[illegible] [illegible]
541.362
W423o

Comb. Theory
541.36
W723c

[illegible] [illegible]

UNIVERSITY
OF FLORIDA
LIBRARIES

1853

ENGINEERING SCIENCES
LIBRARY

Digitized by the Internet Archive
in 2013

http://archive.org/details/physicalmeasurem00unse

PHYSICAL MEASUREMENTS IN GAS DYNAMICS AND COMBUSTION

BOARD OF EDITORS

Theodore von Kármán, *Chairman*
Hugh L. Dryden
Hugh S. Taylor

Joseph V. Charyk, General Editor, 1951–
Associate Editor, 1949–1951
Martin Summerfield, General Editor, 1949–1951

I. Thermodynamics and Physics of Matter. Editor: F. D. Rossini
II. Combustion Processes. Editors: B. Lewis, R. N. Pease, H. S. Taylor
III. Fundamentals of Gas Dynamics. Editor: H. W. Emmons
IV. Laminar Flows and Transition to Turbulence. Editors: L. Lees, C. C. Lin
V. Turbulent Flows and Heat Transfer. Editors: L. Lees, C. C. Lin
VI. General Theory of High Speed Aerodynamics. Editor: W. R. Sears
VII. Aerodynamic Components of Aircraft at High Speeds. Editors: A. F. Donovan, H. R. Lawrence
VIII. High Speed Problems of Aircraft and Experimental Methods. Editors: A. F. Donovan, H. R. Lawrence, F. Goddard, A. E. Puckett, R. R. Gilruth
IX. Physical Measurements in Gas Dynamics and Combustion. Editors: R. W. Ladenburg, B. Lewis, R. N. Pease, H. S. Taylor
X. Aerodynamics of Turbines and Compressors. Editor: W. R. Hawthorne
XI. Design and Performance of Gas Turbine Power Plants. Editor: W. R. Hawthorne
XII. Jet Propulsion Engines. Editor: O. E. Lancaster

VOLUME IX

HIGH SPEED AERODYNAMICS
AND JET PROPULSION

PHYSICAL MEASUREMENTS IN GAS DYNAMICS AND COMBUSTION

EDITORS

PART 1. R. W. LADENBURG
PART 2. B. LEWIS, R. N. PEASE, H. S. TAYLOR

PRINCETON, NEW JERSEY
PRINCETON UNIVERSITY PRESS
1954

Copyright, 1954, by Princeton University Press

London: Geoffrey Cumberlege, Oxford University Press
l. c. card 52-8779

Reproduction, translation, publication, use, and disposal by and for the United States Government and its officers, agents, and employees acting within the scope of their official duties, for Government use only, is permitted. At the expiration of ten years from the date of publication, all rights in material contained herein first produced under contract Nonr-03201 shall be in the public domain.

Printed in the United States of America by
The Maple Press Inc., York, Pennsylvania

FOREWORD

On behalf of the Editorial Board, I would like to make an acknowledgement to those branches of our military establishment whose interest and whose financial support were instrumental in the initiation of this publication program. It is noteworthy that this assistance has included all three branches of our Services. The Department of the Air Force through the Air Research and Development Command, the Department of the Army through the Office of the Chief of Ordnance, and the Department of the Navy through the Bureau of Aeronautics, Bureau of Ships, Bureau of Ordnance, and the Office of Naval Research made significant contributions. In particular, the Power Branch of the Office of Naval Research has carried the burden of responsibilities of the contractual administration and processing of all manuscripts from a security standpoint. The administration, operation, and editorial functions of the program have been centered at Princeton University. In addition, the University has contributed financially to the support of the undertaking. It is appropriate that special appreciation be expressed to Princeton University for its important over-all role in this effort.

The Editorial Board is confident that the present series which this support has made possible will have far-reaching beneficial effects on the further development of the aeronautical sciences.

Theodore von Kármán

PREFACE

Rapid advances made during the past decade on problems associated with high speed flight have brought into ever sharper focus the need for a comprehensive and competent treatment of the fundamental aspects of the aerodynamic and propulsion problems of high speed flight, together with a survey of those aspects of the underlying basic sciences cognate to such problems. The need for a treatment of this type has been long felt in research institutions, universities, and private industry and its potential reflected importance in the advanced training of nascent aeronautical scientists has also been an important motivation in this undertaking.

The entire program is the cumulative work of over one hundred scientists and engineers, representing many different branches of engineering and fields of science both in this country and abroad.

The work consists of twelve volumes treating in sequence elements of the properties of gases, liquids, and solids; combustion processes and chemical kinetics; fundamentals of gas dynamics; viscous phenomena; turbulence; heat transfer; theoretical methods in high speed aerodynamics; applications to wings, bodies and complete aircraft; nonsteady aerodynamics; principles of physical measurements; experimental methods in high speed aerodynamics and combustion; aerodynamic problems of turbo machines; the combination of aerodynamic and combustion principles in combustor design; and finally, problems of complete power plants. The intent has been to emphasize the fundamental aspects of jet propulsion and high speed aerodynamics, to develop the theoretical tools for attack on these problems, and to seek to highlight the directions in which research may be potentially most fruitful.

Preliminary discussions, which ultimately led to the foundation of the present program, were held in 1947 and 1948 and, in large measure, by virtue of the enthusiasm, inspiration, and encouragement of Dr. Theodore von Kármán and later the invaluable assistance of Dr. Hugh L. Dryden and Dean Hugh Taylor as members of the Editorial Board, these discussions ultimately saw their fruition in the formal establishment of the Aeronautics Publication Program at Princeton University in the fall of 1949.

The contributing authors and, in particular, the volume editors, have sacrificed generously of their spare time under present-day emergency conditions where continuing demands on their energies have been great. The program is also indebted to the work of Dr. Martin Summerfield who guided the planning work as General Editor from 1949–1952. The cooperation and assistance of the personnel of Princeton University

Press and of the staff of this office has been noteworthy. In particular, Mr. H. S. Bailey, Jr., the Director of the Press, and Mr. R. S. Snedeker, who has supervised the project at the Press and drawn all the figures, have been of great help. Special mention is also due Mrs. H. E. H. Lewis of this office who has handled the bulk of the detailed editorial work for the program from its inception.

Joseph V. Charyk
General Editor

PREFACE TO VOLUME IX

This volume is concerned with physical measurements in gas dynamics and with the corresponding measurements in combustion processes. It records the varying techniques which can be employed to measure density, pressure, velocity, and temperature in gaseous systems. It deals with the measurements of shock waves, turbulence, condensation studies, and analogue methods. The second half of the volume is concerned with techniques and the measurement of properties in materials undergoing combustion processes.

The first 340 pages of the present volume represent the original proposal for a single volume. To secure a greater uniformity in the size of each volume in the series the second part was added to the first. Professor R. Ladenburg, with a rare editorial initiative and skill, assembled his contributors' material more rapidly than any other editor. Unhappily, he did not live to see the fruits of his effort through the processes of printing and publication. That duty has been most efficiently discharged by his former pupil and colleague Professor Daniel Bershader. Together they have provided an authoritative document in the field of measurement in gas dynamics. The list of their authors and the articles are at once a guarantee of the authority of the work and a tribute of devotion to their late editor. The volume becomes in this way a memorial to Professor Ladenburg's unique abilities in the area in which he so conspicuously excelled.

The second part of the volume will, it is hoped, not be found unworthy to be included with the material assembled by Professor Ladenburg. It has been the writer's responsibility mainly to secure this in respect to Part 2, and to provide a summary of the techniques and measuring tools that can be employed in flames and in combustion processes generally.

The results achieved would not have been possible without the loyal effort and cooperation of some twenty-two authors, the General Editor and his staff, and the Princeton University Press. To them I extend sincere appreciation and thanks.

Hugh Taylor
Volume Editor

CONTENTS

PART 1. PHYSICAL MEASUREMENTS IN GAS DYNAMICS

EDITOR: R. LADENBURG

A. DENSITY MEASUREMENTS

A,1. Analysis of Optical Methods 3

F. Joachim Weyl, Office of Naval Research, Department of the Navy, Washington, D.C.

1.1. Introductory Remarks 3
1.2. The Principal Systems 4
1.3. Quantitative Evaluation 8
1.4. Analysis of Shadowgraphs 20
1.5. Conclusions 23
1.6. Cited References 24

A,2. Shadow and Schlieren Methods 26

J. W. Beams, Department of Physics, University of Virginia, Charlottesville, Virginia

2.1. Introduction 26
2.2. Schlieren Systems 27
2.3. Shadow Methods 38
2.4. Light Sources, Optical Parts, and Photography 40
2.5. Comparison of Schlieren and Shadow Methods 43
2.6. Cited References 44

A,3. Interferometry 47

R. Ladenburg, Department of Physics, Princeton University, Princeton, New Jersey
Daniel Bershader, Department of Aeronautical Engineering, Princeton University, Princeton, New Jersey

3.1. Introduction 47
3.2. Theory of the Mach-Zehnder Interferometer 49
3.3. Construction of the M-Z Interferometer 56
3.4. Evaluation of Interferograms 61
3.5. Applications 69
3.6. Cited References 75

A,4. Electrical Discharge and Afterglow Technique 79

Eva M. Winkler, Aeroballistic Division, Naval Ordnance Laboratory, Silver Spring, Maryland

4.1. Introduction 79
4.2. Nitrogen Afterglow 79
4.3. Air Afterglow 82
4.4. Experimental Aspects of Afterglow Methods 83
4.5. Glow Discharge in Nitrogen and Air 86
4.6. Experimental Aspects of the Discharge Technique 86
4.7. Cited References 87

A,5. Spectral Absorption Method 89

Eva M. Winkler, Aeroballistic Division, Naval Ordnance Laboratory, Silver Spring, Maryland

5.1. Introduction 89
5.2. Oxygen Absorption Method 90
5.3. Ozone Absorption Method 92
5.4. Mercury Vapor Absorption Method 93
5.5. Concluding Remarks 95
5.6. Cited References 96

A,6. X-Ray Technique 97

Eva M. Winkler, Aeroballistic Division, Naval Ordnance Laboratory, Silver Spring, Maryland

6.1. Principle and Accuracy of the Method 97
6.2. Apparatus 100
6.3. Application of the X-Ray Technique 103
6.4. Use of Corpuscular Rays 103
6.5. α Particles and Protons 104
6.6. Electrons 105
6.7. Concluding Remarks 106
6.8. Cited References 107

B. PRESSURE MEASUREMENTS

B,1. The Impact Tube 111

P. L. Chambré, Department of Mathematics, University of California, Berkeley, California
S. A. Schaaf, School of Engineering Science, University of California, Berkeley, California

1.1. Introduction 111
1.2. Viscous Effects 112
1.3. Tolerances in Alignment. Effects of Transverse Velocity Gradient and Free Stream Turbulence 119

1.4. Impact Tube Theory in Free Molecule Flow 120
1.5. Cited References 122

B,2. Pressure Measuring Manometers and Gauges 124
Walker Bleakney, Department of Physics, Princeton University, Princeton, New Jersey
Arnold B. Arons, Department of Physics, Stevens Institute of Technology, Hoboken, New Jersey

2.1. Introduction 124
2.2. Important Characteristics 124
2.3. Low Frequency Gauges 126
2.4. High Frequency Gauges 127
2.5. Mechanical Peak Pressure Gauges 133
2.6. Cited References 134

C. VELOCITY MEASUREMENTS

C,1. Velocity Measurements Using Ions as Tracers 139
Willoughby M. Cady, Physics Division, Naval Ordnance Test Station, Pasadena, California
C,2. Velocity Measurements by Illuminated or Luminous Particles 142
Willoughby M. Cady, Physics Division, Naval Ordnance Test Station, Pasadena, California
C,3. Electric Discharge Anemometry 146
Willoughby M. Cady, Physics Division, Naval Ordnance Test Station, Pasadena, California
C,4. Acoustic Mach Meters 152
Willoughby M. Cady, Physics Division, Naval Ordnance Test Station, Pasadena, California
Cited References and Bibliography (C,1-C,4) 157
C,5. Velocity of Shock Waves by the Light Screen Technique 159
Walker Bleakney, Department of Physics, Princeton University, Princeton, New Jersey
Cited References (C,5) 163

D. TEMPERATURE MEASUREMENTS

D,1. Wall Temperature Determination 167
Gerhard R. Eber, Holloman Air Development Center, Holloman Air Force Base, New Mexico
1.1. Introduction 167
1.2. On the Principle of Wall Temperature Measurements 168
1.3. Thermocouples 169

1.4. Infrared Radiation 170
1.5. Phosphor Luminescence 173
1.6. Applications 176
1.7. Cited References 184

D,2. Shielded Thermocouples 186

Gerhard R. Eber, Holloman Air Development Center, Holloman Air Force Base, New Mexico

2.1. Introduction 186
2.2. Theoretical Considerations 187
2.3. The Influence of Conduction and Radiation 188
2.4. Design of Temperature Probes 189
2.5. Miscellaneous Temperature Measuring Devices 195
2.6. Cited References 196

D,3. Temperature Measurement by Sound Velocity Methods 198

Willoughby M. Cady, Physics Division, Naval Ordnance Test Station, Pasadena, California

Cited References 200

E. SHOCK FRONT MEASUREMENTS BY LIGHT REFLECTIVITY

Donald F. Hornig, Metcalf Research Laboratory, Brown University, Providence, Rhode Island

E,1. Introduction 203
E,2. Theory of the Method 204
E,3. Experimental Technique 205
E,4. Results. The Thickness of Shock Fronts and Rotational Equilibrium 207
E,5. Cited References 210

F. TURBULENCE MEASUREMENTS

Leslie S. G. Kovásznay, Department of Aeronautical Engineering, The Johns Hopkins University, Baltimore, Maryland

F,1. Methods to Distinguish between Laminar and Turbulent Flow 213

1.1. Velocity Profile Measurement 215
1.2. Diffusion Methods 215
1.3. Optical Methods 217
1.4. Glow Discharge Anemometer 218

F,2. Hot Wire Method 219

2.1. Introduction 219

2.2. Hot Wire Probe 223
2.3. Heat Loss in Steady Flow (King's Formula) 228
2.4. Heat Loss of Wire at Supersonic Velocities 233
2.5. Effect of Finite Wire Length on Heat Loss 237
2.6. Angle of Attack 239
2.7. Hot Wire Response to Unsteady Flow 241
2.8. Electronic Equipment (Thermal Lag Compensation, Amplification) 253
2.9. Statistical Processing of the Hot Wire Anemometer Output Signal 263

F,3. Optical Techniques 277

3.1. Introduction 277
3.2. Turbulence Measurements from Shadow Pictures 278
3.3. Interferometer Measurement of Density Fluctuations 282

F,4. Cited References (F,1-F,3) 283

G. CONDENSATION STUDY BY ABSORPTION OR SCATTERING OF LIGHT

Eva M. Winkler, Aeroballistic Division, Naval Ordnance Laboratory, Silver Spring, Maryland

G,1. Introduction 289
G,2. Theoretical Considerations of Light Scattered by Spherical Particles 289
G,3. Measurements 295
G,4. Application to Measurements of Condensation Particles in High Speed Flow 302
G,5. Cited References 304

H. ANALOGUE METHODS

H,1. Free Surface Water Table 309

Ascher H. Shapiro, Department of Mechanical Engineering, Massachusetts Institute of Technology, Cambridge, Massachusetts

1.1. Introduction 309
1.2. The Basis of the Analogy 309
1.3. Experimental Methods 311
1.4. The Validity of the Analogy 314
1.5. Some Typical Results 319
1.6. Appraisal of Water Channel as Experimental Tool 320
1.7. Cited References 321

H,2. Electrolytic Plotting Tank 322

L. Malavard, ONERA, Châtillon-sous-Bagneux (Seine), Paris, France

2.1. General Principles 322
2.2. The Experimental Method 324
2.3. The Experimental Apparatus 325
2.4. Representation of the Circulation around an Obstacle 327
2.5. Study of a Cascade of Profiles 329
2.6. Representation of Axially Symmetric Flows 329
2.7. Fulfillment of Boundary Condition 330
2.8. Lifting Surfaces 332
2.9. Study of Compressible Flows by the Method of G. I. Taylor 333
2.10. The Hodographic Tank 335
2.11. Conical Flows 337
2.12. Conclusions 339
2.13. Cited References 339

PART 2. PHYSICAL MEASUREMENTS IN COMBUSTION

EDITORS: H. S. TAYLOR, B. LEWIS, AND R. N. PEASE

I. MEASUREMENT OF FLAME TEMPERATURE, PRESSURE, AND VELOCITY

F. P. Bundy and H. M. Strong, General Electric Company, Schenectady, New York

I,1. Introduction 343
I,2. Spectral Line Reversal Techniques 346
I,3. Absolute Radiation Methods 359
I,4. Spectral Energy Distribution Methods 361
I,5. Thermocouple and Compensated Hot Wire Methods of Flame Temperature Measurement 364
I,6. Gas Temperature from Pneumatic Apparatus 369
I,7. Temperature from Velocity of Sound 372
I,8. Gas Velocity in Supersonic Flames 376
I,9. Gas Pressure in Supersonic Flames 382
I,10. Cited References and Bibliography 385

J. FLAME PHOTOGRAPHY

William T. Reid, Battelle Memorial Institute, Columbus, Ohio

J,1. Introduction 389
J,2. Direct Photography 389
J,3. Interferometry 396
J,4. Schlieren Photography 398

J,5. Shadow Photography 401
J,6. Solids in Flames 402
J,7. Comparison of Photographic Methods of Locating Flame Front 404
J,8. Cited References 405

K. MEASUREMENT OF BURNING VELOCITY

Ernest F. Fiock, National Bureau of Standards, Washington, D.C.

K,1. Introduction 409
K,2. Effects of the Structure of the Combustion Wave 410
K,3. Burning Velocities from Stationary Flames 412
K,4. Burning Velocities from Moving Flames 422
K,5. Effects of Operating Parameters on Burning Velocity 428
K,6. Summary of Recent Determinations 430
K,7. Cited References 436

L. MASS SPECTROSCOPY

John A. Hipple, Atomic Physics Section, National Bureau of Standards, Washington, D.C.

Chapter 1. Methods of Mass Analysis

L,1. Introduction 441
L,2. Types of Analyzers of Current Interest to Chemists 442
L,3. The Production and Detection of Ions 446

Chapter 2. Application to Chemical Analysis

L,4. Ionization and Dissociation Processes 447
L,5. Special Requirements for Analysis 453
L,6. Recent Developments 453

Chapter 3. Applications to Flames

L,7. Early Studies of Chemical Reactions 456
L,8. Flame Studies with the Mass Spectrometer at Johns Hopkins Applied Physics Laboratory 458
L,9. Cited References 462

M. SPECTROSCOPY OF COMBUSTION

G. H. Dieke, The Johns Hopkins University, Baltimore, Maryland

M,1. Introduction 467
M,2. Instrumentation 468
M,3. Identification of Flame Constituents 482
M,4. Absorption 486
M,5. Data on Equilibrium Conditions 491
M,6. Departure from Equilibrium Conditions 514
M,7. Cited References and Bibliography 522

N. ANALYSIS OF THE COMBUSTION WAVE BY PRESSURE EFFECTS AND SPECTROSCOPY

Nigel Thomas, Princeton University, Princeton, New Jersey

N,1. Introduction 527
N,2. Burner Design and Characteristics 528
N,3. Reaction Zone Structure 531
N,4. Spectroscopic Temperature Measurements 534
N,5. Free Radical Concentration Measurements 544
N,6. Pressure Effects and Burning Velocity 553
N,7. Discussion 561
N,8. Cited References 565

Index 567

SECTION A

DENSITY MEASUREMENTS

F. JOACHIM WEYL
J. W. BEAMS
R. LADENBURG
DANIEL BERSHADER
EVA M. WINKLER

ARTICLE A,1

ANALYSIS OF OPTICAL METHODS

F. JOACHIM WEYL

A,1.1. Introductory Remarks. Many of the optical procedures employed in the examination of compressible gas flows are based on a common fundamental idea: the variations in density across the transluminated medium imply variations in the absolute local index of refraction which in turn affect the traversing light. Appropriate optical apparatus translates the resulting effect into variations in the intensity of illumination on a screen or photographic plate. The possibility of interpreting the record thus obtained is based on the fact that the operation of the system is fully describable by means of idealizations employing for the most part nothing more than the concepts of geometric optics. The individual systems, however, should be and have been investigated from the viewpoint of physical optics [*1*,*2*,*3*,*4*], principally in order to determine under what conditions and in what ranges they will operate, and operate most satisfactorily, according to the laws governing their idealizations.

The subsequent analysis is therefore carried through from the viewpoint that any such optical system is useful only to the extent to which it realizes this ideal. Hence the light transluminating the density inhomogeneity is taken to consist of rays whose course from source to screen is determined by Fermat's law of stationary transit time. According to this law the first variation of the integral along the light path of the local index of refraction $n(x, y, z)$ must vanish:

$$\delta \int n(x, y, z) ds = 0$$

where s denotes the arc length. A path solving this variational problem will therefore satisfy the corresponding Euler equations

$$\frac{d}{ds}\left(n \frac{dx}{ds}\right) = \frac{\partial n}{\partial x}, \qquad \frac{d}{ds}\left(n \frac{dy}{ds}\right) = \frac{\partial n}{\partial y}, \qquad \frac{d}{ds}\left(n \frac{dz}{ds}\right) = \frac{\partial n}{\partial z} \qquad (1.1\text{-}1)$$

and, respectively, the conditions of Snell's law of refraction, which replace them at surfaces of discontinuity of $n(x, y, z)$. It must be remembered, however, that the electromagnetic wave theory of light leads to light paths through nonhomogeneous mediums which differ from those predicted by geometric optics, even if the index of refraction varies continuously and by negligible amounts over distances comparable to the wavelength of light [*5*]; but these deviations do not exceed experimentally detectable limits except in the immediate vicinity of those places where the incidence according to geometric optics is grazing. Refraction phenomena occurring in this region have been exploited by D. F. Hornig in an optical procedure to measure the width of shock waves. This method is discussed in Sec. E.

Fig. A,1.1 illustrates an individual light ray which, in the absence of the disturbance, would have reached the registering screen S at the point Q from the direction θ (characterized, e.g., by three direction cosines) and at time t, but which will actually reach it at the point Q^*, from the direction θ^*, and at time t^*. The insertion of appropriate optical equipment into the light path will furnish on S either a record of the *phase lag* $\tau = t^* - t$, the *deflection* $\epsilon = \theta^* - \theta$, or the *displacement* $Q \rightarrow Q^*$ or, generally, some combination of them. The task of the theory is the twofold one of reconstructing (1) from the record the phase lags, deflections, or displacements responsible for the recorded variations in intensity of illumination, and (2) from the latter in turn the values of the local index of refraction $n(x, y, z)$ encountered by the rays on their way through the disturbance. Once $n(x, y, z)$ has been found, well-known laws allow the computation of the corresponding local densities. This, then, is the most which can be expected of any quantitative evaluation of optical records.

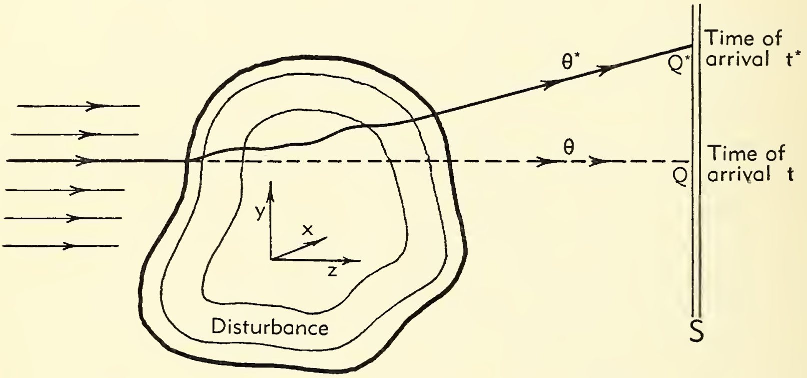

Fig. A,1.1. Comparison of a light path with its unperturbed prolongation through a disturbance.

A,1.2. The Principal Systems. If only the inhomogeneity and no further optical equipment is introduced into a pencil of light, as indicated in Fig. A,1.1, the resulting records are generally called *shadowgraphs*.

They convey information about the mapping $Q \rightarrow Q^*$ but they do this in so implicit a manner that a recovery of the actual displacements from such records, if not impossible, requires complex analysis. The problems arising in this context form the subject of Art. 1.4.

In optical systems where either the deflection $\epsilon = \theta^* - \theta$ or the phase lag $\tau = t^* - t$ is to be recorded, the displacement must be eliminated. For this purpose an objective lens O is inserted into the light path which focuses on the photographic plate S a suitably chosen plane M passing through the disturbance. Under the assumption that *the refractive deviation of the disturbed ray from its undisturbed course inside the inhomogeneity is very small* (infinitesimal), we accept, even after the introduction of the disturbance, the image of the plane M on S as identical to the one projected by the undisturbed light. The validity of this hypothesis of infinitesimal deviation can readily be checked: let a screen carrying a visible coordinate system, e.g. a lattice of mutually perpendicular rulings, be placed in the plane M and photographed through the disturbance; if its image shows no observable distortion, the hypothesis is valid. Proceeding on this basis we shall ascribe the phenomena observed at the point Q^* of Fig. A,1.2a to optical densities supposedly encountered along the straight segment $\overline{A^*B^*}$, while they are actually due to those encountered along the curvilinear passage $\widehat{AB}$. This amounts to replacing the consideration of the actual disturbance with index of refraction $n(x, y, z)$ by that of a fictitious one with refractive index $n^*(x, y, z)$ such that

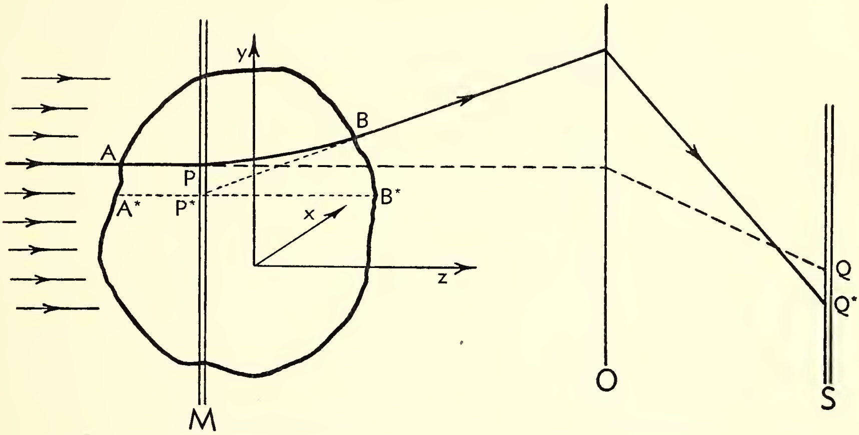

Fig. A,1.2a. Paths of light rays in the presence of a focusing objective lens at O.

$$E_{\widehat{AB}}[n] = E_{\overline{A^*B^*}}[n^*] \qquad (1.2\text{-}1)$$

where $E_C[n]$ stands for the recorded effect if a light ray traverses a disturbance of refractive index n along a path C. The size of the error $n - n^*$ is influenced by the location of the plane M, and in certain analyses, especially in boundary layer investigations, a special effort should be made to position M so as to minimize this error. In general, however, it is negligible for any reasonable location of this plane.

Optical systems producing fluctuations in the intensity of illumination which depend on the phase lag of the disturbed rays must exploit the phenomenon of interference and will therefore have to work with monochromatic light. We refer to them categorically as *interferometric procedures.* The arrangement now generally employed in this connection is that of the four-plate Mach-Zehnder interferometer (see Fig. A,3.2a) whose physical description and optical specifications will be found in Art. 3.2 and 3.3. Suffice it to say here that the effect of the instrument, in proper adjustment, is satisfactorily described as that of producing of the plane M, considered as the locus of several light sources, a (virtual) image M' slightly tilted with respect to the former, as shown in Fig. A,1.2b. Each light source object-image combination on M and M' represents a coherent pair of sources. Interference between the light coming respectively from corresponding points P and P' is therefore possible and their image Q on the photographic plate S will appear to lie on the αth fringe of a pattern of straight equidistant fringes, parallel to the projection on S of the line in which M' intersects M, where $\alpha\lambda_0 = n_0\eta d$. Here λ_0 is the wavelength of the source in the ambient medium and the significance of the geometric quantities η and d is given by Fig. A,1.2b [*4*,*6*,*7*].

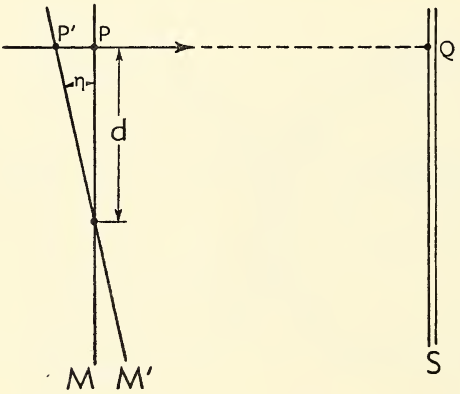

Fig. A,1.2b. The effect of inserting a Mach-Zehnder interferometer into the light path.

The characteristic feature of interferometric arrangements is the possibility of introducing a density inhomogeneity in such a fashion that it is passed only by the light producing the image of M', while the light in which the camera photographs M remains unaffected. The phase lag τ in the ray through P' will therefore retard it further in comparison to its unaffected companion through P, and the image Q will now appear to lie on the βth fringe, where β is determined by $\lambda_0\beta = \lambda_0\alpha + c_0\tau$ with c_0 = velocity of light in the undisturbed ambient medium. Ascribing to every point Q on the photographic plate the coordinates x and y of its original P in the plane M, the so-called fringe shift $\beta - \alpha = S$ becomes a function of x and y.

$$S(x, y) = \frac{c_0}{\lambda_0}\tau = \frac{c}{\lambda}\tau \tag{1.2-2}$$

where λ and c are respectively the wavelength of our source and the velocity of light in vacuo.

Any optical system, which produces records of a density inhomogeneity in which the local brightness of illumination depends on the difference of the individual ray's incident and emergent directions, is generally classified as a *schlieren*[1] *arrangement.* Various experimental arrangements toward this end are described in Art. 2.2, and almost encyclopedic completeness will be found in [*1*]. The operation of such systems is sketched in Fig. A,2.2a. In the absence of the disturbance all points of the photographic plate receive uniform illumination intensity I, proportional to the width a of the light beam allowed to pass over the schlieren edge S_2. Once the disturbance is introduced the refractive deflection, suffered by the rays through any one of its points, will induce a shift in the source image formed by this light in the plane of S_2, and the intensity of illumination at the corresponding point on the photographic plate will now have changed by an amount ΔI proportional to Δa, the component of this shift normal to the knife edge. Primarily concerned with the contrast obtained in the resulting record, we formulate this by writing $\Delta I/I = \Delta a/a$. The schlieren setups now commonly encountered in aerodynamic installations conform to Fig. A,2.2d. Endowing the latter with a coordinate system whose z axis is in the direction of the transluminating light, the y axis normal to and away from the schlieren edge, the x axis, finally, supplementing them to a right orthogonal system, it follows from an elementary optical argument that $\Delta a = f_2 \tan \epsilon_y$ where f_2 is the focal length of mirror E and ϵ_y the angle between the projections into the (y, z) plane of the emergent and incident directions. Carrying again the (x, y) coordinate system from M (the plane on which the camera is focused) into its image on the photographic plate, the local relative brightness becomes a function of x and y:

$$\frac{\Delta I}{I} = C(x, y) = \frac{f_2}{a}\tan \epsilon_y \tag{1.2-3}$$

---

[1] The German word *schliere* designates a local inhomogeneity in a transparent medium.

These arguments readily apply to any arrangement working with parallel straight line edges in the source and schlieren stop, irrespective of whether photogrammetric evaluation or an arrangement of the Ronchi variety [*8*,*9*] is used. In all cases the data ultimately obtained are values of $\Delta a/a$, i.e. the component of the source image shift normal to these edges, measured in terms of the width of the transmitted light band.

A different type of setup is presented by the case of a circular source whose undisturbed image in S_2 is exactly covered by the schlieren stop, which consists of an opaque disk. Thus no light is transmitted to the screen in the undisturbed situation. Any shift of the light source image will produce, however, some illumination whose intensity I is proportional to $\pi a \Delta a$ where, for the present, a is the radius and Δa the total shift of the source image.

$$I \sim af_2 \sqrt{\tan^2 \epsilon_x + \tan^2 \epsilon_y}$$

While occasionally of value for qualitative purposes, this method is not well suited for quantitative analyses on account of the nonlinear dependence of I on the deflection components.

A,1.3. Quantitative Evaluation. The quantitative evaluation of interferometric and schlieren records is based on the dependence of ϵ and τ respectively on the index $n(x, y, z)$ of the transluminated disturbance. In order to derive this dependence, let the positive z axis be chosen, as in Figs. A,1.1 and A,1.2a, in the direction of the incident light, and let $z = B_i(x, y)$, $z = B_e(x, y)$ define, respectively, the surfaces through which the light enters the disturbance and through which it emerges. The system Eq. 1.1-1 can now be recast into the form of a pair of differential equations for x and y as functions of z:

$$\begin{aligned} x'' &= (1 + x'^2 + y'^2)(l_x - x'l_z) \\ y'' &= (1 + x'^2 + y'^2)(l_y - y'l_z) \end{aligned} \tag{1.3-1}$$

where the prime denotes differentiation with respect to z and l_x, l_y, l_z are the components of grad ln $n(x, y, z)$. If now

$$x = \varphi(\xi, \eta; z), \qquad y = \psi(\xi, \eta; z)$$

is the solution of Eq. 1.3-1 with the incident (initial) element $x = \xi$, $y = \eta$, $z = \zeta = B_i(\xi, \eta)$, $x' = y' = 0$, and if $z = \zeta_1$ is determined as the root of the equation

$$0 = z - B_e[\varphi(\xi, \eta; z), \psi(\xi, \eta; z)]$$

the element of the ray at its point of emergence can be written in the form

$$x = \xi_1 = \varphi(\xi, \eta; \zeta_1), \qquad y = \eta_1 = \psi(\xi, \eta; \zeta_1), \qquad z = \zeta_1$$
$$x' = p_1 = \varphi'(\xi, \eta; \zeta_1), \qquad y' = q_1 = \psi'(\xi, \eta; \zeta_1)$$

The point Q^*, where this ray arrives on the photographic plate (see Fig. A,1.2a), carries the coordinates

$$x = \xi_1 - p_1(\zeta_1 - \zeta_M), \qquad y = \eta_1 - q_1(\zeta_1 - \zeta_M)$$

of the point P^* on the plane M: $z = \zeta_M$. The phase lag and deflection, on the other hand, are given by

$$\tau = \frac{1}{c}\int_{\zeta}^{\zeta_1} \{n[\varphi(z), \psi(z), z]\sqrt{1 + [\varphi'(z)]^2 + [\psi'(z)]^2} - n_0\}dz$$

$$\tan \epsilon_x = p_1, \qquad \tan \epsilon_y = q_1$$

These relations define for each pair ξ, η a pair x, y and corresponding values τ, ϵ_x, ϵ_y. In this fashion they determine how the observed values of the latter depend, as functions of the observed coordinates, on the optical density of the disturbance.

Under the assumption of infinitesimal deviation this situation is approximated by

$$\varphi'(z) \equiv \psi'(z) \equiv 0, \qquad \varphi(\xi, \eta; z) \equiv \xi, \qquad \psi(\xi, \eta; z) \equiv \eta$$

hence in particular

$$\xi_1 = x = \xi, \qquad \eta_1 = y = \eta, \quad \text{and} \quad \zeta_1 = B_e(\xi, \eta)$$

This leads to the following estimates of τ, ϵ_x, and ϵ_y as functions of x and y:

$$\tau(x, y) \cong \frac{1}{c}\int_{\zeta}^{\zeta_1} [n(x, y, z) - n_0]dz \tag{1.3-2}$$

$$\tan \epsilon_x = \int_{\zeta}^{\zeta_1} x''(z)dz \cong \int_{\zeta}^{\zeta_1} l_x(x, y, z)dz \tag{1.3-3}$$

$$\tan \epsilon_y = \int_{\zeta}^{\zeta_1} y''(z)dz \cong \int_{\zeta}^{\zeta_1} l_y(x, y, z)dz$$

The Eq. 1.3-1 define any particular ray only along sections where it does not encounter discontinuity surfaces of $n(x, y, z)$. At such a surface both $p = x'(z)$ and $q = y'(z)$ receive finite increments Δp, Δq respectively which are determined by Snell's law of refraction as functions of the finite jump in the index n. This effect is automatically neglected, along with all other deflections, in the estimate (Eq. 1.3-2) of the phase lag; but in the corresponding estimate (Eq. 1.3-3) of the total deflection these finite increments must be added separately to the contribution due to continuous turning of the tangent.

In the evaluations of optical records, which are based on the approximations (1.3-2) and (1.3-3) respectively, the near-equality is replaced by strict equality. Since the left sides represent actually observed values, strict equality can be enforced only at the price of altering $n(x, y, z)$ from its actual value, as symbolically indicated in Eq. 1.2-1. Estimates of the resulting error Δn exist only for two-dimensional flows where n is independent of z [*20,21*] (see also Art. 3.4). Such estimates are required in order to interpret observations made of boundary layers along surfaces which are parallel to the transluminating light.

The evaluation problem thus presents itself as that of determining the function $n(x, y, z)$ from either one of the following relations which are obtained by combining Eq. 1.2-2 with Eq. 1.3-2 and Eq. 1.2-3 with Eq. 1.3-3 respectively:

$$S(x, y) = \frac{1}{\lambda} \int_{\zeta}^{\zeta_1} [n(x, y, z) - n_0] dz \tag{1.3-4}$$

$$C(x, y) = \frac{f_2}{a} \int_{\zeta}^{\zeta_1} \frac{\partial \ln n(x, y, z)}{\partial y} dz \tag{1.3-5}$$

In general this problem has, of course, no unique solution; such will be the case only if the inhomogeneity satisfies certain geometric symmetry conditions which allow an a priori reduction of the number of independent variables in the function $n(x, y, z)$ from three to two.

TWO-DIMENSIONAL CASES. The simplest of all symmetry requirements, insuring that Eq. 1.3-5 and 1.3-6 can be solved for n, is the condition that $n(x, y, z)$ be independent of z. It is evident, however, that such two-dimensional flows can be realized only between a pair of bounding surfaces, generally plane parallel glass plates normal to the direction of translumination, which clearly form part of the inhomogeneity.

Procedures. In the case of the interferometry the effect of the glass plates is eliminated by inserting into the undisturbed companion beam a pair of compensating plates or a compensating chamber whose dimensions match those of the container in which the flow takes place and in which a uniform standard condition of optical density n_0 prevails. Hence Eq. 1.3-4 furnishes

$$n(x, y) = n_0 + \frac{\lambda}{D} S(x, y) \tag{1.3-6}$$

where D is the width of the flow in the z direction.

In the case of a schlieren arrangement the light will receive an additional deflection Δq on emergence into the undisturbed medium, given to within linear terms in the deflection numbers $p = x'(z)$, $q = y'(z)$, with which the ray arrives at this boundary, by

$$\Delta q = \frac{1}{n_0} [n(x, y) - n_0] q$$

Hence

$$C(x, y) = \frac{f_2}{a} \left(1 + \frac{n - n_0}{n_0}\right) \frac{D}{n} \frac{\partial n}{\partial y} = \frac{f_2 D}{a} \frac{1}{n_0} \frac{\partial n}{\partial y}$$

The index of refraction itself can now be computed by integration, starting from some point where n is known

$$n(x, y) - n(x, y_0) = \frac{a}{f_2}\frac{n_0}{D}\int_{y_0}^{y} C(x, \eta)d\eta \qquad (1.3\text{-}7)$$

Error sources. Computations based on formulas (1.3-6) and (1.3-7) are subject to errors of two types:

1. Deviations of the actual physical situation from the idealizations of our theory.
2. Inaccuracy of the observed data.

Errors Δn of the latter type are determined by the amounts ΔS and ΔC to within which on interferometric records the fringe shift and on schlieren records the value of C can be reliably measured. At the same time the ratios

$$\frac{\Delta S}{\Delta n} = \frac{D}{\lambda}, \text{ respectively } \frac{\Delta C}{\Delta n} = \frac{a}{f_2}$$

characterize the "amplification factor" with which changes in density are translated into the optically recorded phenomena, thus setting the characteristic sensitivity levels for these two methods. For more detailed discussions we refer to Art. 2.2 and 3.4.

Errors of type 1 are due to the deviations from two-dimensionality especially in the boundary layers along the confining glass panels, and to the linearization implied by the infinitesimal deviation hypothesis. These have been studied in detail only in the interferometric case [*20*,*21*]. By applying appropriate corrections to the observed fringe shifts the former can be significantly reduced, and it has been shown that the latter are very nearly eliminated if the camera is focused on a plane dividing the distance D between the flow boundaries $z = B_i$ and $z = B_e$ in the ratio 2:1, provided the boundary layer is not too thin (see Art. 3.4). For schlieren records an evaluation based on Eq. 1.3-7 fails to account for shock waves. Any ray grazing such a density discontinuity on the low density side must be credited with an additional finite increment Δq in tan ϵ_y,

$$\Delta q = \cos\theta \frac{\sqrt{n_+^2 - n_-^2}}{n_-} \cong \cos\theta \sqrt{\frac{2\Delta n}{n}}$$

where $\Delta n = n_+ - n_-$ is the jump of the refractive index through the shock and θ the angle included between its downstream normal and the positive y axis. Any such discontinuity appears therefore on the record either as a light or as a dark streak, depending on whether the density increases or decreases in the positive y direction. The amount Δn must be determined from the illumination intensity in the shock streak, using the value of n on that side of the shock which is accessible to formula (1.3-7). (See also Art. 2.2.)

Axially Symmetric Cases. Next in simplicity after the two-dimensional flows are those exhibiting cylindrical symmetry. They can be realized with a satisfactory degree of approximation in the laboratory since they do not require bounding surfaces along which their rotational symmetry would necessarily be destroyed; their theoretical treatment under the classical assumptions of continuum mechanics, although generally not as accessible as that of two-dimensional flows, is still manageable; and finally they have a large number of important technological applications. Their analysis by optical methods has therefore been the subject of careful investigations [*1,9,10,11,12,13,22,26*].

Procedures. With the x axis of our coordinate system chosen as the axis of cylindrical symmetry, the local value of n in the disturbance becomes a function of x and $r = \sqrt{y^2 + z^2}$. For the line element dz along a line parallel to the z axis we have

$$dz = \frac{r dr}{\sqrt{r^2 - y^2}}$$

and the resulting form of relations (1.3-4) and (1.3-5) shows that the determination of $n(r, x)$ is a problem which has to be solved separately for each cross section $x = \text{const}$. The dependence of S, C, and n on x will therefore not be indicated in the sequel. Thus Eq. 1.3-4 and 1.3-5 appear as

$$S(y) = \frac{1}{\lambda} \int_y^R [n(r) - n_0] \frac{d(r^2)}{\sqrt{r^2 - y^2}} \tag{1.3-8}$$

$$\frac{1}{y} C(y) = \frac{2f_2}{a} \int_y^R \frac{d \ln n(r)}{d(r^2)} \frac{d(r^2)}{\sqrt{r^2 - y^2}} \tag{1.3-9}$$

which show them to be integral equations of the classical Abel type. Analytically their solutions can be obtained by applying to both sides once more the operator

$$\int_u^R [\cdot \ \cdot \ \cdot] d(y^2)/\sqrt{y^2 - u^2}$$

and interchanging the order of integrations in the double integral thus produced on the right (see e.g. [*27*]). In the interferometric case, Eq. 1.3-8, a final differentiation followed by an additional small calculation then furnishes

$$n(r) - n_0 = -\frac{\lambda}{\pi} \int_r^R \frac{dS(y)}{\sqrt{y^2 - r^2}} \tag{1.3-10}$$

while in the case of Eq. 1.3-9 we obtain directly

$$n(r) - n_0 = -\frac{n_0 a}{\pi f_2} \int_r^R C(y) \frac{dy}{\sqrt{y^2 - r^2}} \tag{1.3-11}$$

where on the left we have used the approximation

$$\ln \frac{n(r)}{n_0} = \ln \left[1 + \frac{n(r) - n_0}{n_0} \right] \cong \frac{n(r) - n_0}{n_0}$$

A numerical determination of $n(r)$ at specified radii r_i from any of these equations involves a sizeable computing job. It was therefore considered worthwhile in Germany, during the latter part of World War II when interferometry was first coming into extensive use, to construct a special planimetric device which allows the determination of the Stieltjes integral, occurring on the right side of Eq. 1.3-10, from the plotted fringe shift $S(y)$ [*24*]. Independent developments in the United States favored numerical procedures, with an eye toward the use of automatic computing facilities which began to be available at that time.

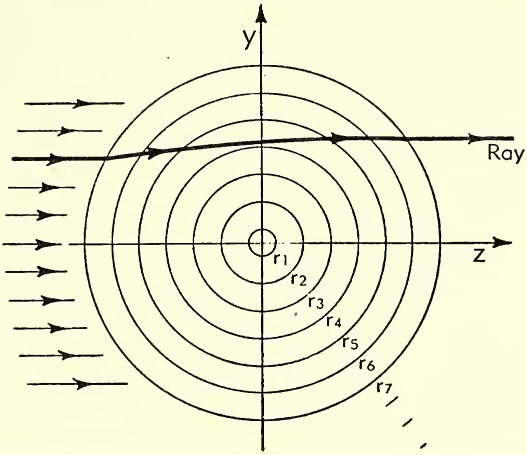

Fig. A,1.3. Zone decomposition of an axially symmetric inhomogeneity.

For this purpose the cross section of radius R is subdivided into zones as in Fig. A,1.3:

$$0 = r_0 < r_1 < \cdots < r_{N-1} < r_N = R$$

The linearity of the operators converting the function

$$\nu(r) = n(r) - n_0$$

into $S(y)$ and $C(y)$, respectively, is exploited by substituting for the latter linear combinations of suitably chosen functions which match the values of the originals at the zone boundaries. Let this be illustrated in the interferometric case: As fringe shift of a disturbance, cylindrically symmetric about the x axis, $S(y)$ is an even function of y, and its value at $y = r_i$ depends only on the density for values $r \geqq r_i$. Hence we select for each index i an even function $F_i(y)$, vanishing identically for $|y| \geqq r_{i+1}$, and approximate $S(y)$ by a linear combination

$$\tilde{S}(y) = \sum_{\mu=i}^{N-1} c_\mu F_\mu(y) \quad \text{for} \quad r_i \leqq y < r_{i+1}$$

From Eq. 1.3-10 it follows that the corresponding approximation for $\nu(r)$ is

$$\tilde{\nu}(r) = \frac{\lambda}{\pi} \sum_{\mu=i}^{N-1} c_\mu f_\mu(r) \quad \text{for} \quad r_i \leqq r < r_{i+1}$$

with

$$f_i(r) = -\int_r^R \frac{dF_i(y)}{\sqrt{y^2 - r^2}}, \qquad F_i(y) = \frac{1}{\pi}\int_y^R \frac{f_i(r)d(r^2)}{\sqrt{r^2 - y^2}}$$

The coefficients c_μ are determined so as to satisfy the triangular system of linear equations

$$S(r_i) = \sum_{\mu=i}^{N-1} c_\mu F_\mu(r_i) \qquad (i = 0, 1, \ldots, N-1) \qquad (1.3\text{-}12)$$

and the values ν_i of $\tilde{\nu}$ at $r = r_i$ are accepted as the desired $\nu(r_i)$:

$$\nu_i = \frac{\lambda}{\pi} \sum_{\mu=i}^{N-1} c_\mu f_\mu(r_i) \qquad (1.3\text{-}13)$$

In selecting the functions F_i a compromise must be made between the quality of the approximation and the simplicity of the resulting reduction procedure. To date only two such selections have been given extensive use.

The first one, due to C. C. Van Voorhis and a refinement of an earlier suggestion by H. Schardin [*22*] who let $\tilde{\nu}$ be a step function, replaces $\nu(r)$ by a piecewise linear approximation $\tilde{\nu}$ [*10*]. It amounts to choosing for $f_\mu(r)$ the function which is zero for $r \leqq r_{\mu-1}$, rises linearly to one at $r = r_\mu$, and falls once more linearly to zero on the next zone, remaining zero for all $r > r_{\mu+1}$. Then Eq. 1.3-13 is satisfied with $c_\mu = \pi\nu_\mu/\lambda$ and Eq. 1.3-12 becomes

$$\lambda S(r_i) = \nu_i a_{ii} + \sum_{\mu=i+1}^{N-1} \nu_\mu (a_{i\mu} - a_{i\mu_{-1}}) \qquad (1.3\text{-}14)$$

where, after an integration by parts,

$$a_{i\mu} = \frac{2}{r_{\mu+1} - r_\mu} \int_{r_\mu}^{r_{\mu+1}} \sqrt{r^2 - r_i^2}\, dr$$

If in particular all zones are of equal width w, then

$$a_{i\mu} = 2w \int_{\mu}^{\mu+1} \sqrt{\omega^2 - i^2}\, d\omega = wA(i, \mu)$$

$$A(i, \mu) = (\mu + 1)\sqrt{(\mu + 1)^2 - i^2} - \mu\sqrt{\mu^2 - i^2} - i^2 \ln \frac{\mu + 1 + \sqrt{(\mu + 1)^2 - i^2}}{\mu + \sqrt{\mu^2 - i^2}}$$

A table of these coefficients for $0 \leqq i \leqq \mu \leqq N - 1$, as well as their first differences

$$A^*(i, \mu) = A(i, \mu) - A(i, \mu - 1)$$

on the index μ, can be computed once and for all,[2] so that the solution of the resulting system of equations

$$\frac{\lambda S(r_i)}{w} = \nu_i A(i, i) + \sum_{\mu=i+1}^{N-1} \nu_\mu A^*(i, \mu), \qquad (i = 0, 1, \ldots, N - 1)$$

can be mechanized along the lines illustrated in Table A,1.3 for the case $N = 6$.

Once a sufficiently extensive table of coefficients A is available, it is possible to reduce with little further difficulty cross sections where one or several zones have been subdivided into a number of smaller equal parts [*11,12,13*]. As an illustration, let the zone boundaries be defined by $r_\mu = \mu w$ where now μ, and hence i, run through the values

$$0, 1, \ldots, j, j + \frac{1}{p}, \ldots, j + \frac{p-1}{p}, j + 1, \ldots, N - 1$$

Then the coefficients $a_{i\mu}$ in Eq. 1.3-14 can be computed as follows:

$$a_{i\mu} = \begin{cases} wA(i, \mu) & \text{for} \begin{cases} \text{all integer values of } i \\ \mu = 0, 1, \ldots, j - 1, j + 1, \ldots, N - 1 \end{cases} \\ \dfrac{w}{p^2} \displaystyle\sum_{\kappa=0}^{p-1} A\,(ip, \mu p + \kappa) & \text{for} \begin{cases} i = j + \dfrac{1}{p}, \ldots, j + \dfrac{p-1}{p} \\ \mu = 0, 1, \ldots, j - 1, j + 1, \ldots, N - 1 \end{cases} \\ \dfrac{w}{p} A\,(ip, \mu p) & \text{for} \begin{cases} \text{all admitted values of } i \\ \mu = j, j + \dfrac{1}{p}, \ldots, j + \dfrac{p-1}{p} \end{cases} \end{cases}$$

A coefficient table of the $a_{i\mu}/w$ and their first differences on μ can thus be constructed and used in the subsequent reduction exactly as the table of the A and A^* values was used in Table A,1.3. Such a procedure serves to furnish more concise information in zones of rapidly varying density

---

[2] Such a table for integer $0 \leqq i \leqq \mu \leqq 49$ has been prepared by R. Ladenburg's group at Princeton University.

Table A,1.3. Calculation of refractive indices from fringe shifts. The columns are filled in proceeding from left to right.

μ \ i	5	4	3	2	1	0
5		$\nu_5 A^*(4, 5)$	$\nu_5 A^*(3, 5)$	$\nu_5 A^*(2, 5)$	$\nu_5 A^*(1, 5)$	$\nu_5 A^*(0, 5)$
4			$\nu_4 A^*(3, 4)$	$\nu_4 A^*(2, 4)$	$\nu_4 A^*(1, 4)$	$\nu_4 A^*(0, 4)$
3				$\nu_3 A^*(2, 3)$	$\nu_3 A^*(1, 3)$	$\nu_3 A^*(0, 3)$
2					$\nu_2 A^*(1, 2)$	$\nu_2 A^*(0, 2)$
1						$\nu_1 A^*(0, 1)$
Column sum	Σ_5	Σ_4	Σ_3	Σ_2	Σ_1	Σ_0
Numerator	$\frac{\lambda}{w} S(r_5) - \Sigma_5$	$\frac{\lambda}{w} S(r_4) - \Sigma_4$	$\frac{\lambda}{w} S(r_3) - \Sigma_3$	$\frac{\lambda}{w} S(r_2) - \Sigma_2$	$\frac{\lambda}{w} S(r_1) - \Sigma_1$	$\frac{\lambda}{w} S(r_0) - \Sigma_0$
Denominator	$A(5, 5)$	$A(4, 4)$	$A(3, 3)$	$A(2, 2)$	$A(1, 1)$	$A(0, 0)$
Result	ν_5	ν_4	ν_3	ν_2	ν_1	ν_0

and may be preferable to the use of the narrower zone width throughout. By keeping down the total number of zones it not only saves labor in hand computations but may actually imply greater accuracy by reducing the accumulation of errors. (If the available table of $A(i, \mu)$ does not go up to indices $Np - 1$, interpolation may be used to determine the values of $a_{i\mu}/w$ for fractional i and $\mu > j$ from neighboring integer entries; an A table up to indices $(j + 1)p - 1$ will then suffice.)

The second method, originating in the Bureau of Ordnance (United States Department of the Navy) [*13*], replaces $S(y)$ by an approximation piecewise linear in y^2. The corresponding function $F_\mu(y)$ vanishes for $y \leqq r_{\mu-1}$, rises linearly in y^2 (i.e. parabolically in y itself) to unity at $y = r_\mu$, and falls once more in the same fashion to zero on the next zone, vanishing for all $y \geqq r_{\mu+1}$. The system (1.3-12) is then solved by $c_\mu = S(r_\mu)$, Eq. 1.3-13 become

$$\nu_i = \frac{\lambda}{\pi} \sum_{\mu=i}^{N-1} [S(r_\mu) - S(r_{\mu-1})] \frac{\sqrt{r_{\mu+1}^2 - r_i^2} - \sqrt{r_\mu^2 - r_i^2}}{r_{\mu+1}^2 - r_\mu^2}$$

and reduce for zones of equal width to

$$\nu_i = \frac{\lambda}{\pi w} \left[S(r_i)B(i, i) + \sum_{\mu=i+1}^{N-1} S(r_\mu)B^*(i, \mu) \right] \qquad (1.3\text{-}15)$$

where

$$B(i, \mu) = \frac{1}{2\mu + 1} [\sqrt{(\mu + 1)^2 - i^2} - \sqrt{\mu^2 - i^2}\,]$$

$$B^*(i, \mu) = B(i, \mu) - B(i, \mu - 1)$$

Evaluations on the basis of Eq. 1.3-15 have been mechanized for execution on IBM equipment[3] as well as the ENIAC [*26*].

The reduction of schlieren records is readily achieved by similar methods: Substituting for $C(y)$ a piecewise linear approximation in y^2 which matches the values of $C(y)$ at the zone boundaries, we shall obtain, for equal zone widths,

$$\nu_i = -\frac{n_0 a}{\pi f_2} \left[C(r_i)A(i, i) + \sum_{\mu=i+1}^{N-1} C(r_\mu)A^*(i, \mu) \right]$$

with the same coefficients A and A^* which have been tabulated for the evaluation of interferograms.

Error sources. In addition to the errors affecting the reduction of optical records from two-dimensional flows, namely, (1) deviations from the idealizations of the theory, and (2) inaccuracies in the observed data, there must now be added a third type:

---

[3] Tables of B^* values on punched cards are available at the Naval Ordnance Laboratory and a Table of B values can be found in [*25*].

3. The replacement of mathematical limit processes by finite arithmetical approximations.

These are the errors in the ν_i, resulting from the replacement of $S(y)$ and $C(y)$ by the approximations $\tilde{S}(y)$ and $\tilde{C}(y)$ respectively, even if the latter assume the true values of S and C at the zone boundaries. In size these errors decrease with increasing zone number N like $N^{-\frac{1}{2}}$ in the interferometric case and like N^{-1} for schlieren records.

Errors of type 2 vary, evidently, as the observational errors ΔS and ΔC. In the schlieren case their size is practically independent of the number of zones employed, but in the case of interferograms their size increases with $N^{\frac{1}{2}}$. It follows that it is unprofitable in the reduction of axially symmetric schlieren records to choose a finer subdivision than one for which the difference $C - \tilde{C}$ is of about the same magnitude as the error ΔC to within which C can be reliably determined. For interferograms, on the other hand, there exists an optimum number of zones such that a deviation either way will increase the total error in the computed values ν_i. Sound estimates for the practical determination of this optimum zone number are not yet available, the estimates in [*13*] and [*26*] erring apparently in opposite directions.

The reason for this difference in the reduction of interferograms and schlieren records lies in the fact that in the former case the index of refraction is obtained from the fringe shift by an operation in the nature of a derivative, while in the latter the relation of relative illumination intensity to $n(r) - n_0$ resembles an integration. Considering that observations $S(r_i)$ are readily obtained, this fact suggests that the strict equalities of Eq. 1.3-12 might be replaced by a least-square procedure of fitting a large number of observations with linear combinations containing comparatively few coefficients c_i. Such a procedure appears particularly attractive if high speed computing equipment is available to execute the necessary calculations.

Errors of type 1, finally, are due to the occurrence of shock waves, to deviations of the flow from axial symmetry, and to the inaccuracies introduced by proceeding on the basis of the hypothesis of infinitesimal deviations. The attitude regarding these errors has on the whole been that of reducing rather than of estimating them. As to refractive deviations, no optical examinations appear to have been made of cylindrically symmetric flow with long enough light paths in fields of high density gradients to warrant their investigation.

The problem of perturbations in rotational symmetry is of importance on account of the singular behavior of Abel's integral equation at the origin. It includes that of locating the axis in a given interferogram. Since any such record generally contains characteristic landmarks, like shocks or model profiles, whose symmetric positioning is of overriding importance, their geometry is used to determine the best location for the axis. Observations are now taken on either side of the axis and the reduction is carried through with the averaged quantities,

$$\bar{S}(y) = \tfrac{1}{2}[S(y) + S(-y)], \qquad \bar{C}(y) = \tfrac{1}{2}[C(y) + C(-y)]$$

In this fashion the functions S and C used in the reduction become even and the errors due to deviations from cylindrical symmetry can be considered as forming part of the observational errors $\Delta S(y)$ and $\Delta C(y)$ respectively.

The presence of shocks in the flow field induces singularities in the functions $S(y)$ and $C(y)$ whose mollification by continuous approximating functions produces sizeable errors. This was spectacularly borne out by a mathematical experiment in which fringe shift values were used to recover, by numerical procedures, a density profile from which they had originally been derived analytically. The characteristic phenomenon is an "overshooting" error on the axisward side of the shock, exceeding by an order of magnitude the errors found elsewhere and subsiding over the next few zones either monotonically or in an oscillating fashion, depending on the method used in the reduction [*10*]. It is possible to eliminate errors of this type almost entirely by splitting $\nu(r)$ into a singular and a reduced portion, determining the former so as to make the remainder sufficiently smooth. If the singularity occurs at $r = r_s$, then

$$\nu(r) = \nu_{\text{sing}}(r) + \nu_{\text{red}}(r), \qquad \nu_{\text{sing}}(r) = 0 \quad \text{for } r \geqq r_s$$

and correspondingly

$$S(y) = S_{\text{sing}}(y) + S_{\text{red}}(y), \qquad S_{\text{sing}}(y) = 0 \quad \text{for } y \geqq r_s$$

Since ν_{red} is supposed to be smooth, it follows that S_{red} varies but slowly in the neighborhood of $y = r_s$. Loosely speaking, therefore, $S_{\text{sing}}(y)$ can be identified as the rapidly varying part of $S(y)$ for values of y near to and less than r_s. Thus, if we are satisfied with a continuous ν_{red}, the singular portion may be chosen as a step function

$$\nu_{\text{sing}}(r) = 0 \quad \text{for } r \geqq r_s, \qquad \nu_{\text{sing}}(r) = n_s \quad \text{for } r < r_s$$

and therefore $S_{\text{sing}}(y)$ of the form

$$S_{\text{sing}}(y) = 0 \quad \text{for } y \geqq r_s, \qquad S_{\text{sing}}(y) = \frac{2n_s}{\lambda}\sqrt{y_s^2 - y^2} \quad \text{for } y < r_s$$

where n_s, the jump in index of refraction across the shock, will have to be estimated from the slope near the origin of a plot of $Y = S(y) - S(r_s)$ against $X = \sqrt{r_s^2 - y^2}$. $S_{\text{red}}(y)$ is now determined by subtracting $S_{\text{sing}}(y)$ from $S(y)$ and used to compute $\nu_{\text{red}}(y)$. Addition of $\nu_{\text{sing}}(r)$ to the latter finally produces $\nu(r)$. If the smoothness in ν_{red} is to extend to derivatives, correspondingly more parameters will have to be estimated by matching the empirical plot of Y versus X with a curve of appropriate type near the origin.

Similar procedures can evidently be applied to the singularities induced by a shock in $C(y)$. While such methods of "deshocking" have been successfully employed in the reduction of interferograms, their use in the evaluation of schlieren records is still to be tried.

A,1.4. Analysis of Shadowgraphs. We return now to Fig. A,1.1 and the shadowgraph records which are obtained if no further optical equipment is introduced into the light path. Let us consider first the mapping $Q \rightarrow Q^* = f(Q)$. On introducing a rectangular coordinate system (x, y) into the plane of the screen, the undisturbed state of illumination can be described by a function $I(x, y)$; and, if the image Q^* of $Q(x, y)$ has the coordinates

$$x^* = \phi_1(x, y), \qquad y^* = \phi_2(x, y)$$

we have for the disturbed state of illumination

$$I^*(x^*, y^*) = \sum_{\text{all } Q \rightarrow Q^*} \frac{I(x, y)}{\left|\dfrac{\partial(\phi_1, \phi_2)}{\partial(x, y)}\right|} \tag{1.4-1}$$

where the sum on the right is to be extended over all points $Q(x, y)$ which are mapped into the point $Q^*(x^*, y^*)$. The denominator is the absolute value of the Jacobian of the mapping. If I and I^* are considered known as functions of their arguments, Eq. 1.4-1 constitutes a relation satisfied by the mapping functions but fails to determine them uniquely. Assuming the validity of the infinitesimal deviation hypothesis not only inside the disturbance but for the entire light path from source to screen leads us beyond this point with the radical linearization

$$x^* = x + \Delta_x(x, y), \qquad y^* = y + \Delta_y(x, y)$$

where Δ_x and Δ_y are functions of x and y which together with their derivatives are small, so that their products and powers can be neglected. Hence

$$\frac{\partial(x^*, y^*)}{\partial(x, y)} = 1 + \frac{\partial \Delta_x}{\partial x} + \frac{\partial \Delta_y}{\partial y} \tag{1.4-2}$$

With the mapping characterized by the functions Δ_x and Δ_y, we turn to the question of their dependence on the values of the refractive index $n(x, y, z)$ encountered by the traversing rays. If L is the distance of the screen from the disturbance, then Eq. 1.3-3 furnishes immediately

$$\Delta_x = L \tan \epsilon_x \cong L \int_{\zeta}^{\zeta_1} l_x(x, y, z) dz, \quad \Delta_y = L \tan \epsilon_y \cong L \int_{\zeta}^{\zeta_1} l_y(x, y, z) dz$$

Substitution in Eq. 1.4-2 shows that under these conditions Eq. 1.4-1 reduces to

$$\frac{I(x, y) - I^*(x, y)}{I^*(x, y)} \cong L \int_{\zeta}^{\zeta_1} \left(\frac{\partial^2}{\partial x^2} + \frac{\partial^2}{\partial y^2}\right) \ln n(x, y, z) dz \quad (1.4\text{-}3)$$

This relation is of the same nature as Eq. 1.3-4 and 1.3-5. In the same sense in which the ratios D/λ and f_2/a are characteristic for the sensitivity of interferometric and schlieren optics respectively, the amplification factor L/D characterizes the sensitivity of a shadowgraph experiment. The effect observed with this sensitivity is, in linear approximation, an averaged second derivative of the index n. Hence quantitative density determinations on the basis of Eq. 1.4-3 require a double integration with attendant computational effort. In addition Eq. 1.4-3 will tend to be least reliable in the description of phenomena most clearly recorded by the shadowgraph technique. Rapid variations in the density gradient imply optical focusing properties of the corresponding flow regions which destroy the one-to-oneness of the mapping $Q \rightarrow Q^*$ and therewith its local linearity on which Eq. 1.4-3 is based. It is therefore not believed that the development of systematic density evaluations on the basis of Eq. 1.4-3 will be profitable.

Nonetheless shadow photography has distinct advantages which, in view of its simplicity, give it a place beside the more sophisticated schlieren and interferometric procedures. Thus turbulent regions show up clearly on shadowgraphs and certain statistical aspects of turbulence in high speed gas flows can be analyzed on the basis of Eq. 1.4-3 which are not accessible to any other method (see F,2). By far the most extensive use of shadowgraph techniques, however, concerns the recording of shock waves and slip discontinuities. Their presence in a flow field produces characteristic optical effects making possible their geometric location with great precision. Methods have been developed, moreover, for using these effects to determine the change in density through discontinuities of this type.

Particular attention in this connection has been given to rotationally symmetric phenomena, such as conical bow waves on projectiles in flight and spherical explosion waves [*14,15,16*]. The characteristic picture on the screen is a band of absolute darkness bounded on one side by an edge of intense brightness subsequently shading off into normal illumination. The outer boundary is the geometric projection of the shock front. This effect is produced by the rays traversing the disturbance in a narrow zone adjacent to the shock surface. The disturbance may therefore be approximated locally by a cylindrical shock wave on whose normal cross section we find the same density distribution as in the plane defined by a light ray grazing the shock surface and by the normal to the latter at the point of tangency; the shock trace in this plane, moreover, can be replaced in the analysis by its osculating circle. The resulting situation is sketched in Fig. A,1.4.

It is now possible to compute the brightness distribution on the screen, and in particular the width of the dark band, for any assumed density profile behind the shock. Thus [14] and [15] obtain in the case of a simple step shock, where the index of refraction jumps from n_0 to n_1, for the width d of the dark band the estimate

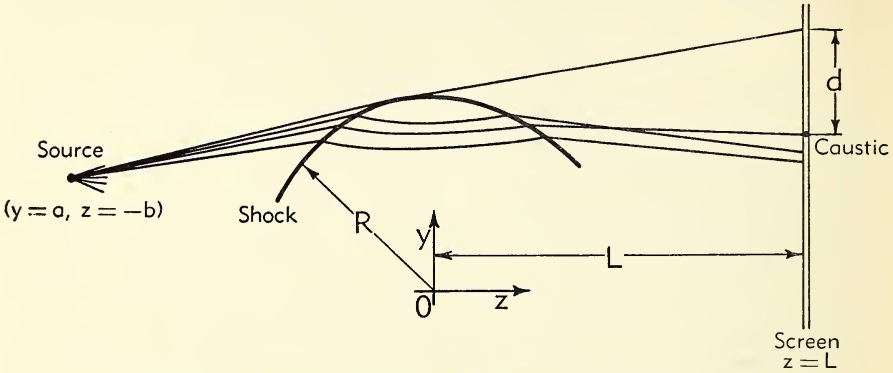

Fig. A,1.4. The shadowgraphic recording of a shock wave.

$$d = \frac{3}{\sqrt[3]{2}}\left(1 - \frac{n_0}{n_1}\right)^{\frac{2}{3}} L^{\frac{2}{3}} R^{\frac{1}{3}}$$

provided the grazing ray is nearly perpendicular to the screen. The validity of this estimate requires also [13] that

$$1 - \frac{n_0}{n_1} \ll \frac{R}{\sqrt{a^2 + b^2}} \frac{b + L}{2L}$$

For the sake of a more refined analysis, P. C. Keenan and H. Polachek [16] have compiled a table giving dark band widths resulting at various screen distances from shocks with linear density decay behind the front. Screen distances vary from three to fifty times the radius of the disturbance, $(n_1/n_0) - 1$ from 10^{-4} to 10^{-3}, and the density gradients from 0 to 5×10^{-3} per disturbance radius. If the same shock wave has been shadowgraphed at two different screen distances this table allows the determination of both the density jump through the shock and the density gradient immediately behind the shock. This table has been used to determine the strength of and density gradient behind the bow shock of a sphere at $M = 1.7$, leading to values in satisfactory agreement with determinations from an interferogram [9].

A variant of the shadowgraph technique, proposed by H. Schardin [*1*] and, independently, by R. R. Halverson [*17*] who has actually used it in the analysis of underwater explosion shocks, consists in photographing a coordinate grid through the disturbance. The distortion of the grid will depend on the density profile behind the shock. By assuming the latter to belong to a two-parameter family, each member of which is characterized by its peak value and a decay constant, Halverson was able to compute a corresponding family of distortions as function of radius and to estimate the parameter values in a given instance by finding among the computed distortion functions the one giving the best fit with the observed one.

A,1.5. Conclusions. The use of optical methods in the analysis of compressible flows is by now a well-established procedure which has attained a considerable degree of engineering sophistication. Wind tunnels, free flight ranges, and especially shock tubes (see Art. 3.5 and VIII,E,6) where the conditions are particularly favorable, have been provided with optical instrumentation, exploiting techniques of measurement which cover effectively the entire range of flows beginning with the onset of compressibility effects at low subsonic speeds and ending with the very high Mach number flows where extreme attenuation renders the detection of density variations by such means impossible. This range includes most of the gas dynamical effects of current interest. The distinctive advantage of all optical methods is that they furnish information about the flow without disturbing it. Moreover their characteristically high qualitative sensitivity makes it possible to obtain quantitative experimental results in the study of gas dynamical effects which allow a direct check on the current theories and some of their underlying assumptions. This is especially true of the modern high precision version of the four-plate Mach-Zehnder interferometer whose records represent a magnification of absolute differences in the index of refraction by a factor equal to the ratio of the diameter of the disturbance to the wavelength of light.

Schlieren systems are at least an order of magnitude more sensitive, but they record density gradients rather than absolute differences. Hence rapid changes by small amounts, such as are encountered in nearly sonic shocks and weak rarefaction fans, may be readily detected on a schlieren record while their location on an interferogram causes difficulty. Interferometers are therefore generally backed up by a schlieren system. Additional advantages of the latter are the significantly greater simplicity of its apparatus and the comparative ease with which axially symmetric flows can be evaluated. Its principal disadvantages stem from the difficulties encountered in obtaining accurate quantitative measurements of the recorded quantity, i.e. the shift of a light source image, and in evaluating the record of a flow with shock waves. Useful quantitative information can be obtained, however, from schlieren records often with little additional effort. The evidently greater potentialities of interferometric procedures have undeservedly stunted the exploitation of these possibilities.

The sensitivity of optical apparatus is compromised in all cases by the fact that an effective evaluation of the records must neglect the deviation of the disturbed light path from its undisturbed course. It is further compromised in the two-dimensional case by the integration of the observed effect through the flow boundaries at which the strict two-dimensionality is necessarily destroyed, and in the axially symmetric case by the approximations inherent in the numerical work required in the evaluation. While the influence of these errors has received considerable attention in the two-dimensional case [*18,19,20,21*], a correspondingly detailed analysis to sharpen the results obtained for cylindrically symmetric flows is yet to be completed [*26*]. It is, however, at least as important to realize as much as possible of the potentiality of these methods also in the axial case.

It is characteristic of the high precision of optical records of compressible flows that their analysis frequently requires and warrants the execution of a considerable amount of computation. This is the case, for instance, in the correction of errors in interferograms of two-dimensional flows, in the reduction of records obtained from axially symmetric flows around free-flight models in a firing range, and for the evaluation of shadowgraphs by ray-tracing methods. Increased use has been made in this connection of modern automatic computing equipment. This development is certain to continue as experimental gas dynamical facilities evolve from qualitative tools for the observation of phenomena into precision instruments for their measurement. In this respect the firing range or wind tunnel, instrumented with interferometers which are backed up by automatic calculating facilities, represents a particularly efficient system for the solution of the complex nonlinear differential equations governing the flow of gases. As such it holds a middle ground between the wind tunnel used on an engineering trial basis and the ultra high speed computer of the future which calculates any three-dimensional compressible flow from its differential equations and the appropriate boundary conditions.

A,1.6. Cited References.

1. Schardin, H. Die Schlierenverfahren und ihre Anwendungen. *Ergeb. exakt. Naturw. 20,* 303–439 (1942).
2. Kinder, W. Theorie des Mach-Zehnder Interferometers und Beschreibung eines Gerätes mit Einspiegeleinstellung. *Optik 1,* 413–448 (1946).
3. Shafer, H. J. Physical optics analysis of image quality in schlieren photography. *J. Soc. Motion Picture Engrs. 53,* 524–544 (1949).

4. Winkler, E. H. Analytical studies of the Mach-Zehnder interferometer. *Nav. Ord. Lab. Rept. 1077,* 1947; *1099,* 1950.
5. Gans, R. Fortpflanzung des Lichts durch ein inhomogenes Medium. *Ann. Physik (4) 47. Folge,* 709–736 (1915).
6. Bennett, F. D. Optimum source size for the Mach-Zehnder interferometer. *Ballist. Research Lab. Rept. 731,* 1950.
7. Bennett, F. D. Effect of size and spectral purity of source on fringe pattern of the Mach-Zehnder interferometer. *J. Appl. Phys. 22,* 776–779 (1951).
8. Ronchi, V. *La provi dei sistemi ottica.* Bologna, 1925.
9. Schardin, H. Das Töplersche Schlierenverfahren. *Ver. deut. Ing. Forschungsheft 367 (5),* 1934.
10. Winckler, J. The Mach interferometer applied to studying an axially symmetric supersonic jet. *Rev. Sci. Instr. 19,* 307–322 (1948).
11. Ladenburg, R., Winckler, J., and Van Voorhis, C. C. Interferometric studies of faster than sound phenomena. Part I: The gas flow around various objects in a free, homogeneous, supersonic air stream. *Phys. Rev. 73,* 1359–1377 (1948).
12. Ladenburg, R., Winckler, J., and Van Voorhis, C. C. Interferometric study of a supersonic air jet at 60 lb/inch^2 tank pressure. *Nav. Ord. Rept. 69–46,* 1946.
13. Weyl, F. J. Analytical methods in optical examination of supersonic flow. *Nav. Ord. Rept. 211–45,* 1945.
14. Hilton, W. F. The photography of airscrew sound waves. *Proc. Roy. Soc. London A169,* 174–190 (1938).
15. Lewy, H. On the relation between the velocity of a shock wave and the width of the light gap it leaves on the photographic plate. *Ballist. Research Lab. Rept. 373,* 1943.
16. Keenan, P. C., and Polachek, H. The measurement of densities in shock waves by the shadowgraph method. *Nav. Ord. Rept. 86–46,* 1946.
17. Halverson, R. R. The evaluation of the time constant of spherical exponentially decaying shock waves from optical distortion. *NDRC Div. 2, Interim Rept. VE-31,* 1945.
18. Saunders, O. A., Fishenden, M., and Mansion, H. D. Some measurements of convection by an optical method. *Engineering 139,* 483–484 (1935).
19. Groth, E. Influence of the boundary layer at the glass panes in the tunnel wall on the evaluation of interference photography at high automatic speeds. *Ministry Supply Transl. GDC 2703,* 1946.
20. Bershader, D. An interferometric study of supersonic channel flow. *Rev. Sci. Instr. 20,* 260–275 (1949).
21. Wachtell, G. P. *Ph.D. Thesis.* Princeton Univ., 1951. Also *Abstract N5, Phys. Rev. 78,* 333 (1950).
22. Schardin, H. Theorie und Anwendungen des Mach-Zehnderschen Interferenz-Refraktometers. *Z. Instrumentenk. 53,* 396–403 (1933).
23. Winckler, J. Interferometric study of supersonic phenomena. Part III: Boundary layer and shock wave interaction observed along probes and wires in supersonic air streams. *Nav. Ord. Rept. 7-47,* 1947.
24. Winkler, E. H. Principle and design of a new type of Stieltjes integrator. *Rev. Sci. Instr. 22,* 406–410 (1951).
25. Gooderum, P. B., and Wood, G. P. Density fields around a sphere at Mach numbers 1.30 and 1.62. *NACA Tech. Note 2173,* 1950.
26. Bennett, F. D., Carter, W. C., and Bergdolt, V. E. Interferometric analysis of airflow about projectiles in free flight. *J. Appl. Phys. 23,* 453–468 (1952).
27. Courant, R. *Differential and Integral Calculus,* Vol. II. Nordeman, New York, 1936.

ARTICLE A,2

SHADOW AND SCHLIEREN METHODS

J. W. BEAMS

A,2.1. Introduction. The function of both the schlieren and shadow methods is to determine small variations in the index of refraction of transparent materials. It can be shown that to a rough approximation the schlieren method measures the first derivative while the shadow method measures the second derivative of the refractive index [*1,2,3,4*].

The basic idea of the schlieren method was originated by Foucault [*5*] for testing lenses and other optical parts, but Töpler [*6*] greatly developed the method and applied it to the study of various air disturbances produced by sparks, explosions, air flows, etc. For the study of rapidly moving shock waves and other transient phenomena Töpler devised a spark light source which could be timed to illuminate a moving air disturbance at the desired instant. As a result "snapshot" pictures of the order of ten microseconds duration could be taken of the phenomena. Following Töpler a large number of workers have applied the schlieren method in various forms to the study of explosions, shock waves, and sound waves. R. W. Wood [*7*, p. 93] in a series of experiments beginning in 1899 photographed the reflection of compression waves from plane and concave mirrors, spherical aberrations, the diffraction produced by an obstacle, the refraction of a CO_2 lens, etc. The pictures graphically illustrate the change in shape of the wave front as it is brought to focus by a lens or concave mirror. The schlieren method has been applied also to the visualization and study of turbulence and convection due to hot wires or surfaces, the air flow around projectiles, jets, sound waves in air and in liquids, electrophoresis boundaries, diffusion boundaries, sedimentation in ultracentrifuges, etc. In recent years, especially, the method has been widely used in investigations of the air flow around bodies placed in high speed wind tunnels.

The shadow method, experimentally, is much simpler than the schlieren method and, since it depends upon the second derivative of the refractive index, is suitable for studies of such phenomena as intense shock waves or where the index of refraction changes very rapidly. The development of the method is usually attributed to Dvorak [*8*] who in 1880 used it to photograph air disturbances. Boys [*9*] in 1893 and Foley

[*10*], beginning in 1905, used the method to obtain beautiful photographs of the reflection, refraction, and diffraction of compression waves produced by sparks. The shadow method also has been used for investigating air jets, air flow around bodies in high speed wind tunnels, turbulence, the air flow and shock waves produced by high speed projectiles, sound waves in gases, liquids, and solids, etc. An excellent review of various shadow and schlieren arrangements, their theory, sensitivity, experimental details, and applications with many characteristic pictures has been written by Schardin [*2*]. The application of the schlieren and shadow methods to the aerodynamics of compressible flow has been discussed by Liepmann and Puckett [*11*, pp. 89–101].

A,2.2. Schlieren Systems.

Description of Schlieren Methods. The general principle of the schlieren system is illustrated by Fig. A,2.2a which is essentially the arrangement used by Töpler, Wood, and others. Light from a source A such as a straight or ribbon filament perpendicular to the page is focused by the lens B on the slit S_1 so that it is uniformly illuminated. The light passing S_1 is focused on the knife edge S_2, which is parallel to the image of S_1, by the long focus, large diameter, so-called schlieren lens C. If now the knife edge S_2 is moved upward into the beam until it just blocks out the image of S_1, no light will reach P (neglecting diffraction effects) provided the lens C is of good optical quality, is free of chromatic and spherical aberration and of astigmatism, and if there are no index of refraction gradients in the air traversed by the light beam. On the other hand, if the air is disturbed in the region D, say by a shock wave, some of the light rays are bent so that they pass above the knife edge S_2 and are focused by the lens G upon the screen or photographic plate P. Consequently, an image of the disturbance is formed on P. It will be noted that, with this arrangement, only the light which is deflected upward by the disturbance passes S_2 so that the regions in which the

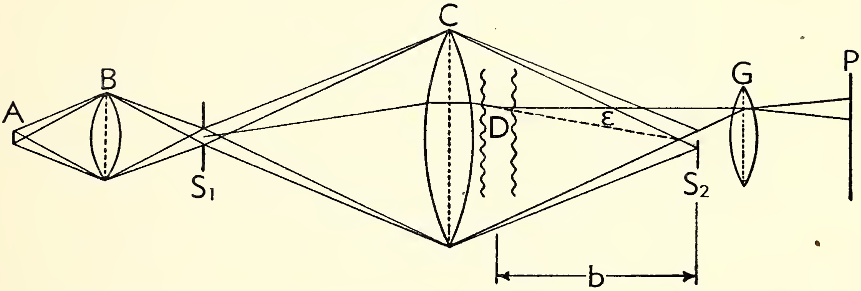

Fig. A,2.2a. A simple schlieren system. Lens G forms image of D on P.

refractive index gradient is such as to deflect the light rays downward or to right or left do not appear on P. In order to bring out the regions where downward deflections occur, it is common practice to adjust the knife edge S_2 to cut off the major portion but not all of the uniformly illuminated image of S_1. To observe the regions which deflect the light to the right or left, the whole optical system may be rotated through a right angle or other shapes of sources and knife edges, such as a point or disk-shaped source or slit at S_1, and a circular light stop at S_2 may be used. If at D a light ray is bent through an angle ϵ by the disturbance as shown (exaggerated) in Fig. A,2.2a, the intensity of illumination on P may be considerably increased. Let a be the unobscured width of the uniformly bright image of the slit S_1 at S_2 perpendicular to the knife edge and b the distance from D to S_2. Then the proportional change in the light intensity I at P is approximately [2,3,11]

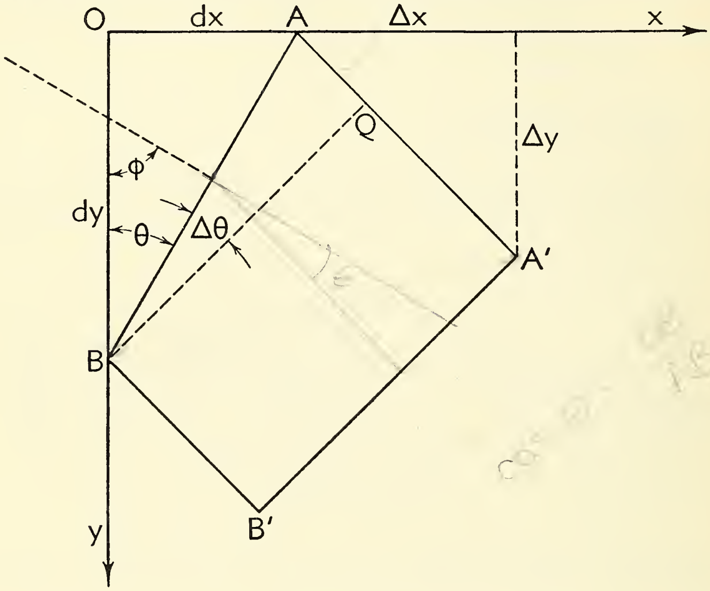

Fig. A,2.2b.

$$\frac{\Delta I}{I} = \frac{\epsilon b}{a} \tag{2.2-1}$$

as long as ϵb is smaller than the obscured image perpendicular to the knife edge. It will be noted that the sensitivity is increased by decreasing a and increasing b as long as diffraction effects can be neglected. Although reference must be made to more comprehensive treatments for the exact determination of the path of a light ray in a medium where the index of refraction varies in three dimensions [1,2,3,4,12], the case where it varies in one dimension only (y direction) is illustrated in Fig. A,2.2b [*13*, pp. 253–273]. Consider a very small segment AB of the wave front of a light wave which makes an angle of θ with the y axis. If now at A the index of refraction is n and at B it is $n + dn$, then, after a time Δt, the wave will move to $A'B'$ then

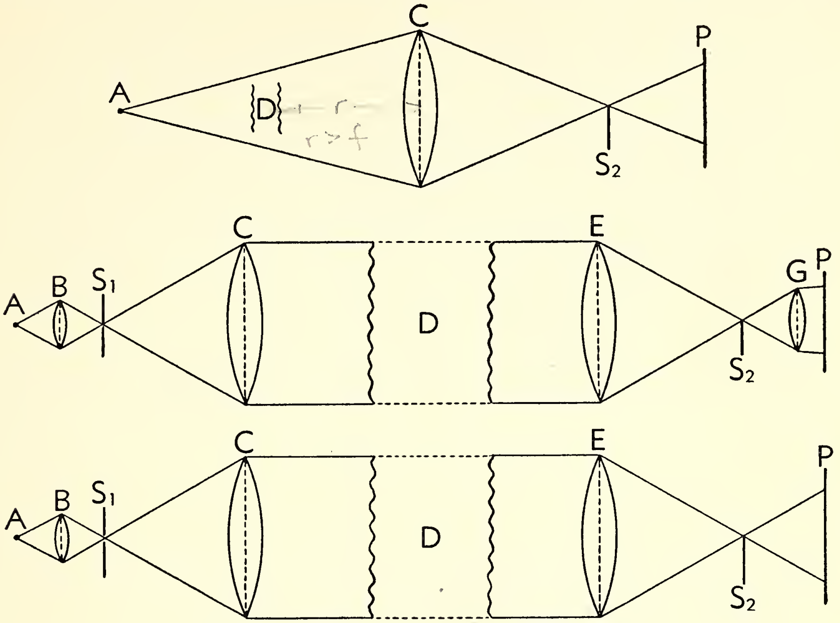

Fig. A,2.2c. Typical schlieren systems.

$$AA' = \Delta l = \frac{\Delta L}{n}$$

and

$$BB' = \frac{\Delta L}{n + dn}$$

where ΔL is the optical path of the wave front. Consequently,

$$\Delta\theta = \frac{AQ}{AB} = \frac{\Delta L}{n}\frac{1}{n}\frac{dn}{dy}\cos\theta = \frac{1}{n}\frac{dn}{dy}\Delta x \tag{2.2-2}$$

or

$$\epsilon = \int_0^l \frac{1}{n}\frac{dn}{dy}\,dl\,\sin\phi$$

where ϕ is the angle between the direction of the ray and dn/dy, i.e. the schlieren method measures the gradient of the refractive index. Since the work of Töpler, many variations of the method have been used by different workers. Three typical arrangements are shown schematically in Fig. A,2.2c. At the top is shown a scheme which utilizes only a single lens *C*. This arrangement requires a point or line source at *A*, and the distance from the region under investigation *D* to the schlieren lens *C* must be greater than the focal length of *C* so that the image of *D* is focused on the screen *P*. It will be observed that the disturbance takes place in a diverging beam as compared to a converging beam in Fig. A,2.2a. In the middle of Fig. A,2.2c is shown an arrangement in which the disturbance *D* takes place in a parallel light beam. For quantitative work there are several advantages in having *D* in parallel light, especially if its dimension parallel to the light beam is appreciable. At the bottom of Fig. A,2.2c is shown another arrangement in which *D* is in a parallel beam and the image of *D* is focused directly on the plate *P* by the lens *E*. In this assembly the distance from *D* to *E* must be greater than the focal length of *E*.

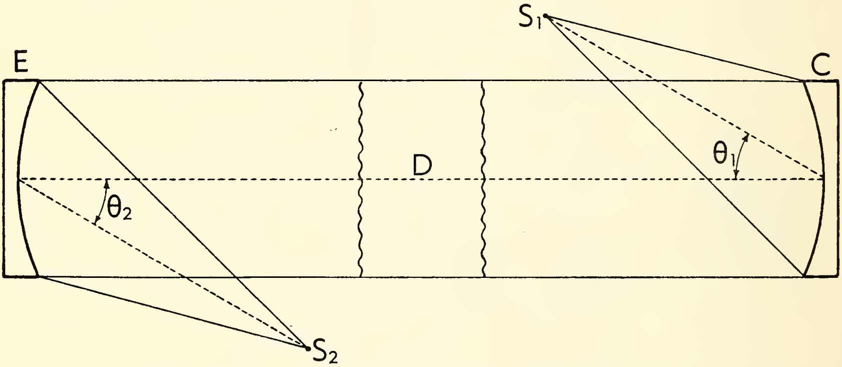

Fig. A,2.2d. Twin concave mirror schlieren system.

It will be noted that for any of the above schlieren arrangements the schlieren lenses *C* and *E* not only must be of the highest optical quality but also must have large diameters and long focal lengths. The large diameter is necessary because the cross section of the disturbance *D* is limited by the cross section of the lens. The long focal length is necessary in order to get the requisite precision and image size. As mentioned before, the schlieren lens should be free of chromatic and spherical aberrations. Also the astigmatism must be small, but it is not as critical as the other properties because of the axial symmetry. (See Art. 2.4.)

In experiments where the region under investigation *D* has a large cross section as in the case of many modern wind tunnels, it is very difficult to obtain lenses of sufficient diameter and focal length, and at the same time with the requisite optical properties and corrections, without almost prohibitive expense. As a result concave mirrors have been widely used. They are completely free from chromatic aberration and in large diameters and long focal lengths are much easier to grind and correct than lenses. Fig. A,2.2d shows a twin mirror system that gives good resolving power. The schlieren mirrors C and E are a carefully matched pair. Usually they are made of glass and their front surfaces are parabolized to better than one tenth of a wavelength of light. The excellence of their optical quality cannot be overemphasized. Also due to their size (more than a foot in diameter) and weight they must be carefully mounted to avoid distortions [*14*]. The angle θ_1 must be approximately equal to angle θ_2 and they should be made as small as possible although angles up to about 7° are used successfully [*11*]. The distance between the mirrors C and E is not critical, but it is good practice to make it greater than twice the focal length of the mirrors. Also the optical system beyond S_2 is simplified if the distance from the disturbance to be observed at D to the mirror E is greater than the focal length of E. The parallel rays entering the region D are bent by the refractive index gradient and are no longer parallel to the beam and, hence, cannot be focused by the second mirror unless the distance from D to the second mirror E is greater than the focal length of E. Also it will be observed that for the case where the disturbance is in parallel light, Eq. 2.2-1 becomes

$$\frac{\Delta I}{I} = \frac{\epsilon f}{a}$$

where f is the focal length of the mirror or lens. (See Fig. A,2.2d.) Because the source slit or knife edge S_1 is off the axis of the mirrors, some astigmatism and coma are introduced, but this is reduced to a minimum by keeping S_1, the axis of the mirrors, and S_2 in the same plane. This plane may be horizontal, vertical, etc., depending upon the direction of the refractive index gradients in D to be observed. With this arrangement the coma is compensated almost completely and the astigmatism lengthens the image of S_1 at S_2 in the direction of the knife edge rather than perpendicular to it so that no appreciable troubles are introduced. Occasionally it is necessary to observe the refractive index gradients in all directions at the same time. This may be accomplished with a point or disk source of light at S_1 and a disk light trap at S_2 which just blocks the image of S_1. This light mask at S_1 may be made, for example, by exposing, say, a lantern slide plate in the position of S_2, then using the developed plate for a light mask. For proper adjustment the knife edges or slits S_1 and S_2 should be of high quality and should be mounted so that they can be raised and lowered, rotated, or moved forward or backward by micrometer adjustments [*2,14*]. Also the mirrors should be accurately adjustable. The mountings of all of the components should be rigid. When properly adjusted for maximum sensitivity, the above system of Fig. A,2.2d responds to very small convection currents and temperature gradients in the light beam as well as the disturbances under investigation at D, i.e. they produce an undesirable background disturbance. Consequently, the distance between the mirrors should not be larger than necessary and care must be taken to prevent room disturbances. Temperature differences of 1°C in air which corresponds to refractive index changes of one part in 10^6 are readily observable [*14*].

Fig. A,2.2e shows a double traverse coincident schlieren system. Light from the source A is focused on the knife edge mirror S_1 by the condensing lens B. The light then goes to the large schlieren concave mirror C where it is returned to the knife edge S_2. The camera lens G is focused on the disturbance D or the region under investigation. In most of the experiments C is a spherical mirror of very long focus and very high quality.

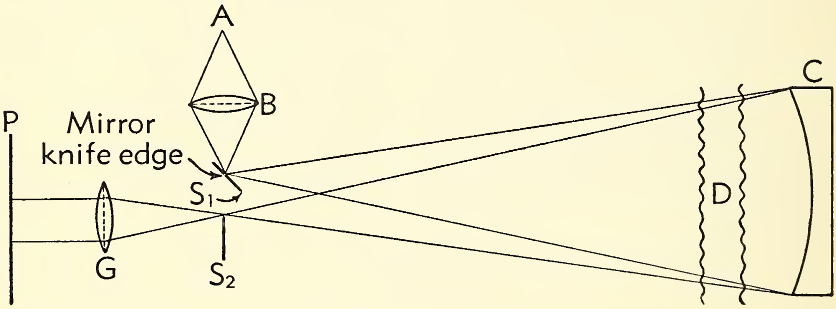

Fig. A,2.2e. Double traverse coincident schlieren system.

It will be observed that the light traverses the disturbance D under investigation twice so that the sensitivity is doubled. On the other hand one beam is converging and the other diverging. Since the two paths through D are not identical, there is a slight blurring or doubling (in case of a shock) of the image which may reduce the resolving power [*15*]. However, in practice this system is especially used to observe very weak disturbances where the light is refracted only a very small amount in one traversal. It can be shown that the sensitivity is

$$\frac{\Delta I}{I} = \frac{4\epsilon f}{a}$$

where f is the focal length of the mirror and the other quantities have the same meaning as in Eq. 2.2-1 [*11*]. This type of schlieren system has been used, for example, in observing phenomena in hypersonic low pressure wind tunnels by McLellan, Williams, and Bertram [*16*]. With a spherical mirror 1 ft in diameter and a radius of curvature of 20 ft they observed density changes across a shock of 1.3 per cent of the free stream density, which was only 6 or 7 per cent of an atmosphere. Optical distortion in the windows of their tunnels limited the precision of their observations.

In Eq. 2.2-1 the refractive index gradient is determined by measuring the light intensity changes on the photographic plate. Often it is more convenient to determine small displacements. One such method is shown in Fig. A,2.2f. (The top diagram gives a side view and the bottom, a vertical projection.) It is known as the Thovert [*17*], Philpot-Svensson [*18,19*] inclined slit method and measures the refractive index gradient in one direction [*20*]. *A* is a light source, preferably monochromatic, such as a high pressure capillary mercury arc with filters [*14*] to give the green line, *B* a collimating or projection lens, S_1 a narrow horizontal slit, *C* the first schlieren lens, *D* the region under investigation, S_2 an inclined slit, *G* a camera lens, *I* a cylindrical lens with a vertical axis, and *P* the photographic plate or viewing screen. Three principal adjustments must be made: first, the image of the horizontal slit S_1 must be thrown on the inclined or diagonal slit S_2, which is just in front of *G*; second, the image of the region *D* must be focused on the photographic plate or viewing screen *P*; and third, an image of the inclined slit S_2 is formed on the photographic plate *P*. The cylindrical lens *I* with vertical axis has no focusing effect on light in the vertical plane, so that each vertical coordinate y in the region *D* corresponds to a vertical coordinate Y on *P* or $Y = K_1y$ where K_1 is the optical magnification of the region *D* on *P*. In the horizontal plane *G* and *I* focus S_2 upon *P* with a magnification factor K_2. If no gradient of the refractive index exists in *D*, a straight vertical line is formed on *P*. On the other hand, in the presence of a gradient the image of the light source on the inclined slit S_2 is displaced either up or down by an amount ϵb where ϵ and b have the same meaning as in Fig. A,2.2a. This causes the image to be horizontally displaced a distance $K_2\epsilon b \tan \varphi$, where φ is the angle the inclined slit S_2 makes with

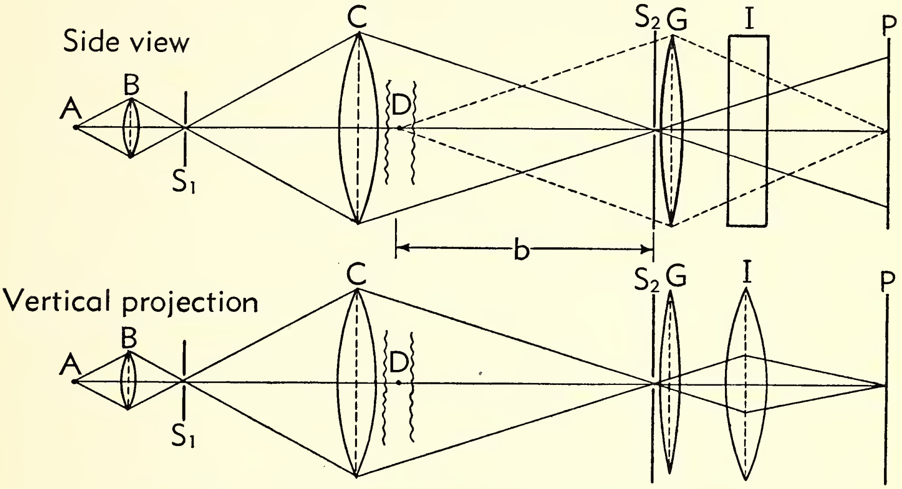

Fig. A,2.2f. Thovert, Philpot-Svensson inclined slit system.

the vertical. Consequently, a curve is automatically recorded on P which gives the refractive index gradient versus the vertical height in the region D. The absolute value of the refractive index is obtained from the integral or area under this curve. If the disturbance D has a large dimension perpendicular to the paper, Fig. A,2.2f (top), and if the vertical refractive index gradient is not uniform perpendicular to the paper across D, then a wide vertical slit should be placed in front of C. The vertical refractive index gradient in the region of D illuminated by the parallel beam is then recorded. The entire region D may be investigated by moving the wide slit across C. The horizontal gradient of the refractive index can be obtained by rotating the whole optical apparatus through a right angle. Also schlieren concave mirrors, Fig. A,2.2d, may be used in place of the schlieren lens. Some experimenters prefer to use a small inclined solid bar at S_2 instead of a slit [*21*]. This gives a dark line on a light background rather than a light line on a dark background. The method was designed originally for observing sedimentation in ultracentrifuges and moving boundaries in electrophoresis where it has wide application, but it is extremely useful in any experiment where quantitative data are essential. Angular deflections ϵ of 10^{-5} radians can be measured with a schlieren mirror of 60 in. focal length and 12 in. diameter.

A number of different optical arrangements may be used with the above method such as shown in Fig. A,2.2c. In fact it is usually preferable to have the region D in parallel light. Also attention should be directed to the Longsworth slit method [*22*] and the Lamm scale method [*13*], as they both give precision comparable with the above methods. The latter method, which essentially consists of photographing a scale or rectangular network through the disturbance and measuring the distortion of the image, is capable of high precision although the reduction of the data is laborious.

In the above schlieren methods the region D under investigation may be of considerable length in the direction of the light beam and still be focused on the photographic plate P, i.e. there may be a comparatively large depth of focus. However, it is often desirable to record only the phenomena which occur in a plane perpendicular to the light beam in D. For this purpose a sharp-focusing schlieren system has been devised recently by Kantrowitz, Trimpi, and Miller [*23*]. The method employs multiple sources and slits (knife edges) with each source and corresponding slit acting as an ordinary schlieren system. The light rays through the region under investigation are approximately parallel but the different beams are oblique to the axis. In this way the disturbances in a given plane in D are accentuated with respect to the other planes with the result that a sharp focus is obtained.

Another method [*1,2,24*] of recording the angular deviation ϵ consists in placing a series of parallel slits in front of or behind the image plane of S_1 at S_2 (Fig. A,2.2a) with the knife edge removed [*32*]. Usually the slits (Ronchi plate) are equally spaced and the distance between the slits is equal to the width of the slits. The slit S_1 is narrowed until the width of its image is not larger than the distance between the slits [*32*]. With this arrangement the background of the schlieren lens (or mirror) and hence the plate or screen at P is covered with straight lines if there is no disturbance at D. However, any refractive index gradients in D will cause the lines to be curved in the region of the disturbance. From the displacement of these lines the angular deviation ϵ can be determined. Diffraction apparently sets the lower limit of the width of the slits that can be used. Darby [*24*] found that 100 lines per inch was about the limit for his apparatus, which had a sensitivity of about 10^{-4} radians per line.

In general the schlieren method is used either for the detection of small refractive index gradients or for the quantitative measurement of these gradients. For the detection of small gradients the apparatus described above, in which the deviation of the light ray ϵ gives rise to the relative light intensity change $\Delta I/I$ on the photographic plate, is almost universally used for studying phenomena in aerodynamics and ballistics. The method also may be made quantitative, but attention must be given to the several variables in the experimental arrangement. If the disturbance is to be photographed, the arrangement must give a maximum contrast between the images of the undisturbed and disturbed regions and at the same time the photograph must be dense enough to be measurable by photometric means. In most cases high contrast photographic plates are preferable even though they are somewhat slower. In order to calibrate the system, a known refractive index gradient such as a small glass prism may be inserted in some corner of the median plane of the disturbance D which allows a check on the formulas used for the optical system. The sensitivity, i.e. $\Delta I/I$, depends directly upon the brightness of the image of S_1 at S_2 and upon its uniformity of illumination. This of course requires as bright and uniform a source as possible to start with and an optical system which sacrifices no more light than necessary. Rectangular sources are usually superior [*11*] and, if they are wide or high enough (for example, a General Electric type H6 lamp) [*14*], they may be placed directly back of the slit S_1 with the elimination of the lens B [*22*]. It is also clear that if the unobscured width a of the image at S_2 is reduced, the sensitivity is increased. However, there is a practical minimum for the width which is set by the diffraction pattern at S_2 and the intensity and size of the source. The sensitivity also increases directly with the focal length of the schlieren mirror or lens, while a large aperture gives high aperture to disturbance ratio which increases the contrast and density on the plate. Shafer [*4*] especially has analyzed theoretically the above factors and has concluded that the effective f ratio of the optical system should be as large as possible, consistent with the brightness of the light source and the availability of the optical parts. He gives a value of $f/10$ for the schlieren system to be used with a Charters [*25*] 1-mm diameter source through which an energy of 5 watt sec is passed in 10^{-6} sec. He also concludes that in general the optimum position of the knife edge should be near the optic axis although the exact position must be determined by the size and brightness of the image of S_1 at S_2. Shafer gives the optimum size of the light source as one whose geometrical image in the focal plane of the objective (schlieren lens) is equal to the width of the "Airy disc" of the objective [*26*].

Suppose the above method is applied to the study of disturbances such as density gradients in a wind tunnel in which the flow is two-dimensional. That is, if the flow is in the x direction and the light beam is in the z direction, the component of the gradient of the refractive index vanishes in the z direction. The index of refraction in air for sodium light can be expressed in terms of the density ρ by the relation

$$n = 1 + 0.000293 \frac{\rho}{\rho_{\mathrm{NTP}}}$$

where ρ_{NTP} is the density at 1 atm and 0°C. As a result Eq. 2.2-2 gives for the components of the angular deflections ϵ_x and ϵ_y in the x and y directions, respectively, as

$$\epsilon_x = \int C \frac{\partial \rho}{\partial x} dz, \qquad \epsilon_y = \int C \frac{\partial \rho}{\partial y} dz$$

where C is a constant.

When the component of the density gradient in the direction of the light beam does not vanish, the interpretation of the pictures is more complicated.

THE SENSITIVITY OF THE SCHLIEREN METHOD FOR STUDIES OF SHOCK AND EXPANSION WAVES. As shown in Art. 2.2, Fig. A,2.2a and Eq. 2.2-1

$$\frac{\Delta I}{I} = \frac{\epsilon b}{a}$$

If now we assume (following references [*2,11,27*]) that we can determine a 10 per cent change in $\Delta I/I$ and set $b/a = 10^4$ (for example $a = 0.006$ in. and $b = 60$ in.), then $\epsilon = 10^{-5}$ radians (about 2 sec of arc).

Of special interest is the question: Under what condition will an oblique shock become visible [*27*]? Assuming the knife edge to be parallel to the front of the oblique shock and, as a typical value, the angle between the shock and the optic axis $\theta = 1° = 0.0175$ radians, it can be shown that all the light incident upon the shock is refracted and the amount of light reflected is negligible. If index 0 characterizes the stagnation conditions at 20°C, index 1 the free flow on the upstream side of the shock, and index 2 on the downstream side, Snell's law of refraction leads to the relation

$$1 + 0.000293\,\frac{273}{293}\,p^0\left(\frac{\rho_1}{\rho^0} - \frac{\rho_2}{\rho^0}\right) = 1 - \epsilon \tan\theta$$

or for $\epsilon = 10^{-5}$

$$\rho_2 - \rho_1 = \rho^0\,\frac{\tan\theta}{27.3p^0} \tag{2.2-3}$$

where p^0 is the stagnation pressure in atm.

If the knife edge is, as usual, parallel or perpendicular to the flow and the shock makes an angle β with the flow, the right side of Eq. 2.2-1 has to be multiplied by $\cos\beta$ or $\sin\beta$, respectively.

More useful than the density difference is the difference between β and the Mach angle μ which is a measure of the shock strength. If M_1 is the Mach number of the flow upstream of the shock, M_n the component of M_1 normal to the oblique shock

$$\sin\beta = \frac{M_n}{M_1} = M_n \sin\mu$$

Furthermore

$$\frac{\rho_1}{\rho^0} = \left(1 + \frac{M_1^2}{5}\right)^{-\frac{5}{2}} \text{ if } \gamma = \frac{C_p}{C_v} = 1.40$$

and

$$\frac{\rho_2}{\rho_1} = \frac{6M_n^2}{M_n^2 + 5}$$

$$\frac{\rho_2 - \rho_1}{\rho^0} = \frac{\rho_2 - \rho_1}{\rho_1}\,\frac{\rho_1}{\rho^0} = \frac{5(M_n^2 - 1)}{M_n^2 + 5}\,\frac{\rho_1}{\rho^0} = \frac{\tan\theta}{27.3p^0} \tag{2.2-4}$$

provided the knife edge is parallel to the shock wave front. Therefore, at given values of θ, p^0, and M_1, also M_n and therefore the minimum difference $\beta - \mu$ which will give a visible schlieren effect is determined.

If the density change across the oblique shock is small, also $\beta - \mu$ is small, $M_n^2 = 1 + \delta$, with $\delta \ll 1$

$$\beta - \mu = \frac{3}{5}\,\frac{\rho^0}{\rho_1}\,\frac{\tan\theta}{27.3p^0\sqrt{M_1^2 - 1}}$$

if $\epsilon = 10^{-5}$ and the knife edge is parallel to the front of the shock wave. For $\theta = \beta - \mu = 1°$ the following table gives the minimum stagnation pressure at which shocks will be visible by schlieren at the assumed rather favorable condition.

M	$p^0_{\min}$ atm
2	0.055
3	0.102
4	0.205
5	0.396
7	1.21
10	4.46

If θ is 5° instead of 1°, the minimum pressures given are approximately five times as large.

A similar consideration will give the conditions for visibility of expansion waves [*27*].

A,2.3. Shadow Methods. As pointed out above in Art. 2.1, the shadow method depends upon the second derivative of the index of refraction and therefore is best suited to recording sudden changes. The apparatus used in the shadow method is much simpler than that used in the schlieren method. Fig. A,2.3a shows a typical arrangement. *A* is a point light source, *D* is the region under investigation, and *P* is a photographic plate or viewing screen. Usually the distance *AD* is greater than 10 ft while *DP* is of the order of 1 or 2 ft, depending upon the magnification desired. The light from *A* in passing through the disturbance *D* is refracted and bent out of its path. If the refractive index gradient, say $\partial n/\partial y$, is constant along the length of *D*, then all the rays are bent by the same amount and no change in the light intensity *I* occurs on the screen or plate *P*. On the other hand, if $\partial n/\partial y$ varies and hence $\partial^2 n/\partial y^2$ is not zero, then the deflection of the rays is not constant. For example in Fig. A,2.3a, if the gradient $\partial n/\partial y$ at *m* is greater than at *l* and *n*, the rays will be deflected by different amounts and n' will lie between l' and m' and a darker region will occur between l' and n' while a lighter region will occur between n' and m'. For example in a shock wave the density increases rapidly to a peak and then approaches a constant value [*11*] so that the image on the plate consists of a dark and light band adjacent to each other [*28*]. As the plate *P* is moved back, this region broadens and becomes more distinct. However, there is usually an optimum distance of a foot or so which gives the best contrast. The distance from the light source *A* to *D* is determined by the intensity of the source and by its size. If *A* is very small as in the case of, say, a concentrated arc lamp or small hole illuminated by a focused spark, the

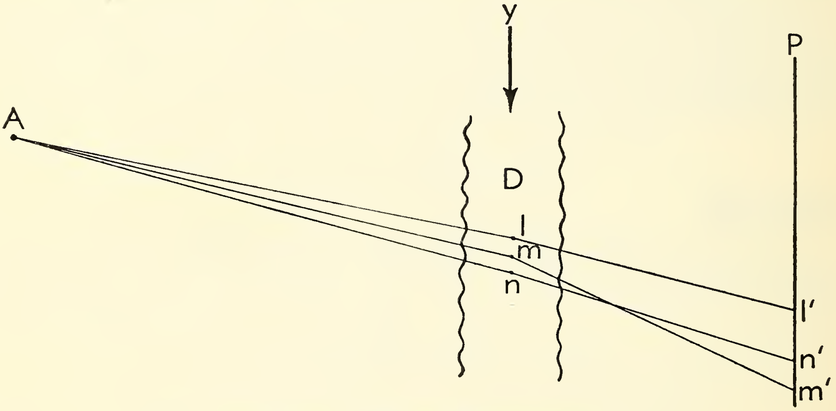

Fig. A,2.3a. Simple shadow system.

distance AD may be made much less than shown in Fig. A,2.3a. The distances of light source A and plate P from the region D under investigation are especially critical if the turbulent nature of the flow is to be studied (see [*45,52*] and F,3).

The above discussion has been limited to one dimension, but for two dimensions [*2,3,11*] the increase of intensity

$$\Delta I = k\left(\frac{\partial^2 n}{\partial x^2} + \frac{\partial^2 n}{\partial y^2}\right)$$

where k is a constant and x and y are the coordinates in a plane normal to the light path.

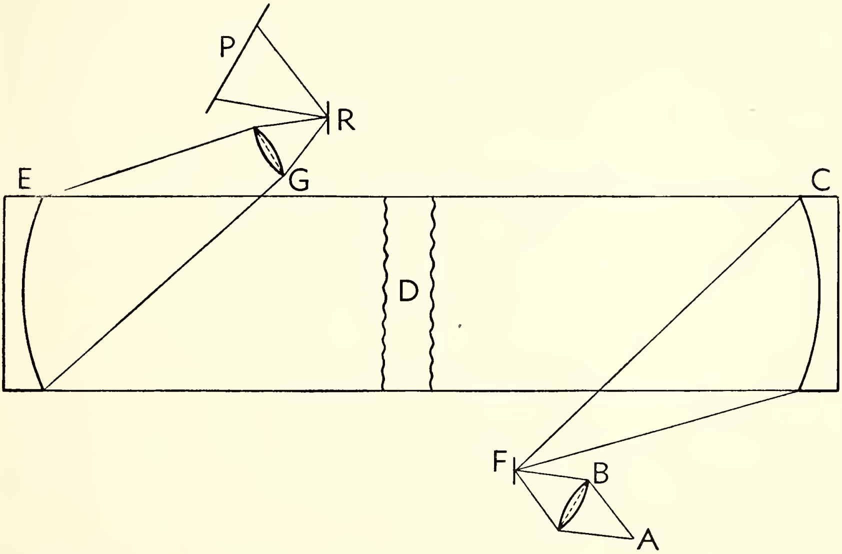

Fig. A,2.3b. Shadow system using parallel light.

Shadowgraphs may be taken in parallel light as shown in Fig. A,2.3b. A is the light source, B a lens, F a flat front surface mirror, C and E the large concave mirrors such as used in Fig. A,2.2d, D the region or plane of the disturbance, G a lens, R another front surface mirror, and P the photographic plate or viewing screen. All of the optical parts should be of first quality and carefully corrected as in the schlieren apparatus. The lens G is so adjusted as to bring the plane of D "in focus" on the photographic plate P. It is therefore possible to obtain "focused" shadowgraph pictures [*29*]. Or if the disturbance is weak, greater shadow effects are obtained by throwing the system slightly out of focus.

Since the shadow method is sensitive to sudden changes in the refractive index, it is often used to study transient phenomena in high velocity jets, the flow of air around rapidly moving bodies, sound waves, shock waves, etc. Consequently either the shutter at R or at F (Fig. A,2.3b) should operate very quickly or the light source at A (Fig. A,2.3a and Fig. A,2.3b) must be made of very short duration to prevent blurring of the image. Rapidly rotating mirrors have been used [*29*] at R or at F and spark light sources are often used at A. These light sources are discussed in Art. 2.4. The shadow method gives the position of the disturbance as well as that of the object which produces it with high precision. It also gives the Mach angles and peak density of the shock waves. As an illustration of the clarity with which the shadow method brings out air disturbances and flow, special reference should be made to the beautiful shadow photographs of projectiles in flight made by Charters and his associates [*25,28*] and to Plate F,1.3. In quantitative studies of the density distribution in air disturbances great care must be given to the proper photographic procedure as well as the photometric measurement of the plates. Usually shadow photographs of shock waves are made at two distances from the disturbance and measurements are made of the width of and intensity across the dark band. Keenan and Polachek [*30*], Clippinger [*31*], and others [*2*] have developed methods of evaluating shadowgraphs and have concluded that they are most useful in determining the density distribution near the front of the shock wave, the slope of the wave, and the peak intensity.

A,2.4. Light Sources, Optical Parts, and Photography. The type of light source required for either the schlieren or shadow method is determined by the type of problem under investigation. In general the schlieren and shadow methods are used to study two kinds of phenomena. The first kind is stationary or changes very slowly with time while the second kind is transient, moving or changing very rapidly.

For the first type of problem almost any kind of light source which is intense enough is satisfactory. The carbon arc and the incandescent lamp especially have been widely used for the first type of phenomenon. In many cases a straight filament or ribbon incandescent lamp may be used without a condensing lens or slit. When monochromatic light is required the mercury lamp with filters is used. For most experiments a high pressure "capillary" mercury arc is suitable since it has both high intensity and a slitlike shape. Also the spectral lines are well spaced and efficient filters are available for isolating the various spectral lines. The spectral lines of course are broadened in the high pressure arc, but it is seldom that the schlieren or shadow methods require highly monochromatic light. A number of investigators have found the H4 and H6 mercury lamps [*14*] especially suitable for their experiments. Because of its very small cross-sectional area and high intensity, the zirconium concentrated arc light is an excellent source, especially when a point source is required. It may be obtained in various sizes depending upon the light intensity requirements [*34*]. Many other light sources are commercially available. Finally, in considering a "white" light source, the sun should not be overlooked because of its high intensity parallel light.

For investigation of the second type or transient phenomenon mentioned above, the experimenter must resort to a fast-acting light shutter or must employ a light source of short duration. In their early experiments, Töpler, Wood, Ferry, and others used a condenser discharge through an electric spark gap. Wood [*4*] developed a slit type intense spark light source by enclosing two sheets of metal between glass plates. The condensed spark takes place between the edges of the two thin metal plates and the light is viewed "edge on." With magnesium sheets as electrodes, Wood obtained extremely intense spark light especially in the spectral region of the 4481A spark lines of magnesium. Condensed discharges through enclosed capillaries or small channels have been developed in recent years for light sources, especially by Charters [*25*], Ladenburg [*35*], and their associates [*36*]. In most cases, the light source is viewed "end on" and is very intense. As long as the phenomena under investigation will permit exposure times of one microsecond or longer, no special care must be taken with these spark sources. However, for the study of the air flow around bodies in supersonic wind tunnels, around high speed projectiles, for the study of turbulent boundary layers, etc., blurring occurs unless the exposure time is reduced well below one microsecond. In general, minimum duration of the spark light source is determined first by the difficulty of getting sufficient energy into the spark and then cutting it off, and second, by the die-away of the light in the spark after the electric current in the spark is stopped. In most practical cases, this die-away time is roughly between 0.01 and 0.1 microsecond. In any type of condensed electric discharge, the resistance of the spark gap changes from almost infinity before the breakdown to a comparatively small value after complete breakdown occurs. That is, the current in the spark must build up from practically zero to a large value in a few hundredths of a microsecond. Consequently, in order for this to occur, the effective inductance in the circuit feeding the spark must be very small and the capacity should be comparatively large. A number of special noninductive condenser spark gap arrangements have been developed which have reduced the effective duration of the spark light to a few tenths of a microsecond [*37*]. Since the principal difficulty with a lumped capacity-resistance-inductance circuit is in matching the impedance of the source to the spark gap, a low impedance transmission line may be employed to considerable advantage [*38*]. In practice the transmission line is open-ended at the output end and shunted at the input end by the spark gap in series with a noninductive resistance equal to the surge impedance of the line. If the line is charged to the desired potential, the spark discharge impresses a discharge wave upon the line. This surge travels to the open end, is reflected, and returns to the input end where it reduces the potential across the spark to zero. The potential across the spark gap is maintained only while the discharge wave is traveling twice the length of the transmission line, and consequently the time can be varied by changing the length of the line. The maximum current in the spark is determined by how small the surge impedance of the line can be made. This can be reduced by using several lines, say RG8/U cable in parallel. Recently Fitzpatrick, Hubbard, and Thaler [*39*] have developed a barium titinate coaxial transmission line (which now can be obtained commercially), with the order of a few ohms surge impedance, which increased the spark light intensity over an RG8/U cable by 1,000 times for 0.1 microsecond flashes. As a result the die-away time of the excited gases in the gap is probably the principal limiting factor on the minimum time of duration of the spark light.

It is clearly possible to take short schlieren or shadow photographs by using a rapidly rotating mirror or a Kerr cell as a light shutter. With the present techniques of rotating mirrors the only limiting factor on the rotational speed obtainable in practice is the strength of the mirror [*40*]. With good highly polished steel mirrors, light flashes or exposures from 10^{-9} to 10^{-10} sec duration can be obtained. These mirrors may be magnetically suspended and driven electromagnetically or they may be air driven [*41*]. Usually they are spun in a vacuum or light gas such as helium in order to reduce optical distortion by shock waves arising from the rapidly moving mirror edges. Kerr cells also may be used as light shutters, although their time of observation is limited by the time constants of the electric circuit of which they represent a minimum of the circuital capacity. However, light flashes of the order of 10^{-9} sec duration can be obtained. The light source used with a rapidly rotating mirror or Kerr cell should be as intense as possible and should be roughly synchronized with the mirror or cell. Consequently high intensity sparks or small exploded metal wires with large capacities across them serve as good light sources.

For quantitative work the optical parts preferably should be as nearly perfect as possible. It can be shown that the difference in the lengths of the light paths of any two rays in an optical system containing lenses or mirrors need not be smaller than $\frac{1}{4}$ wavelength of the light used [*26*]. However, this is often difficult (though not impossible) to obtain and in practice a few wavelengths can usually be tolerated. This also applies to any wind tunnel window through which the light passes. However, it should be pointed out that perfect lenses or mirrors if used in a manner for which they are not constructed give rise to difficulties. For example, a portrait objective should not be used for parallel light, etc. For each system careful calculations should be made using the well-known methods of optics (*2*,*26*,*42*]. The slits and knife edges must not only be accurately adjustable but also they must be precisely made [*1*,*2*,*14*]. For example, an error of one mil in the knife edge would introduce a change in intensity on the plate of about 16 per cent in the problem discussed in Art. 2.2. Because of the long optical paths, diffraction patterns formed by the slits and knife edges are sometimes gross enough to be readily visible. In the case of a slit the diffraction pattern is symmetrical, but for a knife edge the pattern consists of "a system of fringes of decreasing width, outside the edge of the geometrical shadow, while within the edge the illumination falls off rapidly without however passing through maxima and minima" [*42*]. Consequently, a knife edge gives a relatively sharp image. On the other hand, the position of the edge of the image of a knife edge will appear to shift on the photographic plate with exposure time (assuming a constant intensity source) while the central line of the slit image will be relatively independent of the exposure time [*22*,*43*]. In all quantitative work the photographic procedures must be carried through in such a way as to give an accurate recording of the light intensity.

A,2.5. Comparison of Schlieren and Shadow Methods. As pointed out in Art. 2.1 above, theory shows roughly that the schlieren method depends upon the first derivative while the shadow method depends upon the second derivative of the refractive index. Consequently, in phenomena where the refractive index varies relatively slowly, the schlieren method is to be preferred to the shadow method, other things being equal. On the other hand, the shadow method brings out very beautifully the rapid changes in the index of refraction. The shadow method also has the advantage of greater simplicity and somewhat wider possible application. The two methods therefore supplement each other and both should be used whenever possible. Fortunately, in many cases the same apparatus or optical parts can be used for both methods by simple rearrangements and without too much effort on the part of the experimenter. In addition to the first and second derivatives, the refractive index itself can of course be obtained by integration. However, whenever possible, it is preferable to measure a quantity directly rather than obtain it from its derivative. For this reason it is clear that the shadow and schlieren methods should be supplemented by the interference method, which gives the refractive index directly. The complete information which can be obtained by these three methods supplementing one another is beautifully demonstrated by the recent work of Ladenburg and his associates [*35*,*36*,*44*,*45*]. The interference method is taken up in detail in the following article. Recently several experiments have been described which utilize essentially the same optical parts for the schlieren, shadow, and interference methods [*44*,*45*,*46*,*47*]. For additional illustrations of the application of the shadow and schlieren methods, reference should be made to the following articles: for axially symmetric jets [*1,2,11,35,36, 38,48,49*]; for two-dimensional channel flow and wind tunnels [*1,11,16,51, 52,53,54*]; for projectiles [*1,25,28,29,50,55,56,57,58,59*]; for shock tubes [*60,61,62*].

A,2.6. Cited References.

1. Schardin, H. Das Töplersche Schlierenverfahren. Grundlagen für seine Anwendung und quantitative Auswertung. *Ver. deut. Ing. Forschungsheft 367* (*5*), 1–32 (1934).
2. Schardin, H. Die Schlierenverfahren und ihre Anwendungen. *Ergeb. exakt. Naturw. 20*, 303–439 (1942).
3. Weyl, F. J. Analytical methods in optical examination of supersonic flow. *Nav. Ord. Rept. 211–45*, 1945.
4. Shafer, H. J. Physical optics analysis of image quality in schlieren photography. *J. Soc. Motion Picture Engrs. 53*, 524–544 (1949).
5. Foucault, L. *Ann. observatoire Paris 5*, 197 (1859).
6. Töpler, A. Über die Methode der Schlierenbeobachtung als mikroskopisches Hülfsmittel, nebst Bemerkungen zur Theorie der schiefen Beleuchtung; Virboskopische Beobachtungen über die Schwingungsphasen singender Flammen (der chemischen Harmonica) mit Benützung des Schlieren-apparates; Optische Studien nach der Methode der Schlierenbeobachtung. *Ann. Physik u. Chem.* (*J. C. Poggendorff*) *127*, 556–580 (1866); *128*, 126–139 (1866); *131*, 33–55, 180–215 (1867); *134*, 194–217 (1868).
7. Wood, R. W. *Physical Optics*, 3rd ed. Macmillan, 1934.
8. Dvorak, V. Über eine neue einfache Art der Schlierenbeobachtung. *Ann. Physik u. Chem.* (*G. Wiedemann*) *9*, 502–512 (1880).
9. Boys, C. V. On electric spark photographs; or, photography of flying bullets, by the light of the electric spark. *Nature 47*, 415–421 (1893).
10. Foley, A. L., and Souder, W. H. A new method of photographing sound waves. *Phys. Rev. 35*, 373–386 (1912).
11. Liepmann, H. W., and Puckett, A. E. *Introduction to Aerodynamics of a Compressible Fluid.* Wiley, 1947.
12. Gehrecke, E. Dioptrik in Medien mit kontinuerlich variablen Brechungsindex. *Handbuch der Physikalischen Optik*, Part 1, 219–236. Leipzig, 1927.
13. Lamm, O., Svedberg, T., and Petersen, P. O. *The Ultracentrifuge.* Oxford, 1939.
14. Barnes, N. F., and Bellinger, S. L. Schlieren and shadowgraph equipment for air flow analysis. *J. Opt. Soc. Amer. 35*, 497–509 (1945).
15. Taylor, H. G., and Waldram, J. M. Improvements in the schlieren method. *J. Sci. Instr. 10*, 378–389 (1933).
16. McLellan, C. H., Williams, T. W., and Bertram, M. H. Investigation of a two-step nozzle in the Langley 11-inch hypersonic tunnel. *NACA Tech. Note 2171*, 1950.
17. Thovert, J. Recherches sur la diffusion des solutions. *Ann. phys.* (*9*) *2*, 369–427 (1914).
18. Philpot, J. St. L. Direct photography of ultracentrifuge sedimentation curves. *Nature 141*, 283–284 (1938).
19. Svensson, H. Electrophoresis by the moving boundary method. A theoretical and experimental study. *Arkiv Kemi, Mineral. Geol. 22* (*10*), 1–156 (1946).
20. Bridgman, W. B., and Williams, J. W. Optical problems of the ultracentrifuge. *Ann. N.Y. Acad. Sci. 43*, 195–210 (1942).
21. Pickels, E. G. The ultracentrifuge. *Chem. Rev. 30*, 341–355 (1942).
22. Longsworth, L. G. The observation of electrophoretic boundaries. *Ann. N.Y. Acad. Sci. 39*, 187–212 (1939).

23. Kantrowitz, A., and Trimpi, R. L. A sharp-focusing schlieren system. *J. Aeronaut. Sci. 17*, 311–314 (1950).
24. Darby, P. D. Unpublished communication. *Remington Arms*, 1946.
25. Charters, A. C. *Proc. Sixth Intern. Congress Appl. Mech.*, 1946.
26. Hardy, A. C., and Perrin, F. H. *Principles of Optics*, Chap. 3 to 8. McGraw-Hill, 1932.
27. Wolgast, R. C., Kantrowitz, A., and Miller, W. S., Jr. *Rept. Air Eng. Develop. Center*, 1948.
28. Charters, A. C., and Thomas, R. N. The aerodynamic performance of small spheres from subsonic to high supersonic velocities. *J. Aeronaut. Sci. 12*, 468–476 (1945).
29. Soule, H., and Sabol, A. P. Development and preliminary investigation of a method of obtaining hypersonic aerodynamic data by firing models through highly cooled gases. *NACA Tech. Note 2120*, 1950.
30. Keenan, P. C. and Polachek, H. *Nav. Ord. Rept. 86-46*, 1946.
31. Clippinger, R. F. Unpublished communication. *Ballist. Research Lab.*, 1946.
32. Ronchi, V. *La provi dei sistemsi ottica.* Bologna, 1925. *Rev. opt.* (*5*), 1926.
33. Anderson, J. A., and Porter, Russel W. Ronchi's method of optical testing. *Astrophys. J. 70*, 175–181 (1929).
34. Buckingham, E. D., and Deibert, C. R. The concentrated-arc lamp. *J. Opt. Soc. Amer. 36*, 245–250 (1946).
35. Ladenburg, R., Winckler, J., and Van Voorhis, C. C. Interferometric studies of faster than sound phenomena. Part I. The gas flow around various objects in a free, homogeneous, supersonic air stream. *Phys. Rev. 73*, 1359–1377 (1948). Ladenburg, R., Van Voorhis, C. C., and Winckler, J. Interferometric study of faster than sound phenomena. Part II. Analysis of supersonic air jets. *Phys. Rev. 76*, 662–677 (1949).
36. Winckler, J. The Mach interferometer applied to studying an axially symmetric supersonic air jet. *Rev. Sci. Instr. 19*, 307–322 (1948).
37. Kovásznay, L. S. G. High power short duration spark discharge. *Rev. Sci. Instr. 20*, 696–697 (1949).
38. Beams, J. W., Kuhlthau, A. R., Lapsley, A. C., McQueen, J. H., Snoddy, L. B., and Whitehead, W. D., Jr. Spark light source of short duration. *J. Opt. Soc. Amer. 37*, 868–870 (1947).
39. Fitzpatrick, J. A., Hubbard, J. C., and Thaler, W. J. A high intensity short duration spark light source. *J. Appl. Phys. 21*, 1269–1271 (1950).
40. Beams, J. W. High centrifugal fields. *Wash. Acad. Sci. 37*, 221–241 (1947).
41. Smith, E. C., and Beams, J. W. A high constant speed rotating mirror. *Phys. Rev. 79*, 222 (1950); *J. Soc. Motion Picture Engrs. 58*, 159–168 (1932).
42. Wood, R. W. *Physical Optics*, 3rd ed. Macmillan, 1934.
43. Longsworth, L. G. Tests of flowing junction diffusion cells with interference methods. *Rev. Sci. Instr. 21*, 524–528 (1950).
44. Bershader, D. An interferometric study of supersonic channel flow. *Rev. Sci. Instr. 20*, 260–275 (1949).
45. Ladenburg, R., and Bershader, D. On laminar and turbulent boundary layer in supersonic flow. *Revs. Mod. Phys. 21*, 510–519 (1949).
46. Svensson, H. An interferometric method for recording the refractive index derivative in concentration gradients. *Acta Chem. Scand. 3*, 1170–1177 (1949).
47. Gayhart, E. L., and Prescott, R. Interference phenomenon in the schlieren system. *J. Opt. Soc. Amer. 39*, 546–550 (1949).
48. Prandtl, L. Neue Untersuchungen über die strömende Bewegung der Gase und Dämpfe. *Physik Z. 8*, 23–30 (1907).
49. Hartmann, J., and Lazarus, F. The air-jet with a velocity exceeding that of sound. *Phil. Mag. 31*, 35–50 (1941).
50. Stevens, V. I. Hypersonic research facilities at the Ames Aeronautical Laboratory. *J. Appl. Phys. 21*, 1150–1155 (1950).
51. Stack, J. *Nav. Ord. Lab. Rept. 1133*, 1949. Also unpublished communication, 1946.

52. Ackeret, J., Feldmann, F., and Rott, N. Investigations of compression shocks and boundary layers in gases moving at high speed. *NACA Tech. Mem. 1113,* 1947.
53. Liepmann, H. W. The interaction between boundary layer and shock waves in transonic flow. *J. Aeronaut. Sci. 13,* 623–637 (1946).
54. Ferri, A. Investigations and experiments in the Guidonia supersonic wind tunnel. *NACA Tech. Mem. 901,* 1939.
55. Cranz, C., and Schardin, H. Kinematographie auf ruhendem Film und mit extrem hoher Bildfrequenz. *Z. Physik 56,* 147–183 (1929).
56. Mach, E., et al. *Sitzber. Akad. Wiss. Wien, Math. naturw. Kl., Abt. IIa, 92,* 625 (1885); *95,* 765 (1887).
    Mach, E., and Salcher, P. Über die in Pola und Meppen angestellten ballistisch-photographischen Versuche. *Sitzber. Akad. Wiss. Wien, Math. naturw. Kl., Abt. IIa, 98,* 41–50 (1889); Optische Untersuchung der Luftstrahlen. *98,* 1303–1309 (1889).
    Mach, E., and Mach, L. Weitere ballistisch-photographischen Versuche. *Sitzber. Akad. Wiss. Wien, Math. naturw. Kl., Abt. IIa, 98,* 1310–1326 (1889); Über longitudinale fortschreitende Wellen im Gase. *98,* 1327–1332 (1889); Über die Interferem der Schallwellen von grosser Excursion. *98,* 1333–1336 (1889).
57. Cranz, C. *Lehrbuch der Ballistik,* 2nd ed., Vol. 3, p. 259. Springer, Berlin, 1927.
58. Charters, A. C. Free flight roll of a simple arrow projectile. *Nav. Ord. Lab. Rept. 1131,* 1949.

59a. Taylor, G. I., and Maccoll, J. W. The air pressure on a cone moving at high speeds. *Proc. Roy. Soc. London 139,* 278–311 (1933).

59b. Maccoll, J. W. The conical shock wave formed by a cone moving at high speed. *Proc. Roy. Soc. London 159,* 459–472 (1937).

60. Smith, L. *Office Sci. Research and Develop. Rept. 6271,* 1945.
61. Bleakney, W. and Taub, A. H. Interaction of shock waves. *Revs. Mod. Phys. 21,* 584–605 (1949).
62. Becker, J. V. Results of recent hypersonic and unsteady flow research at the Langley Aeronautical Laboratory. *J. Appl. Phys. 21,* 619–628 (1950).

ARTICLE A,3

INTERFEROMETRY

R. LADENBURG

DANIEL BERSHADER

A,3.1. Introduction. The importance of interferometry for the study of high speed aerodynamics is due to the fact that interferometers allow quantitative measurements of density and subsequent calculation of the pressure, temperature, and velocity in a flowing gas without introducing any disturbance into the phenomena to be investigated. In order for the interferometric method to apply, the velocity of the gas stream has to be of the order of, or larger than, the sound velocity. (See Table A,3.1.)

Table A,3.1. M = Mach number; ρ = density.

M	0.2	0.5	0.7	1.0
$\Delta\rho/\rho$	0.02	0.13	0.26	0.58

Then compressibility effects become noticeable and local changes in density and in refractive index occur. Such changes can be measured to a high degree of accuracy by interferometry. A suitable arrangement is the division of amplitude of the light from a monochromatic source by a glass plate, the so-called "beam splitter," into two coherent beams which when reunited may give interference fringes. Fringe maxima occur if the difference in optical path length between the two beams—that is, the product of refractive index n and geometrical path length l—is an even multiple of a half wavelength. Assuming, for simplicity, that the index is constant over each path, there results for the maxima

$$n_1 \cdot l_1 - n_2 \cdot l_2 = 2N\left(\frac{\lambda}{2}\right) \qquad N = 0, 1, 2 \ldots$$

Minima occur if this difference is an odd multiple, $(2N + 1)\lambda/2$. (See for example [*1*] or [*2*].)

Changes of the density ρ of the gas are proportional to changes of its refractive index n. With one beam undisturbed, a change in optical path experienced by the other beam produces in the simple two-dimensional case a proportional shift S of the fringes:

$$\Delta n_1 \cdot l_1 = K \cdot \Delta \rho_1 \cdot l_1 = S \cdot \lambda$$

where $K = (n - 1)/\rho$, the Gladstone-Dale constant, depends only on the wavelength used and on the nature of the gas and is to a large extent independent of the pressure of the gas.

How the other variables such as pressure, velocity, etc., may be obtained from the density in special cases by using aerodynamic relations is discussed in Art. 3.4 and 3.5.

In most applications to gas dynamics one wants to know the density change at a definite position in space along the light beam (for example, at the nose of a two-dimensional object in a wind tunnel or at a given point in a supersonic jet). It is normally required that the fringes be located at this same place in order to obtain the combined photograph-interferogram needed for evaluation purposes (see Art. 3.4).

This condition is fulfilled in the Mach-Zehnder interferometer [*3*,*4*] by suitable adjustment of one or two of its four plates (see especially Art. 3.2 and Fig. A,3.2a). It is the ability of this instrument to locate fringes in any desired place by suitable rotation of the plates that makes it particularly applicable for aerodynamic purposes. Moreover, it permits one to produce as wide a separation of the interfering beams as desired so that even a large wind tunnel can be brought into one beam without disturbing the light path in the other beam. These features have made the Mach-Zehnder (abbreviated M-Z) the main instrument for the quantitative study of high speed aerodynamic phenomena.[1]

The instrument is a modification of the simpler Jamin interferometer [*1*] which consists of two plane-parallel plates of equal thickness whose front sides act as beam splitters and whose rear surfaces act as reflecting mirrors. However, the separation of the two interfering beams is limited here by the thickness of the two plates, and the interference fringes are located at infinity.

In the Michelson interferometer [*1*,*2*], on the other hand, where the two beams are also separated by an arbitrary distance, the localized fringes are always located near one of the mirrors, since coherent rays intersect there (see Art. 3.2 and [*6*]). Besides, the light passes twice through the disturbance, thus making the interpretation somewhat doubtful.

Present techniques do not permit one to make good plane-parallel plates of larger diameter than about 15 in. This limits the size of the working field to be studied with the conventional type of M-Z. In this connection various modifications have been proposed (see Art. 3.3).

---

[1] The history of the M-Z is reviewed by Kinder [*9*] who also gives a long list of references for its properties and applications.

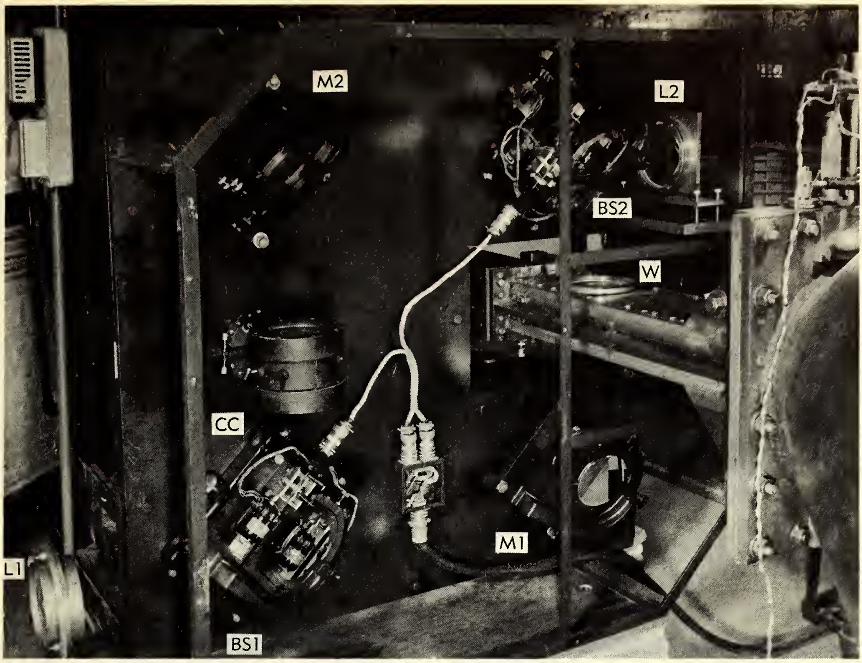

Plate A,3.3. M-Z interferometer mounted on a vertical plate with the nozzle of a two-dimensional supersonic wind tunnel, working section 3 × 3 in. $L1$,$L2$, lenses. $BS1$, $BS2$, beam-splitters. $M1$, $M2$, mirrors. W, upper window on working section. CC, compensating chamber with windows.

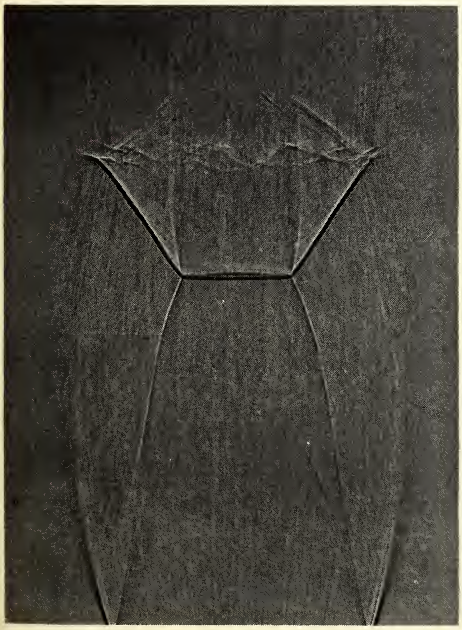

Plate A,3.5a. Shadowgram of an axially symmetric air jet flowing upward from a round orifice of 10 mm diameter, at a reservoir gauge pressure of 70 lb/in.^{2}

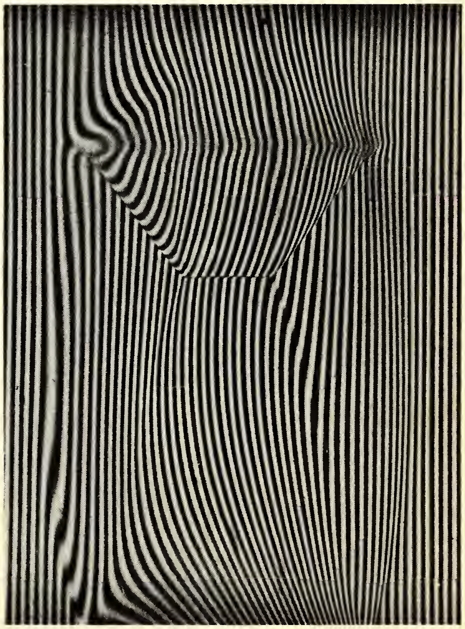

Plate A,3.5b. Interferogram of an air jet flowing upward from a round orifice of 10 mm diameter, at a reservoir gauge pressure of 60 lb/in.^{2} Exposure 300 microseconds.

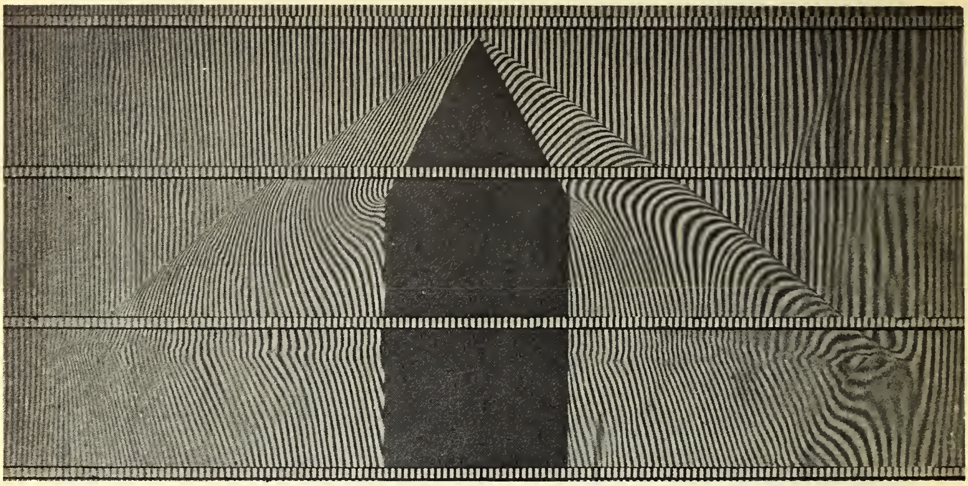

Plate A,3.5c. Interferogram of air flow around 30° cone-cylinder in an "open wind tunnel" at $M = 1.70$. Reservoir gauge pressure 69.5 lb/in.^{2} The horizontal strips contain no-flow fringes (see Art 3.4).

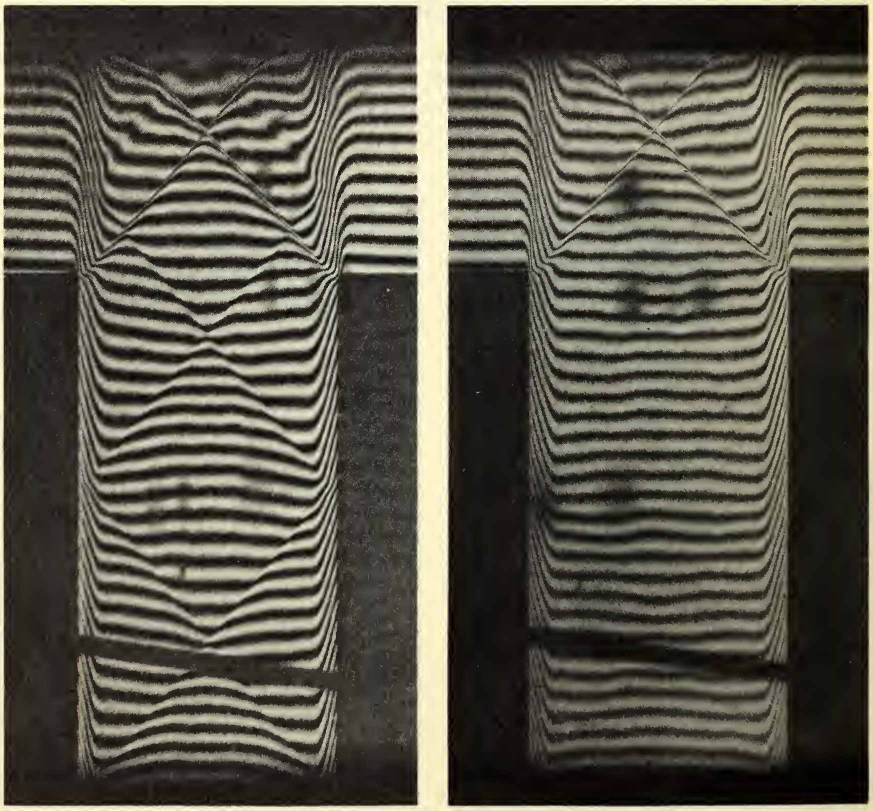

Plate A,3.5d. Interferograms of orifice section of Laval nozzle replacing divergent channel of Fig. A,3.5c. Left, weak shocks due to small errors in the converging part of the channel; right, after improving the channel.

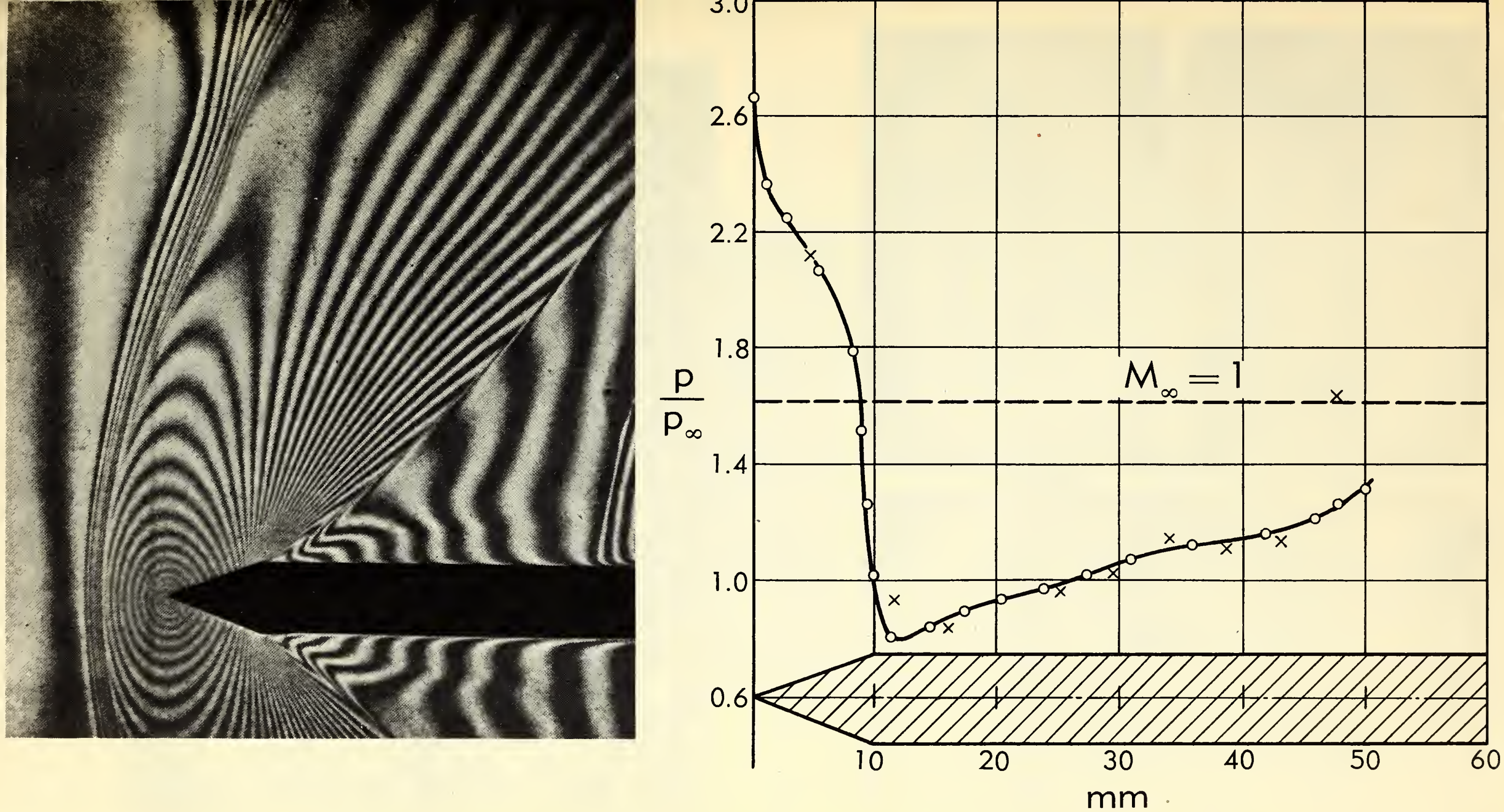

Plate A,3.5e. Contour interference fringes and evaluated pressure distribution of flow around a 40° wedge at $M = 1.40$. Pressures, represented by small circles, to be compared with manometer readings, represented by small crosses [24]. (Ordinates are pressure coefficients p/p_∞ where p_∞ is free stream pressure.) (From [24] by permission of H.M.S.O., London.)

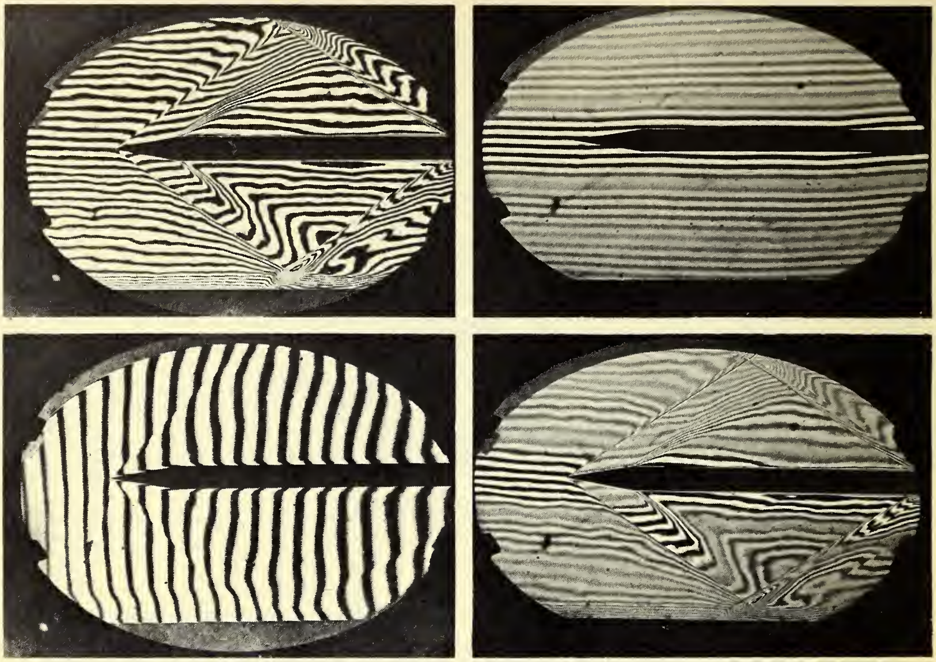

Plate A,3.5f. Interferograms with displacement fringes of the flow at $M = 2.3$ around a 20° wedge in a 3 × 3 in. working section: top left, at 9 cm Hg pressure; bottom left, at 5 mm Hg pressure; right, using unfiltered spark ("white light") at 9 cm Hg pressure, top, air at rest, bottom, at $M = 2.3$.

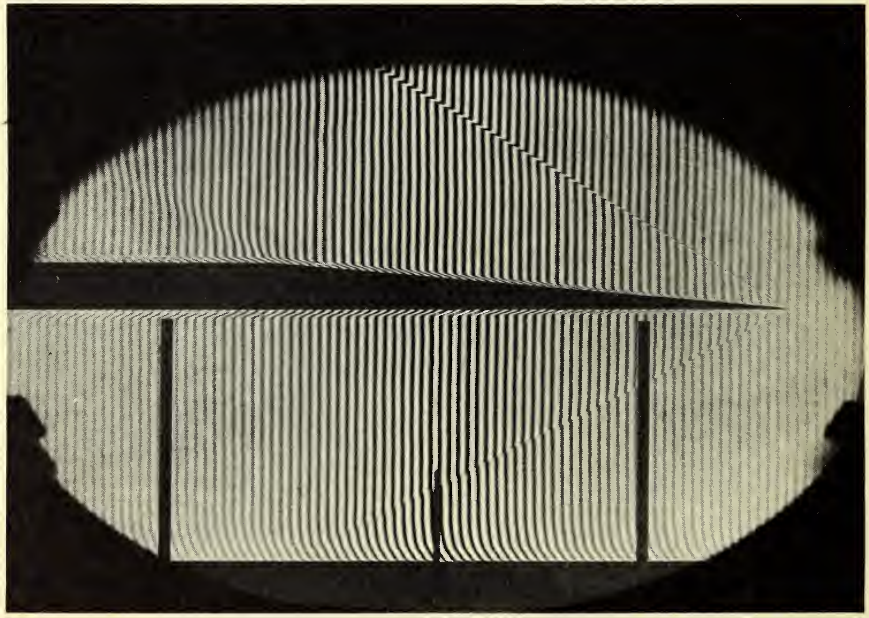

Plate A, 3.5g. Flow around half wedge at $M = 2.3$, stagnation pressure 31 cm Hg, fringes perpendicular to flow.

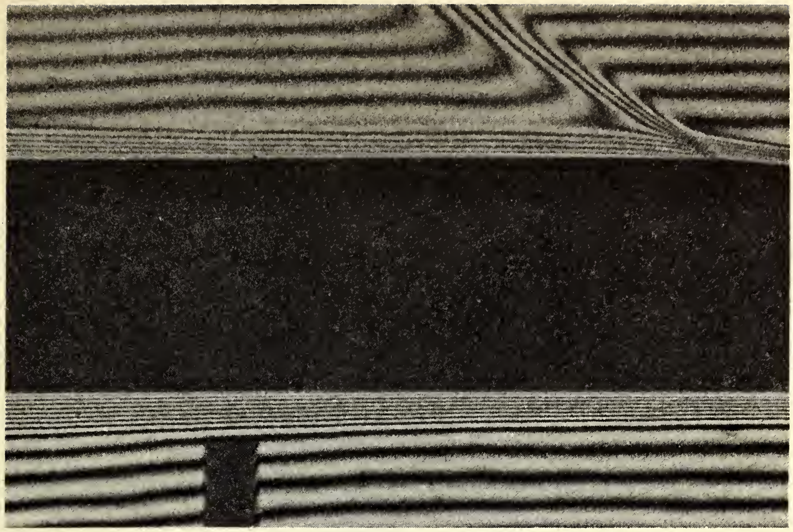

Plate A,3.5h. Enlarged part of the flow around the same model and at the same Mach number as in Plate A,3.5g but with stagnation pressure 240 cm Hg, fringes parallel to flow (note crowded fringes in boundary layer).

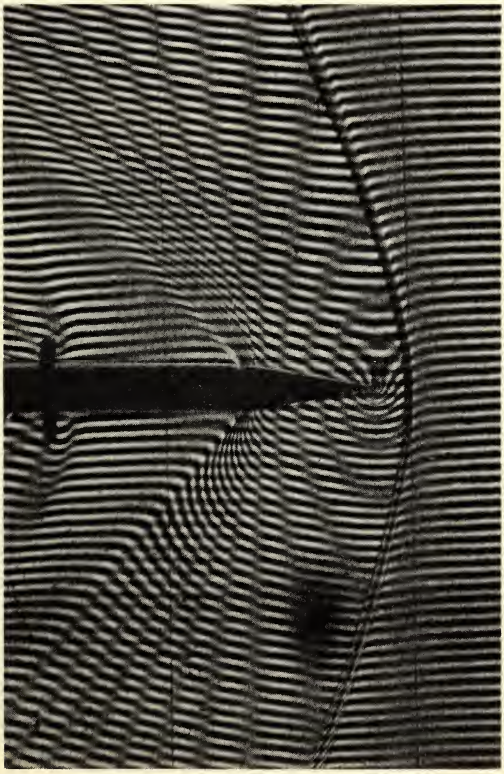

Plate A,3.5i. Density contours obtained with superimposed displacement fringes of the flow around a wedge of 10° half angle at $M = 1.278$.

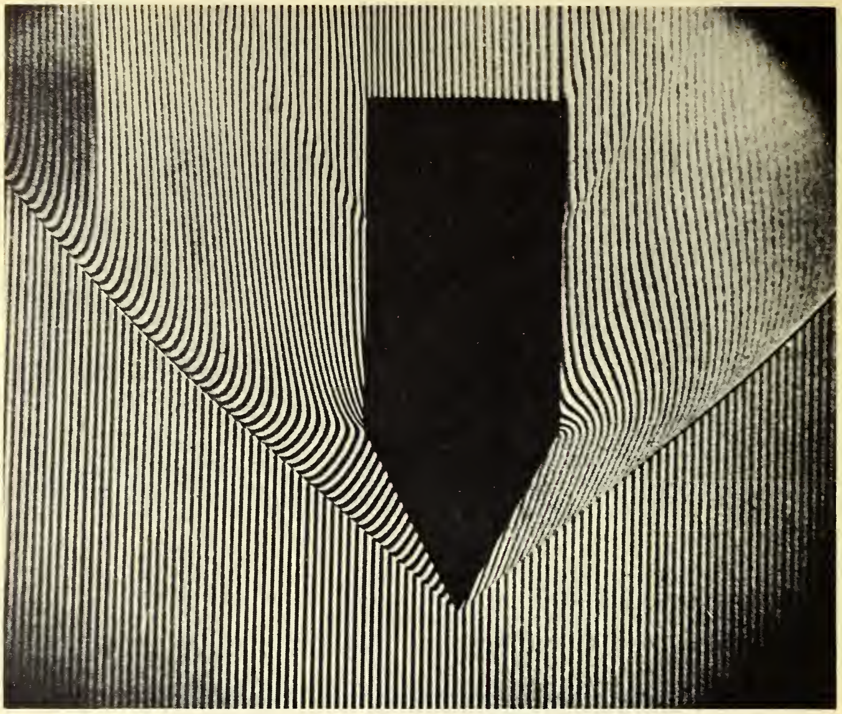

Plate A,3.5j. Flow around projectile cal. 30, 30° half angle cone-cylinder in free flight at $M = 1.77$. To be compared with Plate A,3.5c.

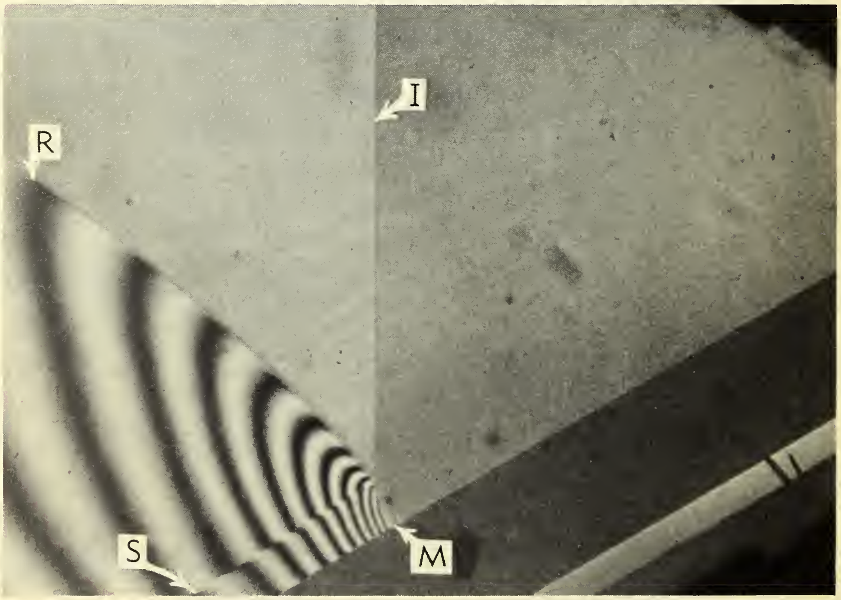

Plate A,3.5k. Mach reflection in a shock tube. *I*, incident shock moving to the right. *R*, reflected shock. *M*, Mach shock. *S*, slip stream originating at the triple intersection.

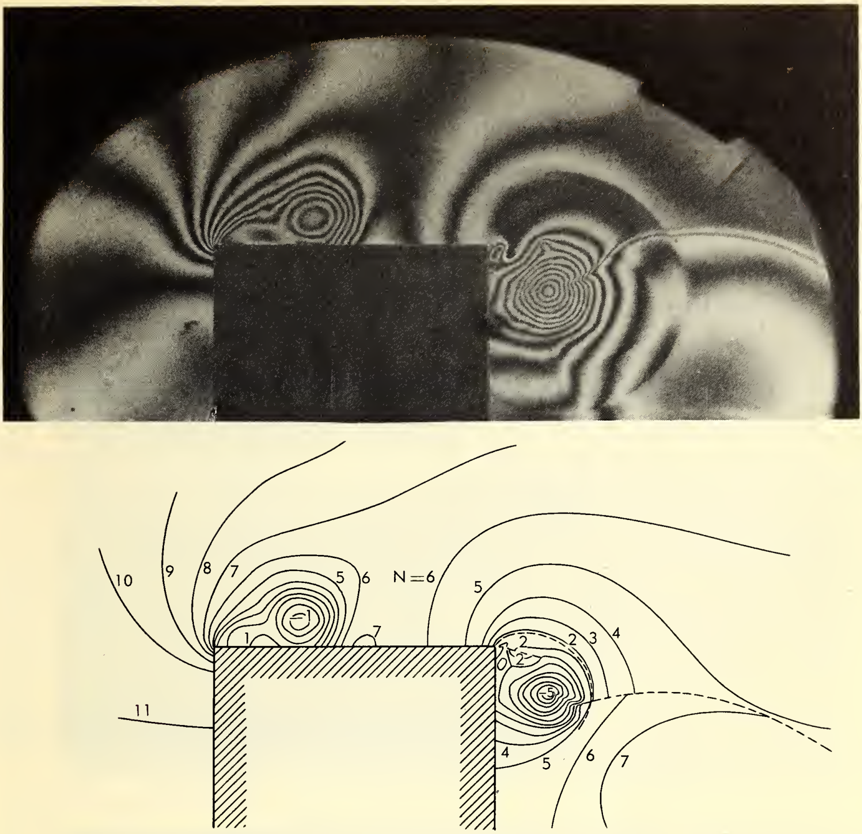

Plate A,3.51. Contour fringes and isopycnals of flow around a rectangular block 277 microseconds after passage of a normal shock moving to the right at $M = 1.34$.

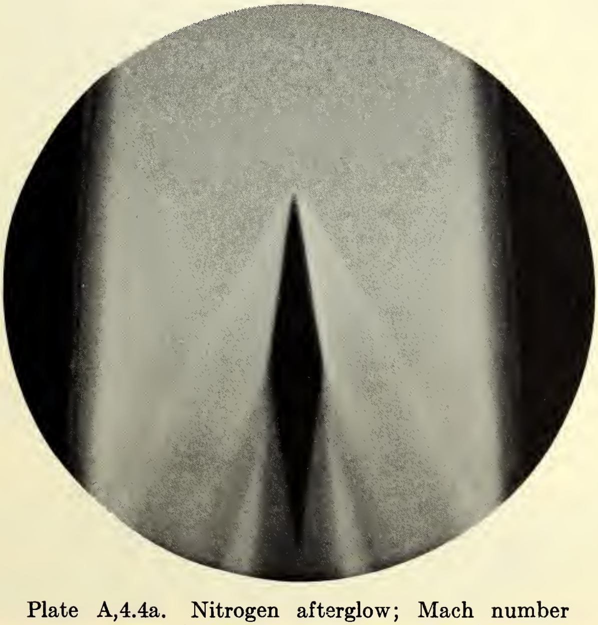

Plate A,4.4a. Nitrogen afterglow; Mach number approximately 2.6. (Courtesy NACA.)

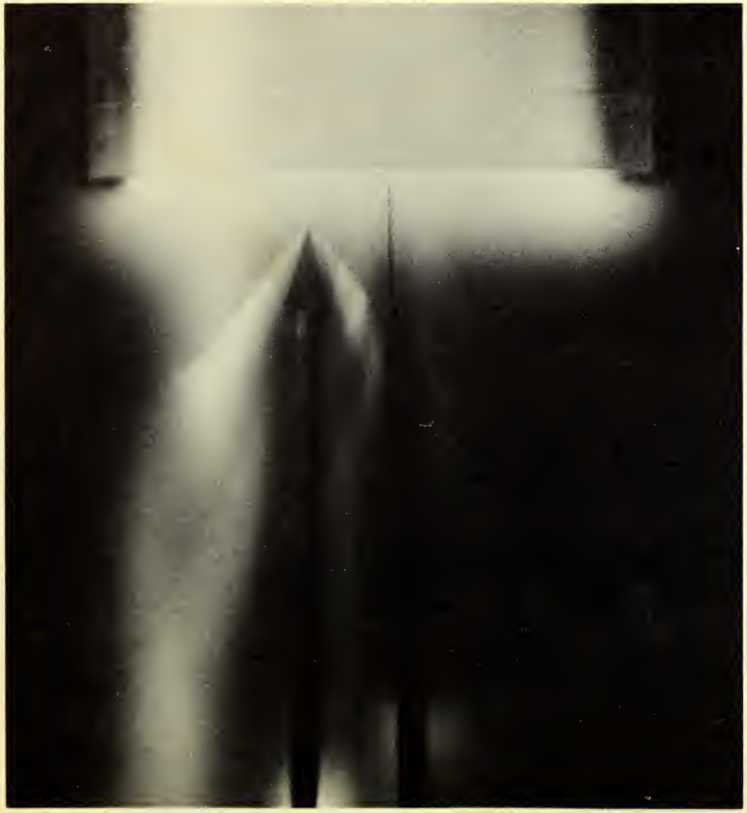

Plate A,4.4b. Nitrogen afterglow; Mach number approximately 2.7. (Courtesy G. J. Maslach, Univ. of California.)

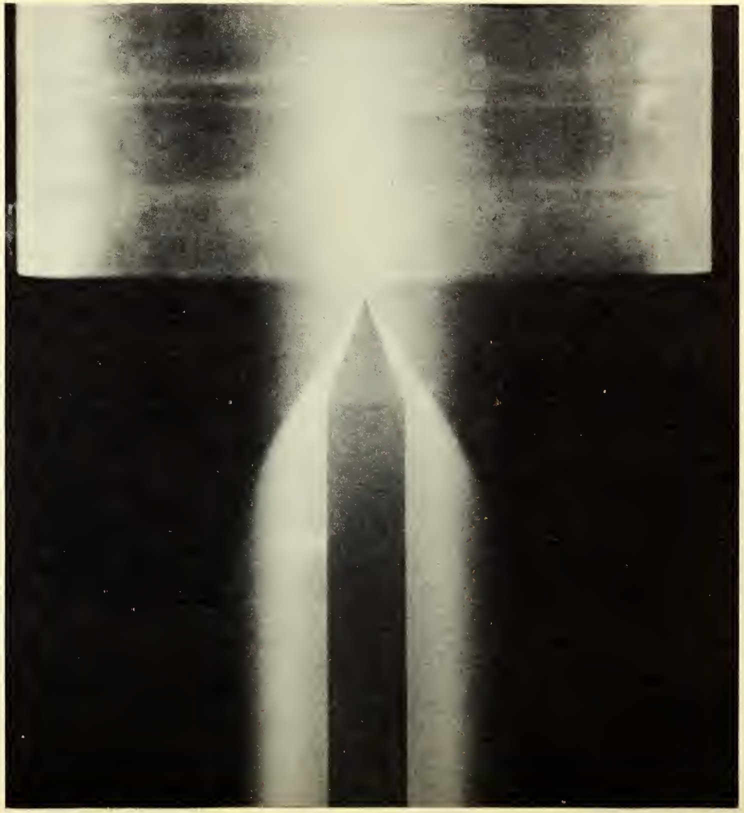

Plate A,4.6. Glow discharge in nitrogen. $M_\infty = 2.6$, $p^0 = 110$ microns, $Re = 760$ per in., 20° half angle cone, 0.7 in. dia support. (Courtesy G. J. Maslach, Univ. of California.)

A,3.2. Theory of the Mach-Zehnder Interferometer.[2]

FRINGE FORMATION IN THE IDEAL M-Z INSTRUMENT. As pointed out in Art. 3.1, the M-Z is a member of a class of instruments in which the amplitude of incident light is divided by a partially silvered mirror, resulting in two beams capable of producing interference phenomena. An "ideal" M-Z may be defined as one in which the plates perform their functions perfectly with no secondary effects on the light beams, and in which the splitter plates are infinitely thin. Any necessary collimating and camera lenses are assumed to be perfect thin lenses, and further, the light is assumed to come from a monochromatic point source. This "idealized" instrument is a useful concept in simplifying the study of fringe formation.[3]

In Fig. A,3.2a the four plates occupy the corners of a rectangle and are all parallel at the start. Parallel monochromatic light falls on $BS1$ at exactly 45° incidence, the plane of incidence coinciding with the plane of centers of the plates, i.e. the plane of the drawing. The dotted line R represents what may be called the reference phase plane. This is a plane normal to the beam and located arbitrarily between the collimator and $BS1$. The light at all points of this plane is in phase, with the result that rays through any two points of R can be made to produce interference. An example is shown in Fig. A,3.2a, using the central ray r^c and another ray r, the subscripts 1 and 2 referring to the portions transmitted and reflected respectively by $BS1$. Upon rotation of $BS2$ through an angle ϵ interference fringes appear on a screen $PO'C$ placed somewhat beyond $BS2$. The phase difference between the rays intersecting at point P is determined by comparing the optical lengths PR_1 and PR_2, representing the distances via the alternate routes from P to the reference phase plane R. Since the lengths OR_1 and OR_2 are equal by construction, the path difference Q between the intersecting rays at P is $OP - OC$. If the distance PC be denoted by $2b$, then we have

$$Q = 2b(\csc 2\epsilon - \cot 2\epsilon) = 2b\epsilon \tag{3.2-1}$$

if terms higher than the second order are neglected in the trigonometric expansions. The path difference vanishes on the bisector of the angle 2ϵ, which approximately also bisects the line PC at the point O' since ϵ is small. Thus, if $Q = N\lambda$, there will be N fringes between O' and P and one has the relation

$$N\lambda = 2\epsilon b \tag{3.2-2}$$

---

[2] For a more complete discussion see especially J. Winckler [*5b*], W. Kinder [*9*], and E. Winkler [*10*], and further see Hansen [*6*], Schardin [*7*], Zobel [8*a*], Steegmaier [*11*].

[3] L. Mach [*12*] has given a simple geometrical theory of his interferometer. He discusses the influence of an extended source and the problem of treating the multiple reflections (half-reflecting coatings for beam splitters were not used until later [*6,44*]), as well as the adjustment of the instrument.

These equations hold only for the special case of rotation of *BS*2 alone. The fringe width $w = b/N$ is given by $w = \lambda/2\epsilon$. More generally, if ϕ is the angle between the interfering beams, the width is

$$w = \frac{\lambda}{\phi} \tag{3.2-3}$$

For example, in Fig. A,3.2d (right) the interference is produced by the rotation of two plates resulting in an angle $2\epsilon_1 + 2\epsilon_2$ between the interfering rays. In that case $w = \lambda/2(\epsilon_1 + \epsilon_2)$.

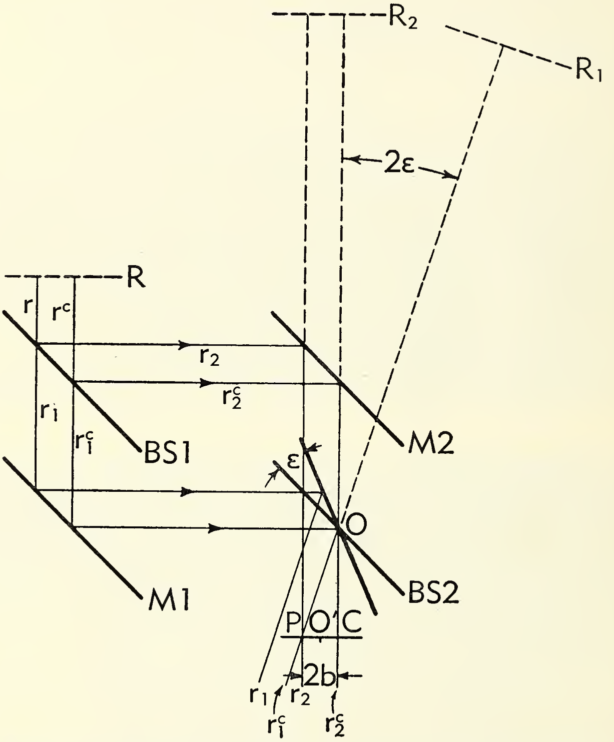

Fig. A,3.2a. Schematic arrangement for M-Z interferometer showing production of interference on the screen *PC*.

With this idealized instrument, interference will be observed everywhere in the field of overlap of the two beams. The fringe number at any point in the field may be computed by the difference in optical path to the two planes R_1 and R_2. Within the size limitations of the optical components, the analysis thus far is a two-dimensional one and therefore the interference phenomena should be identical in planes parallel to the plane of centers. Thus the fringes will appear as bands perpendicular to this plane, i.e. parallel, as always, to the axis of rotation (see Kinder [*9*] Sec. 7).

Interferometers of the M-Z type are made more flexible by providing for plate rotation about an axis in the plane of centers as well as about an axis perpendicular to this plane. This axis should also lie in the plane of the plate and thus would coincide with the trace of the plate as drawn in Fig. A,3.2a. For a small rotation the virtual images of the source lie above one another and fringes appear which are parallel to the plane of centers. The incident beam makes, in this case, an angle of 45° with the axis so that a rotation η turns the reflected ray through an angle $\sqrt{2}\,\eta$ rather than 2η.

FRINGE PRODUCTION WITH A LABORATORY LIGHT SOURCE. In practice, of course, one deals with an instrument having plates of finite thickness with some deviation from the desired plane-parallel homogeneous glass. In particular, difficulties arise from wedge-shaped beam splitters, imperfect and misaligned windows (see Art. 3.3), and beam splitters and mirrors with finite radii of curvature (see [*10,11*]).

However, it is the nonideal nature of the light source which determines the important modifications in the M-Z behavior. Firstly, the finite spectral width of any light source limits the number of obtainable fringes. Taking the limiting case of two line sources differing in wavelength by $\Delta\lambda$, the fringe pattern will "wash out" in the Nth order when the Nth bright fringe of one system falls on the Nth dark fringe of the other. From Eq. 3.2-3 the difference in fringe width Δw is given by $\Delta w = \Delta\lambda/\phi$ and the washout condition is expressed by $N\Delta w = w/2$ or $N = \lambda/2\Delta\lambda$. For $\lambda = 5000$A and $N = 250$ (500 fringes in all, as there would be N fringes on each side of the zero fringe) $\Delta\lambda$ must be limited to 10A.[4] The number of available fringes is important in the study of regions with a high density gradient, for then very narrow fringes are necessary to obtain accuracy. This has the further effect of minimizing the formation of fringe "islands," a phenomenon which may make the evaluation uncertain (see [*5b*]).

For analyzing the problems concerned with the finite *size* of the light source, the latter may be assumed to consist of several point sources. When interference is produced by collimated light from such a source, the amplitude at any point on the observation screen is the result of several pairs of interfering rays rather than of a single pair. Thus, one must be concerned with phase relations among the pairs as well as between the components of any one pair. For if the aperture of the system be given by $2\omega_0$ (Fig. A,3.2b), then interference is obtained only if the path difference between a pair of rays changes by no more than $\lambda/2$ over the entire aperture.

One seeks therefore a relation between the path difference and the angle $2\omega_0$. (Note that there is a whole set of beams—each beam consisting of parallel rays coming from one point of the source—entering the interferometer, the extreme beams making the angle $2\omega_0$ with each other.) Suppose that the central beam enters the interferometer at 45° and that the fringes produced are perpendicular to the plane of centers; then a simple geometrical consideration shows [*9*] that the total number of clear fringes in the field is

---

[4] For further consideration of illumination problems in connection with the M-Z see [*10,11,14*].

$$2N \leqq \frac{1}{\omega_0^2} \tag{3.2-4}$$

Thus, for example, if 400 clear fringes are desired, the maximum value for the aperture $2\omega_0$ is 0.1 radians or 5.7°.

A similar study shows that, when fringes are at some orientation other than perpendicular to the plane of centers, the number of distinct interference fringes will be smaller for the same aperture. For example, if the fringes are parallel to the plane of centers, then with a 45° interferometer the aperture $2\omega_0$ has to be 0.01 radians (0.57°) in order to obtain 100 fringes.

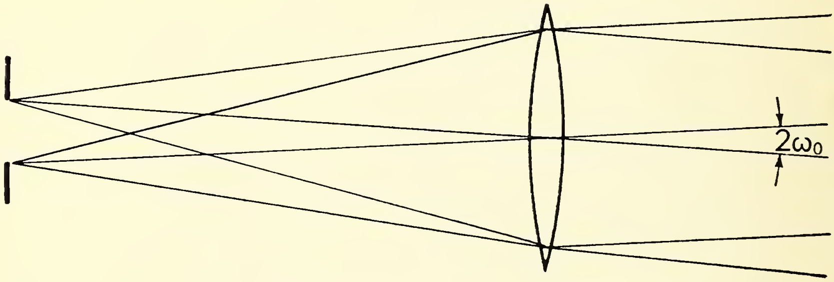

Fig. A,3.2b. Aperture of the light source.

A further disadvantage of fringes parallel to the plane of centers arises from the fact that the direction of fringes is always parallel to the resultant axis of rotation. Thus the plane of most distinct fringes would be parallel to the plane of $BS2$, and therefore at 45° to the central light ray. For applications it is awkward to have the observation screen or photographic plate at 45° to the light beam since this would distort the picture of the test section (see the following subarticle). It is true that the projections of such fringes will be observed on a screen placed normal to the light beam, but the extension of these fringes will be limited by their depth of focus.

The optimum source shape corresponding to any given fringe direction can be derived by a geometrical analysis [*10*] or preferably by vector analysis treatment [*14*]. The result is that the optimum shape of the source for fringes perpendicular to the plane of centers is a circle whose radius, as can be seen from Eq. 3.2-4, is inversely proportional to the square root of the number of desired fringes, and for any orientation the optimum area is one enclosed between two conics in the source plane.

Certain other features of the M-Z contribute to the limit of the allowed aperture.[5] One of these is the finite thickness of the beam splitters. Following an ordinary adjustment for fringes, the splitters may make a small angle ϑ with each other, with the result that the angle of incidence at the two beam splitters may be slightly different. This produces different paths in glass, such differences depending upon the actual angle of incidence, i.e. the path difference due to the glass will be different for rays incident at the angle α as compared with those at $\alpha + \omega$. The variation ΔQ in path difference is given by

$$\Delta Q = \omega \cdot \vartheta \cdot D \cdot F_{\alpha\alpha}(\alpha, n) \tag{3.2-5}$$

where ϑ is the difference in angle of incidence, α the angle of incidence for perfect adjustment, D the thickness of the splitters, n the refractive index of the glass, and

$$F_{\alpha\alpha}(\alpha, n) = \frac{\partial^2 F(\alpha, n)}{\partial \alpha^2}$$

with $F(\alpha, n) = \sqrt{n^2 - \sin^2 \alpha} - \cos \alpha$. Note that ΔQ is positive or negative according to the sign of ω.

A path difference between interfering rays is produced by a difference ΔD in thickness between the two beam splitters. Again, this path difference varies with ω since, for rays incident at the angle α, it is given by $Q = \Delta D \cdot F(\alpha, n)$ while for rays incident at $\alpha + \omega$ the corresponding expression is $Q = \Delta D \cdot F(\alpha + \omega, n)$. More explicitly, the difference between these two values for Q is

$$\Delta Q = \omega \cdot \Delta D \cdot F_{\alpha}(\alpha, n) \tag{3.2-6}$$

In the case of two plates both of thickness D but differing in refractive index by Δn, a path difference is again produced; this path difference varies with ω as follows:

$$\Delta Q = \omega \cdot \Delta n \cdot D \cdot F_{\alpha n}(\alpha, n) \tag{3.2-7}$$

The sum of all ΔQ should be less than $\lambda/2$ over the complete aperture $2\omega_0$ for obtaining interference.

OVER-ALL OPTICAL ARRANGEMENT FOR THE M-Z.[6] A typical optical assembly for the M-Z is shown in Fig. A,3.2c. The light from the light source *LS*, collimated into parallel beams by the lens *L*1, passes through the interferometer and then through the lenses *L*2 and *L*3 (often combined into a single camera lens),[7] which serve to focus the test plane *G* and the interference fringes there upon a photographic plate or ground glass screen *G'*. In the figure, *WS* represents the working section and *CC* the compensating chamber, the latter being used to produce equal optical paths in glass. (*L*1 and *L*2 are replaceable by suitable mirrors.)

---

[5] For a derivation of the results represented by Eq. 3.2-5 through 3.2-7, see Winkler [*10*].

[6] The importance of good focusing of the interference fringes and details for such optical arrangements are discussed by Hansen [*6*], Kinder [*9*], and J. Winckler [*5b*].

The arrangement of the interferometer plates themselves depends on the desired linear dimensions of the instrument and on the angle of incidence α. If the latter is other than 45°, the plate centers will occupy the corners of a parallelogram rather than a rectangle. This may be slightly more awkward for adjustment purposes. Also, at 45° the greatest lateral displacement between the beams is obtained, possibly an important factor in large installations.

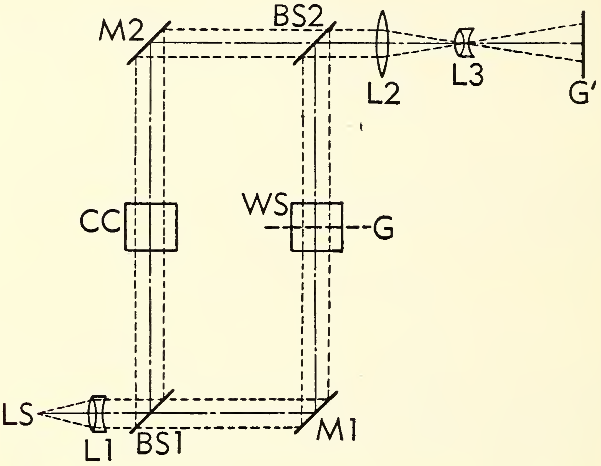

Fig. A,3.2c. Over-all optical arrangement for interferometry.

There are, however, definite advantages in using smaller values for α. One obtains a larger lateral field of view since this varies with cos α. It was seen above (Eq. 3.2-5 through Eq. 3.2-7) that α also enters as a parameter into relations affecting the quality of the fringe pattern. In all cases these conditions become less restrictive with decreasing α. The dependence is shown graphically in [*10*]. The value of α becomes particularly important when fringes are established at some oblique angle β with respect to the normal to the plane of centers. One finds that for a given value $2\omega_0$ of the aperture, the total number of fringes in the field of view decreases both with increasing α and increasing β, although for $\beta = 0$ the number is large for all values of α.

---

[7] In practice, the two-lens system proves to be rather convenient with respect to object-image geometry. The combination of field lens and small, highly corrected camera lens is also less expensive than one large highly corrected camera lens and more easily adapted to schlieren studies.

In practice the test section is placed in one arm of the interferometer and the fringes focused at the test section so that a combination interference-photograph may be taken for analysis. This is feasible because, as pointed out in Art. 3.1, a feature of the M-Z is its ability to produce fringes at any desired place. Fringes produced within the instrument are virtual since the interfering rays do not combine until they reach *BS*2. In the case of virtual fringes the rays appear to an observer to have intersected within the instrument and, since the place of intersection determines the location of interference,[8] a camera lens focused on the plane of apparent intersection will produce a real image of the virtual fringes on a photographic plate. Fig. A,3.2d taken from Kinder [*9*] shows plate orientations in which (left) real fringes are established beyond *BS*2 and (right) virtual fringes are established ahead of *BS*2. Note the linear representation of the instrument in this figure, the way it would appear to an observer beyond *BS*2 who did not know about the actual rectangular arrangement of the plates. Note also that, when interference is established by rotation of two plates as in Fig. A,3.2d, a further rotation of any plate changes the location as well as the structure of the fringes, in contrast to the case when the location of fringes is at the axis of rotation. In the latter case one-plate control is possible since the fringes will remain in focus while their structure is being altered.

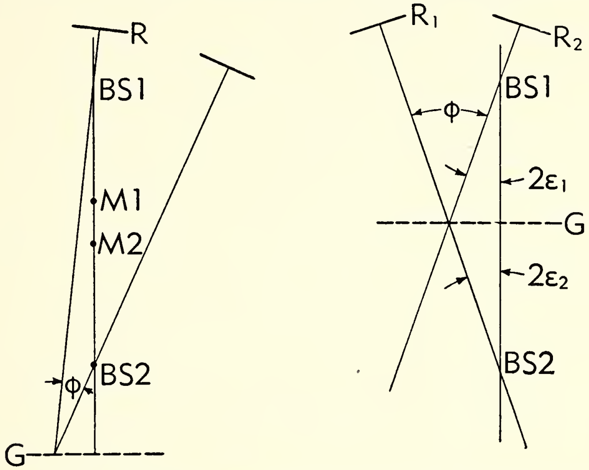

Fig. A,3.2d. Linear representation of the M-Z interferometer.

---

[8] Interferograms of gas flow having regions of high gradient of refractive index transverse to the light beam sometimes show poorer quality fringes as a consequence of the bending of one light beam and the resultant effect on the apparent place of intersection [*11*].

An instrument using single-plate control was suggested by Kinder and Hansen, [*15*] and [*9*], in which the dimensions of the rectangle shown in Fig. A,3.2a are changed so that $M2$ is twice as far as $M1$ from $BS2$. If the test plane is then located midway between $M2$ and $BS2$ such that the optical paths from $M1$ and from the test plane to the observation screen are equal, both planes are then in focus simultaneously on the screen, and the fringe pattern may be controlled by $M1$ without loss of focus. In this case the other three plates may be kept in perfect adjustment, allowing for transmission through the beam splitters at exactly the same incident angles and eliminating thereby the aperture limitation depicted by Eq. 3.2-5. Further, the plane containing the axis of rotation is the most favorable for obtaining a maximum number of fringes with a given aperture. The manipulation of this single-plate control instrument is much easier and simpler than the "conventional" arrangement and is recommended as superior for routine work. (Of course, single plate control would also be obtained by interchange of the above-mentioned dimensions, insertion of the test section between $M1$ and $BS2$ and use of $M2$ as the control mirror. While the aperture limitations of Eq. 3.2-5 could not then, in general, be avoided, rays strongly refracted by density gradients in the test section would travel to the camera without having to penetrate $BS2$ at significantly different angles of incidence.)

When determining the photographic parameters of the optical assembly, one must take the fringe system into account. Problems arising in this connection, such as the relative depth of focus of the interference fringes and the test object, as well as the effect of the aperture of the camera on the fringe contrast in the case of narrow fringes, are discussed by Kinder [*9*].

A,3.3. Construction of the M-Z Interferometer.

Required Properties of the Optical Elements [*4,6,7,8a,9,13*]. An ideal interferometer of the type described in Art. 3.2 would give exactly parallel fringes of constant width. Some M-Z instruments have actually approached this ideal to within 0.1 fringe. Clearly, this tolerance grows more difficult to attain as the size of the plates is increased because of the limited size of available pieces of glass with suitable homogeneity of refractive index for beam splitters and especially if the plane of centers is vertical because of the sagging of the plates. When additional windows are required, as in a wind tunnel or shock tube, these must also be of high quality. A suitable quality glass is BSC1 or BSC2 (Bausch and Lomb notation). In order that the refractive index variation distort the fringe pattern by no more than 0.1 fringe, such variation must not be larger than about 2×10^{-6} for green light and for a plate thickness of 1 inch. The thickness of the plates depends on their size, as larger plates must also be thicker for purposes of grinding and polishing and for protection against too much sagging when mounted with the planes of the plate surface at some angle to the vertical.

M-Z interferometers in actual aerodynamic use up to the year 1953 contain plates up to 9 in. in diameter, with larger ones now under construction. In practice one may be content with a pattern uniform to within a quarter of a wavelength inasmuch as in most cases the position of the displaced (flow) fringes must be measured relative to the undisturbed pattern. For circular plates the quality can often be improved by rotation of one or more components about an axis perpendicular to the plate surface, compensating in this way for the inhomogeneities.[9] The thickness of the two beam splitters should be the same within about 10 wavelengths; otherwise, because of the dispersion by the glass, the path difference would depend on the wavelength to such an extent that the quality of the useful "white light fringes" (see below and Art. 3.4) formed in the neighborhood of zero path difference would be marred. The requirements for the windows of the wind tunnel and of the compensating chamber are similar to those for the beam splitters. Here again, small deviations from plane parallelism, if not too irregular, can often be compensated by suitable relative orientation of circular windows about an axis perpendicular to the surface. Deviations from equal thickness of the four windows may be compensated by a small inclination of the compensating chamber with respect to the light beam. When ordering the plates one should specify them in terms of uniformity of the fringes rather than the properties of the individual plates. Useful interferograms have been obtained with selected plate glass for the windows. For some applications the windows must be of large thickness to sustain sizeable pressure differences.

A suitable coating of the front surface of the beam splitters is important for producing a fringe system having sufficient intensity and for avoiding an undesirable secondary fringe system caused by reflection from the rear surfaces of the beam splitters. The question of intensity is critical since one often requires a monochromatic light source of small size and extremely short duration (10^{-6} seconds or less) for satisfactory flow interferograms (see A,2.4). For special purposes a rotating mirror and camera lens combination is used to reduce the effective light source duration by stopping the motion of the image on the film (Bergdolt, Greenwald, and Slater [*16*]). This is especially important for obtaining pictures of the air density around projectiles flying at high speed. (When fired in atmospheric air at Mach number 4 the projectile would travel through 1.4 mm in 10^{-6} seconds.) Coatings have been developed which are nonmetallic and very efficient, absorbing just a few per cent while giving nearly 50 per cent transmission and reflection. These coatings operate on an interference principle so that each is designed for a restricted wavelength region and for a given angle of incidence; such quantities have therefore to be specified when plates are ordered.

---

[9] Zobel [*8b*] has devised a special method for correcting and improving the fringe pattern by a controllable deformation of the reflecting surfaces.

The full mirrors of the interferometer should reflect more than 90 per cent of the light; on the other hand, if they are adjusted by the method of transmitted light (see below) these mirrors must possess at least a 1 per cent transparency. The rear surfaces of the beam splitters and every window and lens surface should have a nonreflecting coating for the wavelength to be used.

MOUNTING AND CONTROL OF THE PLATES [*8a,10,11,17,18a,30*]. Adjustment of the M-Z instrument requires that each of the plates permit rotation around a horizontal and a vertical axis. In order to avoid any combined translation and rotation, the axis of rotation should lie in the plane of the reflecting surface. Further, one of the plates must be provided with a mechanism for pure translation in order to vary the path difference. The second beam splitter (*BS*2 in Fig. A,3.2a) is usually chosen for this function.

Improper mounting of a plate will produce strains in the glass with a resultant adverse effect on the fringes. The use of snug-fitting rubber gaskets around the rim of the plate should be avoided. The plate diameter should be, for example, 0.003 in. less than the diameter of the holder, with the use of paper gaskets around the rim to provide a loose fit. (For further details of mounting see [*11*].)

It is important that the controls be sufficiently sensitive to provide for a fine adjustment of the fringes as required in the everyday operation of the instrument. For major adjustments, such as the initial one, both coarse and fine controls are desirable. Remote control by use of motors provides for greater flexibility in the relative position of operator and interferometer. The motor may be coupled directly or by a flexible cable to, say, a micrometer head whose shaft then provides the turning moment for a gimbal ring. Synchronous motors of the selsyn variety are convenient, as are a.c.-clock motors which are internally geared down to give shaft speeds of the order of 1 rpm. If the conventional two plate-adjustment is used, then motor control is desirable on both plates. Together with the translation motor, this would give five individual motor controls. If the Kinder arrangement (see Art. 3.2) is used, this reduces to three controls. To decide on the gear ratio one must choose a desired rate of change of fringe width which can be related to the motor speed, the moment arm at the mirror, and the pitch of the micrometer screw.

ADJUSTMENT OF THE M-Z. The four plates have to be adjusted parallel to one another and in such a way that the path difference between the two interfering beams is zero. A small rotation of one of the four plates will then produce fringes whose structure and location must be controlled. This adjustment requires practice, but can be done in different ways and has often been described; see especially [*6,9,17*], also [*4,5,8,44*]. It may suffice here to make some remarks based on practical experience. If the centers of the four plates of the M-Z lie in a vertical plane and the angle of incidence is 45°, their adjustment is simplified by using a cup with mercury for defining a horizontal plane, and by the help of a telescope, which should be supplied with a water level for horizontal and vertical adjustment and with a Gauss eyepiece plus a small lamp for autocollimation. This is illustrated in Fig. A,3.3 (top). Fig. A,3.3 (bottom) shows a procedure for making the two mirrors parallel (see also [*6,53*]). The latter adjustment requires that $M1$ allow some transmission. Another method uses a good pentaprism on an optical bench [*17*]. In any case it is good practice when first mounting the four plates of the M-Z to do it in such a way that the length of the air path of the two interfering beams is as nearly equal as can be done mechanically. A detailed description of the adjustment for single-plate control (Kinder

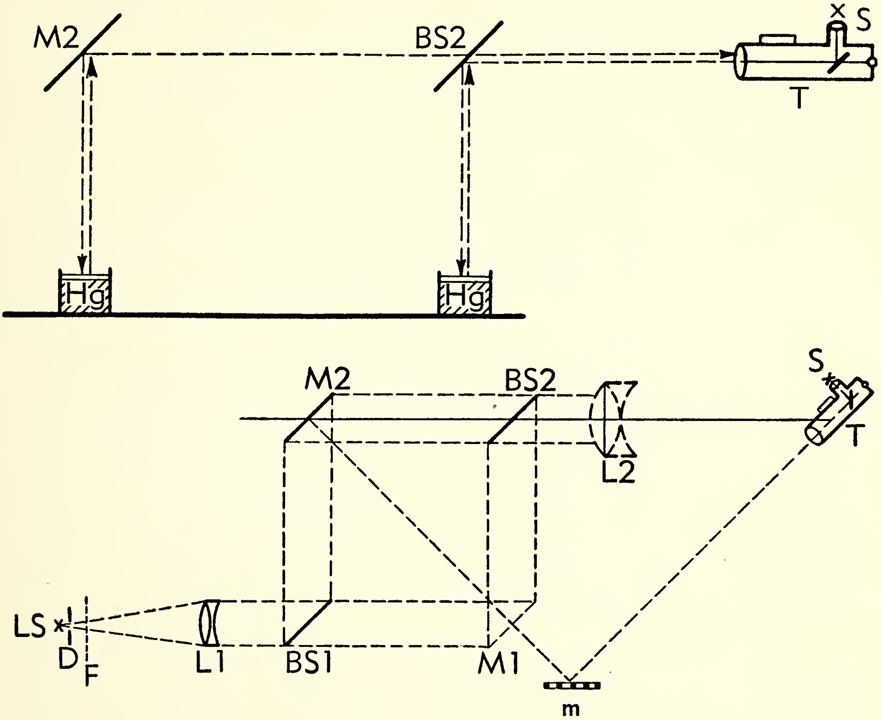

Fig. A,3.3. Adjustment of the interferometer.

arrangement) is given in [*9*], but a simpler procedure is possible in practice [*52*]. The last step of the adjustment consists always in equalizing exactly the path length of the two interfering beams so that the "central" or "white light" fringes from an incandescent lamp or of a tungsten arc appear. Much time can be saved, at least at the first trial, by use of a spectroscope, for example, a small grating, or better, a hand spectroscope. By focusing three or four sharp horizontal fringes on the vertical slit of the hand spectroscope, one can usually see oblique fringes. To adjust the interferometer for central fringes the last beam splitter $BS2$ is translated until the fringes seen in the spectroscope are horizontal. Then the optical path difference is the same for all wavelengths and the adjustment is finished.

Plate A,3.3 shows the optical assembly of the interferometer used in conjunction with a supersonic intermittent wind tunnel by Ladenburg and his group [*23*].

Modifications of the M-Z. Since good beam-splitting plates of more than about 12 in. diameter have not been produced so far, modifications of the M-Z have been proposed which use large plane and concave mirrors, but only small beam splitters. The interferometer suggested by W. E. Williams [*20*] has the disadvantage that the evaluation of the data is extremely difficult, since divergent light passes twice through the disturbance to be investigated. In the instrument suggested by Clippenger and constructed by Bergdolt [*21*], parallel light passing only once through the disturbance is used. The diameter of the beam-splitting plate is only about one-third of the width of the illuminated working field. The original arrangement is shown schematically in Bergdolt's paper. In the instrument as actually constructed the number of optical parts is reduced to simplify the construction, but the restrictions and conditions for such instruments are not fully explored as yet.

A different kind of interferometer has been suggested recently by Kraushaar which does not use beam splitting plates, but two small replica diffraction gratings and two large concave mirrors [*22a*]. It is an outgrowth of a modified Ronchi-schlieren apparatus. Promising results are shown by preliminary tests [*22c*] on an instrument of this type which was built at Langley Field.

During the preparation of this article, the authors' attention was called to another very promising technique that can be classed as interferometric in nature, developed by S. F. Erdmann in Amsterdam [*22b*]. He uses the phase contrast method modified in such a way as to produce a system of interference fringes which permits the quantitative evaluation of densities in a flow field. This new method is, according to the author, rather insensitive to acoustical or mechanical oscillations because the two light beams producing interference are separated from each other only just before entering the focusing optics. (See also [*52,55*]).

A,3.4. Evaluation of Interferograms.

Measurement of Fringe Shifts. Quantitative studies are performed by measuring the fringe shift S in the field under investigation with respect to a reference field of known density. Table A,3.4 gives reference fields for typical applications and the technique for relating the fringe number, and therefore the density (according to Eq. 3.4-2), in the field under investigation to that in the reference field. In general, fairly narrow fringes are used, the width depending on the problem investigated. For obtaining the fringe shift it is necessary to number the fringes and read their positions. This is done by use of a comparator with micrometer motions in two orthogonal directions. A good but expensive instrument is the Bausch and Lomb contour projector, which gives an enlarged image on a ground glass screen.

Table A,3.4

Application	*Reference field*	*To relate unknown field with reference field*
1. Axially symmetric jet discharging into atmosphere	Undisturbed atmosphere	Use displacement fringes to map field with correspondingly numbered flow and no-flow fringes. White light fringes for discontinuities.
2. Projectile in free flight	Undisturbed atmosphere	Use displacement fringes to map field with correspondingly numbered flow and no-flow fringes. White light fringes for discontinuities.
3. Two-dimensional shock tube	Undisturbed gas ahead of shock	White light or "offset" method to follow fringes across shock.
4. Wind tunnel	Compensating chamber or undisturbed flow	White light with displacement fringes or pressure measurements with contour fringes.

If the plate or film is developed correctly, the fringe maxima and minima are equally wide; two readings per fringe are feasible, corresponding to a setting of the instrument cross hairs on the center of the maximum and of the minimum. This method was found by J. Winckler [*5b*] to give better results than an automatic arrangement such as a recording photodensitometer. The variable fringe spacing and contrast as well as the formation of so-called "islands" render the automatic methods less effective. A fringe-shift plotting device ("fringe pattern analyzer") for use with a comparator has been developed by Kendall [*28*] at the Naval Ordnance Laboratory. In his instrument the micrometer screw of the comparator is mechanically coupled to a rotating recording drum.

For the cases 1 and 2 of Table A,3.4 there are undisturbed fringes in the flow picture (see Plates A,3.5b, c, j) corresponding to atmospheric density. This undisturbed pattern may be extrapolated over the flow field and the relative shift obtained between the extrapolated and the actual flow pattern. It is more accurate to take a separate no-flow picture so as to avoid errors arising from small nonuniformities in the undisturbed fringe pattern [*35,40*]. By use of a matching pair of grids and slots the no-flow and flow pictures may be obtained on one plate for analysis (see Plate A,3.5c).

In cases 3 and 4 of Table A,3.4 the reference density, in general, is not atmospheric, but is obtained also from pressure and temperature measurements. In the wind tunnel (case 4) the reference field is not visible on the flow picture; one must take a no-flow picture where the working section and compensating chamber have the same density. The shift of the flow fringes with respect to the no-flow fringes gives the difference between the densities in the compensating chamber and in the working section. To obtain this fringe shift, the fringes on both pictures must be correspondingly numbered with the aid of some device, for example, the white light fringes: a white light source gives sufficiently few fringes (see Plate A,3.5f, right) to identify the zero order fringe.

If shocks are present, white light is again useful in order to follow the fringes through the discontinuity; in the case of a plane shock, the "offset" method may be used, which consists of placing the light source off axis. (See [*27*], Fig. 6.)

Another technique consists of measuring the static pressure and then computing the corresponding local density according to aerodynamic relations. The density in the entire field may then be obtained either by the "displacement" fringes described above or, in the two-dimensional case, by use of "contour" fringes. These are constant density contours (isopycnals) obtained by adjusting all four interferometer plates exactly parallel to one another. If the density field is uniform, it will be covered by a single fringe; in a nonuniform field the fringe pattern consists of these contour fringes. Constant density contours may also be obtained from displacement fringes by superimposing a no-flow fringe pattern upon its corresponding flow picture.[10] Those regions where fringes are just 180° out of phase then become visible as gray strips which represent lines of constant fringe shift and therefore constant density. Under good conditions such lines may be located with an accuracy of $\pm\frac{1}{20}$th fringe (see Plate A,3.5i). This method is less satisfactory in regions where fringes on the superimposed pictures run nearly parallel or have widely different spacing.

COMPUTATION OF DENSITY. If x and y be the coordinates in a plane normal to the direction z of the light, then the change Q in optical path of a light ray intersecting the plane at the point x, y is given by

---

[10] This method has been devised by Bleakney and his group.

$$Q(x, y) = \int_0^L [n(x, y, z) - n_0]dz \tag{3.4-1}$$

where $n - n_0$ is the change of refractive index caused by some disturbance in the region $0 \leqq z \leqq L$. The index n is related to the density of a gas by the Gladstone-Dale equation

$$n - 1 = K\rho \tag{3.4-2}$$

where K is constant for a given wavelength of light and a given gas over a large range of pressures. Further, it is convenient to express the path change Q by the relation $Q = S\lambda$.

If the index n is independent of z, the integral of Eq. 3.4-1 becomes a simple product, and the following relation is obtained between ρ and S:

$$\rho(x, y) = \rho_0 + CS(x, y) \tag{3.4-3}$$

where the constant $C = \lambda/KL$.

Eq. 3.4-1 may also be evaluated when the disturbance has axial symmetry as in the case of a jet issuing from a round orifice. Then each light ray passes along a chord of the circular jet (see Fig. A,1.3c). If the flow direction be x and the distance of the chord from the jet center be y, then

$$S(x, y) = \frac{2}{\lambda} \int_y^R [n(r, x) - n_0] \frac{r\,dr}{\sqrt{r^2 - y^2}} \tag{3.4-4}$$

where $r^2 = y^2 + z^2$ and R is the radius of the jet [*7,39,40*]. The methods of solution of this integral are discussed in Art. 3.1. E. H. Winkler [*19*] has considered the evaluation of Eq. 3.4-4 as a Stieltje's integral and constructed a special planimeter for its computation.

A particular technique has been developed to test for conical flow. This is defined as a flow in which physical variables, including the density, are constant along straight lines emanating from a point called the vertex. Giese, Bennett, and Bergdolt [*31*] have shown that if x be the axis of the flow and y be normal to it, then the "reduced" fringe shift $S(x, y)/x$ is a function of y/x, if the origin of coordinates is located at the vertex of the cone. Thus, for strictly conical flow, the reduced fringe shift for all points x, y in the flow should lie on a single curve when plotted against y/x.

If the flow system is an isentropic one and the stagnation values p^0 and T^0 of the pressure and temperature are known, it is possible to compute values of pressure p, temperature T, velocity u, and Mach number M from the determined densities in the flow from the relations

$$\frac{p}{p^0} = \left(\frac{\rho}{\rho^0}\right)^{\gamma}; \qquad \frac{T}{T^0} = \left(\frac{\rho}{\rho^0}\right)^{\gamma-1}$$

$$u = \sqrt{2c_pT^0\left(1 - \frac{\rho}{\rho^0}\right)^{\gamma-1}} \tag{3.4-5}$$

$$M = \sqrt{\frac{2}{\gamma - 1}\left[\left(\frac{\rho^0}{\rho}\right)^{\gamma-1} - 1\right]}$$

where γ is the ratio of specific heat at constant pressure c_p to that at constant volume c_v. The superscript 0 represents stagnation conditions.

Computations of other physical variables have been made from evaluated densities in boundary layers where the flow is no longer isentropic. For example, the temperature profile is given as the inverse of the density distribution if one assumes constant pressure through the layer (an assumption which may be tested by a pressure hole in the wall). The computation of velocity profiles is a more complicated matter. (See for example [*32*,*26*].)

Precision of the Interferometric Method. A conservative value for the tolerance δS of measured fringe shifts is 0.1 fringes. Eq. 3.4-3 gives for the uncertainty of the density change $\delta(\rho - \rho_0) = 0.1C$. By neglecting $\delta\rho_0$, the following relation is obtained for the per cent uncertainty in the density measurement of the undisturbed flow:

$$100\frac{\delta\rho}{\rho} = 10\frac{C}{\rho} \tag{3.4-6}$$

To obtain the variation of $\delta\rho/\rho$ with Mach number M one writes $\delta\rho/\rho = \delta\rho/\rho^0 \cdot \rho^0/\rho$; the ratio ρ^0/ρ as a function of M can be found in available tables,[11] and ρ^0, the stagnation density, is set at some characteristic value, say, 1.205×10^{-3} g/cm^3 corresponding to standard pressure $p^0 = 76.0$ cm Hg and room temperature $T^0 = 293°$K. Assuming isentropic flow from the settling chamber, one may use Eq. 3.4-6 to obtain a curve of $100\delta\rho/\rho$ versus M, shown in Fig. A,3.4a. In this figure the following values are used: $\lambda = 5.460 \times 10^{-5}$ cm, $K = 0.227$ cm^3/g, $L = 10.00$ cm, $C = \lambda/KL = 2.405 \times 10^{-5}$ g/cm^3. The density change corresponding to the tolerance $\delta S = 0.1$ fringe is then 2.4×10^{-6} g/cm^3 or $0.002\rho^0$.

Note that the percentage uncertainties given in Fig. A,3.4a are computed for atmospheric density in the settling chamber. For larger Mach numbers, above say 4 or 5, the actual density there is usually much higher. For example, at $M = 6.5$ one might use[12] 40 atm and 700°K in the settling chamber so that the uncertainty $100\delta\rho/\rho$ would not be

---

[11] See for example *NACA Technical Note 1592.* Aug. 1948.
[12] See for example *NACA Technical Note 2171.* Sept. 1950.

55 per cent as in Fig. A,3.4a, but $\frac{55}{17}$ or about 3.2 per cent. On the other hand, for small Mach numbers the stagnation density might be lower than atmospheric, so that the uncertainty would be larger than in Fig. A,3.4a.

The interferometric study of the density *distribution* in a flow field is of course more accurate the larger the variation of density. Consider,

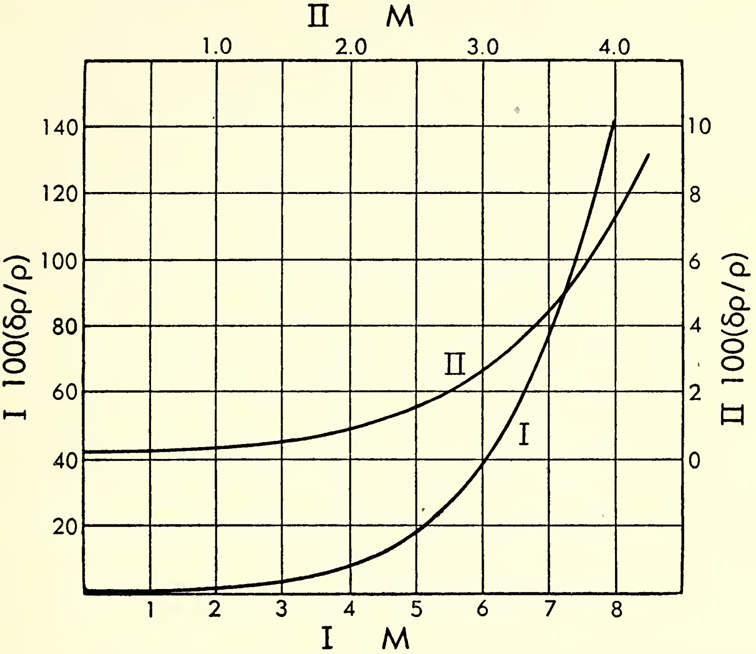

Fig. A,3.4a. Percentage uncertainty in the interferometric measurement of a density ρ as function of Mach number M assuming $\delta\rho = 2.40 \times 10^{-6}$ g/cm³ $= 0.002\rho^0$, corresponding to a stagnation density $\rho^0 = 1.20 \times 10^{-3}$ g/cm³ at $p^0 = 76$ cm Hg and $T^0 = 293°$K. Graph II gives values for M between 0 and 4 on a larger scale than I.

for example, a normal shock wave. The density difference across the shock $\rho_2 - \rho_1$ can be expressed in terms of the upstream Mach number M_1 and the stagnation density ρ^0, provided that there is isentropic expansion from the settling chamber down to the shock:[13]

$$\rho_2 - \rho_1 = \left(\frac{\rho_2}{\rho_1} - 1\right)\frac{\rho_1}{\rho^0}\rho^0 = \rho^0 \frac{M_1^2 - 1}{\left(1 + \frac{\gamma - 1}{2} M_1^2\right)^{\gamma/\gamma-1}} \tag{3.4-7}$$

The uncertainty in measuring the density difference $\rho_2 - \rho_1$ is

$$\delta(\rho_2 - \rho_1) = \sqrt{2}\,\delta\rho$$

---

[13] The tables of *NACA Technical Note 1592* also contain the values of ρ_2/ρ_1 as function of M_1.

since the measurement of ρ_2 as well as of ρ_1 involves the same $\delta\rho$. Curve I of Fig. A,3.4b shows the percentage uncertainty $100\delta(\rho_2 - \rho_1)/(\rho_2 - \rho_1)$ as function of M_1 if 0.1 fringe is assumed again as the tolerance of measured fringe shift. This curve shows that an uncertainty of 0.7 per cent is to be expected in the measurement of the difference $\rho_2 - \rho_1$ at $M_1 = 2$ and that the uncertainty would increase to 17 per cent at

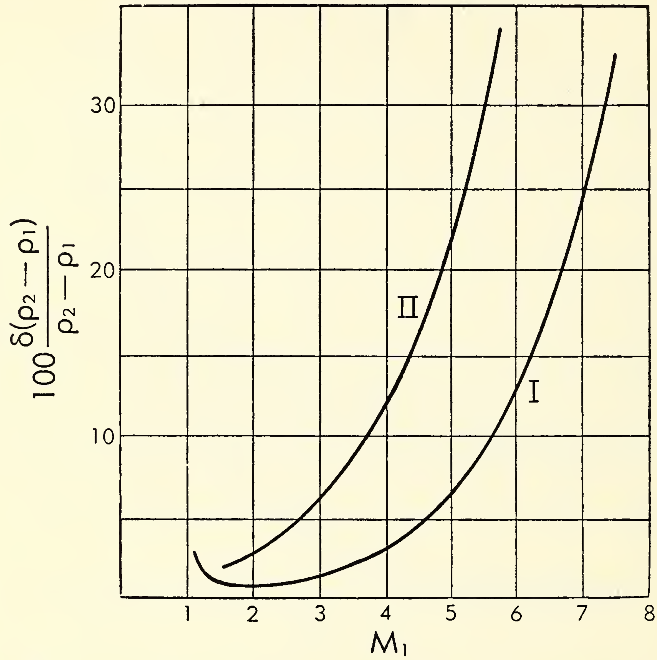

Fig. A,3.4b. Percentage uncertainty as function of M_1 in measuring the density change $\rho_2 - \rho_1$ (I) across a normal shock and (II) across an oblique shock produced by a wedge of half apex angle $\theta = 10°$, assuming atmospheric density in the settling chamber.

$M_1 = 6.5$, if the stagnation density were atmospheric. However, as mentioned above, at large Mach numbers one would use much higher density in the settling chamber. At the conditions assumed before, the uncertainty in the measurement of the density change across a normal shock at $M_1 = 6.5$ would be only 1 per cent.

Of more practical value is the expected accuracy in measuring the density change $\rho_2 - \rho_1$ across an oblique shock produced, for example, by a wedge. For a given apex angle one obtains the density ratio ρ_2/ρ_1 in the same way as above using, instead of the Mach number M_1, its component $M_1 \sin \beta$ normal to the shock wave where the angle β between shock and flow can be easily computed or obtained from tables. Curve II of Fig. A,3.4b gives the percentage uncertainty as function of M_1 in measuring the change $\rho_2 - \rho_1$ across an oblique shock due to a wedge of half-angle $\theta = 10°$. The uncertainty is of course much larger than for a normal shock at the same Mach number, since the density change is much smaller for an oblique shock; but, again, larger densities than atmospheric in the settling chamber would diminish the uncertainties correspondingly (see also E. M. Winkler's report [*34*]).

The boundary along a flat plate in a uniform stream is chosen as another illustration. In such studies one may inquire how accurate the interference method is in determining the density change across the boundary layer as function of the external stream Mach number M_e. For present purposes it is sufficient to choose the simplest assumptions and boundary conditions, namely the plate temperature $T_w = T_0$, the pressure p_e as constant through the layer, the Prandtl number $Pr = 1$, and no pressure gradient in the direction of the flow. Then the density difference between external flow (index e) and wall (index w) $\rho_e - \rho_w$ is given as

$$\rho_e - \rho_w = \left(1 - \frac{\rho_w}{\rho_e}\right)\frac{\rho_e}{\rho^0}\rho^0 = \rho^0 \frac{\frac{\gamma - 1}{2} M_e^2}{\left(1 + \frac{\gamma - 1}{2} M_e^2\right)^{\gamma/\gamma-1}} \qquad (3.4\text{-}8)$$

The uncertainty of the interference method in measuring this density change

$$\frac{\delta\rho}{\rho_e - \rho_w} = \frac{0.1C\left(1 + \frac{\gamma - 1}{2} M_e^2\right)^{\gamma/\gamma-1}}{\rho^0 \frac{\gamma - 1}{2} M_e^2}$$

is about 2 per cent at $M_e = 2$ and increases to about 10 per cent at $M_e = 4$.

So much for the sensitivity of the interferometric method. Some additional accuracy problems deserve mention at this point. The first of these is a refraction error due to the curving of the light rays in any flow region containing an appreciable density gradient transverse to the light path [*35,36,37*]. Such gradients are found in boundary layers, shock waves, and strong expansion waves. If the corresponding gradient of the refractive index is assumed to be parallel to the y direction, then the radius of curvature R of the path is given by

$$\frac{1}{R} = \frac{1}{n}\frac{dn}{dy}\cos\theta = \frac{y''}{(1 + y'^2)^{\frac{3}{2}}} \qquad (3.4\text{-}9)$$

where θ is the angle between the light path and the z direction and $y' = dy/dx$. The curved light path between two points A and B is found to be

$$\widehat{AB}_{\text{opt}} = n(0)\int_A^B (1 + y'^2)dz$$

when $n = n(0)$ for $y = y' = 0$ at $z = 0$. The difference between this actual path and the no-flow path obviously will depend on the depth L of the flow field and the gradient of the index, but involves as well the thickness of the glass exit window and the lens system, which focuses a definite plane in the flow upon the photographic plate. If h is the distance of this plane from the exit window, it has been shown by Wachtell [*37*] that the density error $\delta\rho$ due to the curvature of the light beam in a boundary layer (b.l.) is given in first approximation by

$$\delta\rho = LK\left(\frac{d\rho}{dy}\right)^2\left(\frac{h}{2} - \frac{L}{6}\right) \tag{3.4-10}$$

The result of a detailed investigation [*37*] is that for $h = L/3$ the error $\delta\rho$ will be less than $\frac{1}{20}(\rho_e - \rho_w)$ in the laminar case provided

$$\frac{\epsilon}{L} \geqq \pi\sqrt{\frac{K}{5}(\rho_e - \rho_w)}$$

ρ_e is the "free stream" density (outside the b.l.), ρ_w the density at the wall, ϵ the thickness of the b.l., and K the constant of the Gladstone-Dale equation (Eq. 3.4-2). For turbulent flow, multiply the above expression on the right by about 0.8.

In the analysis of an enclosed flow by the use of windows there will be a deviation from two-dimensionality due to boundary layer on the glass walls. Because of the lower density in the layer, the free stream density computed from the observed fringe shift by means of the glass-to-glass distance will be too low. Some indication of the glass boundary layer density profile must be obtained in order to make a correction. The true external density ρ_e is related to the apparent density ρ_e' as computed from the observed fringe shift by Eq. 3.4-3 in the following manner [*35*]:

$$\rho_e = \rho_e' + \frac{2}{L}\int_0^\epsilon \Delta\rho(z)dz \tag{3.4-11}$$

where ϵ is the width of the glass boundary layer and $\Delta\rho(z)$ is the density difference between the free stream density ρ_e and the value in the boundary layer z mm from the glass wall.

A further difficulty occurring in the study of boundary layers in rectangular channels is the so-called corner effect due to two intersecting boundary layers. An analysis of this effect for the case of a small channel [*35*] showed that it caused only a small ambiguity in the region of the boundary layer profile; however, the corner effect may become appreciable if the thicknesses of the intersecting boundary layers are more than 10 per cent of the depth L of the light path.

In the case of axially symmetric flow, computational errors arise in the neighborhood of shocks or other high density gradients, leading to so-called "overshooting" of the computed densities [*5a*]. Another difficulty lies in the poorer precision of the computed results near the axis of the flow. A discussion of these problems is given in [*39*;*46a*,*b*].

It has to be kept in mind that the interferometric method integrates over the length of the light path and does not show possible inhomogeneities. This constitutes, in a sense, the basic accuracy problem, as the fringe measurement procedure itself can be made with great accuracy [*56*].

A,3.5. Applications. Before discussing the applications of interferometry to supersonic phenomena it may be mentioned that the M-Z interferometer has also been used successfully for subsonic flow; see especially Zobel's extensive studies on a large subsonic wind tunnel [*8c*] and the investigations of heat transfer in free convection by Kennard [*18a*] and by Eckert and Soehngen [*18b*].

AXIALLY SYMMETRIC JETS. The M-Z interferometer was applied to axially symmetric supersonic air jets at first by Mach himself [*38*], later in detailed investigations by Ladenburg, Van Voorhis, and Winckler [*5*,*40*]. By use of the special evaluation methods described in Art. A,1.3 and A,3.4, these authors obtained the complete density distribution in a series of jets issuing from a high pressure supply tank at pressures between 20 and 110 lb/in.^{2} Plate A,3.5a is a shadowgram of an air jet at 70 lb/in.^{2} gauge tank pressure; Plate A,3.5b an interferogram of an air jet at 60 lb/in.^{2} gauge tank pressure. The fringes are oriented parallel to the gas stream and perpendicular to the plane through the centers of the interferometer plates; such fringes are sharper than those parallel to the centers (see Art. 3.2). Although the density distribution is symmetric, the fringes appear asymmetric with respect to the axis of the jet, due to the general shifting of all fringes within one cross section to the left or right depending on whether the density in that part of the jet is larger or smaller than the density in the surrounding room air. Fig. A,3.5a shows the evaluated density distribution in this jet. The pressure, temperature, velocity, and Mach number in the jet can be computed from the known pressure and temperature in the supply tank by use of the adiabatic relations and the energy law $u^2/2 + c_pT = c_pT^0$.

Instead of the inhomogeneous jet one obtains an homogeneous jet of constant density and Mach number, a kind of open wind tunnel, by replacing the cylindrical tube connected through a valve with the supply tank by an axially symmetric Laval nozzle, and by regulating the tank pressure according to the Mach number M so that the jet escapes at atmospheric pressure from the orifice [*40*]. By suspending cylindrically symmetric models in this homogeneous jet one can study the supersonic flow around such models by interferometry and compare the evaluated density and pressure distribution with theory. Plate A,3.5c is such an

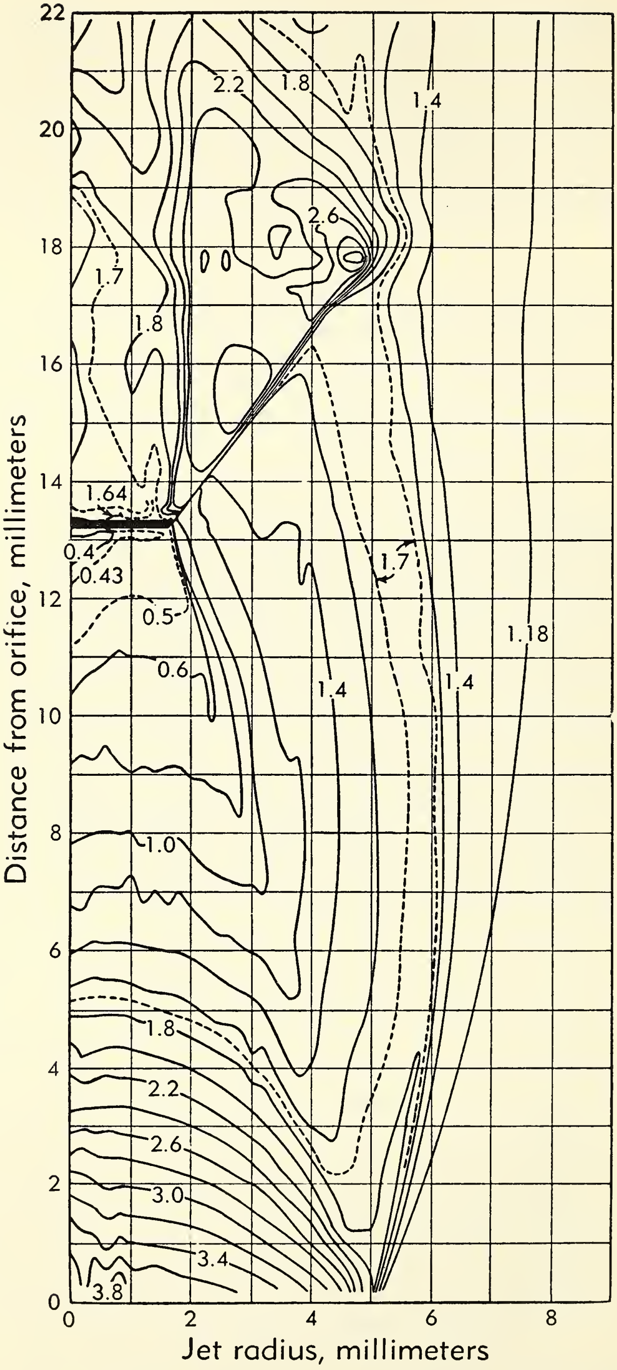

Fig. A,3.5a. Density distribution in the same jet as in Plate A,3.5b. The density contours (isopycnals) are labeled in mg/cm^3; they also represent isobars.

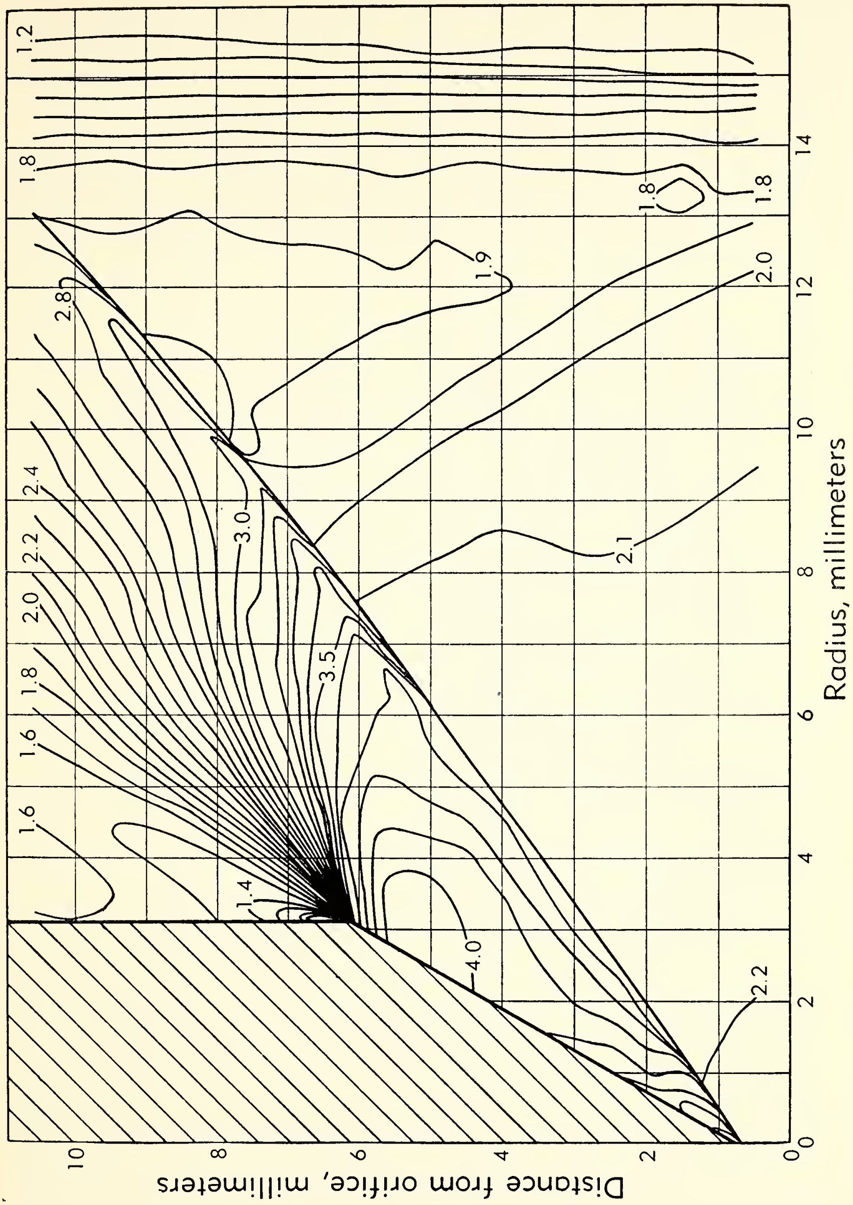

Fig. A,3.5b. Isopycnal chart obtained by evaluation of interferogram Plate A,3.5c. Contours labeled in mg/cm³.

interferogram of the flow around a cone cylinder of 30° half-angle, and Fig. A,3.5b gives the evaluated density distribution. Detached shock-wave patterns, for example around a sphere, may also be studied in this way [*40,41*].

Two-dimensional Channel Flow and Wind Tunnels. Interferograms of two-dimensional flow, which are much simpler to evaluate than interferograms of axially symmetric flow, can be obtained with an apparatus made by attaching steel nozzle blocks to the cylindrical outlet of the supply tank by means of a suitable transition section and by using plane-parallel glass plates for the other sides of the channel. (See Bershader [*35*] and Fig. A,3.5c.) The gas discharges through a valve, the cylindrical tube, and the two-dimensional channel into the atmosphere. The flow is studied by sending the light of one beam of the interferometer through the glass plates while the other beam traverses a "compensating chamber" furnished with two glass windows of the same thickness. As the figure shows, the glass walls extend beyond the orifice of the channel proper so that the flow remains two-dimensional between the plates in spite of being open to the atmosphere. By replacing the divergent channel

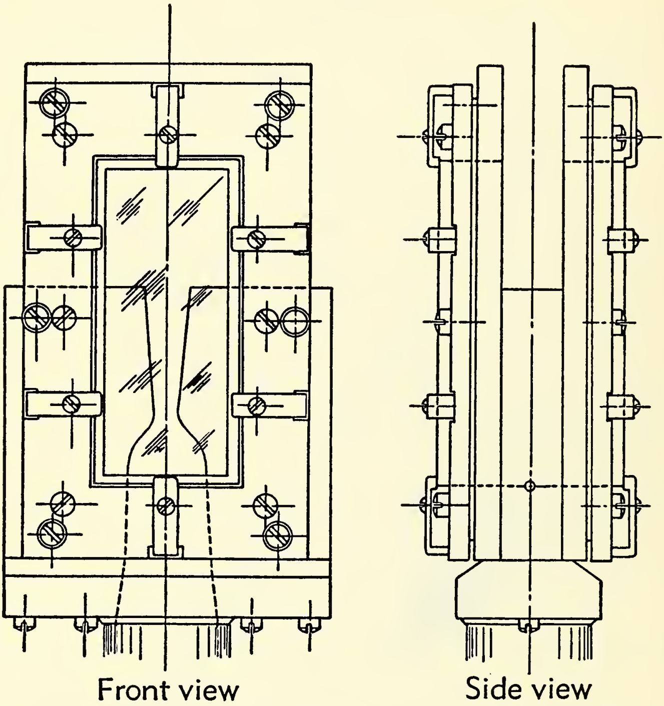

Fig. A,3.5c. Front and side view of two-dimensional channel, air discharging into the atmosphere. Glass walls extend beyond orifice of channel proper.

shown in Fig. A,3.5c with a Laval nozzle, one obtains an intermittent two-dimensional wind tunnel open to the atmosphere. Plate A,3.5d shows interferograms of the orifice section of the Laval nozzle (left) before and (right) after it was improved [*35*]. The weak shocks within the channel visible in the former, corresponding to pressure changes of about 2 per cent, are not visible any more in the latter. Remarkable is the sudden bending of the horizontal fringes in the "boundary layers" at the metal walls as well as at the boundary between the flow and the outside atmospheric air at rest. This fringe curvature is caused by the drop in density associated with a temperature increase within the layer.

If regular wind tunnels are furnished with good optical, preferably plane-parallel, glass windows (see Art. 3.3), the flow in the tunnel and around objects in the channel can be studied in detail with the M-Z interferometer. Before and during the last war, Zobel, using a subsonic wind tunnel of the *Luftfahrtforschungsanstalt* at Braunschweig, studied interferograms of subsonic flow around various two-dimensional models such as cylinders, Joukowski profiles, and NACA radiator cowls [*42*]. Pack and Groth [*24*] used a large supersonic tunnel at Braunschweig and studied the flow around wedges of 20° and 40° half-angle at Mach numbers between 0.7 and 2.0. Plate A,3.5e is one of their interferograms of a 40° wedge with "contour fringes" in a stream of $M = 1.4$. The figure also shows the evaluated pressure distribution and gives, as well, results obtained with a manometer; the agreement is as good as can be expected when using contour fringes. Ladenburg and Bershader [*23,26*] used a small intermittent supersonic wind tunnel whose working section density was variable in the ratio 25:1, and studied the flow around wedges, half-cylinders, and especially boundary layers along the tunnel wall and along a flat plate suspended in the flow. Plate A,3.5f shows interferograms with displacement fringes of the flow at $M = 2.3$ around a 20° wedge under various conditions. Plate A,3.5g is an interferogram at $M = 2.3$ with displacement fringes perpendicular to the flow around a model, one side of which is a plate, the other a half-wedge of 5° angle at $M = 2.3$. Plate A,3.5h is an enlarged interferogram of the boundary layer along the center part of the same model with fringes parallel to the flow at the same Mach number, but at much higher density. Interferometric studies of boundary layers were also carried out by Blue [*50*] and by De Frate [*51*]. Plate A,3.5i shows "superimposed displacement fringes" of the transonic flow around a 10° wedge at $M = 1.278$ obtained by Liepmann and Bryson [*49*]. This method of superimposing an interferogram with quiet air upon one with flowing air, developed by Bleakney and his group, shows the isopycnals directly (see also Art. 3.4).

Projectiles in Free Flight. Of great importance for aerodynamics is the interferometric study of the flow around projectiles in free flight. The first measurements were made by L. Mach more than 50 years ago [*43*]. Before and shortly after the first world war Cranz and his coworkers continued Mach's work, and used the Schardin method (see Art. 1.3 and 3.2) for evaluating the flow around a series of different bullets [*7*; *44*, p. 277; *45*]. Very careful and complete measurements around bullets of various caliber and forms are being carried out at the Ballistic Research Laboratory (BRL), Aberdeen Proving Ground, by Giese, Bennett, and their coworkers [*31*; *46a,b*]. For recent published results see [*54*]. Plate A,3.5j is an interferogram obtained at BRL with a projectile Cal. 30, 30° half-angle cone cylinder, fired at $M = 1.77$, and Fig. A,3.5d is the evaluation. The similarity of these pictures with Plate A,3.5c and Fig. A,3.5b, obtained in an open wind tunnel at nearly the same Mach number, is striking. To summarize briefly the technique used at the BRL, we may say that the projectile is fired down the centerline of a closed, pressurized tube into a stopping chamber. This chamber is filled with sand and separated from the main chamber by a rubber diaphragm. Two 5-in. optically plane windows are situated on an axis perpendicular to the centerline of the range just ahead of the stopping section. Both

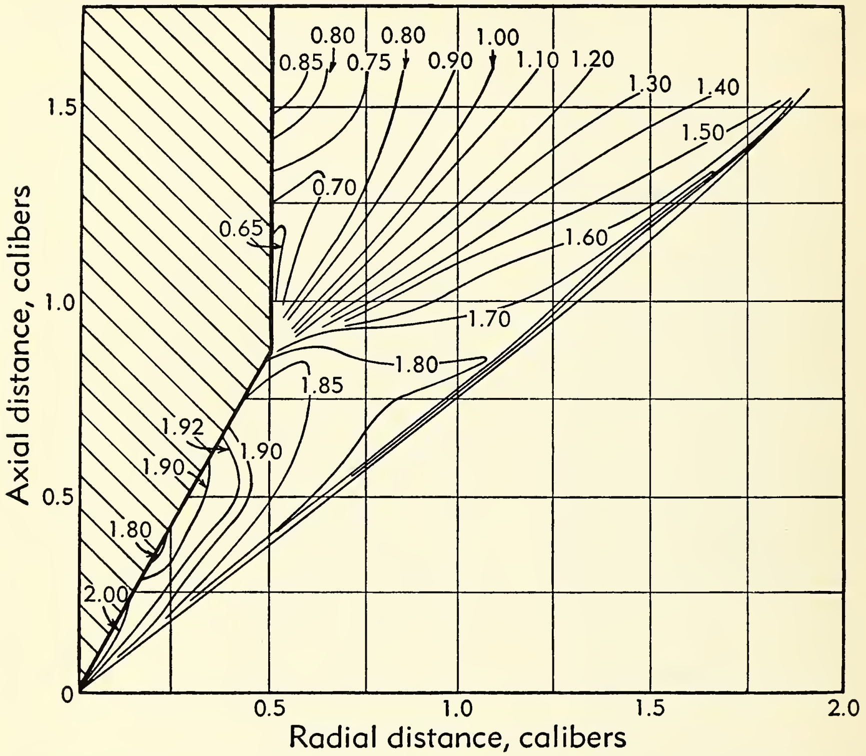

Fig. A,3.5d. Isopycnal chart corresponding to flow of Plate A,3.5j. Densities given in units of room density. To be compared with Fig. A,3.5b.

beams of a 2-in. Mach-Zehnder interferometer, adjusted so that its fringes are parallel to the centerline of the range, pass through the plane windows. The interferometer components, light source, and rotating-mirror camera are situated entirely outside the pressurized chamber. When a projectile is fired it proceeds down the range interrupting a light beam through the forepart of the plane windows. This triggers the spark which takes the interferogram picture. A B-H6 tube is used with a liquid prism monochromator isolating the 5461A or 4358A line of mercury. The rotating mirror sweeps the image of the plane through which the projectile passes, and in which the fringes are in sharp focus, in a direction counter to the motion of the projectile on the film. With proper synchronization, which is not extremely critical, an interferogram of the projectile almost completely free of blur is obtained.

The final evaluation of the interferograms obtained in this way is described in some detail by Bennett, et al. [*46a,b*]. Of great help is the use of high speed computing machines. At the BRL the ENIAC machine is used.

SHOCK TUBE. Very promising are the applications of the M-Z to the shock tube. Such studies have been started by Bleakney and his group [*27,48*]. Plate A,3.5k shows contour fringes of the reflection of a plane shock from an inclined wall [*47*]. The incident shock I travels from the left to the right. The flow field behind it is remarkably uniform; only in the region behind the reflected shock R and Mach shock M is there a detectable variation in the density. The theory of the interaction of shock waves as far as can be given at present is reviewed by Bleakney and Taub [*48*]. Investigations of the flow of a moving plane shock in a shock tube around various models have been carried out by Bleakney, White, and Griffith [*29*]; Plate A,3.5l is a contour fringe interferogram, together with its evaluation, of the diffraction of a plane shock over a rectangular block.

A,3.6. Cited References.

1. Drude, P. *Lehrbuch der Optik.* S. Hirzel, 1906.
2. Williams, W. E. *Applications of Interferometry.* Methuen, 1930.
3. Zehnder, L. Ein neuer Interferenzrefraktor. *Z. Instrumentenk. 11,* 275–285 (1891).
4. Mach, L. Über einen Interferenzrefraktor. *Z. Instrumentenk. 12,* 89–93 (1892); *14,* 279–283 (1894); Über ein Interferenzrefractometer. *Sitzber. Akad. Wiss. Wien, Math. naturw. Kl., Abt. IIa, 101,* 5–10 (1892); Über einige Verbesserungen an Interferenzapparaten. *Sitzber. Akad. Wiss. Wien, Math. naturw. Kl., Abt. IIa, 107,* 851–859 (1898).

5a. Ladenburg, R., Van Voorhis, C. C., and Winckler, J. A supersonic air jet at 60 lb/in.^{2} tank pressure. *Nav. Ord. Rept. 69-46,* 1946.

5b. Winckler, J. The Mach interferometer applied to studying an axially symmetric supersonic air jet. *Rev. Sci. Instr. 19,* 307–322 (1948).

6. Hansen, G. Über ein Interferometer nach Zehnder-Mach. *Z. tech. Phys. 12,* 436–440 (1931); Über die Ausrichtung der Spiegel bei einem Interferometer nach Zehnder-Mach. *Z. Instrumentenk. 60,* 325–329 (1940).

7. Schardin, H. Theorie und Anwendungen des Mach-Zehnderschen Interferenz-Refraktometers. *Z. Instrumentenk. 53*, 396–403 (1933).

8a. Zobel, Th. Development and construction of an interferometer for optical measurements of density fields. Transl. "Entwicklung und Bau eines Interferenzgerates zur optischen Messung von Dichtefeldern." *Deutsche Luftfahrtforschung, Forschungsbericht 1008*, 1938; *NACA Tech. Mem. 1184*, 1947.

8b. Zobel, Th. Optical corrections for interference measurements by controllable deformation of reflecting surfaces. *Air Force Tech. Rept. 5664*, 1948.

8c. Zobel, Th. Strömungsmessung durch Lichtinterferenz. *Deutsche Luftfahrtforschung, Forschungsbericht 1167*, 1940.

9. Kinder, W. Theorie des Mach-Zehnder-Interferometer und Beschriebung eines Gerätes mit Einspiegeleinstellung. *Optik 1*, 413–448 (1946).

10. Winkler, E. H. Analytical studies of the Mach-Zehnder interferometer. Part I, *Nav. Ord. Lab. Rept. 1077*, 1947; Part II, *Nav. Ord. Lab. Rept. 1099*, 1950.

11. Steegmaier, K. Fundamentals of construction and application of interferometers. *Ministry Supply Rept. L.F. 226*, 1943.

12. Mach, L. Über ein Interferenzrefraktometer (II). *Sitzber. Akad. Wiss. Wien. Math. naturw. Kl., Abt. IIa, 102*, 1035–1056 (1893).

13. Eckert, E. R. G., Drake, R. M., Jr., and Soehngen, E. Manufacture of a Zehnder-Mach interferometer. *Wright-Patterson Air Force Base, Tech. Rept. 5721*, 1948.

14. Bennett, F. D. Optimum source size for the Mach-Zehnder interferometer. *Ballist. Research Lab. Rept. 731*, 1950; *J. Appl. Phys. 22*, 184–190 (1951). Effect of size and spectral purity of source on fringe pattern of the Mach-Zehnder interferometer. *Ballist. Research Lab. Rept. 742*, 1950; *J. Appl. Phys. 22*, 776 (1951).

15. Kinder, W., and Hansen, G. Mehrplatten Interferometer. *Deut. Reichspatentschr. 732190*, 1941.

16. Bergdolt, V. E., Greenwald, A. J., and Slater, D. B. Pressurized range for small caliber projectiles in free flight. *Phys. Rev. 76*, 879 (1949).

17. Lamla, E. Über die Justierung des Mach-Zehnderschen Interferometers. *Z. Instrumentenk. 62*, 337–346 (1942). Transl. as *Rept. T-TS-893-RE, Air Matériel Command, Wright Field.*

18a. Kennard, R. B. An optical method for measuring temperature distribution and convective heat transfer. *J. Research Natl. Bur. Standards 8*, 787–805 (1932).

18b. Eckert, E. R. G., and Soehngen, E. E. Studies on heat transfer in laminar free convection with the Mach-Zehnder interferometer. *Air Force Tech. Rept. 5747*, 1948.

19. Winkler, E. H. Principle and design of a new type Stieltje's integrator. *Nav. Ord. Lab. Mem. 10798*, 1950.

20. Clippinger, R. F. Comparison between Jamin-Mach interferometer and the Williams interferometer as applied to the study of air flow around a supersonic projectile of revolution. *Ballist. Research Lab. Rept. 576*, 1945.

21. Bergdolt, V. E. A new interferometer with a large working field. *Ballist. Research Lab. Rept. 692*, 1949.

22a. Kraushaar, R. A diffraction grating interferometer. *J. Opt. Soc. Amer. 40*, 480–481 (1950).

22b. Erdmann, S. F. Ein neues sehr einfaches Interferometer zum Erhalt quantitativ auswertbarer Strömungsbilder. *Ber. F-68 Nat. Luchtvaartlag*, Amsterdam, 1950. *Appl. Sci. Research B2*, 149 (1951).

22c. Sterrett, J. R., and Erwin, J. R. Investigation of a diffraction grating interferometer for use in aerodynamic research. *NACA Tech. Note 2827*, 1952.

23. Ladenburg, R. Application of interferometry to the study of supersonic flow. *Proc. Seventh Intern. Congress Appl. Mech.*, Vol. 2, 388–397 (1948).

24. Pack, D. C., and Groth, E. Investigation of the flow past finite wedges of 20 deg. and 40 deg. apex angle at subsonic and supersonic speeds, using a Mach-Zehnder interferometer, with Appendix: Sensitivity and accuracy of the interference method applied to pressure measurements. *Ministry Supply Aero. Research Council Repts. and Mem. 2321*, 1949.

25. Schubert, F. Zur Theorie des stationären Verdichtungsstosses. *Z. angew. Math. u. Mech. 23*, 129–138 (1943).
26. Ladenburg, R., and Bershader, D. Interferometric studies on laminar and turbulent boundary layers along a plane surface at supersonic velocities. *Nav. Ord. Lab. Rept. 1133*, 1949.
27. Bleakney, W., Weimer, D. K., and Fletcher, C. H. The shock tube: a facility for investigations in fluid dynamics. *Rev. Sci. Instr. 20*, 807–815 (1949).
28. Kendall, J. M. The interferometer fringe pattern analyzer built at the Naval Ordnance Laboratory. *Nav. Ord. Lab. Rept. 1596*, 1951.
29. Bleakney, W., White, D. R., and Griffith, W. C. Measurements of diffraction of shock waves and resulting loading of structures. *J. Appl. Mech. 17*, 439–445 (1950).
30. Greenwald, A. J., and Bergdolt, V. E. The design and construction of a Mach-Zehnder interferometer. *Ballist. Research Lab. Mem. 469*, 1947.
31. Giese, J. H., Bennett, F. D., and Bergdolt, V. E. A simple interferometric test for conical flow. *J. Appl. Phys. 21*, 1226–1231 (1950).
32. Crocco, L. The laminar boundary layer in gases. *Monografie Scientifiche di Aeronautica 3*, 1946. Transl. as *North Amer. Aviation Rept. CF-1038*, 1948.
33. Van Driest, E. R. The turbulent boundary layer for compressible fluids on an insulated flat plate. *North Amer. Aviation Rept. AL-958*, 1949.
34. Winkler, E. M. Comparison of methods for measuring the density in hypersonic tunnels. *Nav. Ord. Lab. Mem. 10936*, 1950.
35. Bershader, D. An interferometric study of supersonic channel flow. *Rev. Sci. Instr. 20*, 260–275 (1949).
36. Howes, W. L., and Buchele, D. R. A theory and method for applying interferometry to the measurement of certain two-dimensional gaseous density fields. *NACA Tech. Note 2693*, 1952.
37. Wachtell, G. P. Refraction effect in interferometry of boundary layer of supersonic flow along flat plate. *Phys. Rev. 78*, 333 (1950).
38. Mach, L. Optische Untersuchung der Luftstrahlen. *Sitzber. Akad. Wiss. Wien, Math. naturw. Kl., Abt. IIa, 106*, 1025–1072 (1897).
39. Weyl, F. J. Analytical methods in optical examination of supersonic flow. *Nav. Ord. Rept. 211–245*, 1945.
40. Ladenburg, R., Van Voorhis, C. C., and Winckler, J. Interferometric studies of faster than sound phenomena. Part I: The gas flow around various objects in a free, homogeneous, supersonic air stream. *Phys. Rev. 73*, 1359–1377 (1948); Part II: Analysis of supersonic air jets. *Phys. Rev. 76*, 662–677 (1949).

41a. Gooderum, P. B., Wood, G. P., and Brevoort, M. J. Investigation with an interferometer of the turbulent mixing of a free supersonic jet. *NACA Tech. Note 1857*, 1949.

41b. Heberle, J. W., Wood, G. P., and Gooderum, P. B. Data on shape and location of detached shock waves on cones and spheres. *NACA Tech. Note 2000*. 1950. Gooderum, P. B., and Wood, G. P. Density fields around a sphere at Mach numbers 1.30 and 1.62. *NACA Tech. Note 2173*, 1–52 (1950).

42. Zobel, Th. Strömungsmessung durch Lichtinterferenz. *Deutsche Luftfahrtforschung. Forschungsbericht 1167*, 1940. Flow measurement by means of light interference. *NACA Tech. Mem. 1253*, 1949.
43. Mach, L. Aufstellung und Apparate für die Interferenzversuche (Weitere Versuche über Projectile). *Sitzber. Akad. Wiss. Wien, Math. naturw. Kl., Abt. IIa, 105*, 621–633 (1896).
44. Cranz, C., ed. Rechnerische Auswertung des Geschossbildes mit Interferenzstreifen (E. Mach, et al.). *Lehrbuch Der Ballistik*, Vol. 3, 277. Springer, 1927; Bemerkungen zu der Benutzung des Mach-Zehnderschen Interferenz-Refraktors sowie der Schlierenverfahren von Dvorak und Töpler. *Ergänzungsband*, 173 (1936).
45. Hauser, F. Über Geschossphotographie. *Z. wiss. Phot. 20*, 257–272 (1921).

46a. Bennett, F. D., Carter, W. C., and Bergdolt, V. E. Interferometric analysis of air flow about projectiles in free flight. *J. Appl. Phys. 23*, 453–468 (1952).

46b. Bennett, F. D. Effect of random errors in fringe shift on interferogram reductions of axi-symmetric flows. *Phys. Rev. 83*, 200 (1951).
47. Bleakney, W., Fletcher, C. H., and Weimer, D. K. The density field in Mach reflection of shock waves. *Phys. Rev. 76*, 323–324 (1949).
48. Bleakney, W., and Taub, A. H. Interaction of shock waves. *Revs. Mod. Phys. 21*, 584–605 (1949).
49. Liepmann, H. W., and Bryson, A. E., Jr. Transonic flow past wedge sections. *J. Aeronaut. Sci. 17*, 745–755 (1950).
50. Blue, R. E. Interferometer corrections and measurements of laminar boundary layers in supersonic stream. *NACA Tech. Note 2110*, 1950.
51. De Frate, L. A. *Application of the Interferometer to the Study of Boundary Layers.* Ph.D. Thesis, Mass. Inst. Technol., 1950.
52. Van de Vooren, A. L. Theory of the Erdmann interferometer for investigation of compressible flows. *Appl. Sci. Research B3*, 18 (1952).
53. Price, E. W. Initial adjustment of the Mach-Zehnder interferometer. *Rev. Sci. Instr. 23*, 162 (1952).
54a. Giese, J. H., and Bergdolt, V. E. Interferometric studies of supersonic flow about truncated cones. *Ballist. Research Lab. Rept. 830*, 1952.
54b. Bergdolt, V. E. Air flow about cone cylinders with curved shock waves. *Ballist. Research Lab. Rept. 832*, 1952.
55. Ingelstam, E. Application of variable contrast methods to the study of aerodynamic fields. *Rev. opt.* (M. Françon, ed.). Paris, 1952.
56. Werner, F. D., and Leadon, B. M. Very accurate measurement of fringe shift in an optical interferometer study of gas flow. *Rev. Sci. Instr. 24*, 121–124 (1953).

ARTICLE A,4

ELECTRICAL DISCHARGE AND AFTERGLOW TECHNIQUE

EVA M. WINKLER

A,4.1. Introduction. In the investigation of phenomena in high speed flow of low density, one faces the problem that methods commonly used for flow visualization can no longer be applied with success. At pressures of the order of 10^{-3} atm and lower, it becomes desirable to utilize alternate methods for obtaining photographs of the flow patterns. In this connection, the afterglow method was suggested by J. Kaplan [*1*]. Development of the afterglow technique has been carried out by the NACA [*2*]; the possibilities of the electrical discharge method were studied by the Berkeley group [*3*]. These preliminary studies on glow methods were made in nitrogen since comparatively few gases produce efficient light emission. Other useful gases are helium, argon, and air. For the application of this technique in low density wind tunnels, air or nitrogen afterglows are probably of greatest interest. The following discussion will, therefore, refer to nitrogen and air only.

A,4.2. Nitrogen Afterglow. If a tube containing nitrogen at low pressures[1] is subjected to a strong electric discharge, a glow may be produced which persists for a considerable time after the exciting discharge has been cut off.

The afterglow was first noticed by Warburg [*4*]; its first detailed experimental investigation and identification of the main bands in the visible spectrum were made by Lewis [*5*]; a large amount of experimental work has since been done in the study of the characteristic properties of the phenomenon. A review of the facts established by these investigations is given in [*6*]. Special mention shall be made only of the more recent work of Rayleigh [*7,8,9*] and of Kaplan [*10*]. Following Kaplan we shall distinguish between the Lewis-Rayleigh afterglow of the active nitrogen, which in its pure form may be produced by a condensed or electrodeless discharge (see Art. 4.4) in nitrogen, and other types of afterglow which may be produced by an ordinary discharge. Since the Lewis-Rayleigh afterglow is of longest duration and is most important if observations are to be made some distance away from the exciting discharge, the following discussion will concern mainly the Lewis-Rayleigh afterglow.

---

[1] Most observations were made at gas pressures of about 60 mm Hg to below 0.1 mm Hg.

Active nitrogen is formed in the discharge. The process of deactivation then furnishes the energy necessary for emission of the afterglow spectrum. This spectrum consists of some bands of the first positive group of the molecular nitrogen spectrum showing a relative enhancement of two bands as compared with the discharge spectrum. These maxima suggest a selective excitation of the 12th and 6th vibrational level of the upper $B^3\Pi g$ state of molecular nitrogen, enhancing the emission of the yellow and green bands (excitation of the 12th level) and the red band (excitation of the 6th level). The wavelengths of the prominent bands and their relative luminosity are [*7*]:

Color	*Wavelength*	*Relative luminosity*
red	6251A	0.345
yellow	5802A	0.940
green	5371A	1.000

They give the afterglow its characteristic golden color. The emission of other bands which might be observed is of shorter duration. For an account of the various theories proposed to explain the emission and intensity of these bands the reader is referred to [*6*] and [*11*]. Since the proper value of the heat of dissociation of the nitrogen molecule has not been definitely established (between the two values of 7.38 ev and 9.76 ev), the formulation of an atomic model of active nitrogen is as yet indeterminate. Calculations of the potential curve of the ground state of the nitrogen molecule by Cario and Reinecke [*12*] lead to the higher value of 9.76 ev for the heat of dissociation. In applying this value to an understanding of the reactions leading to the excitation of the 12th vibrational level of the $B^3\Pi g$ state, Cario and Reinecke propose as the most frequent initial process the recombination of two normal nitrogen atoms in a two-body collision. If the kinetic energy of the colliding atoms is high enough, $T \geqq 250°\text{K}$, an equilibrium is established between a steady dissociation and retention in the $B^3\Pi g$ state with selective excitation of the 12th vibrational level, which makes possible the emission of the bands of the first positive group until all nitrogen atoms are used. With the help of this model, the temperature dependence of the afterglow can be readily explained. For temperatures higher than 250°K, the above model suggests that the luminosity of the afterglow should increase with decreasing temperature, and if the temperature is lower than 250°K the afterglow should decay rapidly. While the rapid decay of the afterglow at the temperature of liquid air is a long-known fact, the existence of a negative temperature coefficient at room temperature was established by

Rayleigh's experiments [*7*]. For the excitation of the 6th vibrational level of the B state, Cario and Kaplan [*13*] have assumed collisions of the second kind between long-lived ^{2}D atoms and metastable A molecules. This process leads to the formation of two molecules in the B state with subsequent emission of the bands of the first positive group. Since all other possible reactions have a much smaller probability, they are considered less important in comparison with the two processes mentioned.

Another process was recently proposed by Kash [*14*] to account for the first positive radiation in the nitrogen afterglow. He suggests a three-body collision involving a highly vibrating $X^1\Sigma$ molecule, a metastable $A^3\Sigma$ molecule, and a neutral nitrogen molecule. This hypothesis was concluded from observations of the intensity decrease as a function of time of the late portion of the afterglow (i.e. the afterglow observed a few tenths of a second after the interruption of the discharge). The decay of the intensity of the first positive radiation is found to be exponential for pressures below 4 mm Hg, and follows an inverse square law for pressures above 4 mm Hg. The exponential curve at the lower pressures is ascribed to the dominance of surface effects at the walls; the inverse square law decay is due to the dominance of volume effects at the higher pressures. In principle, the square law agrees with a two-body collision as well as with a three-body collision. However, the pressure dependence of the decay curves [*14*, Fig. 6] supports the assumption of a three-body collision of two active particles and a neutral nitrogen molecule. For a more detailed reasoning about this process in relation to the observed afterglow intensity, the reader must refer to [*14*, pp. 26–36].

Rayleigh [*7*] observed that, if the glowing gas is compressed or rarefied as a whole and the temperature kept constant, the intensity of the afterglow changed as the inverse cube of the volume. These observations refer to an arrangement wherein the glowing nitrogen was made to diffuse into a large vessel of suitably conditioned walls (see Art. 4.4) and the increase of the luminosity was measured when a steady state was established after the pressure change. Since the variation of the luminosity with pressure is influenced by various reactions that may occur in the volume of the gas and by the effect of the walls of the afterglow vessel, different responses were obtained under other conditions. Studies of the transient response of the luminosity due to the compression at a shock wave, recently made by Benson [*11*], did not verify the third-power relation (see Art. 4.4).

If the afterglow is not produced in pure nitrogen but in the so-called "technical dry nitrogen" containing traces of other gases such as oxygen and hydrocarbons, the color of the afterglow is changed. Oxygen imparts a green to blue color, depending on its concentration. The hydrocarbons produce a violet coloring due to the cyanogen bands. While traces of impurities in the order of a fraction of a per cent of the nitrogen are favorable in prolonging the life of the afterglow [*8*], they may mask some of its characteristic properties. Pressure changes in the glowing gas may be indicated not only by a variation of the intensity but also of the color of the afterglow, necessitating the use of suitable filters to obtain a correct indication of the density of the flow.

A,4.3. Air Afterglow. The afterglow of air has been observed in the pressure range from 10 mm Hg to about 0.002 mm Hg [*15,16,17,18,19,20*]. If the afterglow is produced by an uncondensed discharge, it is found that the afterglow is of a greenish yellow color in the whole pressure range where it can be observed. Its spectrum is continuous, extending from 6700A to 4200A with 30 diffuse bands superimposed. The duration of the glow is $\frac{1}{2}$ sec at the higher pressure, but may be as long as 50 sec at reduced pressure, depending on the pressure and the temperature of the gas and on the electrical intensity of the discharge. The brightness of the glow decreases with decreasing pressure. If the afterglow is produced by a condensed discharge, the greenish yellow afterglow is observable only in the pressure range from 10 mm Hg to about 3 mm Hg [*15,20*]. Below a pressure of 3 mm Hg its color changes abruptly to blue. In this stage the spectrum of the afterglow consists mainly of the emission bands of the NO molecules. The duration of the blue glow is very short—about 0.3 sec. At pressures of the order of 0.8 mm Hg, the blue stage disappears and the orange-yellow color of the nitrogen afterglow becomes prominent.

In general, the properties of the air afterglow have been of far less interest to the physicist than those of the active nitrogen afterglow, so that comparatively few facts can be considered as having been established by experiments. Depending on the intensity of the exciting discharge, there exists a critical pressure at which the afterglow is difficult to obtain; above this value, and especially below, the afterglow is readily obtained and is brightest if the pressure has been regulated to such a value that the discharge is of a bright white color. The critical pressure value shifts to higher absolute values as the frequency of the discharge is increased.

If the afterglow produced at room temperature is caused to diffuse into a vessel which is maintained at reduced temperature, the duration as well as the luminosity of the afterglow is changed in the sense that the decay is more rapid and the glow is of higher luminosity. When the discharge takes place at the temperature of liquid air, the glow is formed only through a short range of pressures; its intensity and duration are greatly reduced as compared to room temperature [*16*].

The density ranges for which the afterglow methods may be used, corresponding to their lower and upper bounds of pressure and the temperature range from room temperature to the temperature of liquid air, are illustrated in Fig. A,4.3.

A,4.4. Experimental Aspects of Afterglow Methods. The commonly used methods of producing afterglow are the electrodeless, the condensed, and the uncondensed discharge. Typical arrangements are shown in Fig. A,4.4. The electrodeless discharge and the high frequency condensed discharge are considered most efficient in producing a bright afterglow. The advantage of the former is that no metal is in contact with the gas. In general, the electrical energy necessary to excite the afterglow is dependent on the size of the discharge vessel and the pressure of the gas. Typical values for the arrangement of the electrodeless discharge in Fig. A,4.4 (top) are: 20,000 volts and condensers of 0.01μf for a gas pressure of about 1 mm Hg. If the condensed discharge in Fig. A,4.4 (bottom) is used, the electrodes should preferably be long and of suitable

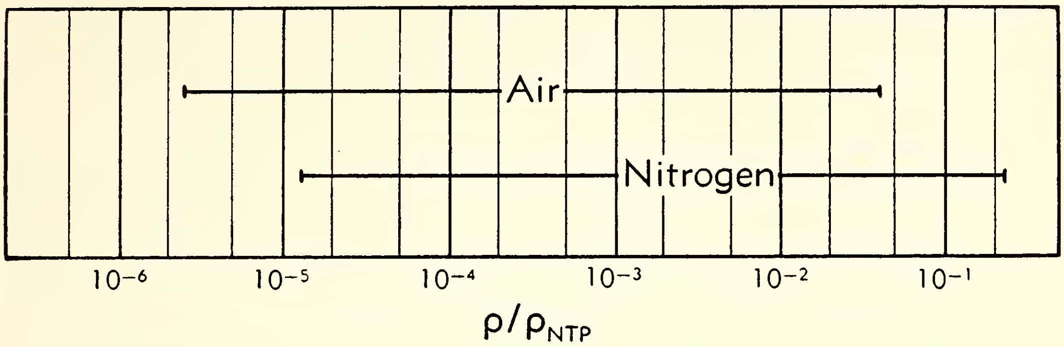

Fig. A,4.3. Useful density range of afterglow methods (ρ_{NTP} = density of the gas at p = 760 mm Hg and T = 273°K).

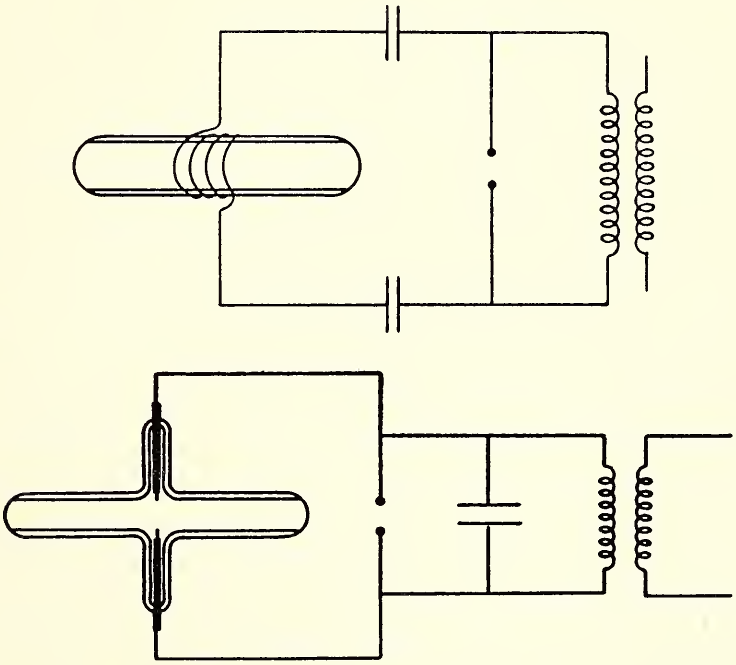

Fig. A,4.4. Arrangements for producing afterglow: (top) electrodeless discharge; (bottom) condensed discharge.

material to facilitate heat dissipation. The preliminary experiments of Williams and Benson [*2*] were made with an alternating current condensed discharge of 7,000 volts. The arrangement is similar to that shown in Fig. A,4.4 (bottom). The tank nitrogen was subjected to the discharge in three consecutive discharge gaps (1 in. wide). The electrodes were made of aluminum rods tipped with tungsten wire. For gas pressures in the range from 3 mm Hg to 10 mm Hg a discharge current of 300 to 500 ma was employed.

Experiments performed mainly to study the laws of decay of the afterglow established various facts with respect to the most favorable conditions for producing the glow. Some of the facts will be mentioned in the following; but for details the reader is referred to the original papers. The properties of the glowing gas are affected by the physical conditions under which the gas is excited, i.e. the purity of the gas, the conditions of the walls of the containing vessel, etc. The persistence of the afterglow is found to be influenced by the size of the vessel and may range from seconds to hours. The intensity and the duration of the afterglow is markedly dependent on the nature of the walls of the containing vessel and on the purity of the gas. Some substances like fluoric acid, if coated on the surface of the walls of the afterglow vessel, served to prolong the life of the glow and to facilitate its production, while others like stopcock grease are destructive to the glow [*7,10,21,22,23*]. Owing to the active nature of excited nitrogen, chemical reactions may accompany the afterglow. Most common is the formation of nitrides. With oxygen or carbon oxides present NO and CN will be formed, as is evidenced by the appearance of some of the NO and cyanogen bands in the afterglow spectrum. Hydrogen, which quenches the glow, does not react with active nitrogen but merely serves as a diluent. Cold clean metals are, in general, not acted upon. This is ascribed to the formation of a protective layer of nitrides on the surfaces. The exception is copper, which acts as a catalyst for the destruction of the active substance.

The energy which is recovered when the afterglow is quenched on the surface of a coil of copper tubing was used to estimate the average energy carried in latent form by the active nitrogen. Values between 0.027 ev to 12.9 ev per nitrogen molecule (which has passed the discharge), and higher, were determined, depending on the conditions of the experiments [*7,11,24*]. A release of this energy to the volume of the gas would raise the temperature of the gas by 90°C and higher while the afterglow is decaying. In the application of the afterglow technique to studies of low density flow, disturbances can be expected from the release of energy.

Estimations, based on an energy of 0.027 ev per nitrogen molecule [*11*], however, indicate that the temperature increase, while the active nitrogen is passing through the test section of a supersonic nozzle, will be negligibly small because the lifetime of the afterglow is considerably longer than the time required for an active nitrogen to travel through the test section.

Other disturbing effects may result from the ionization which is always associated with afterglow. Its source is ascribed partly to the exciting discharge and partly to a collision process between fast electrons and nitrogen molecules in the volume of the glowing gas [*25*]. In flow observations, disturbing effects in the form of corona discharges were observed near metallic surfaces and where rapid expansions of the flow cause a large pressure drop. These discharges were found to be due to the presence of free electrons rather than positive ions in the stream of active nitrogen [*11*,*26*]. These discharges were eliminated by placing a grounded screen upstream of the test section. For the most recent investigation on mass production of intense afterglows in air and nitrogen and the study of some of their properties in a dynamic system, the reader is referred to the work of Kunkel [*27*,*28*].

In practical application to the study of flow phenomena, the exciting discharge has been placed either in a separate discharge tube ahead of the wind tunnel [*2*] or in the settling chamber of the tunnel [*29*]. With the equipment described in [*2*], the discharge tube, settling chamber, and test section are made of Pyrex and insulating plastic, respectively. The test section dimensions were 3.75 in. by 1.5 in. Flow observations were made at a Mach number of 2.6 and test section pressures ranging from 3 to 10 mm Hg. Since it was observed that the supply temperature increased by about 90°C with full power input (3,500 watts), the observations covered the density range from $6 \times 10^{-3}\rho_{\mathrm{NTP}}$ to $1.9 \times 10^{-3}\rho_{\mathrm{NTP}}$, where ρ_{NTP} denotes the density of nitrogen at 0°C and 760 mm Hg. The glow was observed to fill the entire nozzle and test section. Using Super XX film, the flow patterns were photographed with exposure times between 20 to 50 sec with a camera lens of $f/1.5$; see Plate A,4.4a.

With the equipment of [*29*], the tunnel proper was of metal and only a plastic tube was attached immediately ahead of the nozzle entrance; the nozzle was made of Lucite (5.5-in. diameter). The discharge (7,000 volts) occurred between a copper screen at the nozzle throat and an electrode inside the insulated portion of the settling chamber. The glow phenomenon observed persisted for some distance beyond the nozzle exit. Shock waves were clearly visible. Plate A,4.4b shows one of the early photographs obtained with the afterglow method. Using Super XX film and a camera lens of $f/8$, the exposure time was about two minutes.

The position of shock waves is found to be correctly defined by the afterglow flow patterns as compared with schlieren photographs. Time records of the response of the intensity of the Lewis-Rayleigh afterglow to the pressure change across a shock wave (made in a shock tube) show that the initial rise in intensity is followed by a gradual rise behind the shock front. Separate studies of the responses of the main bands of the afterglow [*11*] revealed that while the intensities of both the green and yellow bands rise simultaneously with the arrival of the shock, only the intensity of the green band rises sharply to a plateau. The height of the plateau was found to correspond within ±6 per cent to the density behind the shock [*11*, Table II]. The intensity of the yellow band also rises sharply at first but then is followed by a slower and greater rise. Benson concludes from these records that while the initial rise of the intensity of the yellow band is probably also proportional to the density increase, an additional slower effect which is correlated to the pressure is superimposed. Consequently, for the evaluation of continuous variations of the density behind shock waves, the flow patterns should be photographed through a filter passing only the green band of the afterglow spectrum.

A,4.5. Glow Discharge in Nitrogen and Air. The emission of light accompanying the electrical discharge in gases at low pressures has also been utilized for flow visualization [*3,30*]. Investigations with this technique are probably most conveniently made if the observations are restricted to the extension of the positive column because the luminous intensity of the positive column is, under certain conditions, constant over its entire length. By a suitable selection of the separation of the electrodes, the length of the positive column may be varied so as to extend over the desired portion of the test section. For a given diameter of the discharge tube, the emission intensity of the positive column is a function of the gas pressure and of the electrical intensity of the discharge [*31*]. In the visible region the discharge spectrum in nitrogen and air exhibits mainly the bands of the first and second positive group of the molecular nitrogen spectrum. Although the intensity distribution in the bands is, in general, determined by the gas temperature, the effective temperature may be altered by the discharge, depending on the gas pressure and the current density, and in addition a redistribution of the molecules over the rotational levels of the upper state may occur [*32*]. For both reasons, pressure changes in the gas may be indicated by changes in the intensity as well as the color of the luminous column.

A,4.6. Experimental Aspects of the Discharge Technique. The electrical discharge method has been used for flow visualization by the Berkeley group [*3,33*]. The arrangement is shown diagrammatically in Fig. A,4.6. The 5.5-in. I.D. Lucite nozzle produced a flow Mach number of 2.6. A high voltage insulated grid was attached at the throat of the nozzle so that all gases entering the test section had to pass through the grid. The discharge was produced between the grid and the grounded walls of the test section. With a power input of 25 to 350 watts and 2,500 to 7,000 volts a.c. at the secondary side a sufficiently bright illumination of the flow through the nozzle and test section was achieved. When the wind tunnel was operated with air at a test section static pressure of about 0.1 mm Hg, the discharge filled the nozzle but did not persist far enough downstream of the nozzle exit. Shock waves from a model placed beyond the nozzle exit plane are described as barely visible [*3*]. With nitrogen (from commercial tanks) a more luminous discharge was obtained which was observed to persist several feet downstream of the nozzle exit. Plate A,4.6 shows one of the photographs obtained with the discharge in nitrogen. With a camera lens of *f*/4.5 the exposure time was $\frac{1}{30}$ sec. In general the flow pictures are roughly comparable with those obtainable with the shadowgraph method at higher pressures, but owing to the brilliant illumination near the nozzle exit, details in this portion seem to be obscured. The shock waves are reported to be visible because of changes in both the intensity and the color of the discharge.

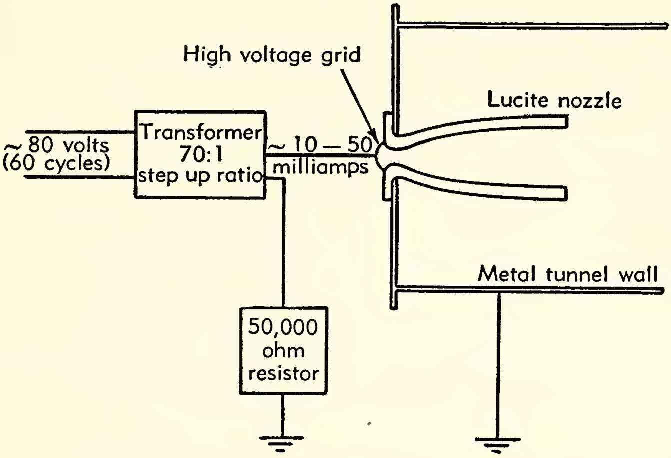

Fig. A,4.6. Arrangement for electric discharge method (after [*3*]).

With the method in the form reported here, no attempts have been made to evaluate the flow pictures with regard to the relation between density changes of the flow and changes in intensity.

A,4.7. Cited References.

1. Report on conference on flow visualization at low pressures. *Univ. Calif. Eng. Projects Rept. HE-150-11,* 1947.
2. Williams, T. W., and Benson, J. M. Preliminary investigation of the use of afterglow for visualizing low-density compressible flows. *NACA Tech. Note 1900,* 1949.
3. Kane, E. D. *Univ. Calif. Eng. Projects Rept. HE-150-51,* 1949.
4. Warburg, E. Phosphorescence des tubes de Geissler. *Arch. sci. phys. et nat. Geneva.* (*4*) *12,* 504, 505 (1884).

5. Lewis, P. Über Fluorescenz und Nachleuchten bei der elektrischen Entladung in Stickstoff. *Ann. Physik 2*, 459–468 (1900).
6. Mitra, S. K. *Active Nitrogen—A New Theory.* Indian Press, Calcutta, 1945.
7. Rayleigh, Lord. New studies on active nitrogen. *Proc. Roy. Soc. London A176*, 1–27 (1940).
8. Rayleigh, Lord. Further studies on active nitrogen. III. *Proc. Roy. Soc. London A180*, 123–139 (1942).
9. Rayleigh, Lord. Further studies on active nitrogen. IV. *Proc. Roy. Soc. London A180*, 140–150 (1942).
10. Kaplan, J. The preparation and properties of auroral afterglows. *Phys. Rev. 54*, 176–178 (1938).
11. Benson, J. M. The physical properties of active nitrogen in low-density flow. *NACA Tech. Note 2293*, 1951.
12. Cario, G., and Reinecke, L. H. Die Dissoziationsenergie des Stickstoffmoleküls und ihre Bedeutung für das Nachleuchten des aktiven Stickstoffs. *Abhandl. braunschweig. wiss. Ges. 1*, 8 (1949).
13. Cario, G., and Kaplan, J. Das sichtbare Nachleuchten des aktiven Stickstoffs. *Z. Physik 58*, 769–780 (1929); *Z. Physik 89*, 523–536 (1934).
14. Kaplan, J., Brook, M., and Kash, S. W. *Univ. Calif. Inst. Geophys. Final Rept. N6onr-27508*, 1951.
15. Herzberg, G. Über das Nachleuchten von Stickstoff und Sauerstoff und den Einflusz der Wände hierauf. *Z. Physik 46*, 878–895 (1928).
16. Trowbridge, C. C. The duration of the afterglow produced by the electrodeless ring discharge. *Phys. Rev. 23*, 279–307 (1906).
17. Kaplan, J. The afterglow in air. *Phys. Rev. 35*, 600–604 (1930).
18. Newman, F. H. Air afterglow. *Phil. Mag. 20*, 777–781 (1935).
19. Strutt, R. J. The afterglow of electric discharge. *Proc. Phys. Soc. London 23*, 66–73 (1910); Das Nachglühen der elektrischen Entladungen in Gemischen von Stickstoff mit Sauerstoff. *Physik. Z. 15*, 274–276 (1914).
20. Tanaka, Y., and Shimazu, M. On the air afterglow. *J. Sci. Research Inst. Tokyo 43*, 241 (1949).
21. Rayleigh, Lord. Active nitrogen of long duration, law of decay, and of increased brightness on compression. *Proc. Roy. Soc. London A151*, 567–584 (1935).
22. Willey, E. J. B. On active nitrogen. Part VII. Further studies upon the decay of the nitrogen after-glow; Part VIII. (i) The influence of photogens and of surfaces upon glow phenomena in nitrogen. (ii) The effects of addition of other gases to luminous nitrogen. *J. Chem. Soc. 133*, Part I, 336–349; 1146–1151 (1930).
23. Purushotham, A. *Proc. Indian Sci. Congr.*, Part III, 42 (1939).
24. Rayleigh, Lord. The surprising amount of energy which can be collected from gases after the electric discharge has passed. *Proc. Roy. Soc. London A189*, 296–299 (1947).
25. Chao, K. T., and Chang, H. P. The process of ionization in active nitrogen. *Phys. Rev. 76*, 970–971 (1949).
26. Jackson, L. C., and Broadway, L. F. An application of the Stern-Gerlach experiment to the study of active nitrogen. *Proc. Roy. Soc. London A127*, 478–689 (1930).
27. Kunkel, W. B. *Univ. Calif. Eng. Projects Rept. HE-150-106*, 1952.
28. Kunkel, W. B. *Univ. Calif. Eng. Projects Rept. HE-150-107*, 1952.
29. Evans, R. A., and Maslach, G. J. *Univ. Calif. Eng. Projects Rept. HE-150-68*, 1950.
30. Molthan, W. Die Ausbreitung eines Dampfstromes im Vakuum und deren Bedeutung für die Wirkung der Diffusionsluftpumpe. *Z. tech. Phys. 7*, 377–388; 452–460 (1926).
31. Francis, V. J., and Jenkins, H. G. Electrical discharges in gases and their applications. *Repts. Progr. Phys. 7*, 230–302 (1940).
32. Herzberg, G. *Molecular Spectra and Molecular Structure*, Vol. I, 2nd ed.; *Spectra of Diatomic Molecules.* Van Nostrand, 1950.
33. Sherman, F. S. *Univ. Calif. Eng. Projects Rept. HE-150-70*, 1950.

ARTICLE A,5

SPECTRAL ABSORPTION METHOD

EVA M. WINKLER

A,5.1. Introduction. Conventional methods of measuring densities or observing flow patterns in high speed gases approach the limits of feasibility if the product of density ρ and test section width l becomes smaller than about 10^{-4} g/cm². An alternate technique which would make visible the flow patterns as well as furnish quantitative data of the density is made possible by utilizing, as a measure of the density, the absorption of radiation by air molecules[1] or by added tracer molecules. Following J. Kaplan's suggestion of the ozone method to the Berkeley group, studies on the applicability of optical absorption methods were initiated several years ago by Evans and his collaborators [*1*].

The utility of any such method is determined by the magnitude of absorption which is to be expected for a given range of gas densities in a test section of specified dimensions. If monochromatic radiation passes through an absorption cell of length l, then the intensity of radiation emerging, after absorption in the gas, is given by

$$I = I_0 e^{-\alpha l} \qquad (5.1\text{-}1)$$

where I_0 is the intensity measured with the cell evacuated, and α is the absorption coefficient in cm^{-1} at NTP. The absorption coefficient is a function of the wavelength of the incident light and depends on the nature of the molecules of the gas, their number concentration, their motion, and their interaction either with one another or with foreign molecules.

Reviewing briefly the spectral absorption regions of air, one notes that it is practically transparent in the range of the infrared, visible, and near ultraviolet spectrum, with the exception of the weak absorption bands of oxygen between λ7710A and λ5380A and between λ2400A and λ2000A [*2*,*3*]. Strong absorption bands of oxygen start at λ2000A and are followed by a continuum between λ1750A and λ1300A [*4*]. The absorption coefficient in this region assumes values suitably large for determining air densities if $\rho l < 10^{-4}$ g/cm² from measurements of I/I_0. Nitrogen remains practically transparent down to λ1450A (band spectrum converging at λ990A beyond which there is a continuum). Tracer molecules suitable for measurements at somewhat longer wavelengths are ozone and mercury vapor. Added in small amounts, their effects on the aerodynamic behavior of air are probably negligible (see footnote 2 below).

---

[1] The discussion in this article is limited to air as the wind tunnel supply gas.

A,5.2. Oxygen Absorption Method. The continuous absorption of oxygen between λ1750A and λ1300A was investigated by Ladenburg and his collaborators [*4*,*5*]. Fig. A,5.2a shows the variation of the absorption coefficient α between λ1750A and λ1300A. The values of this curve refer to oxygen at normal temperature and pressure. At the maximum, α assumes a value of 490; this corresponds to a 50 per cent absorption of λ1450A in a layer of 0.0014 cm of pure oxygen, or 0.007 cm of air at NTP [*5*]. The curve of the absorption coefficient as a function of the wavelength, as shown in Fig. A,5.2a, is correct as long as the influence of temperature on the molecular vibrations of oxygen can be neglected. Since density measurements in wind tunnels will, in general, be made at temperatures where this assumption is fulfilled, the absorption can be considered as independent of the temperature. The absorption measured

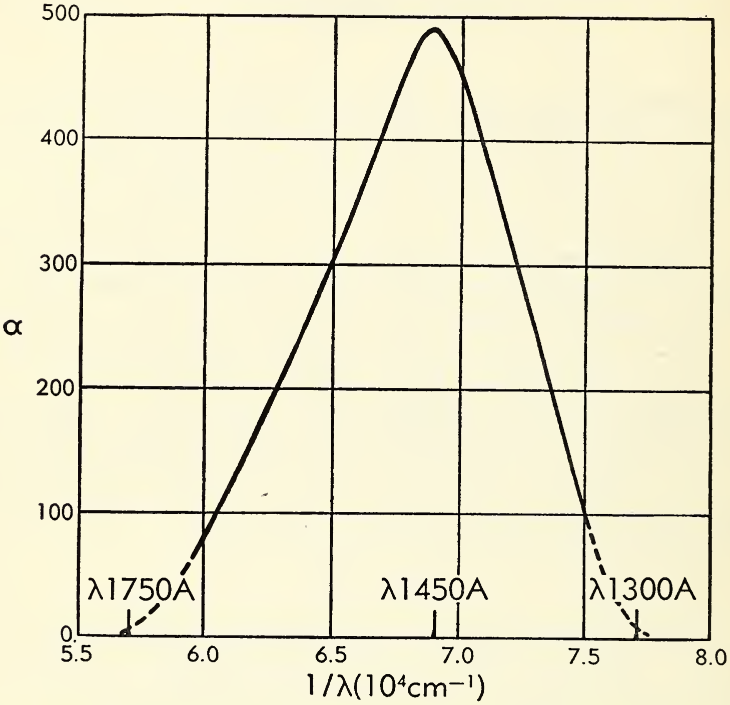

Fig. A,5.2a. Absorption coefficient of oxygen as function of the wavelength; the values refer to oxygen at NTP; (after [*5*]).

with a specified wavelength, in a given path length *l*, is then a function of the number concentration of the oxygen molecules only. The strong absorption suggests that measurements in this spectral range will be particularly advantageous for determining low air densities in wind tunnels of small dimensions. This is illustrated by Fig. A,5.2b, which gives the absorption for three selected monochromatic wavelengths, λ1470A, λ1570A, and λ1650A, as a function of the air density in a 10-cm wide test section.

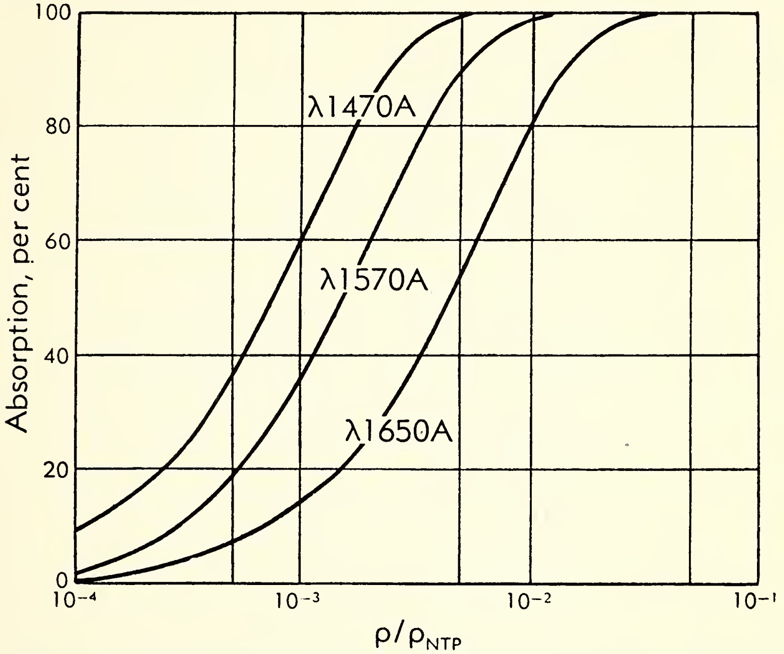

Fig. A,5.2b. Absorption of λ1470A, λ1570A, and λ1650A as function of the air density in a 10-cm wide test section.

For the secondary reactions occurring as a consequence of the absorption of radiation shorter than λ1750A in oxygen, we mention only the formation of ozone (quantum yield about 2). Its effect on the ratio of the specific heat, however, can be neglected for most practical cases.[2]

The equipment needed with the oxygen absorption method is basically simple, consisting of a suitable light source and optical system to produce a parallel beam of light on one side of the test section and a receiver on the opposite side. Because of the spectral range involved, all portions of the light path outside the test section must be enclosed and the housing evacuated or filled with a nonabsorbing atmosphere such as pure helium or pure nitrogen. Windows and optical components must be made either of calcium fluorite or lithium fluoride. While the latter is easier to obtain in larger sizes [*6*] and has somewhat better transmission than the natural fluorite [*7*, Fig. 2], it has the disadvantage that it discolors upon exposure to intense ultraviolet radiation. This is accompanied by a gradual shift of the absorption limit by as much as several hundred angstroms [*8*]. (Heating the crystal or repolishing its surface will, in general, restore the original transparency.)

---

[2] For λ1470A and $\rho/\rho_{NTP} = 10^{-3}$ the absorption in a 10-cm air path is 60 per cent. If we assume an I_0 of about 10^{16} quanta per sec cm^2 [*10*], about 10^{15} ozone molecules will be formed per sec cm^3. This yields a concentration of about 0.5 per cent ozone and $\gamma = 1.3998$ (if $\gamma_{air} = 1.40$ and $\gamma_{ozone} = 1.29$).

Radiation in the range λ1750A to λ1300A may be obtained with sufficient intensity from enclosed sparks (Cd, Zn, or Al) or from gas discharge tubes. Low voltage discharge tubes with a neon-xenon mixture (20 mm neon with 0.5 per cent xenon) [*9,10,11,12*] produce a spectrum which is mainly that of xenon. Applying a strong magnetic field near the window of the discharge tube, Groth [*10*] achieved an output of about 10^{16} quanta per sec cm^2 of λ1470A and λ1295A with the discharge tube operated at 80 volts and 50 amperes. With a discharge in hydrogen at 3 mm pressure and a current of 2 amperes, approximately the same output can be obtained for radiation in the wavelength range 1650A to 1350A. The spectral line desired must either be isolated by means of a monochromator or by the method of focal isolation. For practical purposes, i.e. if the measurements are referred to a calibration curve, the latter method will generally suffice. While it yields only partial isolation of a given spectral region, it has the advantage of encountering a minimum loss of intensity [*13*]. If a photoelectric receiver is used to measure the transmitted intensity, and if the remaining undesired light consists mainly of radiation of longer wavelengths, it may be eliminated by a proper choice of metal for the emitting electrode [*14*, Table 3-2]. For a discussion of the various receivers useful in the vacuum ultraviolet, the reader is referred to [*15,16,17*].

A,5.3. Ozone Absorption Method. The ozone absorption method is based on the strong absorption of ultraviolet light by ozone. Ozone has a region of continuous absorption between λ2900A and λ2300A, with a maximum almost coincident with the wavelength of the mercury resonance line λ2537A. At normal temperature and pressure the absorption coefficient (Eq. 5.1-1) equals 343.5 at λ2537A [*18*]. This corresponds to an absorption of 50 per cent in a layer of 0.002 cm pure ozone. The addition of a small percentage of ozone to the supply gas of a wind tunnel should, therefore, permit density measurements by means of radiation absorption. The absorption to be expected in a 10-cm path for various ozone concentrations is shown in Fig. A,5.3 as function of the air density.

The advantage of this technique, namely that the range where density data are desired can be achieved by varying the ozone concentration, has stimulated detailed investigations on its practical possibilities [*1*]. While the optical instrumentation requirements, a mercury resonance lamp, quartz windows and lenses, pose no particular problems, technical difficulties are encountered in achieving high ozone concentrations from ozonators with capacities sufficient for operation in connection with wind tunnels [*1*]. In practice, a concentration of only 0.1 per cent has been used so far.

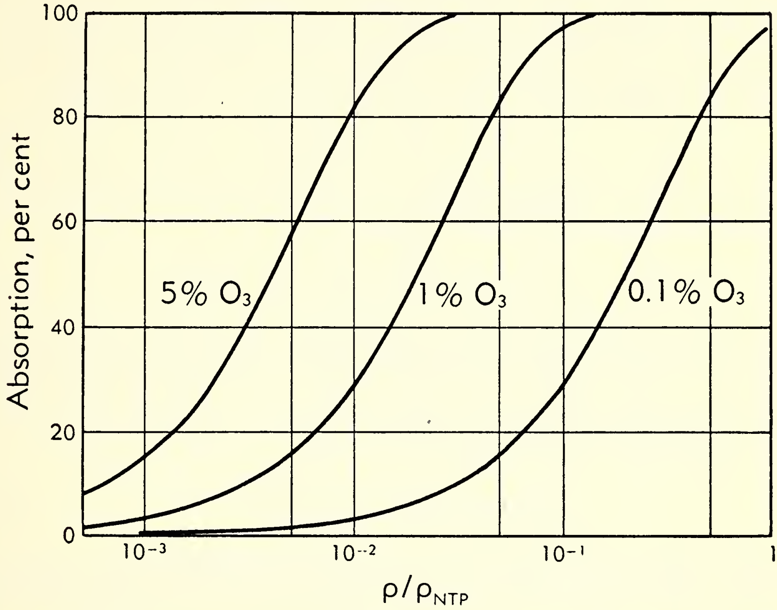

Fig. A,5.3. Absorption of λ2537A in an air-ozone mixture as function of the air density in a 10-cm wide test section and for three different ozone concentrations.

The evaluation of measurements made with the ozone method are made difficult by the instability of ozone. Ozone is easily decomposed by traces of organic matter and by irradiation with ultraviolet light of $\lambda < 3000A$, the amount of decomposition being dependent upon temperature and ozone concentration. For a summary discussion of the possible reactions occurring refer to [*19*]; the preparation and chemical properties of ozone are reviewed in [*20*].

A,5.4. Mercury Vapor Absorption Method. With a small, known amount of mercury vapor added to the supply air of a wind tunnel, the strong absorption of radiation of λ2537A in mercury vapor can be utilized for air density determinations. With a mercury resonance lamp (λ2537A) as light source, the absorption in a column *l* of mercury vapor is given by

$$A = 1 - \frac{\int_{-\infty}^{\infty} e^{-[\omega^2+\alpha(\nu)l]}\, d\omega}{\int_{-\infty}^{\infty} e^{-\omega^2}\, d\omega} \tag{5.4-1}$$

where

$$\omega = \frac{2(\nu - \nu_0)}{\Delta\nu_{\mathrm{E}}} (\ln 2)^2$$

and ν_0 denotes the frequency of the resonance line; the symbols $\Delta\nu_{\mathrm{E}}$ and $\Delta\nu_{\mathrm{A}}$ are the Doppler half-breadth of λ2537A in emission of the resonance lamp and in absorption (of the column l), respectively. The collision broadening is neglected for the present; this is allowable if the mercury vapor pressure is smaller than 10^{-2} mm Hg and the total pressure lower than about 10 mm Hg. The absorption coefficient $\alpha(\nu)$ is given by

$$\alpha(\nu) = \alpha(\nu_0) e^{-(\Delta\nu_{\mathrm{E}}/\Delta\nu_{\mathrm{A}})^2\omega^2} \tag{5.4-2}$$

where $\alpha(\nu_0)$ is the maximum absorption coefficient when Doppler broadening alone is present. For $\alpha(\nu_0)$ we have [*21*]

$$\alpha(\nu_0) = \frac{1.44 \times 10^{-4}}{\Delta\nu_D} N \tag{5.4-3}$$

where N is the number concentration of mercury atoms. With the Doppler breadth $\Delta\nu_D = 7.16 \times 10^{-7}\nu_0 \sqrt{T/\mathfrak{M}} = 6.16 \times 10^7 \sqrt{T}$ for Hg and λ2537A, and if N is expressed by the saturation ratio p/p_∞ and the vapor pressure of Hg, $p(T)$ at the temperature T, we obtain

$$\alpha(\nu_0) = 2.36 \times 10^8 \frac{p}{p_\infty} \frac{p(T)}{T^{\frac{3}{2}}} \tag{5.4-4}$$

In other words, the maximum absorption at λ2537A which can be expected in a test section of given width depends on the temperature of the gas and on the saturation ratio p/p_∞. Using the asymptotic expansion for Eq. 5.4-1 [*21*], the absorption to be expected in a test section of 10-cm width has been calculated for $p/p_\infty = 1$, and as a possible upper limit for $p/p_\infty = 10$. A $\Delta\nu_{\mathrm{E}}/\Delta\nu_{\mathrm{A}}$ of 1.21 was assumed [*21*]; the vapor pressure data of mercury were taken from [*22*]. The results are plotted in Fig. A,5.4 as a function of the temperature. By arbitrarily supposing an absorption of 5 per cent as the lower limit for sufficiently accurate measurements of the density, one sees that the mercury vapor method will be feasible only in cases where the test section temperature is higher than about 210°K for $p/p_\infty = 10$, and 230°K for $p/p_\infty = 1$. These values correspond to flow Mach numbers of about 3 and 2.8, respectively, if the supply air is heated to 600°K.

For gas pressures exceeding about 10 mm Hg, the effect of collision broadening of the absorption line in mercury vapor-air mixtures can no longer be neglected. Owing to this effect a relative decrease of absorption by 3 per cent is to be expected for a test section pressure of 53 mm Hg, and 14 per cent for a test section pressure of 208 mm Hg.[3]

The instrumental requirements for measuring the absorption by the ozone and mercury vapor methods are similar. The λ2537A radiation can be obtained with sufficient intensity and purity from commercial mercury-rare gas discharge lamps (in particular, argon) [*19*, p. 29]; quartz windows and lenses are required for the optical system; the selection of a suitable receiver in this spectral range poses no special problem; photographic film, counters, and photoelectric cells may be used; for a review see [*16*,*17*].

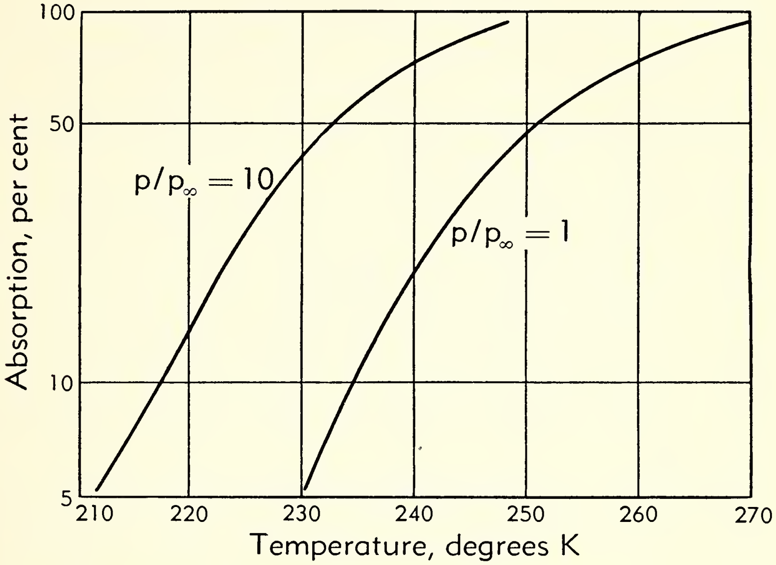

Fig. A,5.4. Absorption of λ2537A in an air-mercury vapor mixture as function of the temperature in a 10-cm wide test section and for two values of the saturation ratio.

A,5.5. Concluding Remarks. Each of the methods discussed above is best suited for measurements in different ranges of air densities.

The oxygen absorption method extends the range in which accurate measurements of the density can be made far beyond the range accessible with other methods.

The ozone absorption method, with presently attainable ozone concentrations, and the mercury vapor absorption method are restricted to measurements of $\rho/\rho_{\text{NTP}} \geqq 10^{-2}$, and $T > 210°\text{K}$, respectively. In the case of the ozone method, the interpretation of measured data will be particularly difficult. Since other methods (Art. 3 and 6) work well in the same density range, the practical value of these methods is questionable.

---

[3] Estimated from the data of [*21*, Table VI].

A,5.6. Cited References.

1. Evans, R. A. *Univ. Calif. Eng. Projects Rept. HE-150-25,* 1947.
2. Mulliken, R. S. Interpretation of the atmospheric absorption bands of oxygen. *Phys. Rev. 32,* 880–887 (1928).
3. Herzberg, G. Ein neuartiges, "verbotenes" Absorptionsbandensystem des O_2-Moleküls. *Naturwissenschaften 20,* 577 (1932).
4. Ladenburg, R., Van Voorhis, C. C., and Boyce, J. C. Absorption of oxygen in the region of short wavelengths. *Phys. Rev. 40,* 1018–1020 (1932).
5. Ladenburg, R., and Van Voorhis, C. C. The continuous absorption of oxygen between 1750 and 1300A and its bearing upon the dispersion. *Phys. Rev. 43,* 315–321 (1933).
6. Stockbarger, D. C. Artificial fluorite. *J. Opt. Soc. Amer. 39,* 731–740 (1949).
7. Schneider, E. G. Optical properties of lithium fluoride in the extreme ultraviolet. *Phys. Rev. 49,* 341–345 (1936).
8. Schneider, E. G. The effects of irradiation on the transmission of lithium fluoride. *J. Opt. Soc. Amer. 27,* 72–74 (1937).
9. Hartek, P., and Oppenheimer, F. Die Xenonlampe, eine Lichtquelle für äusserstes Ultraviolett. *Z. physik. Chem. B16,* 77–80 (1932).
10. Groth, W. Photochemische Untersuchungen im Schumann-Ultraviolett Nr. 3 und Nr. 4. *Z. physik. Chem. B37,* 307–322 (1937).
11. Evans, R. A. *Univ. Calif. Eng. Projects Rept. HE-150-60,* 1950.

11a. Evans, R. A., and Schultz, W. M. *Univ. Calif. Eng. Projects Rept. HE-150-109,* 1952.

12. Dacey, J. R., and Hodgins, J. W. Mercury 1850A and Xenon 1470A resonance lamps as ultraviolet sources for photochemical studies. *Can. J. Research B28,* 90–95 (1950).
13. Duncan, A. B. F. A focal isolation monochromator for the Schumann region. *Rev. Sci. Instr. 11,* 260–261 (1940).
14. Hughes, A. L., and Du Bridge, L. A. *Photoelectric Phenomena.* McGraw-Hill, 1932.
15. Lyman, T. *Spectroscopy of the Extreme Ultra-Violet.* Longmans, Green & Co., London, 1928.
16. Bomke, H. *Vakuumspektroskopie.* J. A. Barth, Leipzig, 1937.
17. Boyce, J. C. Spectroscopy in the vacuum ultraviolet. *Revs. Mod. Phys. 13,* 1-57 (1941).
18. Läuchli, A. Zur Absorption der ultravioletten Strahlung in Ozon. *Z. Physik 53,* 92–94 (1929).
19. Noyes, W. A., and Leighton, P. A. *The Photochemistry of Gases.* Reinhold, 1941.
20. Yost, D. M., and Russell, H., Jr. *Systematic Inorganic Chemistry of the Fifth-and-Sixth Group Nonmetallic Elements.* Prentice-Hall, 1944.
21. Zemansky, M. W. Absorption and collision broadening of the mercury resonance line. *Phys. Rev. 36,* 219–238 (1930).
22. Ditchburn, R. W., and Gilmour, J. C. The vapor pressures of monatomic vapors. *Revs. Mod. Phys. 13,* 310–327 (1941).

ARTICLE A,6

X-RAY TECHNIQUE

EVA M. WINKLER

A,6.1. Principle and Accuracy of the Method. Another method to measure the density of gases makes use of the absorption of soft X rays, i.e. X rays of wavelengths longer than about 2A. In view of the application to aerodynamic studies, this method attracted attention not only as an alternate probeless means for density determination but also because of certain advantages inherent in it. In comparison to optical methods, refraction and diffraction phenomena can practically be neglected with X rays because of the small deviation of the index of refraction from unity and the short wavelength. This is an advantage if measurements are to be made near wall and model surfaces or of steep density gradients. Furthermore, as will be shown in the following, the X-ray absorption method can be used with a specified accuracy for a wide range of densities for any given dimensions of the test section by suitably selecting the X-ray wavelength.

Assuming for the present the X rays to be monochromatic, their attenuation in passing through a layer of matter of thickness l is expressed by an exponential law of the form

$$I = I_0 e^{-\mu l} \tag{6.1-1}$$

where μ, the total absorption coefficient, is a function of the X-ray wavelength λ, the atomic number Z, and the density ρ of the absorbing element. If the absorber is a homogeneous material of more than one element, its mass absorption coefficient μ/ρ is the sum of the mass absorption coefficients of the individual elements weighted according to their relative abundance in the material [*1*, p. 513].

μ may be expressed by the empirical relation

$$\mu = CZ^4\lambda^3\rho + \sigma(Z, \lambda)\rho \tag{6.1-2}$$

where the first term, given in the form suggested by Bragg and Pierce [*2*,*3*], accounts for the true absorption and the second term for the scattering. C is a constant, which, however, changes its numerical value at the critical absorption wavelengths. For $\lambda < \lambda_K$ (λ_K = wavelength of K-absorption limit), and if λ is measured in angstrom units, and A denotes the atomic weight of the absorber, we have $C = 16 \times 10^{-3}/A$; for $\lambda_K < \lambda < \lambda_L$, $C = 5 \times 10^{-4}/A$ [*4*]. The relation 6.1-2 is the most convenient expression of μ for estimating the amount of absorption to be expected under various conditions. It represents μ for air with fair accuracy up to 5A, but gives too large values for longer wavelengths. An empirical expression for calculating the total absorption coefficient with an accuracy of about 1 per cent for any wavelength range and any element has been given by J. A. Victoreen [*5,6*]. This expression for μ is

$$\mu = (C\lambda^3 - D\lambda^4)\rho + \sigma(Z, \lambda)\rho \tag{6.1-3}$$

C and D are constants which may be calculated from the atomic energy states of the absorbing element [*6*, Eq. 3]. For $\lambda < \lambda_K$ the values of C and D for various elements have been tabulated by Victoreen [*6*, Table I].

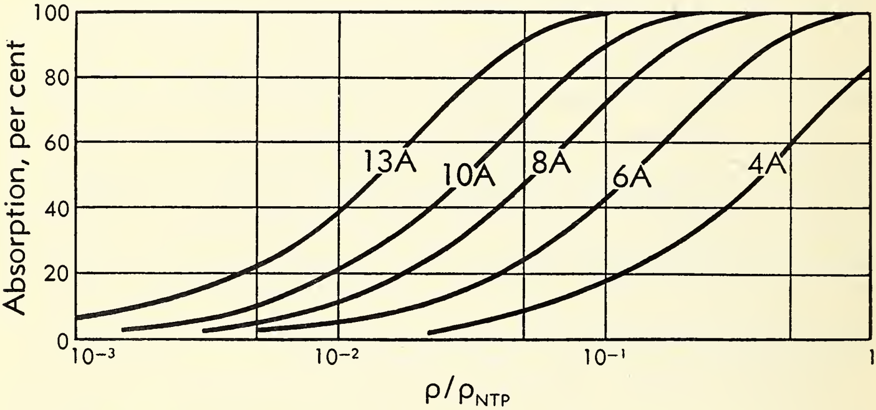

Fig. A,6.1a. Absorption of X rays in a 10-cm air path as function of the density for various wavelengths.

The scattering coefficient $\sigma(Z, \lambda)$ increases slowly with λ and with Z. In the wavelength range suitable for gas density measurements by absorption ($2A \leqq \lambda <$ approximately 20A) the value of $\sigma(Z, \lambda)$ for air amounts to not more than 2 per cent of the true absorption coefficient.[1]

Relation 6.1-1, together with Eq. 6.1-2 or Eq. 6.1-3, may be used to determine the wavelength which is suitable for measuring a desired range of densities in a test section of specified width. Fig. A,6.1a illustrates the absorption of X rays in air in a 10-cm wide test section, as a function of the density, for various wavelengths.

We shall now consider the accuracy with which density data can be determined from absorption measurements. Assuming the relative error of the intensity measurements to be small, we have for the density error approximately

$$\frac{\Delta\rho}{\rho} = -\frac{1}{\mu l}\frac{\Delta I}{I} \tag{6.1-4}$$

---

[1] For exact values of $\sigma(Z, \lambda)$ see [*6*, Table V and Eq. 8].

Here $\Delta I/I$ is the error encountered in measuring the absorption. Disregarding the variation in $\Delta I/I$, the X-ray wavelength determines the accuracy with which the density can be measured in a test section of specified width. In Fig. A,6.1b, the density error is plotted as function of the density for various wavelengths for a 10-cm wide test section. $\Delta I/I$ was assumed to be 1 per cent, which can, in general, be achieved with moderate effort. A discussion of the factors which affect the accuracy of the intensity measurements cannot be given here. For this, the reader is referred to [*7*,*8*,*9*].

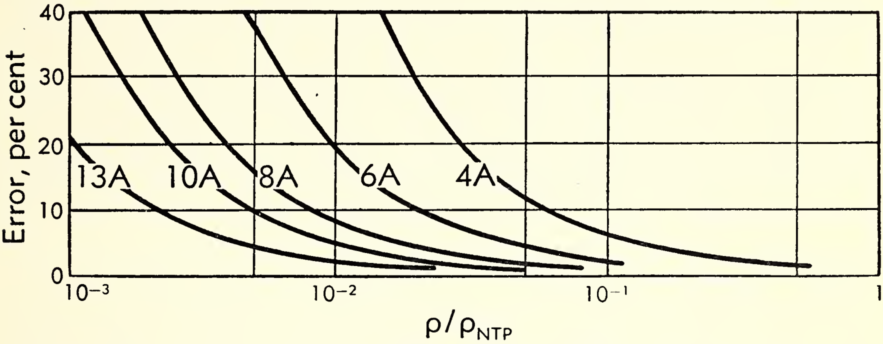

Fig. A,6.1b. Density error to be expected from X-ray absorption measurements in a 10-cm air path as function of the density for various wavelengths, assuming $\Delta I/I = 0.01$.

The use of Eq. 6.1-1 for calculating the density from absorption measurements requires that monochromatic X rays be used. The low intensity with which monochromatic radiation can be obtained would render the method impractical for an application to aerodynamic studies because of the long measuring times which would be needed. It is, therefore, common practice to refer the measurements to a previously made calibration curve. This has the advantage that X rays of any spectral distribution can be used, i.e. characteristic radiation or a continuous spectrum. It is, however, necessary to make certain that the spectral distribution remains reasonably constant during calibration and measurements. If a continuous spectrum is used, its effective wavelength can be controlled by the operating voltage of the X-ray tube. The voltage required to obtain a desired effective wavelength can be estimated from Dauvillier's law $\lambda_{\max} = 1.3\lambda_0$ (for X rays emitted perpendicular to the cathode rays) and the Duane-Hunt relation $\lambda_0 = 12{,}405/V$

$$\lambda_{\text{eff}} \cong \lambda_{\max} = \frac{16{,}126.5}{V} \tag{6.1-5}$$

where V is measured in volts.

With respect to the technique of obtaining absorption data of a flow pattern, we have the choice between making "point by point" measurements or photographing a portion of the flow pattern. The evaluation of "point by point" measurements, for two-dimensional and rotationally symmetric flow, is identical with the evaluation used with the interferometric technique; for details see Art. 1. It is understood that the abovementioned analysis must be modified for the evaluation of photographs made by a conical X-ray beam.

Point by point measurements require that the X-ray tube and the receiver be moved parallel to each other along the traverse. In order to warrant a good geometrical resolution of density gradients, the beam cross section must be very small. The measuring time at one point, using a Geiger counter as receiver, is of the order of a few seconds [*10*], and for the photographic technique of the order of a few minutes; see Art. 6.2. So far transient phenomena cannot be studied in light gases. For measurements in strongly absorbing gases harder radiation can be utilized. X-ray flash tubes with exposure times of 10^{-6} sec and less are then feasible. This technique has been applied by W. Schaafs to the study of sound waves generated by sparks in dielectric liquids [*11*].

A,6.2. Apparatus. The basic arrangement of apparatus is simple. It requires mainly that X-ray tube and receiver, mounted at their respective sides of the test section, either can be properly aligned with respect to each other, or are kept stationary and the model moved instead. An evacuated connection tube between X-ray tube and test section should be provided to avoid absorption in the space between them. For a monitoring of the "zero" X-ray intensity, a reference receiver should be incorporated.

In order to facilitate short measuring times and good geometrical resolution, the X-ray tube should be designed for high emission from a small target area. Since atomic number, melting point, and thermal conductivity determine the maximum radiation intensity obtainable per unit area, the target material should be selected accordingly [*12*, p. 34], except when characteristic X radiation is to be used. In the wavelength range between 2 and 20A, characteristic X rays are available from chromium and aluminum targets, λ2.28A and λ8.32A, respectively. The minimum voltage V_0 required to excite the characteristic radiation can be found from the Duane-Hunt relation by using for λ_0 the wavelength of the K-absorption limit of the target material. Though the line intensity increases roughly with the square of the overvoltage $(V - V_0)$, the overvoltage feasible for use of unfiltered characteristic radiation will be determined by considering the amount of continuous background that can be tolerated. For all other effective wavelengths, the utilization of the continuous spectrum from a tungsten target tube is the best choice.

Only tubes equipped with ray exit windows of low inherent absorption of soft X rays are practical. For wavelengths shorter than about 4A, commercial tubes are adequate if sealed by beryllium, aluminum, or Lindemann glass windows [*13*]. Radiation softer than about 4A, however, is not available with sufficient intensity from commercial tubes because the window thickness of $\frac{1}{4}$ to 1 mm used in permanently sealed tubes cuts the transmission to a few per cent. For X rays between 4 and 10A wavelength thin foil windows, aluminum or cellophane of about 10-micron thickness, give sufficiently high transmission. Such tubes have to be evacuated continuously. Suggestions for their design and construction can be found in many publications [*14,15,16*]. For wavelengths longer than 10A, the absorption loss in 10-micron foils is of the order of 90 per cent. A considerable gain in intensity can be achieved by omitting the window completely. This could be done by arranging a system of continuously evacuated chambers between the X-ray tube and the ray entrance pinhole of the test section. This chamber system, interconnected by pinholes of the size of the desired beam diameter, can be evacuated stepwise by suitably chosen pumps to provide the necessary pressure difference between test section pressure and the high vacuum in the X-ray tube. For illustration, Table A,6.2 compares the suitability of

Table A,6.2

Density to be measured (ρ/ρ_{NTP})	λ_{eff} required for 50% absorpt. in 10-cm path (A)	Tube voltage required (kv)	X-ray intensity 1 cm from target (erg/mm^2 sec)	Tube window	Total absorpt. (%)*	Remaining intensity 60 cm from target (hν/mm^2 sec)	Time to measure intensity within ±1% (sec)†
5×10^{-1}	3.7	4.4	0.5	beryllium	82.0	4,700	2.1
				cellophane	63.0	9,600	1.1
				windowless	55.0	11,700	0.9
10^{-1}	6.2	2.6	0.5	beryllium	99.6	170	60.0
				cellophane	86.5	5,900	1.7
				windowless	63.0	16,300	0.6
5×10^{-2}	7.8	2.0	0.5	beryllium	99.9	44	230.0
				cellophane	94.8	2,800	3.6
				windowless	73.0	15,000	0.7
10^{-2}	13.5	1.2	0.5	cellophane	99.6	380	26.0
				windowless	90.6	8,900	1.1

* This includes the absorption in 0.25 mm Be, 0.02 mm cellophane, or the air remaining in the windowless X-ray tube arrangement, respectively, the absorption in the tunnel entrance and exit windows, of 0.008 mm cellophane, and the absorption in the tunnel air.

† Based on the use of a Geiger counter as receiver.

X-ray tubes with three different kinds of windows for measuring the air density in a 10-cm wide test section. The measuring times given in this table refer to Geiger counters as recording instruments.

Photographic film, ionization chambers, or various types of counters are generally suitable for measuring X-ray intensities. In selecting one or the other, one has to consider the magnitude of the signal to be expected, the time which can be tolerated for one measurement, the accuracy desired, and the convenience in performing the measurements. Some aspects of the various means for measuring X-ray intensities will be given here, but for detailed discussions of the various receivers and the general theory of the methods refer to [*1,9,12,17,18*].

The general advantage of the photographic method, namely that it gives a picture of the flow pattern which can be evaluated at leisure, is somewhat lessened in the application in question. This is due to the fact that photographic film is less sensitive to small X-ray intensities than an ionization chamber or counter [*17,18*]. Because of the limited intensity with which soft X rays are available, rather long exposure times are required. Using the relevant data of [*17*] and [*18*] for the case given in line 1 of Table A,6.2, we find that an exposure time of about 3 min is necessary to achieve an optical density of the film of 1.5 above fog.

To measure the intensity of a narrow X-ray beam, as used for point by point measurements, an ionization chamber or counters are more suitable. Using an integrating type of ionization chamber [*1*, p. 492; *9*], the measuring apparatus can be adapted to the magnitude of the X-ray intensity to be measured by properly selecting the capacity and resistance of the ionization chamber circuit. Considerations of microphonic disturbances, if the receiver has to be mounted at the wind tunnel, reduction of the amplifier background noise, zero drift of the meter, etc., impose restrictions with respect to the lowest X-ray intensity that is practical to measure with an ionization chamber.

Counter equipment [*9*] is most sensitive for low energy X rays and if very small beam cross sections are used. Due to the high gas amplification taking place in a Geiger counter, each X-ray quantum absorbed in the counter filling gas can be recorded. An argon filled counter with a 10-cm length of the sensitive volume has a counting efficiency between 93 and 100 per cent for incoming quanta in the energy region between 4 kv and 2.5 kv. To be suitable for high and low counting rates, the counter should have a short dead time and a low background counting rate, in order to keep to a minimum the corrections necessary due to coincidence losses (quanta not being recorded during the dead time of the counter) and background. The counter may be either connected to a counting rate meter, or it may be used in connection with a scaling circuit. The latter method is preferable for low counting rates because the time required to achieve a desired accuracy can then be varied conveniently.

With respect to the requirements on window thickness and material used with the receiver, and at the entrance and exit of the test section, the same considerations apply as for the X-ray tube. Among the commercially available counters, the Tracerlab TGC-3 counter, for example, is suitable for X rays as soft as 6A. Sealed by a 1 mg/cm^2 mica window, it has a transmission efficiency of 14 per cent for 2 kv X rays [*19*]. For softer radiation much thinner windows will be advantageous. In order to eliminate the absorption loss in a separate exit window, the counter should be sealed to the test section. Pressure regulation in the counter filling gas will then be advisable [*20*] to avoid bulging or breaking of the delicate window due to the pressure difference between test section and counter filling gas.

Scintillation counters for measuring low energy X rays use (NaI + Tl) as the sensing crystal. Their counting efficiency varies from 100 per cent for X rays of 5 kv or harder to about 65 per cent for 2 kv X rays [*21*]. Since windows between test section and the scintillating crystal can be omitted, these counters may be used for low energy X rays with better advantage than Geiger counters.

A,6.3. Application of the X-Ray Technique. So far only few applications have been made of the X-ray absorption technique [*10,22,23,24*]. The objective was not so much a study of certain flow patterns, but the investigations were primarily made to set forth the suitability of particular equipment for aerodynamic studies. Measurements of the free stream density of supersonic flow of Mach numbers between 1.5 and 3.3 were made by Arnold [*22*] and Winkler [*10*], using the point by point method, with an ionization chamber and a Geiger counter, respectively, as the X-ray detector. The sensitivities obtained were $0.02\rho_{\text{NTP}}$ and $0.008\rho_{\text{NTP}}$, respectively, if referred to a 10-cm path. They also applied the technique to measurements of the density change in shock waves at a wedge-shaped model [*10,23*]. Investigations of the density profile of the boundary layer of a flat plate at a Mach number of 0.65 have been made recently by Weltmann, et al. [*24*].[2] In this case a narrow beam of 0.05-mm width was used. The operational data of the X-ray tube were so chosen that a sensitivity of $0.015\rho_{\text{NTP}}$ was achieved. These studies were initially made point by point with a Geiger counter as receiver. Subsequently X-ray film was used to obtain a complete record of one boundary layer station.

A,6.4. Use of Corpuscular Rays. The utilization of the absorption of corpuscular rays has been suggested by various investigators in discussing means of gas density measurements in low density flow. But only recently Schopper and Schumacher [*25*] investigated the practical possibilities of using α particles, protons, and electrons.

---

[2] The author is deeply grateful to the NACA for obtaining this information in advance of its publication.

If a beam of corpuscular rays of energy E passes through matter of density ρ and thickness l, its energy is decreased by two mechanisms. One is the decrease of the energy ϵ of the individual particle, the other is a reduction of the number concentration n of particles per unit area and per second. In general, the attenuation of energy may be written as

$$\frac{dE}{d(\rho l)} = n\frac{\partial \epsilon}{\partial(\rho l)} + \epsilon\frac{\partial n}{\partial(\rho l)} \tag{6.4-1}$$

where $E = n\epsilon$. Depending upon the type of particles used for the absorption measurements either one of the terms of Eq. 6.4-1 will be predominant.

A,6.5. α Particles and Protons. In the case of α particles and protons as the probing beam, only the first term of Eq. 6.4-1 needs to be considered since the number concentration of the heavier particles remains constant practically over the entire length of their range, as illustrated schematically by curve n in Fig. A,6.5. The length of the range in specified material, however, is a function of its density and depends on the initial energy of the corpuscles. Measurement of the residual range, after a test section of specified length, therefore, is a measure of the density in the test section. Such measurements can conveniently be made by determining the differential ionization which varies with the energy

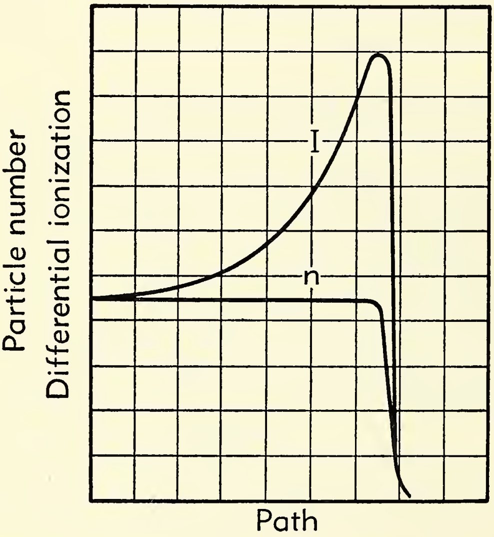

Fig. A,6.5. Particle number n and differential ionization I as function of the traversed path for α particles and protons (schematically).

decrease experienced by the particle; see curve *I* in Fig. A,6.5. The evaluation of density data from measurements of the differential ionization presupposes, of course, that ions formed in the test section do not affect the readings. Such effects can practically be neglected in measurements made in streaming gases, since the newly formed ions will be swept away more or less rapidly.

To illustrate the initial energy of particles necessary for density measurements in air, Table A,6.5 gives the ranges of protons and α particles in air at two different pressures. For a 10-cm path in air of 10 mm Hg pressure and 273°K temperature, for example, the initial proton energy should be 200 kev, and the initial α-particle energy between 200 and 500 kev.

Table A,6.5. Range in air (273°K) of α particles and protons of three different energies, after [*25*].

	Protons		*α Particles*	
Energy	760 mm Hg pressure	10 mm Hg pressure	760 mm Hg pressure	10 mm Hg pressure
100 kev	0.12 cm	9 cm	0.10 cm	7.6 cm
200	0.30	23	0.17	13
500	0.85	64	0.34	26

Since the relative change of particle energy $\partial\epsilon/\partial(\rho l)$ determines the sensitivity of an α particle or proton probe to record small changes in the gas density, and $\partial\epsilon/\partial(\rho l)$ varies with the particle energy [*26*, p. 270], the accuracy of this method can be adjusted to the density to be measured by a suitable selection of the particle energy. For large values of $\partial\epsilon/\partial(\rho l)$ which give a high accuracy, $\partial\epsilon/\partial(\rho l)$ changes, however, strongly with l (see [*26*, Fig. 31]), making a high sensitivity probe practical only in cases where the density is homogeneous along the probing beam. Such a probe, using α particles, was developed by Knapp [*27*]. It permits one to determine the air density at NTP with an accuracy of 0.15 per cent in a measuring time of only 10^{-2} sec.

A,6.6. Electrons. With electrons as the probing beam, particle energies between 50 kev and about 1 kev are suitable for measurements in low density air. In this case, the attenuation can essentially be described by the second term of Eq. 6.4-1. The attenuation is due partly to true absorption and partly to scattering. Assuming a beam of electrons of uniform energy entering a test section filled with a gas of density ρ, the beam spreads due to diffuse scattering. After a certain distance which is dependent upon the scatterer, the diffuse scattering comes to an equilibrium, i.e. the average number of scattered electrons tending to spread the center portion of the beam equals the average number of electrons scattered toward the center of the beam. From there on the attenuation of the center portion of the electron beam can be described by the familiar absorption law

$$n = n_0 e^{-\alpha l} \qquad (6.6\text{-}1)$$

where α the electron absorption coefficient is a function of the electron energy, the density, and atomic weight of the absorber.[3] Fig. A,6.6 illustrates the absorption to be expected in a 10-cm path, after the equilibrium is established, as function of the air density, and for three different electron energies.

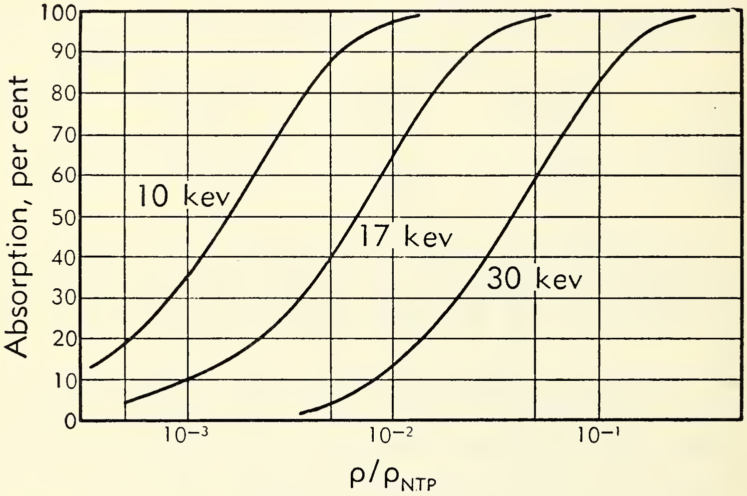

Fig. A,6.6. Absorption of electrons in a 10-cm air path as function of the air density for three different electron energies.

The apparatus needed is basically simple, requiring an electron tube with provisions to focus the beam; for example see [*25*, Fig. 2, p. 704]. For the higher energy electrons the tube may be closed by a Lenard window, but Schumacher and Schopper also incorporated a differential pumping system on the test section side to eliminate the need of a window when using 3 kev electrons. So far the method has been used for probing small air jets and measuring temperatures in burner flames.

A,6.7. Concluding Remarks. The possible advantages of the X-ray technique over the use of other quantitative methods like interferometry and the over-all possibilities of the corpuscular ray methods may be summarized as follows:

X rays may give results at lower density in the wind tunnel than interferometry; for measuring $\frac{1}{100}$ atmospheric density in a 10-cm path, one may obtain an accuracy of 2 per cent by using X rays of 13A. The time necessary to achieve this accuracy would be between 1 sec and about 30 sec (see Table A,6.2).

---

[3] Numerical values are given in [*28*, p. 61].

The study of density profiles in boundary layers may be more exact by using X rays than by use of interferometry, as the position of the edge of the plate studied is well defined with X rays, but cannot be measured directly by optical means. Such studies would require very narrow X-ray beams, and one would need a rather long and steady run for measuring a number of points in the boundary layer separately or obtaining a photographic record of one boundary layer station.

Either of the corpuscular ray probes extends the range where integrated values of the air density can be measured far beyond the range accessible with the conventional methods such as the interferometer. As with the X-ray technique, measurements near solid boundaries may be made without sacrifice of the definition of the position of the boundary, a difficulty encountered with optical methods.

The range where density data are to be measured and the accuracy of the measurements can be varied by a proper selection of the particle energy.

Though neither of the techniques described permits a visualization of the flow in a larger portion of the test section, point by point measurements may be made in a relatively short time.

A,6.8. Cited References.

1. Compton, A. H., and Allison, S. K. *X Rays in Theory and Experiment.* Van Nostrand, 1935.
2. Bragg, W. H., and Pierce, S. H. The absorption coefficients of X rays. *Phil. Mag. 28,* 626–630 (1914).
3. Bragg, W. H. The relation between certain X-ray wavelengths and their absorption coefficients. *Phil. Mag. 29,* 407–412 (1915).
4. Walter, B. *Fortschr. Gebiete Röntgenstrahlen, 35,* 929, 1309 (1927).
5. Victoreen, J. A. The absorption of incident quanta by atoms as defined by the mass photoelectric absorption coefficient and the mass scattering coefficient. *J. Appl. Phys. 19,* 855–860 (1948).
6. Victoreen, J. A. The calculation of X-ray mass absorption coefficients. *J. Appl. Phys. 20,* 1141–1147 (1949).
7. Arndt, U. W. An X-ray tube with adjustable focus. *J. Sci. Instr. 25,* 414–416 (1948).
8. Arndt, U. W. Power supply for an X-ray tube used in conjunction with a Geiger counter spectrometer. *J. Sci. Instr. 26,* 45–47 (1949).
9. Korff, S. A. *Electron and Nuclear Counters. Theory and Use.* Van Nostrand, 1946.
10. Winkler, E. M. Density measurements in supersonic flow by means of the X-ray absorption method. *J. Appl. Phys. 22,* 201–202 (1951).
11. Schaafs, W. Untersuchungen an Funkenschallwellen mit Hilfe von Röntgenblitzen. *Z. Naturforsch. 4a,* 463–472 (1949).
12. Sproull, W. T. *X Rays in Practice.* McGraw-Hill, 1946.
13. Brackney, H., and Atlee, Z. J. Beryllium windows for permanently evacuated X-ray tubes. *Rev. Sci. Instr. 14,* 59–63 (1943).
14. McCue, J. J. G. An X-ray tube using an electric gun. *Rev. Sci. Instr. 14,* 339–341 (1943).

15. Kliever, W. H. A high voltage, demountable X-ray tube. *Rev. Sci. Instr. 10,* 126–128 (1939).
16. Poittevin, M. Rayons X—Tube à rayons X à foyer linéaire de grande brillance. *Compt. rend. 224* (*Part 2*), 1709–1711 (1947).
17. Tellez-Plasencia, H. Théorie générale des méthodes de mesure des Rayons X. *J. phys. radium* (*ser. 8*)*9,* 230–235 (1948).
18. Hörlin, H. The photographic action of X rays in the 1.3 to 0.01A range. *J. Opt. Soc. Amer. 39,* 891–897 (1949).
19. Clarke, E. *Tracerlog 19.* Tracerlab, Boston, 1949.
20. Ter-Pogossian, M. Pressure regulated thin window Geiger-Müller counter. *Rev. Sci. Instr. 20,* 289–290 (1949).
21. West, H. I., Jr. Detection of X rays by means of NaI (Tl) scintillation counters. *Phys. Rev. 81,* 141–142 (1951).
22. Arnold, G. Density measurements with X rays in supersonic flow in the wind tunnel. *F2 A-157-47, Archive No. 66/124, Wright Field,* 1944.

22a. Dimeff, J., Hallett, R. K., Jr., and Hansen, C. F. X-ray instrumentation for density measurements in a supersonic flow field. *NACA Tech. Note 2845,* 1952.

23. Arnold, G. Density measurements on the structure of compression shock waves on wedge-shaped profiles. *F2 A-1434-46, Archive No. 66/192, Wright Field,* 1945.
24. Weltmann, R. N., Fairweather, S., and Papke, D. Application of X-ray absorption to measurement of small air-density gradients. *NACA Tech. Note 2406,* 1951.
25. Schopper, E., and Schumacher, B. Messung von Gasdichten mit Korpuskularstrahlsonden. *Z. Naturforsch,* 6*a,* 700–705 (1951).
26. Livingston, M. S., and Bethe, H. A. Nuclear physics. Part C. Nuclear dynamics, experimental. *Revs. Mod. Phys. 9,* 245–390 (1937).
27. Knapp, D. *Thesis.* Technical Univ., Stuttgart, 1950.
28. *International Critical Tables.* Vol. VI. McGraw-Hill, 1929.

SECTION B

PRESSURE MEASUREMENTS

P. L. CHAMBRÉ
S. A. SCHAAF
WALKER BLEAKNEY
ARNOLD B. ARONS

ARTICLE B,1

THE IMPACT TUBE

P. L. CHAMBRÉ
S. A. SCHAAF

B,1.1. Introduction. The impact (Pitot) tube is one of the standard instruments for measuring the total pressure of a moving gas stream. It consists in essence of an open-ended tube facing the oncoming flow, the other end of the tube being connected to a pressure-sensitive element. The pressure recorded by the latter, except at very low free stream pressure, is the average of the forces acting on a unit surface of fluid particles located at the stagnation point of the instrument. By means of an appropriate analysis the total pressure can be related to certain properties of the gas flow such as, for example, the free stream velocity and the static pressure. Since the pressure is exerted at a stagnation point of the instrument, the total pressure is also referred to as the stagnation pressure or impact pressure. The impact pressure p^0 is a measured quantity and is not necessarily equal to the local reservoir pressure p_i^0 which would be obtained after isentropic deceleration of the flow to zero velocity.

In the flow of an ideal fluid the reservoir pressure p_i^0, the free stream static pressure p_∞, and the free stream Mach number M_∞ are related by [*1*, p. 26]

$$\frac{p_i^0}{p_\infty} = \left(1 + \frac{\gamma - 1}{2} M_\infty^2\right)^{\frac{\gamma}{\gamma-1}} \tag{1.1-1}$$

For very low free stream Mach numbers Eq. 1.1-1 can be approximated by

$$\frac{p_i^0}{p_\infty} \cong 1 + \frac{\gamma}{2} M_\infty^2 = 1 + \frac{1}{2}\left(\frac{\rho_\infty U^2}{p_\infty}\right) \tag{1.1-2}$$

where ρ_∞ and U are the free stream density and velocity respectively. Experimental evidence indicates that for real fluids Eq. 1.1-2 is replaced by [*2*, p. 248]

$$\frac{p^0}{p_\infty} = 1 + C\left(\frac{1}{2}\frac{\rho_\infty U^2}{p_\infty}\right) \tag{1.1-3}$$

where p^0 is the actual measured stagnation pressure and C is a numerical factor which is approximately unity for most conditions of operation except at very low Reynolds numbers.

For supersonic flow of an ideal fluid the gas may be assumed to pass through a normal shock which forms ahead of the instrument. After the shock the fluid is assumed to decelerate isentropically to the stagnation point. The total pressure is then given by [*1*, p. 77]

$$\frac{(p_i^0)'}{p_\infty} = \frac{\left(\frac{\gamma + 1}{2} M_\infty^2\right)^{\frac{\gamma}{\gamma - 1}}}{\left(\frac{2\gamma}{\gamma + 1} M_\infty^2 - \frac{\gamma - 1}{\gamma + 1}\right)^{\frac{1}{\gamma - 1}}} \tag{1.1-4}$$

where $(p_i^0)'$ is the local reservoir pressure after the shock. Considerations of geometric and dynamic similarity show that the ratio of stagnation pressure to static pressure of a real fluid can be expressed for both subsonic and supersonic flow quite generally in the form

$$\frac{p^0}{p_\infty} = \frac{p_i^0}{p_\infty} F\left[Re,\ M_\infty,\ Pr,\ \gamma,\ \frac{\overline{q'^2}}{U^2},\ \frac{\lambda}{r},\ \frac{t}{r/U},\ \theta,\ \frac{r_1}{r}\ \cdots\right] \tag{1.1-5}$$

F is a function of the following dimensionless moduli:

1. The Reynolds number of the flow based on the probe radius, i.e. Re
2. The Mach number of the flow M_∞
3. The Prandtl number of the gas Pr
4. The ratio of the specific heats γ
5. The intensity of the free stream turbulence $\overline{q'^2}/U^2$
6. The Knudsen number, i.e. the ratio of molecular mean free path to probe radius which characterizes the effect of slip, λ/r
7. The ratio of the relaxation time of the gas to a characteristic macroscopic time interval $t/(r/U)$
8. The angle of attack which the probe makes with the flow, i.e. θ
9. The ratio of dimensions of stagnation orifice to the external tube dimensions r_1/r

In the following we concern ourselves with an analysis of the influence of some of these dimensionless parameters on the measurement and interpretation of stagnation point pressures.

B,1.2. Viscous Effects.

Introduction. The method of interpreting total pressure measurements with the help of ideal fluid theory is valid as long as the Reynolds number $Re = Ur/\nu$ is sufficiently large, say $Re > 100$ (r denotes the probe radius and ν the kinematic viscosity of the fluid). For small Reynolds numbers, however, the measured impact pressure increases in a manner dependent on the Reynolds number as well as on the shape of the probe.

The problem has been investigated theoretically and experimentally [*3,4,5*].

Incompressible Case. Consider an impact probe in the form of a body of revolution oriented along the y axis with its vertex at the origin and the oncoming flow having a velocity of (Fig. B,1.2a)

$$u = 0, \qquad v = -U, \qquad w = 0$$

Let the flow along the central stream line leading to the stagnation point decelerate to the edge of the boundary layer which is presumed to form at the nose of the instrument. The radial coordinate of distance from the y axis is x. Then the Navier-Stokes equation in the y direction for the stagnation stream line for which $x = u = 0$ reduces to

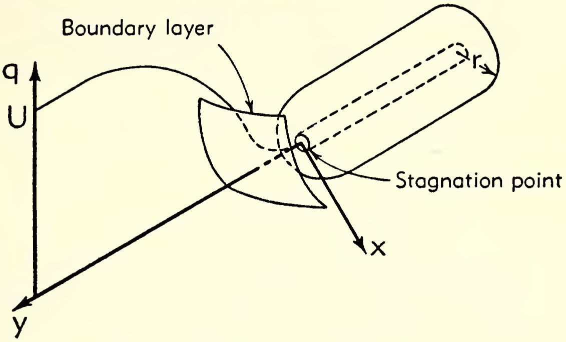

Fig. B,1.2a. Sketch of the velocity distribution about an impact tube with a source-shaped head.

$$\rho_\infty v \frac{\partial v}{\partial y} = -\frac{\partial p}{\partial y} + \mu \nabla^2 v \tag{1.2-1}$$

Making the usual boundary layer assumption that $\nabla^2 v \cong \partial^2 v/\partial y^2$ one obtains

$$\rho_\infty v \frac{\partial v}{\partial y} = -\frac{\partial p}{\partial y} + \mu \frac{\partial^2 v}{\partial y^2} \tag{1.2-2}$$

For constant density and viscosity this can be integrated with respect to y from $y = 0$ to the edge of the boundary layer at $y = \delta$. The result is

$$\frac{1}{2}\rho_\infty v^2 \Big]_0^\delta = -p \Big]_0^\delta + \mu \frac{\partial v}{\partial y}\Big]_0^\delta \tag{1.2-3}$$

Assuming that the fluid does not slip over the surface u, v, $\partial u/\partial x$, and $\partial v/\partial y$ (by the continuity equation) all vanish at $y = 0$. Writing for the measured impact pressure at the stagnation point $p = p^0$ one obtains

$$p^0 = \left(p_\delta + \frac{1}{2}\rho_\infty U_\delta^2\right) - \mu \left(\frac{\partial v}{\partial y}\right)_{y=\delta} \tag{1.2-4}$$

The quantity $(p_\delta + \frac{1}{2}\rho_\infty U_\delta^2)$ is simply the local ideal reservoir pressure outside the boundary layer, i.e. the normal impact pressure p_i^0 obtained in the absence of viscous effects. By the continuity equation,

$$\frac{\partial v}{\partial y} = -2\frac{\partial u}{\partial x} \equiv -2\beta \tag{1.2-5}$$

so that

$$p^0 = p_i^0 + 2\mu\beta \tag{1.2-6}$$

The quantity β, which has the dimension of a velocity gradient, may be determined experimentally or estimated theoretically from the potential flow field about the probe. The dimensions of the latter must be corrected by the boundary layer displacement thickness. For a source-shaped tube,[1] for example, the velocity potential is given by [*6*, p. 54]

$$\phi = Uy + \frac{r_0^2 U}{[x^2 + (y + r_0)^2]^{\frac{1}{2}}} \tag{1.2-7}$$

so that

$$\beta = \frac{U}{r_0} \tag{1.2-8}$$

The quantity r_0 is the radius of curvature of the edge of the boundary layer at the stagnation point. It is taken to be the actual radius of curvature of the probe surface plus a displacement thickness δ^* at the stagnation point, which was evaluated to be [*4*]

$$\delta^* = 0.5576\sqrt{\frac{\nu_\infty}{\beta}} \tag{1.2-9}$$

Hence

$$\beta = \left(\frac{2}{1 + \frac{0.394}{\sqrt{Re}}}\right)\frac{U}{r} \tag{1.2-10}$$

For different probe geometries β can be expressed quite generally in the form

$$\beta = \left(\frac{C_1}{1 + \frac{C_2}{\sqrt{Re}}}\right)\frac{U}{r} \tag{1.2-11}$$

The correction term $2\mu\beta$ may be related to the coefficient C of Eq. 1.1-3. Combining Eq. 1.1-2, 1.1-3, 1.2-6, and 1.2-11 results in

$$C = 1 + \frac{4C_1}{Re + C_2\sqrt{Re}} \tag{1.2-12}$$

The validity of these results for incompressible flow has been investigated experimentally for a forward stagnation point flow on a sphere. A similar analysis for a cylinder was also checked experimentally [7]. The agreement indicated in Fig. B,1.2b is quite good, even for very small Reynolds numbers.

---

[1] A source-shaped tube has a surface contour corresponding to the stagnation stream line of a combination of a point source with a uniform flow.

In the above analysis it has been assumed that the measured pressure is equal to the stagnation point pressure. In practice, the measured pressure is the mean value over the area of the stagnation orifice and is generally lower than the total pressure at $x = y = 0$. A simple analysis shows that the average stagnation pressure p^0_{av} for an orifice of radius r_1, $(r_1 \ll r)$ is given by

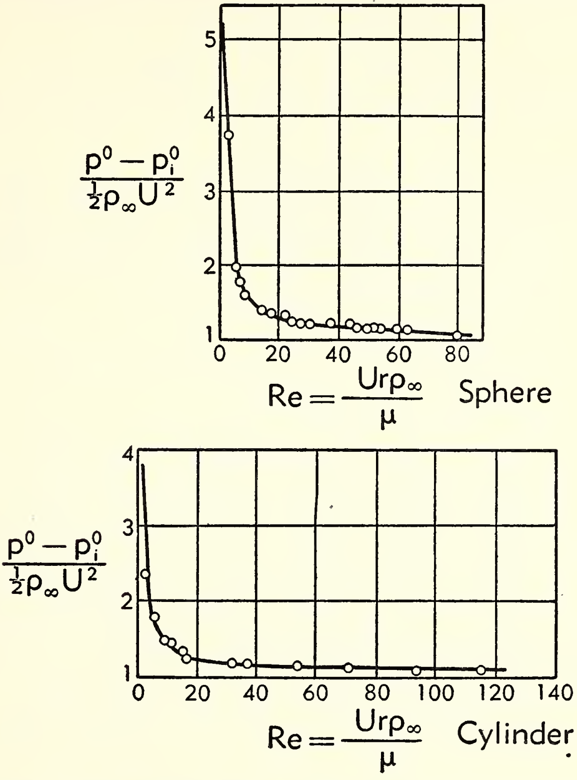

Fig. B, 1.2b. Theoretical and experimental viscous correction to impact pressure on a cylinder and a sphere as given by Homann [4].

$$p^0_{av} = p^0 - \frac{\beta^2 \rho_\infty r_1^2}{4} \qquad (1.2\text{-}13)$$

Experimental verification of this correction is incomplete. Since the flow field in the immediate vicinity of the pressure orifice is quite complicated, due to the possibility of fluid motion inside the orifice opening, the tentative nature of Eq. 1.2-13 must be emphasized. Preliminary experimental work indicates a larger effect of orifice diameter.

Subsonic Compressible Case. For subsonic compressible flow the results given above can be extended by including the effect of compressibility on the potential flow outside the boundary layer, while neglecting the effects of compressibility inside the boundary layer. The Rayleigh-Janzen method [*1*, p. 161] is used to obtain a velocity potential for the subsonic compressible flow about the probe as long as the critical Mach number is not exceeded. This furnishes a corrected value for β in the form

$$\beta_{\text{compr}} \cong \beta_{\text{incompr}} (1 - C_3 M_\infty^2) \tag{1.2-14}$$

For a spherical-shaped probe, for example, it is estimated that [*8*]

$$C_3 = \tfrac{83}{330} \tag{1.2-15}$$

The corresponding viscous correction may be expressed in the form of the ratio of the measured stagnation pressure p^0 to the ideal nonviscous stagnation pressure p_i^0 by dividing Eq. 1.2-6 by p_i^0 and using Eq. 1.1-1, 1.2-11, and 1.2-14 and the perfect gas law to give

$$\frac{p^0}{p_i^0} = 1 + \frac{M_\infty^2}{Re} \left[\frac{2\gamma C_1 (1 - C_3 M_\infty^2)}{1 + \dfrac{C_2}{\sqrt{Re}}} \right] \left[1 + \frac{\gamma - 1}{2} M_\infty^2 \right]^{-\frac{\gamma}{\gamma - 1}} \tag{1.2-16}$$

A series of half-spherical probes of different radii has been tested experimentally. Preliminary results check the validity of Eq. 1.2-16 within the limit of error (of the order of 20 per cent) of the experiments [*5*].

Supersonic Case. The analysis given above breaks down for the case of supersonic flow due to the presence of a detached shock wave in front of the probe. The problem has been investigated experimentally for source-shaped probes in a low density supersonic wind tunnel [*9*]. The Reynolds number was varied by using either probes of different radii or by changing the pressure level of the gas stream. The data extends over a Reynolds range based on probe diameter of 25 to 800 and a Mach number range of 2.3 to 3.6. The results are given in Fig. B,1.2c. It can be seen that the viscous effects in the range of supersonic flow investigated are of importance when the Reynolds number is less than 100.

An important application where the use of a Pitot tube has been explored in the case of supersonic flow is in the measurement of pressure distributions in supersonic boundary layers. The small dimensions involved and interference effects seriously influence the utility of this technique and data interpretation therefrom. Discussions of the problem are given in [*9b,9c*].

See [*21*] for a report on two Pitot-static tubes tested in the Langley 9-in. supersonic tunnel at free stream Mach numbers of 1.93 and 1.62.

Slip and Relaxation Effects. In a low density gas flow the tangential velocity of the fluid at the surface of the probe is not zero.

The gas "slips" over the surface with a velocity q_w which is related to the wall shear τ_w by

$$q_w \cong \frac{\lambda}{\mu} \tau_w \tag{1.2-17}$$

where λ is the molecular mean free path and varies inversely with the density of the gas. If the low Reynolds number, with which the viscous effects mentioned above are associated, arises from the fact that the stream density is low, these effects may be further complicated by the phenomenon of slip.

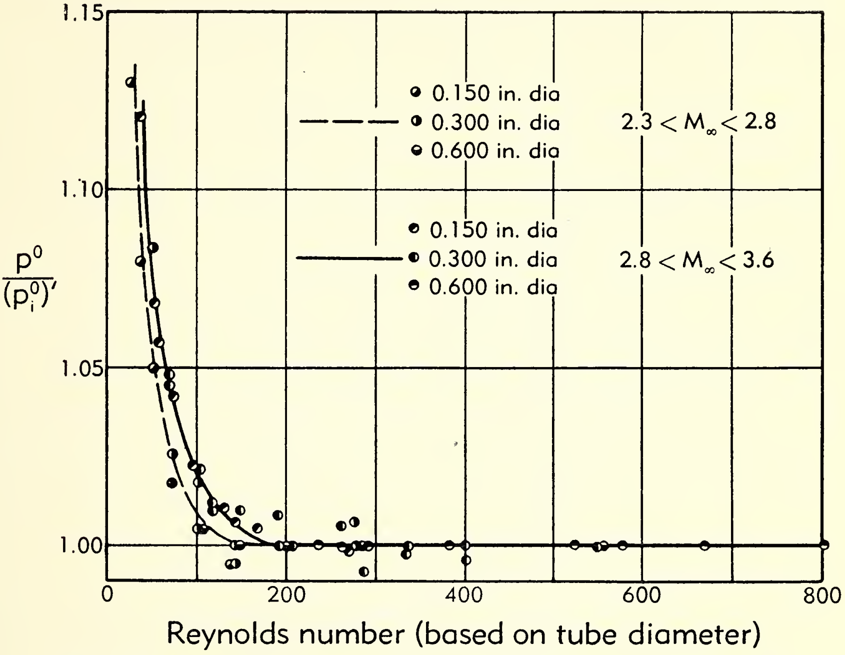

Fig. B,1.2c. Viscous correction to impact pressure in supersonic flow.

The problem has been investigated theoretically [*10*]. At the stagnation point under no slip condition, the normal stress $-\sigma_y$ and the mean pressure p are identical since in the relation

$$\sigma_y = -p + 2\mu \frac{\partial v}{\partial y} \tag{1.2-18}$$

$\partial v/\partial y$ vanishes. The results indicate that the mean pressure at the stagnation point will decrease due to the effect of slip, while the normal stress $-\sigma_y$ increases. As the probe measures $-\sigma_y$ the effect of slip is to increase the viscous correction to the impact pressure. Since the molecular mean free path λ, the Mach number M, the Reynolds number Re, and the probe radius r are related by [*11*]

$$\frac{\lambda}{r} = 1.255\sqrt{\gamma}\frac{M}{Re} \tag{1.2-19}$$

the results can be expressed in terms of M and Re as indicated in Fig. B,1.2d.

The existence of energy dissipation due to lag in the vibrational heat capacity of the gas will also affect the total pressure reading of the instrument. It has been shown both theoretically and experimentally [*12*] that total pressure defects, due to heat capacity lag during and after the compression of the gas at the stagnation point of the impact probe, are to be anticipated. The time interval in which the compression of the gas occurs is essentially determined by a characteristic dimension of the impact probe and the free stream velocity. If this time interval is comparable with or shorter than the time required for the gas to maintain an equilibrium partition of energy, the process is accompanied by an increase in entropy with a resultant drop in impact pressure. Since the relaxation time necessary to excite the vibrational energy is inversely proportional to the static pressure level of the gas, the effect becomes

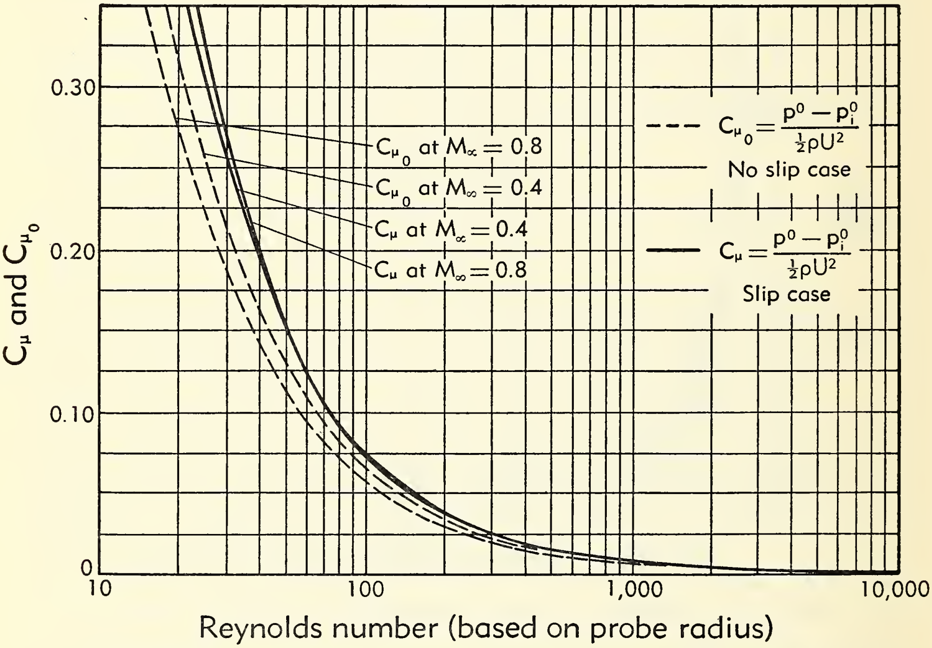

Fig. B,1.2d. Effect of slip on viscous correction to impact pressure on a probe with a half-spherical head in subsonic flow.

significant in low density gas streams with fully excited vibrational energy levels.

B,1.3. Tolerances in Alignment. Effects of Transverse Velocity Gradient and Free Stream Turbulence. In use, the head of the impact tube has to be aligned properly with the gas flow. Since the direction of flow is usually not known exactly, there arises the question of the effects of the angle of yaw on the total pressure measured. The effects vary to some extent with the geometric forms of the impact tube head and the ratio of stagnation orifice size to external dimensions of the instrument. The following comments refer to gas flows in which viscous and relaxation effects are absent.

For incompressible flows the relation between angle of yaw and total pressure has been investigated experimentally for a variety of different head geometries [*13*, pp. 498–500]. It has been shown that instruments with ogive head forms are less sensitive to errors than probes with blunt half-spherical heads. In general an angle of yaw of 5 degrees or less produces little or no error in the reading.

A study of the influence of stagnation orifice size on the reading with different angles of yaw revealed that in the case of half-spherical head the instrument became more sensitive as the orifice size increased [*13*].

Subsonic tests on a round-nosed and flat-nosed total pressure tube revealed characteristics similar to those quoted above [*14*]. In a Mach number range from 0.3 to 0.9 no error was incurred by either tube for angles of yaw from 0° to 10°.

At supersonic speeds theoretical considerations indicate [*15*] that the true stagnation pressure behind a normal shock will not be measured unless the stagnation orifice is small in comparison to the frontal area of the probe. An experimental study of the effect of nose shape on the stagnation pressure measurement has been made [*16*]. Probes with different nose shapes—square, spherical, and conical with 5° half angle—were tested at Mach numbers between 1.5 and 2.2 under various angles of yaw. It was found that up to angles of approximately 10° all measured pressures were within 1 per cent of the theoretical values for all tubes. The blunter-nosed tubes were, however, more independent of attitude at larger angles of attack.

Under certain circumstances the impact tube is employed in flow fields which exhibit regions of transverse total pressure gradients. Under these conditions there exists generally a considerable velocity gradient across the stagnation orifice. Hence it cannot be assumed that the total pressure measured by the tube is the total pressure of the fluid corresponding to the geometric center of the stagnation orifice. This problem has been investigated for an incompressible subsonic fluid [*17*]. It was found that the effective center of the total pressure is displaced from the geometric axis of the instrument toward the region of higher velocity. The amount of the displacement δ depends on the internal and external diameters of the instrument d_1 and d respectively. The correction is given by

$$\frac{\delta}{d} = 0.131 + 0.082\frac{d_1}{d} \tag{1.3-1}$$

The effects of free stream turbulence on the reading of the impact probe have been discussed theoretically [*18*] for incompressible subsonic flows. It appears that the total pressure measured by the instrument is given by

$$p^0 = \bar{p}_\infty + \tfrac{1}{2}\rho_\infty U^2 + \tfrac{1}{2}\rho_\infty \overline{q'^2} \tag{1.3-2}$$

where $\bar{p}_\infty$ is the mean free stream static pressure of the fluid and $\overline{q'^2}$ is the mean square of the turbulent velocity components. In accurate investigations of total pressures near solid surfaces the effects of turbulence become important due to the relative magnitude of the turbulent velocity fluctuations.

B,1.4. Impact Tube Theory in Free Molecule Flow. At very low pressures, when the molecular mean free path is large compared to the impact tube dimensions, the chances of collision of molecules among themselves are much smaller than the chances for collision with the surface of the probe. Hence collisions between molecules can be neglected. Such flows are known as free molecule flows. The interpretation of impact pressures under such conditions is considerably different from the continuum cases discussed in the first part of this section.

Theory. For simplicity consider an impact tube which consists of an orifice in an infinitely thin wall which is oriented perpendicular to the oncoming gas stream of velocity U. The pressure-measuring device is located on the other side of the partition. It is assumed that the gas in the free stream appears to an observer traveling with the macroscopic velocity U to be in Maxwellian equilibrium. From kinetic theory, the number of molecules entering the orifice per unit time from the free stream side is given by [*11*]

$$N_{\text{in}} = \frac{\rho_\infty}{m}\left\{\frac{1}{2}\sqrt{\frac{2RT_\infty}{\pi}}\,e^{-\frac{U^2}{2RT_\infty}} + \frac{U}{2}\left[1 + \operatorname{erf}\left(\frac{U}{\sqrt{2RT_\infty}}\right)\right]\right\} \tag{1.4-1}$$

where ρ_∞, T_∞ are the free stream density and temperature respectively, m is the mass of a molecule of the gas and

$$\operatorname{erf}(s) = \frac{2}{\sqrt{\pi}}\int_0^s e^{-y^2}\,dy$$

If the temperature and density on the other side of the partition are T_1

and ρ_1 respectively, the number of molecules which flow through the orifice toward the oncoming gas stream is given by

$$N_{\text{out}} = \frac{\rho_1}{2m}\sqrt{\frac{2RT_1}{\pi}} \tag{1.4-2}$$

It has been assumed that the gas in the pressure measuring device is

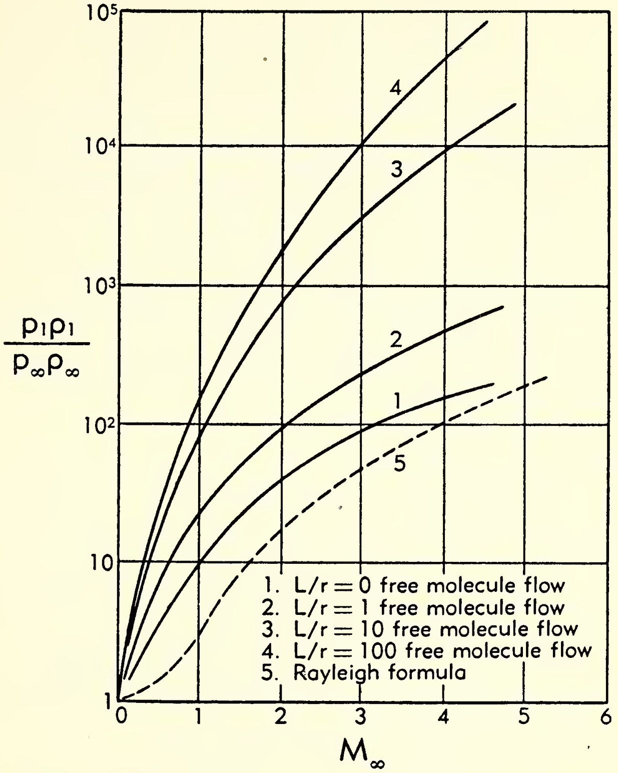

Fig. B,1.4. Ratio of pressure density products as a function of Mach number in free molecule flow.

also in Maxwellian equilibrium. Clearly, equilibrium is attained when $N_{\text{in}} = N_{\text{out}}$. This leads to a relationship of the form

$$\frac{p_1\rho_1}{p_\infty\rho_\infty} = \left\{e^{-\frac{\gamma}{2}M_\infty^2} + M_\infty\sqrt{\frac{\pi\gamma}{2}}\cdot\left[1 + \operatorname{erf}\left(M_\infty\sqrt{\frac{\gamma}{2}}\right)\right]\right\}^2 \tag{1.4-3}$$

where M_∞ is the free stream Mach number.

This analysis has been extended to the case of an impact tube with arbitrary length to internal radius ratio L/r [*19*]. The results are depicted in Fig. B,1.4 where the continuum relation (Rayleigh) has been included for purposes of comparison. Experimental verification is still lacking.

Response Time. Under very low pressure conditions when the molecular mean free path is of the order of a probe's interior dimensions, the time lag for the pressure at the gauge to reach equilibrium following a change in pressure at the stagnation orifice may be considerable unless care is taken to dimension the probe properly. Assuming free molecule flow and diffuse molecular reflection inside the gauge system, an approximate formula may be obtained for the time lag t in the form [20]

$$t \cong C_4\left(\frac{VL}{r_1^3} + \frac{8V}{3r_2^2} + \frac{8\pi r_1^2 L}{3r_2^2} + \frac{4L^2}{\pi r_1}\right) \tag{1.4-4}$$

where V is the pressure gauge volume, L the tube length, r_2 orifice radius, and r_1 tube radius. There exists in fact an optimum internal impact tube radius for any given installation. Too large a radius increases the time lag because a larger volume must be brought into equilibrium while too small a radius increases the time lag by increasing the resistance to flow through the tubing. Since the time lag at higher pressures is less, the restriction on design indicated by this result is sufficiently strong for all operating conditions. The validity of this result has been investigated experimentally in the low pressure range, where it is confirmed within an accuracy of ±20 per cent.

B,1.5. Cited References.

1. Liepmann, H. W., and Puckett, A. E. *Introduction to Aerodynamics of a Compressible Fluid.* Wiley, 1947.
2. Goldstein, S., ed. *Modern Developments in Fluid Dynamics,* Vol. 1. Oxford Univ. Press, 1938.
3. Barker, M. On the use of very small Pitot-tubes for measuring wind velocity. *Proc. Roy. Soc. London, A101,* 435–445 (1922).
4. Homann, F. Der Einfluss grosser Zähigkeit bei der Strömung um den Zylinder und um die Kugel. *Z. angew. Math. u. Mech. 16,* 153–164 (1936).
5. Chambré, P. L., and Smith, H. In *Papers of the Heat Transfer and Fluid Mechanics Institute.* ASME, 1949.
6. Streeter, V. L. *Fluid Dynamics.* McGraw-Hill, 1948.
7. Homann, F. *Forsch. Gebiete Ingenieurw. 7,* 1–10 (1936).
8. Kaplan, C. The flow of a compressible fluid past a sphere. *NACA Tech. Note 762,* 1940.

9a. Kane, E. D., and Maslach, G. J. Impact-pressure interpretation in a rarefied gas at supersonic speeds. *NACA Tech. Note 2210,* 1950.

9b. Spivack, H. M. Experiments in the turbulent boundary layer of a supersonic flow. *North Amer. Aviation Rept. AL-1052,* 1950.

9c. Wilson, R. E. and Young, E. C. Aerodynamic interference of Pitot tubes in a turbulent boundary layer at supersonic speed. *Applied Physics Laboratory, Johns Hopkins University, Report CF-1351,* Dec. 1949.

10. Lin, T. C., and Schaaf, S. A. Effect of slip on flow near a stagnation point and in a boundary layer. *NACA Tech. Note 2568,* 1951.
11. Tsien, H. Superaerodynamics, mechanics of rarefied gases. *J. Aeronaut. Sci. 13,* 653–664 (1946).
12. Kantrowitz, A. Heat-capacity lag in gas dynamics. *J. Chem. Phys. 14,* 150–164 (1946).
13. Wien, W., and Harms, F. *Handbuch der Experimentalphysik IV,* 1. Teil, Akad. Verlagsgesellschaft, Leipzig, 1931.

14. Humphreys, M. D. Effects of compressibility and large angles of yaw on pressure indicated by a total-pressure tube. *NACA Wartime Rept. L5C30*, 1945.
15. Maccoll, J. W., and Codd, T. Theoretical investigations of the flow around various bodies in the sonic region of velocities. *Ministry of Supply, Theoretical Research Rept. 17/45 BARC 45/19*, 1945.
16. Liccini, L. L. *Calibration of Pitot tubes at supersonic speeds.* Work performed at NACA.
17. Young, A. D., and Maas, J. N. The behaviour of a Pitot tube in a transverse total-pressure gradient. *Aeronaut. Research Comm., Repts. Mem. 1770*, 1937.
18. Goldstein, S. A note on the measurement of total head and static pressure in a turbulent stream. *Proc. Roy. Soc. London A155*, 570–575 (1936).
19. Chambré, P. L., and Schaaf, S. A. The theory of the impact tube at low pressures. *J. Aeronaut. Sci. 15*, 735–737 (1948).
20. Schaaf, S. A., and Cyr, R. R. Time constants for vacuum gage systems. *J. Appl. Phys. 20*, 860–863 (1949).
21. Hasel, L. E., and Coletti, D. E. Investigation of two Pitot-static tubes at supersonic speeds. *NACA Research Mem. L8102*, 1948.

ARTICLE B,2

PRESSURE MEASURING MANOMETERS AND GAUGES

WALKER BLEAKNEY

ARNOLD B. ARONS

B,2.1. Introduction. In the entire history of the subject of fluid dynamics probably no physical measurement has outranked in practical importance that of the determination of pressure. This statement applies as strongly to modern trends in the field as it does to any previous time. As a consequence a large amount of thought and experiment has been and continues to be devoted to the development of suitable methods for pressure measurements, and techniques are undergoing rapid changes. It is fruitless, therefore, to undertake to describe in this short article the details of particular pressure gauges since the information is likely to become obsolete in a short time. Rather it is considered more useful to discuss only the principles of gauge design. The subject is so intricate that in spite of the host of instruments now available in great variety, it is frequently necessary for the investigator to design his own pressure measuring equipment to meet the requirements of his own particular problem. The great variety of conditions under which the sensing element must operate makes it impossible to develop a universal pressure gauge.

It would be desirable, of course, to approach the problem by discussing entire systems such as, for example, the pressure gauge or transducer, preamplifier, cables, recorder and playback equipment since the problems arising from the various components are intricately bound together. The magnitude of such an effort precludes the possibility of including such a discussion in this volume. Hence this article is confined solely to the gauge or sensing head itself.

B,2.2. Important Characteristics. It is pertinent to discuss at some length the various characteristics which may be desirable in a pressure gauge, whether or not they are realizable. In practice one must make the best compromise possible in fitting the instrument to the problem.

Frequency response. In many applications the pressure changes so slowly that one is essentially dealing with a steady state. Under these circumstances a response time of several minutes may be involved as in reading a McLeod gauge or mercury manometer, and this may not be objectionable. On the other hand the pressure rise across a shock front progressing into gas at rest may occur in times of the order of 10^{-9} seconds or less. The fluctuating pressures in gun chambers, engines, jets, etc. involve times scattered all the way between these limits. The range of interest in the frequency characteristic extends, therefore, from zero to 1,000 megacycles although no direct pressure sensing device developed so far approaches the upper limit.

Insensitivity to noise. By this is meant the degree to which the device is unaffected by disturbances other than changes in pressure. Such disturbances may consist of electromagnetic fields, acceleration and mechanical shock, fluctuating temperatures and temperature gradients, ionizing radiation, or combinations of these. In modern practice this characteristic has assumed great importance.

Accuracy. As in any measurement, the tolerances are determined by the problem. The term is meant to include here reproducibility and proper damping characteristics so that a changing pressure may be followed faithfully.

Linearity. It is usually considered a great convenience to have the output of a pressure gauge proportional to the pressure change, but this is not absolutely essential and in some cases not even desirable if a great range is encompassed.

Simplicity. This is a highly desirable characteristic from the standpoint of fabrication, adjustment, maintenance, and repair.

Ruggedness. This is a necessary feature in situations where mechanical injury from rough treatment or exposure to corrosive elements is involved.

Size. Aside from convenience in transporting and handling, the size may be a critical characteristic in several respects. The actual confines of the phenomena under investigation may limit the size of instrument (e.g. the measurement of blood pressure within an artery). The size may influence the interaction of the gauge with the fluid, disturbing the quantity being measured. Finally, the reading can only be some sort of average over its sensing element, and so the size limits the amount of detail which can be observed.

Range. Using the best vacuum technique the lowest pressures obtained are thought to be of the order of 10^{-14} atmospheres. Near the other extreme pressures in excess of 10^5 atmospheres have been produced in the laboratory. This is truly an enormous range. Only a minute fraction can be covered by a single gauge; nevertheless the designer tries to cover as much ground as possible.

Sensitivity. Other considerations being equal, one obviously chooses a gauge of high sensitivity since its output signal requires less amplification, thus simplifying the recording equipment.

Output impedance. Those gauges whose outputs are in the form of an electrical signal are characterized by an impedance which must be properly matched to the recording mechanism to achieve the most efficient system. In general low impedance devices are preferred since insulation problems are less acute, signals are more easily transmitted over long lines, and stray electrical signals are less likely to interfere.

Calibration. In some cases the theory of operation is sufficiently straightforward so that the response of a gauge may be computed with confidence from the properties of the materials involved. Or the dynamic response may be inferred from a static calibration for simple systems. In many instances, however, only a dynamic calibration gives a sufficiently reliable basis from which to interpret the results. Ease of calibration is therefore an important consideration.

Record evaluation. The Bourdon gauge indicates the pressure directly by displacement of a pointer over a calibrated scale. On the other hand, certain types yield a frequency-modulated carrier which is usually recorded on tape. To obtain the pressures the tape must be read by a demodulating system. Obviously, the ease and certainty with which the records may be interpreted is a factor in the design of the pressure instrument.

B,2.3. Low Frequency Gauges. The two most important considerations in choosing a pressure gauge for a particular application are the pressure level at which it is to be operated and the speed of its response. There exists a very broad experience in the measurement of low pressures

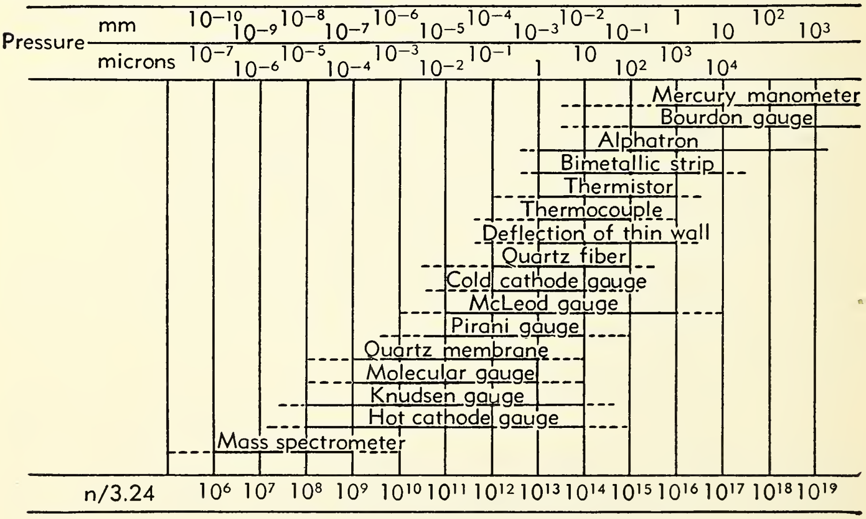

Fig. B,2.3. Chart showing ranges of pressures for different types of gauges. (From [2] by permission of John Wiley & Sons, Inc.)

which has been summarized in a number of books such as those by Strong [*1*] and Dushman [*2*]. For much of this work speed of response has not been a prime consideration. Such well-known instruments as the liquid manometer, McLeod, Langmuir viscosity, Knudsen ionization, Pirani thermocouple, and Phillips ion gauges each have their particular characteristics which fit them for different types of measurement in this field. The range of a number of these gauges is illustrated in the chart of Fig. B,2.3 taken from Dushman [*2*]. The lower limit of the ionization gauge has been somewhat extended by the recent work of Bayard and Alpert [*3*].

The pressure gauges used in wind tunnels usually are liquid manometers arranged in large banks to read pressures at numerous points simultaneously. For intermittent tunnels and transient flows gauges of higher frequency response are required (Art. 2.4). One must not only consider the speed of the sensing element itself in these cases but usually also the effect of the communicating channel [*15,16,17*]. Since the theory and practice of these devices has been so well described in the references cited, no further treatment of their performance will be given here.

B,2.4. High Frequency Gauges. Instruments for measuring fluctuating pressures have a long history. The problem of the "engine indicator" which gives the pressure as a function of position of the piston is about as old as the steam engine itself and the literature on the subject is quite extensive [*4*]. Again, since treatments of this phase of the subject may be found in existing books [*5*] no review will be given here except insofar as the topics discussed below are applicable. In the field of high speed measurements considerable progress has been made in recent years and since this information is not so well assembled the remainder of this article will be pointed in that direction.

Elastic Diaphragm. A great many of the modern gauges depend for a sensing element on a circular diaphragm or plate clamped rigidly at the circumference. A discussion will first be given of the diaphragm without regard to the method by which its deflection is measured, after which a number of complete gauge systems will be described. The deflection of the idealized system at the center under uniform load is given for small displacements by [*6*, p. 492]

$$x = \frac{3(1 - \sigma^2)}{16E} \cdot \frac{pr^4}{t^3}$$

where E and σ are the modulus of elasticity and Poisson's ratio for the material, p is the excess pressure on one side of the diaphragm and r and t denote the radius and thickness respectively. For a given material high sensitivity is obtained by making r large and t small.

The fundamental frequency of vibration for the same diaphragm is given by the relation [7]

$$\omega = 10.21 \left[\frac{E}{12\rho(1 - \sigma^2)}\right]^{\frac{1}{2}} \cdot \frac{t}{r^2}$$

Here ρ is the density of the material. It is seen that high frequencies are obtained by making t large and r small, the opposite of the requirements for high sensitivity. Obviously a balance dictated by the requirements must be struck between the two as far as these characteristics are concerned.

In order to use the plate diaphragm as a sensing element at frequencies approaching its natural value some system of damping must be employed. This may be accomplished in a variety of ways such as: installing a chamber in front of the diaphragm communicating with the fluid of interest through small holes, a similar "shock absorber" on the back side, covering the surface of the diaphragm with a viscous material, incorporating damping material in the supports, etc. Any of these methods changes the natural frequencies, of course, to some extent.

The plate diaphragm is particularly useful in applications where the sensitive element must be mounted flush with a wall in order to avoid interference with a flow; it is cheap and easy to fabricate, strong and rugged. Compared to other devices its natural frequency can be made rather high at usable sensitivities. It suffers from the fact that it is not insensitive to accelerations and temperature fluctuations. Acceleration effects can be reduced by using two diaphragms back to back in the form of a wafer so that signals from the two tend to cancel. In this form, however, it is unsuitable for the flush-wall type of mounting. Thermal effects can be reduced by employing insulating covers and materials of low expansion coefficient. Under extreme temperature conditions a settling chamber must be interposed between gauge and fluid combined with air or liquid cooling. These steps may at the same time be designed to take care of the damping problem.

The deflection of the diaphragm may be indicated in a variety of ways. The most important include the optical lever, optical interference, electrical condenser, variable reluctance, resistance strain principle, and many variations of these methods. For instance the condenser may be used under conditions of constant charge so that the voltage across it becomes a measure of the deflection or it may be employed as one element in an oscillating circuit whose frequency change is a function of the deflection and so the pressure. A brief description is given below of a few actual gauges illustrating these principles.

The gauge described by Buck and Barkas [8] makes use of the interference principle, the diaphragm forming one element of a system analogous to the experiment of Newton's rings. No electronic equipment is involved in the recording mechanism since the motion of the fringes is photographed directly on a moving film. In spite of the bulky nature of this gauge required by the necessary proximity of pickup and recording mechanism, it has given a good account of itself in accuracy and frequency response in many difficult situations.

As an illustration of the condenser method of measuring the deflection of an elastic diaphragm the so-called General Motors gauge [*9*] is fairly typical. The signal is an amplitude-modulated carrier wave, the condenser influencing the amplitude of forced oscillation in a tank circuit near its resonant frequency. This gauge in its commercial form is usable to a frequency of about 10 kcps. Many other condenser pickups are employed with the elastic diaphragm, most of them having adopted the frequency modulation system in which the condenser is a part of the oscillating tank circuit. (See, for example, [*19*].)

An example of the variable reluctance principle applied to the elastic diaphragm may be found in the Bendix[1] gauge. A button of magnetic material attached to the rear face of the diaphragm varies the magnetic reluctance through a small coil in close proximity to the diaphragm. The coil is part of an oscillating circuit and deflection of the diaphragm changes the frequency of this oscillation. The frequency-modulated signal may be recorded (on magnetic tape for example) or passed immediately through a demodulator to give a reading of the pressure. With some modifications the usable frequency limit of the gauge may be pushed up to about 10 kcps for sensitivities designed to record pressure changes of the order of one atmosphere.

Of course there are geometries other than the circular plate which may be used as the strained element in gauges otherwise similar in principle to those mentioned above. The most famous of these variations is the Bourdon tube whose deflection likewise may be indicated in a great variety of ways. A very successful modification of this idea is incorporated in the Wiancko gauge[2] which employs a short section of twisted tube which tends to untwist when pressure is applied to the inside. Attached to the end is a variable reluctance element acting in a push-pull arrangement with two coils in a bridge circuit driven by a suitable a.c. supply. The output from the bridge is an alternating current signal whose amplitude is a measure of the pressure. The balanced construction makes this gauge relatively free from disturbances. For ranges of the order of one atmosphere the upper limit in useful frequency response is 10 kcps or less.

Bulk Properties. There is a whole class of pressure gauges which depend for the sensing element on some bulk property of the material which is loaded by the pressure field. These properties include such phenomena as magnetostriction, piezoelectric effect, and electrical resistance, which evidence themselves when a piece of suitable material is placed under strain by the pressure load. The load itself may be applied in a unilateral direction through a piston or flexible diaphragm which offers no appreciable resistance, or the material may be subjected in some cases to hydrostatic load. The strain in a material element itself may be indicated by attaching resistance or other strain-sensitive materials to the surface of the element.

---

[1] Made by Pacific Division, Bendix Aviation, North Hollywood, Cal.
[2] T. H. Wiancko Co., Altadena, Cal.

Probably the most successful application of this last principle is to be found in the device of Draper and Li [*4*]. A flexible diaphragm transmits the pressure load to a cylindrical post which becomes the sensing element through the strain-sensitive winding attached to its surface. Careful design has resulted in a gauge of very good characteristics fully described in the original paper.

Gauges based on the magnetostriction principle have been developed [*10*] but the sensitivity is quite low. On the other hand, semiconductors such as carbon buttons or piles can be made very sensitive but are not very reliable in holding a constant sensitivity under rough treatment. The change in bulk resistivity of some resistance wire under hydrostatic pressure is appreciable, but a gauge based on this principle is not very sensitive. This arrangement is quite useful for measuring high pressures however.

PIEZOELECTRIC GAUGES. The use of the piezoelectric effect in measuring pressure has been a very attractive idea throughout the history of the subject, and a scientist faced with the problem of high speed measurement is likely to consider this principle first among all the possibilities. At this writing the piezoelectric gauge has had no superiors in certain types of measurements. For instance the bulk of the best high frequency measurements of shock waves in air and water have so far been made with this gauge. Nevertheless its use is beset with certain difficulties. In view of its importance in the field of high speed measurements a more extended discussion of the application of the piezoelectric principle is given below.

General characteristics and performance limitations. Crystals belonging to those classes which do not have a center of symmetry in the lattice structure are known to be piezoactive, i.e. the material becomes polarized when subjected to changes in stress. The resulting charge distributes itself over certain crystalline faces in a manner determined by the crystal symmetry and the nature of the applied stresses. Some material (such as tourmaline, lithium sulfate, barium titanate) are "hydrostatically sensitive," in that changes in *hydrostatic* pressure produce a resultant charge. Other materials (such as quartz, Rochelle salt, ammonium dihydrogen phosphate (ADP)) are not hydrostatically sensitive and develop a net charge only when unilateral forces are applied, the charge developing under the influence of one of the principal stress components (as in quartz) or from shear components only (as in Rochelle salt or ADP).

The charge generated in the crystal distributes itself over the capacitance C, in parallel with the gauge, and the charge then leaks away with the time constant RC, where R, the effective resistance across the gauge, is generally determined by the input resistance of the amplifier. Since the magnitudes of R and C are limited by various practical considerations, piezoelectric gauges are not suitable for measurement of steady or slowly varying pressures and can only be used for the measurement of fairly rapid transients having decay constants very much smaller than RC [*11*]. Thus most piezoelectric pressure measurements involve cathode ray oscilloscope recording.

The charge sensitivity of a gauge is given by the product of K, the effective piezoelectric modulus, and A, the surface area over which the charge is collected. Quartz and tourmaline have sensitivities of the order of 10 micromicrocoulombs/in.^{2} for one lb/in.^{2} change in pressure. ADP is about 10 times more sensitive, barium titanate 10 to 50 times more sensitive, and X-cut Rochelle salt about 100 times more sensitive, for a given area of crystal.

Thus the charge generated by a pressure change Δp is $(KA)\Delta p$; but since the charge is distributed over the parallel capacity C, the resulting voltage signal V is given by $(KA)\Delta p/C$. The effective voltage sensitivity of a gauge is therefore determined not only by its fundamental charge sensitivity but also by the magnitude of the parallel capacity of the cable and padding of the input circuit. Where high effective sensitivity is desired and recording equipment must be at some distance from the gauge position, it is sometimes necessary to reduce C by using a short cable to connect the gauge to a preamplifier (generally a cathode follower to afford high input impedance). The preamplifier acts as an impedance matching device, coupling the high impedance gauge circuit to a longer, low impedance line leading to the oscilloscope amplifier.

Cable capacity varies significantly with temperature and time, and frequent measurement of the shunt capacity C would be necessary in precise piezoelectric work were it not for the charge-step calibration technique due to R. H. Cole [*12*]. This technique provides a simple step response calibration of the entire recording system and simultaneously eliminates the need for direct measurement of the cable capacity.

Since piezo sensitive crystals develop polarization due to shifting of the "center of gravity" of positive and negative charges under the influence of elastic strain, it is to be expected that expansion and contraction under the influence of temperature changes would lead to similar effects. This type of "pyroelectric effect" is frequently the source of serious interference, particularly when measured pressure transients are accompanied by violent temperature fluctuations or when, owing to the use of very high impedance (*RC*) in the input circuit, relatively slow ambient temperature variations cause the generation of sufficient signal to make the oscilloscope spot wander vaguely around on the screen. Hydrostatically sensitive materials (such as tourmaline) are particularly subject to such interference, much more than nonhydrostatically sensitive ones (such as quartz). In the latter case pyroelectric charge would not be developed at all if the temperature changed uniformly through the crystal; whatever signal is developed arises from strain components set up by temperature *gradients.*

Naturally it is impossible to define sharp boundaries to the range of application of crystal pressure gauges, but to give some rough idea as to orders of magnitude of the practical limits of pressure and duration it may be cited that such gauges have been used to measure transient pressure changes from 0.1 lb/in.^{2} to 50,000 lb/in.^{2} It is relatively easy to measure transients of duration up to 0.2 or 0.3 seconds, but measurement of slower phenomena becomes increasingly difficult owing to pyroelectric interference and the stringent input impedance requirement. The high frequency response is limited in most applications by the time required for the pressure pulse to propagate over or through the gauge rather than the natural frequencies of the crystal and mounting, although the latter are disturbing factors. Hence the upper limit is determined by the geometrical size of the gauge. Rise times as short as 10 microseconds have been recorded. As with any high impedance device, microphonic cables and dielectric dispersion in cables or padding condensors are sources of trouble which may be overcome [*11*] by careful design and wise choice of materials.

Selection of piezoactive materials. Of the naturally occurring materials, only quartz and tourmaline are found in sufficient quantity and size of crystal [*13*] to merit consideration for use in pressure gauges, and both materials have been widely used. Since tourmaline is hydrostatically sensitive, it is utilized under circumstances where it is important to minimize vibrations and avoid frequency response limitations introduced by the presence of diaphragms or complicated gauge mountings necessary to insure unilateral loading on nonhydrostatically sensitive materials such as quartz, ADP, and Rochelle salt. However, quartz is cheaper and more readily available than tourmaline in large sizes, and is somewhat less subject to pyroelectric interference, as indicated above. The hydrostatically sensitive materials also respond to a unilateral deformation, in some cases with enhanced sensitivity. Many applications make use of the piezoelectric material in this way, particularly when barium titanate is involved.

Very few of the important synthetics approach quartz and tourmaline in ruggedness and resistance to moisture, although most are considerably more sensitive piezoelectrically. Rochelle salt and the few barium titanate crystals and ceramics tested so far show pronounced relaxation effects when subjected to pressure changes of fairly large amplitude (over 5 or 10 lb/in.^{2}). The effect is manifest in the continued rise of the recorded signal when a gauge is subjected to a step pressure change. This behavior obviously introduces serious low frequency distortion, and at present such gauges offer little promise except in special situations where it may be possible to compromise with or accept low frequency distortion (for the sake of high sensitivity). Recent developments in the technique of processing barium titanate are said to have overcome this difficulty, making this material appear very promising for use in pressure gauges. ADP appears to be reasonably free from distortion, but its lack of hydrostatic sensitivity and ruggedness, and the relatively small increase in sensitivity it affords, have prevented its becoming a strong competitor to quartz and tourmaline. Needless to say, the sensitive synthetics dominate the field of measurement at acoustic levels.

For construction details and response characteristics the reader is referred to the literature [*11*].

B,2.5. Mechanical Peak Pressure Gauges. Frequently, as for example in observing shock waves in air or water, it is of interest to obtain the peak or maximum pressure only. Several simple devices have been developed which, if intelligently used, give this quantity with some reliability. Perhaps the simplest consists of a series of diaphragms of different sizes covering holes in a box. After an event one simply notes the largest unbroken and smallest broken foil which serve to bracket the peak pressure when suitable calibrations are made. Crude as this procedure sounds, the results for blast waves in air are good. A second variation makes use of a deformable diaphragm, the depth of permanent set being interpreted in terms of the peak pressure.

Crusher and indentor gauges [*12*] are essentially single-reading peak pressure measuring devices. The incidence of a pressure wave causes motion of a small piston which flattens a copper ball in the crusher type or indents a copper block with a sharpened point in the indentor type. Although such gauges have proved very useful in underwater explosion work where very high pressures (thousands of pounds per square inch) are encountered and give results in excellent agreement with piezoelectric measurements, they are relatively insensitive devices and are most useful for measurement of high amplitude pressures. However, by careful design, Hartmann [*14*] has applied the indentor gauge to pressures as low as 0.1 atmospheres.

The general form of the equation of motion for such gauges is:

$$M\ddot{x} + F(x) = f(t)$$

where x = displacement of piston; M = effective mass of moving system; $F(x)$ = force function; $f(t)$ = driving function.

If $F(x)$ and $f(t)$ are known, the equation can in principle be solved to obtain the maximum deformation in terms of the parameters of the driving function. The response time of a ball crusher using $\frac{5}{32}$-inch diameter copper balls is of the order of 200 μsec while the response time of indentors is of the order of tens of μsec. If $f(t)$ decays appreciably within the response time, the resulting deformation depends not only upon the pressure amplitude of $f(t)$ but also on the decay rate. Some knowledge of the decay must then be available to make possible the calculation of the peak pressure. In the interpretation of deformations produced by low working pressure, correction must also be made for the fact that there is a slight amount of elastic recovery [*12*].

In the case of the ball crusher gauge, the force function $F(x)$ is found to be linear in x over a fairly wide range. (For $\frac{5}{32}$-inch copper spheres the proportionality constant is about $1.5(10^5)$ lb/ft up to deformations of 0.05 in., corresponding to incident pressure jumps of about 1,600 lb/in.^{2}) The force functions of indentor gauges are initially quadratic in x, and solution of the equation of motion becomes correspondingly more complicated but still feasible.

One method of calibration is accomplished by measuring deformation as a function of energy of impact E, the deformations being produced by dropping weights [*12*]. The force function is then found from the relation

$$F(x) = \frac{d}{dx} E(x)$$

B,2.6. Cited References.

1. Strong, J. *Procedures in Experimental Physics.* Prentice-Hall, 1939.
2. Dushman, S. *Scientific Foundations of Vacuum Technique.* Wiley, 1949.
3. Bayard, R. T., and Alpert, D. Extension of the low pressure range of the ionization gauge. *Rev. Sci. Instr. 21,* 571–572 (1950).
4. Draper, C. S., and Li, Y. T. A new high-performance engine indicator of the strain-gauge type. *J. Aeronaut. Sci. 16,* 593–610 (1949).

5a. De Juhasz, K. J. *The Engine Indicator.* N.Y. Instrument Publishing Co., 1934.

5b. Taylor, C. F., and Taylor, E. S. *The Internal Combustion Engine.* International Textbook Co., 1948.

6. Timoshenko, S. *Strength of Materials,* Part II. Van Nostrand, 1930.
7. Den Hartog, J. P. *Mechanical Vibrations.* McGraw-Hill, 1940.
8. Buck, W., and Barkas, W. H. Dynamic pressure measurement by optical interference. *Rev. Sci. Instr. 19,* 678–684 (1948).
9. Grinstead, C. E., et al. *S.A.E. Quart. Trans. 52,* 534 (1944).
10. Smith, A. W., and Weimer, D. K. Comparisons of supersonic intensities by means of a magnetostriction gauge. *Rev. Sci. Instr. 18,* 188–190 (1947).
11. Arons, A. B., and Cole, R. H. Design and use of piezo-electric gauges for measurement of large transient pressures. *Rev. Sci. Instr. 21,* 31–38 (1950).
12. Cole, R. H. *Underwater Explosions.* Princeton Univ. Press, 1948.
13. Bond, W. A mineral survey for piezo-electric materials. *Bell System Tech. J. 22,* 145–152 (1943).

14. Hartmann, G. K. Unpublished work, Nav. Ord. Lab.
15. Bollay, W. Aerodynamics of supersonic aircraft and missiles. *Nav. Ord. Lab. Rept. 1131*, 1949.
16. Wilson, R. E. Turbulent boundary-layer characteristics at supersonic speeds—theory and experiment. *J. Aeronaut. Sci. 17*, 585–594 (1950).
17. Spivack, H. M. Experiments in the turbulent boundary layer of a supersonic flow. *North Amer. Aviation Rept. AL-1052*, 1950.
18. Campbell, W. R. Performance tests of wire strain gages: I. Calibration factors in tension; II. Calibration factors in compression; III. Calibrations at high tensile strains. *NACA Tech. Note 954*, 1944; *978* and *997*, 1945. Errors in indicated strain for a typical wire strain gage caused by prestraining, temperature changes, and weathering. *NACA Tech. Note 1011*, 1946.
19. Cook, D. B., and Danby, C. J. A simple diaphragm micromanometer. *J. Sci. Instr. 30*, 238–240 (1953).

SECTION C

VELOCITY MEASUREMENTS

WILLOUGHBY M. CADY
WALKER BLEAKNEY

ARTICLE C,1

VELOCITY MEASUREMENTS USING IONS AS TRACERS

WILLOUGHBY M. CADY

C,1.1. The usual method of determining air velocity in a wind tunnel is the Pitot-static system, in which the velocity is inferred from pressure measurements. The pressure is observed both augmented (Pitot) and not augmented (static) by the impact of the stream. The pressure ratio indicates the Mach number. For some applications this method is short of ideal in certain respects. First, it requires probes which disturb the air flow, particularly if the probe is placed shortly upstream from the test object; second, the pressure measurement gives not the true air speed but rather the Mach number; and third, the static pressure is sensitive to the local flow pattern and to the angle of attack.

In this section several methods for measuring the speed of air flow are described, principally in the free stream, which are free of one or more of these defects. None has been widely exploited, and it is too early to say to what extent these methods will find application in flight or in the wind tunnel. In the present article we are concerned with the use of ions as tracers. In essence the method is as follows: At a known place in the flow and at a known time a small volume element of the air is ionized; at a measured later time the ions are noted as they pass a detector at a known position several inches downstream; and the true air speed is deduced directly. This technique of anemometry gives the average speed of the moving volume element; it cannot give localized or instantaneous velocities. In principle the method is excellent in that the ion cloud follows the air flow with great fidelity as a tracer and without exerting any perturbing effect on the flow.

C,1.2. For introducing ions into the airstream, a variety of procedures can be imagined. The ions could be produced outside the flow channel by an arc, or otherwise, and blown through an aperture into the flow spasmodically, but in order to avoid boundary layer effects it is preferable to produce the ions in the flowing air itself by means of an agent which is effective in midstream. Such agents are high energy electron beams, alpha particles, or very soft X rays. A fourth ionizing agent, the electric spark, has been used in at least two researches, although its electrodes unavoidably disturb the flow if supported in the free stream instead of being flush in a boundary of the flow. Each of these ionizing agents can be briefly excited, as is necessary for the measurement of the downstream transit time of the resulting ions.

A beam of high energy electrons can be produced in a vacuum by standard techniques, and allowed to enter the air through a thin window which forms a part of the vacuum envelope. If this window also forms a part of the wall of a wind tunnel, the electron beam will penetrate an appreciable distance into the flow; for example, electrons from a 50-kv tube will travel several millimeters in air at atmospheric density. En route these electrons ionize the air molecules. Since the energy of each electron is thousands of times greater than the energy required to ionize one molecule, the number of ions produced by each electron in the beam is correspondingly large. These are produced most copiously toward the end of the path of the electrons. According to Mellen [*1*] and Lawrence [*2*] the electron beam has not yet been made a fully satisfactory ionizing agent for anemometry.

Ionization by alpha particles has been shown by Wright [*3*] to be promising in air speed measurements. He placed a small radioactive preparation of polonium at the end of a 2-mm hole 1 cm deep in the side of a wind tunnel. About 100,000 α particles emerged per second and traveled through about 4 cm of air at atmospheric pressure, i.e. 3 cm into the stream before they were halted by molecular impacts. A toothed wheel or a 40-cps tuning fork modulated the beam. Some of the resulting ions were collected at a collector downstream, and others at a second collector at a distance l below the first. The time interval τ between the first and second collections was observed, and the air speed $u = l/\tau$ calculated. The use of alpha particles in this connection has apparently not been further exploited or published.

Electromagnetic radiation is capable of ionizing the air if certain conditions are met: it must be sufficiently penetrating in air to permit its transmission at good intensity well into the stream; it must not be so penetrating that it will fail to be absorbed and so fail to ionize densely, and its photons individually must have energy above the photoelectric threshold of air. These conditions are met in only one part of the spectrum, the extreme ultraviolet. The writer is not aware that that region has been used for this purpose.

The use of sparks to produce ions for the study of air flow has been mentioned in the above references [*1,2,3*], and also by Fay [*4*] and Munnikhuysen [*5*]. The last, reporting from Wright Field on the work at Cook Research Laboratories, notes that the gap readily allowed a spark to pass at Mach numbers as high as 1.75 and probably higher. Fay states that a 5,000-volt potential suffices to produce a spark between needle point electrodes spaced 1 mm apart at pressures between atmospheric and $\frac{1}{4}$ mm Hg. The character of the spark may be controlled by control of the external circuit. It should be rather brief, especially for use at the highest velocities, e.g. at $M = 6$ its duration should be limited to 1 μsec lest the cloud of ions be too much strung out along the lines of flow. If the spark is operated at a voltage well above the minimum required to make it pass, it will commence without delay, i.e. in well under 1 μsec; this promptness is sometimes desirable. It is believed that the position of the spark in relation to the gap can be made more reproducible by enclosing all but the tip of each electrode in a material of high dielectric strength.

C,1.3. We now turn to the detection of the cloud of ions as it passes the downstream station. The detector will be a metal button set flush in the wall bounding the flow but insulated from it and connected to an amplifier. Since a net negative charge characterizes the ion cloud, as the cloud passes the detector there is induced in it momentarily a positive charge. Therefore if the circuit is sensitive to the charge on the button [*5*] a single positive peak is recorded oscillographically, while a circuit sensitive to the current flowing from the button [*2*] shows a negative and then a positive peak. There is no need to collect the ions; their inductive effect suffices, although the path of the cloud may be as much as two or more inches from the detector electrode. The instant at which the cloud passes the detector is taken to be the instant of maximum induced charge or zero current; in the latter case this instant can be determined to within about 0.2 msec with the aid of a 10-kc timing wave superposed on the oscillogram. For example, the signal was detected by a probe 6 inches from the spark in a 250-mph stream. The transit time was about 1.3 msec, and the length of the pip was about 0.8 msec. A certain small error may occur at low air speeds in that the time of a pip may be slightly later than the actual time of passage of the ions; this error can be estimated and allowed for by comparing the transit times for a long and a short drift path.

An alternative method [*1,5*] of displaying the data from the ionization anemometer is to trigger each spark by the detected and amplified signal from the ions of the previous spark. In this way the recurrence frequency of the spark is made to depend on the transit time.

The above methods of measurement give the average of the air speed over an appreciable distance rather than the air speed at a point. Their utility is thus likely to be limited to the homogeneous portions of flows. This limitation also applies to several of the methods described in Art. 2 and 4.

ARTICLE C,2

VELOCITY MEASUREMENTS BY ILLUMINATED OR LUMINOUS PARTICLES

WILLOUGHBY M. CADY

C,2.1. We now describe the use of tracer particles somewhat grosser than the ions discussed in Art. 1. A small particle of matter follows with more or less fidelity the motion of the air in which it is floating. By observations on its velocity the velocity of the air is known. A particle which has long been in a steady stream has certainly acquired substantially the stream velocity. However, a particle recently introduced, or one in a stream in which the molecules are accelerated, is of course somewhat sluggish in acquiring the ambient velocity. Let us consider the fidelity of tracer particles, as discussed in Bourot's exhaustive report on their use in a wind tunnel [*6*].

For a particle of 20μ diameter which partakes of the air velocity with an error not exceeding say 70 cm/sec, the Reynolds number is small and the drag upon the particle is essentially viscous. The acceleration whereby it approaches the stream velocity u is then given by

$$\frac{dU}{dt} = K(u - U)$$

whence

$$U = u + (U_0 - u)e^{-Kt}$$

where U_0 is the initial value of the particle velocity. Here the coefficient of entrainment K according to Stokes' law is $3\pi\eta d/m$ for a sphere of diameter d and mass m in a fluid of viscosity η. The particles favored by Bourot are aluminum flakes; for these K is somewhat dependent on the angle of attack, but an average value is taken to be $6.6\eta d/m$. The coefficient K is the reciprocal of the relaxation time, or time required for the particle velocity to achieve 63 per cent compliance. After 4.6 such intervals the compliance is 99 per cent complete. Thus a 4μ aluminum flake 1μ thick, having $K = 15{,}000$, if moving at 300 m/sec in a 301-m/sec stream would in 1/15,000 sec (i.e., 2 cm) acquire a speed of 300.63 m/sec; and after 9.2 cm it will have made good all but one per cent of its velocity debt. If at any time a particle has a speed relative to the stream so great that the Reynolds number considerably exceeds unity, then its initial approach to the stream velocity will be more rapid than the above equation would predict. Where a flow changes direction, essentially the above considerations apply to the lateral acceleration of the particles.

The aluminum flakes used by Bourot are used as supplied for making paint; the stearin with which they come coated is left in place. For the best fidelity it is necessary to sort the particles, rejecting those having K below an assigned K_0. To accomplish this the powder is blown upward into the bottom of a vertical glass tube in which air is slowly ascending with a velocity which is adjusted so that, on the axis, it equals $u_g = g/K_0$. Only those particles will rise in the stream for which $K > K_0$, and these are collected in a bottle into which the stream spills them. The method is slow but effective. Typical speeds u_g are 0.3 to 4 mm/sec, affording K_0 values of 33,000 to 2,500.

C,2.2. Tracer particles have been injected and observed in several ways. In Bourot's experiments, the flakes are introduced into the wind tunnel at a point far enough upstream to allow them to acquire the stream velocity before reaching the test section, and far enough upstream so that the perturbation at the test section, caused by the injection device, is negligible. At such a point there is inserted into the stream a tube carrying a current of particle-laden air from a bottle of aluminum powder. The end of the tube is flared in one dimension to 10 tube diameters and constricted in the other to $\frac{1}{3}$ diameter; the flare is long and gentle, to encourage a uniform efflux of particles from its entire width. The powder is caused to enter the stream at a rate of about 5 g/hr; too fast a delivery rate loads the air appreciably so that the density of the stream is locally increased and the flow is perturbed. The particles should be few enough to allow examination of their individual motion.

The technique of tracer particles affords data on the velocity as well as the direction of flow. Bourot's arrangement includes a high current (140 to 220 amp) carbon arc and parabolic reflector as an illuminant for dark field photography of the tracers, together with a sector disk rotating in the light beam. By this means the illumination is interrupted at, for instance, 500 times per second. A shutter limits the exposure time to a small number of flashes (3 to 10). In the many beautiful photographs [*6*] the trace of each particle has the appearance of a row of dashes. If the spacing of these dashes is measured on the negative and if the interruption rate and optical magnification (or minification) are known, the speed of each particle can be deduced. Two ambiguities remain. First, the method as used by Bourot affords no data on velocity in the line of sight; however, Zwicky [*7*] has suggested that stereoscopic observation would remove this objection. And second, the magnification is not a definite quantity because of the finite depth of field. The depth of field is limited to 8 mm by geometrically confining the illumination; since this depth is small compared with the distance (40 cm) to the camera lens, the ambiguity in the magnification, and in the velocity, is only ±1 per cent.

Although reported only for low velocities, mainly below 30 m/sec, the method of Bourot seems to hold promise at higher speeds as well.

C,2.3. The technique of tracer particles was used by Zwicky and Sutton [7] in 1945–1946. Their method differed from the foregoing in using particles that are self-luminous, in dispensing with the sector disk, and in introducing a rotating mirror in the optical train. Since the mirror is revolved so as to cause the image of the flow channel to move transversely to the streamlines, the image of a tracer particle moves diagonally across the emulsion. The inclination of its trace is the information from which the velocity of the tracer particle may be calculated.

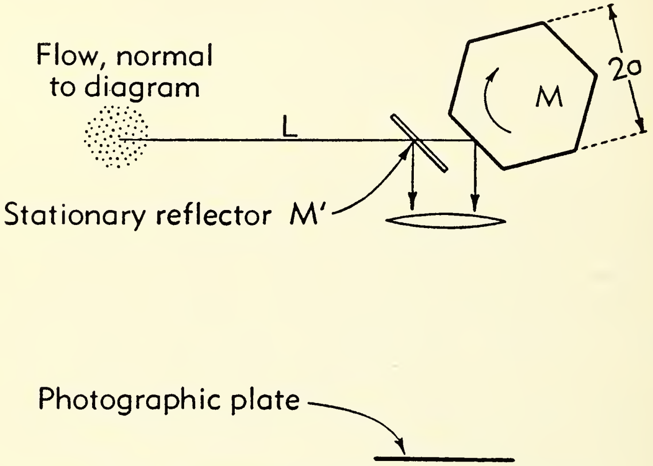

Fig. C,2.3. The use of a rotating mirror in measuring the speed of luminous particles.

Fig. C,2.3 indicates a possible arrangement. It is easy to show that the tracer velocity is given by the calibration formula

$$U = \frac{2\omega L}{\tan \alpha}\left(1 - \frac{a}{\sqrt{2}\,L}\right)$$

where ω is the angular speed of the rotating mirror M, and α is the angle between the photographic image and a trace on the emulsion such as would be produced by a moving tracer particle if observed with the mirror stationary. For ease in measuring α a stationary auxiliary mirror M', partly transmissive and partly reflective, is placed before the rotating mirror. This causes a streak to be impressed on the emulsion by each tracer; the angle α is the angle between the streaks formed by the reflections from M and M'.

A variant of the rotating mirror is the vibrating mirror. If the frequency of vibration is sufficiently rapid, the streak of each particle is seen to be sinuous. From the known frequency of vibration and the measured distance traveled by the particle per undulation it is possible to calculate the particle velocity.

Another type of streak camera uses a moving emulsion and no mirror. The film may be wrapped once around a rotating drum of radius r, or it may be placed on the face of a spinning disk. If the lens is at a distance p from the tracers and q from the emulsion, then the calibration formula is

$$U = \frac{p}{q} \frac{\omega r}{\tan \alpha}$$

Although successfully used in certain aeroballistic problems [*8*], the moving film streak camera is less well adapted than the rotating mirror type for the measurements of fast tracer velocities. The reason is that in the calibration formula for the rotating mirror the term L commonly exceeds the term rp/q in the moving film formula; the moving film camera finds its best application where rp/q can be made large.

C,2.4. Anemometry may be carried out by observing not the drift of tracer particles but the drift of a thermal disturbance. A device on this principle is the Electronic Transit-Time Anemometer (abbreviated ETTA), under development at Rensselaer Aero-Physical Laboratories [*8a*]. A fine wire of 0.0004-inch nickel alloy $\frac{3}{8}$ inch long is stretched transversely to the flow and pulsed for 40 μsec with 1.5 amp. Thus briefly pulsed to a dull red heat, it warms the passing air, which soon passes an identical wire $\frac{3}{8}$ inch downstream. The resistance of the second wire, increased momentarily, is timed with an oscillograph. It is found that the warmed air diffuses so fast that a transit time of over 6 msec is undesirable, and transit times less than 50 μsec are likely to allow considerable errors. An airborne version has been constructed with probes of platinum ribbon of $\frac{1}{2}$-inch span, 0.018-inch chord, and 0.00015-inch thickness. The ETTA is intended for measuring flows from 100 to 5,000 ft/sec to an accuracy of ±2 per cent.

ARTICLE C,3

ELECTRIC DISCHARGE ANEMOMETRY

WILLOUGHBY M. CADY

C,3.1. Atmospheric air is not a perfect electric insulator, for it permits the flow of a more or less feeble current in a region of an electric field between two electrodes. This current depends upon several variables among which are the field strength, the electrode material, spacing and configuration, the production of ions by any outside influence, the pressure, and the air velocity. If all but the last of these are held constant, the dependence of the current on velocity suggests the use of an electric discharge as a device for anemometry. This method gives local and instantaneous values of the velocity rather than values averaged over space or time. It has been exploited at several institutions. Notable is the recent and current research at California Institute of Technology, led by H. W. Liepmann; the following account leans heavily on the work of his students.

When two wires or thin rods are mounted in line in air with their tips separated by a gap of a few thousandths of an inch, an applied voltage of 6 to 12 kv will cause a current of the order of magnitude 10^{-12} to 10^{-9} amp between them. This current depends on a continuing supply of ions produced by ultraviolet illumination, X rays, cosmic rays, or radioactivity. This feeble current would cease if all such ionization from outside were stopped. It is known as the Townsend discharge, or the dark current, or, in German, *Vorstromentladung.* If the voltage is increased, the current rises to 10^{-7} or 10^{-6} amp, and the discharge gradually becomes luminous; it is no longer dependent upon external ionization. The discharge is now known as a corona. Further increase in the current to a few milliamperes causes the discharge to change its character discontinuously: the voltage drops to perhaps 350 volts and the phenomenon, while not spectacular, is now bright enough to warrant being called a glow discharge. Like the corona, the glow discharge is self-sustaining, provided only that the external voltage is maintained. Electron collisions in the gap ionize the air molecules to such an extent that, once the glow is established, an abundant population of carriers of electricity exists between the electrodes; only when the voltage is first applied does an initial transient carry the voltage above its normal value.

Ions bombard the cathode so violently that they disintegrate its surface by causing atoms to "sputter" away from it. If the current is increased beyond a few hundredths of an ampere, there occurs a gradual transition to an arc in which the cathode is so hot that it emits electrons thermionically, and both electrodes vaporize. The Townsend discharge, the corona, and the glow, described below in that order, have all been used in air velocity measurements.

It must be pointed out that the influence of the pressure p upon electric discharges reduces somewhat their anemometric usefulness. If we imagine the calibration of an electric discharge anemometer displayed, for instance, as a family of curves of constant voltage on the u, p plane (the current being held fixed) it becomes evident that the voltage observed in an experiment cannot be interpreted in terms of velocity or pressure alone. The static pressure must in principle be known before the velocity can be deduced from an electric discharge.

C,3.2. The Townsend discharge has been used considerably by Fucks [*9*] in Germany. Electrodes of platinum wire about 1 mm in diameter and hemispherically rounded at the ends gave promising results. To the gap, one or a very few millimeters long, there was applied some 5,000–7,000v. The current was of the order of 10^{-12} amp if no ionization was purposely introduced, but it rose to about 10^{-6} amp if the light from an ultraviolet lamp was focused upon the discharge. Table C,3 is derived from a graph in Fucks' paper; it gives the velocity calibration of a 3-mm gap between 1-mm electrodes at 7 kv, illuminated with ultraviolet. The sensitivity $(udI)/(Idu)$ of this anemometer is seen to be in the range 0.5–1.0. With X-ray ionization in place of ultraviolet, the sensitivity is reportedly less.

Table C,3. The effect of air velocity upon the current in a Townsend discharge (Fucks).

(m/sec)	0	20	75	120
I (μamp)	7.6	3.8	1.9	1.1

An atomic theory of the Townsend discharge as an anemometer has been proposed by Mettler [*10*] on the hypothesis that the wind reduces the current simply by blowing the ions away from the cathode before they can complete their migration.

C,3.3. It was observed by Fucks that the use of pointed electrodes encourages the formation of a discharge different in type from the foregoing, with current adjusted to over 10 μamp. This discharge persists even when the ultraviolet illumination is turned off, whereas the Townsend discharge falls nearly to zero. Although termed by him a glow discharge, it is better regarded in our terminology as a corona. This is only about one-tenth as sensitive to air velocity as is the Townsend discharge. A further disadvantage of the corona as used by Fucks is that it is electrically "noisy" and so does not lend itself to studies of turbulence. This work seems to have stopped in 1945 but to have been revived more recently as mentioned in the bibliography.

The corona as an anemometer has lately been described by Werner [*11*]. (His usage of the term "glow" to describe his discharge has here been altered in consonance with our terminology.) One electrode is a pointed fine platinum wire, usually 2,000–5,000v, negative and pointing toward the face of a grounded disk electrode a few millimeters away. With respect to pressure p the sensitivity $(pdI)/(Idp)$ at a fixed voltage inferred from Werner's graphical data on the current I appears to be about 0.5. Werner reports a velocity sensitivity $(udI)/(Idu)$, which is about twenty-five times lower. It appears that his instrument is a useful barometer under some conditions but that its velocity sensitivity is less than desirable.

C,3.4. Probably the type of discharge best adaptable to air speed determination is the glow. The pioneer in this application was Lindvall [*12*]. Subsequent workers have generally followed his lead in observing the voltages between electrodes operated at constant current. The discharge was studied with a variety of electrode materials, and platinum was found to afford the best compromise between steady operation and immunity from sputtering; the electrodes were about 0.15 cm in diameter with pointed tips. Sputtering was bad when the current rose toward 30 ma, while the discharge tended to revert to a corona intermittently below 10 ma. The best gap length was 0.015 cm, the discharge being unsteady if longer than 0.025 cm and being rather insensitive to air speed if shorter than 0.010 cm. These comments apply also to more recently described work on the glow anemometer. The voltages were of the order of 400v, rising significantly with increasing air speed while the current was controlled to a constant value.

The work of Lindvall on the glow anemometer has recently been extended by Mettler [*10*] and by Morgan and Vrebalovich [*13*]. An important consideration in these studies is the theory of the velocity sensitivity. Four causes may be plausibly suggested: (1) mechanical distortion of the gap by wind forces or by the cooling effect of the wind since the electrodes are heated by the discharge; (2) the effect of wind cooling on the thermionic properties of the electrodes; (3) a pressure effect; and (4) a blowing away of the ions from the space between the electrodes. There are strong reasons for believing that, with well-designed electrodes and holder, the last of these causes is dominant: (1) although the glow is a phenomenon too complex to admit of a complete theory, the theory of a Townsend discharge in flowing air agrees with experiment if the blow-away hypothesis is used; (2) qualitatively the well-known velocity of an ion in compliance with an electric field such as exists in the gap is a very few hundred meters per second, so that the direction of its motion is expected to be strongly influenced by a wind transverse to the field; (3) under some conditions a luminous wake is observed below the discharge and is easily interpretable as ions blown out of the glow; (4) the effect of ambient temperature and pressure on the glow discharge is small; and (5) the current in the anode differs from that in the cathode.

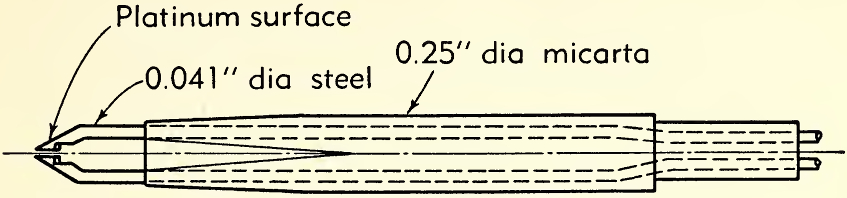

High speed probe

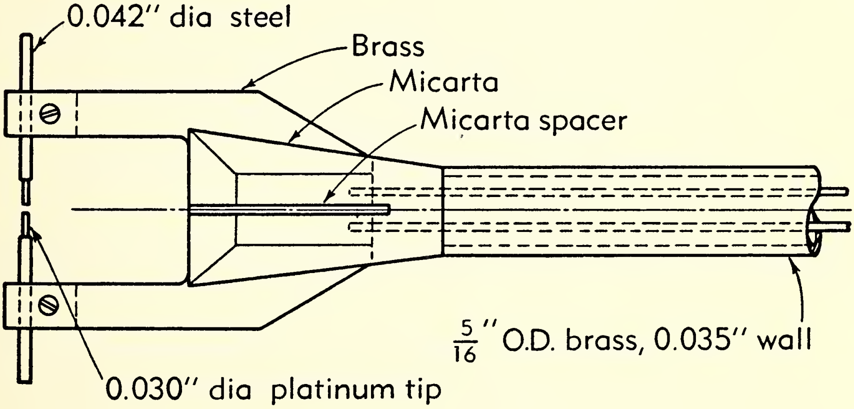

Low speed probe

Fig. C,3.4a. Probes for glow discharge anemometry at high and low air speed (from [*13*]).

Suitable probes for high speed and low speed flow are shown in Fig. C,3.4a. For d.c. use the anode may be made smaller than the cathode, to prevent the active area from wandering. High speed flow may better be studied with the streamlined probe, pointed upstream. The glow is energized by a constant-current source of, e.g. 10 ma, a.c. or d.c. The voltage is either read directly on a scale or displayed on an oscilloscope; the latter may be used to study the wave form in turbulence, but with the reservation that the results are somewhat perturbed by the pressure sensitivity of the glow. The effect of pressure is, however, gratifyingly slight. In one test a rise from 15 to as much as 45 psia caused the voltage to rise from 344 to 362 volts as the current was held at 8 ma; this voltage increment corresponds to about 6 m/sec in a typical calibration curve. In view of the nonlinear character of such curves as are shown in Fig. C,3.4b, it is not convenient to state a value for the sensitivity of the glow anemometer.

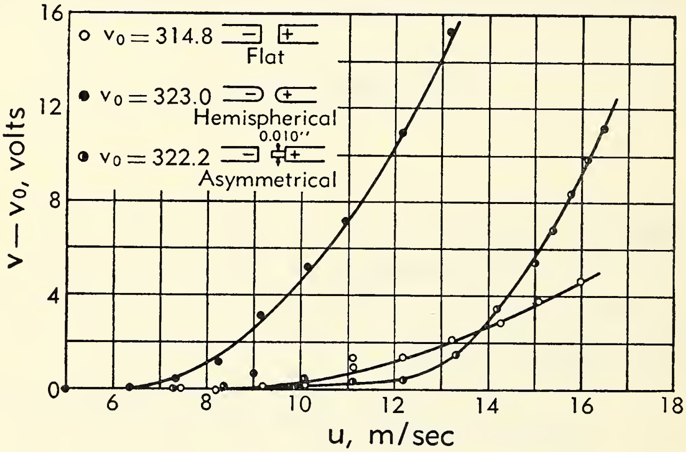

Fig. C,3.4b. The voltage across a 10-ma glow discharge anemometer having 0.0067-inch gaps between 0.030-inch electrodes of various shapes. v_0 is the voltage at $u = 5$ m/sec (from [*13*]).

In d.c. operation, the glow anemometer needs about ten minutes to settle down to a steady voltage; and this voltage is even then subject to a rise of, say, 1 volt per hour if the current is 10 ma, because of sputtering. Therefore, in practice the observations must be made only after the ambient conditions have been steady for ten minutes; and frequent calibration would be necessary for use of the glow as a measuring instrument.

The glow is stable even in the supersonic region. That the discharge persists even under this condition is not surprising, for it is then always in the wake of the shock caused by the electrodes. Although the discharge occurs in the subsonic wake, the potential drop is a function of the free stream velocity and may be used for supersonic anemometry. In the wake the pressure is low and the velocity is subsonic; both factors are cordial to the glow. In fact as the free stream Mach number rises above unity the falling velocity between the electrodes causes the voltage actually to fall. In one case the voltage at $M = 1.22$ was 577v, falling to 520v at $M = 1.44$. The sensitivity of the glow anemometer may well vanish in the neighborhood of transonic flow.

The grave fault with the d.c. glow anemometer is the sputtering away of its cathode and the consequent gradual rise in its voltage. In 1942 Fucks showed that the use of a.c. excitation overcomes this difficulty. A 1944 German report by Fucks and Schumacher [*14*] confirmed this result, giving details and data. Evidently the material lost to one electrode is largely collected by the other and a nearly equal amount is returned to the first in the next half cycle. Fuchs and Schumacher used a frequency of 500 cycles and found the drift due to sputtering to be substantially eliminated. They found that with their apparatus the glow would not persist at air speeds greater than 50 m/sec; the reason for this failure is obscure.

Morgan and Vrebalovich [*13*] have more recently used an alternating current glow. They have shown that the effect of sputtering can be largely eliminated either by reversing the polarity of a d.c. glow a few times per second (7 to 2,000), or by using high frequency excitation (100 kc). Either very high or very low frequency is preferable to 500 cycles because turbulence measurements require that the apparatus itself introduce no disturbance in the range of frequencies characterizing turbulence; cf. F,3. It is understood that the very low frequency of 4 reversals per minute is under consideration. The reignition of the discharge following the dead time during reversal is the occasion for a spike of voltage, which should be electronically excluded from the recording circuit. With high frequency excitation the glow has insufficient time to deionize as the current passes through zero; therefore the glow does not extinguish and the spike is absent.

ARTICLE C,4

ACOUSTIC MACH METERS

WILLOUGHBY M. CADY

C,4.1. The propagation of sound in still air depends, in good approximation, only upon the temperature. In moving air the travel of an acoustic wave is influenced by the Mach number of the flow as well. Arrangements are described which afford such data on sonic propagation as permit calculation of the Mach number; these are termed acoustic Mach meters. Some of the arrangements afford values of the true air speed; these are designated as acoustic anemometers. These instruments are attractive in two important respects: (1) they are absolute in the sense of needing no calibration by other means; and (2) for wind tunnel use they are aerodynamically clean. No probes need be introduced into the stream; the source of sound and the microphone, if any, may be flush-mounted in the walls of the flow channel. These devices measure air flow as averaged over definite and sometimes large distances and times.

C,4.2. One of the three acoustic air speed meters to be described involves the measurement of the transit time or velocity of a pulse of sound, while the others require, directly or indirectly, the measurement of an angle. We summarize first the method requiring no angle measurement, as elaborated by Eisenstein, Clark, and Carlson [*15*, Vol. I], and by Carrier and Carlson [*16*]. Their apparatus is perhaps more properly regarded as an anemometer than as a Mach meter. A spark gap, energized to give a single spark sufficiently loud to emit a shock wave, is mounted flush in the floor of a wind tunnel. The instantaneous configuration of the shock front, at a time following the spark by a controlled interval τ, is photographed with a schlieren optical arrangement. An H6 mercury flash lamp is used as the source of light for this photography. Since the shock is weak after the first two centimeters of travel, it can be regarded as being propagated at the velocity of sound, a, relative to the air, which is moving at velocity u. Thus, if there is no boundary layer, the image of the shock is circular with radius $a\tau$, the center of curvature being displaced downstream a distance $u\tau$. A determination of M is thus possible. If τ is known, the true air speed is also given by the photographs. In agreement with calculation, the photographs show that the wave fronts depart significantly from hemispherical shape, indicating that there is a boundary layer in which the velocity is less than that in the full stream. As a Mach meter this device is useful mainly in subsonic flow, and is less useful in supersonic flow, where the angle of the Mach cone gives the value of M without invoking the aid of the acoustic disturbance from a spark. The method is also useful in hypersonic flow, where the angle of the Mach cone is rather insensitive to changes in M. For anemometry the method is applicable at all speeds.

An application of the same method for measuring air speed in the subsonic region has been reported recently by Hertzberg and Kantrowitz [*17*]. It is useful only in a shock tube for observing the flow in the immediate wake of the traveling shock front. A slight step on the floor of the channel is struck by the traveling shock and becomes the origin of a weak circular acoustic front which is photographed at a known time after its birth. Measurements on the photograph then give both M and u.

C,4.3. Of the two angle-sensitive sonic Mach meters we consider first a device described by Marlow, Nisewanger, and Cady [*18*] which, with equal directness, gives the true air speed and the Mach number. Mounted flush in the floor of the flow channel is a quartz plate so cut and metalized that, when connected to an appropriate oscillator and power amplifier, it will execute thickness vibrations at 344 kcps. Since under these conditions a good plate vibrates in the same phase over its entire surface (e.g. 0.5-inch square), the one-millimeter waves it emits are plane and parallel to the boundary. As the distance from each wave to the boundary increases with the speed of sound the wave is also swept downstream at the velocity u. As photographed through windows in the flow channel with a microsecond spark for illumination, the shadows of the waves are seen to be arranged in echelon as shown in Fig. C,4.3a. The crystal mounting

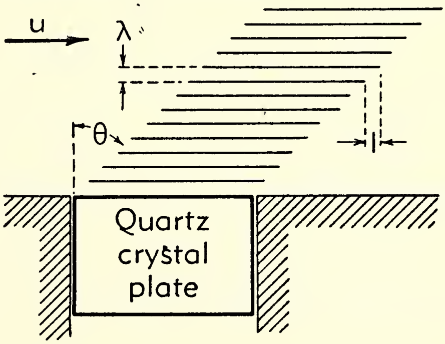

Fig. C,4.3a. Wave fronts produced by a crystal in one form of acoustic air flow meter.

requires careful workmanship if supersonic flow is to be observed, as in that case any irregularity in the channel floor will cause attached shock waves to appear. The crystal face must be truly flush with the floor and the crack around the sides must be as small as possible.

The inclination θ of the boundaries of the beam is related to the Mach number of the flow by the relation

$$M = \tan \theta \tag{4.3-1}$$

The air velocity u can be obtained by noting the relative downstream displacement l of successive wave fronts, for if f is the frequency, then

$$u = fl \tag{4.3-2}$$

This device is rather inferior as a Mach meter or anemometer because the edges of the beam are blurred by diffraction. It also shares with the Carrier-Carlson arrangement the inconvenience of being photographic.

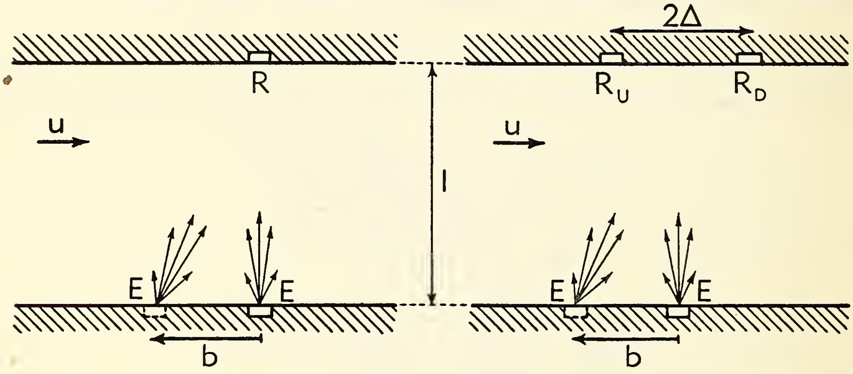

Fig. C,4.3b. The acoustic path in two versions of the STAMNI Mach meter, using one and two receivers. In each version the movable emitter is shown as placed in still air and (dotted) in moving air.

Substantially the same method has been briefly reported independently by Du Bois and Kling [*19*]. Their sonic beam is produced by a Hartmann whistle [*20,21*] operating at 57 kcps (wavelength 6 mm), of which the sound is collimated by a parabolic reflector. The energy enters the wind tunnel through a hole that is closed by a diaphragm which is aerodynamically smooth but acoustically transparent. The method is reported to give values of u which agree within 5 per cent or better with values obtained by pressure measurements.

Another and seemingly more practical acoustic Mach meter has been described by Corey [*22*], who has kindly furnished additional details for this article. Let us consider a region of uniform air flow in which a stationary source of sound waves is immersed, Fig. C,4.3b. A quartz crystal oscillator E operating at 48 kcps (more recently 100 kcps) produces the radiation, which is beamed across the air flow and detected by a quartz crystal microphone R. The emitter is free to be moved along a path which is parallel to the flow and at a distance l from R; its position as measured upstream from a point opposite R is b. Typically $l = 8$ in. The signal amplitude received by R is a function of the position of E on its path. If $u = 0$, then R receives the greatest signal when E is at $b = 0$. For $u \neq 0$ the position of E for maximum amplitude moves upstream a distance $b = ul/a$. When E has been set accordingly, the Mach number is given by

$$M = \frac{b}{l} \tag{4.3-3}$$

When this adjustment is made, the transit time for the sound waves from E to R is at its minimum; in fact the minimization of τ is of more basic significance than the maximization of the amplitude. Experimentally the transit time need not be known, but its variation with b can be measured by observing the relative phase of the voltage applied to E and the sound signals received at R, and adjusting b to retard the phase of the latter as far as possible. The device has been named the Sonic True Air Speed and Mach Number Indicator, abbreviated to STAMNI. It has features in common with the Sonic True Air-Speed Indicator described in [*15*, Vol. II].

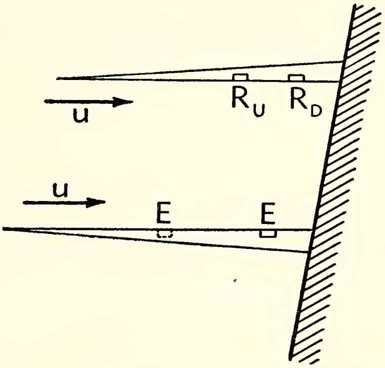

Fig. C,4.3c. The STAMNI emitter and receiver in a possible mounting at the leading edge of a wing.

The emitter and the receiver may be set flush into opposite walls of a wind tunnel. For use in flight they may be mounted in such half-wedges as are shown in Fig. C,4.3c, following recent Princeton aerodynamic studies [*23*], in order that the emitter and receiver may be as nearly as possible in undisturbed air. To prevent serious deviations in the measured values of M by the boundary layers, the length of the acoustic transmission path should be large in comparison with the thickness of the boundary layers.

Corey has suggested that the setting of E for maximum signal can be more accurately accomplished if R is replaced by two identical receivers, one of which, R_D, is at a selected fixed distance 2Δ downstream from the other, R_U, as in Fig. C,4.3b. The pair of receivers is moved along its path to the position at which the received signals are equally intense. With this two-receiver STAMNI the setting can be made more accurately than with the single receiver, simply because the balancing of two signals is usually more precise than the maximizing of one signal. A small displacement of E upstream results in a sharp increase of signal at R_U and a sharp decrease at R_D, so that the position of E for equal amplitudes is easily determinable. A method of data analysis with two receivers is best understood by referring to Fig. C,4.3d. Here a spherical wave front emitted into the flowing air by E is detected by R_U and R_D simultaneously after a transit time τ. Since the setting b of E as measured with respect to the midpoint of the dual receiver is equal to $u\tau$ and the radius of the front is $a\tau$, we may write

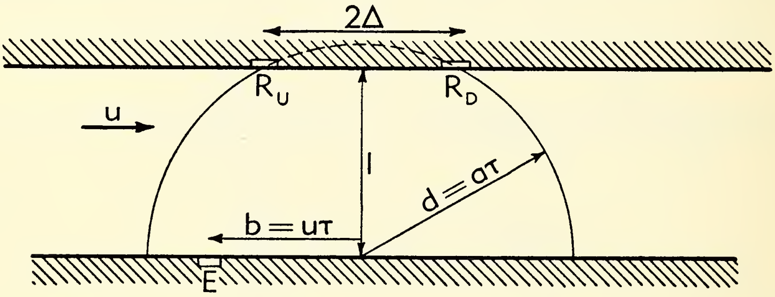

Fig. C,4.3d. Subsonic velocity measurement with the two-receiver STAMNI.

$$M = \frac{u}{a} = \frac{b}{d}$$

or (4.3-4)

$$M = \frac{b}{\sqrt{l^2 + \Delta^2}}$$

In the supersonic case the same equation holds, but Fig. C,4.3d should show E to the left of the semicircle. It is interesting to note that, if the wave front is swept downstream by supersonic air and energizes a receiver, it will again energize the receiver at a later time; the interval is the time during which the receiver is inside the moving spherical front. The propagation of sound in the STAMNI here regarded as a ray phenomenon, has been treated by Corey both as a ray and as a wave problem, with substantially confirmatory results.

At the condition for which Fig. C,4.3d was drawn, viz. equal amplitude at R_U and R_D, the transit time τ is the same for each, and they are operated in phase. If this fact is used in setting the receivers, it is unnecessary to depend on the technically risky comparison of the intensities; rather, the relative phase is used. One is thereby freed of the uncertainty in the directivity of E, R_U, and R_D and the relative sensitivity of R_U and R_D and their amplifiers. In use above Mach one, the phase comparison is somewhat clouded by the fact that each wave front attacks each receiver twice; precautions can, however, be taken to make E directional in order to weaken the undesired portions of the wave front. The phase comparison is made to within $\pm 5°$ by a phase-sensitive amplifier; the unavoidable ambiguity of one or more whole cycles is solved by approximate prior knowledge of the flow. The amplifier contains a bridge of rectifiers that provides a d.c. output for meter indication and which, by the synchronizing signal from the oscillator, discriminates against the noise of the air stream and in favor of the desired sound waves. In this way a signal 100 times smaller in amplitude than the noise can be recovered.

The conditions of air flow measured by the STAMNI are as averaged over the acoustic path. It is reported that Mach number measurements with a two-receiver equal-amplitude 48-kcps STAMNI agree with concurrent measurements by standard wind tunnel methods to within an average deviation of 0.01, and that under favorable conditions the emitter can be placed in relation to the receivers to within a Mach number uncertainty of only 0.001.

C,4.4. Cited References and Bibliography (C,1-C,4).

Cited References

1. Mellen, G. L. Gas-flow speedometer. *Electronics 23*, 80 (1950).
2. Lawrence, R. B. Measurement of gas velocity by pulsed ionization technique. *Final Rept. to ONR from Natl. Research Corp., Contract N7onr-478*, 1951.
3. Wright, F. H. *A method of measuring the rate of ion diffusion in a turbulent air stream.* Ph.D. Thesis. Calif. Inst. Technol., 1948.
4. Fay, J. V. Private communication from Cook Research Laboratories.
5. Munnikhuysen, R. D. *ATI Tech. Data Digest 13*, 7 (1948).
6. Bourot, J. M. Chronophotographie des champs aérodynamiques. *Publs. sci. et tech. Ministère Air, France, 226*, 1949. Also Bourot, J. M., and Moreau, J. J. Mécanique des fluides—Sur la visualisation du tourbillon marginal d'une aile, au moyen de lamelles d'aluminium, en soufflerie aérodynamique. *Compt. rend. 228*, 1567–1569 (1949); Mécanique des fluides—Note sur les zones d'inégale luminosité observées dans certaines visualisations d'écoulements. *Compt. rend. 228*, 1628–1630 (1949).
7. Zwicky, F., and Sutton, G. P. Private communications from Aerojet Engineering Corp.
8. Rinehart, J. S. Simultaneous photography of self-luminous and non-self-luminous effects. *Rev. Sci. Instr. 21*, 939–940 (1950).

8a. de Graffenried, A. L. Private communication from Rensselaer Aero-Physical Laboratories.

9. Fucks, W. Investigation of the operating properties of the leakage current anemometer. Transl. from *Deutsche Luftfahrtforschung*, 1944; *NACA Tech. Mem. 1178*, 1947.
10. Mettler, R. F. *The anemometric application of an electrical glow discharge in transverse air streams*. Ph.D. Thesis. Calif. Inst. Technol., 1949.
11. Werner, F. D. An investigation of the possible use of the glow discharge as a means for measuring air flow characteristics. *Rev. Sci. Instr. 21*, 61–68 (1950).
12. Lindvall, F. C. *Trans. Am. Inst. Elec. Eng. 53*, 1068 (1934).
13. Morgan, A. J. A., and Vrebalovich, T. Investigation of direct and alternating current glow anemometers. *Rept. to NACA from Calif. Inst. Technol., Contract NAw 5776*, 1950.
14. Fucks, W., and Schumacher, G. Tests with an alternating current glow anemometer under steady conditions. *Natl. Research Council, Canada, Div. Mech. Eng., Tech. Transl. TT-58. ATT 37077.*
15. Eisenstein, J., Clark, K. C., and Carlson, F. D. Sonic true airspeed indicator. Vol. I. *OSRD Rept. 5369*, 1945; Vol. II. *OSRD Rept. 5370*, 1945.
16. Carrier, G. F., and Carlson, F. D. On the propagation of small disturbances in a moving compressible fluid. *Quart. Appl. Math. 4*, 1–12 (1946).
17. Hertzberg, A., and Kantrowitz, A. Studies with an aerodynamically instrumented shock tube. *J. Appl. Phys. 21*, 874–878 (1950).
18. Marlow, D. G., Nisewanger, C. R., and Cady, W. M. A method for the instantaneous measurement of velocity and temperature in high speed air flow. *J. Appl. Phys. 20*, 771–776 (1949).
19. Dubois, G., and Kling, R. Mécanique des fluides—Sur la mésure des caractéristiques d'un courant gazeux rapide au moyen d'un faisceau d'ultrasons. *Compt. rend. 228* (*Part 1*), 363–364 (1949).
20. Barish, D. *Acoustical airspeed indicators*. A.E. Thesis. Calif. Inst. Technol., 1950.
21. Hartmann, J. On the production of acoustic waves by means of an air-jet of a velocity exceeding that of sound. *Phil. Mag. 11*, 926–948 (1931).
22. Corey, V. B. Acoustic measurement of airstream parameters. *Inst. Aeronaut. Sci. Preprint 267* (1950).
23. Ladenburg, R., and Bershader, D. On laminar and turbulent boundary layer in supersonic flow. *Revs. Mod. Phys. 21*, 510–515 (1949).

Bibliography

Bleakney, W., Weimer, D. K., and Fletcher, C. H. The shock tube: a facility for investigations in fluid dynamics. *Rev. Sci. Instr. 20*, 807 (1949).

Fucks, W. Schwankungen von Entladungsparametern bei Vorstomentladungen und Schwankungsmessungen. *Z. Naturforsch. 5A*, 89–98 (1950).

Loeb, L. B. *Fundamental Processes of Electrical Discharge in Gases*. Wiley, 1939.

Ower, E. *The Measurement of Air Flow*. Chapman and Hall, 1949.

ARTICLE C,5

VELOCITY OF SHOCK WAVES BY THE LIGHT SCREEN TECHNIQUE

WALKER BLEAKNEY

C,5.1. The use of a beam of light to sense the time at which an object passes a prescribed point is commonplace, and when it becomes desirable to measure the velocity of a shock wave it is natural that some variation of this technique should be tried. In this article, the use of light screens are described as applied to the problem of measuring the velocity of plane shock waves propagated in gases contained in a channel or tube.

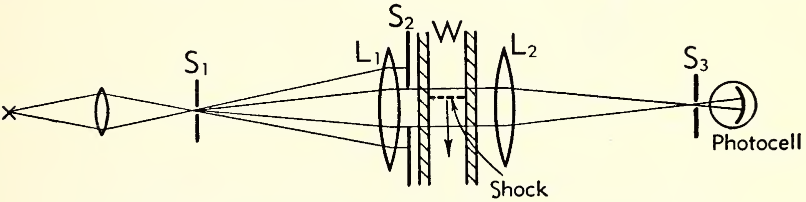

Fig. C,5.1a. Schematic layout of the schlieren optical screen.

Although many variations of the technique are possible, for purposes of discussion one may divide the method as it has been used in the past into two types characterized by the words "schlieren" and "reflection." The first, or "schlieren," system, as the name implies, consists of a miniature schlieren optical arrangement in which the camera or viewing screen is replaced by a photocell. Fig. C,5.1a makes this clear. Light from a suitable source falls upon the slit S_1 and becomes parallel after passing through the collimating lens L_1. It is possible to replace the condensing system shown here by any source of light having a sharp edge at the position of S_1. The beam is further limited to a rectangular shape by the slit or stop S_2 whose edges are parallel to the plane of the oncoming shock front. In addition to defining the parallel beam crossing the tube through the windows W, the stop S_2 is useful in cutting out much of the stray light. The lens L_2 throws an image of the slit S_1 on the plane of slit S_3 behind which is located the photocell, usually in the form of a photomultiplier tube, to receive any light which passes this last slit. Careful alignment of the system so that its axis is parallel to the plane of the shock front is, of course, necessary for optimum performance.

The system is adjusted by moving the slit S_3 from an initial position centered on the light beam in a direction opposed to the direction of motion of the shock front until the light entering the photocell is just cut off. As soon as the shock enters the side of the beam, certain rays of light are refracted sufficiently to pass through the slit S_3 and fall on the photocell. As the shock front traverses the width of the beam, the amount of light reaching the cell remains essentially constant since density gradients behind the shock front itself are usually small. In practice the amplified output signal will have the shape sketched in Fig. C,5.1b. The rise time of the signal may be as short as one or two microseconds and it is this steep front of the signal which is used to identify the time of arrival of the shock front. It will be noted that, in using two such screens to measure velocities, it is the distance between corresponding edges of slits S_2 which must be used as the base line in computing the speed. Since the density gradient normal to the light beam must have a particular sense to throw light on the photocell, the device is sensitive to shock waves going in only one direction. It is possible, therefore, to adjust the system so that it will ignore a shock wave and pick up, for example, its reflection going in the other direction.

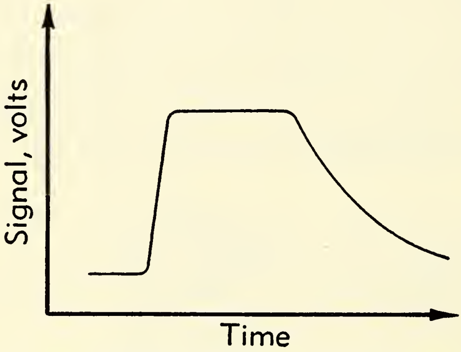

Fig. C,5.1b. Shape of the output signal from the schlieren screen.

Another modification of the schlieren screen [*5*] consists in replacing the photocell by another lens which forms an image of the test section on a particular plane still farther removed from the channel, the arrangement ordinarily used in schlieren photography. A slit S_4 is now placed in this image plane with the photocell directly behind. When the shock wave passes through the test section, its schlieren image is swept over the slit S_4 and a short pulse of light falls on the photocell. The signal will differ from that of Fig. C,5.1b in that the flat top will be eliminated. A possible advantage of this modification lies in the reduction of stray light reaching the photocell.

The "reflection" system is much simpler than the first type in that no lenses are needed. An extended source of light and three knife edges are arranged as in Fig. C,5.1c so that only the limiting ray parallel to the shock front reaches the photocell. As soon as the shock front enters the illuminated region some rays suffer total reflection from the back side, escape the third knife edge, and reach the photocell. As the front progresses, it intercepts more light so that, for the small angles involved, the signal rises linearly with time, and a backward extrapolation locates the beginning of the signal with high precision. The adjustments to be made with this method are similar in most respects to those of the first method and are obvious from the figure. The alignment of the knife edges must be made with considerable care to realize the accuracy of which the arrangement is capable.

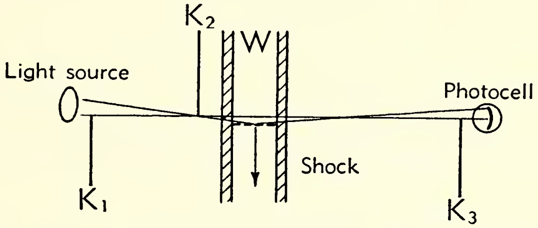

Fig. C,5.1c. Arrangement of the reflection screen.

In dealing with strong shocks involving large changes in the index of refraction, the signals are strong and no difficulties arise. As the two methods are extended to weak shocks, there is a limit beyond which the operation is unsatisfactory. This limit is set by the signal-to-noise ratio emerging from the photomultiplier tube. Contributing factors influencing this ratio are the operating potentials, amount of stray light, and the particular vagaries of individual tubes. To achieve maximum sensitivity for weak shocks, the phototube and its operating characteristics should be selected for high signal-to-noise ratio, and the optical system should be designed for the highest signal-to-stray light ratio. The latter is achieved by maintaining the optical system free of dust, minimizing unwanted reflections, using a narrow light beam, and otherwise cutting out all unnecessary rays by extensive baffling. When the signal-to-stray light ratio is the controlling factor, little can be gained by increasing the brightness of the light source because both signal and stray light increase together.

The amplification, gating, and transmission of the signals from photomultiplier to chronograph may be accomplished by customary practices.

The electronic circuits for these procedures develop rapidly with time and it does not seem worthwhile to give details here. As a guide, however, the reader may wish to consult some general texts [*1,2*] and a few specific papers [*3,4,5*]. The chronograph, of which there are many types, should have a resolving power of about 10^{-7} seconds and should cover the time interval of interest. The electronic cycle counter chronograph and the cathode ray and drum camera combination have both found extensive use in measuring shock velocities in tubes. The first is convenient in that the time interval is given immediately, but one instrument normally takes care of only two light stations. Any number of events can be recorded on the drum camera, but the film must be developed and the record inspected before the result can be found. Unless an immediate measurement of the velocity is needed, the drum oscillograph is recommended because it is generally more reliable. The gating action necessarily included in the counter chronograph leaves open the possibility of undetected interference by extraneous signals.

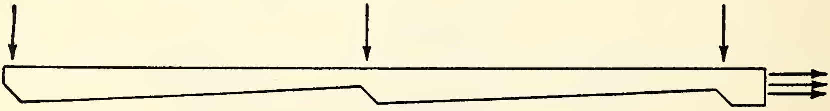

Fig. C,5.1d. Shape of Lucite rod for servicing several light stations with a single photocell.

An ingenious method has been used [*6*] to "pipe" the light from several stations to the same photocell. A rectangular rod of Lucite is placed in such a way as to intercept the light from two or more stations. The back side of the rod is contoured to present a totally reflecting surface to the light rays as shown in Fig. C,5.1d. On emerging from the end of the rod, the light falls on the cell. By this means two or more signals pass through the same phototube and amplifier system, reducing the cost as well as eliminating differential time lags which might be present in different amplification channels. There is a limit, however, to the number of stations which can be attached to the same channel since the signal-to-stray light ratio goes down with the number of stations. In practice three stations piped to one amplification channel have been used without difficulty.

A typical example of a routine record [*6*] is shown in Plate C,5.1 using the reflection method and drum camera. The cathode ray spot sweeps up and down taking 100 μsec for the round trip. The motion of the film displaces successive sweeps sufficiently to prevent overlapping. The small spikes pointing toward the left are time signals 5 μsec apart. The sweep begins and ends on one of these markers. Signals from the light stations result in deflections toward the right, five of which are visible on this record. With equipment of this character, the time of arrival of a signal is easily determined within 1 μsec or in favorable circumstances, and with considerable care in analyzing the record, the uncertainty can be reduced to about 0.3 μsec. An idea of the sensitivity for weak shocks may be had from the results obtained in a shock tube [*3*] of 4 inches width employing the schlieren optical screen. This system picked up reliable signals from a shock in which the density jump in air was one per cent of normal atmospheric density. With either system the signal strength rises with increase in density jump to a certain point beyond which the signal remains constant since the shock can intercept only a limited number of light rays. Hence, once adjusted, no changes are necessary for all shock strengths within the range of the instrument.

In actual performance there is little to choose between the schlieren and reflection systems. The first may offer better discrimination against shocks moving in one direction although in most cases this will be of no interest. The second method will normally be chosen because of its simplicity and cheapness; and being compact it readily lends itself to a rugged construction. Of course there are other devices for detecting the presence of a shock, such as pressure gauges, for example, but in general the precision is not so good as that obtained with the methods discussed above.

C,5.2. Cited References.

1. *Mass. Inst. of Technol. Radiation Laboratory Series,* Vol. 18, 19, 22. McGraw-Hill, 1948 and 1949.
2. Elmore, W. C., and Sands, M. L. *Electronics. National Nuclear Energy Series V-1.* McGraw-Hill, 1949.
3. Bleakney, W., Weimer, D. K., and Fletcher, C. H. The shock tube: a facility for investigations in fluid dynamics. *Rev. Sci. Instr. 20,* 807–815 (1949).
4. Emrich, R. J. Spiral chronograph for measurement of a single millisecond time interval with microsecond accuracy. *Rev. Sci. Instr. 18,* 150–157 (1947).
5. Geiger, F. W., and Mautz, C. W. The shock tube as an instrument for the investigation of transonic and supersonic flow patterns. *Univ. Mich. Eng. Research Inst. Rept.,* 1949.
6. Emrich, R. J. and Curtis, C. W. Attenuation in the shock tube. *J. Appl. Phys. 24,* 360–363 (1953).

SECTION D

TEMPERATURE MEASUREMENTS

GERHARD R. EBER
WILLOUGHBY M. CADY

ARTICLE D,1

WALL TEMPERATURE DETERMINATION

GERHARD R. EBER

D,1.1. Introduction. Experimental procedures for investigating the interaction between the temperature of a solid wall and a compressible fluid adjacent to it, as encountered in such problems as the determination of temperature recovery factors, heat transfer coefficients, or boundary layer transition, require the exact measurement of wall temperatures. Usually, such measurements are made in either one of the two following cases: (1) when a fast-moving fluid is in contact with a solid body at rest, and (2) when fast-moving objects, such as projectiles in free flight, are in contact with still air. Methods applied in the case of low speed flow may be adequate in many applications of the first problem, provided that certain conditions inherent in the effect of high speed are taken care of properly. The second problem remained unsolved for a long time for projectiles too small in size to carry telemetering equipment. Only recently a method has been devised (as described in Art. 1.4) which is promising for temperature measurements above 150°C.

Methods for the measurement of widely ranging temperatures at walls of fixed bodies wetted by high speed flow are usually based on (1) thermoelectric thermometry, (2) resistance thermometry, or (3) radiant energy emission.

The three methods are well covered in the literature. Practices for the measurement of surface temperatures by the use of thermocouples, resistance thermometers, and radiation techniques are summarized by F. C. Houghten and H. T. Olson [*1*]; thermoelectric thermometry has been treated extensively by William F. Roeser [*2*]; and the methods of optical pyrometry for the measurement of surface temperatures of hot bodies have been reported by W. E. Forsythe [*3*]. Thermoelectric thermometry is most extensively applied, whereas resistance thermometry as a means of determining surface temperatures has not received wide attention. The integrating effect of a fine resistance wire spread over a large area of an isothermal surface has obvious advantages for surface temperature measurements compared with the single point measurement obtained from a thermocouple junction. However, the method has not found general application, presumably because of insufficient information on the effect of strain from bending of resistance wires on the calibration.

The use of radiant energy emission is not restricted to high temperatures. Useful methods have been developed which make possible the measurement of temperature by use of infrared radiation down to nearly room temperature, with an accuracy comparable with that of thermoelectric methods.

D,1.2. On the Principle of Wall Temperature Measurements. Several basic requirements must be observed in order to obtain reasonably accurate measurements of the temperature at a solid wall in contact with a fast-moving compressible fluid. Even under conditions where the wall is at recovery temperature and the heat transfer has vanished, the temperature gradient in the fluid is rather large at a short distance from the wall. The temperature-sensing element must be in good contact with the wall and must not be influenced by the temperature of the surrounding fluid. It should have a two-dimensional rather than a three-dimensional extension and must be immersed into the region where the temperature is to be measured.

It is further required that the temperature-sensing element must not produce a disturbance at the measuring point, nor conduct heat away from or to this point, nor change the conditions of heat transfer at the surface if heat transfer is involved. Otherwise, the temperature-sensing element will not measure the true temperature of the wall but a temperature which is constantly disturbed by the sensing element.

Any temperature-sensing element in a wall will indicate its own temperature. Therefore, the principal problem is to devise the sensitive element of a temperature-measuring instrument so that it will assume the wall temperature. Furthermore, when heat transfer is involved between a solid surface and its surroundings, this transfer will include radiation and convection, and in some cases exchange of mass (evaporation or condensation). Therefore it is essential not to interfere with the mode of heat and mass transfer which may be taking place. If transfer of heat by radiation occurs, the emissivity of the surface must not be affected. In most practical cases the temperature-sensing element of the instrument will have an emissivity different from the material of the surface itself. Similarly, if convective heat transfer is involved, the smoothness of the surface must not be affected by the instrument.

It is obvious that conditions exist under which it may be impossible to avoid entirely interference between the temperature-sensing element and the mode of heat transfer. However, by careful calculation of the possible measuring error an arrangement of the temperature-sensing element can always be found which will allow one to measure the true wall temperature quite accurately.

D,1.3. Thermocouples. The measurement of wall temperature by means of thermocouples has found extensive application. Standard techniques in determining the temperature of the junction are well known. Wires of any diameter and of a large variety of suitable materials are commercially available. The main difficulty inherent in the application of thermocouples is the necessity for attaching the junction and the leads in such a way that the isothermal field in the wall will be least disturbed.

In a metal wall, the junction may be soldered or peened directly in the metal. However, care must be taken that the character of the surface will not be changed, nor must the emissivity be affected. Surface thermocouples may be adjusted successfully to the above requirements, giving a sufficiently large heat transfer and minimizing the disturbance of the wall temperature. The simple method of soldering a small plate to the surface and leading the leads away parallel to the surface in an isothermal layer in order to minimize heat conduction losses cannot be applied in compressible flow. Such an attachment would cause shock waves in supersonic flow and disturb the flow in the surrounding boundary layer. It may change entirely the thermal conditions which prevail without this measuring device. Hence, in compressible flow the temperature-sensing element must be mounted flush with the surface, making the arrangement for the temperature measurement more elaborate. For the measurement of surface temperatures in insulating materials, good results may be obtained by using small inserts of copper or silver of about $\frac{1}{8}$-inch diameter and $\frac{1}{100}$ inch thick glued into the wall flush with the surface. Fig. D,1.3 shows such a thermocouple arrangement, which is frequently used to measure recovery temperatures on bodies in supersonic flow. Such small plates easily assume the temperature of the surface and follow rapidly any changes in temperature because of the low heat capacity and the practically two-dimensional extension. The heat transfer through the surface area of the insert will compensate for the heat conduction through the lead wires. Coating the insert with a thin layer of lacquer

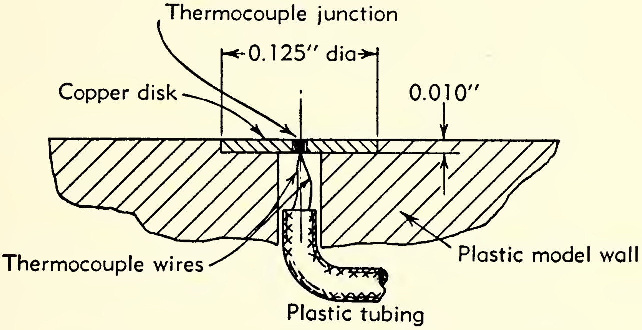

Fig. D,1.3. Arrangement of surface thermocouple.

having an emissivity similar to that of the wall material, will reduce the influence of radiation to a minimum.

In all wall temperature measurements, it is advisable to check the effect of the thermal conductivity in the lead wires and the heat transfer to or from the junction very carefully in order to determine the measuring error for each particular application.

Another useful method for determining wall temperatures is to evaporate or galvanize a small band of thermocouple material on the surface of the wall in such a fashion that both layers overlap at the measuring point and form an extremely sensitive thermojunction. The lead wires are soldered to the thin layer at a location where the wire will not cause a disturbance at the measuring point. This method is particularly useful in the case of temperature measurements in sandwiched walls for the determination of the heat flux in the wall, and may be applied on metal walls as well as walls of heat-insulating materials. The necessary precautions mentioned above for avoiding any change in the thermal characteristics of the walls apply here as well.

A different method for measuring surface temperatures with thermocouples has been described by N. Sasaki [*4*]. Using this method, a thermocouple junction must, by heating or by cooling, be adjusted to a temperature equal to that of the surface to be measured. The junction is then brought into contact with the surface. When the instrument in the thermoelectric circuit of the junction does not deflect during a short contact of the junction with the surface, it is concluded that the surface temperature is equal to the temperature of the measuring junction.

D,1.4. Infrared Radiation. The measurement of surface temperatures by means of thermal or infrared radiation is well known and widely employed. Experimental methods are described in the literature [*5*,*6*].

However, when the temperature changes rapidly, or when a temperature exists only for an extremely short time, or when the surface temperature of an object moving with high speed, such as an airplane or projectile, is to be measured, the usual methods are frequently not applicable because of the time lag involved. During recent years, the development of lead sulfide photoconductive cells has introduced the possibility of utilizing thermal radiation to determine surface temperatures under these adverse conditions. The high sensitivity of such a cell combined with its short time response has made it into one of the most useful detectors of thermal radiation [*7*,*8*,*9*,*10*].

Considering a black body, the energy density of radiation increases with the fourth power of its absolute temperature and is distributed over a large range of wavelengths. A lead sulfide photoconductive cell used as a detector of the energy emitted from the surface responds only to a limited range of wavelengths of the total radiation. The signal from this conductor, however, varies with a much higher power of the absolute temperature. Such detectors are insensitive to infrared radiation at wavelengths beyond 3.3 microns. Fig. D,1.4a shows a typical spectral sensitivity curve of a lead sulfide cell.

The response time of lead sulfide cells may be made as low as a few microseconds. L. G. Mundie, E. M. Pell, and L. W. Jones [*11*] have investigated a large number of lead sulfide cells and have determined their characteristics.

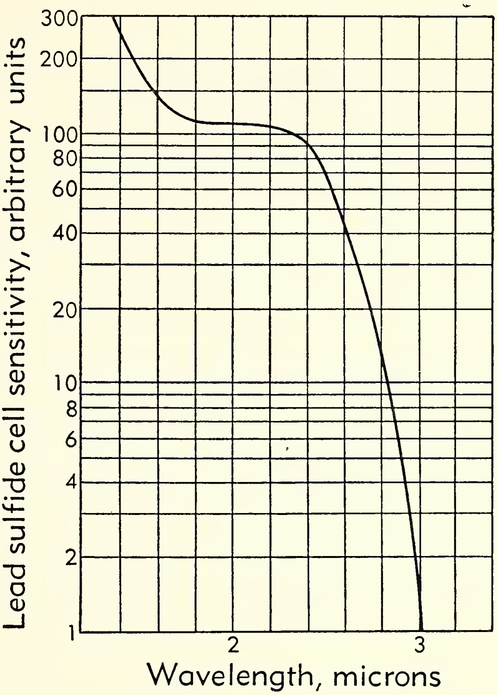

Fig. D,1.4a. Spectral sensitivity of lead sulfide cell.

Experiments have been performed by the same group at the Naval Ordnance Laboratory [*12*] in an attempt to determine the accuracy with which a lead sulfide cell can measure the surface temperature of both stationary and fast-moving objects, thus indicating the usefulness of lead sulfide cells for practical applications. The fundamental assumption on which the measurements were based is that the response of the lead sulfide cell detector to thermal radiation from a heated object different from zero will increase in a monotonic manner as the temperature of the surface is raised. The correctness of this assumption is substantiated by the experiments.

An arrangement for a general purpose infrared optical pyrometer is to interrupt periodically the radiation from a blackened heated object

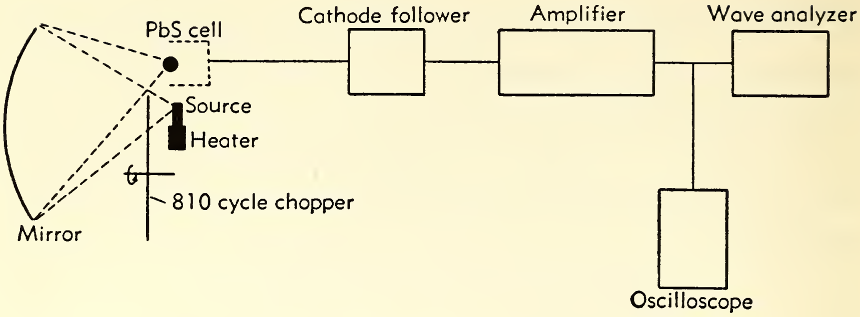

Fig. D,1.4b. Experimental arrangement for temperature measurements with lead sulfide cells.

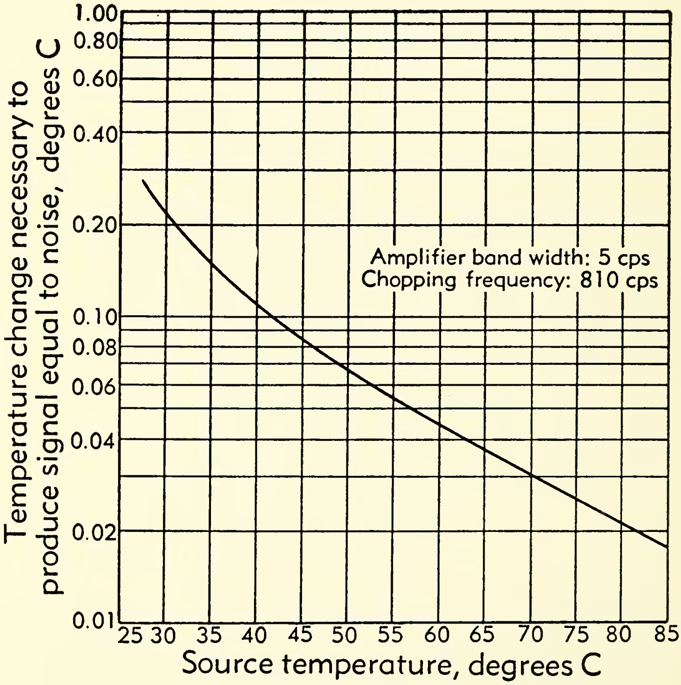

Fig. D,1.4c. Detectable temperature change of lead sulfide cell vs. source temperature.

by means of a chopping blade and then focusing it on the cell by a concave mirror, as shown schematically in Fig. D,1.4b. To reduce the noise from the cell a tuned amplifier with a narrow band pass of 5 cps is used to measure the signal. It was found that at temperatures above 45°C a few hundredths of a degree centigrade change in temperature is detectable with this type of instrument. Temperatures which exist for one or two seconds only can be measured with an accuracy of ±0.22°C at 30°C and

±0.02°C at 80°C, as illustrated in Fig. D,1.4c. Temperatures which exist for only a few microseconds can be measured with accuracies of ±8°C at 160°C and ±2°C at 210°C.

For measurements of surface temperatures of objects moving at high speed, a broad band amplifier must be used because only a simple impulse of extremely short duration is involved. A practical arrangement is to use an amplifier with a band pass extending from 10^2 to 10^6 cps and an oscilloscope to measure the amplifier output. Since such a frequency band includes more noise, signal-to-noise ratios are much smaller at each temperature.

The experimental procedure is then to observe on the oscilloscope the signal generated by the lead sulfide cell when the image of the fast-moving object whose surface temperature is to be measured crosses the sensitive area of the cell, momentarily replacing the image of the heated background. The object is momentarily imaged on the lead sulfide cell by a concave mirror. Prior to and following the image of the object, the heated background surface of known temperature itself is imaged on the detector.

If the temperature of the object differs from that of the background, a pulse is observed on the oscilloscope. If the background and object temperatures are identical, the oscilloscope shows a flat trace. By adjusting the background temperature to that of the object the advantages of a null method can be realized. On the other hand, calibration of the pulse heights causes no particular difficulties.

The application of this method requires that the spectral emissivities of the surface and the background are equal and that all surrounding objects are at room temperature. It is also desirable to have as high an emissivity as possible. This can be achieved by coating the surfaces with blackening material.

Signals for background temperatures of 150°C and higher can be obtained with detectors now available. The probable experimental error at 150°C is about ±10°C, and this error decreases as the temperature is raised. The method may be applied to the measurement of the temperature rise of fast-moving objects during flight for increases in excess of 150°C, by duplicating the equipment and measuring the temperature at two stations placed along the path of the flying object.

D,1.5. Phosphor Luminescence. The temperature dependence of the luminescent efficiency of superlinear phosphors and the variation of this dependence with the exciting intensity is a property which may be used for the measurement of surface temperatures. F. Urbach, N. R. Nail, and D. Pearlman [*13*] have investigated numerous phosphors and have developed two methods for observing, measuring, and recording photographically surface temperatures ranging from room temperature to about 200°C. Both methods are based on the same principle but are different in their application. Using the first method, the surface under investigation is coated with a luminescent phosphor and illuminated with ultraviolet radiation. The temperature distribution can be observed from the pattern of brightness or color of the luminescent coating and isotherm charts can be drawn. Using the second method, no coating is required. A temperature-sensitive phosphor screen is placed in the focus of a suitable optical system. The distribution of the thermal radiation from the surface is imaged on the screen and is visible as a brightness pattern. Urbach and coworkers have proposed the terms "contact thermography" and "projection thermography" for the first and the second methods, respectively.

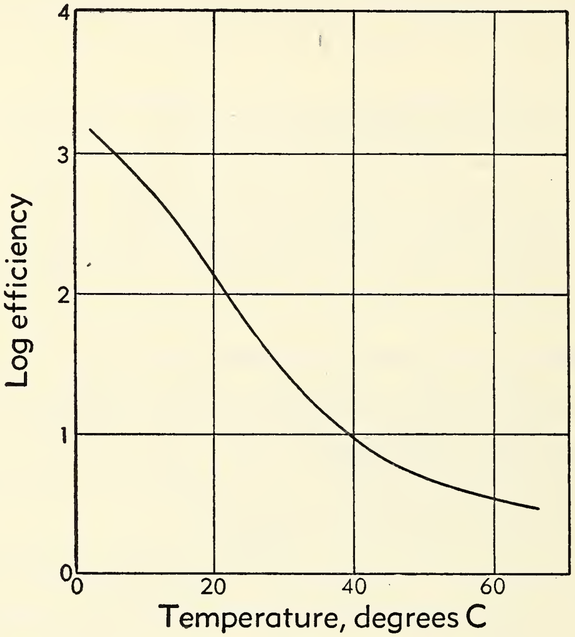

Fig. D,1.5a. Temperature dependence of the efficiency for a zinc-cadmium-sulfide phosphor.

The thermometric sensitivity of the phosphors used is dependent on the temperature coefficient and the accuracy with which changes of this coefficient can be measured. A method has been developed which measures successfully small changes in luminescent brightness as an indicator of the temperature and which has great advantages in its application. The temperature dependence of the luminescent efficiency has been made large so that no elaborate measurements are needed. The changes in brightness or color are very well suited for photographic recording and visual observation.

From the large number of phosphors investigated it was found that zinc-sulfide, zinc-cadmium-sulfide, and zinc-cadmium-selenide phosphors have the strongest temperature dependence. For the zinc-cadmium-sulfide phosphor selected by Urbach and coworkers for their investigations, up to 20 per cent brightness change per degree centigrade was obtained. An example of the temperature dependence of the efficiency for a zinc-cadmium-sulfide phosphor is given in Fig. D,1.5a.

The efficiency in this case represents essentially the ratio of phosphorescent brightness to some standard brightness. By plotting the natural log of the efficiency, one sees directly the temperature sensitivity of the per cent change of brightness, the quantity of practical importance.

The flexibility of the phosphors is remarkable. The temperature dependency curves may be changed to cover a wide range simply by varying the composition of the base or the activators or by using mixtures selected on the basis of whether range or sensitivity is desired for a particular application. Furthermore, the temperature curves can be shifted by varying the exciting intensity. Thus range and sensitivity may be adjusted to any particular need.

Contact thermography makes possible the direct determination of temperature distributions by photoelectric photometry. The sensitivity depends upon the type of photometric method used. The necessary calibrations can be obtained easily. However, the application of this method is subject to certain limitations. The thermal characteristics of the surface may be altered by the coating so that emissivity and convective heat exchange of the coated surface might be different from those of the uncoated surface. At temperatures higher than about 200°C the stability of the coating must be taken into account. The necessity of working in a darkroom or at low ambient illumination imposes restrictions on the application.

The adjustment or response time of the phosphorescence to temperature changes is of importance in the study of transient phenomena. Such times differ greatly for different phosphors, but are rather low for phosphors of the ZnS-CdS type used in this application. With moderately strong ultraviolet excitation, such as that provided by a mercury arc, one may safely take the adjustment time to be under 0.3 seconds, possibly considerably less.

Preliminary experiments[1] by members of the Ladenburg group at Princeton indicate that contract thermography is a useful tool in the study of the growth of turbulence in the boundary layer of wind tunnel models [*27*].

The influence of the coating on the modus of heat transfer may be eliminated by use of projection thermography, the second method proposed by Urbach and coworkers. The physical arrangement of this method is shown in Fig. D,1.5b. A temperature-sensitive phosphor screen is placed in the focal plane of a concave mirror. The mirror forms an image of the object to be measured on the phosphor screen and has an opening in the center through which the image on the screen can be recorded photographically. An ultraviolet emitting lamp is used for excitation of the screen and an ultraviolet absorbing filter is placed in front of the camera. The sensitivity of the phosphors mentioned above is sufficient to form visible images by thermal radiation. The image of the object is not very clearly defined.

---

[1] See report by L. C. Bradley III, "Temperature-sensitive phosphor used to measure surface temperatures in aerodynamics," *Rev. Sci. Instr.* *24*, 219–220 (1953).

The accuracy with which temperature differences of nearly black radiators may be detected with projection thermography is at present about 4° to 5°C. This shows that the method is far less sensitive than contact thermography. The great advantage is its simplicity. Since no coating is needed, the exciting lamps may be arranged in any manner without definite relation to the object under investigation. The object itself may be located outside of the reach of the observer. This makes the method attractive for application in supersonic wind tunnels. Furthermore, projection thermography is not restricted to low ambient illumination since filters eliminating the visible light may be used.

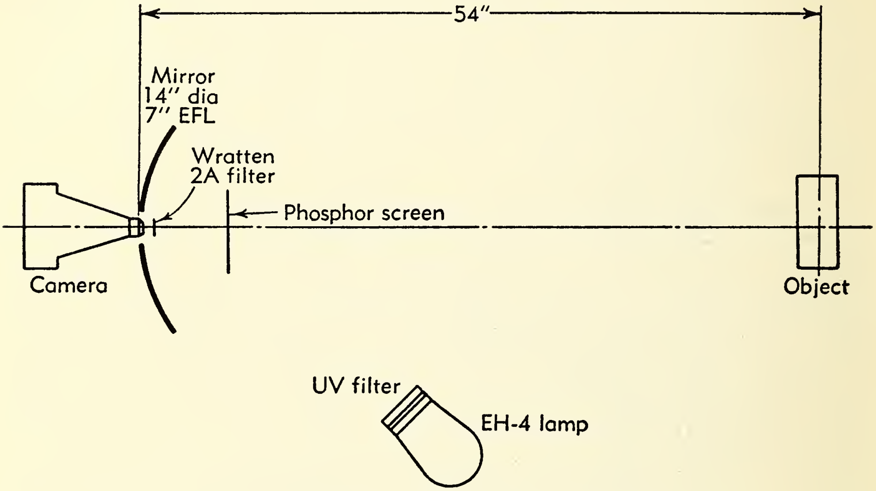

Fig. D,1.5b. Arrangement for projection thermography.

D,1.6. Applications. Two applications of wall temperature measurements are discussed in more detail: (1) the determination of temperature recovery factors, and (2) the determination of heat transfer coefficients. Reference is made to V,F of this series for the physical principle and theoretical aspect of aerodynamic heating and high speed heat transfer.

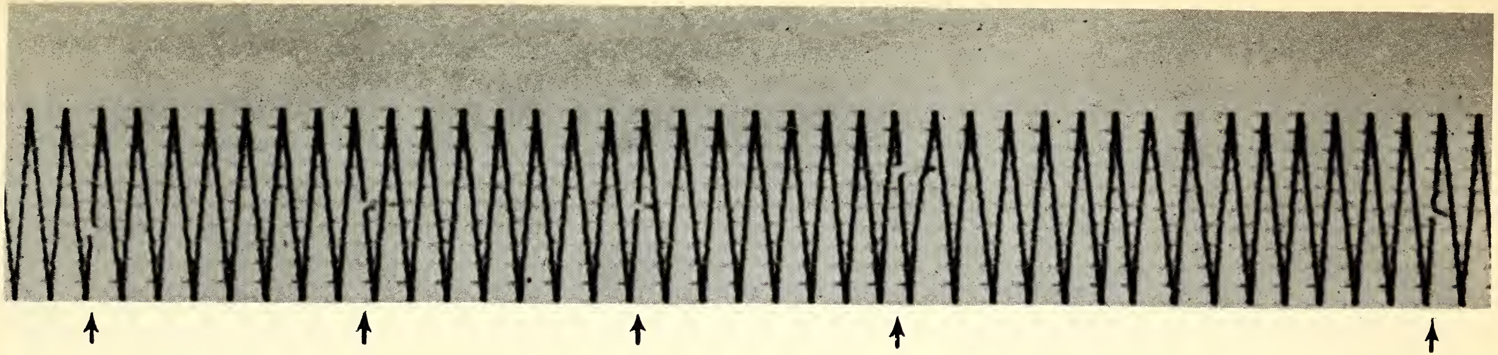

Plate C,5.1. Reproduction of an actual chronograph record. Time pulses point toward the left, light signals toward the right. The arrows indicate location of light signals.

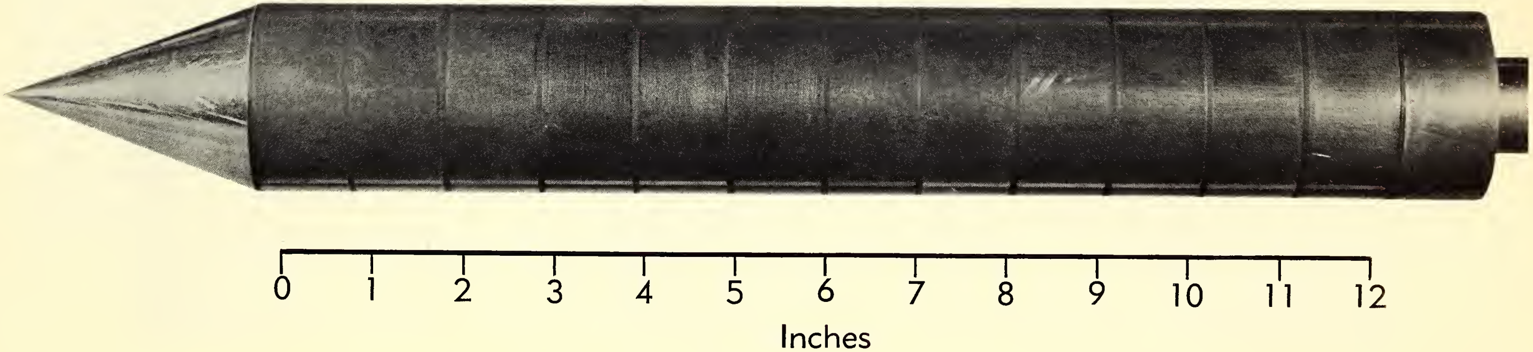

Plate D,1.6. Sectionalized cone-cylinder model for transient heat transfer measurements.

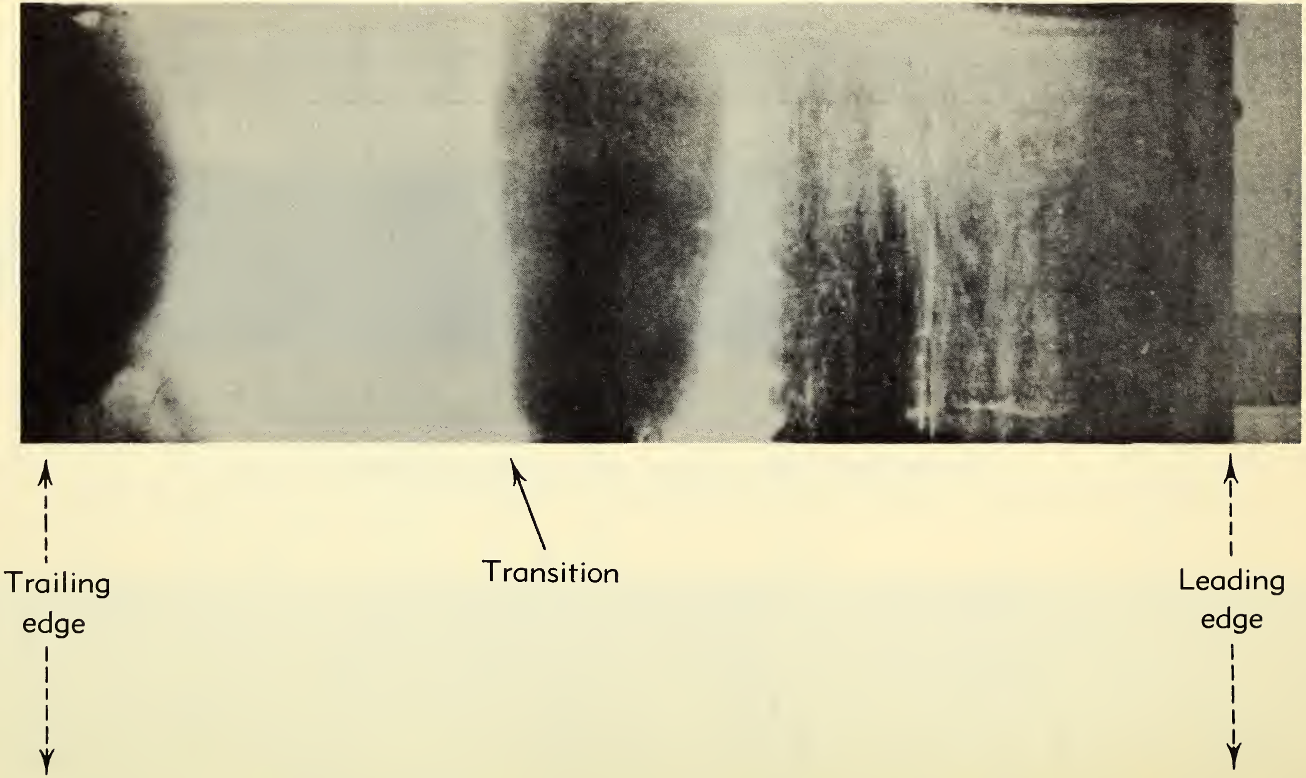

Plate F,1.2. Transition on airplane wing, "China clay" method. (From [2].)

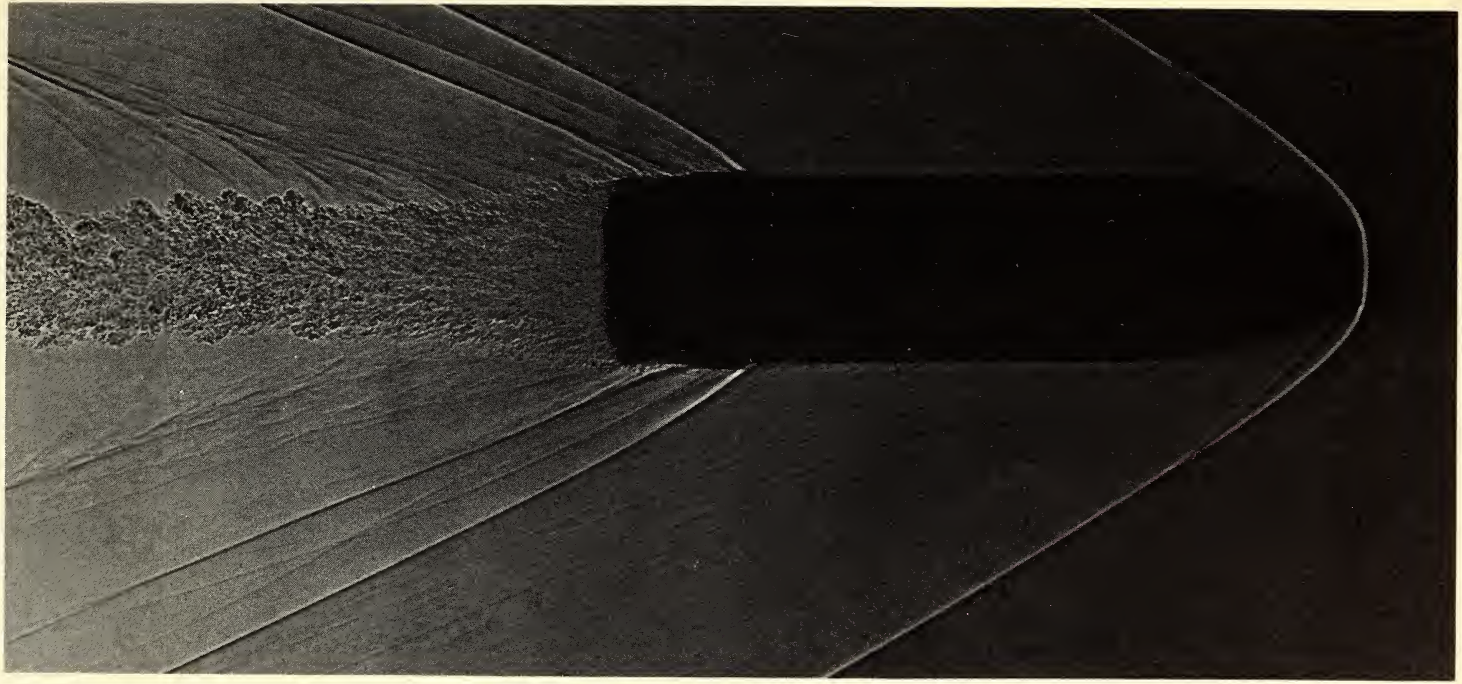

Plate F,1.3. Shadow picture of projectile in supersonic flow.

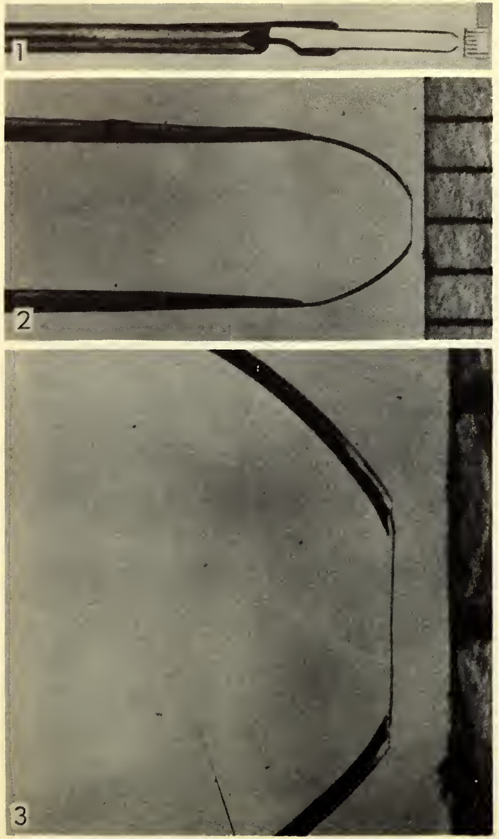

Plate F,2.2a. Hot wire probe. 1, complete exploring head. 2, sewing needles with soldered loop of Wollaston wire. 3, loop of Wollaston wire. (From [*44*].)

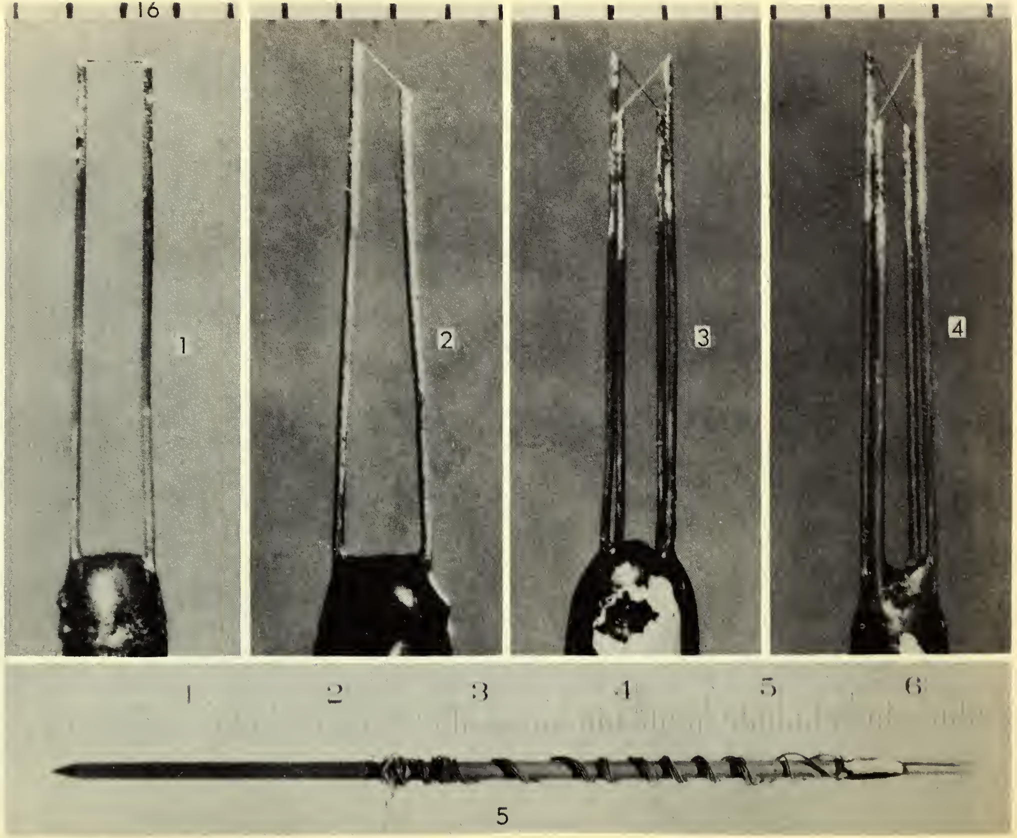

Plate F,2.2b. Magnified view of hot wire arrangements. 1, for measuring u'. 2 and 3, for measuring turbulent shearing stress. 4, for measuring v' and w'. 5, one complete instrument. Actual size of 1, 2, 3, and 4 shown by $\frac{1}{16}$-inch scale at top. (From [*8*].)

Tungsten wire 0.003 in. dia.

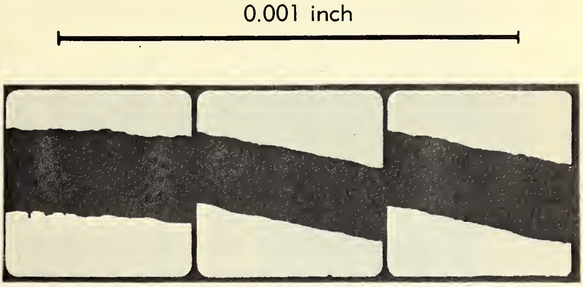

Tungsten wire gold plated 0.00015 in. dia.

Plate F,2.2c. Electron microscope photographs of tungsten wires. (From [*9*].)

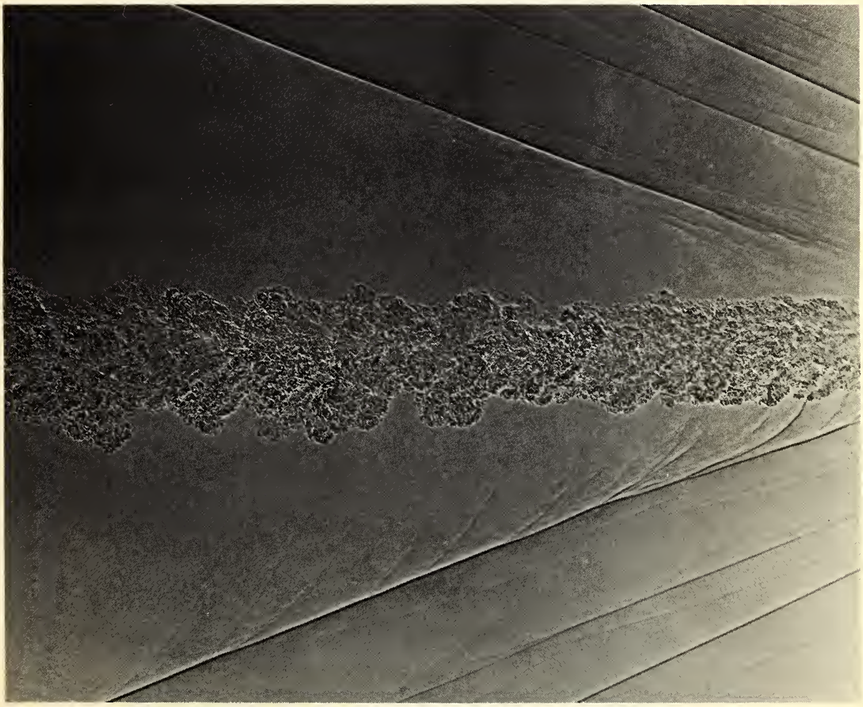

Plate F,3.2. Turbulent density fluctuations in wake of projectile.

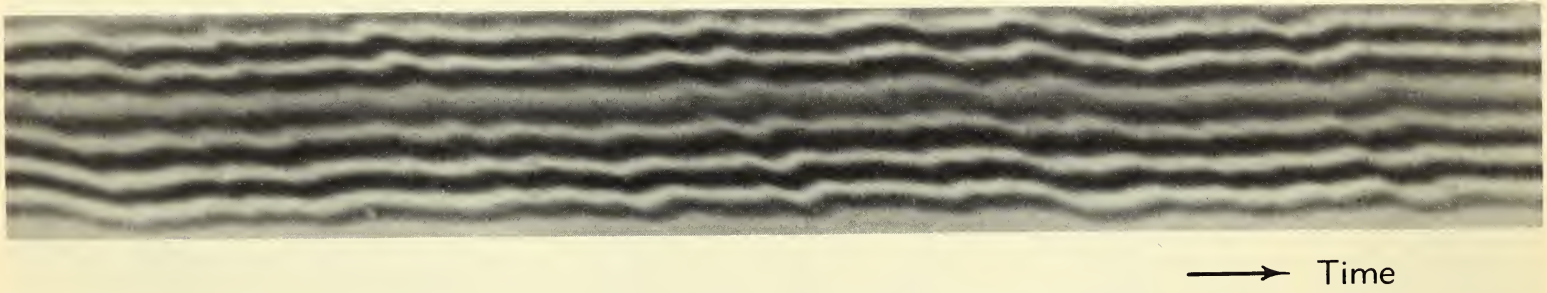

Plate F,3.3. Time record of turbulent fluctuations by the interferometer.

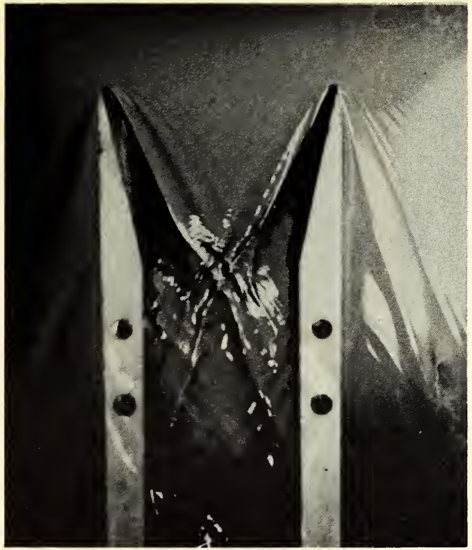

Plate H,1.3a. Photograph by reflected light (see Fig. H,1.3b).

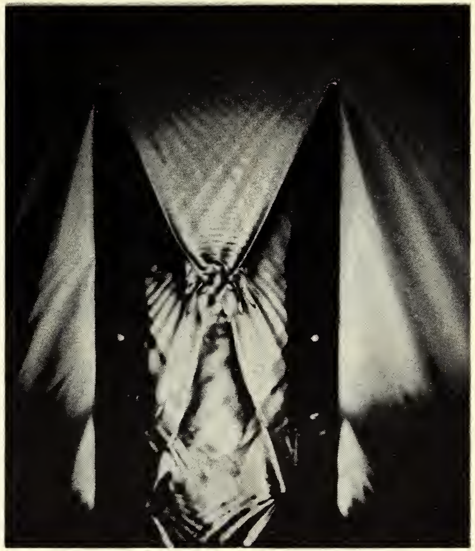

Plate H,1.3b. Photograph by transmission of diffuse light (see Fig. H,1.3c).

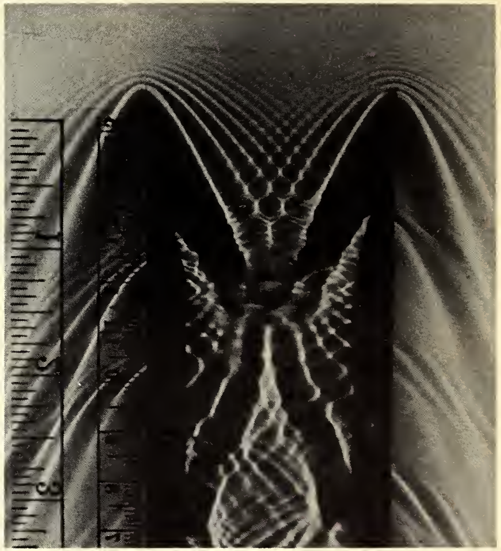

Plate H,1.3c. Photograph by transmission of parallel light (see Fig. H,1.5).

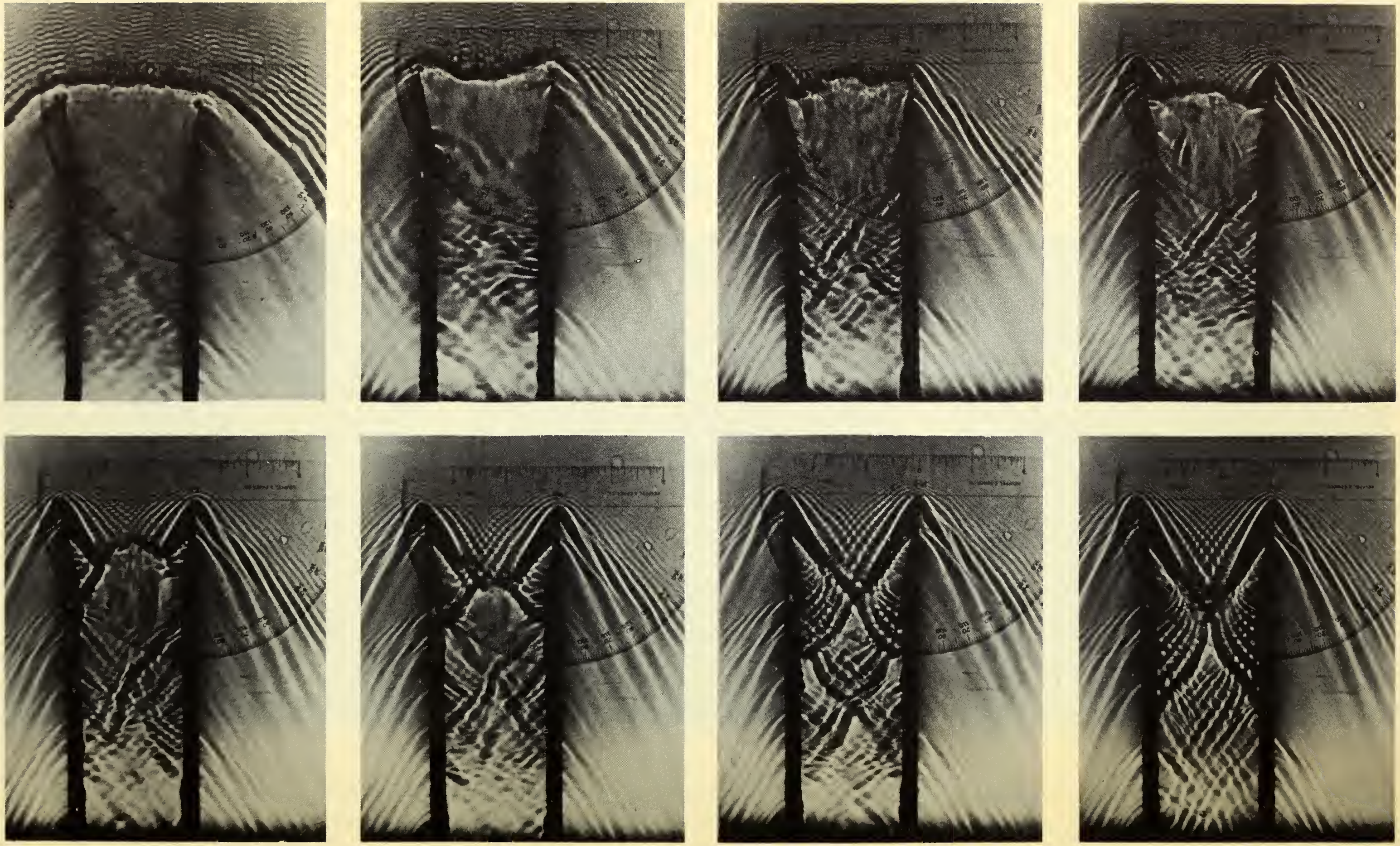

Plate H,1.5. Motion picture frames showing starting of fixed geometry supersonic diffuser.

Determination of Temperature Recovery Factors. The temperature which the insulated surface of a body at supersonic speeds assumes due to aerodynamic heating is called the adiabatic wall or recovery temperature. Its value depends on the local Mach number (or static temperature) outside of the boundary layer and the frictional dissipation of kinetic energy in the boundary layer.

The recovery of temperature is usually expressed in terms of the temperature recovery factor r, defined as the ratio of the actual temperature rise $(T_w - T_\infty)$ of the wall temperature above that of the free stream temperature to the adiabatic temperature rise $(T^0_\infty - T_\infty)$, viz.

$$r = \frac{T_w - T_\infty}{T^0_\infty - T_\infty} = \frac{\frac{T_w}{T^0_\infty}\left(1 + \frac{\gamma - 1}{2} M^2_\infty\right) - 1}{\frac{\gamma - 1}{2} M^2_\infty} \qquad (1.6\text{-}1)$$

T^0_∞ = Total Temp [illegible] of Tunnel [illegible]

During recent years, a considerable number of experimental investigations were conducted in order to determine temperature recovery factors in supersonic wind tunnels at speeds ranging from subsonic to about five times the speed of sound [*14* to *21*]. In general, two-dimensional and axially symmetric bodies of simple geometric shape, such as flat plates, cones, ogives, and cone-cylinders in axial flow, were employed by the various investigators for their experiments.

A critical review of the results shows that the determination of temperature recovery factors requires not only precise temperature measurement but also proper consideration of several factors influencing the measurement of recovery temperatures. The most important of these factors are: the thermal conductivity and heat capacity of the model material; the temperature history of the boundary layer; radiative heat exchange between the model surface and the surrounding wind tunnel walls; the surface finish of the model wall; and the free stream turbulence in the wind tunnel flow. The relative importance of the above factors varies depending on the measuring technique employed for a particular investigation.

Laminar temperature recovery factors on pointed bodies such as cones and ogives built from shells of ~~about~~ $\frac{1}{32}$-inch thickness [*15*,*16*,*17*,*20*] agree very well with theory, whereas those on flat plates [*18*,*21*] are consistently higher, as illustrated in Fig. D,1.6a, where the local recovery factor is plotted as a function of the local Reynolds number based on wetted length and surface conditions for density and viscosity. Such a difference cannot be real. It appears that the higher temperatures measured on flat plates with laminar boundary layer are caused by the asymmetric thermal conditions near the leading edge of the models. The leading edge of a flat plate usually consists of a wedge of about 10° total angle with one face adjusted parallel to the flow. Due to the entropy increase through the oblique shock in front of the wedge the recovery temperature at the face of the wedge which is at an angle with the flow is higher than that of the face which is parallel to the flow. Heat is conducted to the opposite side of the wedge and a recovery temperature higher than that of the perfect insulated case is attained at the face parallel to the flow. The error depends on the angle of the wedge, the thermal conductivity of the wedge material, and the convective heat transfer characteristics. It becomes smaller as the distance from the leading edge becomes larger. Therefore, a correction must be applied for recovery temperatures behind the leading edge of flat plates.

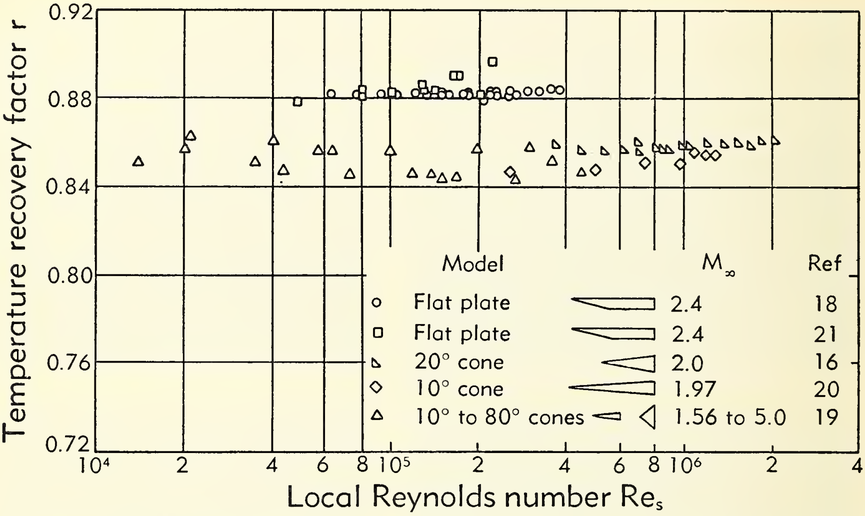

Fig. D,1.6a. Laminar temperature recovery factors on flat plates and cones.

At some distance from the tip or leading edge of a model where the boundary layer becomes turbulent, the recovery factor increases from the lower laminar value to the higher turbulent value, usually passing through a maximum in the transitional region. To measure the true recovery temperature under such nonuniform temperature conditions, care must be taken to minimize the effect of heat conduction in the wall parallel to flow direction. Two techniques have been applied to meet the above limitation: one requires the use of thermal insulating material for the wall thus approaching the case in which the heat flow within the wall is negligible and does not affect the recovery temperature; the other method uses a model made out of a thin metal shell of practically zero mass, which, again, results in negligible heat conduction in the flow direction because of the small cross section of the wall. Neither method is entirely satisfactory. However, it appears that sufficiently far back from the transition region both methods yield identical results as illustrated in Fig. D,1.6b.

Continuously as well as intermittently blowing wind tunnels have been employed to measure recovery temperatures. In a continuous wind tunnel a constant temperature distribution in the model wall is established after some time. In an intermittent tunnel the duration of a blow is usually insufficient to establish equilibrium conditions. The recovery temperature is then measured by precooling the model wall to the anticipated recovery temperature before blowing the tunnel. When the temperature recorded during the blow does not change with time, it is postulated that recovery temperature and wall temperature are identical. If, however, the recovery temperature is nonuniform along the wall, it is practically impossible to precool the entire wall to the correct recovery temperature. Therefore, the recovery temperature at a certain point under consideration is influenced by heat transfer occurring upstream of this point and will settle at an apparent higher recovery temperature if the wall temperature at any portion upstream of the measuring point is above its recovery temperature or vice versa.

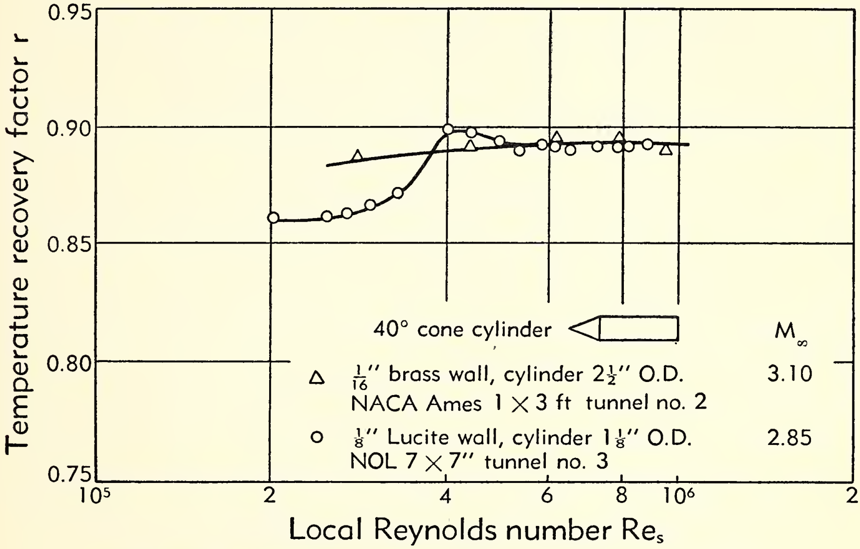

Fig. D,1.6b. Temperature recovery factors on 40° cone-cylinder models of heat-conducting and heat-insulating material.

Conventional high speed wind tunnels operate with supply air of atmospheric temperature or slightly higher. Under these conditions the temperature difference between the model surface and the tunnel walls is small and the error from radiative heat exchange on recovery temperature measurements is negligible. If, however, the model surface temperature differs largely from the tunnel wall temperature as it does in wind tunnels using heated supply air and having cooled nozzles, correction must be made for radiation. For simple geometric configurations the radiation error may be computed in the usual manner; in more complex cases the correction for radiation must be determined as a function of the temperature difference between model and tunnel walls from a separate investigation.

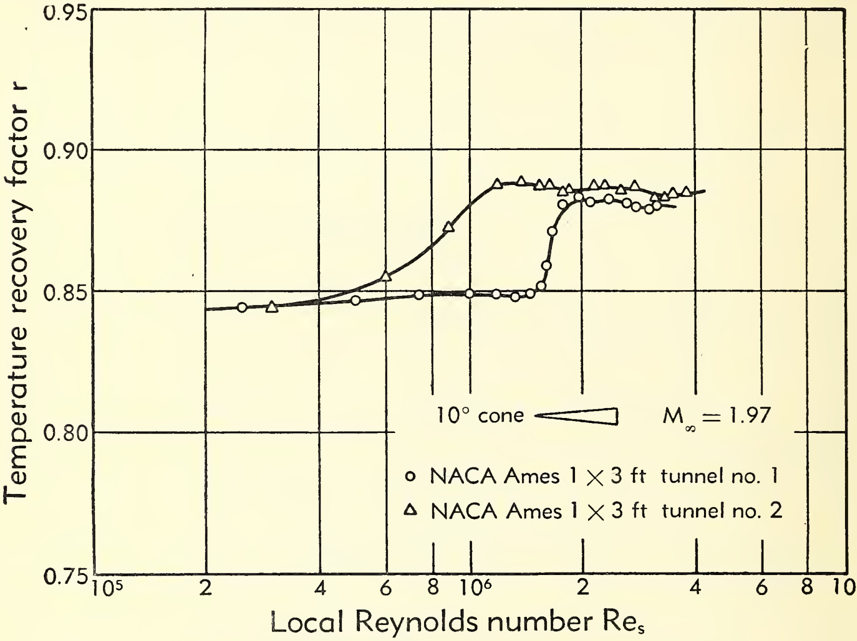

Fig. D,1.6c. Effect of free stream turbulence on the temperature recovery factor on a 10° cone.

It has been stated that the recovery temperature may be affected by the surface roughness of the model. It is common practice to express surface roughness as rms values in microinches (μin.), although it is realized that it is an oversimplification to describe the complex geometry of a surface by a single number. As far as reported, the rms values of the bodies investigated were between about 6 microinches for highly polished surfaces and 100 microinches for rather rough surfaces. Experimental evidence is that, within this range, the surface finish does not influence the numerical value of the laminar or turbulent recovery temperature beyond the measuring accuracy. As the surface becomes rougher the transition zone of the boundary layer moves upstream.

The level of free stream turbulence, being different in various wind tunnels and varying in the same tunnel with the supply pressure and Mach number, has an effect on the transition of the boundary layer from laminar to turbulent. This effect becomes evident in recovery temperature measurements which show the change from laminar to turbulent values farther upstream in a tunnel which has an apparently higher turbulence. Fig. D,1.6c illustrates recovery factors determined on a 10-degree total angle cone at $M_\infty = 1.97$ in the NACA Ames 1 × 3 ft supersonic wind tunnels no. 1 and 2 [*20*]. Tunnel no. 1 is a continuous closed return type tunnel, whereas tunnel no. 2 is a blow-down tunnel of about 5 to 18 minutes blow duration.

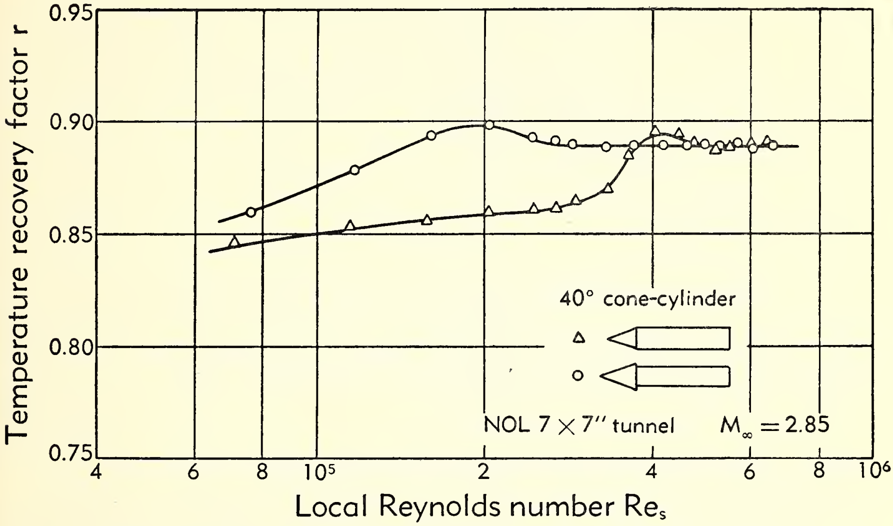

Fig. D,1.6d. Temperature recovery factor on a 40° cone-cylinder Lucite model without and with artificial turbulence promotion.

Turbulence in the boundary layer has been promoted by artificial means by various investigators in making their measurements of recovery temperatures. The effect of such turbulence promotion on recovery temperatures is again evident in the transition region. Fig. D,1.6d shows as an example the recovery factor for a 40° cone-cylinder model at $M_\infty = 2.85$ measured in the NOL 7 × 7 in. continuous wind tunnel without and with artificial promotion of turbulence. Turbulence was promoted by using a cone having a base about 12 per cent larger in diameter than the cylinder diameter.

Determination of Heat Transfer Coefficients. The experimental determination of convective heat transfer characteristics in high speed flow constitutes another example of the application of wall temperature measurements. The heat flow from a solid wall to the surrounding medium or in opposite direction may be measured either under steady state or under transient heat flow conditions. Under steady state conditions the wall of the model is continuously heated or cooled internally and heat is exchanged with the flow. The wall assumes a constant temperature which is measured. The rate of heat flow may be determined either from the mass flow and the temperature change of a heating or cooling liquid, from the voltage and current of an electric heating system, or from the heat flux through a calibrated heat flux meter sandwiched into the wall.

With q as the rate of heat flow, A the surface area, and T_w and T_r the wall temperature and recovery temperature respectively, the heat transfer coefficient h can be determined from the equation

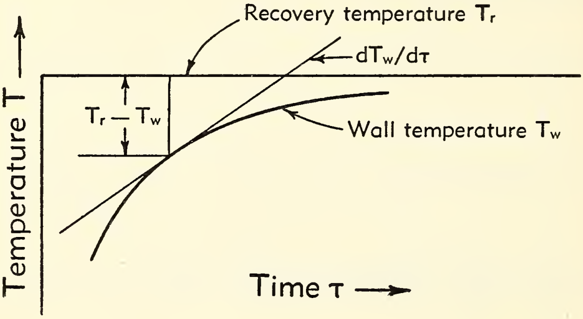

Fig. D,1.6e. Transient method for heat transfer measurement.

$$q = Ah(T_r - T_w) \tag{1.6-2}$$

Applications of this method are given in VIII,F,5.

In the transient method the heat capacity of the wall must be known. By measuring the wall temperature as a function of time and assuming that heat is transferred only between the wall and the surrounding medium, the heat transfer coefficient h may be obtained from a heat balance

$$q = mc_p \frac{dT_w}{d\tau} = hA(T_r - T_w)$$

$$h = \frac{mc_p}{A} \frac{dT_w/d\tau}{T_r - T_w} \tag{1.6-3}$$

where m is the mass, c_p the specific heat of the wall material, and $dT_w/d\tau$ the slope of a temperature-time record obtained during the measurement. An analysis of the method is illustrated in Fig. D,1.6e.

This method has been applied by London, Nottage, and Boelter [*22*] in low speed flow, by Eber [*19,23*] in supersonic wind tunnels, and by Fischer and Norris [*24*] and others in free flight testing. It is the only one which can be used for investigations where steady state conditions cannot be attained, although it is not restricted to such applications. Average as well as local heat transfer characteristics may be obtained with this method.

Plate D,1.6 presents a sectionalized cone-cylinder model employed at the Naval Ordnance Laboratory for the determination of local heat flow rates. The model is composed of a 40° solid cone and cylindrical copper sections of 1-inch length, $\frac{1}{8}$-inch wall thickness, and 2-inch diameter. The sections are mounted on a core of heat insulating material (Linen Bakelite) and insulated from each other by $\frac{1}{16}$-inch ribs of the same material. A section of the model is shown in detail in Fig. D,1.6f.

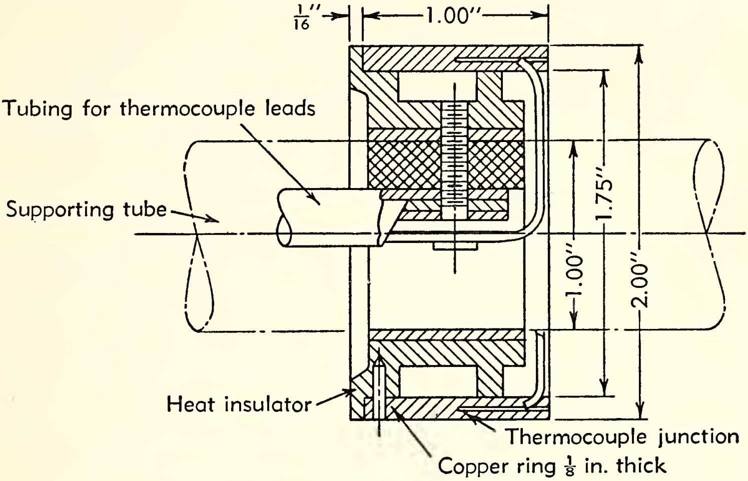

Fig. D,1.6f. Cross section of heat transfer model segment.

In order to apply the transient method successfully in securing heat transfer data, certain precautions must be taken and the limitations of the technique must be known. To use the method in an intermittent wind tunnel one must start with the entire wall at a uniform temperature above or below recovery temperature. This may be achieved by special heating or cooling devices. Hence the temperature gradient is zero throughout the model at the beginning of a measurement. During the measurement the wall temperature will either drop or rise according to the heat flow and may become nonuniform if the rate of heat flow is not constant along the surface. However, if the deviation from the initial temperature is small during the measuring period, the temperature gradient in longitudinal direction, because of the difference in rate of heat flow, will be small and the error introduced by heat conduction negligible. Likewise the temperature gradient normal to the surface will be negligible if the wall is made of a material of high thermal conductivity and small thickness. If for particular applications the wall must be rather thick, a correction may be applied for the heat conduction in the wall by measuring its normal temperature gradient. When the time of operation is short, the time constant of the wall ($1/[hA/mc_p]$) must be small in order to keep the temperature change within reasonable limits and to keep small the error in reading the slope of the temperature-time curve. This in turn requires a temperature-recording instrument with a fast response rate.

If the temperatures are such that a radiative heat exchange occurs between the wall surface and its surroundings, correction must be made in the usual manner.

To evaluate the rate of heat flow determined from the slope of the temperature-time curve and the thermal capacity of the wall in terms of heat transfer coefficients, two factors need proper consideration—the recovery temperature and the surface temperature distribution. If the time of operation is sufficiently long, the recovery temperature may be measured after temperature equilibrium has been attained, provided that longitudinal heat conduction in the model is negligible. If the heat conduction cannot be neglected, the recovery temperature may be determined from a model of identical shape designed for the determination of recovery factors. In special cases the recovery temperature may be determined from the known recovery factors for identical boundary layer flow conditions. However, it is known that the recovery factor depends in a complicated manner on the flow history. For the conditions with heat transfer upstream of a certain point under consideration, the recovery factor will be different from that of a perfect insulator. Therefore, in determining heat transfer coefficients from the rate of heat flow, an error in the temperature difference ($T_r - T_w$) may be introduced, the magnitude of which may be appreciable in certain cases.

It is an inherent feature of the transient method that the surface temperature distribution cannot be kept uniform. It has been shown by Chapman and Rubesin [*25*], Lighthill [*26*], and others that heat transfer coefficients for nonuniform temperature distributions are different from those for uniform temperature distributions and may be entirely inappropriate to present heat transfer characteristics. In certain critical regions where the heat flow changes its direction, large corrections must be made for the nonuniformity of the temperature distribution.

If the model for a specific application of the transient method is designed properly, it is always possible to avoid both critical regions and large nonuniformity of temperature distribution along the wall.

D,1.7. Cited References.

1. Houghton, F. C., and Olson, H. T. *Temperature, Its Measurement and Control in Science and Industry*, p. 855. Reinhold, 1941.
2. Roeser, W. F. *Temperature, Its Measurement and Control in Science and Industry*, p. 180. Reinhold, 1941.
3. Forsythe, W. E. *Temperature, Its Measurement and Control in Science and Industry*, p. 1115. Reinhold, 1941.

4. Sasaki, N. New method for surface-temperature measurement. *Rev. Sci. Instr. 21,* 1–6 (1950).
5. Lee, E., and Parker, R. C. Use of lead sulphide photo-conductive cells for high-speed pyrometry. *Nature 158,* 518 (1946).
6. Larsen, B. M., and Shenk, W. E. *Temperature, Its Measurement and Control in Science and Industry,* p. 1150. Reinhold, 1941.
7. Cosherrom, R. J. Development of sensitive lead sulphide photoconductive cells. *OSRD Rept. 5998,* 1945.
8. Sosnowski, L., Starkiewicz, J., and Simpson, O. Lead sulphide photoconductive cells. *Nature 159,* 818 (1947).
9. Moss, T. S. Spectral sensitivity of lead sulphide layers. *Nature 159,* 476 (1947).
10. Sutherland, G. B. B. M., Blackwell, D. E., and Fellgett, P. B. Use of lead sulphide cells in infra-red spectroscopy. *Nature 158,* 873 (1946).
11. Mundie, L. G., Pell, E. M., and Jones, L. W. An experimental study of nineteen lead sulfide photo-conductive cells. *Nav. Ord. Lab. Mem. 9929,* 1948.
12. Scanlan, W. W., Mundie, L. G., and Shadle, P. W. Temperature measurements with lead sulfide cells. *Nav. Ord. Lab. Mem. 10830,* 1950.
13. Urbach, F., Nail, N. R., and Pearlman, D. The observation of temperature distributions and of thermal radiation by means of non-linear phosphors. *J. Opt. Soc. Amer. 39,* 1011–1019 (1949).
14. Eckert, E., and Weise, W. Measurement of temperature distribution on the surface of unheated bodies in high velocity flow. *Forsch. Gebiete Ingenieurw. 13,* 246–254 (1942).
15. Eber, G. Experimentelle Untersuchung der Bremstemperatur und des Wärmeüberganges an einfachen Körpern bei Überschallgeschwindigkeit. *Archiv 66/57,* Peenemünde, 1941.
16. Wimbrow, W. R. Experimental investigation of temperature recovery factors on bodies of revolution at supersonic speeds. *NACA Tech. Note 1975,* 1949.
17. Eber, G. R. Determination of temperature-recovery factors on cones in the NOL 40 × 40 cm supersonic wind tunnel No. 2. *Nav. Ord. Lab. Mem. 10107,* 1950.
18. Stalder, J. R., Rubesin, M. W., and Tendeland, T. A determination of the laminar, transitional, and turbulent boundary layer temperature-recovery factors on a flat plate in supersonic flow. *NACA Tech. Note 2077,* 1950.
19. Eber, G. R. Recent investigation of temperature recovery and heat transmission on cones and cylinders in axial flow in the NOL aeroballistics wind tunnel. *J. Aeronaut. Sci. 19,* 1–6 (1952).
20. Stine, H. A., and Scherrer, R. Experimental investigation of the turbulent boundary layer temperature-recovery factor on bodies of revolution at Mach numbers from 2.0 to 3.8. *NACA Tech. Note 2664,* 1952.
21. Slack, E. G. Experimental investigation of heat transfer through laminar and turbulent boundary layers on a cooled flat plate at a Mach number of 2.4. *NACA Tech. Note 2686,* 1952.
22. London, A. L., Nottage, H. B., and Boelter, L. M. K. Determination of unit conductances for heat and mass transfer by the transient method. *Ind. Eng. Chem. 33,* 467 (1941).
23. Eber, G. R. Heat transfer measurements on cones in the NOL 40 × 40 cm supersonic wind tunnel No. 2. *Nav. Ord. Lab. Mem. 10106,* 1950.
24. Fischer, W. W., and Norris, R. H. Supersonic convective heat-transfer correlation from skin-temperature measurements on a V-2 rocket in flight. *Trans. ASME 71,* 457–469 (1949).
25. Chapman, D. R., and Rubesin, M. W. Temperature and velocity profiles in the compressible laminar boundary layer with arbitrary distribution of surface temperature. *J. Aeronaut. Sci. 16,* 547–565 (1949).
26. Lighthill, M. J. Contributions to the theory of heat transfer through a laminar boundary layer. *Proc. Roy. Soc. London A202,* 359–377 (1950).
27. Bradley, L. C., Van Voorhis, C. C., and Bershader, D. Experiments on a phosphorescence method for study of surface temperatures in a supersonic flow field. *Phys. Rev. 91,* 469 (1953).

ARTICLE D,2

SHIELDED THERMOCOUPLES

GERHARD R. EBER

D,2.1. Introduction. The need for an accurate determination of the thermodynamic state of a gas flowing at high subsonic and supersonic velocities has become highly important in high speed aerodynamics and related fields. A considerable amount of research work has been expended in recent years in order to develop temperature probes suitable to measure gas temperatures for various particular purposes. The importance of an accurate temperature measurement in a gas is obvious, considering that fundamental properties such as total energy, conductivity, viscosity, specific heat, and velocity of sound are determined from the temperature.

In general the thermodynamic state of a gas is determined by its pressure and temperature. However, for a rapidly moving gas two principal states may be defined: the "static" temperature to be observed by a thermometer moving together with the gas, and the "total" temperature to be observed with a stationary thermometer in the flow at which the gas is brought to a complete rest and at which its kinetic energy is converted adiabatically into a temperature rise.

The static temperature cannot be measured directly with an existing temperature probe at velocities at which the effect of the compressibility becomes appreciable (above Mach numbers of about 0.3). The reason is that the gas velocity around a stationary probe inserted into the gas flow will always be reduced in the boundary layer. It may be noted that the static temperature of a gas can be determined indirectly by measuring the static pressure and either the density of the gas, the velocity of sound, or the index of refraction. The total temperature can be measured with a relatively small error at the stagnation point of a temperature probe provided that, in the case of large temperature differences between the temperature sensing element and the surrounding walls, the probe is protected by radiation shields. A conventional temperature probe inserted into a rapidly moving gas stream will indicate a temperature between the "static" temperature and the "total" temperature depending on the shape of the probe, its orientation, radiation, and various other factors.

D,2.2. Theoretical Considerations. The stagnation temperature T^0, of a perfect gas which results from adiabatically reducing the velocity of the gas from free stream velocity to zero is related to the static temperature T_∞ and the flow Mach number M_∞ through the equation [*1*]

$$\frac{T^0}{T_\infty} = 1 + \frac{\gamma - 1}{2} M_\infty^2 \tag{2.2-1a}$$

γ denotes the ratio of the specific heats of the gas. This equation reduces for air with $\gamma = 1.4$ to

$$\frac{T^0}{T_\infty} = 1 + 0.2M_\infty^2 \tag{2.2-1b}$$

and is valid for both subsonic and supersonic flow conditions. This stems from the fact that a shock wave ahead of a temperature probe in supersonic flow effects only the entropy and not the total heat content of the gas. Investigations of total temperature probes, however, show that the indicated total temperature T_p is less than the theoretical value T^0 because of the loss of heat to the surroundings. Therefore a temperature recovery factor r of a probe may be defined as the ratio of the indicated temperature rise $T_p - T_\infty$ to the adiabatic temperature rise $T^0 - T_\infty$

$$r = \frac{T_p - T_\infty}{T^0 - T_\infty} \tag{2.2-2}$$

Consequently a probe giving a recovery factor equal to 1 will measure the total temperature and must be considered as very efficient. However, since from Eq. 2.2-1 two of the unknown quantities, namely T^0 and M_∞, must be determined to find the third, it is important that the recovery factor of a probe is constant over an appreciable range of Mach numbers and flow conditions. Therefore a probe with a recovery factor smaller than 1 but constant over a wide range is also a useful temperature probe. Then in selecting a suitable probe for temperature measurements in high velocity flow, a choice must be made between probes designed to measure stagnation temperatures as closely as possible and other temperature probes calibrated accurately for temperature recovery factors.

A survey of investigations shows that total temperature probes are preferable to other probes. A probe designed to establish a stagnation zone ahead of the temperature sensing element is insensitive to small changes in size and shape. The calibration of such a probe shows a better reproducibility than that of a probe for which the flow characteristics in the boundary layer determine the recovery factor.

Although a total temperature probe for a particular purpose will have to be designed with this purpose in mind, there are certain physical characteristics common to any satisfactory probe in compressible flow. These characteristics may be summarized as follows:

Temperature Sensing Element. Any suitable temperature sensing element, thermocouple or resistance thermometer, of low heat capacity may be used. To reduce heat conduction along the leads of a thermocouple, the leads should be exposed to the temperature of the stagnation chamber over a certain length. The low heat capacity will reduce the time lag of the thermocouple.

Radiation Shield. A radiation shield must surround the temperature sensing element of the probe. The temperature of the shield will be different from that of the sensing element and therefore influence the indicated temperature through radiative heat exchange. To minimize this effect the shield should be made of a material of low heat conductivity and its surface should have a low emissivity. The effectiveness of the radiation shield can be improved by using more than one radiation shield around the stagnation chamber containing the temperature sensing element.

Vent Holes. Because the temperature of the air in the stagnation chamber will drop below stagnation temperature due to heat conduction and radiation, a number of vent holes must be provided to replace the air. The size of these vent holes must be small so that the air in the probe does not assume an appreciable velocity. A certain amount of flow will increase the heat transfer to the thermocouple by convection and thus reduce the time lag.

Shape of the Probe. A blunt probe with a strong normal shock wave in front of it will help to increase the temperature in the boundary layer around the probe and therefore reduce the heat loss from the probe. A strong normal shock will also reduce the influence of flow inclination.

D,2.3. The Influence of Conduction and Radiation.

The temperature which a sensing element of a probe indicates is an equilibrium temperature resulting from a heat balance between the heat transferred from the gas to the temperature sensing element and the heat transferred from this element to the surroundings by conduction and radiation.

A total temperature probe supported from a wall having the temperature T_w, lower than that of the total temperature T^0 of the gas in which the probe is inserted, will indicate a thermometric error $(T^0 - T_p)_C$ due to conductive heat exchange along the lead wires and the supporting stem.

This error may be computed from the equation [2]

$$(T^0 - T_p)_C = \frac{T^0 - T_w}{\cosh (mL)} \tag{2.3-1}$$

where

$$m = \sqrt{\frac{hS}{kA}}$$

[illegible]

[illegible]

[illegible]

[illegible]

$$[illegible]$$

[illegible]

[illegible]

[illegible]

[illegible] **Design of Temperature Probes.** [illegible] devices are denoted as "high velocity thermocouples." In the design of these thermocouples the radiation error is usually reduced by a single or several (up to five) radiation shields, and the heat transfer by convection to the thermocouple is increased by use of an aspirator, operated by compressed air, which draws the hot gas past the thermocouple junction.

A different type of shielded thermocouple probe for use in gas turbines was recently developed by Dahl and Fiock [*5*]. The design of this probe is simple and very effective. It is based on the consideration that the emissivity of base metal thermocouples with oxidized surfaces of 0.8 to 0.95 can be substantially reduced by using materials (such as gold and silver, with an emissivity of 0.03 to 0.05, or platinum, with an emissivity of 0.12 to 0.18) which are not subject to oxidation and therefore will retain their effectiveness as radiation shields at all temperatures below their melting points. A shielded thermocouple of this type is shown in Fig. D,2.4a. It is simple to construct, reasonably rugged, has small physical dimensions, and responds rapidly to sudden changes in gas temperature. The reading of the thermocouple depends on the gas mass flow.

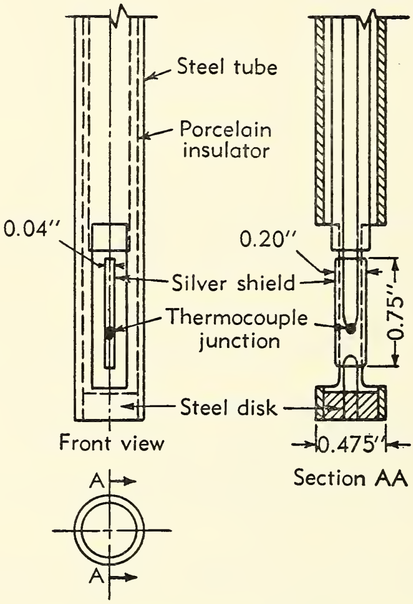

Fig. D,2.4a. Shielded thermocouple probe of A. I. Dahl and E. F. Fiock. (From [*5*].)

In working with aircraft engine superchargers, velocities up to that of sound and temperatures up to 400°F are encountered. There the compressibility effect cannot be neglected. One of the first useful total temperature probes, a diffuser type, was developed by Franz [*6*], (Fig. D,2.4b). The gas enters the stagnation chamber of the probe, built around the thermocouple junction, through a diffuser. The speed of the gas is slowed down to a fraction of its original velocity, and the temperature is measured at the position of minimum velocity. The gas escapes through small holes drilled into the wall downstream from the thermocouple. The recovery factor of this instrument was found by Franz to be equal to 1 up to 650 ft/sec velocity. A similar diffuser type temperature probe, designed by Eckert [*7*], gives a constant recovery factor of 0.99 up to 980 ft/sec.

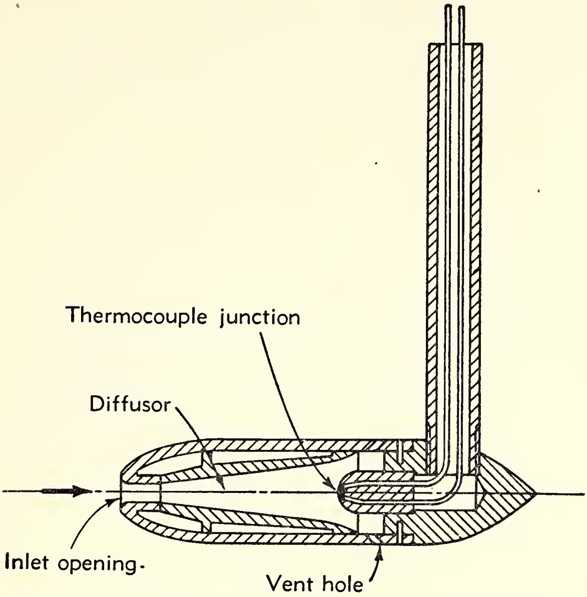

Fig. D,2.4b. Diffuser type total temperature probe of A. Franz.

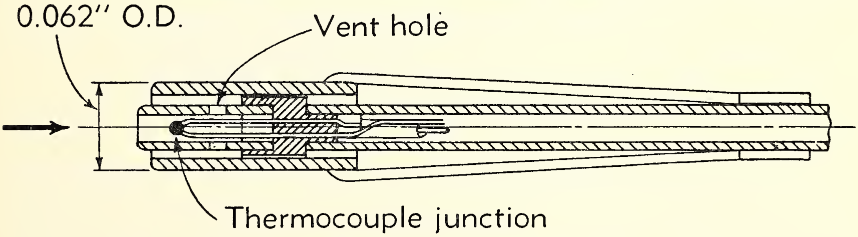

Fig. D,2.4c. MIT total temperature probe of H. C. Hottel and A. Kalitinski. (From [*8*].)

Numerous small total temperature probes were investigated by Hottel and Kalitinski [*8*]. As a result of the investigation, a temperature probe called MIT probe (Fig. D,2.4c) was developed which was found to be satisfactory with regard to temperature recovery as well as scattering of the calibration data. It is insensitive to angles of yaw up to ±12°. Further development at Pratt and Whitney revealed that a much simpler probe giving almost identical results could be constructed. It is easy to manufacture and rugged enough to withstand the severe vibration encountered in supercharger testing. This probe, its recovery factor, and orientation sensitivity are shown in Fig. D,2.4d. Special probes for the measurement of total temperatures in the flow through turbo-compressors and gas turbines were designed at the NACA Lewis Laboratory [*9*]. One of the configurations, a diffuser type probe with two stagnation chambers, is shown together with its calibration in Fig. D,2.4e. The chamber walls of the probe are made of metal tubing and both chambers have bleed holes. To reduce heat conduction an adapter of laminated silicone plastic is inserted between the shields and the supporting rod. The probe may be used up to temperatures of 500°F. Calibration of the probe with air

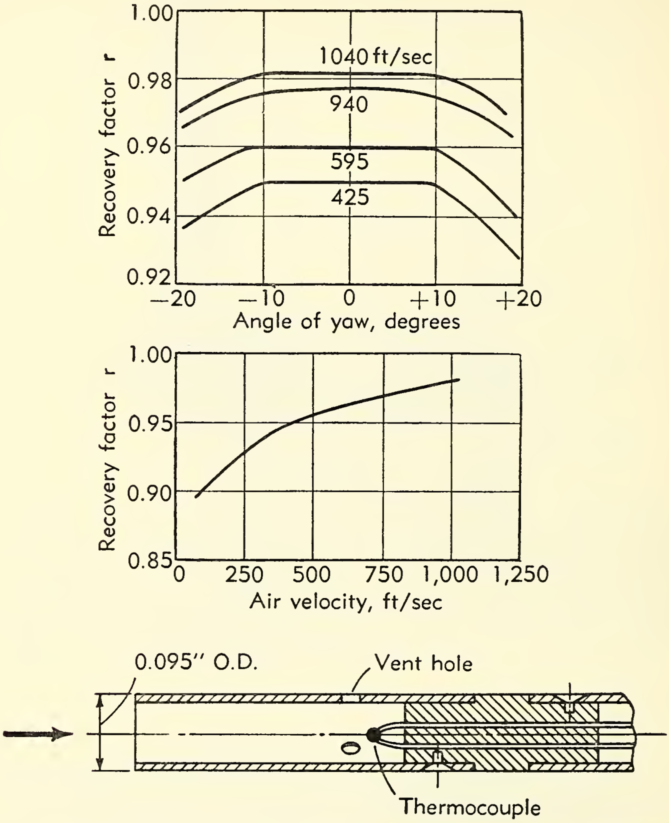

Fig. D,2.4d. Sensitivity and recovery factor of Pratt and Whitney probe. (From [*8*].)

of about 80°F stagnation temperature shows a recovery factor of 0.98 at a Mach number of 0.9, which is somewhat lower than that of similar probes with one stagnation chamber. However, the probe is insensitive to angles of yaw of ±30°.

In exhaust pipes of airplane engines velocities comparable with those in superchargers and temperatures up to 2,000°F are encountered. Here the compressibility effects are small as compared with the radiation losses, and total temperature probes have not been developed to date for this particular purpose. An investigation by King [*10*] leads to the result that a small quadruple-shielded thermocouple will give readings, with an error not in excess of 10°F at 1200°F and 20°F at 1800°F, at air or exhaust gases with velocities of the order of 400 ft/sec in a bare pipe.

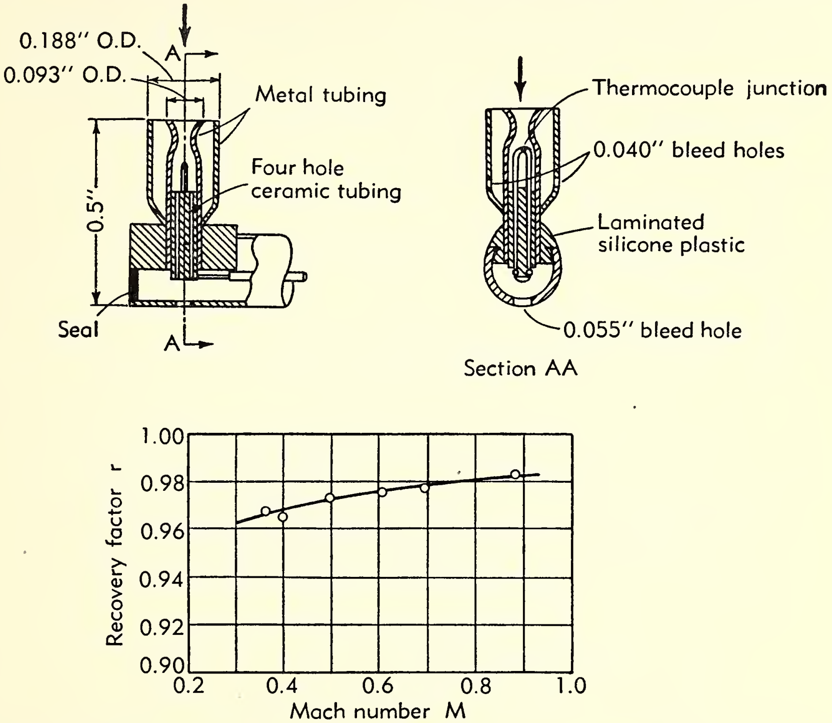

Fig. D,2.4e. NACA high recovery thermocouple probe.

Particular need exists for the determination of total temperatures in the test section of supersonic wind tunnels in order to calibrate the wind tunnel for heat transfer measurements. The total temperature in conventional supersonic wind tunnels is usually below 150°F. Goldstein [*11*] has designed and calibrated a diffuser type probe for this purpose. The probe is made of Lucite and the thermocouple junction is located 0.05

inches ahead of the stagnation point of a hemisphere inside of the stagnation chamber. The probe has a calibration factor of 0.992 ± 0.002 in a Mach number range between 1.3 and 2.0. The ratio of vent area to entrance area was found at an optimum value between 0.50 and 0.63. The probe is insensitive to angles of yaw of ±9°.

In supersonic wind tunnels designed to create Mach numbers above 5, usually designated as hypersonic wind tunnels, the problem of total temperature measurements is more difficult. Due to the liquefaction of the air in these tunnels when air of room temperature is used, the air must be heated. Then the efficiency of the shielding discussed above becomes questionable because of the large temperature difference between the stagnation temperature and the surface temperature of the shielding. A probe designed by Eva Winkler at the Naval Ordnance Laboratory for measurements in hypersonic wind tunnels is shown in Fig. D,2.4f. The design is based on the same assumptions valid for lower Mach numbers. Because of the high temperatures, silica is used as the material for the holder of the temperature sensing element and the shield around the stagnation chamber. Inside and outside surfaces of the stagnation chamber are coated with platinum in order to minimize radiation effects. Calibration data of this probe are as yet available only up to Mach number 3.2, giving a constant recovery factor of 0.995 ± 0.002 in the entire range. For recent results see [*18*].

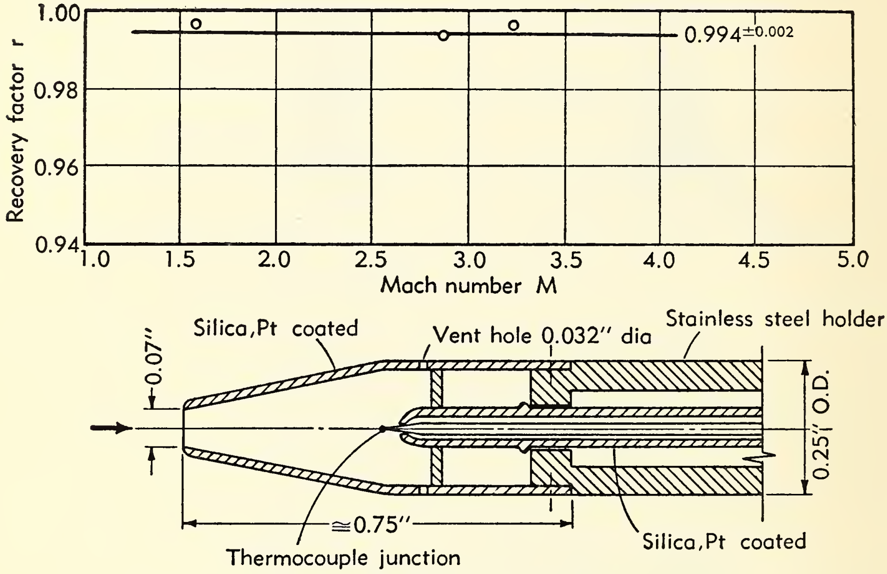

Fig. D,2.4f. NOL total temperature probe of E. Winkler.

In recent years attempts have been made to determine total temperatures in flow boundary layers. Probes of extremely small dimensions have been used in order to keep the distortion of the flow around the probe at a minimum. A useful probe was developed at NAA [12]. Hypodermic needle tubing with 0.032″ O.D. was used with vent holes of 0.010″ diameter drilled into the tubing. A very low lag of the thermocouple was achieved by using 0.005″ Cu-const. wire for the junction and a heat insulating material to reduce heat conduction between the temperature sensing element and the holder. The recovery factor of this probe was determined in the isentropic flow along the axis of the wind tunnel nozzle and found to be 0.948 and constant within ±1 per cent between Mach numbers 1.2 and 2.8, as shown together with the probe in Fig. D,2.4g.

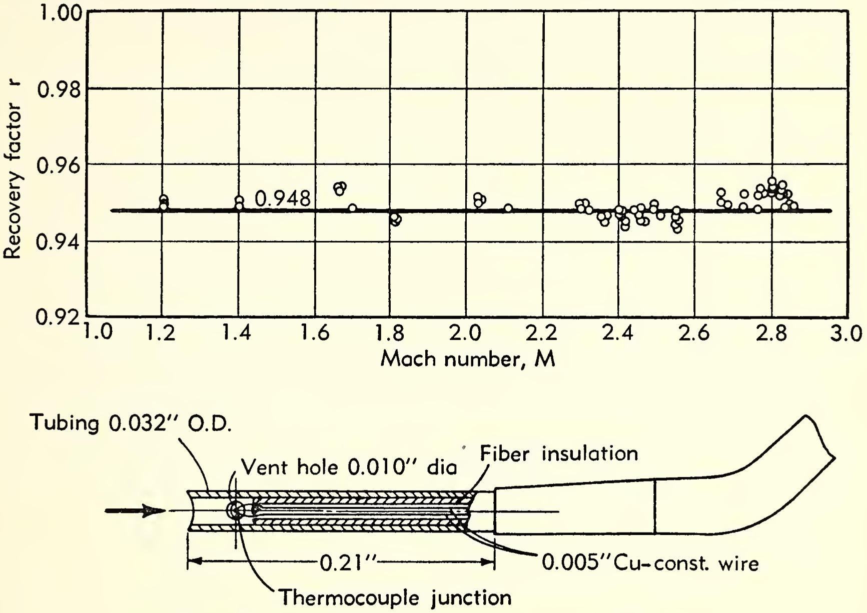

Fig. D,2.4g. NAA total temperature probe for boundary layer work by H. M. Spivack.

D,2.5. Miscellaneous Temperature Measuring Devices.

Thermocouple Wires in Perpendicular Flow. Butt-welded thermocouples of cylindrical shape have been frequently used for temperature measurements in high speed flow. The temperatures indicated by such thermocouples are insensitive to flow inclinations and well reproducible; however, the recovery factor determined from these measurements is dependent on the Mach number in a nonlinear manner and apparently is influenced by the diameter of the wire as an effect of the Reynolds number. Furthermore, the application is limited to low temperatures because radiation losses cannot be eliminated with this type of probe.

VORTEX THERMOMETER. Based on the discovery of Ranque [*13*] that a temperature decrease occurs in the center of a vortex, Vonnegut [*14*] developed a temperature measuring device by mounting a thermometer in the center of an air vortex created by a simple housing. The temperature decrease in the vortex balances out the aerodynamic heating effect. The high speed of rotation creates a pressure difference between the outside and the center of the air revolving in the housing. The temperature drop in the center is produced by expansion of the air on the way from the periphery to the center. The process taking place in a vortex tube is discussed in detail in the literature [*15,16*].

HOT WIRE RESISTANCE THERMOMETER. Hot wire instrumentation and technique is discussed in F,2. However, it might be mentioned here that the fine wire of a hot wire instrument can be conveniently used for the determination of temperatures at transonic and supersonic velocities where small dimensions and low response time are essential as, for example, in boundary layer work. A useful device of this type, developed by Lowell [*17*], can be used at total temperatures up to 525°F, Mach numbers up to 2.4, and twice the total atmospheric density. The recovery factor of such a fine wire is principally a function of the Mach number, the Reynolds number being of almost negligible effect. Therefore if the Mach number is known and the recovery factor experimentally determined, the total (or static) temperature may be obtained by using the wire as a resistance thermometer.

By use of the simple relation

$$T = \frac{R - R_0}{\alpha R_0} \tag{2.5-1}$$

where T is the temperature of the wire, R and R_0 are the wire resistance at the temperature T and at the ice point respectively, and α is the temperature coefficient of the wire, a sufficiently accurate temperature determination can be obtained. However, errors introduced by radiation, strain gauge effects, and conduction of heat to or from supports must be considered in each case.

D,2.6. Cited References.

1. Handbook of supersonic aerodynamics. Formulae for isentropic channel flow. *Nav. Ord. Rept. 1488(1)*, 1950.
2. Jakob, M., and Hawkins, G. D. *Heat Transfer and Insulation.* Wiley, 1947.
3. Knoblauch, O., and Hencky, K. *Anleitung zu genauen technischen Temperaturmessungen.* R. Oldenburg, München, 1926.
4. Mullikin, H. F. In *Temperature, Its Measurement and Control in Science and Industry*, p. 775. Reinhold, 1941.
5. Dahl, A., and Fiock, E. F. Shielded thermocouples for gas turbines. *Trans. ASME 71*, 153 (1949).

6. Franz, A. Pressure and temperature measurement in supercharger investigations. *NACA Tech. Mem. 953,* 1940.
7. Eckert, E. Temperature recording in high speed gases. *NACA Tech. Mem. 983,* 1941.
8. Hottel, H. C., and Kalitinski, A. Temperature measurements in high velocity air streams. *J. Appl. Mech. 12,* A-25 (1945).
9. Scadron, M. D., Gettleman, C. C., and Pack, G. J. Performance of three high-recovery-factor thermocouple probes for room-temperature operation. *NACA Research Mem. E50I29,* 1950.
10. King, W. J. Measurement of high temperatures in high velocity gas streams. *Trans. Am. Soc. Mech. Engrs. 65,* 421 (1943).
11. Goldstein, D. L., and Scherrer, R. Design and calibration of a total-temperature probe for use at supersonic speeds. *NACA Tech. Note 1885,* 1949.
12. Spivack, H. M. Experiments in the turbulent boundary layer of a supersonic flow. *North Amer. Aviation Rept. CM-615,* 1950.
13. Ranque, G. J. Expérience sur la détente giratoire avec productions simultanées d'un échappement d'air chaud et d'un échappement d'air froid. *J. phys. radium 7, 4,* 112-S (1933).
14. Vonnegut, B. Vortex thermometer for measuring true air temperatures and true air speeds in flight. *Rev. Sci. Instr. 21,* 136 (1950).
15. Fulton, C. D. Ranque's tube. *J. Am. Soc. Refrig. Engrs. 58,* 473–479 (1950).
16. Kassner, R., and Knoernschield, E. Friction law and energy transfer in circular flow. *Air Force Tech. Rept. F-TR-2198ND,* 1948.
17. Lowell, H. H. Design and applications of hot-wire anemometers for steady-state measurements at transonic and supersonic airspeeds. *NACA Tech. Note 2117,* 1950.
18. Winkler, E. Design and calibration of total-temperature probes for use at high supersonic speeds and elevated temperatures. *Phys. Rev. 91,* 469 (1953).

ARTICLE D,3

TEMPERATURE MEASUREMENT BY SOUND VELOCITY METHODS

WILLOUGHBY M. CADY

D,3.1. In still air the velocity of sound in a gas of molecular weight $\mathfrak{M}$ is given by the approximate relation

$$a = \sqrt{\frac{\gamma RT}{\mathfrak{M}}} \tag{3.1-1}$$

The same formula describes also the propagation velocity of a vanishingly-weak shock front. Hence the absolute temperature T of the air may be expressed as

$$T = \frac{\mathfrak{M}a^2}{\gamma R} \tag{3.1-2}$$

in terms of known or measurable quantities. The thermometric method implied in Eq. 3.1-2 affords a value of the temperature averaged over the distance and time required for the measurement of a. Since for moving air Eq. 3.1-1 gives the velocity of sound in relation to the air stream, the measurement of a by a stationary observer must be made in such a way that the air velocity either fails to enter the equation used in reducing the data or else is known and allowed for. The data gathered for thermometry by acoustic methods usually allow a calculation of air speed as well as temperature. Some of the pertinent apparatus has, therefore, been described in C,4; in the present article only its thermometric use is discussed.

D,3.2. The techniques of Eisenstein, Clark, and Carlson [*1*], although reported by them in connection with a study of an acoustic air-speed indicator, are capable of yielding temperature values. The apparatus is mentioned in C,4. The portion of the expanding spherical wave front which is parallel to the floor of the flow channel is propagated with a velocity component a away from the floor. This speed can be computed as $a = l/\tau$ where l is the distance from that part of the wave to the floor at the time τ when the wave was photographed. Eq. 3.1-2 then gives the temperature. The method is invalid for thermometry of the free stream if there is a boundary layer at a temperature different from that of the free stream. Nevertheless, a valid value of the temperature can be obtained from photographs made at two times τ_1 and τ_2, at which the wave front has reached distances from the wall l_1 and l_2 well beyond the boundary layer. In this case we have $a = (l_2 - l_1)/(\tau_2 - \tau_1)$ whence T is found by Eq. 3.1-2.

D,3.3. The apparatus of Marlow, Nisewanger, and Cady [*2*], described in C,4 and Fig. C,4.3a as an anemometer, is also a thermometer. In this role it permits the measurement of the wavelength of the sound in a high frequency beam by noting the shadows of the sound waves as formed in the light of a brief spark. The known frequency f and measured wavelength λ of the waves then provide the speed of sound as $a = f\lambda$, from which T is known.

The measurement of temperature by this method can be made with fair precision and reproducibility. It has been performed in a shock tube where, in the immediate wake of a shock front traveling into still air, the temperature was reliably known from the measured shock velocity and shock wave theory. In a typical experiment, before the shock passed the wavelength was $\lambda_1 = 1.00$ mm; in the wake it was $\lambda_2 = 1.18$ mm. The temperature ratio deduced was $T_2/T_1 = (\lambda_2/\lambda_1)^2 = 1.39$, whereas the measured shock velocity led to the prediction $T_2/T_1 = 1.44$. It is not known where the cause of the discrepancy lies.

The wavelength can be measured as the spacing of the waves along a common normal. If the flow is rapid, however, it would be preferable to measure the spacing of the waves along any line of known inclination which is chosen to cross all the observable wave fronts. Following the obvious trigonometric correction the wavelength is thus given with optimum certainty.

Methods closely similar to those just described have been discussed by H. Ramm as having been tried in Germany at Kochel during the war. This discussion, reported by Goll [*3*], presents qualitatively several schemes, some of which appear to have succeeded. These include the generation of sound waves at high frequency above the Laval nozzle of the tunnel in the hope of observing them in the supersonic stream below. This promising suggestion failed to lead to useful results because of the low intensity of the sound transmitted through the nozzle and presumably because of the noise. A Hartmann whistle produced sound waves which made possible the study of subsonic flow to Mach 1 with schlieren optics.

D,3.4. A method has been studied by J. V. Fay [*4*] of Cook Research Laboratories in which the air temperature is determined by simultaneous acoustic and ionic measurements. The latter have been mentioned in

C,1. The sound produced by an electric spark is detected after a transit time τ_a by a microphone a distance l_a below the spark. Meanwhile, the ions produced by the spark are moving toward an ion detector situated at a distance l_i below the spark and which is reached by the ions at time τ_i. Since $\tau_a = l_a/(a + u)$ and $\tau_i = l_i/u$, we find

$$a = \frac{l_a}{\tau_a} - \frac{l_i}{\tau_i} \tag{3.4-1}$$

whence T may be found.

It is clear that this method gives u as well as T.

D,3.5. Last among the acoustic thermometers we mention the Sonic True Air-Speed and Mach Number Indicator described by Corey [*5*] and discussed in C,4. Basically this instrument is a Mach meter. If, however, the acoustic signals are pulsed instead of being continuous, the transit time for a pulse becomes measurable. With continuous, i.e. not pulsed, sound waves, a somewhat involved procedure can be used whereby the wavelength can be roughly measured by noting the phase changes accompanying known variations in the transmission path, deducing therefrom the number of waves in the transmission path within an accuracy of a minor fraction of a wave, and refining this number by noting again the phase of the arriving waves to obtain the final value of the transit time and thence a and T.

D,3.6. Cited References.

1. Eisenstein, J., Clark, K. C., and Carlson, F. D. Sonic true airspeed indicator. Vol. I. *OSRD* (*Div. 17*) *Rept. 5369*, 1945.
2. Marlow, D. G., Nisewanger, C. R., and Cady, W. M. A method for the instantaneous measurement of velocity and temperature in high speed air flow. *J. Appl. Phys. 20*, 771–776 (1949).
3. Goll, M. E. Measurement of temperature of airflow with sonic waves. *Air Force Rept. RP-IRE-61*, 1946.
4. Fay, J. V. Private communication from Cook Research Laboratories.
5. Corey, V. B. Acoustic measurement of airstream parameter. *Inst. Aeronaut. Sci. Preprint 267*, 1950.

SECTION E

SHOCK FRONT MEASUREMENTS BY LIGHT REFLECTIVITY

DONALD F. HORNIG

SECTION E

SHOCK FRONT MEASUREMENTS BY LIGHT REFLECTIVITY

DONALD F. HORNIG

E,1. Introduction. At the head of an advancing shock wave is a region, the shock front, in which the density, pressure, temperature, and flow velocity change almost discontinuously. At the present time no adequate theoretical description of the shock front is available (III,E,1) but according to Thomas [*1*] the entire transition takes place in a few mean free paths for all but very weak shock waves, e.g. for a shock of Mach number 2 the compression takes place in about 2 mean free paths, equivalent to 1×10^{-5} cm or 2×10^{-10} sec for a shock moving in stationary air at NTP.

The only experimental method which has yielded any quantitative data regarding the details of the front is the measurement of its optical reflectivity as a function of the wavelength of the light and the angle of incidence [*2*]. If the shock front were a discontinuity, the change in density $\Delta\rho$ across the front would give rise to a corresponding discontinuous change Δn in the index of refraction. The two quantities are related by the expression

$$\frac{\Delta\rho}{\rho_1} = \frac{\Delta n}{n_1 - 1} = \frac{\Delta n}{n_0 - 1} \cdot \frac{\rho_0}{\rho_1} \tag{1-1}$$

where ρ_1 and n_1 are the density and index of refraction, respectively, of the medium ahead of the shock, and ρ_0 and n_0 are the same quantities in a standard state, e.g. at NTP. In this case light can be reflected from the interface, and the reflectivity R is given by the expression

$$R = \frac{1 + \tan^4\theta}{4} (\Delta n)^2 = \frac{(1 + \tan^4\theta)(n_0 - 1)^2}{4\rho_0^2} (\Delta\rho)^2 \tag{1-2}$$

where θ is the angle of incidence. This expression is obtained from the usual laws of reflection if $R \ll 1$ [*2*] and the condition is fulfilled even in the strongest shocks, except at very nearly grazing incidence.

The reflectivity thus gives a method of measuring the density change across a shock front. Since the density change in question is that immediately across the front, it may be used to detect delays in energy equipartition in the gas, e.g. if the rotational and vibrational temperatures do not change in crossing the front, the density change found will always be that of a monatomic gas. This type of measurement has been carried out in nitrogen and is described in Art. 4.

If the shock front is not a discontinuity, the parts of the incident ray reflected from various depths of the front differ in phase and the resulting reflected intensity is diminished. It is this fact which forms the basis for the measurement of the shock front profile. This effect is important whenever the transition region has a thickness of the order of the wavelength λ of the light used and, since this is indeed the case for shocks in gases at NTP, such measurements have been successful.

E,2. Theory of the Method. The theory of the effect on reflected intensity when there is a continuous change in the index of refraction is simple [*2*]. If $R \ll 1$ (and this condition is satisfied only too well), the amplitude of the waves reflected from successive infinitesimal interfaces, across which $dn = (dn/dx)dx$, need only be added with suitable phase differences, yielding the equation

$$R = \frac{1 + \tan^4 \theta}{4} |F(y)|^2 \tag{2-1}$$

where

$$F(y) = \int_{-\infty}^{\infty} \frac{dn}{dx} e^{-2\pi i y x} \, dx \tag{2-2}$$

and

$$y = \frac{2 \cos \theta}{\lambda} \tag{2-3}$$

In order to use this equation it is necessary to assume some functional form for the index of refraction and then to adjust parameters to fit the measured data. The function

$$n(x) = n_1 + \frac{\Delta n}{1 + e^{-\frac{4x}{L}}} \tag{2-4}$$

is very close to the shape predicted theoretically [*1,2*]. In this function the parameter L is the thickness of the shock front, defined as

$$L = \frac{\Delta \rho}{(d\rho/dx)_{\max}} = \frac{\Delta n}{(dn/dx)_{\max}} \tag{2-5}$$

For the index of refraction defined by Eq. 2-4, the reflectivity is given by the expression

$$R = \frac{1 + \tan^4 \theta}{4} (\Delta n)^2 \left[\frac{\pi^2 L \cos \theta/\lambda}{\sinh (\pi^2 L \cos \theta/\lambda)} \right]^2 \tag{2-6}$$

Eq. 2-2 is that for a Fourier transform, so that if any other functional form for $n(x)$ is explored, the corresponding $F(y)$ can be conveniently obtained from standard tables of Fourier transforms [*3*].]

E,3. Experimental Technique. The requirements for the successful measurement of shock front reflectivities are an intense collimated beam of nearly monochromatic light and a method for detecting the weak reflected beam against a background of scattered light [*2*]. The magnitude of the reflectivity in a typical case, reflection at an angle of 75° from a shock of Mach number 1.3 in nitrogen at 2.5 atmospheres, is approximately 4×10^{-6}. A schematic drawing of an optical system which has been used successfully in measuring shock reflectivities is shown in Fig. E,3 [*4*]. In this apparatus a carbon arc, run just below the hissing stage, is used as a light source; monochromatization of the light is obtained with interference filters; and the remainder of the optical system is designed to produce a 1-degree divergence of the beam in the plane of the drawing and a 3-degree divergence perpendicular to this plane. The divergences are determined by the dimensions of the effective source. The purpose of the mask is to restrict the dimensions of the parallel beam

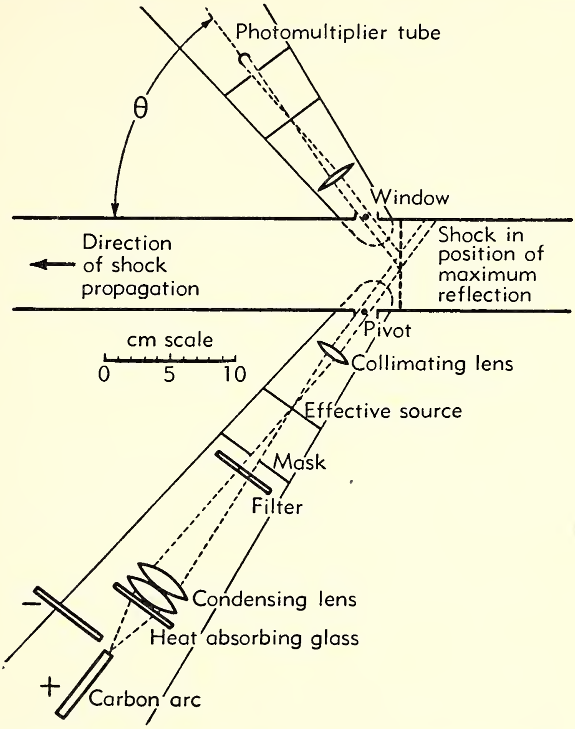

Fig. E,3. Optical system for the measurement of shock front reflectivity. (From [*4*].)

to those of the area of shock which is being measured, in this case about 1 cm × 1 cm. The reflected light is received on a photomultiplier tube.

Up to now reflectivity measurements have been carried out on a moving shock in a shock tube (VIII,E,6), although they might also be carried out on a quasi-stationary shock in a wind tunnel. The moving shock method has two practical advantages because of the low intensity of the reflected light: (1) the measurement of the pulse height obtained when the moving shock intersects the incident light beam discriminates between the reflected light and stray light due to scattering from dust, optical elements, etc; (2) it is possible to keep the background scattering at a lower level in a shock tube (static conditions) than in a flowing system. The moving shock method has the disadvantage that the measurement must be carried out during the time the shock intersects the incident beam at an appropriate point, approximately 20 microseconds.

A conventional recording system can be used for these measurements, using only the amplifier contained in a Du Mont Type 304-H oscilloscope or its equivalent. In one form of the apparatus [*4*] the fluctuations in source intensity are eliminated by passing a comparison beam around the shock tube and comparing the reflected pulse with the standard signal.

Other high intensity sources (A,2.5) may also be used, and E. F. Greene of Brown University has recently found that a 1,000-watt projection lamp yields as high an intensity for this purpose as the carbon arc since the heat filter may be eliminated. However, it is much more sensitive to vibration. At present, reflectivity measurements can only be reproduced with an average deviation of ±10 per cent; it is not certain whether this is due to instrumental factors such as short term fluctuations in the source intensity or to instability in the shock wave itself.

The conditions under which reflectivity measurements can be made are severely limited due to two factors: (1) reflectivities lower than 10^{-7} cannot be measured at the present time so that the initial pressure p_1 and the Mach number of the shock must be high enough to obtain adequate reflectivity, and (2) the thickness of the shock must be of the order of 1 to 3×10^{-5} cm if a significant variation of reflectivity with $\lambda/\cos\theta$ is to be obtained. It is always possible, in principle, to meet both requirements if either p_1 or M is defined, but in general it is not possible to fix both arbitrarily. As an example, the thickness of shocks with $M = 1.11$ were measured in the range $p_1 = 7$ to 11 atmospheres while shocks with $M = 1.38$ were studied in the range $p_1 = 3.5$ to 6 atmospheres.

Fortunately, because of the scaling law, $Lp_1 =$ constant for shocks of given M (see Art. 4), results can always be scaled to an arbitrary p_1. This same scaling law also makes it possible to extend effectively the range of $\lambda/\cos\theta$ by varying p_1 since the reflectivity curve, Eq. 2-6, depends on $\lambda/L\cos\theta$. That is, the reflectivity spectrum, R_a for $p_1 = p_a$, is determined from the spectrum R_b for $p_1 = p_b$ by the equation

$$R_a\left(\frac{\lambda}{\cos\theta}\right) = \frac{p_a^2}{p_b^2} R_b\left(\frac{p_b\lambda}{p_a \cos\theta}\right) \tag{3-1}$$

The usual process of making measurements therefore consists in measuring the reflectivity of shocks of fixed M at 2 to 3 wavelengths in the visible region of the spectrum, at several angles of incidence between 60° and 80°, and at several initial pressures. Using Eq. 3-1 the results can all be plotted on a single curve as a function of $\lambda/\cos\theta$ and the theoretical curve, e.g. Eq. 2-4, fitted to it to yield a value of the thickness.

E,4. Results. The Thickness of Shock Fronts and Rotational Equilibrium. Despite the lack of precision in the measurements which have been made so far, significant experimental results have been obtained. In the first place, the Boltzmann equation yields the fundamental scaling law that at a given temperature the thickness of a shock front, measured in mean free paths, depends only on the pressure ratio across the front, $S = p_2/p_1$. In experimental terms, the thickness is inversely proportional to the initial pressure p_1 at constant S. That is

$$Lp_1 \sim \frac{L}{l} = f(S)$$

The thickness L has been measured by fitting the experimental curves for reflectivity as a function of $\lambda/\cos\theta$ to Eq. 2-4 and some typical results [*4*] are given in Table E,4a. Within the accuracy of these experi-

Table E,4a. Thickness of shock fronts in argon and nitrogen. (From [*4*].)

Gas	p_1 (atm)	Velocity (km/sec)	Mach no.	p_2/p_1	ρ_2/ρ_1	Thickness (10^{-5} cm)	Thickness scaled to $p_1 = 1$ atm (10^{-5} cm)	Thickness (mean free paths ahead of shock)
A	7.27	0.3574	1.113	1.299	1.169	2.15	15.6	23
	10.73	0.3582	1.115	1.304	1.172	1.43	15.3	22
	6.66	0.4046	1.259	1.734	1.384	1.24	8.2	12
	3.20	0.4104	1.275	1.782	1.405	2.50	8.0	12
	6.11	0.4424	1.377	2.120	1.548	1.12	6.8	10
	3.48	0.4476	1.393	2.176	1.570	1.80	6.3	9
N_2	11.00	0.3971	1.128	1.318	1.217	1.86	20.5	32
	6.73	0.4011	1.139	1.347	1.235	2.48	16.7	26
	2.62	0.4523	1.285	1.760	1.488	2.59	6.8	10
	5.19	0.4530	1.286	1.767	1.491	1.63	8.5	13
	2.62	0.4978	1.414	2.167	1.712	2.20	5.7	9
	4.63	0.4993	1.418	2.181	1.720	1.38	6.4	10

ments, about 15 per cent, the scaling law has been verified in argon and nitrogen for a range of p_1 from 2.5 to 11 atmospheres. It may be expected to hold with even greater validity in the lower pressure region since for purely binary collisions the Boltzmann equation is exact. The thickness of the shock fronts was found to be significantly greater than predicted by Thomas [*1*], using the best theory that can be based on the Navier-Stokes equations.

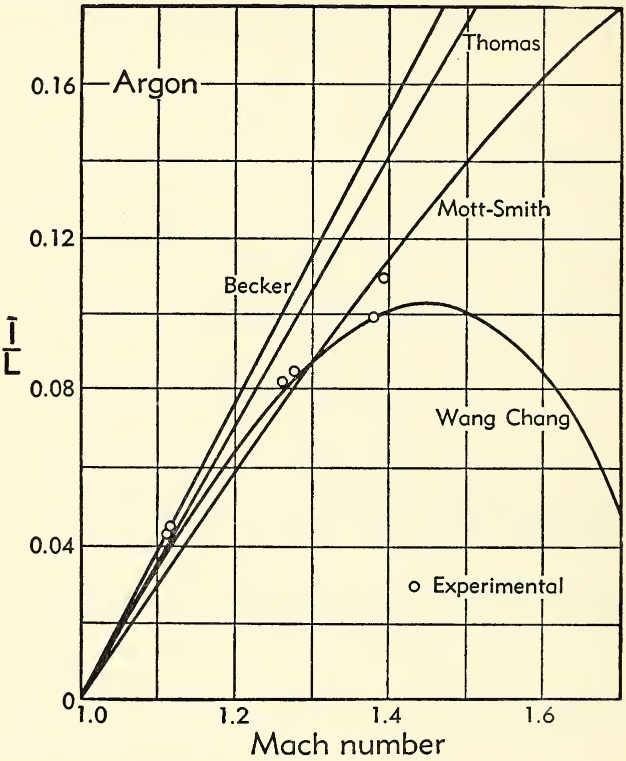

Fig. E,4. Comparison of experimental and theoretical thickness of shock fronts. $\bar{l}$ is the mean free path. (From [*4*].)

The function $f(S)$ has been obtained, in various degrees of approximation, by Becker [*5*], Thomas [*1*], Wang Chang [*6*], and Mott-Smith [*7*]. In Fig. E,4 the thickness derived from the most recent experimental curves on argon is compared with the various theories. For convenience the variable $\bar{l}/L$ is plotted vs. the Mach number rather than S. It appears that a curve which coincides with that of Wang Chang at small and of Mott-Smith at large Mach numbers will agree reasonably well with experiment.

It has also been demonstrated from reflectivity measurements that the rotational temperature of nitrogen does not come to equilibrium with the translational temperature immediately as the gas is heated in the front. If there is a large delay in equilibrating the rotation, the gas will have the thermodynamic properties of a monatomic gas in the front but gradually will relax to its final values. If the final density ρ_F is known (e.g. from the velocity of the shock (VIII,E,6) which depends only on initial and final conditions [*8*]) it is possible to find the density change across the front if the process is stationary.

To do so we need note that, if all gradients are negligible behind the front (i.e. if the relaxation takes place through a region great compared to the shock front thickness), we may write the equations of conservation of mass, momentum, and energy separately for the initial, intermediate, and final states. These are

$$\rho_1 u_1 = \rho_2 u_2 = \rho_F u_F \tag{4-1}$$

$$p_1 + \rho_1 u_1^2 = p_2 + \rho_2 u_2^2 = p_F + \rho_F u_F^2 \tag{4-2}$$

$$u_1^2 + \frac{2\gamma_2}{\gamma_2 - 1}\frac{p_1}{\rho_1} = u_2^2 + \frac{2\gamma_2}{\gamma_2 - 1}\frac{p_2}{\rho_2} \tag{4-3}$$

$$u_1^2 + \frac{2\gamma_F}{\gamma_F - 1}\frac{p_1}{\rho_1} = u_F^2 + \frac{2\gamma_F}{\gamma_F - 1}\frac{p_F}{\rho_F} \tag{4-4}$$

where u = flow velocity, ρ = density, p = pressure, and γ = specific heat ratio, all in a coordinate system in which the shock front is at rest. Noting that u_1 is the propagation velocity of the shock wave, it can be obtained explicitly in terms of the final conditions by combining Eq. 4-1, 4-2, and 4-4, and in terms of the conditions immediately behind the front by combining Eq. 4-1, 4-2, and 4-3. If the process is a stationary one, these velocities must be equal so that

$$u_1^2 = \frac{2\gamma_F \rho_F p_1}{\rho_1[(\gamma_F + 1)\rho_1 - (\gamma_F - 1)\rho_F]} = \frac{2\gamma_2 \rho_2 p_1}{\rho_1[(\gamma_2 + 1)\rho_1 - (\gamma_2 - 1)\rho_2]} \tag{4-5}$$

Consequently,

$$\frac{\rho_2}{\rho_1} = \frac{\dfrac{1 + \gamma_2}{\gamma_2}}{\left[\dfrac{\rho_1}{\rho_F}\left(\dfrac{1 + \gamma_F}{\gamma_F}\right) + \dfrac{\gamma_2 - \gamma_F}{\gamma_2 \gamma_F}\right]} \tag{4-6}$$

This argument is equivalent to that used by Stepanov [*9*]. In the case in which only translational degrees of freedom are affected in the shock front, γ_2 is characteristic of a monatomic gas. When the reflectivity of such a front is measured, one expects to find a curve characteristic of a monatomic gas which reaches a limiting value, given by Eq. 1-2 with $\Delta\rho$ taken from Eq. 4-6, and then rises slowly to the limit for the final conditions. These limiting measurements can be made with considerable precision. The results of a series of runs on nitrogen are summarized in Table E,4b [4]. It is seen that, in a front during which a nitrogen molecule undergoes 50 collisions, the density change is exactly that expected for complete equilibration but that, in a front in which a molecule undergoes only 20 collisions, the equilibration is about 85 per cent complete. It seems likely that collisional processes in gases can be investigated in this fashion for any process which occurs in the range 10–200 collisions.

Table E,4b. Evidence for rotational heat capacity lag in nitrogen. (From [4].)

p_1 (atm)	Mach no.	Calculated $\frac{\Delta\rho}{\rho_1}$		Experimental $\frac{\Delta\rho}{\rho_1}$	Number of collisions in shock front
		$\gamma_2 = 1.667$	$\gamma_2 = 1.4$		
11.00	1.128	0.053	0.217	0.225 ± .006	48
11.01	1.131	0.057	0.222	0.224 ± .004	48
5.19	1.286	0.268	0.491	0.446 ± .011	22
4.63	1.418	0.443	0.720	0.675 ± .012	19

E,5. Cited References.

1. Thomas, L. H. Note on Becker's theory of the shock front. *J. Chem. Phys. 12,* 449–457 (1944).
2. Cowan, G. R., and Hornig, D. F. The experimental determination of the thickness of a shock front in a gas. *J. Chem. Phys. 18,* 1008–1017 (1950).
3. Campbell, G. A., and Foster, R. M. Fourier integrals for practical applications. *Mathematical Physics Monograph B-584. Bell Telephone System Tech. Publ.,* 1942.
4. Greene, E. F., Cowan, G. R., and Hornig, D. F. The thickness of shock fronts in argon and nitrogen and rotational heat capacity lags. *J. Chem. Phys. 19,* 427–434 (1951).
5. Becker, R. Stosswelle und Detonation. *Z. Physik 8,* 321–362 (1922).
6. Wang Chang, C. S. *Rept. UMH-3-F, Univ. Michigan, Dept. Eng. Research,* 1948.
7. Mott-Smith, H. M. The solution of the Boltzmann equation for a shock wave. *Phys. Rev. (2) 82,* 885–892 (1951).
8. Rayleigh, Lord. *Proc. Roy. Soc. London A84,* 268 (1911).
9. Stepanov, P. E. *J. Exptl. Theoret. Phys. U.S.S.R. 17,* 377 (1947).
10. Bethe, H. A., and Teller, E. Deviation from thermal equilibrium in shock waves. *Ballist. Research Lab. Rept. X-117,* 1940.

SECTION F

TURBULENCE MEASUREMENTS

LESLIE S. G. KOVÁSZNAY

ARTICLE F,1

METHODS TO DISTINGUISH BETWEEN LAMINAR AND TURBULENT FLOW

LESLIE S. G. KOVÁSZNAY

The main characteristic of turbulent phenomena is their irregular random nature. Although turbulence exhibits disorder, in most cases of interest it has certain statistical properties that are reproducible in experiments.

When devising techniques for measuring turbulent flows there are fundamentally two types of approach: (1) to take into account the statistical nature of turbulence and measure directly the effects that are the result of some average behavior; (2) to attempt the measurement of point by point values in three-dimensional space and in time, omitting statistics completely in this phase but later applying statistical averaging processes to the data collected from these point by point field measurements. The first method is more straightforward and the results are easier to visualize since some over-all statistical property of the turbulent motion is described. On the other hand, the large amount of information obtained from a point by point record may obscure the statistical concepts that are desired. Therefore, some statistical processing is required (determination of correlation or spectra) before the results of the measurements can be assessed.

In most treatments the turbulent flow field is decomposed into a mean value and a turbulent fluctuation. Decomposition is defined in such a way that the mean value of the fluctuation field is zero. (Appropriate mean value, whether it is time, space, or ensemble average, is selected.)

The simplest form of information about a turbulent flow region is a "yes" or "no" type of information. Some measurements indicate that, if both turbulent and nonturbulent regions exist in a flow, the line of demarcation is rather well defined (at least instantaneously) between the nonturbulent and turbulent domains.

Logically the next more complicated situation would be to measure some "level of activity" in the turbulent region, namely, to associate some quantity with the degree of turbulent activity. This leads to attempts to measure the intensity of turbulent fluctuations by the hot wire or by other point value methods. However, point value methods give more information than just the intensity level.

The inherent averaging properties of some techniques, especially those of the optical techniques, permit the obtaining of a statistical type of information directly without the point by point method. However, the optical methods have the great disadvantage that the type of statistical average thus obtained is fixed by the method used and it is beyond the control of the experimenter.

In accordance with the previous reasoning, turbulence measurements can be classified into three basic types:

1. Methods to distinguish between laminar and turbulent flow.
2. Measurements of point values by a probe. The most important is the hot wire method, but other types, e.g. ionization, dark current probes, or glow discharge, would fall into this group. The technique consists of electronic amplification and appropriate electronic circuits to perform the statistical operations.
3. Optical methods. The fact that the light rays passing through a turbulent region with density fluctuations present are affected throughout the depth of the turbulent region produces a particular statistical averaging effect in depth. On the other hand, this cannot be changed as long as the same optical technique is used.

The simplest type of information about a flow field that may or may not be turbulent is the detection of the presence of turbulence. Since this is a discrete two-state ("yes" or "no") proposition, it depends on a clear-cut criterion to determine when turbulence is considered to occur. There must be some threshold above which the flow is considered turbulent. One fortunate circumstance is that instantaneous flow pictures by the shadow method in compressible flows (Plate F,1.3) and also hot wire records in the transition region of boundary layers clearly indicate that the change from a nonturbulent (laminar) flow state to a turbulent flow state is not gradual but abrupt and therefore very distinct. One reason that transition regions have appeared to be gradual and smooth is due to the fact that the turbulent and laminar regions appear intermittently in time and their relative occurrence gives a smooth curve. Another reason is the so-called transverse contamination in two-dimensional flow [*46,47*]. This effect may produce an increasing region of turbulent and a decreasing region of laminar flow along the boundary layer of the model so that a shadowgram integrating over the span of the model in a wind tunnel shows a gradual transition [*53*].

In order to distinguish qualitatively between laminar and turbulent flow, the properties that give the greatest "contrast" between the two states must be investigated. Probably the most striking property of turbulence is the great increase of diffusion. This leads to detection methods that involve the diffusion properties. The methods fall into three groups: (1) mean velocity profile measurements in the boundary layer; (2) diffusion methods; (3) optical methods.

F,1.1. Velocity Profile Measurement. The velocity distribution across the boundary layer is even qualitatively different in laminar and turbulent layers. Although the total thickness of the boundary layer rapidly increases at transition, the velocity gradient close to the wall increases with the increased skin friction, so that the local velocity close to the wall increases when turbulence sets in. This fact permits an easy indication of transition without measuring the complete velocity profile, simply by placing a total head tube very close to the wall and measuring the variation of total head along the boundary layer. At transition there is an almost discontinuous rise in the total head values that is easily detectable. Naturally the thickness and the approximate velocity distribution of the laminar and turbulent boundary layers should be estimated so as to make sure that the total head tube is in the part of the boundary layer where this change is prominent. Fig. F,1.1 shows the comparison between the two boundary layer profiles and the type of rise that occurs. One of the difficulties is that the transition point may vary in a wide region by moving back and forth at random, giving a statistical distribution of intermittency of turbulent flow that smooths out the sharp jump.

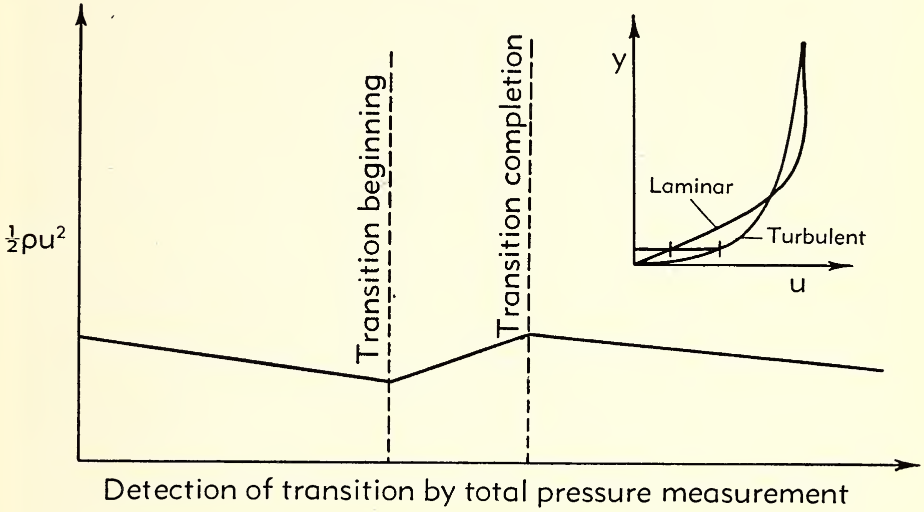

Fig. F,1.1. Detection of transition by total pressure measurement.

F,1.2. Diffusion Methods. Basically the velocity profile measurement is also a diffusion method if the change of boundary layer profile is regarded as the result of the change in the rate of diffusion of momentum. However, the concept of diffusion proper may be restricted to some diffusible scalar property such as heat or some concentration of substance.

The original method for detection of turbulence, used by Osborne Reynolds, consisted of diffusion of a dye in water. The same method is applicable in air by using a thin smoke filament. At the point where turbulence sets in, the smoke or dye is diffused so fast that its concentration suddenly drops to such a low value that it is practically undetectable, and the onset of turbulence is marked by the sudden disappearance of the smoke or dye filament. This method has proved to be very profitable in liquid experiments and also in air as long as the velocities are low. The velocity is limited by the practical fact that smoke in sufficient density cannot be produced so that it would still be detectable when diluted by the action of turbulent diffusion. Wind tunnel experiments indicate that the limit of applicability of the smoke method is approximately 180 miles per hour [*1*]. Additional inconveniences of this method are the elaborate lighting and optical schemes necessary to obtain good photographic records.

There is a great desire to use diffusion techniques in such a manner that they give a more or less permanent record without taking pictures of the flow field. This permits investigation of inaccessible surfaces such as models in windowless wind tunnels or even in free flight. If some chemically active substance is used instead of smoke, there may be sufficient contrast of chemical action on a surface to show the differential rate of diffusion between laminar and turbulent flow in the boundary layer. There is a great variety of substances that can give either positive or negative effects in a turbulent flow. If, for instance, the surface of an airplane wing is treated with white lead paint and the airplane flies through a small cloud of chlorine, the larger diffusive properties of the turbulent boundary layer increase the amount of chlorine brought into action on the surface. A so-called positive effect is obtained, namely, the chemical action is noticeable where the boundary layer was turbulent and unnoticeable in the laminar region. On the other hand, if some chlorine is "oozed" from an orifice ahead of the turbulent region, the filament of chlorine gas holds together in the laminar region and produces a marked streak, but disappears in the turbulent region where the diffusion reduces the concentration to such a low level that it does not make noticeable marks. This is called a negative effect since the method responds to laminar flow and disappears in the turbulent region. Detailed information and formulas are given in [*1*] and [*3*].

Probably the most practical method for wind tunnel work is based on the differential rate of diffusion in the form of the differential rate of evaporation of a liquid from an appropriately treated surface. If the surface is coated with a thin film of liquid, the turbulent region, due to its higher rate of diffusion, causes a higher rate of evaporation. The disappearance of the liquid can be rendered visible by some appropriate artifice. If a substance in powdered form that has a refractive index equal to that of the liquid is chosen, it becomes invisible in the liquid and the original surface determines the reflectivity of that portion of the surface. On the other hand, as soon as the liquid is evaporated the powder substance gives its own reflectivity, that may be appreciably higher. This is the basis of the so-called China clay method developed in Great Britain during the war and used with considerable success in developing the laminar flow airfoil. China clay is a white powder that can be used as a coating with an appropriate binder and can be worked down into an extremely smooth surface still retaining very good (nonspecular) reflectivity. If this China clay surface is sprayed with an appropriate liquid that has the same refractive index as the particles, the surface appears dark when moist and the white surface reappears after evaporation. The method gives very clear indication of the boundary layer transition region, although it gives additional indications of high evaporation rates close to the leading edge where the diffusion rate is high in the laminar region. A typical record is shown in Plate F,1.2, and the whole method is summarized in [*2*].

F,1.3. Optical Methods. In compressible flow, especially in supersonic flow, optical techniques are usually available and they may be adapted to give information about transition points in the boundary layer. The shadow method responds approximately to second derivatives of the density with respect to the coordinate axes perpendicular to the light beam. Since it emphasizes fast variations in the density, this method is the most appropriate to detect turbulence. Its principal disadvantage is that turbulent boundary layers on wind tunnel windows may obscure the whole field. This effect can be minimized if both the light source and the shadow plate are as close to the windows as possible. This improvement, however, is limited to large wind tunnels where there is sufficient length to form a good shadow picture. In small wind tunnels, visible indications of the beginning of the turbulent region in the boundary layer along a model have been obtained by taking shadowgrams near the model in parallel light or by taking schlieren pictures with the knife edge perpendicular to the flow. The interpretation of those pictures is rendered difficult due to transverse contamination since such optical methods integrate over the span of the model. A rather sensitive criterion for distinguishing between the laminar and the turbulent state of the boundary layer is the measurement of the "temperature recovery factor" (see D,1 and IV,D). Since tests in free flight do not require windows, the shadow pictures do not have background disturbance, and a very clear detection between laminar and turbulent flow is possible. Plate F,1.3 shows transition on a shell fired at supersonic velocity.

There is one serious difficulty in the interpretation of the shadow picture with respect to boundary layer transitions. Transition is usually defined on an average basis that implies either a large number of experiments or experiments on the basis of quantities that respond to the average situation. A shadow picture taken at an instant does not permit the averaging except at the prohibitive expense of taking a great number of pictures and statistically averaging the results. This suggests that the shadow technique or any other method based on an instantaneous situation with respect to transition should be interpreted with great care and, if quantitative data is required, a sufficient number of pictures should be taken. Further details of the shadow method for detecting or measuring turbulence are given in Art. 3.

F,1.4. Glow Discharge Anemometer. The thermal lag of the hot wire, which can be overcome only by using cumbersome electronic compensation, always has been the chief obstacle against its wider use. There is a continued interest in finding some new method that will replace hot wires. One of the most significant of the suggested methods is the glow-discharge anemometer.

The discharge current between two electrodes placed in air is a function of the physical properties of the air (density, temperature, pressure, moisture) and also of the air velocity as well as of the voltage imposed. Preliminary experiments were performed both in the dark current region and in the so-called glow discharge region. The general nature of the results is the following: Using dark discharge the current is so small (order of 10^{-9} amp) that the detector requires very large input impedances, where the capacitive lag is comparable to the hot wire's thermal lag. On the other hand, using visible glow discharge, the results are not well reproducible since the electrodes wear out quickly due to sputtering. At the present time the over-all sensitivity, accuracy, and reproducibility of the hot wire method is still superior. For further information see [*51*].

ARTICLE F,2

HOT WIRE METHOD

F,2.1. Introduction. The hot wire method is used for measuring a fluctuation flow field in space and in time with a sufficient resolution to obtain complete records that are unavailable at present by any other method.

The essential principle of the hot wire method is the following: If a small body is placed in a moving medium and heated to a temperature higher than that of the medium, heat exchange occurs between the body and the medium. The rate of heat loss depends on the geometrical and physical properties of the body, the physical characteristics of the medium, and the characteristics of the flow conditions. The instantaneous conditions for equilibrium are modified by a transient response of the whole system both with respect to fluid mechanical and thermal readjustment. The heat input is electrical and is controlled by an electric current.

In the case of a thin wire that is long compared to its diameter, the temperature distribution along the wire length is not uniform and the measured resistance gives an average temperature along its length. There are two typical cases for operation of a wire. In one case, the wire heating current is kept constant, which results in a wire temperature fluctuation according to the cooling effect of the flow. In the other case, the heating current is controlled in such a manner that an appropriate amount of heat is being generated to maintain a constant temperature. In all practical applications the wire is in an in-between state where both its temperature and heating current vary slightly, although it is attempted to keep one of the variations so small that it can be taken into account only as a correction. The response of the wire may be the resistance value itself, the heating current that is required to maintain a constant resistance, or the developed voltage drop across the wire. In the latter case both resistance and heating current may fluctuate.

The use of the hot wire method immediately introduces the problem of statistical averages. The usual situation in a turbulent experiment is that the equipment and the probe are fixed to a frame of reference so that the medium is flowing with an appreciable velocity. Due to decomposition of flow field into a mean and a turbulent flow, the turbulent pattern is swept by at a rate determined by the local mean flow velocity. The real difficulty is caused by the fact that most of the turbulence theories treat the problem from a frame of reference fixed to the moving fluid so that the mean velocities can be discarded. On the other hand, experiments are performed in wind tunnels where the mean velocity is not zero. A useful hypothesis, introduced by G. I. Taylor [*4*], for turbulence of very low intensity assumes that the turbulent pattern is swept along the wind tunnel almost unaltered. In this case, the fluctuations in time, observed in the wind tunnel, are equivalent to a space scanning of the pattern in the x direction. For convenience a turbulent field with no mean velocities can be referred to as "box turbulence" in contrast to the wind tunnel turbulence. This interchange of time and space variables, although an approximation, has proved very useful for assessing the relative merits of time and space resolution, and it is also applied in concrete measurements (e.g. determining the microscale λ by Townsend's method) [*29*].

Several choices are available for taking averages with the hot wire technique. The turbulence theories use time, space, or ensemble averages. The hot wire gives a time record at a point which may or may not be interpreted as a one-dimensional space record of the corresponding "box turbulence" (subject to the validity of Taylor's hypothesis). Complete space averaging would be extremely difficult by the hot wire method. On the other hand, there is a definite possibility of taking the equivalent of an ensemble average [*34*]. The ensemble average is the average over a great number of experiments performed under the same conditions. If the hot wire output is measured at one instant and again at later instants so widely separated in time that it can reasonably be assumed that each reading is a separate experiment, the average of the results can be regarded as an ensemble average. This can be achieved electronically by sampling the hot wire output at an extremely slow rate to make certain that the subsequent samples are statistically independent of each other.

If the measuring probe is sufficiently small, it may be considered to have zero dimension, and the strict point value of the field quantity can be obtained. Similarly, if the probe has no time lag, the instantaneous value of the field quantity is registered.

Before the functional relationships of hot wire response to various parameters are established, inventory can be taken of the physical quantities that may influence the reading by the probe. Since velocity is one of the most important variables in turbulent flow, it is reasonable to search for methods that are sensitive to velocity and its orientation. Being a vector, it can be specified by three components or by absolute magnitude and two orientation angles. The next important flow parameter is density. This is a scalar quantity and in a great variety of problems can be regarded as a constant. Response to density has an important place in compressible flow. This is also true of temperature and pressure.

The properties of the medium, such as specific heat, heat conductivity, and viscosity, may also have an important bearing on the response of the probe. It is assumed that all of these parameters influence the hot wire in some manner that can be determined by appropriate calibration. Since the hot wire is usually heated by an electric current, it is possible to control conditions with this additional parameter. Fortunately both theory and experiment indicate that there is a possibility of obtaining explicit forms of functional dependence between the pertinent variables. Response to the various flow parameters usually can be separated, if not in a single experiment, at least by a set of experiments either with multiple wires or readings taken by the same wire repeatedly under different conditions (angle or current). Naturally this general reasoning remains the same for other types of probes besides the hot wire anemometer, e.g. ionization or glow discharge probes. These would also have a complex response to a number of flow parameters as well as an independent parameter controlled by the experimenter, such as the imposed high voltage on the gap.

From a general point of view, any probe can be regarded as an instrument that interacts with the flow field in such a manner that exchange of energy or matter (ions) is involved. Since most methods of measurement can be reduced ultimately to the detection of a small amount of energy, it is safe to speculate on the ground that the ultimate resolution of all these methods is governed by the minimum amount of air (or other medium) that is required to exchange the minimum detectable energy with the probe. This reasoning would indicate that there should be an inherent minimum resolution "volume" for all such methods. The ultimate limit of this resolution by any method would be established by the thermal motion of the medium where statistical fluctuations of energy content would jeopardize any further detection. At the present time the hot wire method has not reached this limit, but has gone sufficiently far toward this ultimate goal.

The hot wire probe, like any other measuring instrument, has a finite resolution both in space and time. The probe does not respond instantaneously and it averages in some manner over a small volume in space. The resolution in space is governed by the physical dimensions of the probe, which are usually a few tenths of a centimeter in one direction and probably one or two orders of magnitude smaller in the other two directions. In the third dimension, namely, the direction of the flow, the resolution is governed principally by the time lag, since masses of air passing across the wire appear as a sequence in time. The thermal lag of the hot wire is of the order of one millisecond with conventional wire materials and diameters. This is insufficient time resolution for most applications. The real advantage of the method lies in the fact that this time lag obeys a law of simple mathematical form that permits the use of an appropriate electronic circuit to compensate for the time lag and extend the time resolution by more than a factor of ten, and sometimes even by a factor of one hundred. The space resolution along the flow direction, which results from the time resolution using Taylor's hypothesis, may be smaller or larger than the space resolution along the wire length, depending on the velocity range and on the quality of time response attained by the electronic equipment. Fig. F,2.1 shows the variation of "resolution-length" with upper frequency limit of the equipment for which the thermal lag can be compensated, considering the mean velocity as the principal parameter. The diagram indicates that conventional hot wire equipment gives adequate resolution along the flow direction compared to the finite wire length at low velocities. On the other hand, this may be questionable at very high velocities where the dominating limitation is the frequency response and not the wire length.

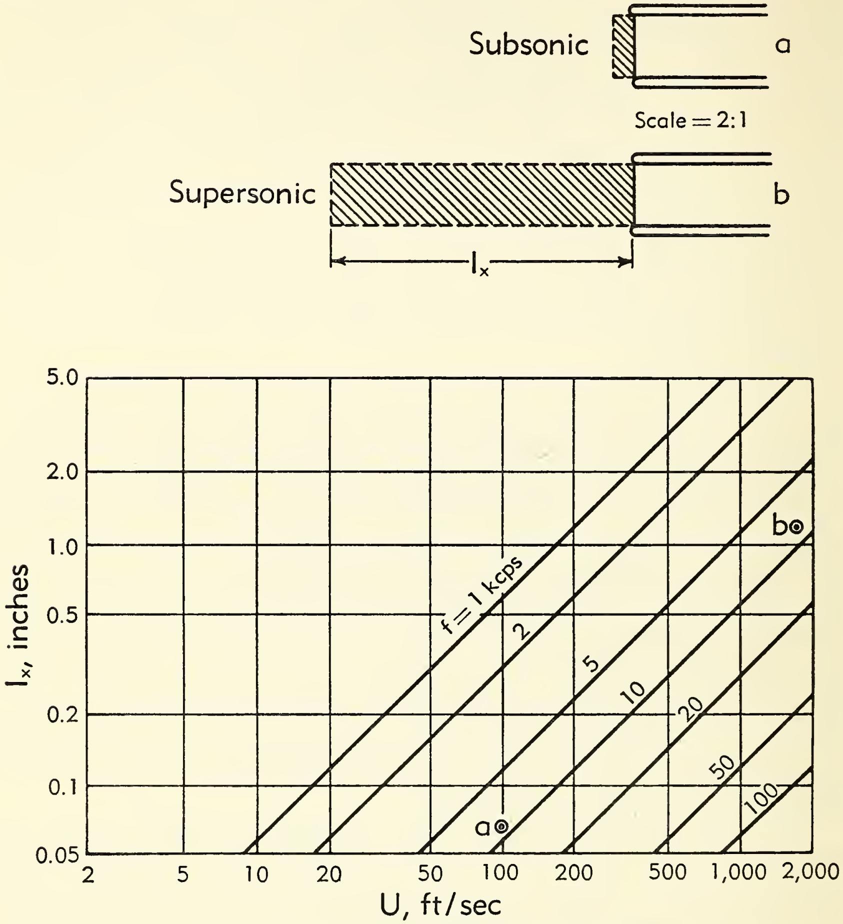

Fig. F,2.1. Resolution length of the hot wire anemometer at various speeds. (From [*52*].)

F,2.2. Hot Wire Probe. The hot wire probe consists of one or more fine wires. The wire material is generally metal and the thickness depends upon handling difficulties. The wire diameter is governed by opposing requirements, and compromises are made according to the problem at hand. Since the heat capacity of the wire is proportional to its cross-sectional area, it decreases proportionally to the square of the wire diameter. The mechanical strength also decreases with decreasing cross section. The wire has an air drag load that is governed by the wire length to diameter ratio. Another type of load is the bombardment of the wire by solid particles. Very little is known about this type of load since the statistical distribution of solid particles in an air stream is difficult to establish. A third type of load that can cause mechanical failure is the vibration of the support prongs due to fluctuations in the air flow (e.g. vortex streets produced by the prongs themselves). The oscillating prongs may break the wire, and if the wire does not break, the prongs may still cause the strain gauge type of resistance fluctuations that can be mistaken for flow fluctuations.

The wire materials are chosen on the basis of contradictory requirements such as high temperature coefficient of resistivity and high mechanical strength. On the basis of high temperature coefficient of resistivity, almost all alloys are ruled out except when the wire is operated at extremely high temperatures where some platinum-iridium alloys can be used profitably and the lower temperature coefficient of resistivity is not such a serious drawback. For standard turbulence measurements two metals, platinum and tungsten, seem superior to others. Platinum has the advantage that it is commercially available in rather long samples in a great variety of diameters. An extremely fine wire with a diameter as small as 0.5 micron (0.00002″) can be made by the Wollaston process. The silver sleeve provided by this technique is also very convenient for soldering the wire to needle tips. These advantages made the Wollaston process platinum wire the standard hot wire material for low speed turbulence work. Since tungsten wire has much greater mechanical strength compared to platinum wire, it is almost the unique material to use under mechanically adverse conditions. Successful runs in supersonic flow have been made with thin tungsten wires [*5,9*]. Tungsten has the great disadvantage that it oxidizes in air above 300°C and requires more elaborate handling because it cannot be soft soldered. The usual technique is to electroplate the tungsten with copper and fasten the wire to the prongs by soft soldering the copper sleeve [*8*]. An alternate method is to spot weld the bare tungsten wire to the prongs. Unfortunately, tungsten wires are not obtainable in diameters as small as platinum wires because no Wollaston process is available for tungsten. The usual technique is to get tungsten wires bare drawn down to 7.6 microns (0.00030″) and further reduce the diameter by chemical etching. This is usually successful down to 3.8 microns (0.00015″). Attempts have been made to go further but the resulting wire is very nonuniform in cross section and breaks easily.

If the choice of wire material and wire diameter is regarded as a problem of compromise between contradictory requirements, a "figure of merit" can be developed for various wire materials based on the following reasoning: The hot wire is required to give maximum voltage response for 1 per cent turbulent velocity fluctuations. Its static response depends principally on the voltage drop across the wire, the temperature above room temperature, and the coefficient of resistivity. The voltage drop across the wire depends principally on the length to diameter ratio, if other operating conditions remain constant. On the other hand, the wire length is limited by mechanical considerations and the mechanical stresses developed in the wire are also dependent upon the length to diameter ratio. Therefore, if a length to diameter ratio that results in the maximum permissible stress in the wire is used, and the temperature in the wire is such that it gives maximum sensitivity, the "figure of merit" is based on the maximum sensitivity attained under highest temperature and highest permissible stress [*5*].

$$\text{“figure of merit”} = \alpha^{\frac{3}{2}}(T_w - T_e)^{\frac{3}{2}}{}_{\max} r^{\frac{1}{2}} \sigma_\tau \tag{2.2-1}$$

where σ_τ is the maximum tensile strength (hot condition), r the specific resistivity, α the temperature coefficient of resistivity, T_w the operating temperature of the wire, and T_e the equilibrium (or air) temperature. A different "figure of merit" has been introduced by H. H. Lowell in [*6*]. Table F,2.2 gives customary wire diameters with corresponding resistance values and temperature coefficients of resistivity.

Table F,2.2

Material	Platinum	Tungsten	Platinum-iridium alloy	Unit
Composition	100	100	80–20	per cent
Maximum useable temperature	800	300	750	C°
Specific resistivity	10	5.5	32	10^{-6} ohm-cm
Temperature coefficient of resistivity	0.00320	0.00350	0.00085	1/C°
Tensile strength (yield point)	0.02	2.00	0.700	10^{10} dynes/cm^2
Figure of merit	0.8–1	10–12	10–12	
Minimum available diameters	1.25	3.8	38	10^{-4} cm
	0.00005	0.00015	0.0015	inch

To make hot wire probes requires a little experience, but the necessary skill can be acquired. Wollaston wires can be used in two different ways to make probes. One technique is to etch off the silver coating in nitric acid before using the wire. In this case a short length of Wollaston wire is placed in nitric acid. The best concentration can be attained if the density of the nitric acid and distilled water mixture is 1.19 (roughly one-third nitric acid and two-thirds distilled water). The Wollaston wire must be free of grease and preferably washed in ether before the etching process. The nitric acid does not start to etch the silver easily unless there are some impurities in the solution. A small amount of silver nitrate ($AgNO_3$) or an electric current (1.5 volt dry cell battery with 10,000 ohm resistor in series) starts the etching process. The wire sample must be connected to the positive electrode. When the silver is completely etched off, the platinum wire has a very uniform appearance under a microscope, and it can be handled easily if a small "weight" (a little piece of Scotch tape) is attached to the end of the wire to keep it stretched vertically. The wire then can be soft soldered to the two prongs using acid flux and a soldering iron with temperature control. The wire gets its appropriate tension from the surface tension of the molten solder and there is no difficulty in obtaining rather straight wires with no excess tension in them.

The alternate method is to solder the Wollaston wire in a semicircular shape between two prongs and etch a portion of the silver sleeve in a drop of nitric acid with the aid of a small electric current (as given above). In this manner the silver-coated portion of the Wollaston wire serves as additional prongs, and rather short probes (1 mm long) can be obtained (see Plate F,2.2a). This method is easier, quicker, and more convenient for single wire probes. On the other hand, in a multiple wire array where length and geometrical definitions are more important, etching the wire before soldering is more suitable.

A recent method [*7*] to obtain extremely short probes consists of etching the Wollaston wire in a very small jet of sulphuric acid with an electric current. In this technique the jet diameter determines the shortest length of the probe. Wires 0.3 mm in length have been obtained with wire diameter of 1.25 microns.

Tungsten wires are handled in an entirely different manner. The tungsten wire can be purchased bare or coated with platinum or gold, but no appreciable advantage has been experienced with gold-plated wires. The customary method for handling tungsten is described in [*8*]. The wire is pulled through a small plating bath that consists of two small vessels containing copper sulphate electrolyte. The distance between the two baths determines the central uncoated portion of the wire. The hole through the bath is so small that the surface tension prevents the electrolyte from entering the central portion. The electrolytic copper sulphate solution with some sulphuric acid added (water, 1,000 gr; $CuSO_4$, 250 gr; H_2SO_4, 70 gr) and a plating current of the order of 100 microamps can be used to obtain sufficient quality of plating in 5 to 10 minutes. It is best to plate a series of wire samples without cutting them off. A string of coated and uncoated portions can be seen on the wire since the red color of copper is easily distinguished from the dull black appearance of tungsten. The individual wire samples then can be cut off and mounted with a drop of sealing wax on a small piece of ordinary copper wire and placed in a bottle for later use. The copper-coated ends will take the solder easily and can be soft soldered to the supporting prongs of the probe. Plate F,2.2b shows standard types of hot wire probes prepared with tungsten wires.

An alternate method is to spot weld the wires by discharging a small condenser through a graphite electrode (pencil lead). No satisfactory results have been obtained with this method using the finest wire available. Platinum-iridium wire has been used and is extensively described in [*6*]. However, its use as yet has been confined to rather large diameters (0.0015″) in steady state applications where thermal lag does not enter into consideration. The use of thin quartz fibers with a metallic coating has been suggested as a possible method of obtaining a low heat capacity system, but no significant results from this method have been published as yet.

The surface conditions of the very fine wires may modify their response, especially in the "molecular" region where the heat transfer is governed by the surface accommodation coefficient. In order to determine surface conditions on a 3.8-micron etched tungsten wire, electron microscope pictures have been taken [*5,9*]. Sample pictures of two wires are given in Plate F,2.2c, showing that the surface is reasonably smooth for such small diameters. The picture indicates that the measurement of wire diameter by optical or electron microscopic methods is rather inadequate due to the bad definition. This strongly suggests that all wire responses must be determined on the basis of calibration instead of being computed from the physical constants and geometrical dimensions of the wire.

A probe may consist of several wires. The angular sensitivity of a single wire can be used to advantage by an appropriate combination of oblique wires. Spatial derivatives also may be obtained by using several wires displaced at fixed distances.

The simplest type of angular probe would be a single wire with variable angle of attack to the mean flow direction. The wire sensitivity with respect to flow angle can be approximated as a cosine law. If two wires are placed obliquely to the flow with the same angle but opposite orientation, the differential response gives an almost linear range of angular sensitivity. The two-wire probes thus obtained measure fluctuations in the angle of the stream which can be identified, for small turbulence levels, as the cross components of the velocity fluctuations.

If the wires are in the same plane, the probe is called a "V" meter; if they are not in the same plane, it is called an "X" meter. Both single probes and X meters are shown in Plate F,2.2b.

A different type of direction meter can be obtained by placing two parallel wires so close together that they mutually influence each other's heat loss. Any angular change would cause more heat loss in one wire and less in the second one. This type of meter is described in [*40*], and it may have great advantage in boundary layer work due to its small dimension across the flow. However, its accurate fabrication constitutes a major difficulty and its use is not widely accepted.

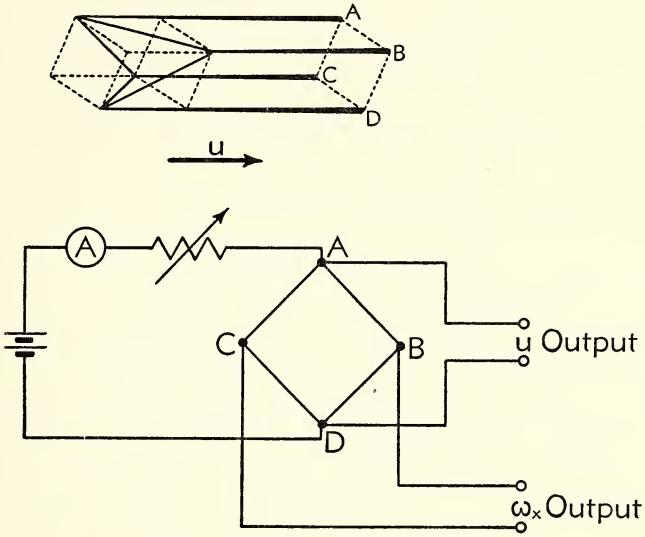

Fig. F,2.2a. Vorticity meter.

Other types of multiple-wire arrangements can be obtained for various purposes. An interesting array of six wires, described in [*41*], permits the measurement of velocity fluctuations independent of temperature fluctuations by using an arrangement which cancels out temperature effect.

With four appropriately-placed wires it is possible to obtain a probe that is sensitive to one component of the vorticity of the velocity field. Fig. F,2.2a shows the arrangement for the longitudinal component of vorticity (ω_x). The four wires have the same angular orientation with respect to the mean flow and are all of equal length. A heating current passes through opposite points of the bridge, and the voltage fluctuations are detected at the other two opposite points of the bridge (galvanometer points). The velocity fluctuations in the flow direction have no effect because the four wires decrease or increase their heat loss simultaneously and the bridge balance remains unaffected. The cross component of velocity fluctuations changes the ratio in the two arms simultaneously leaving the bridge balanced. Spinning of the probe or corresponding rotation in the air stream causes increase of the heat loss in two diametrically opposite arms and a decrease in the other diametrically opposite arms, giving response to vorticity. A detailed analysis shows that a completely matched four-wire system responds to the vorticity components along the x axis (the direction of mean flow), and calibration of the probe can be performed easily by spinning the probe with a known angular velocity. Fig. F,2.2b shows a calibration performed in this manner.

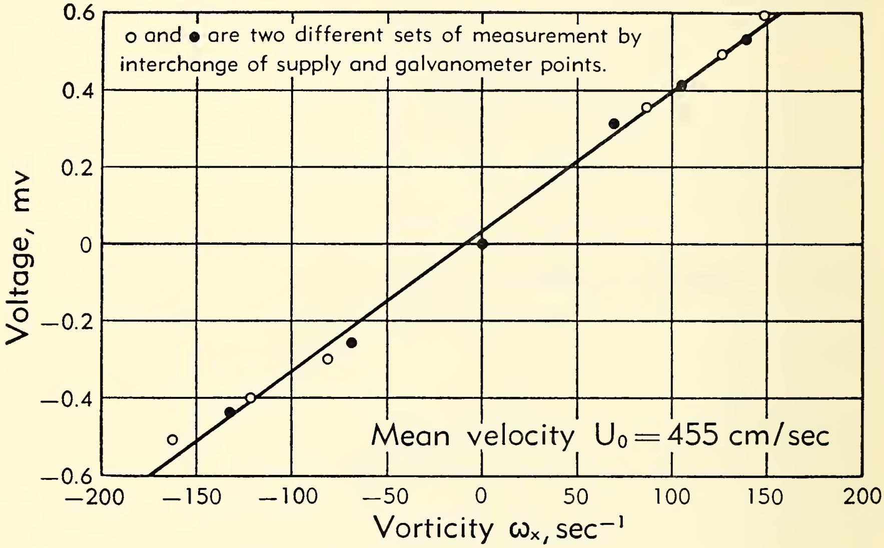

Fig. F,2.2b. Response of vorticity meter.

F,2.3. Heat Loss in Steady Flow (King's Formula). The fundamental information needed in order to use a hot wire probe is the law that governs heat transfer from a single wire depending on the relevant physical parameters. There are no theoretical results available that consider the problem with all of its complications. On the other hand, sufficient information can be obtained from rather simple considerations and the exact behavior can be determined by calibration.

A hot wire can be regarded as a cylindrical object of great length compared to its diameter, made of some electrically conducting material, and placed in a uniform flow field of some medium that can be characterized by a number of physical quantities. The pertinent physical parameters encountered in the problem are:

	Geometrical	
l	length	
d	diameter	of the wire
α	angle of attack	
	Flow parameters	
U	magnitude of velocity	
ρ	density	
p	pressure	
T	temperature (absolute)	
	Wire parameters	
	material	
T_w	temperature of wire (or its distribution)	
	Properties of the fluid	
c	specific heat per unit mass (usually c_p at constant pressure)	
μ	viscosity (function of T alone)	
k	heat conductivity (function of T alone)	
γ	ratio of specific heats	

The heat loss can be expressed as the energy transferred from the wire to the fluid per unit time, and in general this must be a function of all the parameters listed above. Dimensional reasoning can reduce these parameters to nondimensional groups. Some are well established nondimensional parameters used in fluid mechanics and heat transfer. The heat loss itself can be made nondimensional by forming the Nusselt number and regrouping the other parameters:

Nu	Nusselt number $= \dfrac{H}{\pi l k \Delta T}$
$\dfrac{l}{d}$	length-to-diameter ratio
α	angle of attack
Re	Reynolds number $= \dfrac{U\rho d}{\mu}$
M	Mach number $= \dfrac{U}{a}$
Pr	Prandtl number $= \dfrac{\mu c_p}{k}$
γ	ratio of specific heats $= \dfrac{c_p}{c_v}$
τ	temperature loading $= \dfrac{T_w - T_e}{T^0}$

The properties of the wire material have been omitted intentionally from this picture because surface properties cannot be assessed by present techniques. The radiation heat loss is usually negligible, but in cases where it is not, it must be subtracted from the total heat loss before treating the problem of forced convection. The wire shows a heat loss in still air which is partly radiation, partly conduction loss, partly free convection. It cannot readily be computed theoretically. The wire usually is operated at such a high imposed flow velocity that the free convection effect can be neglected. This is definitely not true in the case of extremely low velocity measurements where the heat convection must be handled separately and the wire calibrated accordingly.

For an easier understanding of the problems, limiting cases are first considered. A very important simplification arises if the following assumptions are made:

1. The wire is exposed to an air stream perpendicular to its length.

$$\alpha = \frac{\pi}{2}$$

2. The fluid is incompressible. $M \to 0$
3. The Prandtl number is constant. $Pr = \text{const}$
4. The ratio of specific heats is constant. $\gamma = \text{const}$
5. The temperature loading is vanishingly small.

$$\tau = \frac{T_w - T_e}{T^0} \to 0$$

In this case the heat loss is a function of the only remaining parameter, the Reynolds number. The dependence of the Nusselt number on the Reynolds number for a simplified case was first theoretically treated and experimentally established by L. V. King [*10*]. King found that the Nusselt number is a linear function of the square root of the Reynolds number, and he measured the numerical constants to compare them with his theoretical results. The effect of finite length can be treated as a correction because the wire is long compared to its diameter. The problem of compressibility has not been sufficiently well treated theoretically, although several attempts to do so have been made [*11*].

In 1914, L. V. King developed a theory for the hot wire heat loss in incompressible flow. His method is based on the following assumptions:

1. The medium is an incompressible perfect fluid.
2. The heat transfer does not modify the flow field.
3. The cross section of the wire is a circle (or ellipse).

The method is essentially conformal mapping and the cross section of the wire is mapped into a straight line. Constant heat flux is assumed along the transformed contour which, in effect, means that the heat flux on the original cylinder is maximum perpendicular to the flow direction where the velocity is maximum, and the heat flux is zero at the front and rear stagnation points. With these assumptions King expresses the total heat loss at a particular temperature, using the condition that the gas attains full wire temperature at the rear stagnation point. The heat loss is expressed as a transcendental function of the relevant parameters and the Nusselt number is expressed in asymptotic form as a linear function of the square root of the Reynolds number. For low Reynolds numbers (less than 1) this law breaks down and King gives a logarithmic formula for this region. King, in his original paper, does not express the parameters in nondimensional form. The heat loss equation in its original form is

$$Q = l(T_w - T_e)(k + \sqrt{2\pi k \rho c_p U d}) \tag{2.3-1}$$

where Q is the heat loss per unit time, T_w the wire temperature, and T_e the temperature of the wire if unheated (air temperature or equilibrium temperature in high speed flow). King stated that this equation is valid if

$$\frac{\rho c_p U d}{k} > 0.08 \qquad \text{or} \qquad Pr \times Re > 0.08$$

This can be transformed easily into the nondimensional form:

$$Nu = \frac{Q}{\pi l \Delta T k}, \qquad \Delta T = T_w - T_e$$

$$Nu = \left(\frac{1}{\pi} + \sqrt{\frac{2}{\pi} PrRe}\right) \tag{2.3-2}$$

If $Pr = \text{const}$

$$Nu = A\sqrt{Re} + B \tag{2.3-3}$$

where A and B are constants. By comparing his theoretical results with experiments, King proves that the functional dependence is expressed correctly, although the numerical constants computed from the theory differ sometimes as much as 30 or 40 per cent.

A simple reasoning makes plausible the square-root type of dependence of heat loss on velocity (Reynolds number). The growth of momentum boundary layer and thermal boundary layer are proportional, and the factor of proportionality depends on the Prandtl number, which for air is of the order of unity. The boundary layer growth is proportional to the square root of the distance from the leading edge, and the average friction coefficient is analogous to the average heat transfer coefficient, which in turn suggests the square-root type of dependence.

Measured data support an empirical power law in which the exponent of the Reynolds number is approximately 0.5. An extensive set of measurements is given by McAdams [*12*] in Fig. F,2.3 for Reynolds numbers from 0.1 to 10^5.

It is difficult to establish absolute coefficients in the heat transfer law

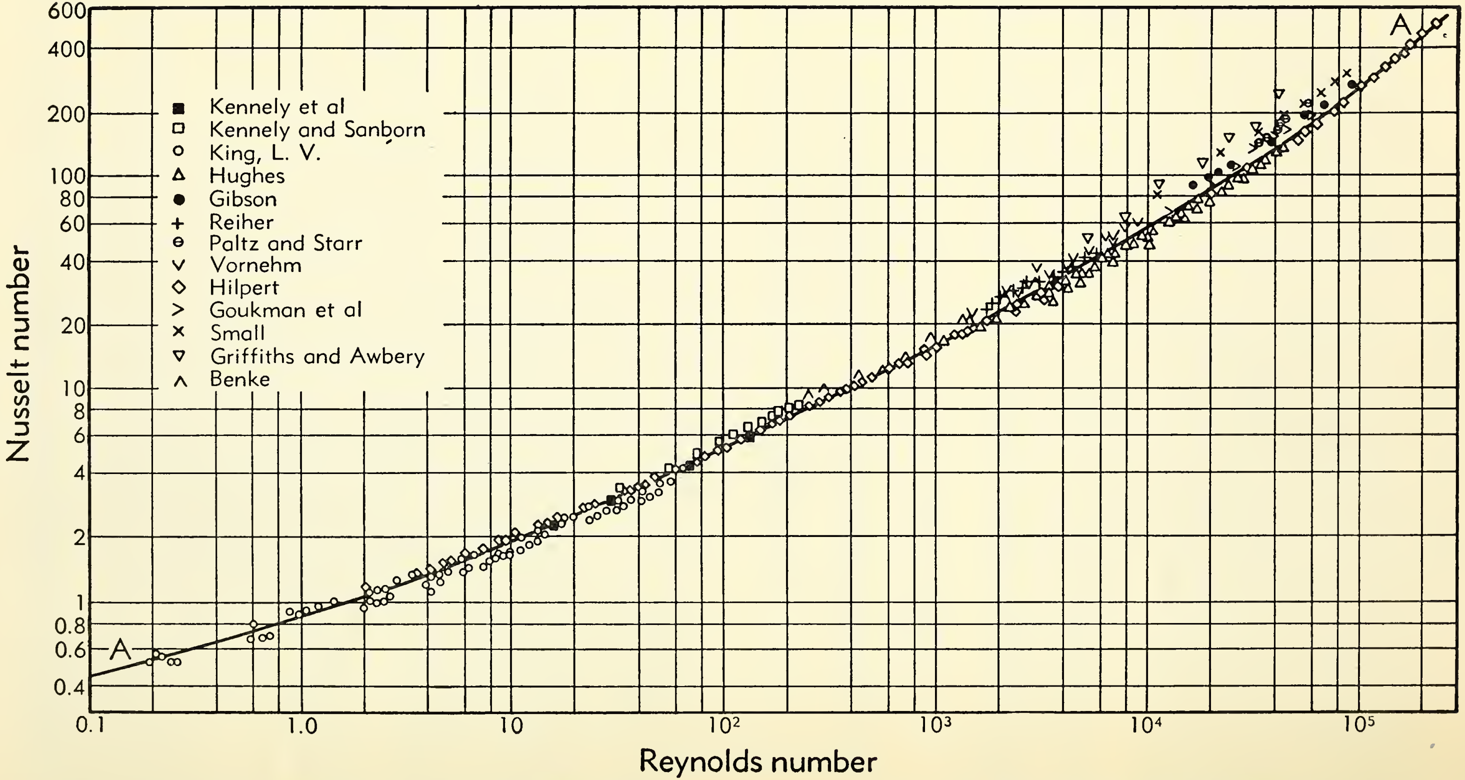

Fig. F,2.3. Heat loss of cylinders (McAdams). (From [*12*] by permission of the McGraw-Hill Book Company.)

because accurate data of wire diameter and physical constants of the material are not available for extremely thin wires. Since the smallest practical hot wire diameters range from two to ten wavelengths of visible light, optical methods for determining the wire diameter are not very accurate.

The effect of finite wire length on heat loss measurement is treated in Art. 2.5. For all practical purposes, when the length-to-diameter ratio exceeds 100, this effect can be taken into account as a correction and only modifies the total heat loss by a constant factor almost independent of the velocity.

All experimental results, corroborated by King's theoretical results, establish the following features of the hot wire heat loss calibration:

1. The intersection on the vertical axis (heat loss) changes with the wire length to diameter ratio, moving upward for shorter wires.

2. The slope of the calibration curve does not vary much from one wire sample to another.

3. The curve consists of straight line portions with noticeable breaking points at certain critical Reynolds numbers. For low speed (incompressible) calibrations there is a noticeable change in slope near Reynolds numbers 10 and 40 corresponding to the change in the flow field when the two attached eddies appear at the rear of the cylinder ($Re = 10$) and when the Kármán vortex street first appears ($Re = 40$). Detailed measurements of the vortex street are given in [*13*].

F,2.4. Heat Loss of Wire at Supersonic Velocities. The hot wire behavior is not essentially different in the compressible and incompressible cases except that compressibility involves additional parameters. For example, the definition of "air temperature" becomes ambiguous.

At high velocities there is the choice of specifying either stagnation temperature T^0 or free stream temperature T_1. In supersonic flow there is sufficient argument to support the additional choice of the free stream temperature T_2 behind a normal shock wave, especially since the hot wire, being a blunt object, causes a normal shock wave ahead of the wire. Similarly, the other flow parameters have different definitions, and the first step is to establish what the pertinent parameters are. Since most supersonic wind tunnels operate at constant Mach number and the density can be varied continuously, the simplest type of experiment is to determine the hot wire heat loss under varying mass flow conditions at constant Mach number.

Operation of a wire is simplest when it is unheated. The unheated wire placed in a supersonic stream reaches a temperature that will be called equilibrium temperature, and it can be determined by small heating currents extrapolated to no heat transfer. For hot wire purposes, this equilibrium point can be regarded as the "air temperature." If the air stream flow conditions are kept constant, the hot wire temperature rises above this equilibrium temperature approximately proportionally to the heat output.

On the other hand, if reference is made to some temperature of the flow field, it is convenient to refer to the stagnation temperature (T^0) in the air stream, since this is a well-defined quantity in both subsonic and supersonic flow and is not affected by the flow going through shock waves. If the wire is heated to a fixed temperature above equilibrium temperature, the resulting heat loss is a function of the cooling effect of the air flow, and in general can be expressed in terms of the Nusselt number, which is a function of Mach number, Reynolds number, Prandtl number, and the degree of heat input compared to the energy contained in the air stream. When evaluating the nondimensional parameters, there is a certain amount of choice in defining them. For convenience in evaluating the Nusselt number, the use of the temperature difference, i.e. the difference between the average wire temperature and the average equilibrium temperature, is suggested. The coefficients of viscosity and heat conduction are evaluated at stagnation temperature of the air stream. The velocity and density, occurring in the Reynolds number only as a product, can be taken either at free stream or behind a normal shock condition, since the mass flow is the same.

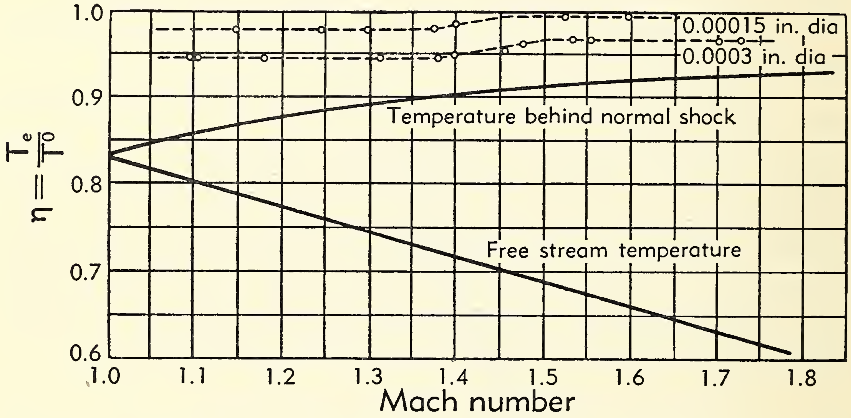

Fig. F,2.4a. Equilibrium temperature of hot wire at supersonic speed (dashed lines). (From [*9*].)

The temperature loading can be defined as the ratio of the temperature difference to the stagnation temperature. This gives the nondimensional ratio of energy input to thermal energy contained in the medium. Detailed experimental results are given in [*5*] and [*9*]. The principal conclusions are the following:

1. The equilibrium temperature varies slightly with Mach number and almost negligibly with Reynolds number. It is very close to the

stagnation temperature (only a few per cent lower) and the difference is constant when expressed as a percentage of the stagnation temperature (not expressed in the form of the conventional recovery factor). See Fig. F,2.4a.

2. For small overheating ratios the heat loss is expressed in the form of the Nusselt number. It does not vary with Mach number if the Reynolds number is given in terms of the mass flow, wire diameter, and viscosity at stagnation temperature. The variation with Reynolds number is very similar to the subsonic case, namely, the Nusselt number is linear with the square root of the Reynolds number. If extrapolated to zero Reynolds number, the intersection on the Nu_0 axis is negative. See Fig. F,2.4b. Naturally this is not related to physical reality but indicates only that the heat loss depends on the square root of the Reynolds number as it does in the subsonic case. However, at low Reynolds numbers with a high Mach number, the free molecular flow probably obeys entirely different laws [*48*]. The lack of variation with respect to Mach number is not so surprising in view of the fact that the flow arrives at the hot wire through an almost normal detached shock wave that produces a subsonic flow around the front part of the cylinder, where most of the heat transfer probably takes place. The Mach number of this subsonic flow does not vary greatly with free stream Mach number, and the heat transfer properties are governed by mass flow and by heat conductivity and viscosity around stagnation conditions.

3. The variation of heat loss with respect to temperature loading is nonlinear and deviates 15 to 20 per cent from the linearity when the overheating ratio becomes unity, i.e. the wire is heated to a temperature twice the stagnation temperature of the medium. See Fig. F,2.4c. This 15 to 20 per cent deviation from linearity may cause twice as much deviation in the slope of the temperature heat loss curve and therefore in the sensitivity for fluctuations.

The fact that the equilibrium temperature of the hot wire is so close to the stagnation temperature makes it rather convenient for measuring stagnation temperature fluctuations where other instruments (thermocouples) are either too large or too sluggish in response (see D,2).

At the present time, relatively little information is available on hot wire response at high subsonic Mach numbers, chiefly due to the lack of detailed measurements in which Mach number and mass flow (Reynolds number) are varied separately. The published results are given in [*6*]. It has been found that humidity effects and interference from the supports are sufficiently great to overshadow the variations that are being sought. The general trend of available experiments shows that heat loss varies with the square root of the Reynolds number but has some Mach number dependence and probably some humidity effect.

The hot wire heat loss does not seem to depend on Mach number at

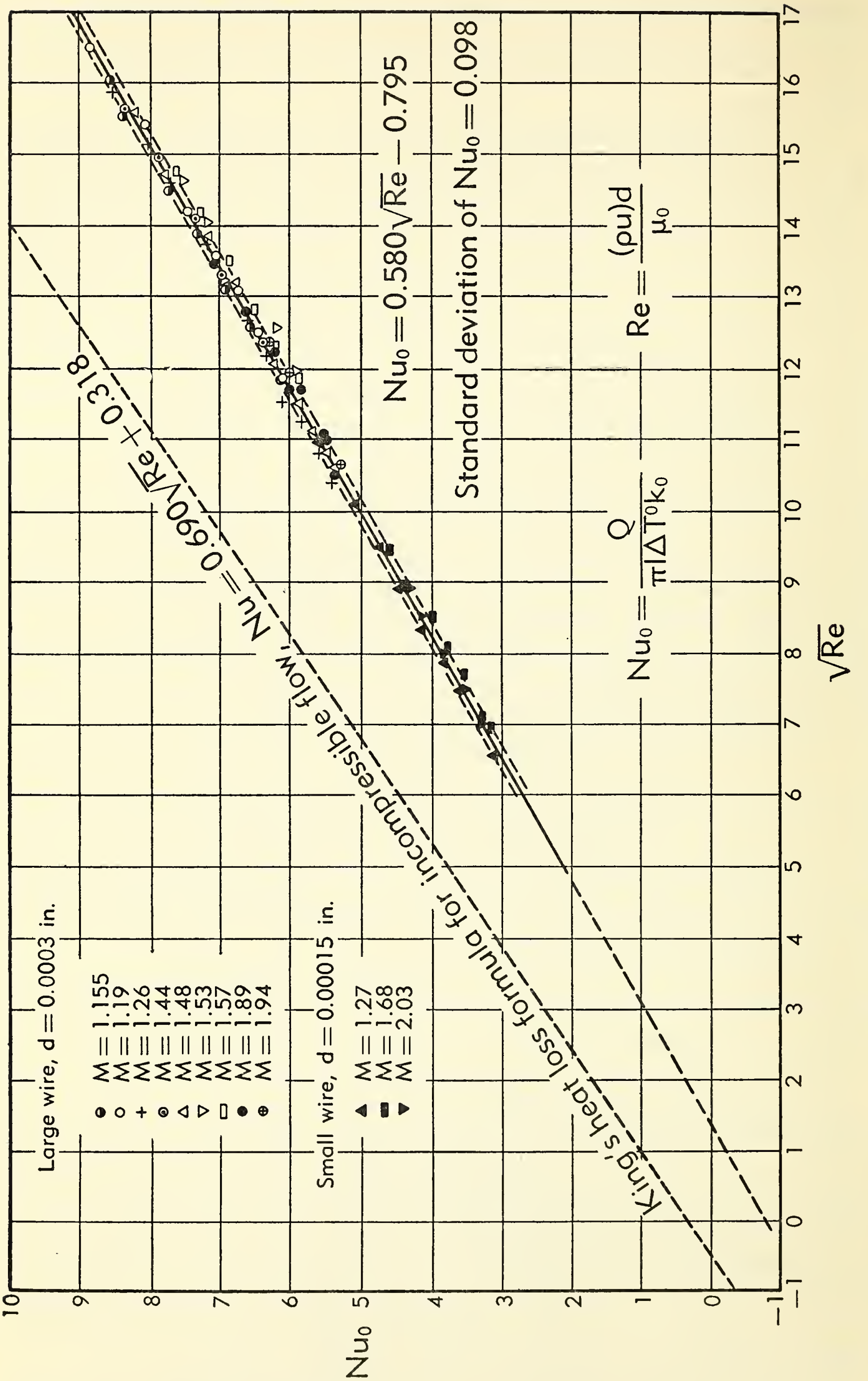

Fig. F,2.4b. Heat loss of hot wire in supersonic flow. (From [9].)

supersonic velocities; yet it differs from low speed data. See Fig. F,2.4b (King's formula). It is probable that there is a family of curves for transonic flow with Mach number as parameter.

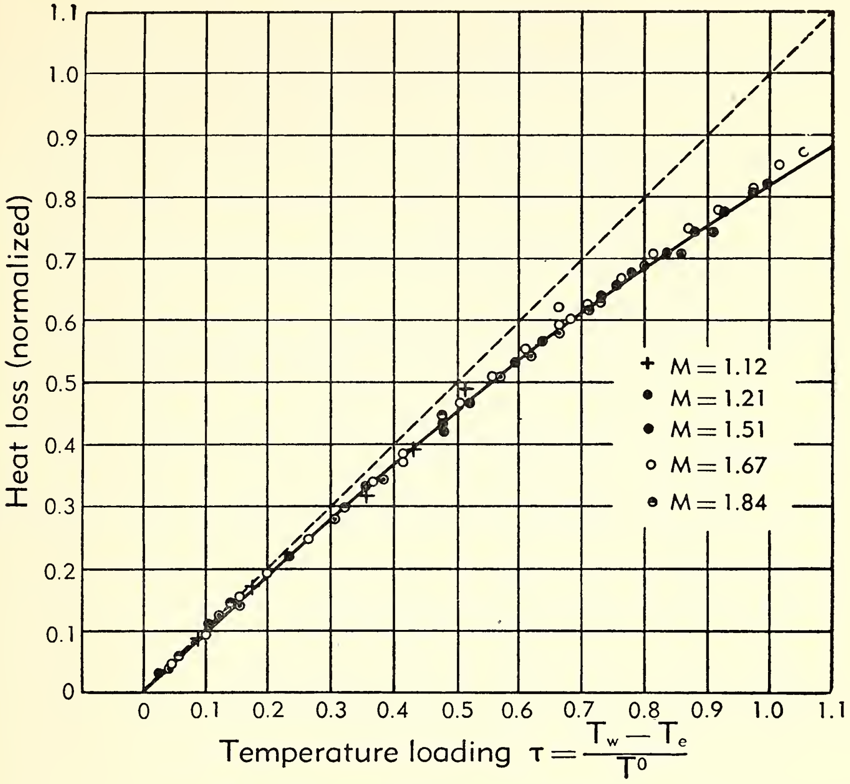

Fig. F,2.4c. Nonlinear dependence of heat loss on temperature at supersonic speed. (From [*9*].)

F,2.5. Effect of Finite Wire Length on Heat Loss. Since most hot wires are rather fine, their length-to-diameter ratio usually exceeds 100. The wire materials, on the other hand, are good heat conducting metals. A substantial part of the heat generated in the mass of the metal is conducted toward the cooler ends of the wire and at the same time a part is transferred to the moving air. If linear relationship is postulated between local heat loss and local temperature difference, and if one-dimensional heat conduction in the metal along the wire is assumed, the result is a hyperbolic cosine distribution of wire temperature along its length. If the heating current and cooling conditions (velocity, density, air temperature) are fixed, the uniform temperature of a wire of infinite length would be higher. Electrical measurements determine the average resistance, and therefore the average temperature, along the length of the wire. The end effect on heat loss can be computed on the following basis and conveniently put into nondimensional form.

Introduce:

A	area of wire
k	heat conductivity of wire material
H	heat loss per unit length due to forced convection
$\bar{H}_m$	average heat loss per unit length for finite wire
$\theta = T_w - T_e$	temperature difference along wire
$\bar{\theta}$	average of θ along wire
θ^*	uniform temperature of infinitely long wire
H^*	heat loss for infinite wire
I	heating current
$h = \dfrac{H}{\theta} = \dfrac{H^*}{\theta^*}$	local heat loss per degree due to forced convection
r_0	resistance per unit length at air temperature

$$\bar{a} = \alpha\bar{\theta}, \qquad a^* = \alpha\theta^*$$

The governing differential equation is:

$$Ak\,\frac{d^2\theta}{dx^2} - H = -I^2 r_0(1 + \alpha\theta) \tag{2.5-1}$$

For infinite wire $\theta = \theta^* = \text{const}$

$$h = \frac{I^2 r_0(1 + \alpha\theta^*)}{\theta^*}$$

or

$$h = \alpha I^2 r_0\,\frac{1 + a^*}{a^*}$$

The average heat loss $\bar{h} = \alpha I^2 r_0\,\dfrac{1 + \bar{a}}{\bar{a}}$

$$\frac{h}{\bar{h}} = \frac{(1 + a^*)\bar{a}}{(1 + \bar{a})a^*}$$

The ratio $\bar{a}/a^*$ can be determined by solving the differential equation and integrating along the wire length. The distribution of temperature

$$\theta = \theta^*\left(1 - \frac{\cosh \dfrac{2x}{l}\dfrac{1}{S}\sqrt{\dfrac{\bar{a}}{a^*}}}{\cosh \dfrac{1}{S}\sqrt{\dfrac{\bar{a}}{a^*}}}\right) \tag{2.5-2}$$

$$\frac{\bar{a}}{a^*} = f(S), \qquad S = \frac{d}{l}\sqrt{\frac{1 + \bar{a}}{Nu_0}}\sqrt{\frac{k}{k_0}}$$

$$Nu_0 = \frac{\bar{H}_m}{\pi l \bar{\theta} k_0}$$

$$\left.\begin{aligned} \sqrt{\frac{k}{k_0}} &= 91 \text{ for tungsten}\\ \sqrt{\frac{k}{k_0}} &= 54.4 \text{ for platinum}\end{aligned}\right\}\text{ at }300^\circ\text{K}$$

The graph for $f(S)$ is given in Fig. F,2.5. For very long wires $S \rightarrow 0$ and

$$\frac{\bar{a}}{a^*} \cong 1 - 1.1S \qquad \text{for} \qquad S < 0.2$$

Fig. F,2.5 shows the correction factor. Since tungsten has a thermal conductivity almost four times as large as platinum, the heat loss effect is approximately twice as large. This is somewhat counterbalanced by the fact that longer wires can be used safely if they are made of tungsten due to its greater mechanical strength. The nonlinearity of heat loss with respect to temperature difference somewhat changes the distribution of temperature along the wire length. This case has been extensively treated by Betchov [*14*], and it is of special interest if both the nonlinearity and the transient readjustment of wire temperature are taken into account.

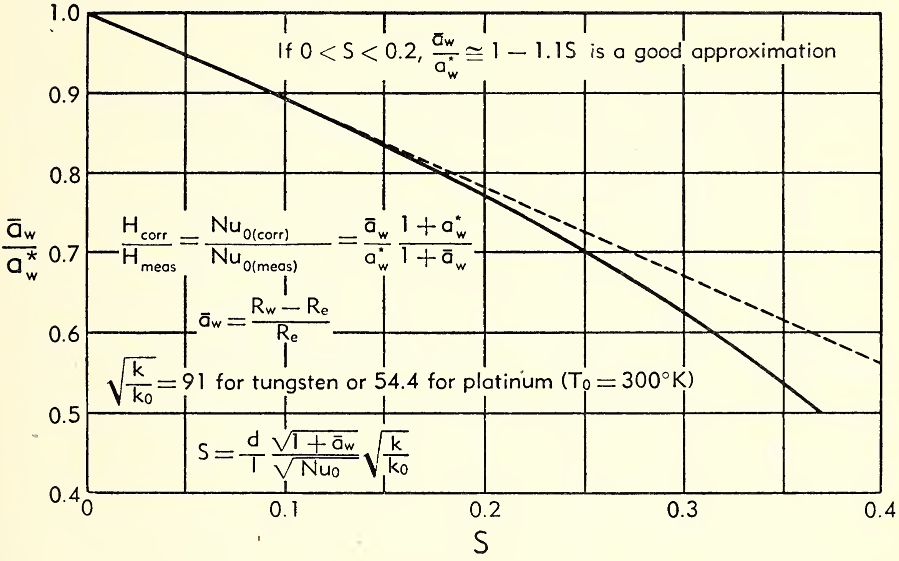

Fig. F,2.5. Effect of finite wire length on heat loss. (From [*5*].)

F,2.6. Angle of Attack. Since the hot wires are oriented at oblique angles to the main flow to measure cross components of turbulent velocity fluctuations, the dependence of heat loss on angle of attack is important. Theoretical predictions can be made from King's equation by taking into account two effects simultaneously: (1) the projection of the hot wire perpendicular to the air flow changes proportionally to the cosine of the angle; (2) the cross section of the wire becomes elliptical, with the smaller axis of the ellipse being the wire diameter and the larger axis changes inversely proportionally to the cosine of the angle. The effective velocity that would yield the same heat loss

$$U_{\text{eff}} = \frac{U}{2}(\cos\beta + 1) \tag{2.6-1}$$

where β is the angle between the mean flow velocity and the normal of the wire. A simple cosine type of dependence

$$U_{\text{eff}} \cong U\cos\beta \tag{2.6-2}$$

is customarily assumed by most experimenters. It is difficult to determine experimentally the correct dependence of heat loss on angle of attack

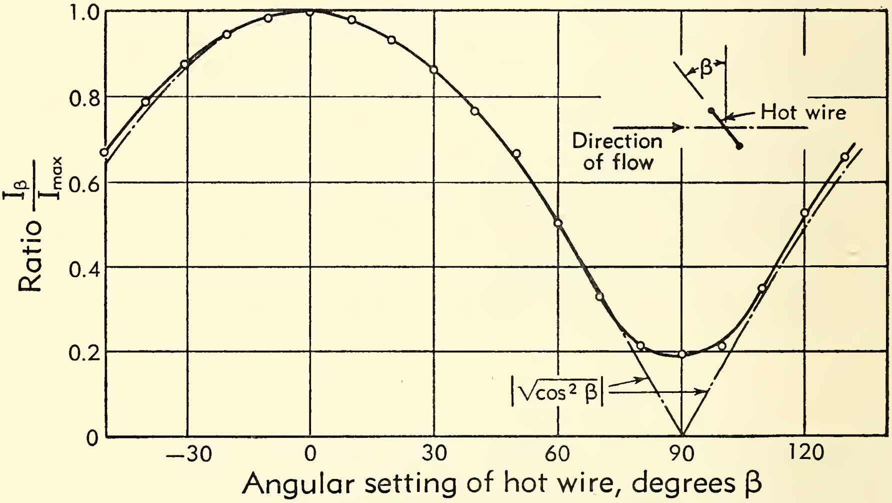

Fig. F,2.6. Directional characteristics of hot wire at constant resistance. (From [*16*].)

because the supporting prongs greatly affect the flow around the wire when the wire is almost parallel to the flow. Results are given in [*15*] and [*16*]. Considerably less systematic effort has been made to determine the dependence of heat loss on angle of attack than on velocity. Since the two wire probes (X or V) must be calibrated at location, no theoretical results are needed to evaluate the angular fluctuation sensitivity. Fig. F,2.6 shows angular dependence of heat loss, taken from [*16*]. The dash line is an empirical interpolation formula.

F,2.7. Hot Wire Response to Unsteady Flow. Since the hot wire is used principally for recording turbulent fluctuations in the flow field, the question can be raised whether the hot wire heat loss determined in steady flow can be applied to determine instantaneous behavior in unsteady flow. If it is assumed that the hot wire heat loss for a transient can be expanded into a Taylor series with respect to time, the order of magnitude of the time derivatives can be estimated. When transformed to a nondimensional basis, the readjustment time can be estimated to be the same order of magnitude as a characteristic time of a typical unsteady flow around a cylinder, namely the Kármán vortex street. The period of the Kármán vortex street depends on the velocity and the diameter of the cylinder. The frequency can be expressed:

$$f = S\frac{U}{d}$$

where S = Strouhal number.

The Kármán vortex street first occurs at $Re = Ud/\nu = 40$; if, for example, $\nu = 0.14$ cm²/sec and $S = 0.125$, $d = 0.001$ cm (0.0004 in.), and $U_{\min} = 5600$ cm/sec (18.6 ft/sec), one finds a Kármán vortex street frequency of 70,000 cps, which is rather high compared to any phenomena expected to be measured with the hot wire anemometer at this low speed. An example at high speed with $S = 0.2$ (assumed from low speed measurements), $d = 0.0004$ cm, and $U = 50{,}000$ cm/sec results in a characteristic frequency of 25 megacycles, which is positively beyond the reach of any equipment. It can be concluded that the transient readjustment of the flow field around the wire is a negligible effect in all conventional hot wire applications due to the very small characteristic time that can be formed with the wire diameter and velocity compared to the much larger thermal lag of the wire itself. The thermal lag is usually of the order of one millisecond. The principal difficulty with respect to transient readjustment is the finite mass of the wire as shown in the following subarticle.

The hot wire responds to changes in the heating current or in the cooling effect of the flow (velocity, density, and temperature of the medium) according to a certain response equation. In order to derive this equation, the conservation of energy is assumed. The amount of heat produced in the hot wire is equated with the heat loss and the accumulation of thermal energy within the wire. For slow variations the thermal lag can be neglected and quasi-equilibrium treatment is satisfactory. The heat loss equated with heat generated becomes for low speed:

$$I^2R_w = (T_w - T_e)(A\sqrt{U} + B)$$

that can be transformed into

$$\frac{I^2}{I_0^2} = \frac{2a'_w}{1 + a'_w}\left(\sqrt{\frac{U}{U_0}} + 1\right) \tag{2.7-1}$$

where I_0 and U_0 are calibration constants of the wire. If $U = 0$ and $a'_w = 1$, $I = I_0$, $B^2/A^2 = U_0$, the intercept of the a'_w = const lies on the $\sqrt{U}$ axis. This reduces the hot wire equation to a convenient nondimensional form.

The nondimensional form of the hot wire steady state equation can be represented by a surface in the I^2, $\sqrt{U}$, a'_w coordinate system. Keeping one variable constant, the usual hot wire characteristics are obtained as orthogonal sections.

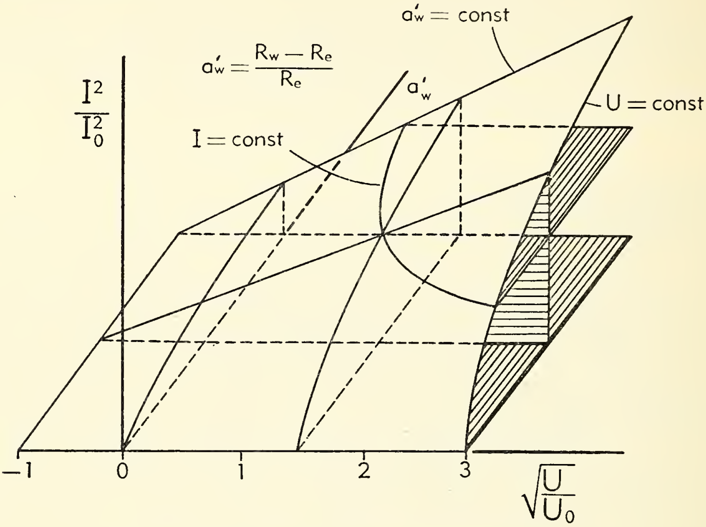

Fig. F,2.7a. The hot wire in thermal equilibrium.

At constant temperature, a'_w = const, the square of the heating current is a linear function of the square root of the velocity. At constant current, I = const, the overheating ratio a'_w decreases with increasing velocity. At constant velocity, U = const, the temperature increases faster than linearly with increasing heating current (Fig. F,2.7a).

The Time Constant. If temperature conditions along the hot wire can be described by a single parameter alone, the principle of the conservation of energy leads to a rather simple equation. Let W be the amount of thermal energy generated per unit time, i.e. the electric power dissipated into heat; let H be the heat loss of the wire per unit time. The thermal energy generated in the wire is a function of the heating current and the wire temperature since the resistance of the wire varies with temperature. The heat loss in the simplest case is a function of the mass flow and of the temperature difference between wire and air. The wire is exposed to a mass flow and to the temperature of the medium. It can also be assumed that the wire is exposed to an air stream which can be split into a mean motion and a fluctuation. The variables become:

$$H = \bar{H} + \Delta H, \qquad T_w = \bar{T}_w + \Delta T_w, \qquad I = \bar{I} + \Delta I, \qquad T_e = \bar{T}_e + \Delta T_e$$

$$W = \bar{W} + \Delta W, \qquad \rho U = \overline{\rho U} + \Delta(\rho U)$$

$$\Delta H = \left(\frac{\partial H}{\partial T_w}\right)\Delta T_w + \left(\frac{\partial H}{\partial T_e}\right)\Delta T_e + \left(\frac{\partial H}{\partial(\rho U)}\right)\Delta(\rho U)$$

$$\Delta W = \left(\frac{\partial W}{\partial I}\right)\Delta I + \left(\frac{\partial W}{\partial T_w}\right)\Delta T_w$$

The heat loss and heat generated are equal for the mean quantity and the difference between the instantaneous heat generated and the instantaneous heat lost is accumulated as thermal energy.

$$W - H = \frac{dE}{dt} \tag{2.7-2}$$

where E is the thermal energy stored. For fluctuations that are small compared to the mean, a small perturbation method can be used. Assuming $E = CT_w$ where C is the thermal heat capacity of the wire

$$A\Delta(\rho U) + B\Delta I + D\Delta T_e = \Delta T_w + \mathfrak{M}\frac{d\Delta T_w}{dt} \tag{2.7-3}$$

$$A = -\left(\frac{\partial H}{\partial(\rho U)}\right)\frac{1}{\left(\frac{\partial H}{\partial T_w}\right) - \left(\frac{\partial W}{\partial T_w}\right)} \tag{2.7-4}$$

$$B = \left(\frac{\partial W}{\partial I}\right)\frac{1}{\left(\frac{\partial H}{\partial T_w}\right) - \left(\frac{\partial W}{\partial T_w}\right)} \tag{2.7-5}$$

$$D = -\left(\frac{\partial H}{\partial T_e}\right)\frac{1}{\left(\frac{\partial H}{\partial T_w}\right) - \left(\frac{\partial W}{\partial T_w}\right)} \tag{2.7-6}$$

$$\mathfrak{M} = \frac{C}{\left(\frac{\partial H}{\partial T_w}\right) - \left(\frac{\partial W}{\partial T_w}\right)} \tag{2.7-7}$$

where $\mathfrak{M}$ has the dimension of time and is called the time constant of the wire in the particular operating condition. This time constant is not a characteristic quantity of the wire but is a function of the operating conditions, and its value increases with increased wire temperature and decreases with increasing cooling effect. The reasoning given above is valid for small fluctuations around the mean values and therefore is a first order approximation for vanishing small fluctuations. If the fluctuations are very large (15 to 20 per cent of the mean), this simplified treatment is insufficient since the value of the time constant varies even within a single cycle and cannot be considered a constant at all. If explicit expressions are available for H and W, specific formulas for both the hot wire sensitivity and the time constant can be obtained easily.

This reasoning did not involve any properties of the electrical circuit. In actual use the hot wire is an integral part of the electrical circuit and this fact is reflected in its characteristics. The resistance fluctuations of the wire are proportional to the temperature fluctuations

$$\Delta R = \alpha R_f \Delta T_w \tag{2.7-8}$$

where R_f is the resistance of the wire at a reference temperature and α is the temperature coefficient of resistivity. Thus Eq. 2.7-3 becomes

$$\alpha R_f A \Delta(\rho U) + \alpha R_f B \Delta I + \alpha R_f D \Delta T_e = \Delta R + \mathfrak{M} \frac{d\Delta R}{dt} \tag{2.7-9}$$

The resistance fluctuations are detected as voltage fluctuations taken either from the wire terminals or across a Wheatstone bridge of which the wire forms one arm. When the voltage fluctuation signal is taken from the wire terminals

$$\Delta e = I \Delta R + R_w \Delta I \tag{2.7-10}$$

Combining this with Eq. 2.7-9

$$\bar{I} R_f \alpha A \Delta(\rho U) + (\bar{I} R_f \alpha B + R_w) \Delta I + \bar{I} R_f \alpha D \Delta T_e + \mathfrak{M} R_w \frac{d\Delta I}{dt} = \Delta e + \mathfrak{M} \frac{d\Delta e}{dt} \tag{2.7-11}$$

Eq. 2.7-11 indicates that not only the mass flow, air temperature, and heating current fluctuations contribute to the voltage signal but also the time derivative of the heating current. When the hot wire is heated from a current source of internal impedance Z_s defined as

$$\frac{\partial(\Delta I)}{\partial(\Delta e)} = -\frac{1}{Z_s} \tag{2.7-12}$$

the current fluctuations are opposite to the voltage fluctuations. The finite impedance then acts like negative feedback both by reducing sensitivity and reducing thermal lag. Substituting Eq. 2.7-12 into Eq. 2.7-11, we obtain

$$-F \Delta(\rho U) + G \Delta T_e = \Delta e + \mathfrak{M}' \frac{d\Delta e}{dt} \tag{2.7-13}$$

with

$$\mathfrak{M}' = \frac{\mathfrak{M}}{1 + \dfrac{I B \alpha R_f}{R_w + Z_s}} \tag{2.7-14}$$

$$F = \frac{\bar{I} A \alpha R_f}{1 + \dfrac{I B \alpha R_f + R_w}{Z_s}} \tag{2.7-15}$$

$$G = \frac{\bar{I}D\alpha R_f}{1 + \dfrac{IB\alpha R_f + R_w}{Z_s}} \tag{2.7-16}$$

For incompressible flow the sensitivity coefficients become simple:

$$\mathfrak{M}' = \frac{\mathfrak{M}}{1 + 2a'_w\epsilon} = \frac{na}{I^2(1 + 2a'_w\epsilon)} \tag{2.7-17}$$

$$F = \frac{\bar{e}a'_w Ez}{2\bar{\rho}\bar{U}} \tag{2.7-18}$$

$$G = \alpha R_w IE \frac{R_f}{R_e} \tag{2.7-19}$$

where n is the thermal lag constant and

$$z = \frac{1}{1 + \sqrt{\dfrac{(\rho U)_0}{\rho U}}} \tag{2.7-20}$$

$(\rho U)_0$ is the calibration constant of the wire (intercept on the $\sqrt{\rho U}$ axis extrapolated for zero heat loss)

$$E = \frac{1 - \epsilon}{1 + 2a'_w\epsilon} \tag{2.7-21}$$

$$\epsilon = \frac{R_w}{Z_s + R_w} = \frac{\bar{e}}{e_{\text{open}}} \tag{2.7-22}$$

$\bar{e} = \bar{I}\bar{R}_w$ is the mean voltage drop across wire and e_{open} is the open circuit voltage of the hot wire supply circuit if the hot wire is removed. (For series current control it is simply equal to battery voltage.)

The real constant of the wire is the thermal lag constant n, which is directly related to the physical properties of the wire. It is proportional to the cross section of the wire, the specific heat, density, and resistance per unit length, and for a specific material it varies with the fourth power of the diameter. For constant operating conditions (velocity and wire temperature) the time constant is approximately proportional to the 1.7 power of the diameter.

According to Eq. 2.7-19 the hot wire response to temperature fluctuations is given, and if the sensitivity for velocity fluctuations is reduced and approaches zero, the sensitivity for temperature fluctuations predominates. This means that the wire must be heated with an extremely low heating current to make the velocity sensitivity vanish. The time constant will also approach a limit.

$$\lim_{a'_w \to 0} \mathfrak{M}(\rho U, a'_w) = \frac{\mathfrak{M}(\rho U, a'_w)}{1 + a'_w} \tag{2.7-23}$$

This indicates that the time constant for temperature fluctuations equals the time constant for velocity fluctuations divided by $(1 + a'_w)$.

The voltage fluctuations across the wire caused by current fluctuations consist of two parts: one is the portion $R_w \Delta I$ which would occur across any resistor; the other is $I \Delta R_w$ which is dependent on the resistance variation due to current fluctuations. Thus the total voltage fluctuation

$$\Delta e = \left(R_w + I \frac{\partial R}{\partial I}\right) \Delta I \tag{2.7-24}$$

The term $I(\partial R/\partial I)$ can be called the "transresistance" of the wire and for the incompressible case to which King's law applies

$$R_T = I \frac{\partial R}{\partial I} = 2a'_w R_w \tag{2.7-25}$$

If the wire is placed in a Wheatstone bridge balanced for the mean values, the only voltage fluctuations are caused (on first order approximation) by the resistance fluctuations of the wire. The bridge unbalance voltage

$$\Delta e_B = I \Delta R \tag{2.7-26}$$

If the unbalanced voltage is amplified and the output current of the amplifier is fed back to the bridge with a negative sign, the resistance fluctuations are suppressed. This is called the constant temperature negative feedback system. The amplifier can be characterized by its transconductance g_m

$$g_m = -\frac{\partial \Delta I}{\partial \Delta e_B} \tag{2.7-27}$$

Substituting Eqs. 2.7-26 and 2.7-27 into Eq. 2.7-9 we obtain

$$\frac{\mathfrak{M}}{1 + R_T g_m} \frac{d\Delta I}{dt} + \Delta I = \frac{1}{1 + \dfrac{1}{R_T g_m}} \left(\frac{\partial I}{\partial(\rho U)} \Delta(\rho U) + \frac{\partial I}{\partial T_e} \Delta T_e\right) \tag{2.7-28}$$

If the negative feedback is large ($R_T g_m \gg 1$), the time constant, as well as the voltage fluctuations, is suppressed in the ratio $1/(1 + R_T g_m)$, and the wire approaches constant temperature conditions. The derivatives on the right-hand side of Eq. 2.7-28 are the constant wire temperature static response derivatives. If e.g. $R_T g_m = 100$, the thermal lag of the circuit is reduced to one hundredth of the thermal lag of the wire alone. The difficulty of physically realizing a large transconductance amplifier without phase errors is the chief obstacle of the wide use of such a scheme. If the hot wire is used for large fluctuations, however, this method offers the unique advantage that the compensating circuit does not need to be set to a particular time constant value [*22,23*].

Hot Wire Sensitivity for Fluctuations in Supersonic Flow. The hot wire placed in a supersonic stream responds to fluctuations in mass flow and to fluctuations in equilibrium temperature. Since the equilibrium temperature is very close to stagnation temperature (see Fig. F,2.4a) the conversion into stagnation temperature fluctuations is rather simple and accurate. The heat loss in supersonic flow can be expressed from the empirical law [9]:

$$H = \pi l k_0 (T_w - T_e)\left(A\sqrt{\frac{\rho U d}{\mu_0}} - B\right)\left(1 - C\,\frac{T_w - T_e}{T^0}\right) \tag{2.7-29}$$

where A, B, C, are nondimensional constants. The voltage fluctuations (assuming constant current source $Z_s = \infty$)

$$\Delta e = -100\Delta e_M \frac{\Delta(\rho U)}{\rho U} + 100\Delta e_T \frac{\Delta T^0}{T^0} \tag{2.7-30}$$

where Δe_M and Δe_T are the sensitivity coefficients for mass flow and stagnation temperature fluctuations.

By logarithmic differentiation of Eq. 2.7-29

$$\Delta e_M = \frac{\bar{e} a'_w}{2} z\phi \tag{2.7-31}$$

$$\phi = \frac{1}{1 - C' a'_w \dfrac{1 + a_w}{g}} \tag{2.7-32}$$

$$\Delta e_T = \bar{e}\phi\left(\frac{\eta g}{1 + a_e} - 0.385 y a'_w - \eta C' a'_w\right) \tag{2.7-33}$$

where

$\bar{e} = I R_w$ is the d.c. potential drop across wire

$$a_w = \frac{R_w - R_{273}}{R_{273}}, \qquad a'_w = \frac{R_w - R_e}{R_e}$$

$$a_e = \frac{R_e - R_{273}}{R_{273}}, \qquad g = \alpha T^0, \qquad \eta = \frac{T_e}{T^0}$$

$$z = \frac{1}{1 - \sqrt{\dfrac{Re^*}{Re}}}, \qquad y = \frac{\sqrt{Re} - 2\sqrt{Re^*}}{\sqrt{Re} - \sqrt{Re^*}}$$

$$Re = \frac{\rho U d}{\mu_0}, \qquad Re^* = \frac{B^2}{A^2}, \qquad C' = \frac{C}{1 - C a'_w \dfrac{1 + a_e}{g}}$$

The values of the constants from [9] are: $A = 0.58$; $B = 0.80$; $C = 0.18$. $Re^* \cong 1.0$ to 1.8 depending on the ratio of wire length to diameter.

The factor ϕ expresses the nonlinear response between wire temperature and heat loss (Fig. F,2.4c).

Since the sensitivity for mass flow fluctuations increases almost linearly with wire temperature (overheating ratio a'_w) and the sensitivity for stagnation temperature fluctuations decreases slightly, the two kinds of fluctuations may be separated by taking several readings with different wire temperatures. The mean square readings of voltage fluctuation:

$$\overline{\Delta e^2} = \Delta e_M^2 \overline{\left[100 \frac{\Delta(\rho U)}{\overline{\rho U}}\right]^2} + \Delta e_T^2 \overline{\left(100 \frac{\Delta T^0}{\overline{T^0}}\right)^2} - 2\Delta e_M \Delta e_T \overline{\left[100 \frac{\Delta(\rho U)}{\overline{\rho U}}\right]\left(100 \frac{\Delta T^0}{\overline{T^0}}\right)} \tag{2.7-34}$$

Taking three readings, the mean square of mass flow fluctuations, the stagnation temperature fluctuations, and the correlation between the two can be separated. Taking additional readings the results can be improved by using the least squares method.

In certain special cases, when some assumptions can be made on the basis of compressible flow theory, the mass flow fluctuations and stagnation temperature fluctuations can be used to determine the velocity and density fluctuations separately. In such a case, when the turbulent pattern is being carried along with the main flow, the pressure fluctuations can be neglected compared to velocity and density (temperature) fluctuations. In this special case

$$\frac{\Delta U}{\overline{U}} = P\left[\frac{\Delta(\rho U)}{\overline{\rho U}}\right] + Q\frac{\Delta T^0}{\overline{T^0}} \tag{2.7-35}$$

$$\frac{\Delta \rho}{\bar{\rho}} = (1 - P)\left[\frac{\Delta(\rho U)}{\overline{\rho U}}\right] - Q\frac{\Delta T^0}{\overline{T^0}} \tag{2.7-36}$$

with

$$P = \frac{1}{1 + (\gamma - 1)M^2}, \qquad Q = \frac{1 + \frac{\gamma - 1}{2} M^2}{1 + (\gamma - 1) M^2}$$

where M is the Mach number and $\gamma = c_p/c_v$, ratio of specific heats. Other assumptions (e.g. isentropic sound waves) give different functions for P and Q. This subject is extensively treated in [*9*].

EFFECT OF NONLINEARITY FOR LARGE FLUCTUATIONS. The evaluation method for velocity fluctuations is based on the small perturbation theory applied to the equation of the hot wire and gives correct results only if the velocity, temperature, and current fluctuations are a small fraction of the respective mean values. On the other hand, if the fluctuations are of the order of 50 per cent or more of the respective mean values, the peculiar nonlinear properties may change the picture completely.

The hot wire is not sensitive to the direction of flow as long as the velocity vector is in the plane perpendicular to the wire. For oblique angles of attack the sensitivity depends only on the angle between the wire and flow direction. The wire does not respond differently to the velocity direction; therefore no information on the sign of the velocity component can be recovered in a fluctuating field where the mean is occasionally vanishing. (This is typically the case near the edge of a turbulent jet where the mean velocity is close to zero, since turbulent bursts appear intermittently in almost still air and the turbulent fluctuations are well over 50 per cent of the mean.) This is a property that makes it difficult to use the hot wire in meteorological applications where the mean velocity may vanish and reversal of the flow is possible. Nonlinearity appears principally due to the inherent nonlinear dependence of heat loss on absolute magnitude of the velocity and to the geometry resulting from the oblique angle of attack of the wire. Depending on these two conditions, the nonlinear effects can be computed for either a two-dimensional or three-dimensional isotropic flow field.

In the case of a two-dimensional flow, if the hot wire is perpendicular to the plane of the flow field, it is sensitive to the absolute magnitude of the velocity vector in two dimensions and the nonlinear effect is confined to the peculiar dependence of the wire response on the absolute magnitude of the velocity. In three-dimensional flow, on the other hand, the respective behavior of velocity fluctuations along the three axes completely obscures and, in some cases, even compensates or partially compensates for the inherent nonlinear effect of the wire.

The errors in hot wire measurements in a flow field of large fluctuations are twofold:

1. Due to the nonlinear effect, the large fluctuations are partially "rectified" and the mean values measured by the wire contain appreciable errors depending on the turbulence level. In the two-dimensional case, this error results also in apparent mean velocity indication lower than the true velocity because the hot wire resistance velocity diagram is convex from below. The fluctuation sensitivity does not change much in the two-dimensional case because the nonlinearity of the response curve up to the second order gives the same slope for the tangent and the secant, and the effect appears only in the third order.

2. In three dimensions there is a partial compensating effect from the other velocity components because the velocity fluctuations in the third dimension give reduced cooling effect due to obliqueness.

In practical operation the deviation from the fluctuation sensitivity based on the linearized theory is not appreciable up to a turbulence level of 20 per cent, but the mean velocity measurements must be evaluated with caution in highly turbulent flow.

Time Constant Calibration by Superimposed Fluctuations. As long as the simple linearized theory applies, the wire responds with the same time constant value irrespective of whether the fluctuations are occurring in the velocity (mass flow), in the air temperature (equilibrium temperature), or in the heating current. Since it is rather difficult to produce velocity fluctuations with controlled amplitude and shape, various methods have been developed to check the simple small perturbation theory and to determine experimentally the time constant value. Even if the theory applies, it is difficult to measure the wire diameter and physical constants to compute the correct time constant value.

The first method consisted of oscillating the wire in a moving air stream so that the velocity to which the wire was exposed fluctuated sinusoidally about its mean value. The difficulty was that, as frequency increased, oscillation of the wire produced great stresses due to inertia forces. This method has not been applied successfully beyond 150–200 cps. On the other hand, these frequencies were not high enough to obtain accurate measurements if the hot wire time constant was small.

Another method, first used by Ziegler [*11,18*], is to place the hot wire in a d.c.-a.c. bridge, supplying the mean heating current from a d.c. source and superimposing an a.c. signal (sine wave). The unbalance of the bridge is proportional to the resistance fluctuations of the wire, and the resultant signal can be fed to an amplifier so that the frequency response can be studied. The principal inconvenience of this technique is that the bridge unbalance, caused by the varying impedance of the other arms of the bridge, and the thermal lag have a similar effect on the output signals.

Square waves have proved to be much more convenient for use in an a.c.-d.c. bridge. The two great advantages are: the square waves, containing a wide spectrum of frequencies, give simultaneous checks of the entire used frequency band; they also give distinctly different responses for bridge unbalance (added square wave shape signal with positive or negative sign) and imperfect compensation (positive or negative slope in square wave).

The output of the bridge gives a signal consisting of exponential segments (Fig. F,2.7b), and the time constant can be measured either from the exponential law or, more conveniently, fed into a compensated amplifier and restored to its original square shape. The required compensation setting gives the time constant value of the wire.

If the compensation is changed, the slope of the restored square wave varies. This method can be extended to any high frequency square wave as long as the bridge has sufficient quality up to the same frequency (Fig. F,2.7c). The square wave shape gives a very sensitive check on the compensation performance. In Fig. F,2.7d three settings of compensation are compared. The correct compensation, 5 per cent overcompensation, and 5 per cent undercompensation are so distinctly different that the estimated mean inaccuracies are approximately 2 per cent. (The interlacing pattern facilitates detection.)

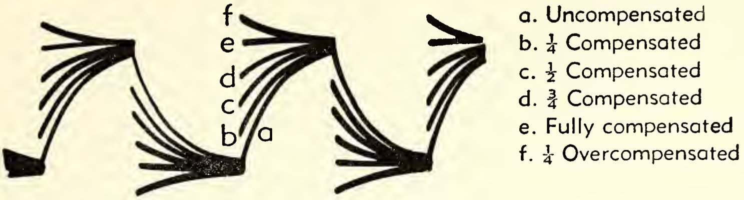

Fig. F,2.7b. Various degrees of compensation: time constant, 0.4 milliseconds; square wave frequency, 500 cps. (From [*52*].)

Another method is to introduce two distinct sine waves [*42*]. The attenuation ratio, which is a function of the time constant, is measured. This enables determination of the time constant in the presence of a high intensity random noise because the two discrete sine waves can be isolated by rather sharp narrow band filters and their ratio monitored. The time constant of the compensation is then adjusted accordingly.

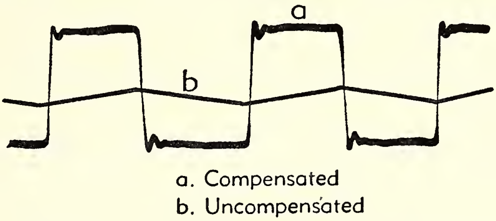

Fig. F,2.7c. Effect of compensation at high frequency: time constant, 0.4 milliseconds; square wave frequency, 5,000 cps. (From [*52*].)

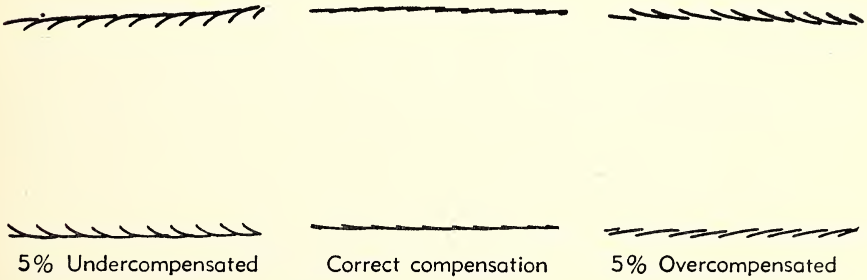

Fig. F,2.7d. Sensitivity of the square wave method: time constant, 0.4 milliseconds; square wave frequency, 400 cps. Note: scope synchronized to $\frac{2}{7}$ of square wave frequency. (From [*52*].)

There is also the possibility of using a square wave or sine wave power signal by modulating the high carrier frequency sources. This would have the advantage that the imposed signal could be much more easily separated before amplification by a low-pass filter. As yet there have been no published results of this technique.

A direct method for checking the transient response of a hot wire in a known unsteady flow field is the use of a shock tube. The shock tube is a long pipe divided by a thin diaphragm into two chambers. If the pressure is different in the two chambers and the diaphragm is suddenly ruptured, the pressure wave travels through the expansion chamber and, if there is sufficient length, the pressure wave steepens into a discontinuous shock wave. The velocity, density, and temperature jump discontinuously at the shock and this gives a velocity, temperature, and density field that varies as a step function of time for the stationary hot wire (see VIII,E,6). Preliminary experimental results indicate that there is no serious disagreement with the simplified linearized theory and its experimental results. Fig. F,2.7e shows a record of the uncompensated and compensated hot wire output due to a traveling shock wave.

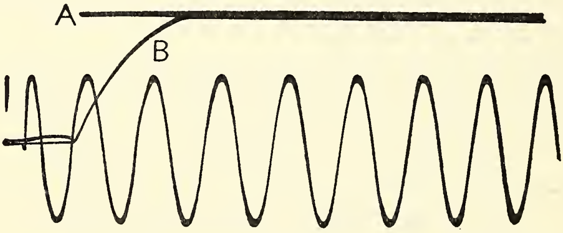

Fig. F,2.7e. Compensated (A) and uncompensated (B) record from shock wave: Wollaston wire 0.0001″ diameter; heating current, 21.42 ma, $a'_w = 0.47$, time constant $= 0.225 \times 10^{-3}$ sec. Calibrating sine wave 5 kc 75 mv rms.

Effect of Thermal Wave Propagation Along the Wire. In the previous reasoning it has been assumed that the wire temperature, even if it is not uniform along the length of the wire, can be described in terms of a single characteristic temperature (probably the average temperature) alone. This implies that, at different heating conditions, the temperature distribution is either similar or, if not similar, the integral effects are self-compensating. If the thermal wave propagation along the wire due to a transient readjustment is taken into consideration, the results, worked out by R. Betchov [*7,14*], indicate that under some conditions the average hot wire response may differ for velocity fluctuations, air temperature fluctuations, or heating current fluctuations, and the corresponding time constants may be different in each case. The situation is complicated by the fact that if the propagation along the wire is considered as a second order effect, there is another second order effect, namely, the nonlinear response of the wire with temperature. The two effects may or may not cancel each other depending on the particular operating conditions and choice of wire material. The nonlinearity is especially great in supersonic flow; the corresponding readjustment time constants have not been worked out as yet.

F,2.8. Electronic Equipment (Thermal Lag Compensation, Amplification).

Compensation by Inverse Circuit. The effect of thermal lag is identical to a linear filter having the same time constant that could be realized by inductance and resistance or capacitance and resistance (Fig. F,2.8a). Such a circuit can be used conveniently as a "dummy hot wire" arrangement in order to check the hot wire compensation network both for sine wave or transient response. The hot wire transient response equation (see Eq. 2.7-13) is

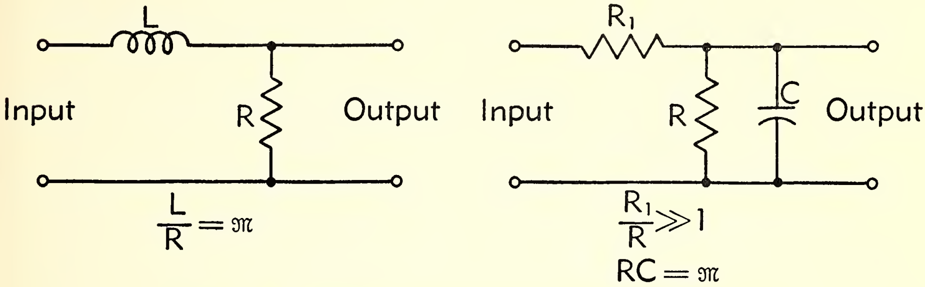

Fig. F,2.8a. Equivalent circuits for hot wire thermal lag.

$$e + \mathfrak{M}\frac{de}{dt} = e_v \tag{2.8-1}$$

where e is the voltage drop across hot wire and e_v the voltage drop that would occur without thermal lag (static response). This is a linear equation, and the filter transfer function can be expressed for sine waves of frequency $\omega = 2\pi f$

$$e_v = A \exp(i\omega t), \qquad e = B \exp(i\omega t)$$

$$\frac{B}{A} = \frac{1}{1 + i\mathfrak{M}\omega} = \frac{1}{\sqrt{1 + \mathfrak{M}^2\omega^2}} \exp(-i \tan^{-1} \mathfrak{M}\omega) \tag{2.8-2}$$

The thermal lag effect can be compensated by an appropriate circuit having the opposite filter characteristics. This was first recognized by Dryden and Kuethe [*30*]. In the case of the response given above, this would be

$$1 + i\mathfrak{M}\omega$$

This implies a type of circuit that has increasing amplification for increasing frequency and infinite amplification for infinite frequency.

Naturally this cannot be realized physically because the amplification must have an ultimate "ceiling," and this will impose a maximum frequency limit. All realizable circuits inherently have this characteristic, and a typical circuit has the response

$$\frac{1 + i\mathfrak{M}\omega}{1 + i\mu\omega}$$

where μ is another time constant associated with the circuit.

If $\omega \rightarrow \infty$, this tends to $\mathfrak{M}/\mu = \kappa$ (called "ceiling-to-floor ratio"), where the amplification at infinite frequency tends to have a definite value. Since the relative amplification for zero frequency is unity by definition, the quality of the compensating circuit can be described by the "ceiling-to-floor ratio," which gives the available margin to improve the frequency characteristics. It can be expressed conveniently in the form of $\kappa = \mathfrak{M}\omega_{\max}$, and various hot wire circuits, depending on the application, give different ceiling-to-floor ratios from 10 to 300 or more.

The physical realization of the circuit may have considerable variation. There are five characteristic types shown in Fig. F,2.8b.

1. Inductance-Resistance Circuit. The circuit is fed from a constant current source and the time constant is given by the ratio of self-inductance to resistance. The principal disadvantages of this circuit are that the nominal amplification (amplification for zero frequency) varies with the setting of the time constant and that the inductance coil has a rather low resonance frequency. In the vicinity of this frequency and beyond it, the circuit does not correspond to the equivalent circuit given in the diagram [*30*].

2. Capacitance-Resistance Circuit. This is the most common type of circuit used, either directly or with some modification. The amplification does not vary with the time constant setting. The ceiling-to-floor ratio depends on the ratio of resistances, R and R_0. The main difficulty of this circuit is that the time constant control elements, R and C, are floating above the ground and form a rather high impedance, so that any parasitic capacitance across the resistor R_0 impairs proper functioning.

3. Mutual Inductance Type of Compensation. According to Eq. 2.8-1 the compensation can be achieved if two signals are added, one being proportional to the hot wire voltage, the other being the time derivative of it. The ratio of the "straight" and "differentiated" signals gives the time constant. A simple method of differentiating is by mutual inductance. The emf of the secondary of the transformer is proportional to the time derivative of the primary current. Detailed information on this type of circuit is given in [*19*].

4. Resistance-Capacitance Circuit with Negative Feedback. This circuit is equivalent to the second type (2) and can be achieved by

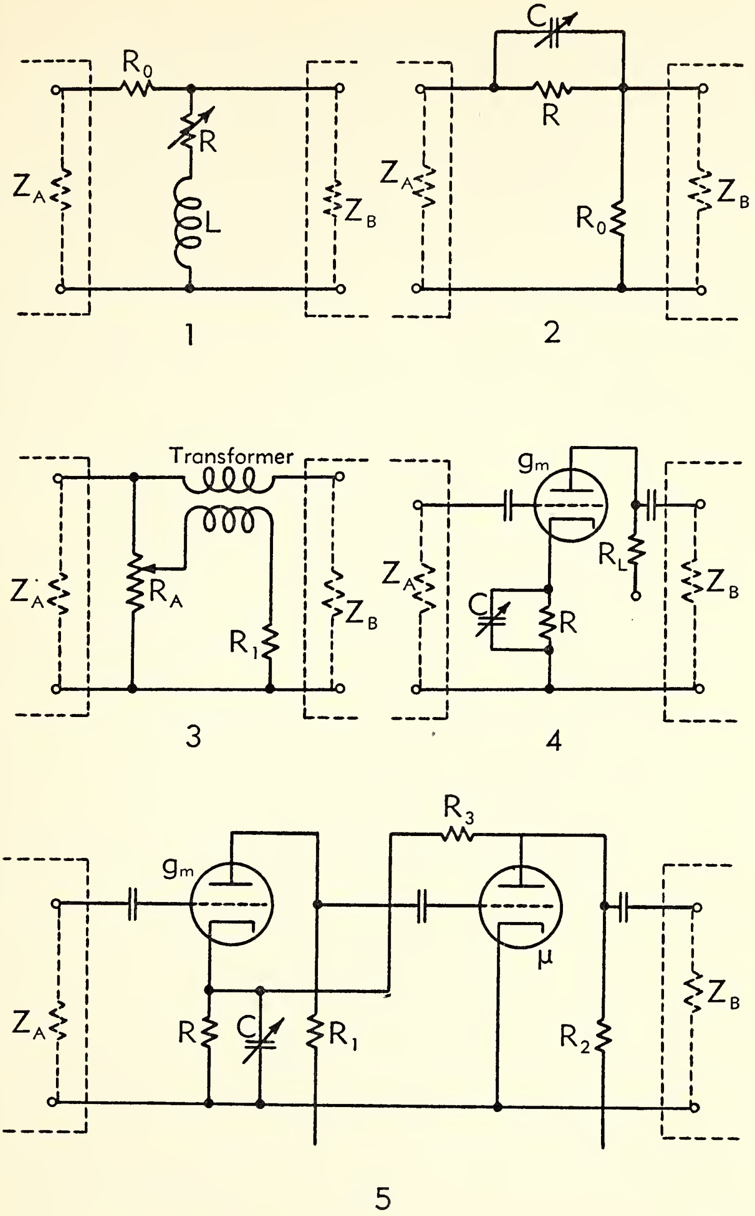

Fig. F,2.8b. Compensation systems. (From [*52*].)

placing the time constant determining *RC* element into a negative feedback loop [*29*]. The cathode bias resistor is bypassed by the appropriate amount of capacitance. It can be used either in a single stage or with additional negative feedback from the succeeding stage (5). The advantages of this arrangement lie in the fact that the *RC* circuit can be made of sufficiently low impedance and no loss of gain appears in the amplification. All other compensation systems have the disadvantage that the signal drops down again to a level where thermal noise may be appreciable due to the great attenuation of the compensating circuit.

5. DIFFERENTIATING CIRCUIT. If compensation is required only for high frequencies and it is certain that the signal does not contain low frequency components, it is easy to achieve compensation by a plain differentiating circuit according to Eq. 2.8-1 and 2.8-2. This may be extremely useful in the case of rotating machinery where no frequencies are expected below the fundamental frequency of the blades, or in applications where the hot wire is used as a time marking device and the compensation is required only for producing sharp pulses.

The quality of compensation can be observed by a square wave test (Fig. F,2.7b and Fig. F,2.7c).

CONSTANT TEMPERATURE NEGATIVE FEEDBACK COMPENSATION. As demonstrated in Art. 2.7, there is an entirely different way of compensating for the thermal lag of a wire, namely, by preventing the change of temperature and maintaining the amount of heating current in the wire that keeps its temperature at a constant value. This can be achieved by detecting the resistance (not the voltage) of the wire to control an amplifier. Since the resistance is a function of the heating current, a feedback with opposite sign suppresses the resistance fluctuations of the wire. This means that the wire, with its specific characteristics, becomes an integral part of the feedback loop, and all considerations for the feedback loop should be extended to the wire itself. Naturally, the temperature change, and therefore the resistance fluctuation, of the wire does not become exactly zero but is substantially reduced to a smaller fraction of the original value depending on the feedback ratio. The thermal capacity of the wire, appearing in the form of a time constant, gives a response inversely proportional to the frequency, which, in this case, becomes "flattened out" by the negative feedback, and the over-all effect is a reduction of the time constant by a factor approximately equal to the feedback ratio, e.g. with a feedback ratio of 100 the temperature fluctuation of the wire will be suppressed to 1 per cent of its original value. If the wire possesses a time constant of 1 millisecond, this will be reduced to approximately 10 microseconds.

The main advantage of this system is that there is no need to adjust the time constant value in the compensating circuit. This is especially advisable if the wire is used to measure large fluctuations where the simple linearized theory does not apply, and therefore no fixed time constant value exists, because the instantaneous "time constant" changes even during a single cycle. The quality of the resulting frequency response depends on the feedback ratio just as the quality of a conventional compensation depends on the "ceiling-to-floor ratio." A simple schematic diagram of this system is given in Fig. F,2.8c. The hot wire is placed in a bridge, the unbalance voltage of the bridge is amplified and the output of the high transconductance amplifier is fed back into the bridge. If the air velocity increases, the wire becomes cooler, the bridge becomes unbalanced, and the amplifier receives a signal that in turn increases the output current, bringing the wire to a higher temperature and the bridge back to balance.

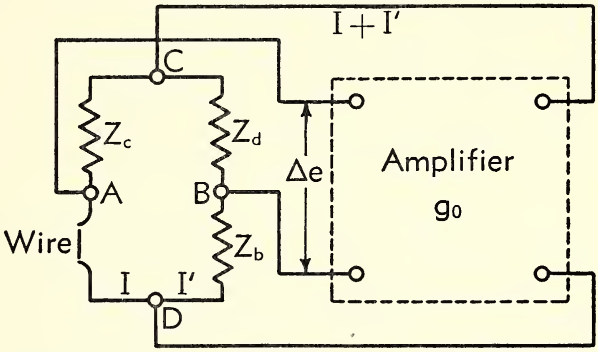

Fig. F,2.8c. Constant temperature feedback system.

Since the hot wire is a low impedance device, it requires heavy current. The transconductance of the amplifier must be high. The transresistance of the hot wire is given in Eq. 2.7-25, and the feedback ratio becomes R_Tg_m where g_m is the transconductance of the amplifier and must be of the order of 0.5 to 5.0 mhos in practical cases.

The high feedback ratio, with a small incidental phase distortion in the amplifier, bridge, and associated equipment, may produce a positive feedback somewhere in the frequency range. This leads to oscillations in the system, although the amplitude remains bounded, because the additional a.c. heating of the oscillations makes the feedback more negative and unbalances the bridge toward the "safe side." The frequency response of the bridge plays an important role since the unbalanced bridge becomes the source of additional positive or negative feedback depending on the direction of the bridge unbalance. A detailed analysis of the situation can be found in [*22*,*23*]. The schematic diagram given in Fig. F,2.8c requires a high transconductance d.c. amplifier. This difficulty can be avoided by using a carrier frequency system; on the other hand, this necessitates good quality instrument modulation and demodulation. The carrier system can be applied to advantage if the fluctuations to be measured are large and the frequency requirements are modest, so that the carrier frequency can be in the higher audio or in the lower ultrasonic frequency range [*49*].

[illegible]. Amplifier Considerations. The peculiar nature of the hot wire amplifiers is due to the very low impedance of the hot wire probe and to the necessity for very high gain (especially at very high frequencies where the lost frequency response must be "boosted" by compensation). In the constant temperature system, high amplification is also needed to achieve a higher feedback ratio.

Before selecting a particular amplifier, the following decisions must be made:

Frequency band. It is possible to compensate for higher frequencies, but additional gain in the equipment is required. The frequency band must be estimated in relation to the thermal noise level. Since the conversion between time and space coordinates is generally a good approximation, the upper frequency limitations can be well interpreted in terms of space resolution limitations. (See Fig. F,2.1.) The frequency resolution is estimated from the minimum spatial structure that is expected to be measured.

If turbulent kinetic energy (turbulence level) is the only goal of the measurement, the frequency band can be quite modest due to the fact that the power spectrum of turbulent signals is usually a monotonically decreasing function of the frequency with most of the contributions in the lower frequency domain. Again, if the goal of the measurement is the microscale or some other quantity connected with the space derivatives of the velocity field, high frequency response should be at a premium. High subsonic or supersonic velocities mean a higher "scanning velocity" of the turbulence pattern; therefore the resolution of higher frequency components in a time record necessitates the use of a channel that can reach these frequencies. The low frequency limit is usually chosen between 1 and 10 cps and is determined by the physical limitations of the coupling condensers. The low frequency limitations are not so critical since corresponding "eddy" dimensions are usually larger than the entire turbulence producing apparatus.

Sensitivity. The minimum signal to be measured sets the limit of noise that can be tolerated. The process of reduction of the noise level to the bare thermal noise involves technical complexity and requires special care with respect to shielding, hum, grounding system, microphonic effects, and other minor technical difficulties. All of these problems in construction and maintenance are the price of high sensitivity. If all other sources of noise and disturbance are eliminated, the ultimate limitation of the sensitivity will be the thermal noise of the input circuit. The hot wire usually has an impedance of 10 to 50 ohms. The first amplifier stage has a thermal noise that is equivalent to a "noise generating resistor" of 300 to 1,000 ohms. This means that, under normal conditions (direct coupling between wire and amplifier), it is the thermal noise of the first tube that determines the noise level of the system.

If a transformer coupling between the wire and the amplifier is used, the mismatch between the wire and the first stage can be improved and the thermal noise reduced by a factor of 2 to 5. The difficulties of a transformer coupling are the limitation in frequency response at the low frequency end and the a.c. load from the transformer to the wire that reduces sensitivity in a ratio which is rather complicated to compute (shunting effect).

Another solution of the mismatch problem is to use a system in which the first stage has an equivalent noise generating resistance of the order of 10 to 50 ohms. Since the noise generating resistance of triodes depends mainly on the transconductance, single tubes with very high transconductance or a bank of tubes in parallel [*24*] can be used.

The signal-to-noise ratio is not a characteristic quantity of a hot wire amplifier, since the value varies widely with signals to be measured. The absolute value of rms noise level referred to the input (in microvolts) describes the situation much better. The input noise level is high if the compensating circuit is used. This is due to the fact that the compensation adds extra amplification at high frequencies, although the nominal amplification is still low. If the compensation "ceiling-to-floor" ratio is high, the noise level varies almost in the same ratio. Fig. F,2.8d shows the theoretical variation of rms noise level with frequency. It is a function of both the time constant setting and the upper cutoff frequency and is expressed as a multiple of the noise for a 10 kcps bandwidth with no compensation. The noise level of a compensated amplifier for high frequencies increases as the $\frac{3}{2}$ power of the frequency limit.

"Poor Man's" Compensation. In conventional compensation systems the frequency-dependent circuit is placed in the amplifier in such a way that the low signal level is first brought to a level high enough that the attenuation of the compensating circuit does not drop the signal level below the noise level of the succeeding stage. If compensation can be achieved before feeding the signal to the amplifier, a conventional amplifier (vacuum tube voltmeter type) can be used for further amplification and detection. Such a compensation system is made possible by using the transformer type as given in Fig. F,2.8b. If the transformer is placed between the wire and the amplifier, both compensation and partial impedance matching (at least at high frequencies) can be obtained. A detailed description and analysis is given in [*20*]. Fig. F,2.8e gives a schematic outline of the circuit with the hot wire placed in a bridge. The bridge unbalance voltage is the uncompensated hot wire signal. The transformer primary coil is connected through a variable resistor across the bribge. The secondary coil is connected in series with the wire output.

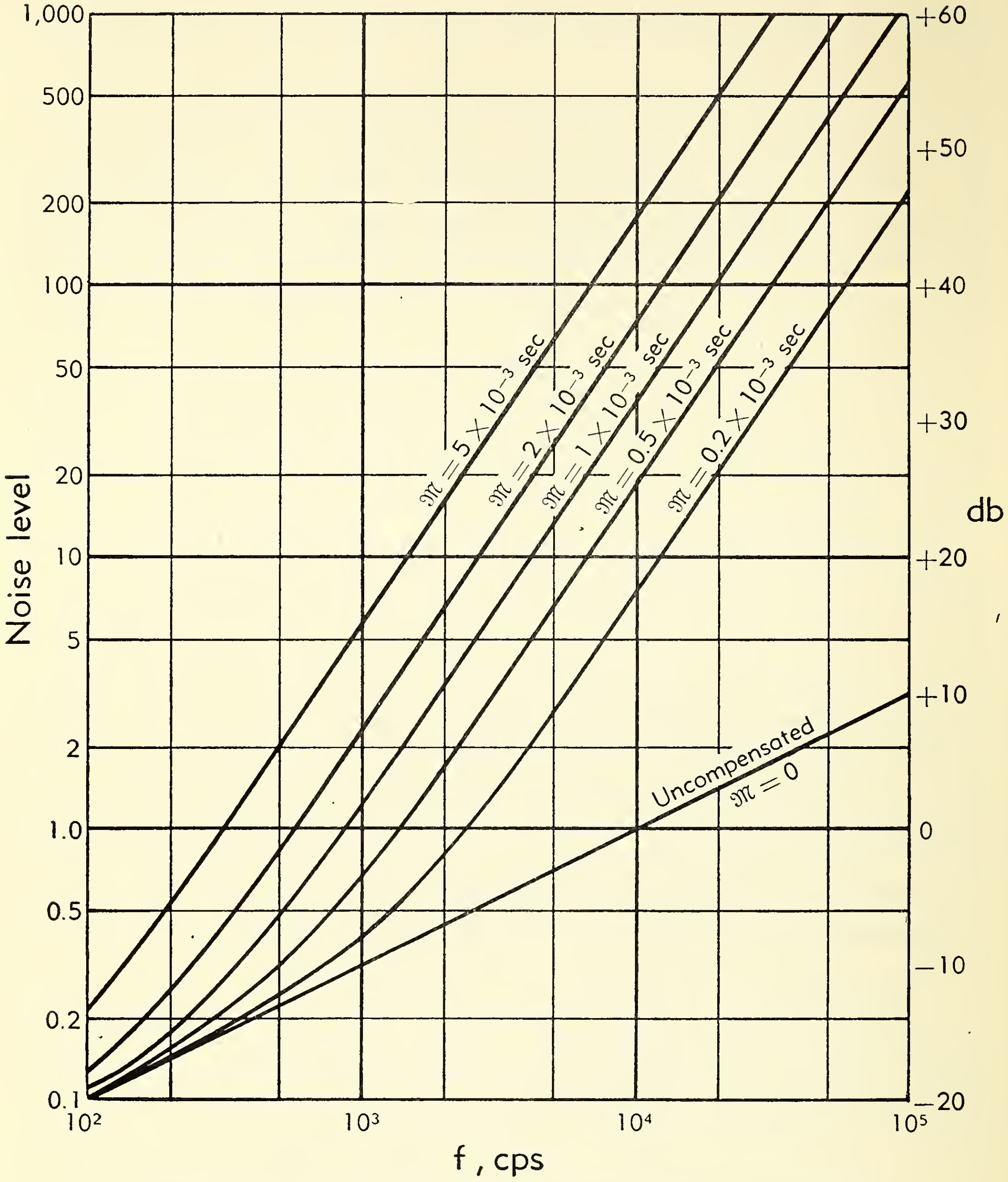

Fig. F,2.8d. Noise factor of compensated amplifiers compared with flat 10 kcps bandwidth amplifier. (From [*52*].)

The mutual inductance of the transformer and the turn ratio must be high (50 to 150). If the primary self-induction is low, the transformer primary coil has a current roughly proportional to the uncompensated hot wire voltage. The secondary is practically unloaded since the input impedance of the amplifier is very high. Therefore the transformer acts as a pure differentiating circuit and the voltage appearing across the secondary coil adds a differentiated voltage to the uncompensated hot wire voltage. This is exactly what is required for compensation:

$$e_v = e + \mathfrak{M}\frac{de}{dt}$$

The time constant value is determined by the mutual inductance of the transformer and the total impedance appearing at the transformer primary terminal. It can be adjusted with the variable resistor R_1 in series with the transformer primary. The transformer voltage vanishes at a low frequency and the hot wire is plainly coupled to the amplifier. In this case the system does not have the disadvantage of a transformer coupling. On the other hand, the shunting effect of the transformer primary circuit across the bridge modifies the hot wire sensitivity and, at the same time, the time constant value. This can be computed using the formulas

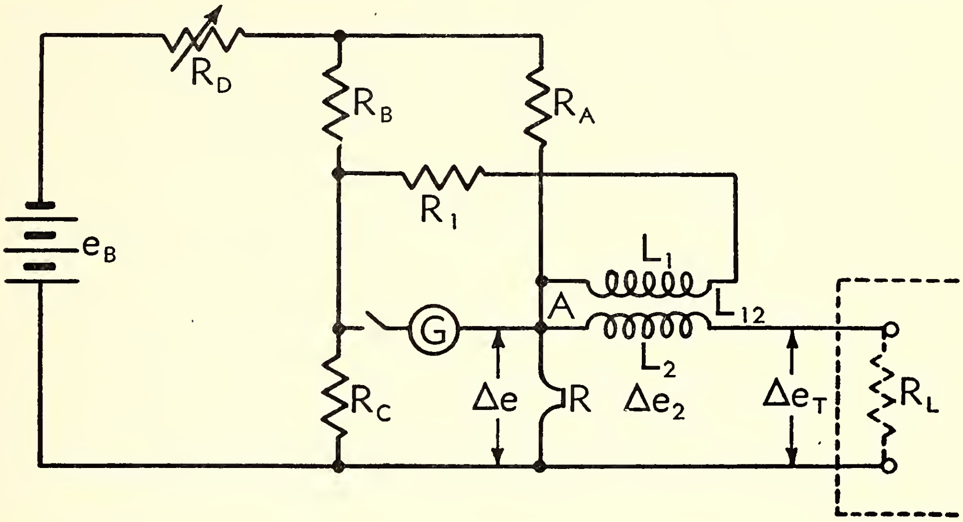

Fig. F,2.8e. "Poor man's" compensation.

$$\mathfrak{M} = \frac{\mathfrak{M}_0}{1 + 2a'_w\epsilon}, \qquad E = \frac{1 - \epsilon}{1 + 2a'_w\epsilon}$$

If $\epsilon = 0.5$ and $a'_w = 0.5$, there is a 33 per cent reduction in the time constant and a 67 per cent reduction in the sensitivity.

Output Signal Considerations. The compensated hot wire amplifier delivers an output signal that is proportional to some turbulent fluctuating quantity (temperature, velocity, density, etc.). In order to record the fluctuations or to measure their statistical properties (correlation, spectra, probability density), additional equipment is necessary. The input requirements of the additional instrument, e.g. oscilloscope, spectral analyzer, etc., determines the output specifications of the amplifier.

In the simplest case the turbulent fluctuations are observed on a cathode ray oscilloscope without any further processing. Since most oscilloscope inputs are of rather high impedance (in the range of megohms) and the required output voltage is low (20 to 50 millivolts), the oscilloscope does not put heavy requirements on the output circuits. If the output is sufficient for other equipment, the oscilloscope can be connected to it also.

The simplest type of statistical average is the mean square value of the fluctuation. This can be obtained most conveniently by means of a vacuum thermocouple. Unfortunately this is a low impedance instrument and responds to current, not to voltage. The current output of an amplifier is more limited than the voltage output chiefly because it can be obtained only by using power tubes of high current rating. The highest impedance vacuum thermocouple available requires 1.5 ma current and its impedance is of the order of 800 ohms. This puts a minimum requirement on the amplifier current output, which, in turn, determines the voltage necessary to drive the power stage. Transformer coupling is usually out of the question owing to its poor frequency response in the very low frequency range (1 to 10 cps).

The usual arrangement is capacitance-resistance coupling or direct coupling in a push-pull stage. In the case of capacitance coupling the time constant of the *RC* circuit must be sufficiently large to pass the lowest frequency. This requires either bulky capacitors or large resistors in series with the thermocouple. Large resistors need additional voltage output in the power stage to take care of the high impedance thermocouple circuit. In the case of the push-pull power stage the thermocouple can be connected from cathode to cathode by direct coupling, but some provision must be made for the d.c. balance.

Hot wire amplifiers differ in one essential way from ordinary amplifiers. An amplifier is usually tested for nonlinearity with sine waves. The nonlinear effect is maximum at the peaks of the sine waves, that is, when the instantaneous value is $\sqrt{2}$ times the rms value. However, in the case of a signal of the random noise type, such as turbulence, the probability of amplitudes has a Gaussian distribution with a "tail" reaching to infinity; therefore occasional high peaks must be considered and the nonlinear effect becomes pronounced at a much lower rms value than it does with sine waves. As a practical limit nonlinearity cannot be tolerated at values lower than three times the rms value. Therefore the overload limits must be almost twice as conservative as for sine waves.

The maximum over-all amplification is determined by the minimum signal to be measured. It is required that input signals having rms values equal to the rms value of the thermal noise be measured conveniently. In other words the thermal noise of the first stage should give an output meter recording which is 5 to 15 per cent of the safe maximum signal.

This entire reasoning applies to "straight" amplification. However, the thermal lag compensation gives additional amplification, depending on the required ceiling-to-floor ratio. A practical example of a hot wire amplifier is given below. (This equipment was built as a joint project between the National Bureau of Standards and The Johns Hopkins University in 1949–1950.)

Total amplification (straight)	10,000
Ceiling-to-floor ratio	250
Maximum amplification	2.5×10^6
Input noise level uncompensated	3 to 4 microvolts (rms)
Input noise level compensated	50 to 500 microvolts (rms)
Time constant	0 to 5.0 milliseconds
Maximum output signal before clipping	40 volts
Input signal causing overload at maximum gain	4 millivolts
Gain control attenuator 17 steps, each step in the ratio	$1:\sqrt{2}$
giving a total ratio	1:256
Impedance of the thermocouple circuit	20,000 ohms
Total transconductance at maximum gain	1 mho
Frequency response	2 to 70,000 cps

The spectrum of turbulence rapidly falls off toward higher frequencies. The amplifier noise, on the other hand, increases with increasing frequency because of the additional gain (6 db/octave) due to compensation. Therefore the signal and the noise spectrum always intersect at some frequency beyond which practically no information is obtained from the measurement. This necessitates some kind of variable frequency cutoff filter in order to minimize the noise contribution from a frequency band that contributes no information to the signal.

F,2.9. Statistical Processing of the Hot Wire Anemometer Output Signal.

ANALYSIS OF A SINGLE SIGNAL. The simplest mean quantity is the mean square measured by the thermocouple. A more involved analysis gives the relative distribution of energy with respect to frequency, which is called the power or energy spectrum of the signal. Inferences can then be made to the spatial wave number spectrum, which occupies an important position in turbulence theory. The energy spectrum is measured essentially by filter circuits that have a narrow passband, and the energy contribution in the selected band is measured by some mean square meter. Mathematical relations establish a one-to-one correspondence between the energy spectrum and the spatial correlation coefficient [*4*]. An entirely different type of information can be obtained by feeding the hot wire amplifier output into a statistical analyzer. As the frequency analyzer measures the contributions from various frequencies, the statistical analyzer measures the contributions from various amplitudes. Probability values indicate which fraction of the total time the signal spends in the neighborhood of any specified value.

The signal can be differentiated with respect to time once or twice, and the ratio of mean square values of the signal and its derivative can be interpreted as an important parameter of the turbulent flow (the microscale).

If there is a memory device available and part of the signal can be stored (magnetic tape or sound track), a 2-point (or more) statistical analysis is possible with respect to time, and correlation functions between the two points separated in time can be measured [*21*].

Two-Signal Analysis. If two hot wires are placed at two different points in the turbulent fluctuating field, two complete time recordings can be taken and several statistical quantities, involving the combination of the two signals, can be formed, revealing spatial parameters pertinent to the distribution of turbulent fluctuations in space.

The customary method of measuring correlation between two signals is the so-called "sum and difference" method. If the sum and the difference of the two signals are formed and the mean square of each combination is measured, the difference between the two mean square signals is proportional to the mean product of the two signals according to the equations below.

If $f(t)$ and $g(t)$ are the two signals

$$\overline{[f+g]^2} = \Sigma^2, \qquad \overline{[f-g]^2} = \Delta^2$$

$$\Sigma^2 - \Delta^2 = 4\overline{fg}, \qquad \Sigma^2 + \Delta^2 = 2\overline{f^2} + 2\overline{g^2}$$

$$R = \frac{\overline{fg}}{\sqrt{\overline{f^2}}\,\sqrt{\overline{g^2}}} = \frac{\Sigma^2 - \Delta^2}{\Sigma^2 + \Delta^2}\left(1 + \frac{\overline{g^2}}{\overline{f^2}}\right)\frac{1}{2}\sqrt{\frac{\overline{f^2}}{\overline{g^2}}} \tag{2.9-1}$$

if $\overline{g^2} = \overline{f^2}$,

$$R = \frac{\Sigma^2 - \Delta^2}{\Sigma^2 + \Delta^2} = 1 - \frac{2\Delta^2}{\Sigma^2 + \Delta^2} \tag{2.9-2}$$

$$1 - R = \frac{2\Delta^2}{\Sigma^2 + \Delta^2} = F\left(\frac{\Delta^2}{\Sigma^2}\right)$$

If the mean square of the two signals is made equal before forming the sum and difference, the equation is simplified and the correlation coefficient becomes a unique function of the ratio of the mean square of the sum and the mean square of the difference. This suggests the possibility of using some kind of ratio-sensitive meter that can be calibrated in terms of the correlation coefficient. Unfortunately the sum and difference method inherently becomes inaccurate when the correlation approaches zero, mainly because the method is primarily sensitive to $1 - R$ and not to R.

A different method for determining the correlation is to measure directly the mean product of the two signals. This can be done by an electrodynamometer, essentially an instrument that gives readings proportional to the product of the currents in the two coils. On the other hand, the self-induction of the electrodynamometer coils gives rather poor frequency response, and the instrument cannot be used for signals containing substantial contributions above 800 cps.

An alternate method is to produce instantaneous multiplication by a pentagrid tube balanced modulator and to average the product with an output instrument. This method seems especially suitable for low correlation coefficients. On the other hand, the alignment of the balanced modulator with sufficiently high quality presents a certain amount of difficulty.

Basically the correlation process should be performed on the signals obtained from two hot wires after proper compensation and amplification. In practice, on the other hand, it is satisfactory to combine the two signals before amplification and compensation, provided that the time constants of the two wires are nearly equal. The only operations involved are forming the sum and difference, amplification, and compensation. All are linear operations. The order of the sequence in this case is immaterial, and considerable saving in complexity of the electronic equipment can be achieved by making a combination of the signals before amplification. On the other hand, if the two wires have widely different time constants, i.e. they are operated in different regions or at different temperatures, separate amplification and compensation is imperative. The frequency response fundamentally alters the correlation coefficient. This is obvious from the transformation between correlation and spectrum, since they are Fourier transforms of each other. A modification of the spectrum by a nonuniform frequency response naturally alters the correlation.

SHEAR CORRELATION. A rather important case of correlation between two signals is the correlation coefficient between two perpendicular components of the velocity fluctuations at the same point. Forming the sum and difference in this case is conveniently done by the two wire probes themselves (X probes or V probes), since one of the wires gives a sensitivity proportional to the sum and the other proportional to the difference of the two velocity components. Output of wire A is $a(t)$ and of wire B is $b(t)$. For small fluctuations,

$$a(t) = \alpha u(t) + \beta v(t) \tag{2.9-3}$$

$$b(t) = \alpha u(t) - \beta v(t) \tag{2.9-4}$$

where $u(t)$ and $v(t)$ are the velocity fluctuations along and across the mean flow, and α and β are sensitivity constants.

$$\overline{(a+b)^2} = 4\alpha^2\overline{u^2} \tag{2.9-5a}$$

$$\overline{(a-b)^2} = 4\beta^2\overline{v^2} \tag{2.9-5b}$$

$$\overline{a^2} - \overline{b^2} = 4\alpha\beta\overline{uv} \tag{2.9-5c}$$

$$\overline{a^2} + \overline{b^2} = 2\alpha^2\overline{u^2} + 2\beta^2\overline{v^2} \tag{2.9-5d}$$

By taking four measurements separately, the mean square fluctuations obtained from the first wire, from the second wire, from the sum, and from the difference can give the values of the mean square fluctuations of both components and the correlation between them [*25*,*26*,*27*,*28*].

Velocity Temperature Correlation. Another important correlation is the correlation coefficient between velocity and temperature fluctuations at the same point. As given in Eq. 2.7-8, a simple hot wire gives response to both the temperature and the velocity (mass flow) fluctuations; but the two fluctuation sensitivities vary differently with varying temperature of the wire. If the wire is almost unheated, there is mainly temperature fluctuation sensitivity (the wire acts as a resistance thermometer). On the other hand, when heated to a high temperature, the velocity (mass flow) sensitivity is predominant. Taking n readings of the mean square fluctuations at n different wire temperatures, n equations for three unknowns (mean square velocity fluctuations, mean square temperature fluctuations, and velocity-temperature correlation) are obtained, and they can be solved for the three unknowns if n is at least three. In case of more than three equations, they can be solved by the method of least squares. Exactly similar reasoning gives a possibility of solving for the mass flow fluctuation, stagnation temperature fluctuation, and stagnation temperature mass flow correlation in the case of supersonic flow [*25*,*26*,*27*].

Triple Correlation. The type of triple correlation that is of interest in turbulence is the correlation between a fluctuation and the square of another fluctuation, e.g. $\overline{f(t)[g(t)]^2}$. The practical difficulty that arises is that the triple correlation is never very high; therefore the correlation measurement between the squared signal and the other signal must be accurate to give any relative accuracy in the triple correlation. Actual circuit arrangement is given in Fig. F,2.9a and is described in detail in [*29*]. The calibration of a triple correlation measuring device can be obtained only from signals that have a known triple correlation, e.g. some periodic signal that contains a certain amount of second harmonic component of proper phase.

Time Correlation. Correlation coefficients are usually measured in turbulence between signals that are obtained from two different points in the field. On the other hand, it is possible to take the two signals at the same point but at different times. The formulation of such a correlation

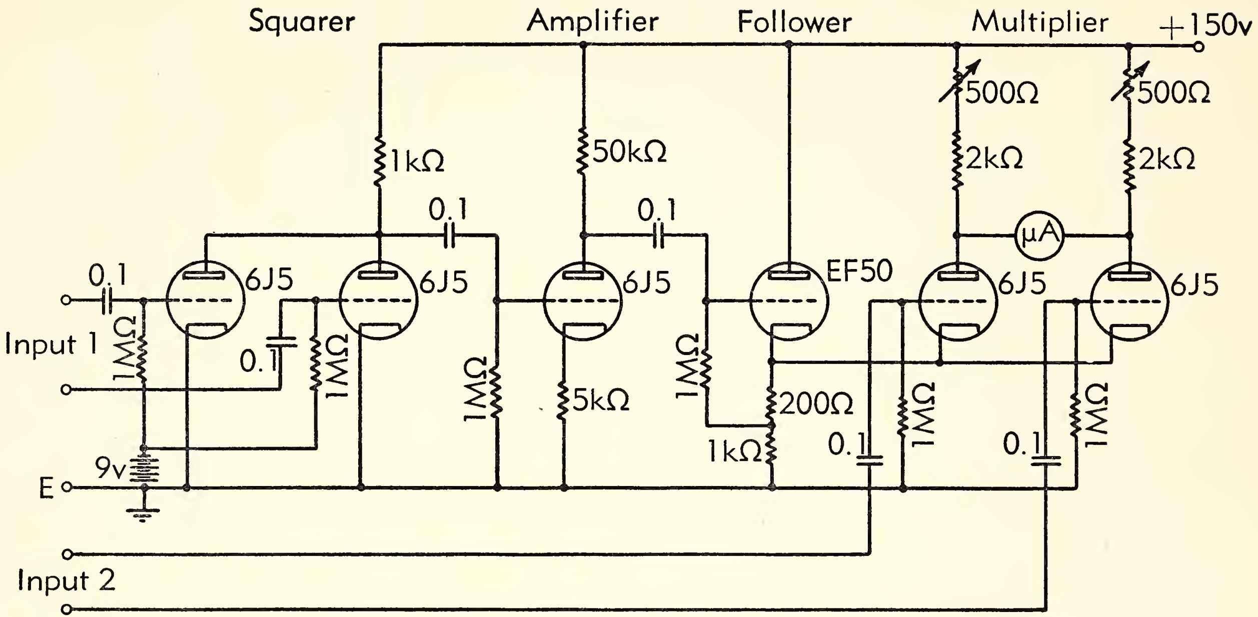

Fig. F,2.9a. Circuit for measurement of triple correlations (Townsend). (From [*29*].)

]

necessitates the use of some dependable delay mechanism producing a time difference between the two signals. This delay can be obtained by some recording medium, e.g. magnetic tape, sound track, or possibly electrostatic recording. The measurement of time correlation has the direct advantage that it is comparable to energy spectrum measurement without resorting to the time-space conversion hypothesis. Such measurements have been carried out by Favre [*21*].

Energy Spectrum. For analyzing the spatial structure of the turbulence pattern, two alternative methods are available to describe the same phenomena: one is the correlation function, the other is the spectrum. The relationship between correlation and spectrum is a one-to-one correspondence as long as the functions satisfy certain requirements. This relationship, first established by Wiener [*43*], makes it possible to use whichever of the two descriptions may be more accessible to the measurement or more revealing in terms of a theoretical model. Naturally the hot wire measurements give a time function, and the corresponding correlation is defined as a space function. The connection between time and space is a debatable point in the interpretation of experimental results. The relationship between the spectrum (in terms of time frequency) and the correlation (in terms of space separation), first stated by G. I. Taylor [*4*], is

$$R(x) = \int_0^\infty F(f) \cos\left(\frac{2\pi f x}{U}\right) df \tag{2.9-6}$$

$$F(f) = \frac{4}{U} \int_0^\infty R(x) \cos\left(\frac{2\pi f x}{U}\right) dx \tag{2.9-7}$$

where $R(x)$ is the correlation coefficient between velocity fluctuations in the x direction at points x distance apart. $F(f)$ is the energy spectrum of turbulent velocity fluctuations in the x direction normalized in such a way that

$$\int_0^\infty F(f)df = 1$$

f is the frequency (cps), and U the mean velocity in the x direction.

The spectrum can be measured by electronic devices, and the measurement does not involve two hot wire probes as does the correlation. From a theoretical point of view the contribution to the energy by various frequency (wave number) components is easier to visualize than the corresponding role of the correlation function. The measurement of spectrum is carried out by several different methods.

The easiest method of measuring the energy spectrum involves the use of high and low pass filters of variable cutoff frequencies. These filters pass signals containing contributions only above or below certain specified frequencies. If the total energy above a certain frequency is measured as a function of the cutoff frequency, the integral function of the energy spectrum is obtained. In order to get the energy spectrum, differentiation is required with respect to the frequency. This makes the method somewhat inaccurate, especially at extreme frequencies where the per cent change in the integrated energy is very small, causing the spectrum function to be very inaccurate [*31*].

The most conventional method of measuring the energy spectrum is to pass the signal through a narrow band filter and measure the mean square fluctuation of the signal distorted by the band filter. Depending on the shape of the band, corrections must be made for the relative sensitivity of the method according to the variations of the band shape and response. Basically there are two types of variable band filter instruments. In one type the band shape for all frequency settings is similar in terms of per cent of the absolute central frequency, and in the other the band shape is a constant for all frequencies. In the first case the equivalent bandwidth increases with increasing frequency. The resulting measurement gives the spectrum function directly only if divided by the frequency (or a quantity proportional to it). In the case of a fixed band shape the result of the measurement gives a quantity proportional to the energy spectrum, but the factor of proportionality that established the absolute level still depends on the equivalent bandwidth.

If the energy spectrum of the analyzed signal is denoted by $E(f)$ and the mean square output of the filter is $E_1(f_1)$, the total energy gives the normalization

$$\overline{u^2} = \int_0^\infty E(f)df \tag{2.9-8}$$

The spectrum of the output signal

$$E_1(f_1) = \int_0^\infty |Y(f_1, f)|^2 E(f)df \tag{2.9-9}$$

where $Y(f_1, f)$ is the filter transfer function (usually complex) and f_1 the nominal analyzing frequency. If the band shape is the same for all frequencies

$$Y(f_1, f) = Y(f - f_1) \tag{2.9-10}$$

and the integral

$$\int_0^\infty |Y(f - f_1)|^2 df = f_B \tag{2.9-11}$$

can be defined as the "equivalent bandwidth." If the bandwidth is small and the spectrum function is "slowly varying"

$$E_1(f_1) = f_B E(f_1) \tag{2.9-12}$$

For constant percentage bandwidth

$$Y(f_1, f) = Y\left(\frac{f}{f_1}\right) \tag{2.9-13}$$

and

$$\int_0^\infty \left| Y\left(\frac{f}{f_1}\right)\right|^2 df = Cf_1 \tag{2.9-14}$$

$$E_1(f_1) = Cf_1E(f_1) \tag{2.9-15}$$

For a single sine wave tuned to the peak of the band, there is no difference in performance between the two types of analyzers; however, for random signals, e.g. white noise, in the constant percentage bandwidth analyzer, the response increases in proportion to the widening of the band.

Circuits which contain the constant percentage equivalent bandwidth are usually selective amplifiers with a negative feedback through a Wien bridge. The nondimensional frequency response of this type of circuit is the same for all central frequencies; therefore the attenuation in the side bands is simply proportional to the ratio of the detune frequency to the central frequency (see Eq. 2.9-13).

Constant band shape filters are physically realized by superheterodyne circuits transposing the frequency band in the neighborhood of a fixed frequency and using the fixed filter for band filter, which guarantees constancy of the band shape. There are two cases. In one, the local oscillator of the superheterodyne varies as the analyzing frequency; the difference frequency is in the neighborhood of the zero frequency and a simple sharp cutoff low pass filter provides the fixed frequency band filter; in the other case a high combination frequency is chosen. Outside of the useful band, a high Q filter, e.g. crystal, is used at a fixed frequency (20 to 100 kcps).

The band shape of a spectral analyzer is determined by sine waves. If the signal is a stationary random function, the output of the filter will be also a stationary random function. The output mean square instrument has a finite integration time resulting in a fluctuating reading. The statistical fluctuations of the output expressed as a fraction of the mean reading will be inversely proportional to the product of the integrating time and the bandwidth of the filter. The necessity of long averaging time puts a practical lower limit on the permissable bandwidth. Another limit is set by keeping peak values within the operating limits of the multiplication element (balanced modulator) of the superheterodyne system. As the bandwidth is reduced, a smaller fraction of the total energy is included. This must be within the sensitivity of the system.

It can be proven that the energy spectrum of the time derivative of a function is the energy spectrum of the original function weighted with the square of the frequency. However, the total integral of the spectrum weighted with the frequency square is proportional to the mean square value of the derivative and is related simply to the microscale of turbulence λ. This gives a possibility for measuring the microscale of turbulence by differentiating the hot wire output with respect to time and comparing the mean square value of the derivative to the mean square value of the function.

$$\frac{1}{\lambda^2} = \frac{4\pi^2}{U^2} \int_a^\infty f^2 E(f) df \qquad (2.9\text{-}16)$$

The actual circuiting and detailed treatment can be found in [*29*].

The formation of the mean square of the derivative can be obtained with certain restricted statistical safeguards by counting the zeros of the original random function as shown below under heading: Probability Functions.

The energy spectrum of turbulent fluctuations can be regarded as the contribution from various frequencies (wave numbers).

By similar reasoning the shear spectrum can be defined as the contribution to the quantity $\overline{uv}$. This quantity can be measured with a hot wire probe that is sensitive to u and v separately and with a conventional spectrum analyzer as described above. The two hot wires of a V′ meter are sensitive both to the longitudinal and transversal velocity components, but the coefficients of sensitivity are different for the two components. One wire gives an output proportional to $u + v$, and the other an output proportional to $u - v$. Taking the mean square of the sum and the mean square of the difference of the two signals, the shear term $\overline{uv}$ is obtained. If the individual signals are put through a narrow band before taking the mean square, the mean square of the sum and difference can be measured within the narrow band and the contribution to the term $\overline{uv}$ from the narrow band can be determined. Naturally this method is sufficiently accurate only when the shear correlation coefficient is rather high since the inaccuracy is governed by the difference of the mean squares compared to the inaccuracy in the mean squares themselves. This sets the practical limit to cases where the coefficient of the shear correlation is of the order of 0.1 or higher. Experimental results are given in [*33*].

PROBABILITY FUNCTIONS. The probability functions give a description of a random function entirely different from correlations or spectra. The probability of finding certain values of a function is a quantity that describes the occurrence of amplitude irrespective of spatial or time structure. The simplest method of obtaining the probability density of a random signal is to put the signal on a cathode ray oscilloscope and take long time exposures. The photographic density is proportional to the time that the cathode ray spot remains in the region, and if the photographic process is properly calibrated, the probability density can be determined by measuring the photographic density as a function of amplitude. This method was first used by Simmons [*32*] to measure the mean square of turbulent fluctuations when no other rms meter was available.

If a random function $u(t)$ lies between the values u_1 and $u_1 + du_1$, for a fraction of the total time $p(u_1)du_1$, $p(u_1)$ is called the probability density. The normalization of $p(u_1)$ is

$$\int_{-\infty}^{+\infty} p(u_1)du_1 = 1 \tag{2.9-17}$$

The measuring techniques essentially produce a discrimination between various values and add up the time spent within a "band" of amplitudes. Different electronic solutions are available. The simplest is given by Townsend [*29*] with a variable electronic gate circuit. Two sharp cutoff circuits are operated in such a way that a difference of the two outputs occurs only if the signal is higher than one of the two cutoff biases but smaller than the other. In this way the output signal is an "on and off" type of pulse signal, being "on" whenever the analyzed signal is within the gate. The integration is performed by a d.c. instrument of considerable inertia and damping and the calibration of the circuit can be performed by a variable amplitude square wave. If the square wave is symmetrical, the function has a certain positive value 50 per cent of the time, and thus the gate circuit can be calibrated.

A different technique is to use discrete counting to perform the averaging process instead of a running integration of a d.c. signal. The output of the gate circuit is an "on and off" type of square wave signal with pulses of definite duration and spacing. When the pulse is "on," signals in the gate can be analyzed. If short duration pulses from an independent source are provided (either periodic or random), the product of the two pulse systems is a new pulse system which has pulses only when the two pulse trains overlap. This is what is called electronic sampling of a function. The random square wave function describes the occurrence of certain amplitudes that are being sampled by a periodic or random pulse. This reduces the problem of integration to a coincidence count. The principal advantage of this scheme is that the integration process is not tied to any particular type of integrating circuit which gives a limited response; by totaling counts both the integration time and the sampling rate can be chosen at will.

If an extremely slow sampling rate is selected, each sample can be regarded as an independent experiment which, in turn, gives an average that can be considered as an ensemble average rather than as an ordinary time average. Details of the sampling method are given in [*34*].

The desire to perform integration by totaling counts with some discrete process led to the development of measuring the mean square derivative of a function by counting the number of zeros, i.e. counting the number of crossings of the time axis. The zero count does not give the average of the mean square slope. It does this only if the function and its time derivatives are statistically independent. The independence means that, when sampling the function at certain amplitudes, the relative distribution of all values of the slope is the same irrespective of the values chosen for the function. If Gaussian distribution of the function and its derivatives is assumed in addition to the statistical independence, the zero count can be related directly to the mean square slope, and the microscale can be inferred from the zero count [*34*]. The mathematical treatment is given in [*35*].

The probability density of a random function can be characterized by its various moments. The first moment is zero by definition; the second moment is what is ordinarily called mean square; the third and fourth moments characterize skewness and kurtosis respectively. The skewness factor is defined as

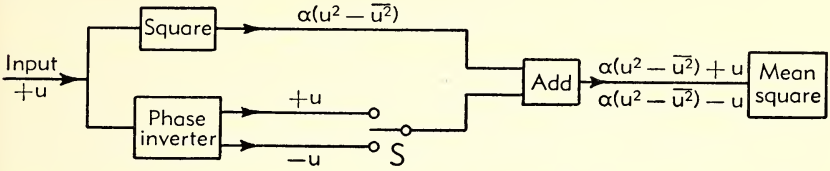
Square
$\alpha(u^2 - \overline{u^2})$
Input
$+u$
Add
$\alpha(u^2 - \overline{u^2}) + u$
$\alpha(u^2 - \overline{u^2}) - u$
Mean square
Phase inverter
$+u$
$-u$
S

Fig. F,2.9b. Block diagram for measurement of skewness and kurtosis (Townsend).

$$S = \frac{\overline{u^3}}{(\overline{u^2})^{\frac{3}{2}}} \tag{2.9-18}$$

and the flattening factor or kurtosis as

$$\beta_4 = \frac{\overline{u^4}}{(\overline{u^2})^2} \tag{2.9-19}$$

The skewness factor has a significant role in turbulent theory because its finite value reflects the nonlinear nature of the governing dynamic equations. The flattening factor, on the other hand, is a direct measure of the intermittency in a partly turbulent, partly nonturbulent flow [*50*].

Both quantities can be found by integration if the probability density curve is available. On the other hand, there is a direct method for measuring both of them without resorting to the point-by-point measurement of the probability density just as in measuring the second moment (mean square) [*50*]. The circuit shown in Fig. F,2.9b essentially consists of a squaring circuit with an adding and subtracting feature. If the squaring circuit has an a.c. output, its output is essentially the difference between the instantaneous square and the mean square. By adding or subtracting the original signal from the squared signal, two signals are obtained whose mean squares also contain third and fourth order terms. By appropriate combinations it is possible to solve for the mean cube and the mean fourth powers which yield the skewness and flattening factors. Depending on the position of the switch (S in Fig. F,2.9b), the mean square output is measured.

$$\theta_+ = A\overline{[u + \alpha(u^2 - \overline{u^2})]^2}$$

$$\theta_- = A\overline{[-u + \alpha(u^2 - \overline{u^2})]^2}$$

$$\theta_1 = A\overline{[u]^2} \qquad \text{(squared signal switched off)}$$

$$\theta_2 = A\alpha\overline{(u^2 - \overline{u^2})^2} \qquad \text{(direct input switched off)}$$

$$\theta_+ - \theta_- = 4A\alpha\overline{u^3} \tag{2.9-20}$$

$$1 + \frac{\theta^2}{\theta_1^2}\frac{\alpha^2}{A^2} = \frac{\overline{u^4}}{(\overline{u^2})^2} \tag{2.9-21}$$

The joint probability distribution of two random variables is defined as the fraction of time that one variable is between u and $u + du$ and the other variable is between v and $v + dv$ simultaneously. If great accuracy is not required, the measurement can be made simply by feeding each signal to a pair of the deflecting plates of a cathode ray tube. The luminous spot describes a random Lissajous figure, and taking a long time exposure, the total amount of light that arrives at any point is proportional to the joint probability density of the two variables. The photographic density obtained is a function of the total amount of light, therefore, of the joint probability density. For greater accuracy two gate circuits and a coincidence circuit between the outputs of the two gate circuits can yield the joint probability density. The different second moments of the joint probability density give the mean square of the two signals separately, and the correlation between them.

$$\int_{-\infty}^{+\infty}\int_{-\infty}^{+\infty} u^2p(u, v)dudv = \overline{u^2} \tag{2.9-22}$$

$$\int_{-\infty}^{+\infty}\int_{-\infty}^{+\infty} v^2p(u, v)dudv = \overline{v^2} \tag{2.9-23}$$

$$\int_{-\infty}^{+\infty}\int_{-\infty}^{+\infty} uvp(u, v)dudv = \overline{uv} \tag{2.9-24}$$

Fig. F,2.9c shows the arrangement for measurement of joint probability density by the photographic method.

Corrections for Finite Wire Length of the Hot Wire Probe. The hot wire probe, however small, is of a finite dimension, and it averages over this finite dimension. This averaging process may distort the experimental results in the case when the measured quantity varies appreciably along the wire. A unified treatment of measuring random fields by a finite probe is given in [*36*].

When the effect of the finite probe dimension is small, simple corrections can be used. These corrections have been worked out for the mean square of the velocity fluctuations, for measurement of correlation coefficient between the velocity of two different points [*37*], and for measurement of energy spectrum by a finite probe [*36*].

The measured correlation is related to the true correlation by an integral equation, but if only the measured correlation is known, it is difficult to solve for the true correlation. A simple graphic method is given in [*36*]. If the measured correlation is plotted against the square of the distance between two points and the average slope is determined at every point, the true correlation in terms of measured correlation is given as

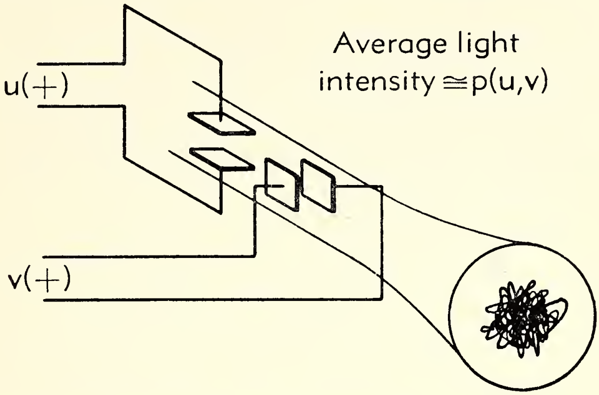

Fig. F,2.9c. Measurement of joint probability density for two variables.

$$R(r) = \mathcal{R}(r)[1 - \Delta R(0)] + \Delta R(r) \tag{2.9-25}$$

where

$$\Delta R(r) = \mathcal{R}(\sqrt{r^2 + 0.1l^2}) - \mathcal{R}(r) \tag{2.9-26}$$

$\mathcal{R}(r)$ is the measured correlation coefficient, $R(r)$ the true correlation coefficient, and l the length of the wire.

It is interesting to note that the correction can be both positive and negative; it vanishes in cases where the correlation coefficient is an error function. The correction for the mean square fluctuation is simply given as

$$\frac{\overline{u^2}_{\text{meas}}}{\overline{u^2}_{\text{true}}} = R(0.316l)$$

in terms of the quantities defined above.

The effect of finite wire length on spectrum measurements can be computed only if isotropy is assumed in the field, because this is the only case in which the so-called three-dimensional spectrum has a one-to-one relationship to the measured one-dimensional spectrum. The measured spectrum falls off compared to the true spectrum with a function depending on the ratio between the wire length and the wavelength corresponding to the particular wave number. Unfortunately this weighting function operates on the three-dimensional spectrum and its expression for the one-dimensional spectrum is rather involved. On the other hand, if some simple analytic assumption is made for the three-dimensional spectrum, the integration can be carried out. For example, if the three-dimensional true spectrum is assumed to obey a power law, the one-dimensional spectrum has the same power law. If both spectra vary with a $(-n)$ power of the frequency (wave number), the measured spectrum obeys the same $(-n)$ power law for low frequencies but attains a $-(n + 1)$ power asymptotically at high frequencies. In a logarithmic plot, both power laws appear as straight lines and the intersection of the two asymptotes occurs at the frequency where the corresponding wavelength is comparable to the wire length. Numerical details are given in [*36*].

ARTICLE F,3

OPTICAL TECHNIQUES

F,3.1. Introduction. Turbulence measurement with the hot wire or any other type of probe inherently requires a finite probe in the flow field, necessarily disturbing the flow field itself. There are cases in which excessive temperature or other circumstances make the use of probes impossible. Flow fields of this nature are still accessible by optical methods which extract certain information about the turbulent flow field. The light passes through the entire cross section of the flow to be analyzed and is affected by changes in the refractive index of the medium. In gases the refractive index is practically a linear function of the density; therefore all optical methods reveal information only about the density. The optical methods (except for the so-called sharp focusing schlieren) respond to the average density along the light ray, which introduces an averaging process that is outside the control of the experimenter. The turbulence measurement must be designed in such a way that this integration takes into account the statistical properties. The sensitivity of optical methods to density fluctuations restricts the use of these techniques to turbulent fields with a substantial change in density.

Turbulence is strikingly noticeable on shadow pictures, taken with short duration spark light sources (0.5 to 5 μsec) because the shadow method emphasizes the strong gradients in the density. In a turbulent flow field the density fluctuations are usually small. However, since the characteristic dimension of the density "patches" is also small, the gradient and higher derivatives are large.

The interferometer has the advantage that its readings are directly proportional to the average density across the flow field. Taking a record of the variations in average density is equivalent to measuring the average density along a light beam which is analogous to measuring with a hot wire that stretches across the field. This feature of the interferometer makes it useful for obtaining information similar to that which can be obtained with a very long hot wire. However, this can be regarded as a workable scheme only in cases where the hot wire cannot be used (especially in combustion).

The schlieren method can be used for measurement of turbulent density fluctuations, but is less readily interpreted than the shadow or interferometer method since this technique involves more parameters (knife edge orientation, relative displacement, etc.) than either of the previous two.

F,3.2. Turbulence Measurements from Shadow Pictures. The density fluctuations of a homogeneous turbulent field can be described by a scalar random field in three dimensions. If a certain thickness of this homogeneous field is exposed to parallel uniform light (Fig. F,3.2a), the local density variations act as little positive (convex) or negative (concave) lenses focusing this light. By placing a screen at some distance from the flow field, a random light intensity pattern which is related to the properties of the density fluctuations themselves can be seen. This granulated pattern (Plate F,3.2) changes slightly according to the distance of the screen from the turbulent flow field. If this distance is large enough, local turbulent density fluctuations may cause the light beam to converge into a focal point beyond which the one-to-one correspondence between the mapping and the actual turbulent density field ceases to exist. If the screen is placed close enough, the probability of a focal point occurring in front of the screen is slight, and the light beam maps the field on the screen in one-to-one correspondence. Under these conditions the evaluation of a shadow picture is considerably easier and certain statistical properties of the three-dimensional density fluctuations can be recovered by analyzing statistically the two-dimensional shadow pictures taken on the screen [*38*].

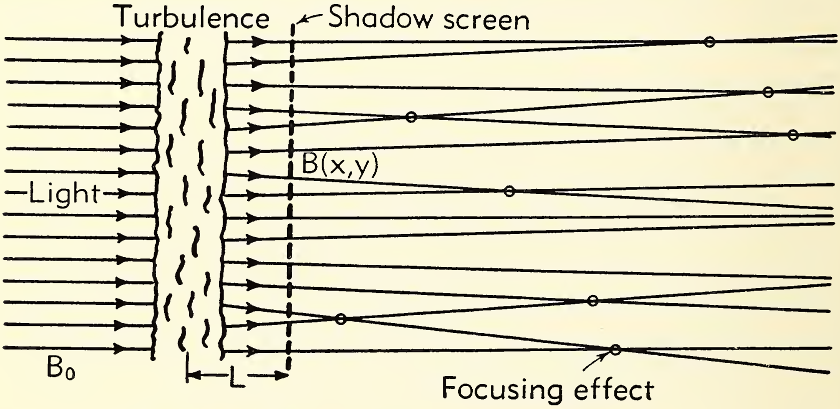

Fig. F,3.2a. Forming of shadow picture. (From [*38*].)

The mathematical relationship between the three-dimensional fluctuating field and its shadow picture is rather involved, but it can be simplified if the three-dimensional field is isotropic, in which case the power spectrum of the three-dimensional density field and the power spectrum of the two-dimensional shadow pictures are simply related. Fig. F,3.2a shows the formation of a shadow picture. The response of the shadow picture is treated in [*45*] (see A,1.4). If the distance between disturbance and screen is much smaller than the focusing distance, the light intensity compared to the intensity of the undisturbed light on the screen becomes

$$\frac{B_0 - B(x,y)}{B(x,y)} = LK \int_{-Z}^{+Z} \left(\frac{\partial^2 \rho}{\partial x^2} + \frac{\partial^2 \rho}{\partial y^2}\right) dz \qquad (3.2\text{-}1)$$

where ρ represents density fluctuations (departures from the mean), B is the light intensity obtained on the shadow picture, B_0 the undisturbed light, x, y, z are rectangular coordinates, L is the distance between disturbance and screen, and K the Gladstone-Dale constant.

The relationship is linear and the light intensity fluctuations on the screen are directly proportional to the second derivative of the density integrated along the light path.

If the density fluctuation field is isotropic, it can be characterized by a single function, called the three-dimensional spectrum of the density field, which describes the contribution to the mean density fluctuation by oblique sine waves having a wavelength $\lambda = 2\pi/k$

$$\overline{\rho^2} = \int_0^\infty E(k)dk \qquad (3.2\text{-}2)$$

The observed one-dimensional spectrum measured by a probe (hot wire) is so related to the three-dimensional spectrum that

$$E_1(k_1) = \int_{k_1}^\infty \frac{E(k)}{k} dk \qquad (3.2\text{-}3)$$

(Note: this is valid only for scalar properties.) The correlation measured between probes at a distance x apart

$$\overline{\rho(\xi)\rho(\xi + x_1)} = T(x_1) = \int_0^\infty E_1(k_1) \cos (k_1x_1)dk_1 \qquad (3.2\text{-}4)$$

The shadow picture has an intensity fluctuation $h(x, y)$. The "two-dimensional" spectrum of $h(x, y)$

$$E_2(k) = 2\pi \int_0^\infty r\beta(r)J_0(kr)dr \qquad (3.2\text{-}5)$$

This is a Fourier-Bessel transform of the correlation in the shadow pattern where

$$\beta(\xi) = \overline{h(x, y)h(x + \xi, y)}$$

and J_0 is zero order Bessel function. From Eq. 3.2-1, 3.2-4, and 3.2-5:

$$k^4E(k) = \text{const} \int_0^\infty \xi\beta(\xi)J_0(k\xi)d\xi \qquad (3.2\text{-}6)$$

relating the measured correlation of the shadow picture to the three-dimensional spectrum of density fluctuations.

The measurement of the correlation, $\beta(\xi)$, is carried out optically in the following manner. The transparency of the photographic plate (positive plate) is a simple monotonic function of the original light intensity of the shadow picture. By splitting the transparency into a mean and a fluctuation, $t(x, y) = \bar{t} + \Delta t(x, y)$. If two photographic plates are superimposed, the resulting transparency is the product of the two transparencies. By using two identical plates shifted out of register by the amounts ξ and η, the resulting transparency becomes

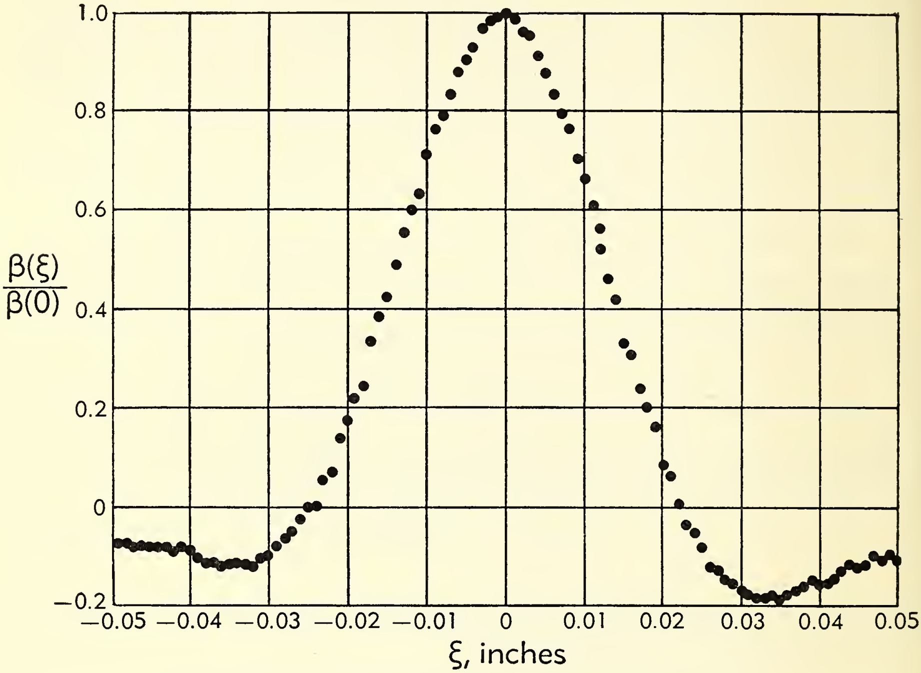

Fig. F,3.2b. Correlation coefficient of the shadow pattern.

$$t_{\text{res}} = [\bar{t} + \Delta t(x + \xi, y + \eta)][\bar{t} + \Delta t(x, y)]$$

Taking the average of the resulting transparency over an area

$$\bar{t}_{\text{res}} = \bar{t}^2 + \overline{(\Delta t)^2}\beta(\xi, \eta) \tag{3.2-7}$$

This gives a simple method for measuring the correlation from shadow pictures. Although the nonlinear features of the photographic process must be taken into account, the measurement is rather easy to perform. A typical measured correlation curve is given in Fig. F,3.2b. The transformation from the correlation measured on the two-dimensional plate to the three-dimensional spectrum of the three-dimensional fluctuation field involves the Fourier-Bessel transformation given in Eq. 3.2-6.

Because of the weighting factor k^4 the determination of the power spectrum at low wave numbers (frequencies) becomes relatively inaccurate.

In order to get an idea of the comparison between information obtained by the hot wire and by the shadow method, the correlation of the shadow method has been computed with the assumption that the ordinary correlation is Gaussian. The two curves are given in Fig. F,3.2c.

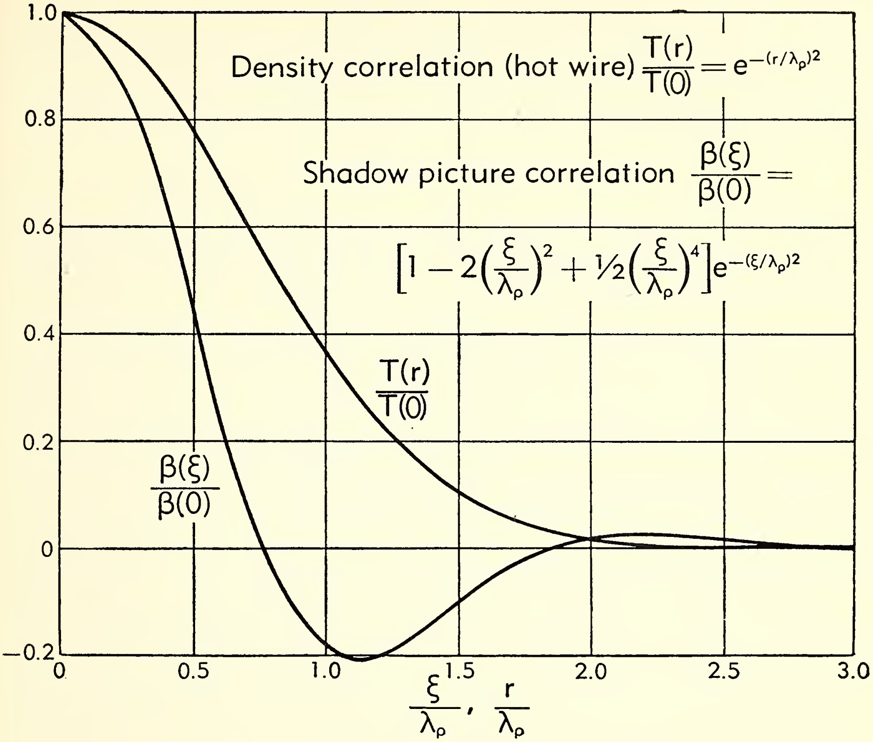

Fig. F,3.2c. Correlation coefficient of density fluctuations compared with the correlation coefficient of the shadow picture (isotropic turbulence).

Theoretically it is possible to recover the entire density correlation curve from the measured shadow correlation if the turbulence is isotropic [*36*].

The ordinary density correlation in isotropic turbulence is $T(r)$

$$T(r) = \frac{\overline{\rho^2}}{8\pi L^2 K^2 Z} \int_r^\infty \beta(\xi)\psi(\xi, r)d\xi \tag{3.2-8}$$

where

$$\psi(\xi, r) = \xi\left[\left(\frac{2r^2 + \xi^2}{r}\right)\cos^{-1}\left|\frac{r}{\xi}\right| - 3\sqrt{\xi^2 - r^2}\right]$$

L is the distance from disturbance to screen, K the Gladstone-Dale constant, $2Z$ the thickness of the turbulent region, and $\overline{\rho^2}$ the mean square density fluctuation.

In isotropic density fluctuation fields $\beta(\xi)$ must have zero first and third moments (integrated $0 \leqq \xi \leqq \infty$). The microscale of turbulent density fluctuation λ_ρ can be found directly

$$\lambda_\rho^2 = -6 \frac{\int_0^\infty \beta(\xi)\xi^2 d\xi}{\int_0^\infty \beta(\xi) d\xi} \tag{3.2-9}$$

where λ_ρ is defined as

$$-\frac{1}{\lambda_\rho^2} = \frac{1}{2}\frac{T''(0)}{T(0)}$$

Comparison between hot wire and shadow measurements indicate that this is a feasible method for measuring the microscale of density fluctuations.

F,3.3. Interferometer Measurement of Density Fluctuations. The interferometer gives information equivalent to a very long hot wire placed across the entire flow field. Because of the averaging along the light beam, the power spectrum of the interference fringe fluctuations (recorded in time) falls off compared to the true power spectrum of the density fluctuations in the same manner as it would for a very long hot wire described in Art. 2.9. The actual measurement of the interference fringe fluctuations can be obtained by projecting a portion of the fringe system of an interferometer on a slit and recording the "wiggling" of the fringe on fast moving film as a time variation [*39*] (Plate F,3.3). The time record can be analyzed similarly to the output of the hot wire and correlation (time correlation) or power spectrum can be determined. The sensitivity of this method unfortunately is not very high, principally due to the inherent low sensitivity of the interferometer. The response of the interferometer is proportional to the change in the refractive index multiplied by the length of the light path, which by dimensional reasoning can be presented as the product of a characteristic density multiplied by a characteristic length. Since the velocity involved in compressible flow is usually of the order of the speed of sound and the viscosity does not vary much, it can be safely stated that the fringe shift is roughly proportional to some characteristic Reynolds number in the flow, which automatically rules out the possibility of measuring flow fields at arbitrarily low Reynolds numbers with the interferometer. The effect of this reasoning on the measurement of turbulent density fluctuations is that the low Reynolds number range of the turbulent energy spectrum is inaccessible to this measuring method. The turbulent eddy sizes can be defined either by physical dimension or Reynolds number. If the density of the flow field is increased, the Reynolds number of an eddy of a given size increases; however eddies of smaller sizes will also appear corresponding to Reynolds numbers that were previously represented by larger eddies. Thus there will always be a limiting eddy Reynolds number at which the sensitivity fails. In practical cases explored, the total fringe shift fluctuation did not amount to more than one fringe. On the other hand, if the density fluctuations are large, e.g. combustion, and there is no other possible way of gaining information about the turbulent density field, this method can be used because it is relatively easy and comparable to the hot wire method.

F,4. Cited References.

1. Preston, J. H., and Sweeting, N. E. Experiments on the measurement of transition position by chemical methods. *ARC Rept. and Mem. 2014*, 1945.
2. Richards, E. J., and Burstall, F. H. The "China-Clay" method of indicating transition. *ARC Rept. and Mem. 2126*, 1945.
3. Preston, J. H. Visualization of boundary layer flow. *ARC Rept. and Mem. 2267*, 1946.
4. Taylor, G. I. The spectrum of turbulence. *Proc. Roy. Soc. London A164*, 476–490 (1938).
5. Kovásznay, L. S. G., and Törnmarck, S. I. A. Heat loss of hot-wires in supersonic flow. *Bumblebee Rept. 127*, 1950.
6. Lowell, H. H. Design and applications of hot-wire anemometers for steady-state measurements at transonic and supersonic airspeeds. *NACA Tech. Note 2117*, 1950.
7. Betchov, R., and Welling, W. Quelques expériences sur la non-linéarité des fils chauds. *Proc. Koninkl. Ned. Akad. Wetenschap.* (*4*) *53*, 432–439 (1950).
8. Schubauer, G. B., and Klebanoff, P. S. Theory and application of hot wire instruments in the investigation of turbulent boundary layers. *NACA Wartime Rept. W-86*, 1946.
9. Kovásznay, L. S. G. The hot-wire anemometer in supersonic flow. *J. Aeronaut. Sci. 17*, 565–572 (1950).
10. King, L. V. On the convection of heat from small cylinders in a stream of fluid. *Phil. Trans. Roy. Soc. London A 214*, 373–432 (1914).
11. Tsien, H. S., and Finston, M. Hot-wire anemometer in high speed flows. *Project Meteor Rept. 28*, 1948.
12. McAdams, W. H. *Heat Transmission.* McGraw-Hill, 1942.
13. Kovásznay, L. S. G. Hot-wire investigation of the wake behind cylinders at low Reynolds numbers. *Proc. Roy. Soc. London A198*, 174–190 (1949).
14. Betchov, R. Théorie non-linéaire de l'anémomètre à fil chaud. *Proc. Koninkl. Ned. Akad. Wetenchap. 52*, 195–207 (1949).
15. Simmons, L. F. G., and Bailey, A. A hot-wire instrument for measuring speed and direction of airflow. *Phil. Mag.* (*7*) *3*, 81–96 (1927).
16. Weske, J. R. Measurement of the arithmetic mean velocity of a pulsating flow of high velocity by the hot-wire method. *NACA Tech. Note 990*, 1946.
17. Ziegler, M. The application of the hot-wire anemometer for the investigation of turbulence of an airstream. *Proc. Koninkl. Ned. Akad. Wetenchap. 33*, 723–736 (1930).
18. Ziegler, M. A complete arrangement for the investigation, the measurement and the recording of rapid airspeed fluctuations with very thin and short hot wires. *Proc. Koninkl. Ned. Akad. Wetenchap. 34*, 663–672 (1931).

19. Kovásznay, L. S. G. Calibration and measurement in turbulence research by the hot-wire method. *NACA Tech. Mem. 1130*, 1947.
20. Kovásznay, L. S. G. Simple hot-wire anemometer. *Rept. Aero/JHU CM-573*, 1949.
21. Favre, A. Statistical measurements of time correlation. *Proc. Seventh Intern. Congress Appl. Mech. 2*, 44–45 (1948).
22. Kovásznay, L. S. G. Simple analysis of the constant temperature feedback hot-wire anemometer. *Aero/JHU CM-478*, 1948.
23. Ossofsky, E. Constant temperature operation of the hot-wire anemometer at high frequency. *Rev. Sci. Instr. 19*, 881–889 (1948).
24. Kunstman, R. W. Operating manual and service information for the constant current hot-wire anemometer. *Tech. Rept. 7, Eng. Exptl. Station, Univ. of Illinois*, 1950.
25. Corrsin, S. Extended applications of the hot-wire anemometer. *Rev. Sci. Instr. 18*, 469–471 (1947).
26. Corrsin, S. Extended applications of the hot-wire anemometer. *NACA Tech. Note 1864*, 1949.
27. Corrsin, S., and Uberoi, M. Further experiments on the flow and heat transfer in a heated turbulent air jet. *NACA Tech. Note 1865*, 1949.
28. Laufer, J. Some recent measurements in a two-dimensional turbulent channel. *J. Aeronaut. Sci. 17*, 277–287 (1950).
29. Townsend, A. A. The measurement of double and triple correlation derivatives in isotropic turbulence. *Proc. Cambridge Phil. Soc. 43*, 560–570 (1947).
30. Dryden, H. L., and Kuethe, A. M. The measurement of fluctuations of air speed in turbulent flow. *NACA Tech. Rept. 320* (1928).
31. Simmons, L. F. G., and Salter, C. An experimental determination of the spectrum of turbulence. *Proc. Roy. Soc. London 165*, 73–89 (1938).
32. Simmons, L. F. G., and Salter, C. Experimental investigation and analysis of the velocity variations in turbulent flow. *Proc. Roy. Soc. London A145*, 212–234 (1934).
33. Corrsin, S. An experimental verification of local isotropy. *J. Aeronaut. Sci. 16*, 757–758 (1949).
34. Liepmann, H. W. On the use of a counting method for the measurement of mean value in turbulent flow. Unpublished *NACA Rept.*
35. Rice, S. O. Mathematical analysis of random noise. *Bell System Tech. J. 24*, 46–156 (1945).
36. Uberoi, M. S., and Kovásznay, L. S. G. Influence of resolving power on measurement of correlations and spectra of random fields. *Project Squid Tech. Rept. 30*, 1951.
37. Dryden, H. L., Schubauer, G. B., Mock, W. C., and Skramstad, H. Measurements of intensity and scale of wind-tunnel turbulence and their relation to the critical Reynolds number of spheres. *NACA Tech. Rept. 581*, 1937.
38. Kovásznay, L. S. G. Technique for the optical measurement of turbulence in high speed flow. Heat Transfer and Fluid Mechanics Institute, Berkeley, Calif., 1949. Published by *Am. Soc. Mech. Engrs.*, 1949.
39. Ladenburg, R., Winckler, J., and Van Voorhis, C. C. Interferometric studies of faster than sound phenomena. Part I. The gas flow around various objects in a free, homogeneous, supersonic air stream. *Phys. Rev. 73*, 1359–1377 (1948).
40. Wien, W., and Harms, F. *Handbuch der Experimentalphysik. 4/1*, p. 660. Akad. Verlagsgesellschaft, Leipzig, 1935.
41. Fay, R. D. Improvement in hot-wire anemometers. *J. Franklin Inst. 183*, 783–785 (1917).
42. Runyan, R., and Jeffries, R. J. Empirical method for frequency compensation of the hot wire anemometer. *NACA Tech. Note 1331*, 1947.
43. Wiener, N. Generalized harmonic analysis. *Acta Math. 55*, 117–258 (1930).
44. Dryden, H. L. Turbulence and diffusion. *Ind. Eng. Chem. 31*, 416–425 (1939).
45. Weyl, F. J. Analytical methods in optical examination of supersonic flow. *Nav. Ord. Rept. 211-45*, 1945.

46. Liepmann, H. W., Roshko, A., and Dhawan, S. On reflection of shock waves from boundary layers. *NACA Tech. Note 2334*, 1951.
47. Charters, A. C. Transition between laminar and turbulent flow by transverse contamination. *NACA Tech. Note 891*, 1943.
48. Stalder, J. R., Goodwin, G., and Creager, M. G. Heat transfer to bodies in a high-speed rarefied-gas stream. *NACA Tech. Note 2438*, 1951.
49. Tournier, M., Laurenceau, P., Heubès, J., and Seigneurin, A. Sur l'utilisation des courants de haute fréquence pour le chauffage des anémomètres à fil chaud. *Recherche aeronaut. 19*, 11–19 (1951).
50. Townsend, A. A. Local isotropy in the turbulent wake of a cylinder. *Australian J. Sci. Research A1*, 161–174 (1948).
51. Werner, F. D. An investigation of the possible use of the glow discharge as a means for measuring air flow characteristics. *Rev. Sci. Instr. 21*, 61–68 (1950).
52. Kovásznay, L. S. G. Development of turbulence-measuring equipment. *NACA Tech. Note 2839*, 1953.
53. Ladenburg, R., and Bershader, D. Optical studies of boundary layer phenomena on a flat plate at Mach number 2.35. *Final Tech. Rept. to Office of Naval Research, Palmer Lab., Princeton*, 1952.

SECTION G

CONDENSATION STUDY BY ABSORPTION OR SCATTERING OF LIGHT

EVA M. WINKLER

SECTION G

CONDENSATION STUDY BY ABSORPTION OR SCATTERING OF LIGHT

EVA M. WINKLER

G,1. Introduction. In high speed wind tunnels where the static temperature drops below the saturation line of any one of the constituents of the streaming gas, condensation may occur. The study of condensation phenomena such as the onset of condensation, the rate of growth of the droplets, and the determination of the amount of matter condensed may be facilitated by optical observations. This may be done by utilizing the scattering phenomena observed when light is transmitted through a turbid medium. Since size and number concentration of the particles causing the turbidity determine the character and intensity of the scattered light, respectively, they may be evaluated, under certain conditions, from light scattering data. Light scattering has been utilized, so far, in relatively few cases for the study of condensation phenomena in high speed gases or vapors. Stodola [*1*] and Yellott [*2*] observed these phenomena in Laval nozzles with dry and wet steam and estimated the size of the droplets and their growth from the colors displayed in the transmitted and scattered light. Similar observations of the condensation of water vapor in air have been made by Head [*3*] and recently by Wegener and Lundquist [*4*]. Air condensation in hypersonic wind tunnels has been observed by Becker [*5*], Stever [*6*], and Wegener [*7*]. These observations are qualitative insofar as the light scattering was used mainly to indicate that condensation is present and varies with the stagnation temperature and the stagnation pressure.

The conditions under which condensation phenomena may occur, their kinetics, the expected sizes and concentrations of the particles in high speed flow are discussed in III,F. Here we are considering only the physical aspects of the light scattering and describe some of the methods for determining particle sizes and particle number concentrations.

G,2. Theoretical Considerations of Light Scattered by Spherical Particles. Scattering of light due to suspended particles was first demonstrated by Tyndall [*8*], and a few years later was investigated theoretically for small particles by Rayleigh [*9*]. In this case the intensity of the scattered light was found proportional to the inverse fourth power of the wavelength. For particle sizes comparable or larger than the wavelength of the incident light, however, the simple theory is inadequate. To describe the character of the scattered light, it is necessary to account for the size, shape, and orientation of the scattering particles. This amounts to finding a strict solution of the diffraction problem in its most general sense, i.e. an integration of Maxwell's equations for a plane parallel wave which is incident on an arbitrary surface separating two mediums possessing different optical properties. A strict solution is possible only for particles of simple geometrical forms. The problem was solved by Mie for spherical particles suspended in a transparent, homogeneous, and isotropic medium [*10*]. For other than spherical particles, the theory is still incomplete. Gans [*11*] and Möglich [*12*] considered ellipsoidal particles.

The methods of determining particle sizes and particle number concentrations from light scattering observations are based largely on the Mie theory and the contributions of Debye [*13*], Rayleigh [*14*], and Cabannes [*15*]. To illustrate the complexity of the phenomena as well as the restrictions imposed in evaluating light scattering data in practical cases, a brief account of theoretical considerations is included. However, for details on the various theoretical investigations the reader is referred to the original papers and the comprehensive reviews given by Stratton [*16*] and van de Hulst [*17*].

A plane electromagnetic wave is assumed to be incident on a suspended sphere of radius R. The electromagnetic field inside and outside the sphere is characterized by the dielectric constants, the conductivities, and the magnetic permeabilities. The integration of Maxwell's equations leads to sums of products of Legendre functions and spherical Bessel functions. Mie expressed the solution of the problem as a series of partial solutions where each partial solution corresponds to a forced mode of oscillation of the spherical particle at the frequency of the incident light. The sum of all solutions gives a formal expression of the diffracted field. Mie then represents the incident plane wave in terms of linear combinations of spherical waves on which the diffracted waves are superimposed. This sum gives the total field intensity at any point inside or outside the sphere. Finally, the amplitude coefficients are determined by consideration of the boundary conditions at the scattering surface of the sphere.

If the scattered light is resolved in two plane-polarized components which are mutually perpendicular and the intensity of the unpolarized incident light is set equal to unity, we obtain

$$I_{\mathrm{I}} = \frac{\lambda^2}{8\pi^2 r^2} i_1, \qquad I_{\mathrm{II}} = \frac{\lambda^2}{8\pi^2 r^2} i_2 \tag{2-1}$$[1]

---

[1] Mie writes $\frac{1}{4}$ instead of $\frac{1}{8}$; for an explanation of the factor $\frac{1}{2}$ reference is made to the discussion in [*18, 19,* and *17,* Chapter 5].

where λ is the wavelength in the medium surrounding the sphere and r is the distance from the sphere to the observer (which must be large compared with R). The expression for i_1 and i_2 and the formulas connected with them are included here, without further ado, as a reference for the following discussions. For their derivation and detailed interpretation the reader must be referred to [*10,16,17*]. Using the representation as given in [*20*],[2] we have

$$
\begin{aligned}
i_1 &= \left| \sum_{n=1}^{\infty} \left\{ \frac{a_n}{n(n+1)} \pi_n + \frac{p_n}{n(n+1)} [\cos \gamma\, \pi_n - \sin^2 \gamma\, \pi'_n] \right\} \right|^2 \\
i_2 &= \left| \sum_{n=1}^{\infty} \left\{ \frac{a_n}{n(n+1)} [\cos \gamma\, \pi_n - \sin^2 \gamma\, \pi'_n] - \frac{p_n}{n(n+1)} \pi_n \right\} \right|^2
\end{aligned}
\tag{2-2}
$$

where

$$
\begin{aligned}
a_n &= (-1)^{\frac{n+1}{2}} (2n+1) \frac{s'_n(\beta) s_n(\alpha) - m s'_n(\alpha) s_n(\beta)}{s'_n(\beta) \phi_n(\alpha) - m \phi'_n(\alpha) s_n(\beta)} \\
p_n &= (-1)^{\frac{n+3}{2}} (2n+1) \frac{m s_n(\alpha) s'_n(\beta) - s'_n(\alpha) s_n(\beta)}{m \phi_n(\alpha) s'_n(\beta) - \phi'_n(\alpha) s_n(\beta)} \\
s_n(x) &= (\tfrac{1}{2}\pi x)^{\frac{1}{2}} I_{n+\frac{1}{2}}(x), \qquad c_n(x) = (-1)^n (\tfrac{1}{2}\pi x)^{\frac{1}{2}} I_{-n-\frac{1}{2}}(x) \\
\pi_n &= \frac{\partial P_n(\cos \gamma)}{\partial(\cos \gamma)}, \qquad \pi'_n = \frac{\partial^2 P_n(\cos \gamma)}{\partial(\cos \gamma)^2} \\
\phi_n(x) &= s_n(x) + i c_n(x) \\
\beta &= m\alpha, \qquad \alpha = \frac{2\pi R}{\lambda}
\end{aligned}
\tag{2-3}
$$

In these expressions primes denote the derivatives with respect to the argument, m the index of refraction of the sphere relative to that of the surrounding medium, and γ the angle between the direction of propagation of the scattered light and the inverse direction of propagation of the incident light. The symbol i_1 is the component whose electric vector vibrates perpendicular to the plane of observation (plane containing the direction of observation and the direction of propagation of the incident light). The electric vector of i_2 vibrates perpendicular to that of i_1. The $I_{n+\frac{1}{2}}(x)$ and $I_{-n-\frac{1}{2}}(x)$ are Bessel functions of half-integral order and the $P_n(x)$ Legendre polynomials of the nth degree. The coefficients a_n give the strengths of the electric partial waves, and p_n the strengths of the magnetic partial waves.

The above formulas show, in general, that the scattering is rotationally symmetric with respect to the transmitted beam. For any value of the particle radius R, the coefficients of the series a_n and p_n will become small, beginning with a certain n; accordingly, the a_n and p_n with higher subscripts can be neglected. Therefore, the radiation scattered by small spheres can be described by a finite number of partial waves. The number of partial waves to be considered increases with the particle size. Mie showed that the nth magnetic wave is of the same order of magnitude as the $(n + 1)$th electric wave. For particles of $R \ll \lambda$, for example, only the first electric mode of oscillation has an amplitude factor of appreciable magnitude. This mode of oscillation is then equivalent to an electric dipole radiation. With the foregoing values of a_1, π_1, and π_1', we obtain

---

[2] This also gives numerical values of the scattering functions for $m = 1.33$; 1.44; 1.55; 2.00; and some complex indices of refraction.

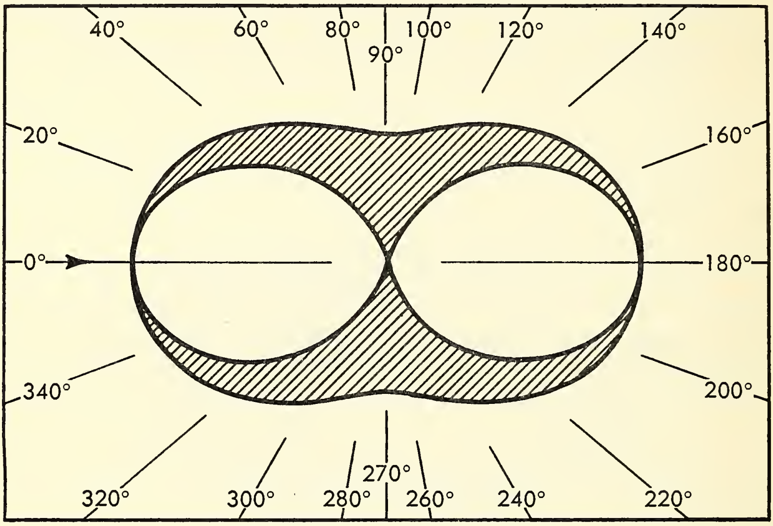

Fig. G,2a. Scattering diagram for lim $2\pi R/\lambda \rightarrow 0$ and $m \neq 1$; the radius vector in the shaded area corresponds to the amount of light polarized; (numerical values from [*20*]).

$$i_1 = \frac{64\pi^6 R^6}{\lambda^6} \left|\frac{m^2 - 1}{m^2 + 2}\right|^2, \qquad i_2 = \frac{64\pi^6 R^6}{\lambda^6} \left|\frac{m^2 - 1}{m^2 + 2}\right|^2 \cos^2 \gamma \tag{2-4}$$

and

$$I = I_{\mathrm{I}} + I_{\mathrm{II}} = \frac{8\pi^4}{r^2} \frac{R^6}{\lambda^4} \left|\frac{m^2 - 1}{m^2 + 2}\right|^2 (1 + \cos^2 \gamma) \tag{2-5}$$

This is Rayleigh's formula. The intensity distribution of the scattered light is symmetric with respect to a plane which is perpendicular to the incident beam and which intersects the midpoint of the scattering particle. Maxima of the intensity are located at $\gamma = 0°$ and $\gamma = 180°$; in the symmetry plane, $\gamma = 90°$, i_2 vanishes, i.e. the scattered light is plane-polarized. A scattering diagram for lim $2\pi R/\lambda \rightarrow 0$ and $m \neq 1$ is shown in Fig. G,2a.

With increasing value of α, higher modes of oscillation contribute to the scattered radiation. Because of the constant phase relations existing between the various partial waves, they are able to interfere upon their superposition. The scattering diagrams then become unsymmetric and the light scattered at 90° is no longer completely plane-polarized. More light is now scattered in the direction of the transmitted beam. This is illustrated by Fig. G,2b which gives the angular distribution of i_1 and i_2 for $\alpha = 1$ and $m = 1.33$ (water droplets in air). This example required use of the first and second electric and of the first magnetic partial waves.

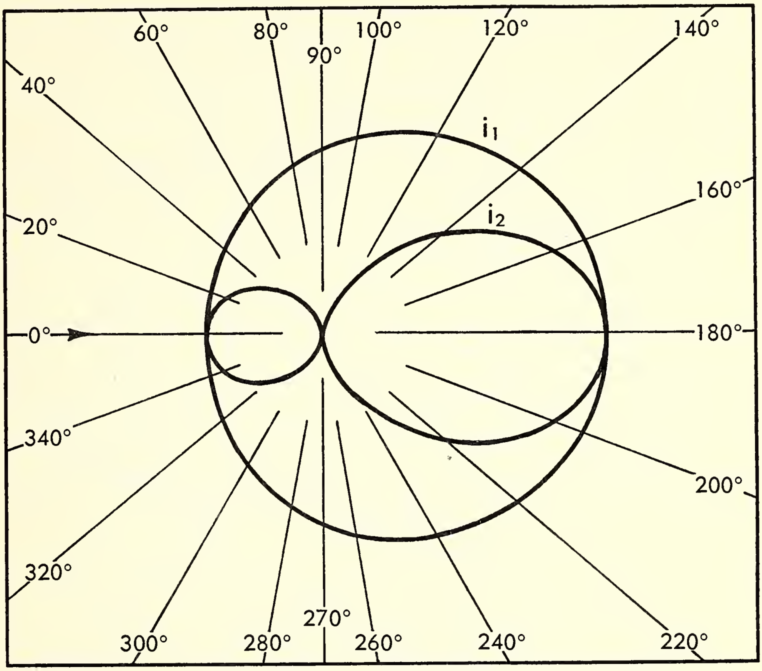

Fig. G,2b. Polar diagrams of i_1 and i_2 for $\alpha = 1$ and $m = 1.33$ (numerical values from [*20*]).

When α exceeds a specific value, which depends on m, the polar diagrams of i_1 and i_2 begin to display maxima and minima in an irregular fashion, as shown in Fig. G,2c. With further increase of α, the diagrams become more and more complex. Finally they merge into the diffraction pattern for circular disks, according to Kirchhoff's theory.

So far we have considered the scattering of individual particles. In practical cases, where the scattering of a large number of particles will be observed, the application of the above equations requires that the particles be considered as independent scatterers. If this is so, the intensity of light scattered by any one particle bears no fixed relationship to that of any other particle, and the total intensity of scattered light is the sum of the intensities from all the particles. A system of particles located randomly in space can be considered as incoherent scatterers if the ratio of distance of separation of the particles to the particle radius is larger than about 100, as La Mer points out [*21*]. If, however, the concentration becomes larger, the light scattered by different particles is no longer incoherent, and interference will occur upon the superposition of the waves scattered by different particles. Since such concentrations are not to be expected for condensation occurring in wind tunnels, its further discussion is omitted. For details refer to the original papers on light scattering of nonindependent particles [*22*,*23*,*24*].

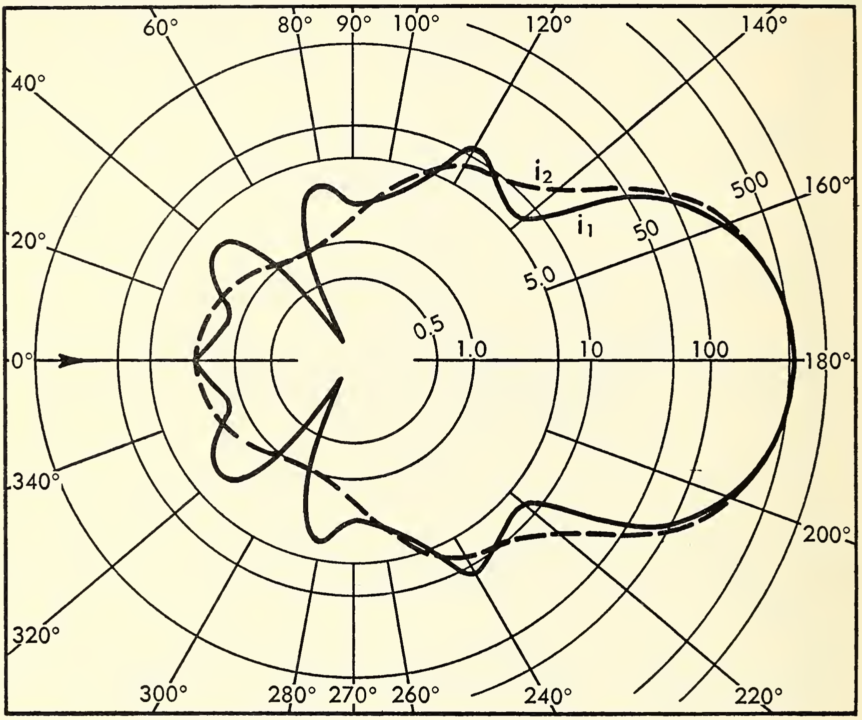

Fig. G,2c. Polar diagrams of i_1 and i_2 for $\alpha = 5$ and $m = 1.33$ (numerical values from [*20*]).

The assumption made in the beginning, namely, that the particles are considered optically isotropic, is insufficient for many cases. The light scattered by polyatomic molecules like N_2, O_2, or H_2O is not completely plane-polarized in any direction as predicted by the Rayleigh formula. This is due to the optical anisotropy of the molecules. To account for this, the expression for the intensity of scattered light, Eq. 2-5, for $\gamma = 90°$, must be multiplied by $(1 + \Delta)/(1 - \frac{7}{6}\Delta)$ where Δ is the degree of depolarization for unpolarized incident light [*15*]. With $\Delta = 1.99 \times$

10^{-2} for H_2O molecules [*25*], we find that about 4 per cent of the light scattered at $\gamma = 90°$ will be unpolarized. For $\gamma \neq 90°$ a more elaborate factor is required [*26*]. For large anisotropic particles the depolarization has been computed by Gans [*11*]; a detailed discussion is given in [*27*].

G,3. Measurements.

METHODS OF MEASURING PARTICLE SIZES AND PARTICLE NUMBER CONCENTRATIONS. Particle sizes and particle number concentrations may be determined from observations of the transmitted light or of the scattered light. In the first case we determine the total amount of light abstracted from the transmitted light; secondly, for particles larger than about 4μ radius, we measure the diffraction rings formed around the transmitted beam. Observations in the scattered light may utilize the intensity or the polarization of the light scattered in a certain direction; if white light is incident, the polychromatism of the scattered light may be used. The suitability of the various methods depends to a certain extent on the size of the particles. If the number concentration N, or the mass concentration, is known, one single measurement can be employed to obtain R. If both N and R are unknown, more than one measurement is needed. In general, accurate measurements require that the suspended particles are of uniform size. For obtaining average values, a moderate polydispersity can be tolerated, depending on the method used. A wide distribution of sizes, however, will obscure the characteristics in the intensity distribution, polarization, and colors displayed by the scattered light as well as the wavelength dependence of the attenuation of the transmitted light.

In the following some of the methods which could be applied to observations on moving gases are discussed. Their bounds are illustrated in most of the examples for particles of $m = 1.33$. We shall assume throughout that the particles are homogeneous and uniform in size. The surrounding medium is assumed isotropic, transparent, and homogeneous. The incident light is assumed to be unpolarized and monochromatic, except as noted.

For some of the methods, special pieces of equipment have been developed in the past decade, resulting from the extensive research on aerosols by La Mer, Sinclair, and others. Since a description of these instruments and their operation is beyond the scope of this article, for detailed information the reader is referred to the original papers.

MEASUREMENTS OF THE TRANSMITTED LIGHT. The attenuation of light passing through a turbid medium follows the law

$$I = I_0 e^{-\epsilon l} \tag{3-1}$$

where I_0 is the intensity of the incident light, ϵ the extinction coefficient, or turbidity, and l the path length in the medium. In the general case ϵ accounts for pure scattering and for absorption. Integration of Mie's equations over the surface of a sphere of radius R yields

$$\epsilon = N \frac{\lambda^2}{2\pi} \text{R.P.} \left[\sum_{n=1}^{\infty} (-1)^{n+\frac{3}{2}} (a_n - p_n) \right] \tag{3-2}$$

where N is the number concentration of the particles, and R.P. denotes that only the real part of the expression in the brackets is to be taken. a_n and p_n are given by Eq. 2-3. The bracketed term depends, for a given m, on α only.

The evaluation of ϵ from measurements of the attenuation at a given λ will yield N times R to some power. If N or R are known, the other quantity is simply evaluated. To discuss the extent to which this method is useful if both R and N are unknown, it is convenient to consider, following Stratton and Houghton [*28*], the variation of the extinction coefficient per cross-sectional area of the particle, $\epsilon/2\pi NR^2$, with α. For a Rayleigh scatterer $\epsilon/2\pi NR^2$ increases as α^4; with increasing particle size the exponent of α changes periodically and for very large particles becomes zero. Corresponding to this variation of the exponent, $\epsilon/2\pi NR^2$ reaches a maximum for moderate values of α. The position and height of the maximum depends on m. For large α, $\epsilon/2\pi NR^2$ oscillates with diminishing amplitude about the value 2 as α increases,[3] [*17*,*29*]. The

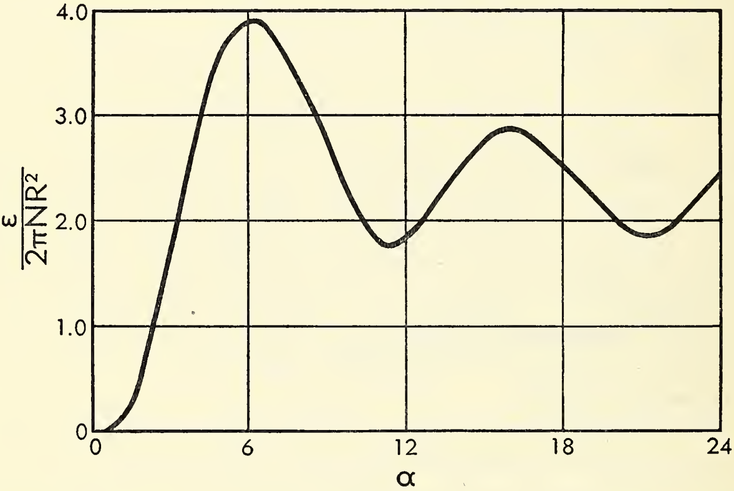

Fig. G,3a. Extinction coefficient per cross-sectional area as function of α; $m = 1.33$; (numerical values from [*20*] and [*29*]).

---

[3] The apparent paradox that large particles scatter twice the amount corresponding to their geometrical size is explained in [*30*, p. 86].

course of the extinction coefficient per cross-sectional area is shown in Fig. G,3a for $m = 1.33$. The Rayleigh region extends up to $\alpha \leqq 0.1$. For $\alpha > 0.1$, measurements made at various wavelengths can be evaluated for R as well as for N if they are referred to the above curve.

In application of the method it is convenient to start out with a set of ϵ/N vs. λ curves computed for various values of R, as illustrated in Fig. G,3b. Measurements of the maximum extinction, for example, as a function of the wavelength can then be compared with these curves. The abscissa value of the maximum determines R, and the ratio of the ordinate value of the measured curve to that of the computed curve gives N. The maxima of extinction for various values of R lie on a straight line which, for $m = 1.33$, is $R = \lambda$. Employing only visible or near infrared light, it is seen that this method is useful for particles between $R = 3.8 \times 10^{-5}$ cm to 10^{-4} cm if $m = 1.33$. For other values of m the position of the first maximum is approximately given by $2\pi R(m - 1)/\lambda = 2$ [*17*, p. 56].

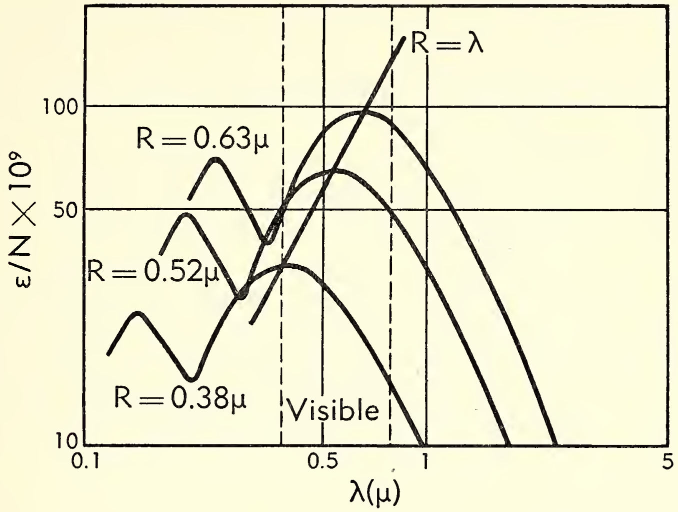

Fig. G,3b. Extinction coefficient per particle as function of λ, for various values of R; $m = 1.33$.

If the particles are nonuniform in size, the measurements yield an average value of R and an average number concentration. The amount of nonuniformity that can be tolerated depends on the relative number concentration of the particles of various sizes. For a large distribution of sizes, however, the characteristics of the ϵ vs. λ curves will be lost. Particular care must be taken in attenuation measurements to exclude large extraneous particles which, when present even in a small number in an otherwise monodisperse medium, compromise the conclusiveness of the data.

Measurement of the slope of the ϵ vs. λ curve also can be evaluated to obtain R. The relative transmission at two or more wavelengths gives the slope and therewith R; the absolute intensity of the transmitted light at one wavelength furnishes the number concentration. The smallest particle size that can be determined with this technique corresponds to an α value of about 0.1 for $m = 1.33$, or with $\lambda_{\min} = 0.38$ microns, $R = 6 \times 10^{-6}$ cm. Such measurements can easily be made with an instrument called the slope-o-meter. This instrument, developed by Hochberg (Columbia University, 1942), is essentially a photoelectric spectrophotometer. It permits measurement of the intensity of, for example, the blue transmitted light and the difference between the intensities of the blue and infrared transmitted light. (For details about this instrument see [*30*, p. 111].)

An estimate of the particle size and the particle size distribution can be obtained by observing the residual colors of white transmitted light [*31*]. For R values smaller than that corresponding to the maximum, the scattering decreases as the wavelength increases, as may be concluded from Fig. G,3c; thus mainly blue light will be scattered and the transmitted light will be yellow to red. If R is larger than corresponds to the maximum, the transmitted light will show a green to blue color. If the particle radius is close to the maximum, the residual color will be bluish red. If the distribution of particle sizes corresponds to about the wavelength range of the visible light, i.e. $R_{\max}/R_{\min} = \lambda_{\text{red}}/\lambda_{\text{violet}}$, no residual color will be seen.

For particles large in comparison to the wavelength of light, the diffraction rings formed around the transmitted light beam may be utilized for particle size determination. The measurements are generally made with parallel monochromatic light, and the diameters of the dark interference rings are measured as seen in a telescope which is focused at infinity. As given in most standard texts on optics, e.g. [*32*, p. 300], the angle at which the first minimum is observed is

$$\sin \varphi = 1.22 \frac{\lambda}{2R} \tag{3-3}$$

This formula may be used if $R \geqq 4$ microns; for smaller particles it loses its validity [*33*].

Measurements of the Scattered Light. Since the intensity, the polarization, and the color of the light scattered in the various directions are functions of the particle radius, R may also be determined from measurements of the scattered light. For very small particles, for which the Rayleigh formula is valid, the intensity distribution and the polarization of the light are symmetrical to $\gamma = 90°$, Fig. G,3a, and with white light incident the scattered light is of blue color. In this case only the product NR^6 can be determined from the measurements. With increasing R, asymmetries in intensity and polarization of the scattered light develop.

The ratio of the intensity of the light scattered at two equal angles ϕ on either side of $\gamma = 90°$ is a function of α alone [*34*]. This function, Fig. G,3c, is monotonic as long as there are no other maxima or minima in the scattering diagram but those already present in the Rayleigh case. For $m = 1.33$, this corresponds to the range $0.2 \leqq \alpha \leqq 2.5$ [*35*]. With the wavelength range $0.38\mu \leqq \lambda \leqq 1\mu$, we have the bounds 1.2×10^{-6} cm $\leqq R \leqq 4 \times 10^{-5}$ cm. Additional measurements of the total intensity scattered at one angle allow a determination of the number concentration [*21,29*].

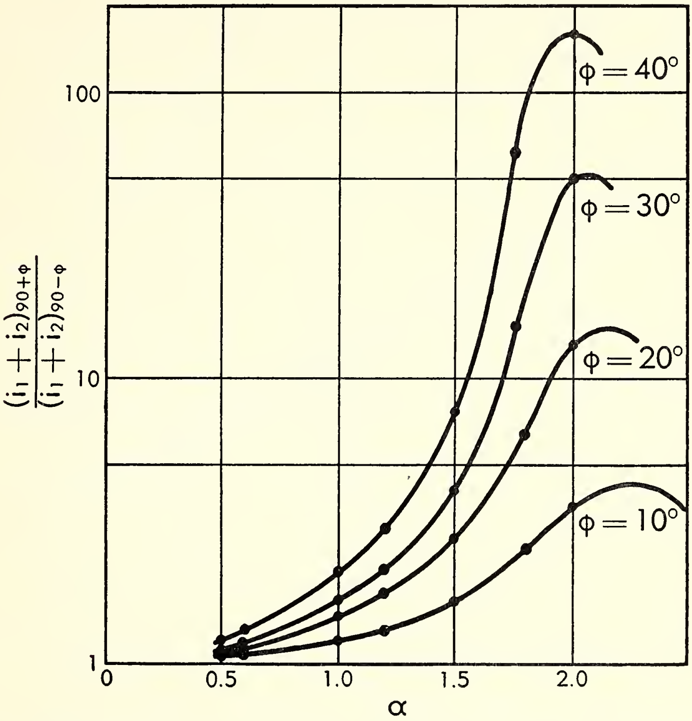

Fig. G,3c. Dissymmetry of the intensity of the scattered light as function of α, for $m = 1.33$ and various angles of observation (numerical values from [*20*]).

The polarization as expressed by the ratio i_2/i_1 (Eq. 2-2) varies, in general, in an irregular fashion with α. But for values $\alpha < 2.5$ and an angle of observation of 90°, it is a monotonic function of α as shown in Fig. G,3d. The lower bound of α for which this method is useful is given by that value of α where i_2/i_1 becomes sufficiently different from zero. This depends on the value of m. For water droplets in air, Fig. G,3d, α must be about 1. With $0.38\mu \leqq \lambda \leqq 1\mu$ the range of particle sizes that can be measured in this case is 6×10^{-6} cm $\leqq R \leqq 4 \times 10^{-5}$ cm. Measurements of i_2/i_1 may be made with a polarization photometer as described in [*30,36,37*].

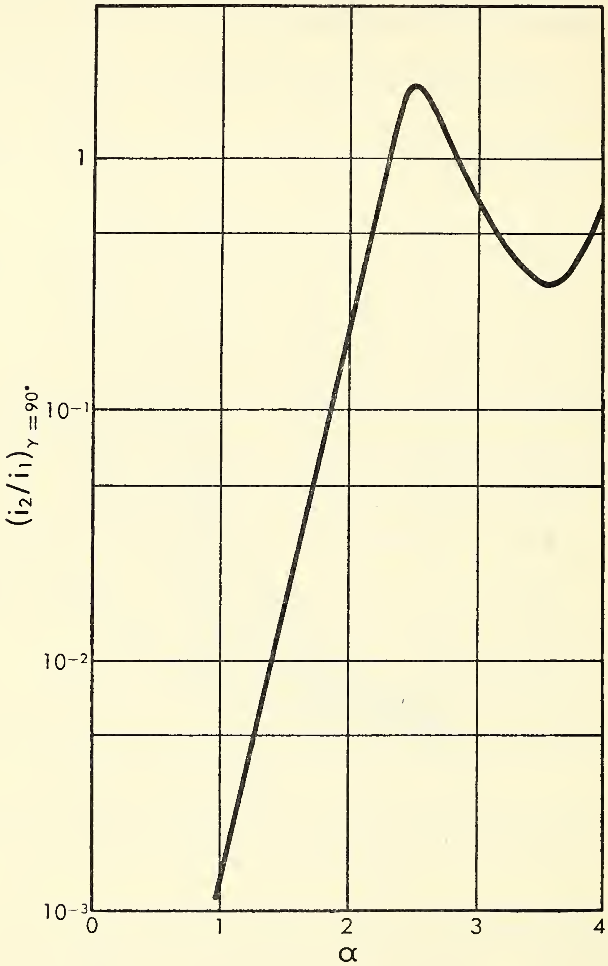

Fig. G,3d. Polarization of the scattered light as function of α, for $m = 1.33$ and $\gamma = 90°$ (numerical values from [*20*]).

If white light is incident in a medium of monodispersed particles of radius R, the scattering diagram will be the superposition of all scattering diagrams corresponding to the α-range $2\pi R/\lambda_{\min} \geqq \alpha \geqq 2\pi R/\lambda_{\max}$. If R is very small, only the blue component will be scattered with noticeable intensity. With increasing R, the longer wavelengths contribute increasingly to the intensity of the scattered radiation. Owing to the particular shapes of the radiation envelopes for various α values, different frequencies prevail in the resulting scattering diagram at different angles of observation. As γ is varied from near 0° to near 180°, the sequence of colors violet to red will be observed. Near $\gamma = 90°$ the sequence is reversed. This phenomenon is most pronounced for the component i_1; i_2 displays a different and usually less prominent spectrum. With increasing particle size the color sequence repeats. La Mer, who named these sequences "Tyndall spectra of higher order," showed that they provide a quick and accurate means for particle size determinations [*38*]. The

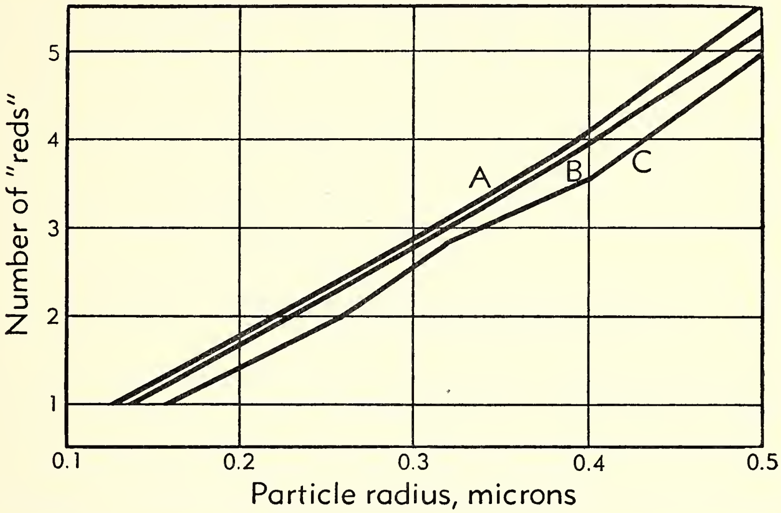

Fig. G,3e. Number of "reds" observed plotted against radius; A for $m = 2.0$, B for $m = 1.43$, C calculated for all indices; (after [*38*]).

number of distinct "reds" which can be observed is found to depend very little on m and is equal to about ten times the particle radius in microns, Fig. G,3e. In addition, observation of the angular position of the "reds" increases the accuracy of the particle size determination, as is illustrated by Fig. G,3f. Using the visible part of the spectrum, this method is suitable for particles in the range of radii $0.1\mu \leqq R \leqq 1.2\mu$. For a description of experimental arrangements convenient for rapid and accurate number and position measurements of the Tyndall spectra of higher order in the visible and ultraviolet, see the detailed discussion of a specially developed instrument (with code name "Owl") in [*30, 39, 40*]. Perhaps more than any of the other methods, the utilization of the Tyndall spectra of higher order depends on the uniformity of the particle sizes. A deviation of the particle size of about 1 per cent is sufficient to inhibit the appearance of the fifth and sixth order spectra [*38*].

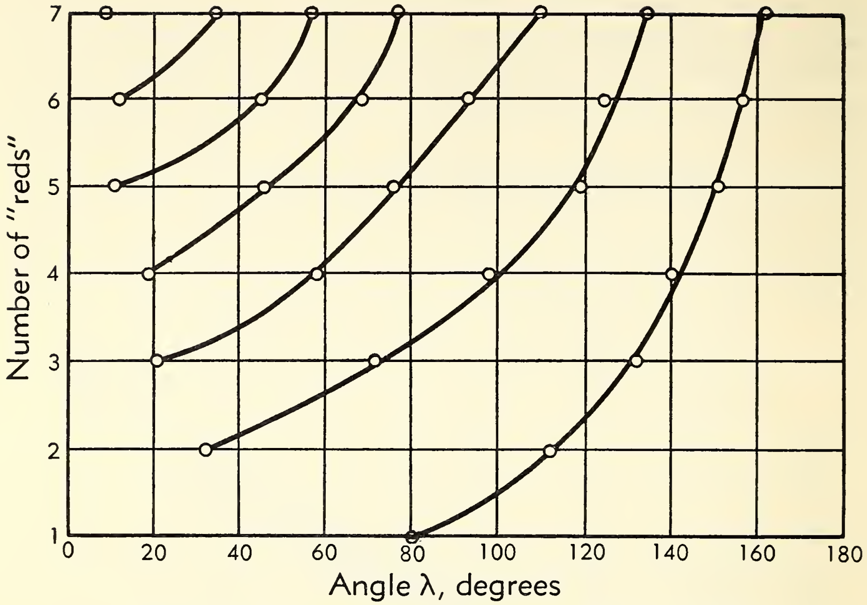

Fig. G,3f. Angular position of "reds" observed in scattered light; $m = 1.43$; (after [*38*]).

G,4. Application to Measurements of Condensation Particles in High Speed Flow. The methods described before have been applied in a variety of cases to particle size and concentration measurements in the study of aero- and hydrosols by La Mer and his collaborators. These studies yielded a broad quantitative knowledge of sols of particles of indices of refraction larger than or equal to 1.33 [*38*]. Only a few observations have been made of the optical properties exhibited by condensation particles in wind tunnels. Aside from the early observation of condensation particles and their growth in steam [*1,2*], water vapor condensation in air was studied by Head [*3*] and later by Wegener and Lundquist [*4*].

While the investigations of Head [*3*] give some interesting results on the onset of condensation as function of pressure, temperature, and water vapor content of the supply air, the technique used does not permit an evaluation as to size and number of particles involved. Only a lower and upper bound of the particle sizes at the start of condensation in the nozzle is deduced from visually observing, in one case, the polarization of light scattered at $\gamma = 90°$, and in the other case from measurements of diffraction rings formed around the transmitted light.

A more refined technique was used by Wegener and Lundquist in an attempt to resolve the discrepancy between wind tunnel results that condensation shocks cannot be avoided if the tunnel is operated with moist air, and the findings of Head [*3*] and Cwilong [*41*] that, if moist air is rapidly expanded to temperatures below 150°K, no condensation occurs. Using a Liebessart spark as light source and a 931A photomultiplier tube as receiver, with maximum sensitivity at 4000A and mounted at right angles to the incident beam of light, they measured the intensity of total light scattered by the condensation particles at a temperature of 130°K in the shock tube at different initial humidities. While visual observations gave negative answers, the sensitive photomultiplier tube recorded the scatter signal to increase almost linearly with the initial humidity. Since no supplementary measurements were made, an evaluation as to particle size and number concentration was not possible.

Observations of air condensation were made by various investigators concerned with the study of high Mach number flow [*5,6,7*]. As regards the condensation particles, they are qualitative only. Quantitative studies of condensation particles in supercooled air flow were made by Durbin in the NACA 11-inch hypersonic tunnel [*42*]. Though the results obtained from these studies may be considered as the first phase in a more detailed quantitative investigation of air condensation particles, a description of the technique used is included here to illustrate the type of equipment adaptable to wind tunnel tests.

The arrangement is shown diagrammatically in Fig. G,4. To obtain the particle size, the dissymmetry method is used. A narrow beam of light, about 1 cm wide, from a GE B-H6 mercury arc filtered by a Wratten filter 77A, is transmitted through the test section of the tunnel and the scattered light is picked up by two photocells (type RCA 1P21) placed symmetrically with respect to the incident monochromatic light. The photocell output is recorded, after amplification, on Brown recorders. To determine the particle number concentration, the attenuation of the transmitted light is measured. Prior to the test run a determination of the proper zero intensity is made by measuring the attenuation of light when passing through the test section filled with atmospheric air, and then with the test section evacuated. From these measurements the effect of the windows and the contribution of the molecular scattering is evaluated and the proper I_0 determined. With the particle radius known from the scattering measurements, the particle number concentration is computed from the measured intensity ratio I/I_0 as indicated by Eq. 3-1 and 3-2. For this purpose the spherical scattering functions of particles having an index of refraction of 1.20 (oxygen and nitrogen) have been computed by the NBS group under A. N. Lowan. Numerical tables of these functions are appended to [*42*].

At a Mach number of 6.9, with a supply pressure of 6.8 atmospheres and the supply temperature equal to room temperature, the radius of the condensation particles was determined to about 5×10^{-6} cm and their concentration to 10^{10} particles per cm^3. These values are obtained assuming the droplets to consist of oxygen and nitrogen only, i.e. neglecting contributions from other condensed particles, such as water vapor or carbon dioxide, or the possibility that the nitrogen and oxygen may have condensed on water vapor or carbon dioxide particles.

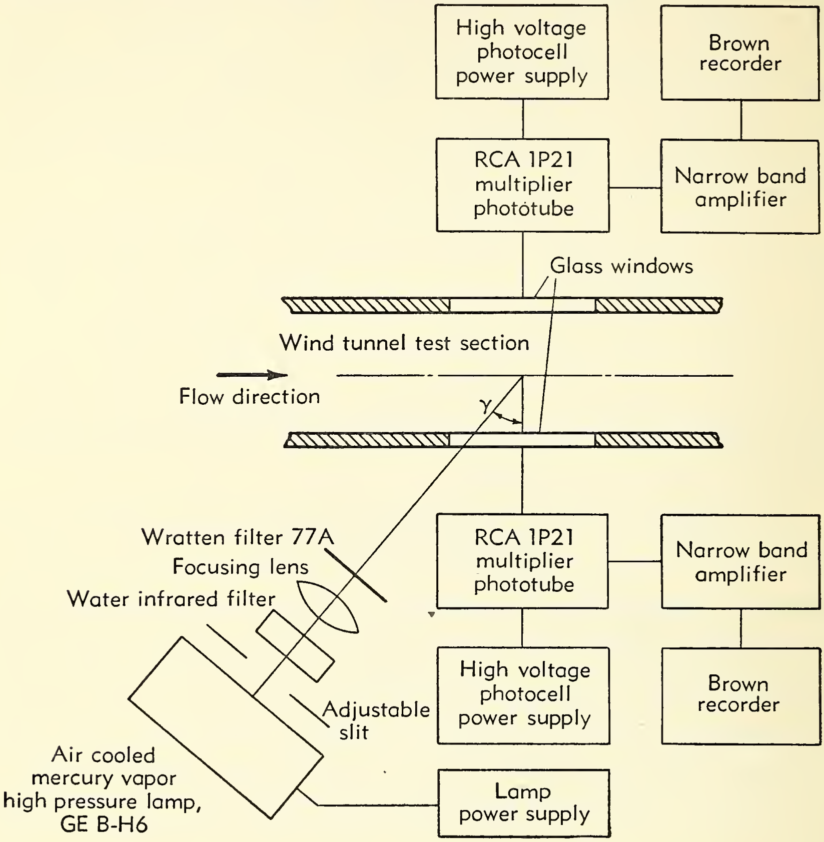

Fig. G,4. Arrangement for light scattering method used for condensation experiments in the Langley 11-inch hypersonic tunnel (after [*42*]).

G,5. Cited References.

1. Stodola, A. *Steam and Gas Turbines*. McGraw-Hill, 1927.
2. Yellott, J. I., and Holland, C. K. The condensation in diverging nozzles. The condensation of flowing steam: condensation in diverging nozzles. *Engineering* *143*, 647–649; 703–705 (1937).
3. Head, R. M. *Investigation of Spontaneous Condensation Phenomena*. Ph.D. Thesis. Calif. Inst. Technol., 1949.
4. Wegener, P., and Lundquist, G. Condensation of water vapor in the shock tube below 150°K. *J. Appl. Phys.* *22*, 233–234 (1951).
5. Becker, J. V. Results of recent hypersonic and unsteady flow research at the Langley Aeronautical Laboratory. *J. Appl. Phys.* *21*, 619 (1950).
6. Stever, H. G., and Rathbun, K. C. Condensation of air in hypersonic wind tunnels. *Mass. Inst. Technol. Aero. Eng. Dept. Rept.*, 1950.

7. Wegener, P., Reed, S., Jr., Stollenwerk, E., and Lundquist, G. Air condensation in hypersonic flow. *J. Appl. Phys. 22*, 1077–1083 (1951).
8. Tyndall, J. On the blue colour of the sky, and on the polarization of light. *Phil. Mag. 37*, 384–394 (1869).
9. Rayleigh, Lord. On the electromagnetic theory of light. *Phil. Mag. 12*, 81–101 (1881).
10. Mie, G. Beiträge zur Optik trüber Medien, speziell kolloidaler Metallösungen. *Ann. Physik (3) 25*, 377–445 (1908).
11. Gans, R. Ultramikroskopische Studien. (Methoden zur Formbestimmung subultramikroskopischer Teilchen.) *Ann. Physik (3) 62*, 331–357 (1920).
12. Möglich, F. Beugungserscheinungen an Körpern von ellipsoidischer Gestalt. *Ann. Physik 83*, 609–734 (1927).
13. Debye, P. Der Lichtdruck auf Kugeln von beliebigem Material. *Ann. Physik 30*, 57–136 (1909).
14. Rayleigh, Lord. The incidence of light upon a transparent sphere of dimensions comparable with the wavelength. *Proc. Roy. Soc. London A84*, 25–46 (1911).
15. Cabannes, J., and Rocard, Y. *La diffusion moléculaire de la lumière.* Les Presses, Univ. de France, Paris, 1929.
16. Stratton, J. A. *Electromagnetic Theory.* McGraw-Hill, 1927.
17. van de Hulst, H. C. *Optics of Spherical Particles.* Drukkerij Duwaer and Zonen, Amsterdam, 1946.
18. Sinclair, D. Light scattering by spherical particles. *J. Opt. Soc. Amer. 37*, 475–480 (1947).
19. Brillouin, L. The scattering cross section of spheres for electromagnetic waves. *J. Appl. Phys. 20*, 1110–1124 (1949).
20. Lowan, A. N. *Tables of Scattering Functions of Spherical Particles.* Natl. Bur. Standards Appl. Math. (4), 1949.
21. La Mer, V. K. Monodisperse colloids and higher-order Tyndall spectra. *J. Phys. & Colloid Chem. 52*, 65–76 (1948).
22. Smoluchowski, M. Molekular-kinetische Theorie der Opaleszenz von Gasen im kritischen Zustande, sowie einiger verwandter Erscheinungen. *Ann. Physik 25*, 205–226 (1908). On opalescence of gases in the critical state. *Phil. Mag. 23*, 165–173 (1912).
23. Einstein, A. Theorie der Opaleszenz von homogenen Flüssigkeiten und Flüssigkeitsgemischen in der Nähe des kritischen Zustandes. *Ann. Physik 33*, 1275–1298 (1910).
24. Ornstein, L. S., and Zernike, F. Accidental deviations of density and opalescence at the critical point of a single substance. *Proc. Roy. Acad. Sci. Amsterdam 17*, 793–806 (1914).
25. Landolt-Börnstein. *Physikalisch-Chemische Tabellen, Ergänzungsband 2*, 5th ed. Springer, Berlin, 1931.
26. Martin, W. H. The scattering of light by liquids: effect of direction on polarization and intensity. *Proc. Roy. Soc. Canada III*, 151 (1923).
27. Oster, G. The scattering of light and its applications to chemistry. *Chem. Revs. 43*, 319–365 (1948).
28. Stratton, J. A., and Houghton, H. G. A theoretical investigation of the transmission of light through fog. *Phys. Rev. (2) 38*, 159–165 (1931).
29. Houghton, H. G., and Chalker, W. R. The scattering cross section of water drops in air for visible light. *J. Opt. Soc. Amer. 39*, 955–957 (1949).
30. Sinclair, D. Optical properties of aerosols. *Handbook on Aerosols.* Atomic Energy Commission, 1950.
31. Ruedy, R. Absorption of light by small drops of water. Transmission of light by water drops 1 to 5μ in diameter. *Can. J. Research A21*, 79–88; 99–109 (1943); *A22*, 53–66 (1944).
32. Wood, R. W. *Physical Optics.* Macmillan, 1923.
33. Mecke, R. Experimentelle und theoretische Untersuchungen über Kranzerscheinungen in homogenen Nebel. *Ann. Physik 61*, 471–500; *62*, 623–648 (1920).
34. Debye, P. P. *Ph.D. Thesis.* Cornell Univ., 1944.

35. Blumer, H. Strahlungsdiagramme kleiner dielektrischer Klugeln. *Z. Physik 32,* 119–134 (1925); *38,* 304–328 (1926).
36. Kerker, M., and La Mer, V. K. Particle size distribution in sulfur hydrosols by polarimetric analysis of scattered light. *J. Am. Chem. Soc. 72,* 3516–3525 (1950).
37. La Mer, V. K., and Sinclair, D. *Rept. 32200. Dept. of Commerce, Office of Publication Board,* 1943.
38. Sinclair, D., and La Mer, V. K. Light scattering as a measure of particle size in aerosols. *Chem. Revs. 44,* 245–267 (1949).
39. Johnson, I., and La Mer, V. K. The determination of the particle size of monodispersed systems by the scattering of light. *J. Am. Chem. Soc. 69,* 1184–1193 (1947).
40. Kenyon, A. S., and La Mer, V. K. Light scattering properties of monodispersed sulfur sols. I: Monochromatic ultraviolet angular scattering. II: Effect of the complex index of refraction upon transmittance. *J. Colloid Sci. 4,* 163–184 (1949).
41. Cwilong, B. M. Sublimation in a Wilson chamber. *Proc. Roy. Soc. London A190,* 137–143 (1947).
42. Durbin, E. J. Optical methods involving light scattering for measuring size and concentration of condensation particles in supercooled hypersonic flow. *NACA Tech. Note 2441,* 1951.

SECTION H

ANALOGUE METHODS

ASCHER H. SHAPIRO
L. MALAVARD

ARTICLE H,1

FREE SURFACE WATER TABLE

ASCHER H. SHAPIRO

H,1.1. Introduction. The analogy between pressure waves in a compressible gas and gravity waves on the free surface of a liquid has long been known mathematically [*1*, Art. 170] and is qualitatively evident merely through a comparison of wave patterns observed in supersonic wind tunnels with wave patterns observed on the surface of a thin rapidly flowing sheet of water.

That this analogy might be used to study two-dimensional gas flows by means of experiments with a rectangular water channel seems first to have been suggested by Jouguet [*2*] and to have been put to practical execution by Riabouchinsky [*3*], von Kármán [*4*], and Preiswerk [*5*]. The active development of supersonic aircraft and the huge cost of supersonic wind tunnels have stimulated additional investigations [*6,7,8,9,10,11*] into the question of what practical information might be obtained from "subsonic and supersonic water channels." This article is based largely on [*11*].

H,1.2. The Basis of the Analogy. The analogy lies in the similarity of the equations of motion for the two-dimensional frictionless isentropic flow of a perfect gas with $\gamma = 2$, on the one hand, and, on the other hand, the quasi-two-dimensional frictionless flow of an incompressible liquid in a horizontal channel with a free surface. Pressure waves in the gas flow correspond to "long" gravity waves in the water flow, that is, waves whose wavelengths are very large compared to the depth of the channel. The shock wave of gas dynamics is the "hydraulic jump" of hydraulics. Although the liquid is incompressible, the free surface flow has an "elasticity" because the depth of water may change, producing changes in the mass flow per unit area; thus changes in depth of the free surface flow correspond to density changes in the two-dimensional gas flow. It is to be noted in this respect that the free surface flow is not truly two-dimensional inasmuch as the depth changes; the term quasi-two-dimensional is here used to denote that the vertical fluid velocities and accelerations are very small.

EQUATIONS OF GAS FLOW. For the two-dimensional gas flow, the basic governing equations are as follows:

Energy equation:

$$c_pT + \frac{q^2}{2} = c_pT^0 \tag{1.2-1}$$

Speed of sound:

$$a = \sqrt{\gamma RT} \tag{1.2-2}$$

Mach number:

$$M \equiv q/a \tag{1.2-3}$$

Isentropic relations:

$$\frac{p^0}{p} = \left(\frac{T^0}{T}\right)^{\gamma/(\gamma-1)} \tag{1.2-4}$$

$$\frac{\rho^0}{\rho} = \left(\frac{T^0}{T}\right)^{1/(\gamma-1)} \tag{1.2-5}$$

Continuity equation:

$$\frac{\partial\rho}{\partial t} + \frac{\partial(\rho u)}{\partial x} + \frac{\partial(\rho v)}{\partial y} = 0 \tag{1.2-6}$$

Combining Eq. 1.2-1, 1.2-2, and 1.2-3, one obtains

$$\frac{T^0}{T} = 1 + \frac{\gamma - 1}{2} M^2 \tag{1.2-7}$$

Equations of Free Surface Liquid Flow. Ignoring vertical components of velocity and acceleration, the pressure will vary in the vertical direction according to the hydrostatic law, and thus the resultant velocity will be constant on vertical lines. Assuming the flow to be quasi-two-dimensional in this sense, taking the floor of the channel to be in the x,y plane, and using h to denote the depth of water, the governing equations are as follows:

Energy equation:

$$h + \frac{q^2}{2g} = h^0 \tag{1.2-8}$$

Speed of propagation of "long gravity waves":

$$c = \sqrt{gh} \tag{1.2-9}$$

Froude number:

$$Fr \equiv \frac{q}{c} \tag{1.2-10}$$

Continuity equation:

$$\frac{\partial h}{\partial t} + \frac{\partial(hu)}{\partial x} + \frac{\partial(hv)}{\partial y} = 0 \tag{1.2-11}$$

Combining Eq. 1.2-8, 1.2-9, and 1.2-10, one obtains

$$\frac{h^0}{h} = 1 + \frac{(Fr)^2}{2} \tag{1.2-12}$$

It may now be noted that, if $\gamma = 2$, the equations for the gas motion are formally similar to the equations for the free surface liquid motion, the following tabulation summarizing the analogous quantities:

Gas flow, $\gamma = 2$	*Hydraulic analogue*
Mach number, $M \equiv q/a$	Froude number, $Fr \equiv q/c$
Density ratio, ρ/ρ^0	Height ratio, h/h^0
Pressure ratio, p/p^0	$(h/h^0)^2$
Temperature ratio, T/T^0	h/h^0

All the familiar relations of isentropic gas dynamics may be applied immediately to the hydraulic analogue merely by setting $\gamma = 2$ and using this table of correspondences.

H,1.3. Experimental Methods.

Supersonic Test Section. The analogy with gas dynamics suggests the use of a conventional two-dimensional converging-diverging nozzle for producing a uniform parallel supersonic water flow. However, because the vertical motions are not entirely negligible, the nozzle contours obtained by the method of characteristics (as used for two-dimensional wind tunnels) do not produce a truly uniform flow in the test section, and it is difficult to avoid unwanted waves.

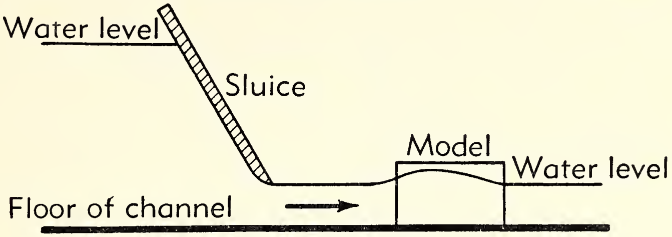

Fig. H,1.3a. Schematic cross-sectional view of channel, showing sluice nozzle.

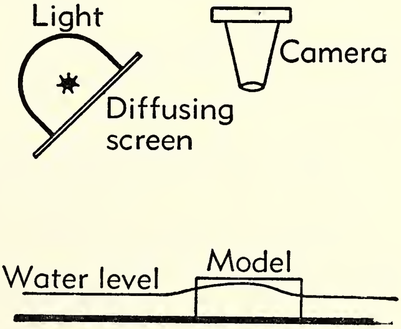

Fig. H,1.3b. Visualization of wave pattern by reflection of diffuse light from water surface (see Plate H,1.3a).

This difficulty is eliminated through the use of a sluice-type nozzle (Fig. H,1.3a) which, experience has shown, produces a test section flow with a very smooth surface. Furthermore the sluice nozzle permits the Mach number to be varied merely by adjusting the height of the water upstream of the sluice gate, whereas a given Laval nozzle is restricted to a single Mach number. The sluice nozzle is simple to construct and may be designed easily for variable test-section depth.

Plate glass makes a convenient floor for the test section since it has

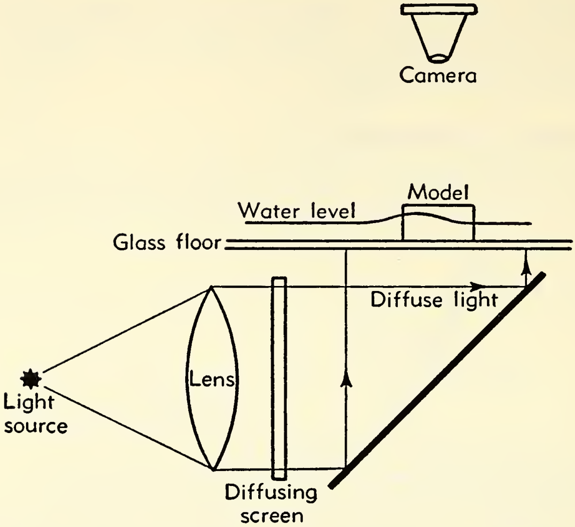

Fig. H,1.3c. Visualization of wave pattern by transmission of diffuse light through water surface (see Plate H,1.3b).

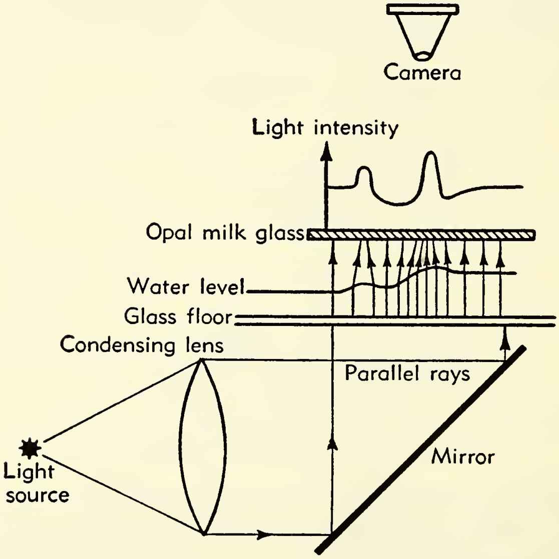

Fig. H,1.3d. Visualization of wave pattern by transmission of parallel light through water surface, with image thrown on screen (see Plate H,1.3c).

a very smooth surface and also lends itself to a wide variety of photographic techniques.

The effects of friction in decelerating the flow in the test section may be cancelled approximately by the gravity force obtained through tilting the channel by a small amount, the proper amount of tilt being most easily found by trial.

PHOTOGRAPHIC METHODS. There are many methods of photographing wave patterns. Three that have been used successfully are shown schematically in Fig. H,1.3b; H,1.3c; and H,1.3d. Plates H,1.3a; H,1.3b; and H,1.3c show photographs of a single flow pattern taken with each of the three methods of lighting.

MEASUREMENT OF WATER DEPTH. The most convenient arrangement for surveying water depths seems to be a needle probe mounted on a traversing system which may be moved in any of three rectangular coordinate directions. The instant at which the probe touches the water surface is usually marked very clearly by the sudden appearance of capillary ripples.

To avoid the height-distorting effects of surface tension near model surfaces, static pressure holes in the model below the water surface may be used.

MEASUREMENT OF FROUDE NUMBER. A measurement of the volume flow of water together with the water height and channel dimensions leads to a calculation of the average velocity of flow but includes the effects of boundary layers.

Measurements of the water height upstream of the nozzle and in the test section also lead through the Bernoulli equation to an approximate value of the test-section velocity, friction again being ignored.

The Froude number may be estimated from measurements of wave angles and height ratios for flow past a thin wedge of known included angle. For reasons given in Art. 1.4, this method is reliable only with water depths of the order of 0.25 inch. Experiments [*11*] show that with this depth the measured Froude number is consistent with the Froude number obtained by other methods, but with larger depths the wave angles give incorrect results.

A "supersonic Pitot tube" specially designed for the hydraulic analogue is described in [*11*].

CHOICE OF WATER HEIGHT. To obtain the best approximation to the analogue, it is necessary (1) to minimize the effects of capillary waves, and also (2) to make the radius of curvature of the free surface large compared with the water depth so that vertical velocities and accelerations will be negligible.

Item (2) may best be managed by making the model under test large compared with the water depth.

For item (1), two courses are open. First, a water height of about

0.25 inch may be used; as shown in Art. 1.4, for this height the capillary waves behave most nearly like gravity waves. Second, depths of a foot or more may be used (requiring proportionately larger channels and models as noted in item (2)), with the aim of making the gravity waves so large that capillary effects are secondary.

H,1.4. The Validity of the Analogy. The assumptions of the analogue will now be reviewed with a view to assessing the significance of data obtained with a free surface water table.

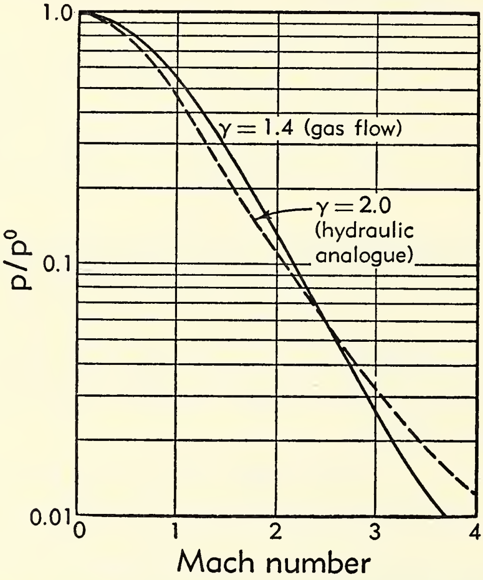

Fig. H,1.4a. Pressure ratio vs. Mach number for isentropic flow, showing effect of γ.

Ratio of Specific Heats. For moderate subsonic speeds or for small perturbations of an otherwise uniform air stream, the various linearized theories indicate that the pressure distribution is independent of the specific heat ratio. Hence under these conditions there is no objection to the fact that the hydraulic analogy refers to a gas with $\gamma = 2$.

For high speeds or for large changes in velocity, the effect of specific heat ratio is not so large as to change the order of magnitude of numerical results; but, on the other hand, the effect is sufficiently large to rule out the feasibility on this score alone of employing the water channel to obtain design data for direct application to air flows. To illustrate the errors owing to the difference in γ, Fig. H,1.4a shows the relation between pressure ratio and Mach number for isentropic flow, and Fig. H,1.4b shows the pressure ratio and streamline radius for Prandtl-Meyer corner flow.

It was noted by E. S. Taylor that the equivalent value of γ depends on the cross-sectional shape of the water channel. The value $\gamma = 2.0$ is peculiar to the rectangular cross section, but almost any desired value of γ may be obtained through proper selection of the cross-sectional shape. Perhaps the most convenient alternative is the triangular cross section, for which $\gamma = 1.5$. Because of the experimental difficulties in studying the steady flow past models in a channel of triangular section, however, it seems likely that this cross section is chiefly applicable to the study of nonsteady wave motions in ducts.

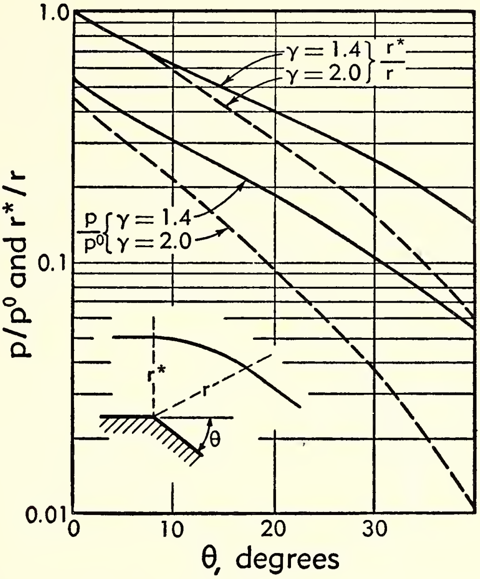

Fig. H,1.4b. Pressure ratio and radius ratio vs. turning angle for Prandtl-Meyer flow, showing effect of γ.

Viscosity and Heat Conductivity. The fluid viscosity, which for purposes of the analogue is ignored in both the gas flow and the water flow, may be accounted for, at least approximately, by carrying out the model and prototype tests at the same Reynolds number. However, in the water flow there is a boundary layer on the floor of the channel as well as on the sides of the model. Furthermore, the low water speeds (of the order of 1 ft/sec) probably make it impractical to duplicate the Reynolds number of a high speed air flow. Lastly, the boundary layer of a low speed liquid does not behave in the same way as that of a high speed compressible gas because of aerodynamic heating effects in the latter case.

Therefore, if the flow pattern is sensitive to viscous effects, as in the case of shock-boundary layer interactions, the water channel can provide at best only descriptive information.

Shocks. When shocks are present the analogy is not valid because the energy equation is a governing relationship in the flow of a gas but plays no part in the flow of an incompressible liquid. Across a shock the stagnation temperature of the gas is constant but the total head of the water flow suffers a decrease.

The relations for the hydraulic jump therefore are not the same as those for the compression shock of a gas with $\gamma = 2$. Fig. H,1.4c shows for example that, compared with a gas having $\gamma = 1.4$, the error in pressure ratio across a normal shock in water is about twice as large as the error for a gas with $\gamma = 2$ and is about 25 per cent between $M = 1.5$ and $M = 3.0$. For weak shocks, both normal and oblique, the change in entropy across the shock is small and the analogue then does not suffer appreciably.

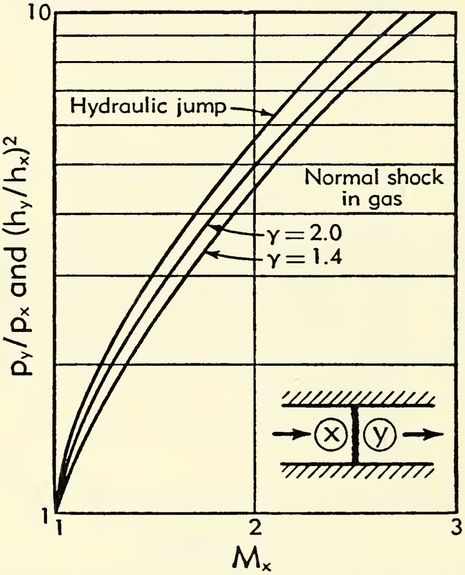

Fig. H,1.4c. Pressure ratio across gas shock and square of height ratio across hydraulic jump, both vs. Mach number.

Vertical Motions. In arriving at the analogue it is assumed that the water flow is two-dimensional. However, this would appear to rule out vertical components of velocity and changes in water depth and leads to the contradiction that accelerations are not permitted. The answer to this seeming paradox is that the analogy refers to a limiting case where the vertical components of velocity and acceleration are negligibly small. In practice this means that the slope of the water surface must be very small and suggests the use of large models compared with the water depth.

Wherever there are rapid changes in water depth, as in shocks or Prandtl-Meyer expansions, the vertical motions are of first order importance. Many of the discrepancies between water channel and wind tunnel experiments seem to be associated with the fact that vertical motions are ignored in the analogy.

Surface Tension. The water surface acts as a stretched membrane, and disturbances in the surface are propagated as capillary waves of small wavelength and large propagation speed. These waves are of course not a part of the analogy.

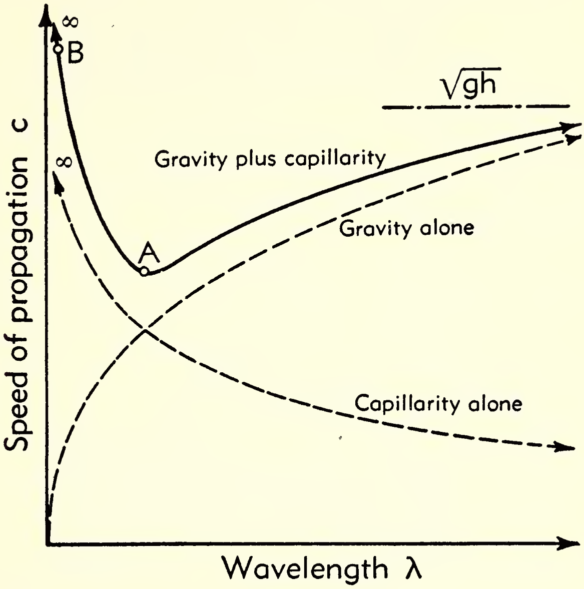

Fig. H,1.4d. Propagation speed vs. wavelength for combined gravity and capillary waves.

In water channel experiments the capillary waves are important chiefly as a nuisance in making height measurements and in interpreting photographs of wave patterns.

Wave Propagation. The effects of ignoring vertical accelerations and surface tension may be looked at from a different point of view which is more illuminating.

In considering the flow past a body immersed in a fluid, we may imagine that each surface element of the body is a source of disturbance which propagates its influence through the body of fluid as a series of pulses in wavelike fashion. The resulting flow pattern is the summation of the disturbances produced by all parts of the body.

If we suppose that the immersed body produces gravity waves and capillary waves of small amplitude, we find from the classical solution

[*1*, Art. 226, 227, 229] to this problem that there are an infinite number of natural modes by which the disturbance may be propagated, each mode having a particular wavelength and a corresponding speed of propagation, according to the formula

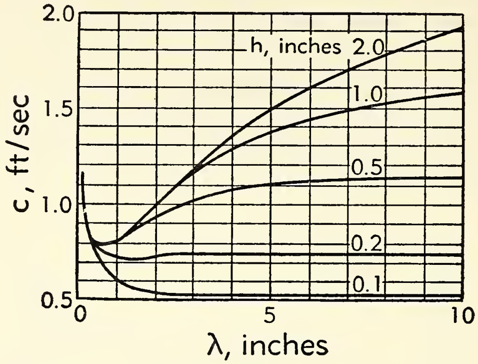

Fig. H,1.4e. Propagation speed vs. wavelength for pure water at 1 atm and 70°F.

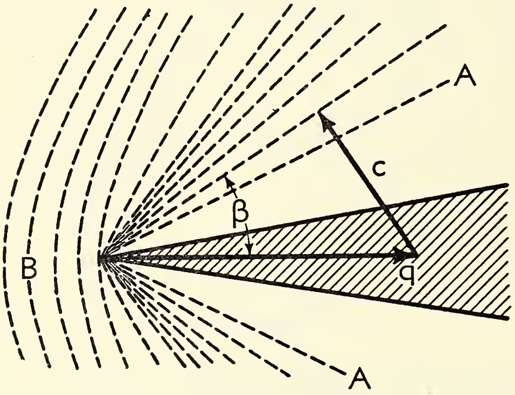

Fig. H,1.4f. Schematic wave pattern for supersonic flow past wedge. *A* represents wave of minimum propagation speed. *B* represents capillary "head" ripples, the propagation speed of which equals the speed of flow (see Fig. H,1.4d).

$$c^2 = \left(\frac{g\lambda}{2\pi} + \frac{2\pi\sigma}{\rho\lambda}\right) \tanh \frac{2\pi h}{\lambda}$$

where λ is the wavelength and σ is the surface tension.

Fig. H,1.4d shows graphically the form of the relation between propagation speed and wavelength and indicates also the shape of the curves when either gravity or capillarity alone is acting. Fig. H,1.4e gives numerical values for water at various depths.

Fig. H,1.4f shows the nature of the flow pattern past a thin wedge according to these considerations. Although the analogue requires a sudden change of direction across a single wave, the actual flow consists of a gradual turn through a series of waves.

It is seen from Fig. H,1.4e that capillary waves behave most like gravity waves for depths of about 0.25 inch.

H,1.5. Some Typical Results. Plate H,1.5 shows successive stages in the starting of a supersonic fixed-geometry diffuser taken from frames of a motion picture made with an ordinary motion picture camera.

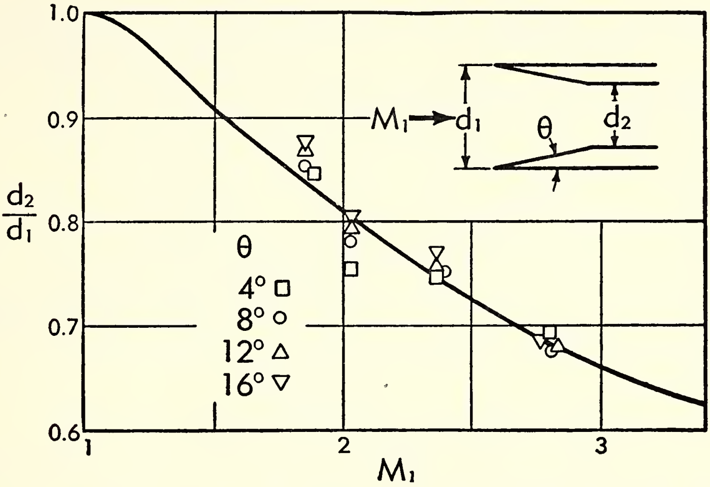

Fig. H,1.5a. Contraction ratio vs. Mach number for starting of fixed geometry supersonic diffuser. Solid line represents results based on one-dimensional analysis without friction.

Fig. H,1.5a shows the measured relation between Mach number and limiting contraction ratio for starting of a fixed-geometry supersonic diffuser. Although the agreement with the simple one-dimensional theory is fairly good as regards starting, other tests showed poor agreement as regards choking of the diffuser with decreasing Mach number.

Because the wave speeds are only of the order of 1 ft/sec, the hydraulic analogue is especially convenient for the study of unsteady flows, such as occur in the inlet and exhaust ducts of reciprocating machinery and in wave machines like the Comprex.

For example, in a study of moving waves using a triangular channel [*11*] the results of Fig. H,1.5b were found for a traveling shock, indicating that a simple one-dimensional theory which ignores friction is in good accord with experiment.

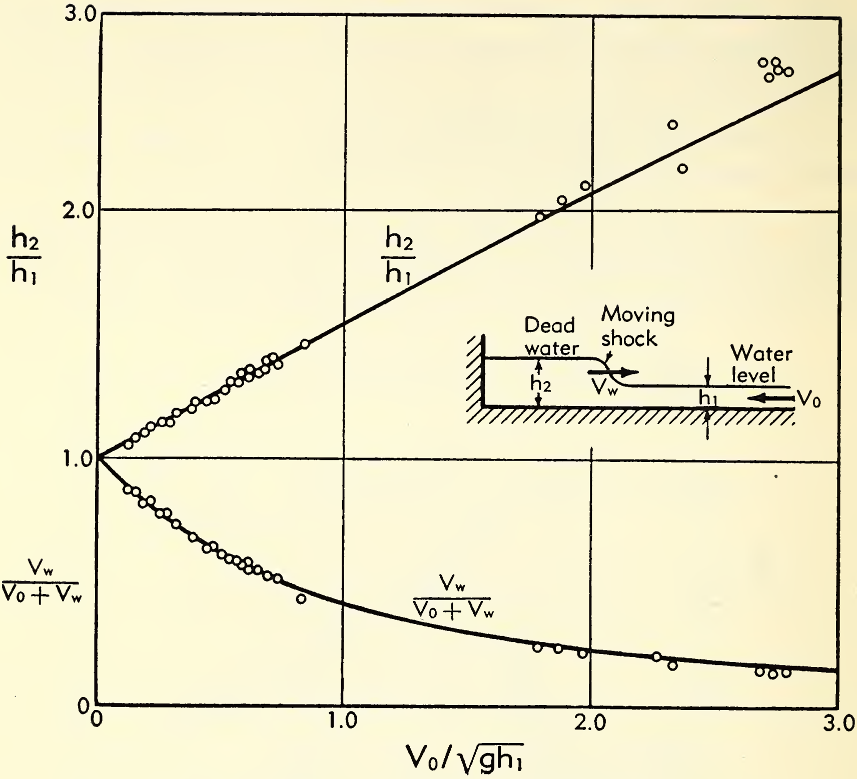

Fig. H,1.5b. Moving shock in triangular water channel. Height ratio and ratio of flow velocities relative to shock, both vs. dimensionless approach velocity. Solid lines represent one-dimensional analysis without friction.

H,1.6. Appraisal of Water Channel as Experimental Tool. The usefulness of the free surface water table must be judged by its ability to shed light on problems of current importance in two-dimensional flow.

It does not seem likely that the analogue will yield quantitative nformation which may be used directly for design purposes.

On the other hand, the water table has been strikingly successful in reproducing most qualitative aspects of high speed flows. It has the great advantages of simplicity, low cost, rapid operation, and gives the operator a chance to "play" with various flow patterns. It is especially suitable for observing unsteady and transient flow patterns.

Despite the many questionable features of the analogue, the water channel is a valuable auxiliary tool. It justifies itself through economy of time and effort and is useful for making qualitative studies and quantitative experiments of a comparative nature.

H,1.7. Cited References.

1. Lamb, H. *Hydrodynamics,* 6th ed. Dover, 1945.
2. Jouguet, E. Quelquesproblèmes d'hydrodynamique générale. *J. math. pures appl.* (*8*) *3,* 1–63 (1920).
3. Riabouchinsky, D. Mécanique des fluides—Sur l'analogie hydraulique des mouvements d'un fluide compressible. *Compt. rend. 195,* 998–999 (1932). Mécanique des fluides—Quelques nouvelles remarques sur l'analogie hydraulique des mouvements d'un fluide compressible. *Compt. rend. 199,* 632–634 (1934).
4. Kármán, Th. von. Eine praktische Anwendung der Analogie zwischen Überschallströmung in Gasen und überkritischer Strömung in offen Gerinnen. *Z. angew. Math. u. Mech. 18,* 49–56 (1938).
5. Preiswerk, E. Application of the methods of gas dynamics to water flows with free surface. Part 1: Flows with no energy dissipation. Part 2: Flows with momentum discontinuities (hydraulic jumps). *NACA Tech. Mem. 934* and *935,* 1940.
6. Orlin, W. J., Lindner, N. J., and Bitterly, J. G. Application of the analogy between water flow with a free surface and two-dimensional compressible gas flow. *NACA Tech. Note 1185,* 1947.
7. Einstein, H. A., and Baird, E. H. Progress report of the analogy between surface shock waves on liquids and shocks in compressible gases. *Calif. Inst. Technol. Hydrodynamics Lab. Rept. N-54,* 1947.
8. Bruman, J. R. Application of the water channel compressible gas analogy. *North Amer. Aviation Rept. NA*-47-87, 1947.
9. Jacobs, D. H. An investigation of water channel photography. *North Amer. Aviation Rept. AL-129,* 1947.
10. Johnson, R. H., Nial, W. R., and Witbeck, N. C. Water analogy to two-dimensional air flow. *Gen. Elec. Rept. 55218,* 1947.
11. Shapiro, A. H. An appraisal of the hydraulic analogue to gas dynamics. *Mass. Inst. Technol. Meteor Rept. 34,* 1949.

ARTICLE H,2

ELECTROLYTIC PLOTTING TANK

L. MALAVARD

H,2.1. General Principles. The use of the electrolytic plotting tank for the study of aerodynamic problems is one of the methods of experimental calculation by analogy based on the production of a physical phenomenon different from that being analyzed but the theory of which obeys the same laws. Analogy considerations permit the reduction of the solution to numerical data on the basis of measured experimental quantities during the test.

For the history of these methods, the reader is referred to previous publications concerning them [*1*].

In the electrolytic tank method the experimental analogy is based upon distributions of electric current in a conductive medium; such distributions depend upon an electric potential V which, in a three-dimensional homogeneous medium, is a harmonic function

$$\nabla^2 V = \frac{\partial^2 V}{\partial x^2} + \frac{\partial^2 V}{\partial y^2} + \frac{\partial^2 V}{\partial z^2} = 0 \qquad (2.1\text{-}1)$$

For every problem in the determination of a harmonic function $\varphi(x, y, z)$ under given conditions, an analogical setup can therefore be worked out in which the function φ will, within a factor, become identified with the electric potential $V(x, y, z)$ of a suitably defined conductive model.

The most important applications are to plane problems. If in such a case one considers a homogeneous conductor of a *slowly varying* thickness $h(x, y)$, the potential V is practically independent of the thickness coordinate z and satisfies the partial differential equation

$$\frac{\partial}{\partial x}\left(h\frac{\partial V}{\partial x}\right) + \frac{\partial}{\partial y}\left(h\frac{\partial V}{\partial y}\right) = 0 \qquad (2.1\text{-}2)$$

There is also a "current function" W associated with V which can be defined by

$$dW = -\sigma h\frac{dV}{dn}\,ds = \sigma h\left(\frac{\partial V}{\partial y}\,dx - \frac{\partial V}{\partial x}\,dy\right) \qquad (2.1\text{-}3)$$

an expression which represents the electric flux through the element of area projected as arc "ds" on the xOy plane and in which σ gives the supposedly constant value of the electric conductivity.

The two functions V and W are related by:

$$\frac{\partial V}{\partial x} = -\frac{1}{\sigma h}\frac{\partial W}{\partial y}, \qquad \frac{\partial V}{\partial y} = \frac{1}{\sigma h}\frac{\partial W}{\partial x} \tag{2.1-4}$$

One can therefore consider an electric plane model composed essentially of a homogeneous conductor of variable thickness $h(x, y)$ for the practical determination of each function $\varphi(x, y)$ as a solution of

$$\frac{\partial}{\partial x}\left(\lambda\frac{\partial\varphi}{\partial x}\right) + \frac{\partial}{\partial y}\left(\lambda\frac{\partial\varphi}{\partial y}\right) = 0 \tag{2.1-5}$$

where $\lambda(x, y)$ is a given function always of the same sign. Moreover, for a function φ there is a corresponding associated function ψ defined by the relations

$$\frac{\partial\varphi}{\partial x} = \frac{1}{\lambda}\frac{\partial\psi}{\partial y}, \qquad \frac{\partial\varphi}{\partial y} = -\frac{1}{\lambda}\frac{\partial\psi}{\partial x} \tag{2.1-6}$$

which satisfies the partial differential equation

$$\frac{\partial}{\partial x}\left(\frac{1}{\lambda}\frac{\partial\psi}{\partial x}\right) + \frac{\partial}{\partial y}\left(\frac{1}{\lambda}\frac{\partial\psi}{\partial y}\right) = 0 \tag{2.1-7}$$

Representation by analogy is therefore possible in two ways [*2*] according to whether one identifies either the function φ or the function ψ with the electric potential V. One can take (within additive constants)

either analogy A: $\varphi = mV, \qquad \psi = nW, \qquad$ from which $h = \dfrac{m}{n}\dfrac{\lambda}{\sigma}$

or analogy B: $\varphi = m'W, \qquad \psi = n'V, \qquad$ from which $h = \dfrac{n'}{m'}\dfrac{1}{\sigma\lambda}$

m, n, m', n' being the scale constants. According to the analogy used, the thickness of the conductive body to be shaped must be either proportional to or inversely proportional to λ. This thickness h will be constant for the models related to the study of harmonic functions with two variables.

In the most general cases the conducting medium used is a liquid; a weak electrolyte contained in a tank of which the shape defines the function to be represented. Very thin metal sheets or plates of a semiconducting material have also been used [*3*]. For experiments which must be rapid and economical though sufficiently accurate, one can use a recently perfected method which makes use of a special kind of con ducting paper [*4*].

H,2.2. The Experimental Method. The essentials of the experimental method will be described here, taking into consideration simple applications for determining the flow of incompressible fluids [*5*]. Later on we will see how the method can be used for the study of compressibility phenomena.

Let us consider the plane and permanent flow of an incompressible fluid having speed U at infinity around an obstacle with any contour C. We start by supposing that there is no circulation around C. One can use either analogy A or analogy B by identifying with the electric potential in the tank (which contains the electrolyte at a constant but shallow depth) either *the velocity potential* φ or the *stream function* ψ of the hydrodynamic flow. At a distance from the obstacle the flow is uniform and the lines φ and ψ = const are straight and parallel to Oy and Ox respectively (Fig. H,2.2); therefore for the analogy A (or B) the electric current for the tank will be fed from two electrodes on the sides of the tank and parallel to Oy (or to Ox). The obstacle in the center of the tank is represented by a cylinder of cross section C of fairly small dimensions so that the wall effects shall be negligible. The contour of C is a streamline. Therefore *in the analogy A this contour* (which is a line of electric current) *will be represented by a cylinder made of insulating material, whereas in analogy B it must be an electric equipotential line and will therefore be made from a material of high conductivity.*[1]

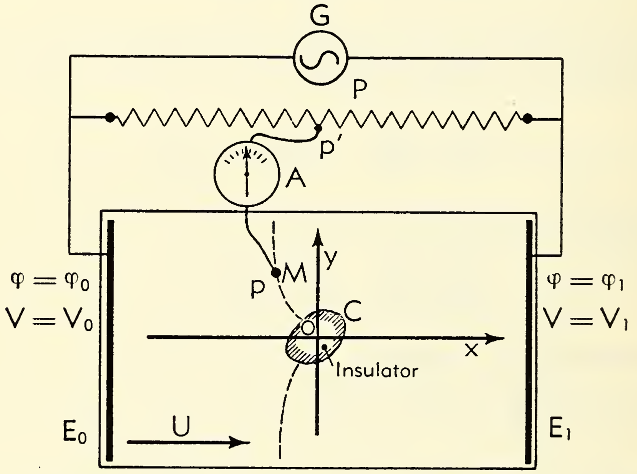

Fig. H,2.2. Tank for the study of plane flows, analogy A.

Fig. H,2.2, a diagram of the electric setup, depicts the case of analogy A. To the terminals of generator G are coupled, in parallel, the tank and a measuring potentiometer P the graduations of which will define the potentials according to a suitably chosen scale (for example 0 to 100 at the generator terminals, which will then give $m = (\varphi_1 - \varphi_0)/100$). The measure of the electric potential V at a point M in the tank is made by the opposition method. An exploring point p made of a thin metallic wire dipping vertically into the tank is moved to point M; it is connected through a zero indicator to plug p' in such a way that no current flows through A. The value of the potential sought is read off opposite the graduation on P. By moving p in the tank in such a way as to maintain A at zero without altering the setting of P, one can trace by points the corresponding equipotential in the tank. The tracing of these positions on a graph can easily be made by a simple mechanical device.

---

[1] A material similar to that used for the tank electrodes; the conductivity of the electrolyte must be much weaker.

The same method will be used for analogy B. One can thus obtain a picture of the field of flow by the orthogonal network of the lines φ and $\psi = \text{const}$. It is interesting to note that the plotting thus obtained permits a practical definition of conformal transformations between any plane areas [*6*] and [*3*, pp. 255–256].

H,2.3. The Experimental Apparatus [*3*]. In the investigation into plane phenomena one uses rectangular tanks of about the following size: length 2 m, width 1.50 m, depth 10 to 15 cm. These tanks are usually made of insulating slabs of glass, marble, slate, etc; they are carried on metal supports fitted with adjusting screws so as to ensure that the bottom surface shall be strictly horizontal.

The most convenient electrolyte is tap water which, in towns, generally has a resistivity of between 2,000 and 10,000 ohm/cm. Its conductivity is generally very homogeneous and its use gives results which are as satisfactory as those obtained from closely defined chemical solutions.

The materials for the supply electrodes or the conducting models can be of red copper, brass, or Duralumin, etc. It is essential that the surfaces of the electrodes be scaled or at least carefully cleaned and degreased before each experiment. Carbon electrodes are the best for avoiding the parasitic phenomenon of polarization. To this end one can cover metal electrodes with a thin coat of a specially prepared colloidal suspension of powdered graphite.

To avoid the phenomenon of electrolysis the electric current to the tank is always alternating. The frequency ordinarily used is between 600 and 1200 cps; the current supply is from a low frequency[2] generator of the usual kind. The power required depends upon the analogical models used for the experiments. It can vary from 1 to 20 watts; the voltage used is between a few volts to a few multiples of 10 volts.

The measuring potentiometer is made up of carefully calibrated resistances mounted on either side of p' so that an automatic device gives a constant total resistance of 1,000 ohms. By means of graduations on the control knobs the voltage applied to the terminals can be read off directly to within one part in ten thousand.

---

[2] If really necessary one can use 60 cps current from the mains, but this frequency is rather weak and does not fully eliminate the phenomenon of polarization.

The most useful type of zero indicator is a cathode ray oscillograph showing Lissajous figures. On the horizontal plates of the cathode tube the difference of potential (between p and p') to be canceled is transmitted by means of an amplifier, the gain being of the order of 3,000 to 10,000, while to the other pair of plates is applied the alternating voltage of the main supply. When there is no phase shift the Lissajous figure observed on the screen is a straight line inclined in one direction or the other; the zero reading is indicated when the straight line is horizontal. The chief advantage of this arrangement is that it will immediately detect on the screen any source of error due to parasitic phase shift brought about accidentally by the effects of capacity, induction, or polarization; the occurrence is shown by an increase in size of the spot which takes the form of an ellipse.

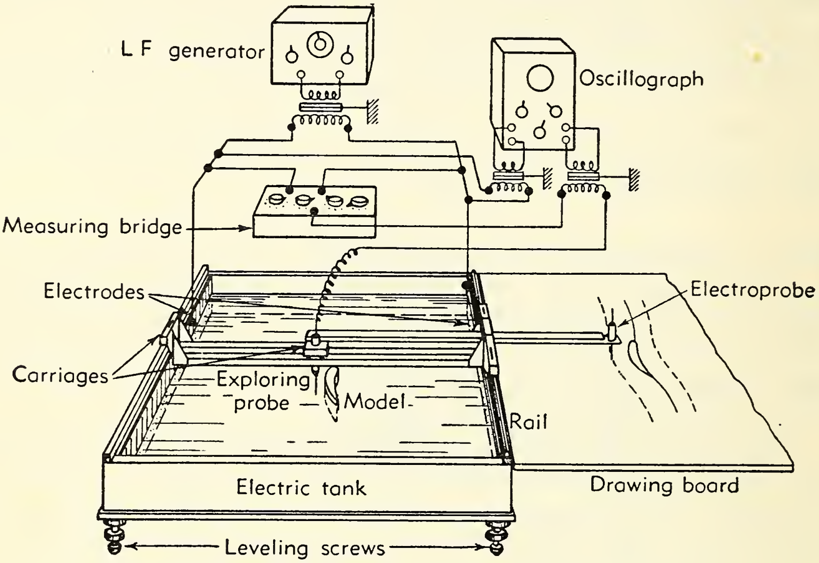

Fig. H,2.3. General arrangement of an electric tank.

A mechanical device which is positioned above the tank and which carries the exploring probe reproduces the probe positions on a graph. As will be seen in Fig. H,2.3, there are two superimposed carriages which make up a "coordinatograph." The smaller carriage links the exploring probe to an arm which can move over a drawing board. At the other end of the arm there is a scriber, electrically controlled, which perforates the paper on the board whenever a position is to be marked.

A device of this kind allows the plotting of the points of equipotentials to within 1 to 3 tenths of a millimeter and measures electric potentials to within one or two ten thousandths of the input voltage.

H,2.4. Representation of the Circulation around an Obstacle. This is very simple by analogy B: the potential function φ being identified with the electric current function W, the circulation $\Gamma = \int_C d\varphi$ is equal to

$$\frac{n'}{\sigma h} \int_C dW$$

But $\int_C dW$ represents the electric flux flowing through C. It is necessary in this case to feed the conducting model which is the obstacle and thus acts as an auxiliary electrode delivering the electric current

$$I = -\frac{n'}{\sigma h} \int_C dW$$

This method is frequently used for the analogue representation of flows around wing profiles. The value of the circulation—a priori unknown—is defined by the Kutta-Joukowski rule according to which the line of current constituting the airfoil has to leave it exactly at the trailing edge. In the tank this line is represented by the equipotential of the model. Very close to the trailing edge of the model is then placed a fine electrode that will constitute a point through which this equipotential must pass. The zero indicator is connected between the model and the electrode; the intensity I is then regulated so as to ensure an equal value of their two potentials.

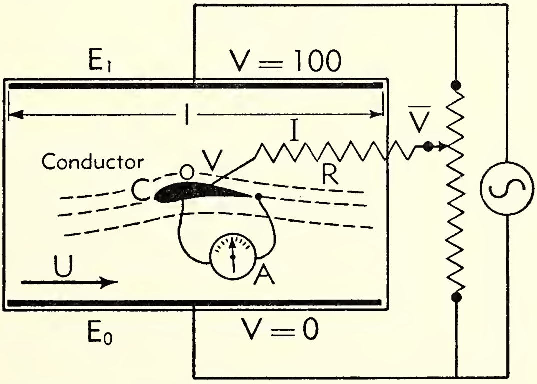

Fig. H,2.4a. Representation of circulation, analogy B.

It is interesting to note that, once the intensity has been regulated, the *measure* of the intensity gives the unknown value of the circulation.

One can easily show that[3]

$$\frac{\Gamma}{U} = -l\,\frac{\bar{V} - V}{100}\,\frac{R'}{R}$$

where $\bar{V} - V$ is the difference in potential between the model and the electrode.

The representation of circulation in analogy A is a little more difficult. The velocity potential φ is multiform; after one complete turn around the obstacle, φ has undergone a variation equal to Γ. This must also be true for the electric potential. One can achieve this representation by making a "cut" which can be chosen along the equipotential MN issuing from the contour C and this can be done by means of two auxiliary electrodes E_2 and E_3 which are separated by a thin insulating plate.

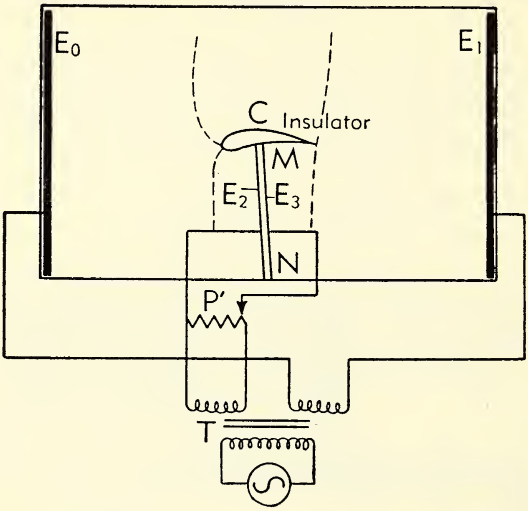

Fig. H,2.4b. Representation of circulation, analogy A.

The circulation is represented by the difference of potential to be obtained between these two electrodes, a difference which is adjusted in order to satisfy the Kutta-Joukowski condition by a potentiometer P' which itself is fed by transformer T (Fig. H,2.4b). The information concerning the equipotential MN can be deduced from the field of lines of current obtained by analogy B.

The method which has been described for the study of a single profile can be generalized without difficulty to analyze the flow about a combination of profiles (multiplanes, profile with leading edge slot, and double or single flaps with slot, etc.). The Kutta-Joukowski condition must, of course, be ensured for each one of them by a suitable electric supply for each model.

---

[3] For the notations see Fig. H,2.4a. R' is the electric resistance measured between the electrodes E_0 and E_1 after the model is removed.

H,2.5. Study of a Cascade of Profiles.

An interesting application of this method to a cascade of profiles can be made. Analogy B is used; the experiment can be limited to a given number of profiles, for example 5 or 7, and it is possible to represent schematically the lines of current ending in the outer profiles by the straight electrodes E_0, E_0', and E_1, E_1'. The potentials of the profiles are adjusted at different values which increase in arithmetical progression. For a given position of E_0E_1 the deflection caused by the cascade can be obtained by determining the direction of the electrodes E_0', E_1' in such a way that the Kutta-Joukowski condition is satisfied for the intermediate profiles. This is done by pivoting E_0' and E_1' about the trailing edges of the outside profiles.

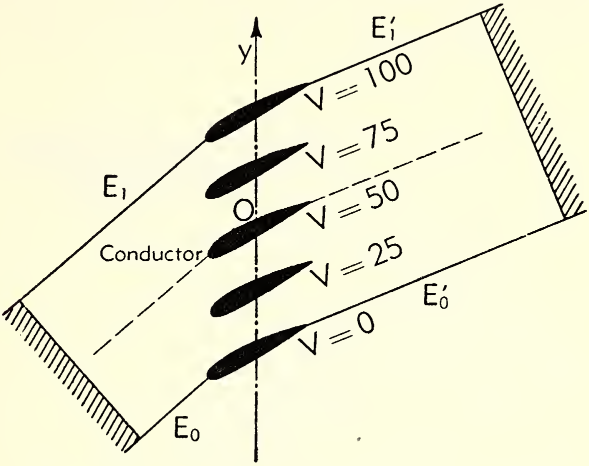

Fig. H,2.5. Diagrammatic arrangement for the study of a cascade of profiles.

The experimental technique is simplified if the demands on the tank are limited to a conformal representation of the given cascade into a cascade of straight line segments; this permits the completion of the experiment by calculation [7]. In analogy B the profiles fixed rigidly are not fed (zero circulation and deflection) and are orientated in a uniform field of the tank so as to satisfy the Kutta-Joukowski condition for the intermediate profiles. This then gives the undeflected flow in the band around these profiles; completing the operation by the application of the other analogy gives (φ, ψ plane) the conformal representation sought.

H,2.6. Representation of Axially Symmetric Flows.

In the three-dimensional harmonic fields with axial symmetry, the velocity potential φ and the stream function ψ can be defined in a meridian half-plane xOy in which Ox represents the axis of symmetry. The two functions are connected by the relations

$$\frac{\partial\varphi}{\partial x} = \frac{1}{y}\frac{\partial\psi}{\partial y}, \qquad \frac{\partial\varphi}{\partial y} = -\frac{1}{y}\frac{\partial\psi}{\partial x} \tag{2.6-1}$$

In the application of analogy A one must use a tank with a flat *inclined* bottom so that the electrolyte forms a conducting wedge whose edge represents the axis Ox (this, by the way, amounts to showing a slice of the three-dimensional field between two meridian planes). The slope of the bottom of the tank is generally fairly slight (a dihedral angle of 5° to 15°). The bottom surface of the insulator models, whose cross sections represent the meridian contours of the obstacle, is cut at an angle so as to rest level on the sloping bottom of the tank. Thus flows in convergent-divergent nozzles or flows around streamlined bodies of revolution can be studied. This latter case is shown in Fig. H,2.6.

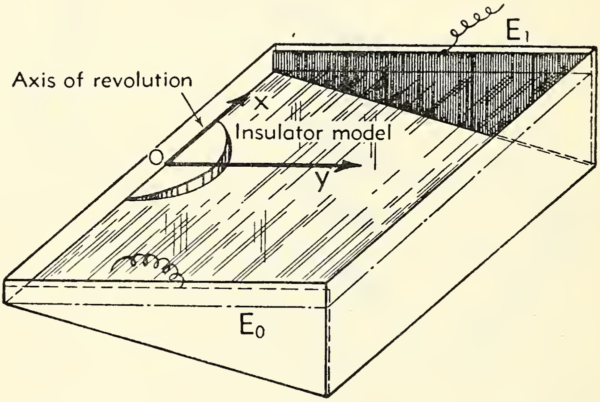

Fig. H,2.6. Tank with sloping bottom for the study of axially symmetric problems.

To represent the stream function in a meridian field—analogy B—it is necessary to use a tank in which the depth is inversely proportional to the distance to the axis (tank with hyperbolic bottom). Unless special contrivances are used, this limits the application to cases in which the axis of revolution is outside the range of definition of the field.

H,2.7. Fulfillment of Boundary Condition [*3,5*]. In the problems considered so far, the analogical interpretation of boundary conditions was immediate. When boundary problems of the classical types (Dirichlet, Neumann, or Fourier) must be resolved, the following arrangement is used: the walls of the tank which represent the boundaries of the field are fitted with small electrodes e_1, e_2, e_3, . . . , etc. which are relatively large and are separated by fairly narrow insulating spaces. Each electrode

e is fed by a potentiometer p which allows the setting of its potential at a suitable value or the discharge through the electrode of a determined electric current. By the first setting a given law of potential can be established for the contour; this is the Dirichlet problem. By the second setting the Neumann conditions can be satisfied: the current discharged by a small electrode of *surface area* s is equal to

$$i = -\sigma \left(\frac{dV}{dn}\right)_m s \tag{2.7-1}$$

in which $(dV/dn)_m$ is the mean value of the normal[4] derivative of the electric potential, which can be identified in practice, if the electrode is small enough, with the value $d\varphi/dn$ calculated at the middle point. The adjustment of the intensity i to a suitable value can be reduced to an adjustment of the difference of potential $\bar{V} - V = iR$ at the terminals of a known resistance R positioned between the potentiometer and the electrode. For the determination of σ and h see references [*3*] and [*5*].

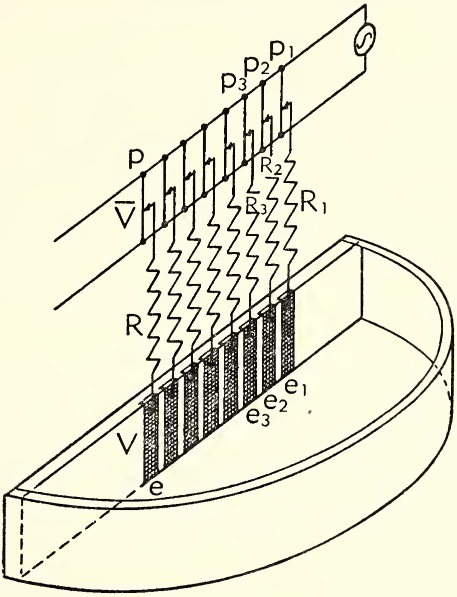

Fig. H,2.7. Tank with small electrodes and electrical supply circuits.

In mixed problems of the Fourier type the linear relationship[5]

$$V - a\frac{dV}{dn} = b \tag{2.7-2}$$

between the potential and its normal derivative can be satisfied automatically for each electrode; taking into account Eq. 2.7-1 it can, in fact, be identified with Ohm's law $\bar{V} - V = iR$ for the circuit which feeds this electrode provided one chooses the resistance R equal to $a/\sigma s$, the potential $\bar{V}$ being adjusted to the value b.

---

[4] The normal n being directed toward the interior of the field.

[5] The coefficients a (which must be positive) and b are in general functions of the point considered on the boundary.

In these setups, the given and continuous laws of the potentials or of the normal derivatives thus are replaced by approximate laws of variation by steps in which each step corresponds to an electrode e.

The models are made by cutting out the small electrodes from thin sheet metal and inserting them into suitable grooves in the insulated walls of the tank. The walls also can be covered with a highly conductive paint scratched away at intervals so as to obtain the required insulating strips.

This experimental setup has been used for numerous problems related to the vortex theory of wings and propellers. In this way the last setup of Fourier type is at the basis of analogical calculating machines (calculators of wings and propellers) used in the calculation of the aerodynamic characteristics of wings or propeller blades of any shape. By simple electric measurements these sets of equipment will give in a few minutes the spanwise distribution of the circulation for a wing or a propeller blade; the accuracy ranges about a few thousandths [*5,8*].

H,2.8. Lifting Surfaces. In similar manner the tank and its electric apparatus are used to solve problems relating to the theory of lifting surfaces. The aerodynamics of flight at high speed has resulted in new shapes of highly swept wings of small aspect ratio concerning which it is essential to be able to evaluate the aerodynamic stresses at supersonic, subsonic, and low speeds. A numerical solution for this last case is often the most difficult to find.

It is known how the problem stands in the linear theory. In a uniform airstream of which the general speed U is parallel to Ox, one considers an infinitely thin, low cambered wing near to the plane xOy and defined by its projected area S on this plane and the slope distribution $g(x, y)$ along Ox. From the trailing edge issues a vortex sheet which extends over area Σ of xOy. Let $Ux + \varphi(x, y, z)$ be the velocity potential. The function φ harmonic in the space can be studied only in a half-space limited to plane xOy, and in this plane it will be characterized by the following conditions: (1) $\varphi = 0$, outside area $S + \Sigma$ in plane xOy; (2) on S the normal derivative of φ is known at each point, $\partial\varphi/\partial y = Ug(x, y)$; (3) on Σ, φ depends only on y; (4) on the trailing edge boundary the values of φ and of its derivatives in S and in Σ must fit.

To deal with the question by analogy [*9*], φ will be identified with the electric potential in a deep tank of large dimensions;[6] the plane xOy is the free surface of the electrolyte. The area of this plane exterior to $S + \Sigma$ is represented by a large electrode connected to one of the poles of the generator and of which by definition the potential gives the zero on the scale.

---

[6] One can also apply the analogy to the potential of accelerations [*10*].

To take into account condition (2) (Neumann's problem) it is necessary to arrange the area S by a paving of small electrodes (50–100 for a half-wing) and adjust the electric current given off by each one according to the value $g(x, y)$ calculated at the middle point. According to (3) the surface Σ is represented by a certain number of electrodes parallel to Ox and made of thin metallic strips; each strip is fed under conditions which are determined by making all adjustments satisfy (4).

The electric adjustments are relatively quick. After they have been made, the potentials of the electrodes of S are measured, thus giving a chart of the values of φ for the wing. The aerodynamic elements can be deduced therefrom since the circulation between the leading edge and the point x, y is equal to 2φ.

H,2.9. Study of Compressible Flows by the Method of G. I. Taylor [*2*]. The velocity potential $\varphi(x, y)$ of a permanent plane flow of a compressible fluid satisfies the equation

$$\frac{\partial}{\partial x}\left(\rho\frac{\partial\varphi}{\partial x}\right) + \frac{\partial}{\partial y}\left(\rho\frac{\partial\varphi}{\partial y}\right) = 0 \tag{2.9-1}$$

in which $\rho(x, y)$ represents the density varying from one point to another. This equation compared to relation 2.1-2 shows that $\varphi(x, y)$ can be identified with the electric potential $V(x, y)$ provided that the bottom of the tank is such that the depth $h(x, y)$ at each point is proportional to the density $\rho(x, y)$. In the same way the stream function $\psi(x, y)$ can be obtained in a tank of which the depth $h(x, y)$ is inversely proportional to $\rho(x, y)$. As the density ρ is known only as a function of the speed (by means of the characteristic equation of the fluid and Bernoulli's equation), it is necessary to proceed by successive approximations. Starting from an approximate value of the function ρ (for example ρ_1 = const which amounts to taking incompressible flow as a first approximation) a first law for depth h_1 is deduced by means of an electric tank experiment. The measurement of the electric gradient at each point gives the value of the corresponding velocity and thus a new approximate value ρ_2 of the density. The experiment is repeated with new corresponding depths h_2, the speeds are measured, and one then proceeds to a third approximation (ρ_3, h_3) and so on. The convergence of the approximations is satisfactory so long as the zones of excess velocities are not too small.

In practice the bottoms of the tanks are fashioned from materials which can be cut and formed easily, such as paraffin wax, hard wax, or a mixture of the two which, with the help of certain devices, permits the shaping of a tank bottom of variable depth in a fairly short time. The determination of the speed at any point is performed by measuring the maximum electric gradient dV/dl at the corresponding point in the tank. This gradient is deduced from the difference in potential ΔV measured between two fine wire probes (0.1 mm), very close together ($\Delta l = 1$ to 2 mm), dipping vertically into the tank along the same line of current. This is done by first placing the two probes on the same equipotential (an operation which is performed by connecting them to the zero indicator) and then by turning them through 90°. The measurement of this gradient can be made with a degree of precision greater than 1 per cent provided one gives special attention to the amplifier circuits and takes the following precautions: that the probes dip into liquid by the same amount during the experiment; that the measurement of ΔV is made by a method of opposition by using a gradient of known reference so as to eliminate the evaluation of Δl; that one avoids all resistive or capacitive losses during the measurements by using a Wagner bridge to ensure that the mean potential of the probes is equal to that of the earth [*3*, pp. 243–246].

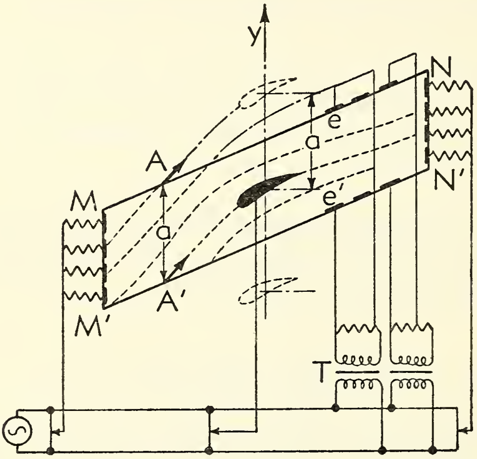

Fig. H, 2.9. Representation of cascades in compressible flows.

The representation of the circulation is done in the same way as for the incompressible fluid This method has been used in the study of subsonic flow around a circle and wing profiles or in nozzles. It can be used for representing compressible flows past a cascade of profiles. It is desirable in this case, in order to avoid having to model a tank bottom of too large an area, to base the form of the tank bottom on the periodic character of the aerodynamic field. The character of the flow is the same when in moving parallel to Oy (Fig. H,2.9) one passes from point A to point A' where the distance AA' is equal to the gap a between two profiles: (1) the speed vector is the same at these two points; (2) the stream function ψ increases by a constant amount. Under these conditions one can limit the picture to a band $MNM'N'$ which will contain a *single* profile and be of a width equal to a. In the tank, which will be shaped to reproduce the parallelogram $MM'NN'$, the function ψ is identified with the electric potential; the walls MN and $M'N'$ are covered with small electrodes which are fed in opposite pairs (e, e') under constant voltage (condition (2)), by means of a transformer T (the flux entering by e' is equal to that leaving by e; condition (1) is thus satisfied). It remains to provide a suitable feed to the walls MM' and NN' according to linear laws of potential so as to set the chosen direction of the upstream flow and satisfy the Kutta-Joukowski condition for the airfoil. The bottom of the tank is fashioned by successive approximations as mentioned above.

Finally it should be noted that this method can also be used for axially symmetric flows, at least insofar as the potential function $\varphi(x, y)$ is concerned; the depths $h(x, y)$ must then be proportional to the product ρy of the density ρ and the distance y from the point considered to the axis of revolution. The bottom of the tank is inclined and modeled.

H,2.10. The Hodographic Tank [*11*]. The study of plane flows of compressible fluids is often undertaken by replacing the spatial variables (x, y) by the independent variables (q, θ), modulus and argument of the velocity at a point; the flow is defined in the hodographic plane. A corresponding electric analogy may be conceived, the principle of which is explained below.

In the hodographic plane the velocity potential φ and the stream function ψ of a compressible fluid are connected by the well-known relations:

$$\frac{\partial\varphi}{\partial q} = -\frac{\rho_0}{\rho q}(1 - M^2)\frac{\partial\psi}{\partial\theta}, \qquad \frac{\partial\varphi}{\partial\theta} = q\frac{\rho_0}{\rho}\frac{\partial\psi}{\partial q} \tag{2.10-1}$$

M is the local Mach number. These equations can be compared with the analogical equations (2.1-4) which may be written in polar coordinates:

$$\frac{\partial V}{\partial r} = -\frac{1}{\sigma h r}\frac{\partial W}{\partial\theta}, \qquad \frac{\partial V}{\partial\theta} = \frac{r}{\sigma h}\frac{\partial W}{\partial r} \tag{2.10-2}$$

The comparison of the relations (2.10-1 and 2.10-2) allows one to determine easily the relation (r, q) and to define the depth law $h(r)$. The electric tank is circular and its center O corresponds to the origin of the q, θ plane; the bottom is axially symmetric about the vertical axis passing through O; the form of the meridian is defined by the law $h(r)$. Mach number 1 corresponds to an infinite depth; it is therefore necessary to limit the use of the tank to a slightly lower Mach number, for example, 0.96.

The use of the tank is particularly indicated for the study of high speed jets and generally for any study of compressible flow with a free surface. It can be used also to determine the contour of an obstacle to which there is a corresponding distribution of given speeds. For example let us consider the following simple case: a symmetric streamlined body is placed at zero incidence in an airstream of uniform velocity at infinity. The streamline $XAEPX'$ (Fig. H,2.10), coinciding with the axis OX and the contour of the body, is found in the plane of speeds in the shape of a closed curve which defines the limit of the hodographic zone and, in analogy A, represents the insulated boundary of the tank.

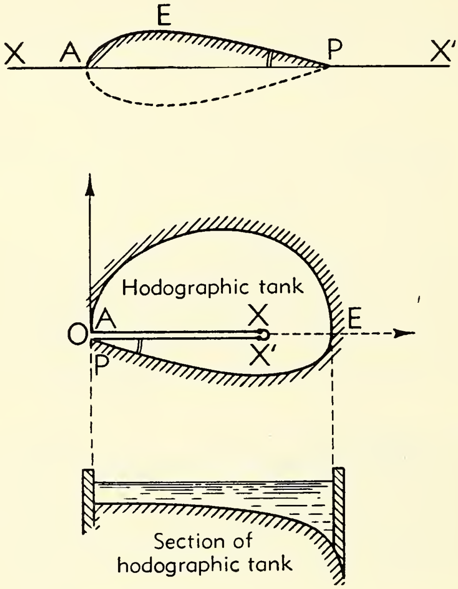

Fig. H,2.10. Representation of a flow in the hodographic plane.

The two coinciding rectilinear segments AX and $X'P$ define in the *hodographic plane* the two edges of a *cut* which extends from the origin (zero speed: points A and P of the profile) to a point XX' of which the distance to O represents the modulus of the speed at infinity. The picture of the uniform flow is then given by a *singularity* located at this point and easy to define.

For the experiment the circular tank described above is limited to the contour $XAEPX'$ molded in paraffin wax. The cut $AXX'P$ consists of a thin insulating screen and the singularity (XX') consists of two small electrodes cut to a suitable shape and separated by a narrow insulating space. These two electrodes are connected to the terminals of the generator and feed current to the tank.

The experimental study is made as follows: the hodograph, that is to say the contour $XAEPX'$ of the tank, is given; during the experiment the distribution of the electric potential is plotted on the contour and by integration the shape of the corresponding obstacle is deduced.

This method has been used for the study of symmetric wing profiles. The degree of precision obtained has been satisfactory; in cases where it has been possible to check with known theoretical results, the errors for the relative thickness of the profile were not more than 0.001 to 0.003.

H,2.11. Conical Flows. Certain problems of conical flows can be resolved by electric tank methods. It is known that in this type of flow the speed vector remains unchanged along any conical line emanating from point O. The movements depend upon only two variables: to know the speed distribution, it is sufficient to study the flow in a plane perpendicular to the stream at infinity, a plane which can be set at a distance $\beta = \sqrt{M^2 - 1}$ from O so as to cut the Mach cone issuing from this point along a circle C of unit radius.

It can be demonstrated that the disturbance velocities u, v, w created by the body are, inside of C, harmonic functions which can be considered as real parts of three analytic functions $U(Z)$, $V(Z)$, $W(Z)$ connected by the compatibility relations

$$-\beta dU = \frac{2Z}{Z^2 + 1}\, dV = \frac{2iZ}{Z^2 - 1}\, dW \qquad (2.11\text{-}1)$$

which express that the flow derives from a potential. The pressure coefficient at each point of the obstacle is proportional to u.

According to the applications, either u, v, or w can be identified with the electric potential of a plane circular tank of which the contour represents the circle C. Let us consider some simple nonrestrictive examples [*12*].

Let us determine the pressures on a *lifting* delta wing with dihedral $AOD = \theta$ (Fig. H,2.11a). The conditions which define the problem are as follows:

1. on C, u, v, w are zero.
2. on OD, $w \cos \theta - v \sin \theta = \alpha$ (α = const is the incidence of the wing). By means of Eq. 2.11-1 it can be deduced that the imaginary part of $[Z(dU/dZ)]$ is zero [*12*, pp. 173].

By identifying the function u with the electric potential and by reducing the tank by a half, taking into account the symmetry about Oy, the above-mentioned conditions show that the half-circumference BAB' must be conductive while the contour $BODOB'$ must be insulated with OD forming a cut. And, lastly, at D there is a singularity of the form $U(Z) \sim K(Z - Z_D)^{-\frac{1}{2}}$ represented by an arc of equipotential (making a small electrode) and an arc of streamline (insulated), both in the shape of arcs of a cardioid. The tank thus is supplied by the half-circumference BAB' and the small electrode.

Measurements of the electric potential along the two edges of the insulating cut ODO give the values of speeds u and therefore the pressure at any point of the wing.

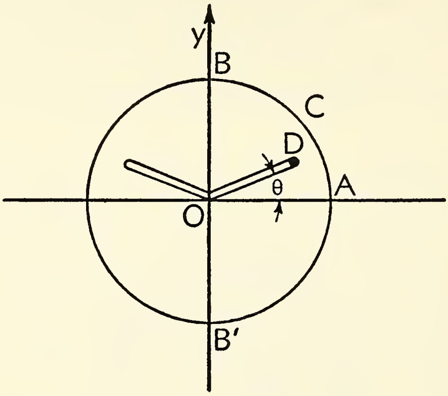

Fig. H,2.11a. Conic flow, delta wing with dihedral.

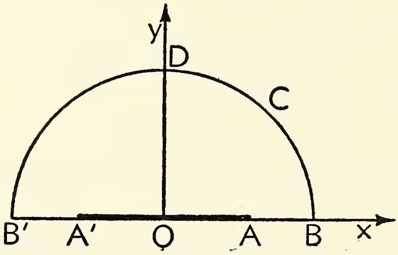

Fig. H,2.11b. Conic flow, case of the flat cone.

Let us consider a second example [*12*, p. 77ff.], that of a flat cone of any section within the cone of Mach. The image of this cone will be the segment AA' of plane Z (Fig. H,2.11b). Along this segment w is known, and on C we still have $u = v = w = 0$. This time function w can be identified with the electric potential of a semicircular tank BDB'; the symmetric problem and the lifting problem can be dealt with separately.

In the first case w is zero on AB and $A'B'$; the contour $ABDB'A'$ is therefore conductive and at zero potential. The segment AA' is covered with small supply electrodes the potentials of which are adjusted to the known values of w on AA' (problem of Dirichlet). By then measuring the strength of the current supplied by each electrode—a strength which, within a factor, represents the normal derivative $\partial w/\partial Y$ at the corresponding point of AA'—one deduces, by means of the compatibility relation 2.11-1

$$\left(\beta \frac{\partial u}{\partial X} = \frac{2X}{1 - X^2} \frac{\partial w}{\partial Y}\right)$$

the tangential derivative $\partial u / \partial X$ from which the value of u at each point of the wing finally is obtained, the integration constant having been deduced from the particular value of u at the center O which is determined from the measurements of the potentials along OD.

In the lifting case u is zero on AB and $A'B'$, which are represented by insulating walls, but it is also necessary to place in A and A' singularities similar to those mentioned in the previous example and in which the potentials must be adjusted to cancel out the electric flux entering at points B and B'. The other adjustments and measurements in this experiment are then made in the same way as in the symmetric case.

H,2.12. Conclusions. The applications which have been described illustrate the two methods of using the electric tank, i.e. either as a simple device for making quick plots of flows or as a calculating machine reducing certain mathematical relations to figures. In the first application the representation of the phenomenon is direct while in the second there is frequently a transformation of the initial problem.

In either case the electric tank is a convenient means of linking theory and experiment. In the development of certain experimental researches much profit could be drawn from combining wind tunnel tests and theoretical studies in the electric tank.

H,2.13. Cited References.

1. Pérès, J. Les méthodes d'analogies en mécanique appliquée. *Proc. Fourth Intern. Congress Appl. Mech. 1*, 9–19 (1938).
2. Taylor, G. I., and Scharman, C. F. A mechanical method for solving problems of flow in compressible fluids. *Proc. Roy. Soc. London A121*,194–217(1928).
3. Malavard, L. *Techniques générales du laboratoire de physique.* Vol. 2. Presses Centre natl. Recherche sci., Paris, 1950.
4. Malavard, L. Sur une nouvelle technique dans le calcul expérimental par analogies rhéoélectriques. *Recherche aéronaut. Paris 20*, 61–68 (1951).
5. Malavard, L. Étude de quelques problèmes de la théorie des ailes. *Publs. sci. et tech. Ministère Air, France, 153*, 1939.
6. Malavard, L. The use of rheo-electrical analogies in certain aerodynamical problems. *J. Roy. Aeronaut. Soc. 51*, 739–756 (1947).
7. Malavard, et al. Calcul des répartitions de vitesse sur les profiles des grilles planes. *Recherche aéronaut. Paris 4*, 33–46 (1948).
8. Siestrunck, R. Ecoulement à potentiel dans les machines hélicoïdales simples. *ONERA Publ. 32*, Paris, 1949.
9. Legras, J., and Malavard, L. Étude au bassin électrique du problème de la surface portante. *Proc. Sixth Intern. Congress Appl. Mech.*, Paris, 1946.
10. Campbell, W. F. Two electrical analogies for the pressure distribution on a lifting surface. *Natl. Research Council Can. Rept. Ma-219*, 1949.

11. Malavard, L. *Méthodes de calcul dans des problèmes de mécanique.* Presses Centre natl. Recherche sci., Paris, 1949.
12. Germain, P. Théorie générale des mouvements coniques. *ONERA Publ. 34,* Paris, 1949.

SECTION I

MEASUREMENT OF FLAME TEMPERATURE, PRESSURE, AND VELOCITY

F. P. BUNDY
H. M. STRONG

SECTION I

MEASUREMENT OF FLAME TEMPERATURE, PRESSURE, AND VELOCITY

F. P. BUNDY

H. M. STRONG

I,1. Introduction. The accurate measurement of flame temperatures has occupied the attention of many investigators for nearly eighty years. During this period many schemes have been proposed and tried. Today, because of the great amount of research and development in combustion systems, increased attention is being given to the problem of devising more satisfactory methods of measuring flame temperatures. The methods which have been developed make use of the radiation and absorption properties of gases, of temperature sensitive probes, and of the velocity of sound or critical flow velocities in the gases. Some representative methods of each type are described in this section.

Flame temperature indications must be interpreted in the light of our knowledge of combustion processes. When a gas is in thermodynamic equilibrium, there is an energy balance among its degrees of freedom and a definite temperature can be assigned to it. If the gas is being heated by chemical reactions it is likely to gain energy through particular degrees of freedom, and equilibrium among all the degrees of freedom will not exist. It is then impossible to assign a unique temperature to the flame gases. This condition is quite common at the flame front or wherever active combustion is going on. Another example of nonequilibrium is the electric discharge tube, in which energy is fed mainly into electronic states of excitation of gas atoms and molecules instead of into translational energy, where it would be manifested as increased temperature of the gas in the ordinary sense.

Any spectroscopic phenomenon which depends on the temperature of the gas can be used for temperature measurement. If the spectroscopic behavior is associated with a particular degree of freedom in the system of gas molecules, it indicates the temperature of that degree of freedom to which it is coupled. This will also be equilibrium temperature provided the life times of the emitters or absorbers of radiation being observed are long enough to attain equilibrium with all degrees of freedom.

The part of this text describing the measurement of temperature by optical methods is based on Kirchhoff's law of black body radiation and on Wien's function for the distribution of radiation from a black body radiator. For a full account of radiation laws, the reader may wish to consult a text such as Richtmyer's *Introduction to Modern Physics* (see bibliography).

Kirchhoff's radiation law states that when a number of bodies in proximity to one another are all at the same temperature, the amount of radiant energy emitted by any particular body is the same as the amount it absorbs from the surrounding bodies. Referring to the different individual bodies by the subscripts 1, 2, 3, etc., Kirchhoff's law may be stated in the following manner:

$$\frac{I_1}{A_1} = \frac{I_2}{A_2} = \frac{I_3}{A_3} = \cdots = 1$$

I is the rate of energy emitted for each unit of area and A is the rate of absorption of energy for each unit of area.

A black body is one which absorbs all energy incident on it and emits the maximum energy for its temperature; all others absorb and emit somewhat less than this amount of energy. A black body is simulated by a cavity and the properties of black body radiation can be observed through a small hole in such a cavity. By comparing the radiation of other bodies with that of a cavity, the emissivity or absorptivity of the other bodies is found. The emissivity or absorptivity of a body is defined as the ratio of the energy it emits or absorbs to that of a black body. That is,

$$\frac{I}{I_b} = \text{emissivity } \epsilon = \frac{A}{A_b} = \text{absorptivity}$$

I_b and A_b refer to the amount of energy emitted and absorbed by a black body and ϵ is the emissivity of the body which emits and absorbs energies I and A. When the temperature of the body is the same as the "black body temperature" of the radiation it receives, then I and A are equal. The part of the energy incident on the body which is not absorbed is reflected or transmitted through it.

Very often a body is selective as to wavelength in its absorption and emission. We then refer to ϵ_λ, its emissivity (or absorptivity) at a particular wavelength. A gray body is one whose emissivity or absorptivity is less than that of a black body but is about the same for all wavelengths.

The distribution of energy in a black body spectrum is continuous and is given with sufficient accuracy for the visible and near infrared regions of the spectrum by Wien's function

$$I_b = \frac{c_1}{\lambda^5} e^{-c_2/\lambda T} d\lambda d\sigma$$

in which I_b is the rate of emission of energy from a black body in the wavelength interval $d\lambda$ and from the area $d\sigma$; c_1 and c_2 are fundamental physical constants; and T is the absolute temperature.

The spectroscopic methods for measuring gas temperature may be classified in the following categories: (1) resonance spectral line reversal which has been adapted to both the visible and infrared spectral regions, (2) distribution of intensity in the rotational lines of band spectra, (3) two-color pyrometry, (4) absolute radiation, and (5) Doppler widths of spectral lines. Examples of method (1) on both isothermal and non-isothermal flames, and methods (3) and (4) will be described. The bibliography, in Art. 10, includes references to various modifications of these methods for which there is not space in this section.

Method (2) and its various modifications are described in M,3.

Method (5), the measurement of flame temperatures from the Doppler widths of spectral lines, has been developed and successfully applied by Gaydon and Wolfhard [*1*] on low pressure flames in which the concentration of the emitter is quite low. A particular advantage of this method in their application is that the Doppler widths give an accurate indication of translational energies even though the spectral line brightnesses are at least partially due to chemiluminescence. For details concerning this method, the reader is referred to the original paper.

Nonspectroscopic methods of flame temperature measurement are useful when the flame or some parts of the flame are not spectroscopically active or where the flame is not accessible to spectroscopic observations. Thermocouples or compensated hot wire probes are useful in such flames up to temperatures of about 1300°K (1900°F). The two-orifice method is also practical for temperature measurement in these circumstances.

The determination of temperature from measurement of the velocity of sound in the flame gases has some particular advantage in that it measures the temperature of the translational energy regardless of whether equilibrium exists among the various degrees of freedom and it is not limited to any particular temperature range. However, to apply this method it is necessary to know the composition and ratio of specific heats of the flame gases quite accurately. These advantages and conditions also apply to the methods employing the critical flow of gases through nozzles (i.e. the "pneumatic" methods).

In the case of flame gases traveling at supersonic speeds, it is often desirable to know pressures and velocities in different parts of the flame as well as temperature in order fully to determine its state. Recently, spectroscopic methods closely related to some of the flame temperature measuring methods have been developed and these are described in detail in the following articles.

I,2. Spectral Line Reversal Techniques.

Classical method. The sodium line reversal[1] method of flame temperature measurement was introduced by Féry in 1903 [*2*] and its validity was established later by Kohn [*3*]. The apparatus required is illustrated in Fig. I,2a. A tungsten ribbon lamp shines through the flame containing sodium vapor,[2] whose temperature is to be measured, and on to the slit of a spectroscope. The NaD lines[3] will be seen through the spectroscope superimposed on the continuous background from the lamp. Adjustment of the lamp brightness temperature to the temperature of the flame will cause the NaD lines to match with the lamp background. An optical pyrometer temperature reading on the lamp then gives the flame temperature directly.

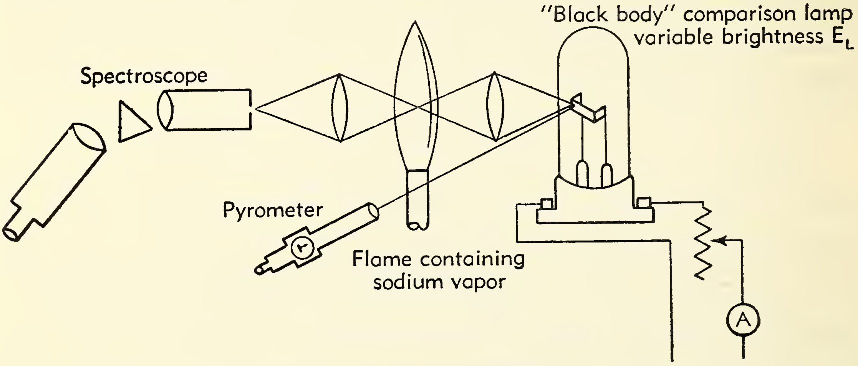

Fig. I,2a. Sodium line reversal flame temperature measuring apparatus.

The theory of SLR is based on Kirchhoff's radiation law. It is expressed by the equation for the matching condition[4]

$$E_L = E_F + (1 - a_F)E_L \tag{2-1}$$

Thus, the background brightness E_L must be equal to the flame brightness E_F plus what gets through the flame from the lamp $(1 - a_F)E_L$. The

---

[1] Sodium line reversal will hereafter be referred to by the symbol SLR.

[2] Salt spray may be blown into the flame with the unburned fuel or a sodium compound added to the fuel to give sodium vapor in the flame. Only very small amounts are required.

[3] NaD is the symbol for sodium D lines.

[4] The E's are called brightness for convenience in the discussion. E is defined in terms of Wien's radiation distribution law as follows:

$$I = \frac{c_1}{\lambda^5} e^{-c_2/\lambda T} d\lambda d\sigma$$

I is the rate of radiation of energy at wavelength λ in the wavelength interval $d\lambda$ from an element of surface $d\sigma$. For the NaD lines $c_1/\lambda^5 = 5.25 \times 10^{16}$. E as used here is defined as

$$E \equiv \frac{I \times 10^5}{5.25 \times 10^{16} d\lambda d\sigma} \equiv 10^5 e^{-c_2/\lambda T}$$

absorptivity of the flame is a_F and $(1 - a_F)$ is the fraction of the incident energy which the flame will transmit. For a flame of uniform temperature, the entire NaD line contour[5] matches with the background when the lamp brightness temperature is equal to the flame temperature, i.e. Eq. 2-1 applies to every wavelength region within the SLC. If instead of one temperature zone there are two or more zones of differing temperatures in the path of the measuring beam, Eq. 2-1 does not apply to all parts of the SLC simultaneously and the temperature reading obtained will be intermediate between the temperatures of the different zones. This is explained in the second part of this article..

The amount of sodium vapor in the flame does not influence the result, except as noted below, provided there is enough to make the D lines visible in the spectroscope.

Various modifications of the optical system in Fig. I,2a are possible provided they are such that lamp and flame brightness are being compared. This means that only that portion of the flame radiation may be used which lies within the cone traversed by the lamp radiation. In the apparatus illustrated this is accomplished by imaging the lamp image in the flame on the slit of the spectroscope so that the observer sees this image spread out in a spectrum. The matching is done within the limits of this lamp image. The NaD lines usually extend outside the lamp image.

For flames that are dangerous to the observer a modified form of SLR apparatus illustrated in Plate I,2a can be used [4]. An optical density wedge or rotating spiral disk imaged on the slit and again on the photographic film provides a background of brightness temperatures graduated parallel to the NaD lines. The tungsten arc target button is imaged in the flame and again on the prism. A diaphragm at the prism limits the cone of radiation to that of the radiation from the tungsten target, thereby establishing the brightness comparison condition described above. It is also necessary for every ray leaving the lens on the left to pass through the flame and the lens on the right. The type of film record obtained with NaD lines, exaggerated in width and separation, is shown diagrammatically in Plate I,2a. The entire operation of the apparatus can be by remote control.

Plate I,2b shows a typical film record obtained by the authors on a rocket motor flame. A rotating spiral disk was used to graduate the background brightness and the two bright horizontal lines were caused by two rings of slots in the spiral disk at the 1800 and 2100°K temperature positions. These two reference marks determine the scale for the entire background. Note that the reversal point was at 2360°K.

Effect of flame zones of different temperatures. Whenever the comparison lamp beam shines through a flame that has distinct temperature zones, a SLR match like those illustrated in Plates I,2a and I,2b will be obtained, but the temperature indicated will be intermediate between the highest and lowest temperatures in the path of the measuring beam [*5*; *6*, pp. 641–647; *7*; *8*; *28*]. If the low resolving power spectroscope normally used in SLR work were now replaced by an instrument capable of fully resolving the shape of the SLC, then, with background brightness kept the same as in the preceding observation, part of the SLC would appear brighter than the background and part of it darker. The low resolving power spectroscope averages the over and under intensities together to give an apparent match. Eq. 2-1 applies now only to the wavelength within the SLC that does match the background brightness. Changing the comparison lamp brightness changes the position on the SLC where a match is obtained.

---

[5] NaD line intensity contour will hereafter be referred to by the symbol SLC.

The factors that control the intermediate temperatures observed on complex flames are the shape of the NaD lines, the temperature for each zone, and the order in which the zones occur in the line of sight. Because of the importance of the NaD line shapes, this will be discussed in more detail.

All spectral lines have bell-shaped intensity distributions that cover a narrow band of wavelengths. The half widths W of these distributions are defined as the wavelength span covered by the SLC between its center and the place where its intensity is one-half the line center intensity. In the case of thermally excited resonance lines, like the NaD lines, the width of the line in both emission and absorption for a thin zone of vapor is due chiefly to the spread of the Doppler shift in wavelength caused by the thermal motions of the atoms and to the disturbing influence of neighboring atoms or molecules on the fields of the emitting or absorbing atoms. As the radiation from a thin zone passes through successive layers of an extensive cloud of absorbing and emitting atoms, the initial radiation is strongly absorbed at the line center and weakly absorbed in the line extremities. At the same time, successive zones add their own radiation. The result of this interplay between emission and absorption is a spectral line which approaches full black body brightness at the line center first, then gradually reaches this limit farther into the line extremities. This is called absorption broadening and its effect is illustrated in Fig. I,2b.

The transmission factor for radiation passing through a cloud of sodium vapor is the customary exponential, with the addition of a SLC wavelength shape factor sf. It is $e^{-z(sf)}$, sf indicating that the amount of transmission depends on the position of the radiation within the SLC; $z(sf)$ is the "optical depth" at $\Delta\lambda A$ from the line center in the ordinary sense that when the exponent of e is unity, the intensity of incident radiation at this $\Delta\lambda$ is reduced to e^{-1} of its initial value on passage through the cloud; z is proportional to the density of absorbing atoms and the path length. The value of sf is given with sufficient accuracy by the expression

$$sf = \frac{W_0^2}{W_0^2 + \overline{\Delta\lambda}^2} \tag{2-2}$$

W_0 is the half width of a NaD line, in emission or absorption, for a very thin wafer of hot sodium vapor. Its value is 0.049A for most flames at atmospheric pressure; $\Delta\lambda$ is the separation in angstroms from the line center of the point on the line contour being considered. At the line center $\Delta\lambda = 0$, $sf = 1$.

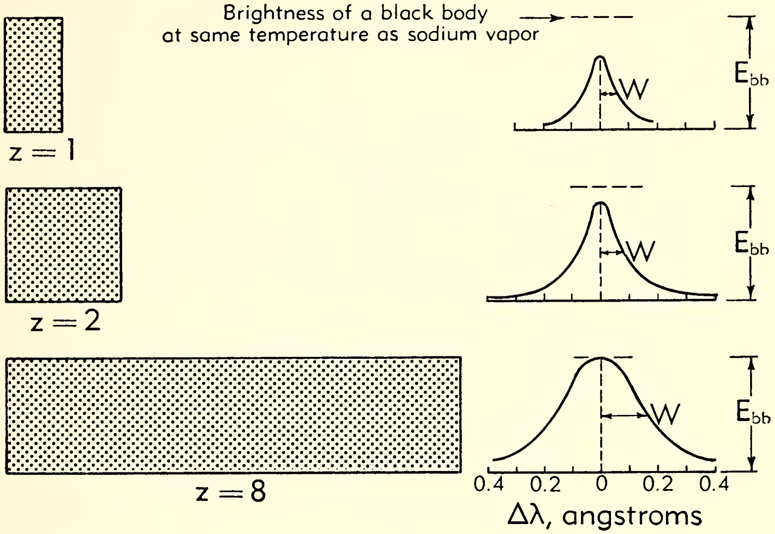
Brightness of a black body at same temperature as sodium vapor
W
E_bb
z = 1
W
E_bb
z = 2
W
E_bb
z = 8
0.4 0.2 0 0.2 0.4
Δλ, angstroms

Fig. I,2b. Illustration of effect of absorption broadening.

For a cloud of sodium vapor whose radiation is in thermal equilibrium with the translational energies of the atoms and molecules, its absorptivity is $[1 - e^{-z(sf)}]$. This is the a_F in Eq. 2-1. By Kirchhoff's radiation law this is also equal to the emissivity of the sodium vapor cloud. Therefore, the radiation emitted by the cloud of sodium vapor has the wavelength energy distribution (or SLC) $E_{\Delta\lambda}$, given by

$$E_{\Delta\lambda} = E[1 - e^{-z(sf)}] \tag{2-3}$$

where E is the black body brightness as defined in footnote 4, p. 346.

Using transmission and emission factors defined above, the energy distribution may be obtained for the radiation from a zone of sodium vapor at temperature T_1 passing through and being selectively absorbed in another zone at temperature T_2 but being reinforced by radiation from this second zone. It is

$$E_{\Delta\lambda} = E_1[1 - e^{-z_1(sf)}]e^{-z_2(sf)} + E_2[1 - e^{-z_2(sf)}] \tag{2-4}$$

The subscripts 1 and 2 refer to their respective zones. This is illustrated in Fig. I,2c for the radiation from two flames burning at two different temperatures. Illustrative values for z_1, z_2, E_1, and E_2 are included in Fig. I,2c.

When a tungsten ribbon lamp also shines through flames (1) and (2) in Fig. I,2c, one additional term must be included on the right side of Eq. 2-4; it is $E_Le^{-(z_1+z_2)(sf)}$, in which E_L is the lamp brightness, a term which remains constant over the wavelength interval covered by the SLC. $e^{-(z_1+z_2)(sf)}$ is the transmission factor for the lamp radiation passing through both flames. A plot of the energy distribution for various values of lamp brightnesses E_L shining through the two flames is shown in Fig. I,2d. These are patterns which would be seen in a spectroscope of very high resolving power during a SLR test on these two flames.

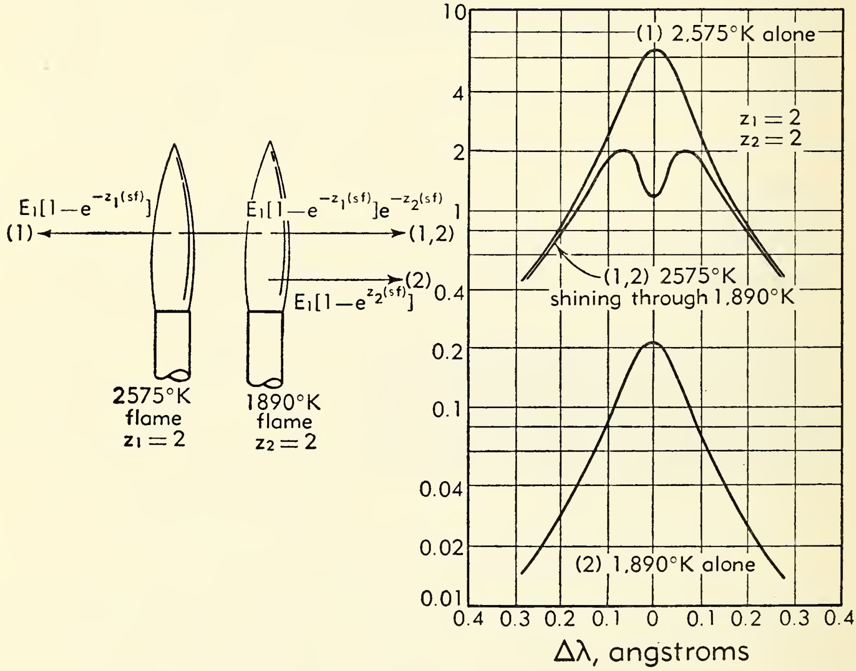

Fig. I,2c. Energy distributions in radiation from two flames.

For an ordinary spectroscope, a SLR match would be observed at $E_L = 2.25$, $T_L = 2285°K$, curve (b) in the example given, because the amount of overintensity above the 2285°K brightness level would be lumped with and would cancel the underintensity beneath this brightness level. These over- and underintensities are shaded in Fig. I,2d. In curve (c) the SLC is brighter than E_L and in curve (a) it is darker than E_L.

Analytically, the condition for a SLR match in a low resolving spectroscope is (following Eq. 2-1) that the lamp brightness integrated over the entire SLC interval is equal to the brightness from the flames plus the brightness from the lamp penetrating the flames integrated over the same SLC interval. It is

$$E_L \int_{\mathrm{SLC}} d\lambda = E_1 \int_{\mathrm{SLC}} [1 - e^{-z_1(sf)}]e^{-z_2(sf)}\, d\lambda + E_2 \int_{\mathrm{SLC}} [1 - e^{-z_2(sf)}]d\lambda$$
$$+ E_L \int_{\mathrm{SLC}} e^{-(z_1+z_2)(sf)}d\lambda \quad (2\text{-}5)$$

E_L, E_1, and E_2 are constant over the SLC.

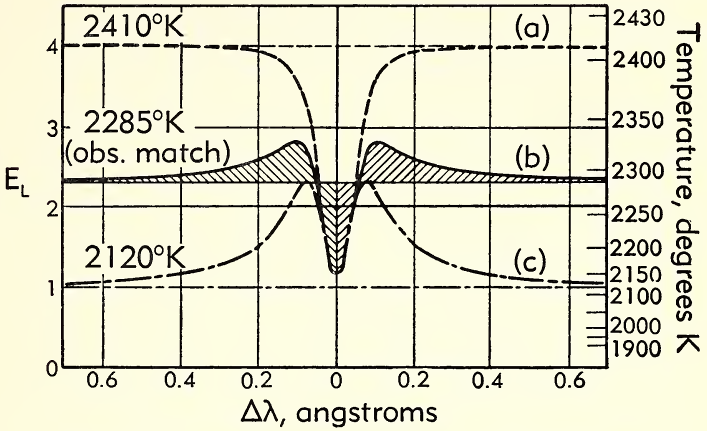

Fig. I,2d. Energy distributions in SLR on two flames of temperatures 2575°K and 1890°K.

Eq. 2-6 may be arranged in a form that can be graphically integrated as follows:

$$E_L = \frac{\int_{\mathrm{SLC}} \{E_1[(1 - e^{-(z_1+z_2)(sf)}) - (1 - e^{-z_2(sf)})] + E_2(1 - e^{-z_2(sf)})\}d\lambda}{\int_{\mathrm{SLC}} [1 - e^{-(z_1+z_2)(sf)}]d\lambda} \quad (2\text{-}6)$$

A graphical integration of the terms $[1 - e^{-z(sf)}]$ was done, the results of which are shown in Fig. I,2e for values of z between 1 and 22. In this plot z represents z_1, z_2, $(z_1 + z_2)$, or any required additive combination of the z's. For example, the value of

$$\int_{\mathrm{SLC}} [1 - e^{-(z_1+z_2)(sf)}]d\lambda$$

for $z_1 = 4$ and $z_2 = 1$ would be obtained from the graph at $z = 5$.

Setting

$$A = \int_{\mathrm{SLC}} [1 - e^{-(z_1+z_2)(sf)}]d\lambda, \quad B = \int_{\mathrm{SLC}} [1 - e^{-z_2(sf)}]d\lambda$$

Eq. 2-6 becomes

$$E_L = \frac{E_1(A - B) + E_2B}{A} \tag{2-7}$$

Thus the SLR matching brightness E_L in this example is given by the values z_1 and z_2 of the optical depths of the two flames and the black body brightnesses E_1 and E_2 corresponding to their temperatures T_1 and T_2. The authors found that Eq. 2-7 gave values of E_L which determined T_L to within 5 per cent of experimentally observed values.

For the convenience of the reader, values of E at $\lambda = 5893\text{A}$ for various values of T in degrees Kelvin are plotted in Fig. I,2f.

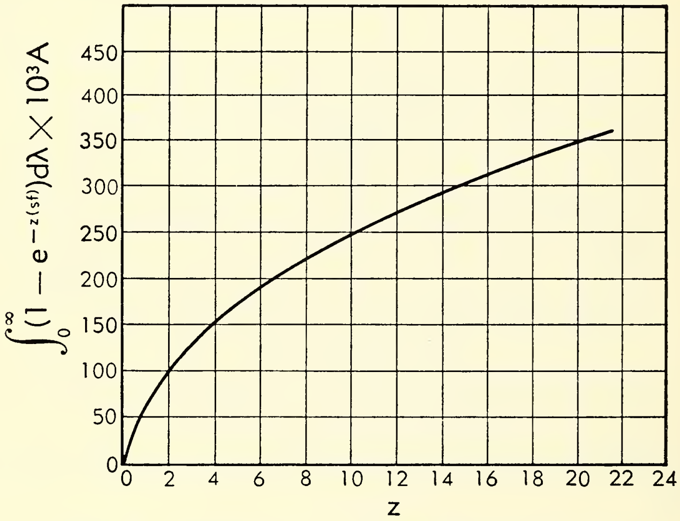

Fig. I,2e. Values of $\int[1 - e^{-z(sf)}]d\lambda$ as a function of z.

The above principles can be used to measure the temperature of an inner zone of a complex flame like that illustrated in Fig. I,2g. For an observation through the flame center (Obs. 1) an equation similar to Eq. 2-7 applies. It is

$$E_L = \frac{E_2(X - Y) + E_1(Y - Z) + E_2Z}{X} \tag{2-8}$$

in which

$$X = \int_{\text{SLC}} [1 - e^{-(z_1+2z_2)(sf)}]d\lambda, \quad Y = \int_{\text{SLC}} [1 - e^{-(z_1+z_2)(sf)}]d\lambda,$$

$$Z = \int_{\text{SLC}} [1 - e^{-z_2(sf)}]d\lambda$$

Observation (Obs. 1) determines the value of T_L and E_L. Obs. 2 determines the value of T_2 and E_2. When these values of E_L and E_2 together with the appropriate values of X, Y, and Z as determined from the optical depths z_1 and z_2 of the flame zones are substituted in Eq. 2-8, the black body brightness E_1 corresponding to the inner zone temperature T_1 can be calculated.

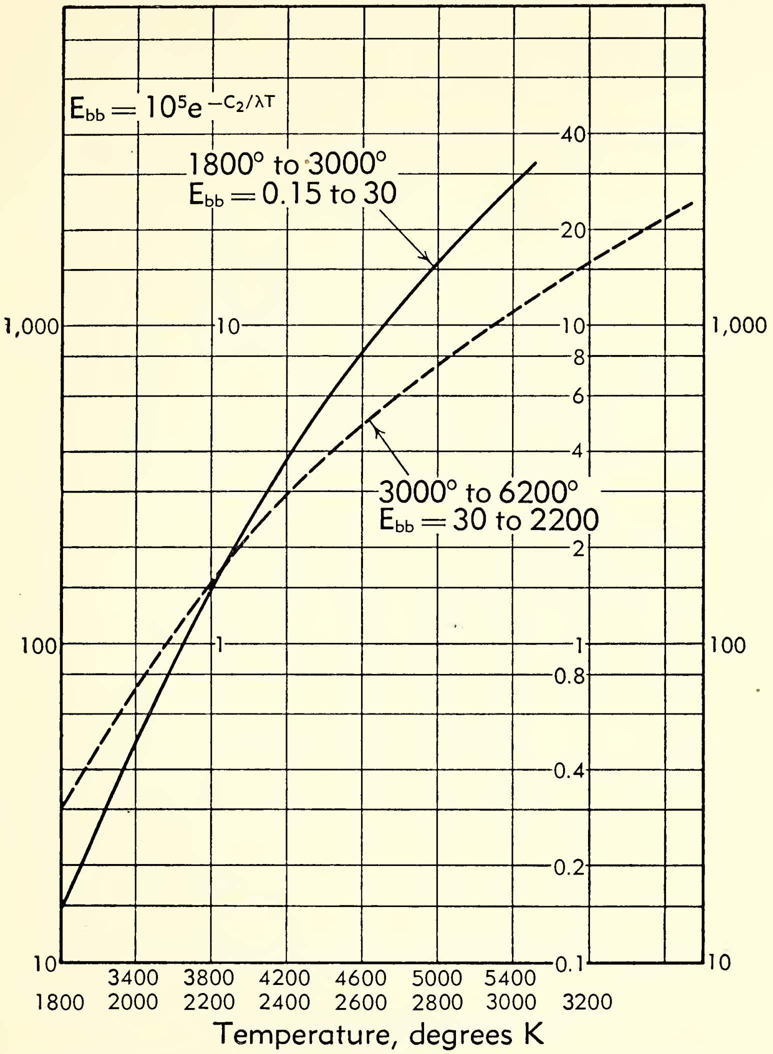

Fig. I,2f. Values of E at 5893A as a function of Kelvin temperature.

The absolute values of z_1 and z_2 are not required. The curve in Fig. I,2g shows that for a constant ratio the intermediate temperature obtained by SLR, Obs. 1 is nearly constant[6] for $z_2 > 2$. The value of this ratio is the determining factor and in the example illustrated it is assumed that the distribution of sodium vapor is uniform throughout the flame so that the ratio z_1/z_2 is equal to the ratio of core diameter to shell thickness. In this case $z_1/z_2 = 4$. Hence, with sufficient sodium vapor in the flame, it is safe to assign values of z_1 and z_2 such that $z_1 = 4z_2$. The proper weighting factors $(X - Y)$, $(Y - Z)$, etc. will then be obtained.

---

[6] $z = 1$ for 6.6×10^{12} Na atoms/cm^2 in the line of sight.

In case one zone differs widely from the other in temperature and pressure, the ratio z_1/z_2 may deviate from the geometric ratio. It is then necessary to estimate the correction to be applied to the geometric ratio to obtain a more representative value of z_1/z_2. For more accurate results, the method and apparatus to be described next are recommended.

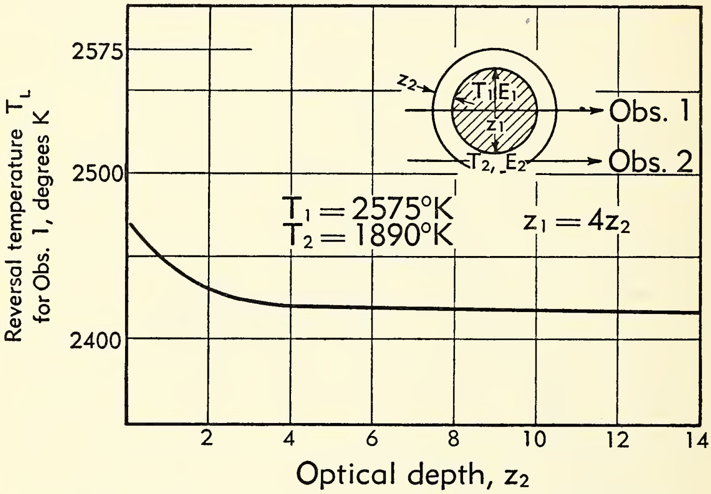

Fig. I,2g. Theoretical SLR temperatures for a complex flame as a function of optical depth.

High resolution SLR apparatus. The method of SLR temperature measurement which is described above depends on certain assumptions regarding the shape of the SLC, which, though generally satisfactory, might not apply for flames at unusually low pressure or of unusual composition. Also, an estimate of the optical depths of the different zones is required which, if substantially in error, would give one the wrong estimate of the inner zone temperature. The method now to be described avoids these difficulties but requires the use of a spectroscopic instrument of high resolving power and a microdensitometer.

This method [7] is based on an equation obtained from Eq. 2-8 by letting the optical depth in the integrated terms approach zero. The new equation is

$$E_L = \frac{z_2E_2 + z_1E_1 + z_2E_2}{z_1 + 2z_2} \tag{2-9}$$

as it would be written to apply to Obs. 1, Fig. I,2g. In the general case of n zones in the path of the measuring beam having n different temperatures and black body brightnesses E_r (r = 1 to n) associated with them, Eq. 2-9 would read

$$E_L = \frac{\sum_{r=1}^{n} z_r E_r}{\sum_{r=1}^{n} z_r} \tag{2-10}$$

The accuracy of Eq. 2-9 is very good for small optical depths. For the example in Fig. I,2g this equation gives a value of E_1 about 7 per cent smaller than that given by the accurate equation when $z_1 = 1.2$. The error in the temperature reading due to this error in the computed value of E_1 is 0.6 per cent, which is smaller than experimental errors.

The spectroscopic resolving power needed to make observations at these low optical depths or at selected points on the SLC is at least 10^5. This is the value of $\lambda/\Delta\lambda$, where $\Delta\lambda$ is the smallest separation in wavelengths which the instrument will resolve. Ordinary spectroscopes have $\lambda/\Delta\lambda = 6 \times 10^3$ to 10^4. The Fabry-Perot interferometer is a convenient instrument to use and has sufficient resolving power. Its use is more fully described in some detailed reports on the subject [*7,9*].

The apparatus is basically a SLR apparatus like that in Fig. I,2a with an interferometer substituted for the spectrograph and a sodium vapor lamp[7] for the tungsten arc. When illuminated by the monochromatic NaD lines from the SVL and flame the interferometer gives a series of circular interference fringes each one of which reveals the SLC. The continuous radiation of a tungsten arc would obscure these fringes; hence it must be replaced by the SVL. An example of the application of this method on two flames burning at two different temperatures will be given. The two-flame experiment permits independent measurement of each of the two zones represented by the two flames as a check on the method.

The arrangement of apparatus and flames is shown in Fig. I,2h. A rotating spiral disk, here represented by an optical density wedge, provided a background of graduated brightness. The observations were recorded photographically and are as follows:

Exposure 1. SVL shining through spiral disk, flames 1 and 2.
Exposure 2. Flames 1 and 2 without SVL.
Exposure 3. Repeat of exposure 1.
Exposure 4. SVL shining through flame 2.
Exposure 5. Flame 2 without SVL. Because of its relatively low temperature, its brightness was only about one-fourth that in the other exposures.
Exposure 6. SVL only.

---

[7] Sodium vapor lamp will hereafter be referred to by the symbol SVL.

These interference patterns are shown in Plate I,2c. The exposures were all of equal time duration. Exposure 6 on the SVL alone shows clearly the brightness grading effect of the rotating spiral disk on the SVL radiation.

The next step is to take microdensitometer traces along radii of the circular interference patterns. By superimposing the trace for the SVL exposure alone on the trace for the SVL shining through both flames, the SLR matching brightness and temperature for the flame combination are revealed by the points where the traces cross. This is illustrated in Fig. I,2i on three of the fringes taken from exposures 3 and 6. The SLR matching temperature was 2210°K and the background (SVL) brightness, E_{SVL}, was 1.71. The set of three smaller fringes taken from exposures 4 and 6 illustrate the SLR match on flame 2 alone. This flame had a temperature of 2000°K and was used as the standard to calibrate the SVL.

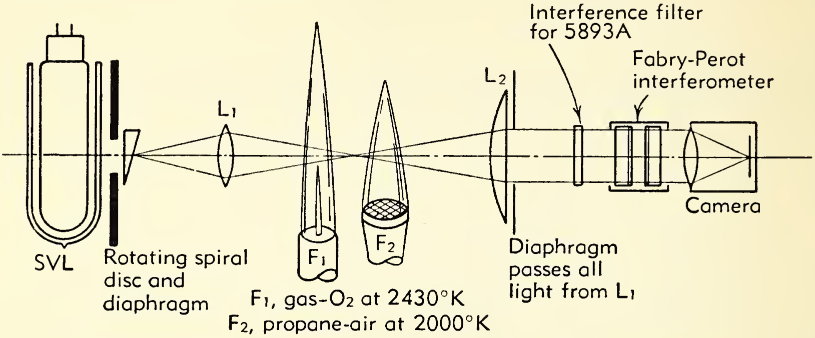
Interference filter for 5893A
Fabry-Perot interferometer
L₂
L₁
Camera
SVL
Rotating spiral disc and diaphragm
F₁
F₂
Diaphragm passes all light from L₁
F₁, gas-O₂ at 2430°K
F₂, propane-air at 2000°K

Fig. I,2h. High resolution SLR apparatus. Test on two flames.

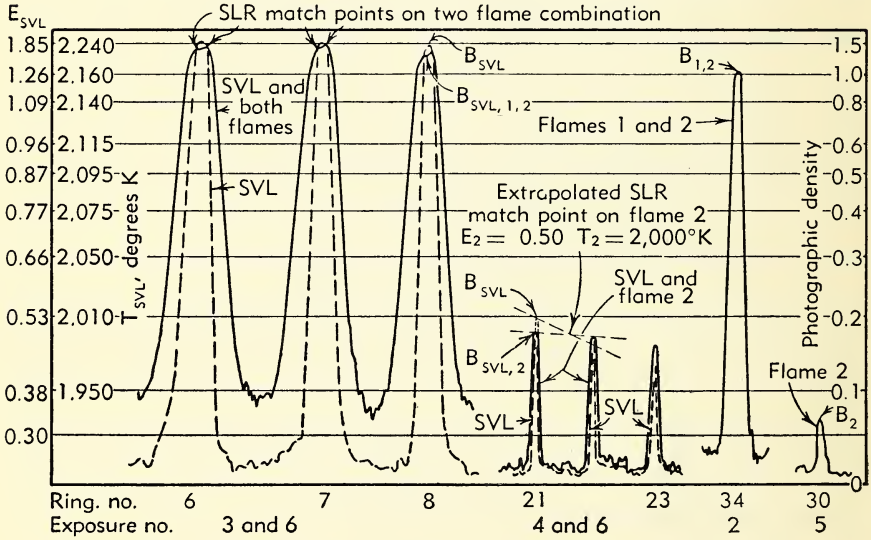

Fig. I,2i. Samples of microdensitometer traces taken on Plate I,2c.

A particular advantage of this method is that the optical depths of the different zones can be determined quite accurately. These optical depths are computed from measurements of the amount of light from the SVL which passes through the flame. In this example, the transmission, $e^{-(z_1+z_2)}$, of the two-flame combination at the NaD line centers ($\Delta\lambda = 0$) is

$$e^{-(z_1+z_2)} = \frac{B_{\mathrm{SVL},1,2} - B_{1,2}}{B_{\mathrm{SVL}}} \tag{2-11}$$

in which the B's are line center brightnesses taken from the E_{SVL} scale on the densitometer traces. The symbol B has been used in place of E to distinguish brightnesses used in optical depth calculations from brightnesses used for temperature calculations in Eq. 2-9, 2-10, and 2-13.

Similarly, the transmission e^{-z_2}, of flame 2 alone, which is here used to represent the outer shell of a complex flame, is given by

$$e^{-z_2} = \frac{B_{\mathrm{SVL},2} - B_2}{B_{\mathrm{SVL}}} \tag{2-12}$$

Eq. 2-11 and 2-12 give the value of $(z_1 + z_2)$ and z_2. The optical depth of flame 1, z_1, here used to represent the inner core of a complex flame, is obtained by subtraction: $z_1 = (z_1 + z_2) - z_2$.

Three fringes are required in each case to determine the B values in Eq. 2-11 and 2-12. One fringe must show the SVL brightness, another must show the brightness for the SVL shining through the flame combination for Eq. 2-11 or through flame 2 alone for Eq. 2-12, and the third fringe must show the brightness of the flame combination or of flame 2 alone without the SVL. Examples of such fringes having the points marked where the respective B values were taken are illustrated in Fig. I,2i. Note that the low-numbered fringes selected from near the center of the interference pattern are wider than the high-numbered fringes taken at some distance from the center. This is due to the characteristics of the interferometer. The widths of the NaD lines in angstrom units remain constant throughout any one pattern.

In practice it is well to use several sets of fringes to obtain averaged values of the z's because local fringe variations produced by the interferometer and photographic materials cause fluctuations in the z's obtained from different sets of fringes.

The SLR equation which applies in this two-flame example is

$$E_{\mathrm{SVL}} = \frac{z_1 E_1 + z_2 E_2}{z_1 + z_2} \tag{2-13}$$

E_1, the black body brightness of flame 1, is the unknown brightness to be determined. The experimental values of E_{SVL}, E_2, z_1, and z_2 were taken from the densitometer traces, samples of which are shown in Fig. I,2i, and are given in Table I,2 below. The temperature T_1 of flame 1 obtained from the calculated value of E_1 along with the value of T_1 measured by a conventional SLR test on flame 1 alone are also given in this table.

Table I,2. Experimental values of terms in Eq. 2-13.

E_{SVL}	E_2	z_1	z_2	E_1 (calc)	T_1 (calc)	T_1 (meas)
1.71	0.50	0.43	1.02	4.63	2445°K	2430°K

While the example illustrated indicates that a high degree of accuracy is possible, the limitations in the resolving power of the interferometer and in the accuracy of photographic intensity measurements would generally limit the accuracy of such temperature measurements to about ±3 per cent at this temperature level.

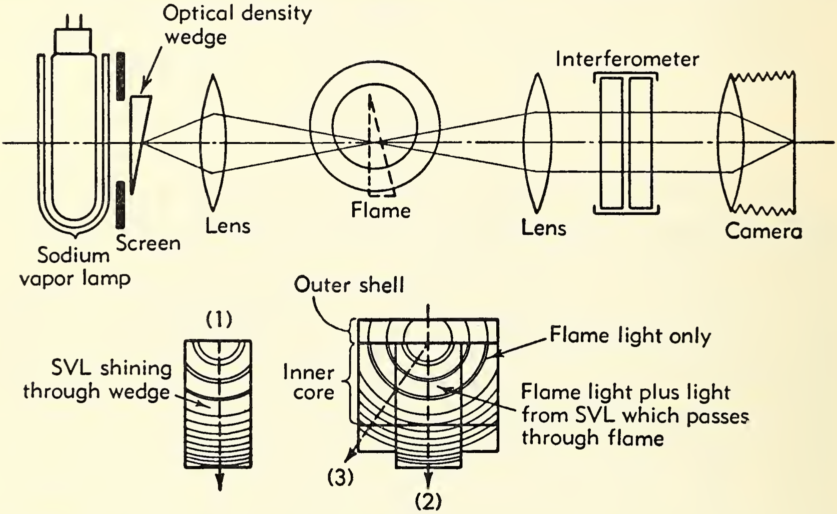

Fig. I,2j. High resolution SLR apparatus applied to a complex flame.

This method can be used on complex flames in the manner illustrated in Fig. I,2j. Also illustrated in Fig. I,2j are the interference patterns that would be obtained for the SVL shining through the wedge only and for the SVL shining through the wedge and flame. In the latter, the wedge image is clearly outlined in the interference pattern. Densitometer traces taken along the dashed arrows (1), (2), and (3) give the data needed to obtain the temperature in the outer shell, the temperature for a line of sight through both zones of the flame, and the various brightness values needed for computing optical depths of each zone of the flame. Using Eq. 2-9 or 2-10, the black body brightness of the inner zone may be calculated.

This method enables one to determine optical depths and temperatures of different zones of a flame quite accurately but has the disadvantage of requiring the use of an interferometer and a microdensitometer.

Intensity must be measured by photographic methods which require considerable care.

I,3. Absolute Radiation Methods. Wien's law for the radiation emitted into the hemisphere of space on one side of an area $d\sigma$ of a black body at temperature T, wavelength λ, and spectral interval $d\lambda$ is

$$I_b = \frac{c_1}{\lambda^5} e^{-c_2/\lambda T} d\lambda d\sigma \tag{3-1}$$

If the emitting body is a luminous, partially transparent flame the emissivity ϵ_λ may be considerably less than unity and the radiation is

$$I = \epsilon_\lambda I_b \tag{3-2}$$

Obviously, if I can be measured with a calibrated instrument, and if ϵ_λ can be determined in some way, the temperature of the flame can be calculated from the black body radiation law as follows:

$$\frac{I}{\epsilon_\lambda} = I_b = \frac{c_1}{\lambda^5} e^{-c_2/\lambda T} d\lambda d\sigma \tag{3-3}$$

One of the common methods of determining the emissivity of a flame is to find the ratio of the flame brightness when viewed against a mirror as compared to being viewed against a black background. If the ratio of the mirrored to unmirrored brightness is R_λ and the reflectivity of the mirror is r_λ, the emissivity is

$$\epsilon_\lambda = \frac{r_\lambda + 1 - R_\lambda}{r_\lambda} \tag{3-4}$$

In general it is difficult to make all the corrections necessary to reduce the actual radiation reading to the ideal solid angle of radiation assumed in the radiation law. It is more practical in actual cases to calibrate a given apparatus, which has its characteristic optical aperture and spectral band of sensitivity, against a flame of known temperature or a standard tungsten strip lamp. If the apparatus gives a reading D_0 for a flame of known temperature T_0 and emissivity $(\epsilon_\lambda)_0$, the constant K of the apparatus is found from

$$\frac{D_0}{(\epsilon_\lambda)_0} = Ke^{-c_2/\lambda T_0} \tag{3-5}$$

Once this constant is determined the apparatus may be used to measure the temperatures of other flames.

An example of this method is a photoelectric pyrometer developed by Hett and Gilstein [*10*]. Their apparatus is illustrated diagrammatically in Fig. I,3a. There are two nearly coincident lines of sight through the flame, one extending from the mirror through the flame, lens, filter, and aperture to the upper photocell, and the other from the black surface through the flame, lens, filter, aperture, and prism to the lower photocell. Thus the output of the upper photocell is proportional to the mirrored flame brightness while that of the lower photocell is proportional to the brightness of the flame alone. The apertures at the left and the corresponding black and mirrored surfaces at the right are located at the conjugate focuses of the lens. The outputs of the photocells are fed through amplifiers to a cathode ray oscilloscope having two electron beams with zero positions normally near the edges of the scope as shown in Fig. I,3b. Any output from the photocells causes the cathode ray spots to deflect toward the center. The cathode ray screen is photographed continuously by a camera in which the film moves at a uniform velocity in a direction perpendicular to the deflection of the cathode ray spots. In this way traces of the kind illustrated in Fig. I,3b are obtained, the fluctuating deflections indicating rapid corresponding fluctuations in flame temperature.

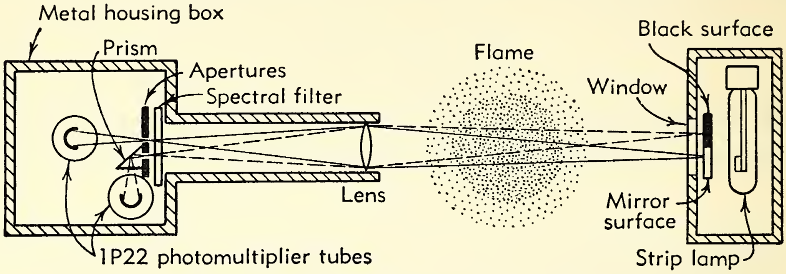

Fig. I,3a. Photoelectric pyrometer of Hett and Gilstein.

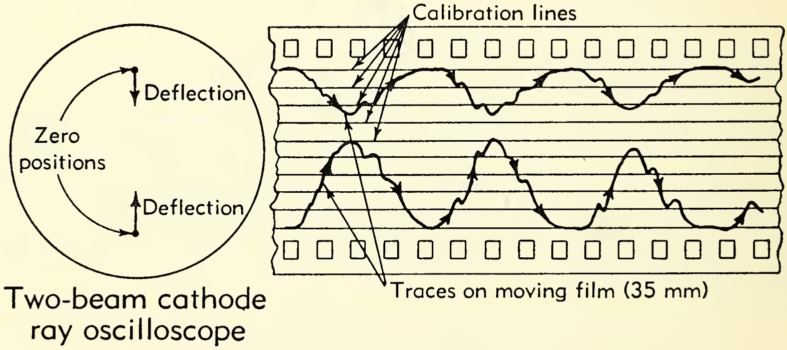
Calibration lines
Deflection
Zero positions
Deflection
Two-beam cathode ray oscilloscope
Traces on moving film (35 mm)

Fig. I,3b. Method of presentation of data from Hett and Gilstein's photoelectric pyrometer.

The instrument is calibrated by removing the plate bearing the black and mirrored surfaces, placing a calibrated tungsten strip lamp in their place, and rerunning the camera film over the same strip of film with the lamp set at different known brightness temperatures. After the calibration trace is on the film the flame emissivity and temperature can be calculated and plotted against the time axis. One of the chief advantages of this type of instrument is that it can follow extremely rapid fluctuations of emissivity and temperature and hence is useful in studying rapid or fluctuating combustion phenomena.

In the use of this instrument it is necessary to choose a region of the radiation spectrum which does not contain any spectral lines or bands unless the spectral interval is small in comparison to the line or band width and the lines or bands are known to be in thermal equilibrium with the flame gases. Such equilibrium is not attained in flames in which there are some combustion processes taking place. The spectral interval is usually determined by interference-type filters which have transmission band widths of the order of 100A between the 50 per cent transmission points, in which case, because of this large band width, line and band spectrum radiation cannot be properly used. Thus the flames to which this method can be readily applied must have a considerable amount of continuous radiation, usually from smoke particles of some kind.

Sanderson, et al. [*11*] have also developed and used a photoelectric pyrometer of the general type described above. An older method based on the same principle but using an optical pyrometer has been described briefly by Hottel and Broughton [*12*]. Recently, Bundy and Strong [*13*] developed a method based on the same principle of comparing the black body brightnesses of flames by measuring the spectral brightness at given wavelengths within the sodium line contour with and without a mirror behind the flame. In this case a spectroscopic instrument of high enough resolving power must be used to display the intensity contours of the individual sodium D lines. One of the chief advantages of this method is that it can be employed to determine the temperatures of inner zones of flames of complex temperature structure, while one of its chief disadvantages is that the method of recording is photographic and the use of a good recording microdensitometer is required.

I,4. Spectral Energy Distribution Methods.

Two-color pyrometry. The distribution of brightness with the wavelength of the radiation from a black body at temperature T is given by

$$I_b = \frac{c_1}{\lambda^5} e^{-c_2/\lambda T} d\lambda d\sigma \tag{4-1}$$

For nonblack bodies having emissivity ϵ_λ at wavelength λ the brightness distribution is

$$I_g = \epsilon_\lambda \frac{c_1}{\lambda^5} e^{-c_2/\lambda T} d\lambda d\sigma \tag{4-2}$$

This brightness corresponds to an apparent black body temperature T_A given by the equality

$$\epsilon_\lambda \frac{c_1}{\lambda^5} e^{-c_2/\lambda T} = \frac{c_1}{\lambda^5} e^{-c_2/\lambda T_A} \tag{4-3}$$

Hence

$$\epsilon_\lambda = e^{-\frac{c_2}{\lambda}\left(\frac{1}{T_A}-\frac{1}{T}\right)} \tag{4-4}$$

The radiation from flames which emit a more or less continuous spectrum comes mainly from tiny particles of soot or other suspended solid or liquid matter in the flame gases. In general the emissivity of such flames varies with the wavelength because of the selective absorption effects of the small particles for radiation of different wavelengths [*12*,*14*,*15*,*16*,*17*,*18*]. The emissivity of a flame is numerically equal to its absorptivity, which in turn is equal to the difference between unity and the transmissivity, i.e.

$$\epsilon_\lambda = 1 - e^{-k_\lambda L} \tag{4-5}$$

in which L is the length of the optical path in the flame and k_λ is the absorption coefficient. Hottel and Broughton [*12*] show that over considerable wavelength intervals the absorption coefficient is given by

$$k_\lambda \cong \frac{k}{(\lambda)^\alpha} \tag{4-6}$$

where $\alpha \cong 1.39$ for luminous hydrocarbon flames in the wavelength range of 0.5 to 0.7 microns. Thus, using Eq. 4-6, 4-5, and 4-4,

$$\frac{1}{T_A} - \frac{1}{T} = -\frac{\lambda}{c_2} \ln\left[1 - e^{-kL/(\lambda)^\alpha}\right] \tag{4-7}$$

Now if T_R and T_G are two monochromatic color temperatures obtained on the same flame at wavelengths λ_R and λ_G which lie within the range covered reasonably well by Eq. 4-6, two equations like Eq. 4-7 may be written in which all the terms are known except T and kL. By solving these two equations simultaneously, T and kL may both be found. Hottel and Broughton [*12*] have had considerable success with this method using a special optical pyrometer with color filters which transmitted effective wavelengths of 0.6651 and 0.5553 microns. More recently Rössler [*19*] also has reported favorable results.

Probably the most ingenious adaptation of the method has been by Uyehara, Myers, Watson, and Wilson [*20*] in measuring continuously the temperature of the gas in a diesel engine combustion chamber during the power stroke. Their apparatus is illustrated in Fig. I,4a. The light from the luminous gases in the combustion chamber of the engine emerged through a thick quartz window and was brought to focus by a lens on a "limiting diaphragm," the aperture of which essentially served as the slit of the prism spectroscope which separated the light into a spectral array in the plane of the phototubes. The two apertures in front of the phototubes permitted only that radiation centering around λ_1 (0.6960 microns) to fall upon one tube, and only that centering around λ_2 (0.9020 microns) to fall upon the other. The electrical output from each phototube was amplified and indicated as a deflection on a cathode ray oscillograph tube, the horizontal sweep of which followed the crank angle of the engine under test. The deflection constants of the oscillograph amplifier system were determined by placing a calibrated tungsten strip lamp in place of the combustion chamber and noting the deflection for various known brightness temperatures of the lamp. Proper corrections for the emissivity of the tungsten filament of the calibrating lamp and for the transmissivity of the quartz window were made. The traces made on the oscillograph screens during one cycle of the engine operation, along with the gas pressure record, were photographed by a camera adapted for the purpose. A typical result is shown in Fig. I,4b.

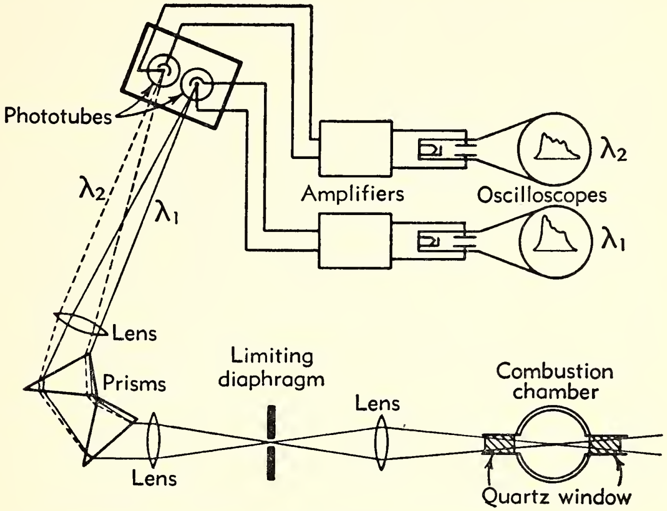

Fig. I,4a. Apparatus of Uyehara, et al., for measuring flame temperature in the combustion chamber of a diesel engine by the two-color method.

In general, the two-color intensity method of flame temperature measurement is convenient and accurate under proper conditions. In its use care must be taken to avoid any regions of the spectrum in which there are spectral bands or lines which originate from chemiluminescence associated with combustion processes, as such radiations are not in thermal equilibrium with the average of the flame gases. There are many examples of this. Wolfhard and Parker [*16,17*] have found, for example, that the two-color temperature of burning photoflash powders may be several hundred degrees higher than can be accounted for by the chemical energy available, or as measured by line reversal or absolute radiation methods. They attribute this difference to unusually large variation of the absorptivity with wavelength due to the small size of the particles suspended in the flame.

Intensity distribution in the lines of band spectra. A specialized form of the two-color or multicolor method of determining the temperatures of flame gases consists in determining the distribution of intensities of the individual lines of a band in a band spectrum emitted by the flame. This distribution of intensity is controlled by the probabilities of the spectral transitions in the molecules and the density of population of the molecules in the different levels of rotational energy. As the latter has a Boltzmann temperature distribution when thermodynamic equilibrium prevails, the intensity distribution varies with the temperature, the higher order lines becoming brighter relative to the lower order ones as temperature increases. This method is discussed in detail by Dieke in M,3 and hence is not described here.

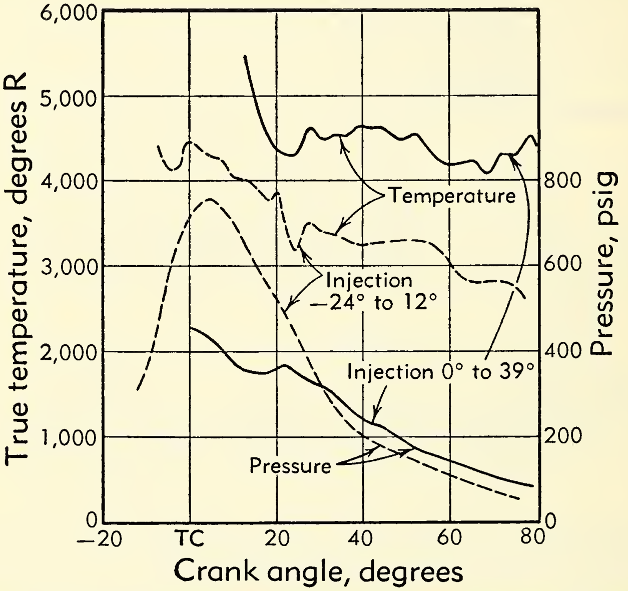

Fig. I,4b. Typical variation of flame temperature and pressure with crank angle in a diesel engine from apparatus of Uyehara, et al.

I,5. Thermocouple and Compensated Hot Wire Methods of Flame Temperature Measurement.

Thermocouples in low velocity flames. Thermocouple probes when immersed in flame gases attain an equilibrium temperature such that the rate of heat gain by the junction through gas conduction, convection, directed impact of gases against the junction, surface friction of gases flowing over the junction, and radiation from the flame is just equal to the rate of heat loss by radiation from the junction to the cool surroundings of the flame and by conduction along the thermocouple wires. For flame gases whose velocity with respect to the thermocouple probe corresponds to a Mach number of 0.1 or less, the effects of directed impact and surface friction are small compared to the other factors and are usually neglected for practical purposes. In this low velocity region, thermocouple probes tend to indicate temperatures below flame temperatures due to the radiation and conduction losses from the junction. In the high velocity region (Mach number greater than 0.1), thermocouple probes are additionally heated by friction and by the adiabatic heating of the gas when its motion is stopped at the probe. The junction may then indicate a temperature higher than the static temperature of the gas. The amount of deviation of indicated temperature from static temperature depends on the size of the probe, its orientation in the gas stream, the Mach number, and the gas temperature.

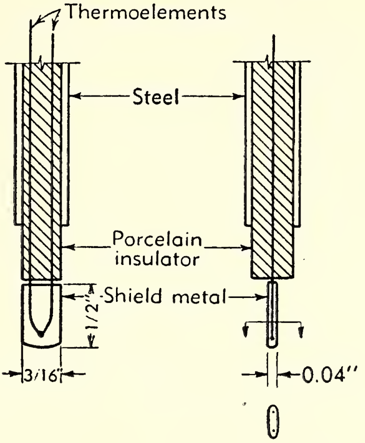

Fig. I,5a. Thermocouple with pressed radiation shield.

At low gas velocity there are only the radiation and conduction losses to compensate for and this can usually be done without difficulty. If small lead wires are used and the junction is immersed deeply enough in the flame, conduction losses become negligibly small. Radiation losses, methods of shielding thermocouple junctions against radiation losses, and radiation loss corrections have been studied by Mullikin [*21*, p. 775], Dahl and Fiock [*22*], and Fiock, Olsen, and Freeze [*6*, p. 655]. Probably one of the most convenient types of radiation shields is illustrated in Fig. I,5a [*22*; *6*, p. 655]. Taking advantage of the low emissivity of silver and gold, 0.03 to 0.05, they made shields by flattening small tubes of silver or gold around the junctions. These were found to be as effective as any radiation shield previously devised. Silver shields are useful in flames up to 1500°F. At higher temperatures gold or platinum shields, whose melting points are higher, had to be substituted. Platinum has an emissivity in the range 0.12 to 0.18 and requires a larger radiation correction factor. Platinum-shielded junctions should not be used in exhaust gas at temperatures below about 650°C.

Dahl and Fiock [*22*] give temperature corrections for silver- or gold-shielded junctions in terms of the indicated temperature, burner wall temperature, and mass flow rate of gas. A set of correction curves is shown in Fig. I,5b. Starting with the indicated temperature, one follows vertically to the interpolated curve for the burner wall temperature, horizontally to the mass flow rate, thence vertically down to the correction to be added to the indicated temperature in order to obtain the correct reading.

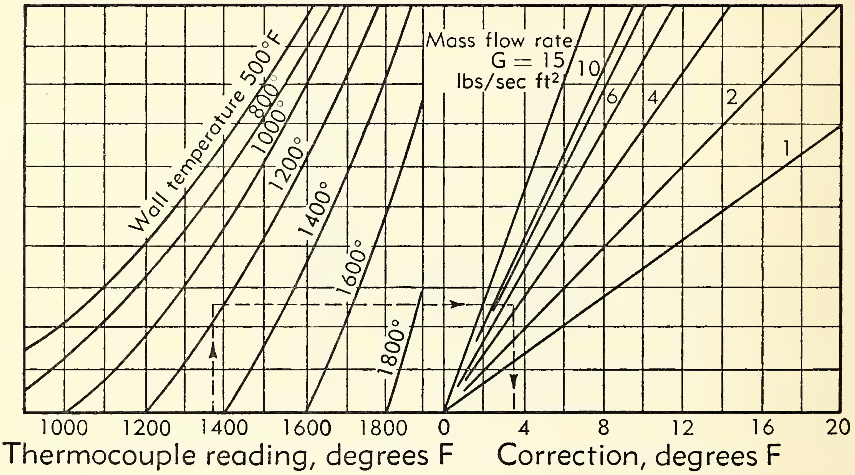

Fig. I,5b. Correction chart for Ag- and Au-shielded thermojunctions (Dahl and Fiock).

In the region of the flame where active combustion is going on, there is a possibility that a junction shielded with one of the platinum group metals will be additionally heated by chemical reactions taking place on its surface. There is also the chance, in the case of liquid fuels, that droplets of unburned fuel will cool the junction. It is not known how to compensate for these factors, and thermocouple readings in such zones cannot be trusted.

Behavior of thermocouples in high velocity air. The behavior of thermocouples in high velocity air streams has been investigated by Zhukovskiĭ [*23*], by Hottel and Kalitinsky [*24*], and by Olsen, Dahl, and Freeze [*25*]. A typical experimental arrangement used for investigating this problem is that of Olsen, et al, shown in Fig. I,5c. In the high velocity streams at (2) a butt-welded junction stretched across the air stream as shown gave an indicated temperature T_j that was higher than the static temperature T_s that would be indicated by an instrument traveling with the air stream. T_j was lower than the total temperature T_t indicated by the thermocouple at (1). Defining a recovery factor r as

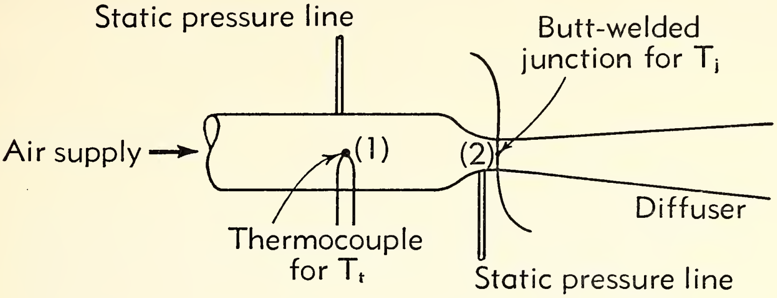
Static pressure line
Butt-welded junction for T_j
Air supply
(1)
(2)
Diffuser
Thermocouple for T_t
Static pressure line

Fig. I,5c. Apparatus to study thermocouple performance in high velocity air stream (Olsen, Dahl, and Freeze).

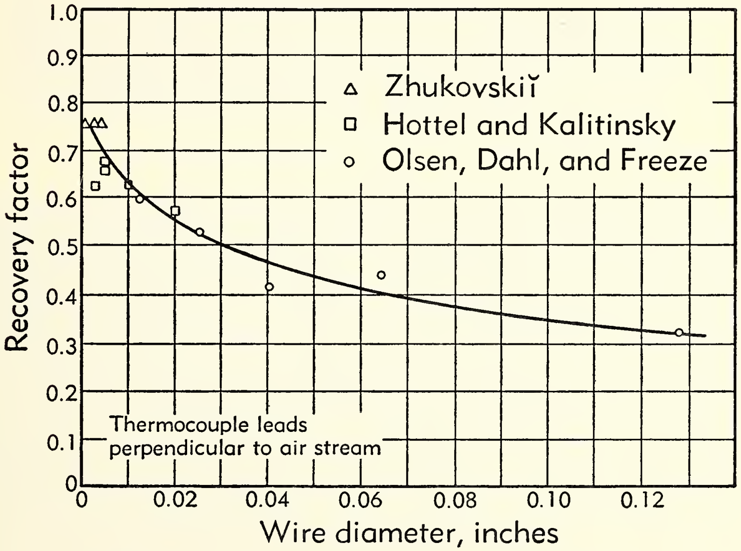

Fig. I,5d. Recovery factor for different wire sizes at velocities up to 700 ft/sec (Mach number ≅ 0.7).

$$r = \frac{T_j - T_s}{T_t - T_s}$$

recovery factors were found to be constant for a given wire diameter for velocities up to about 700 ft/sec or a Mach number of about 0.7. Recovery factors as a function of wire diameter are shown in Fig. I,5d, taken from Olsen, et al, for wires stretched across the air stream. For thermocouples axially located at (2), recovery factors were somewhat higher. At Mach numbers above 0.7, T_j approached the total temperature T_t. The ratio T_t/T_j for different Mach numbers is shown in Fig. I,5e for thermocouples perpendicular to the gas stream.

The value of T_s was computed from the relation required by conservation of energy,

$$T_t - T_s = \frac{U^2}{2gJC_p} \tag{5-1}$$

in which U is the gas velocity, $g = 32.2$ ft/sec², $J = 778$ ft lb/BTU, and C_p is the mean specific heat. U was obtained from measurements of T_t and of static pressure at (1) and (2).

In high temperature, high velocity (Mach number greater than 0.1) gas streams, the indicated temperature will be influenced both by the effects of directed impact of the gases against the probe, as described for low temperature gases above, and by radiation effects. The difference between indicated temperature and total or static temperature would have to be worked out for particular cases.

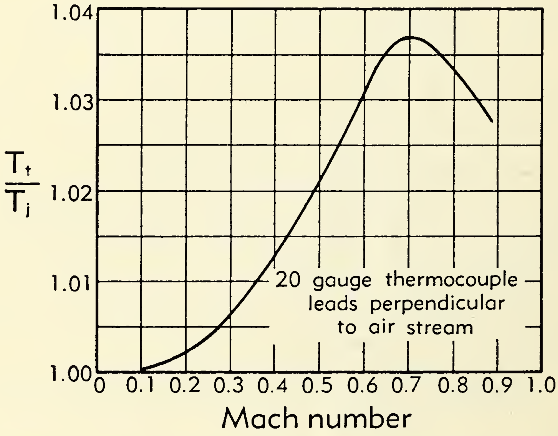

Fig. I,5e. Ratio T_t/T_j as a function of Mach number for air at T_t = 100° to 220°F (Dahl and Freeze).

Compensated hot wire method for measuring flame temperature. The radiation and conduction losses from a wire temperature probe immersed in a flame can be compensated for by passing an electric heating current through the wire just sufficient to make up for these losses. The method is applicable to transparent flames in a region of the flame where all burning is complete so that no chemical reactions can take place on the surface of the wire. The wire temperature, representing the flame temperature, is read with an optical pyrometer, the reading being corrected for the emissivity of the wire.

This test may be accomplished as follows: First, the wire to be used is heated electrically in a good vacuum, its temperature being observed

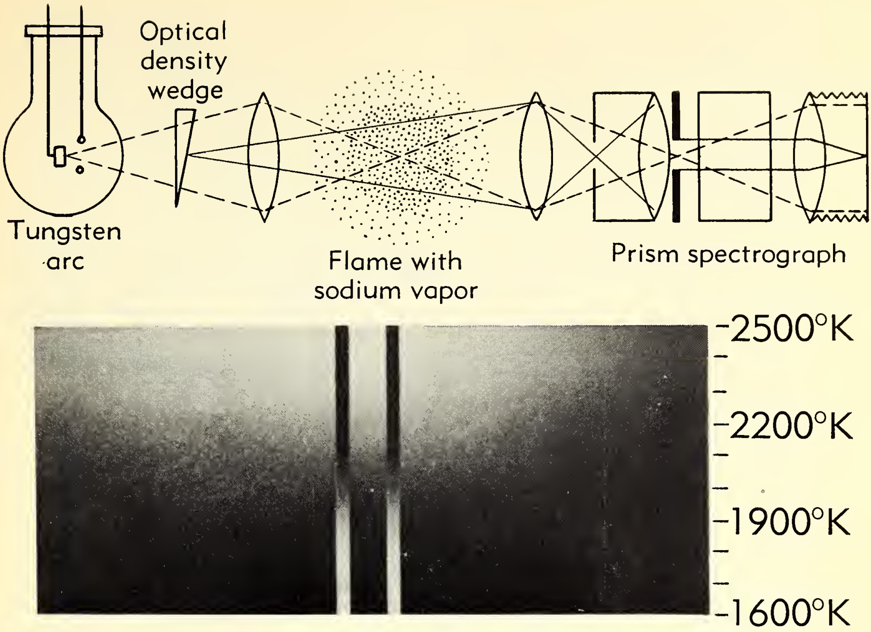

Plate I,2a. Sodium line reversal apparatus adapted for remote control.

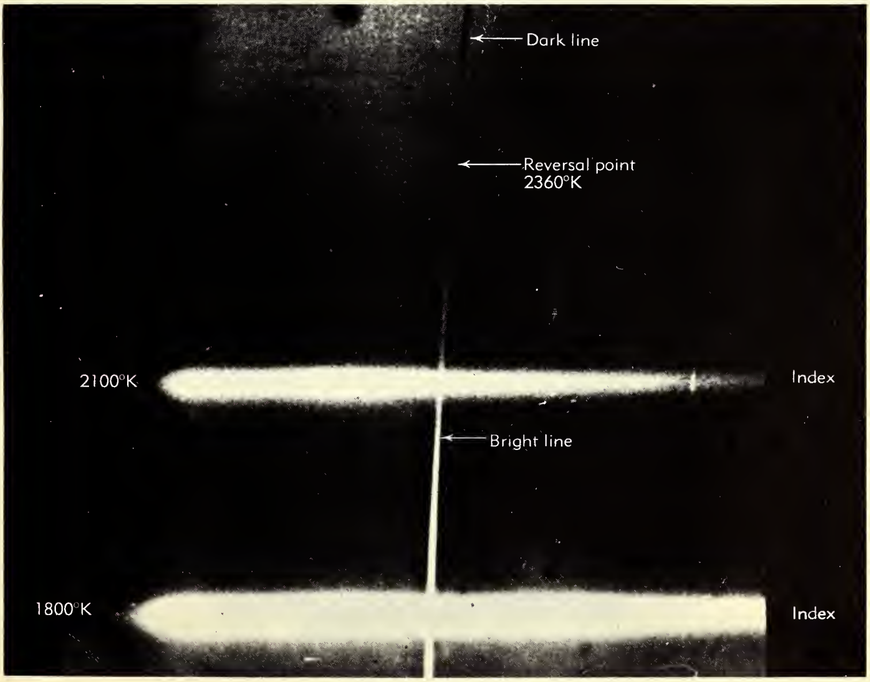

Plate I,2b. Sodium line reversal film record taken on a rocket motor flame.

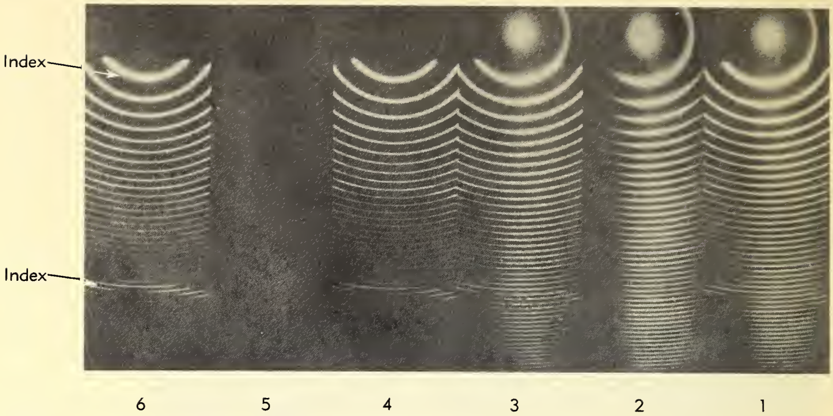

Plate I,2c. Interference patterns obtained with SLR apparatus Fig. I,2j. Note background brightness grading effect of rotating spiral disk in exposure 6.

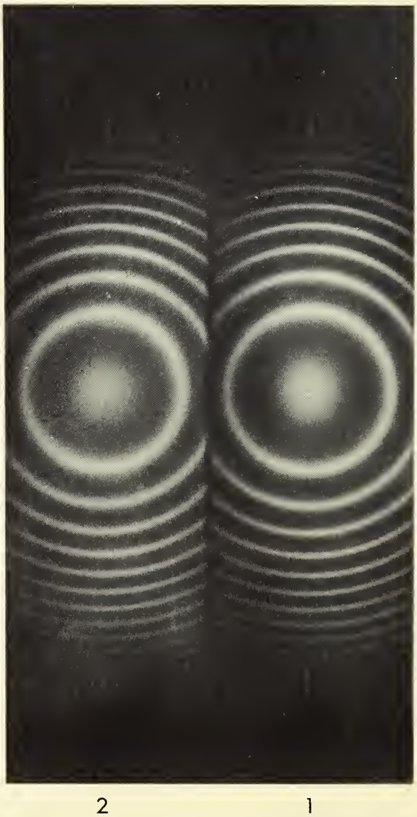

Plate I,8a. Typical pair of Doppler shift interference patterns.

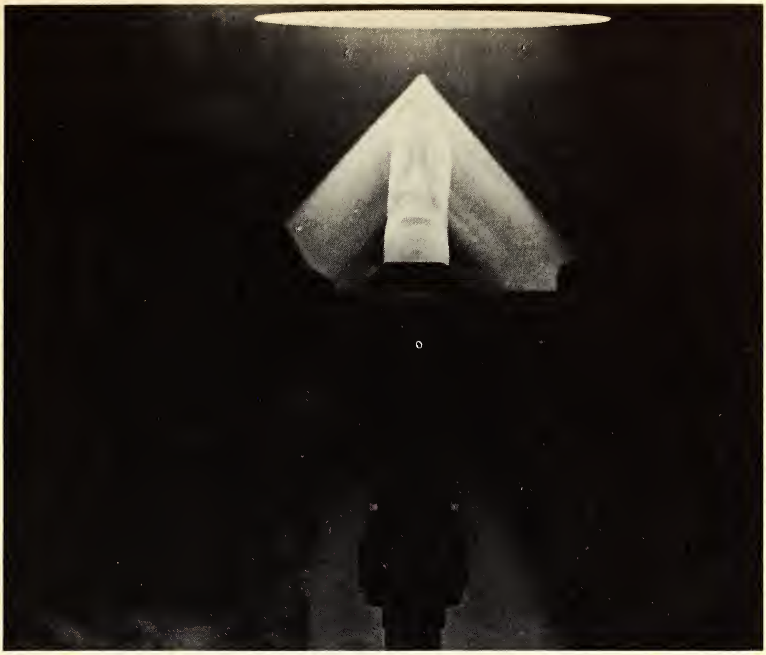

Plate I,8b. Photograph of shocks produced in a supersonic rocket flame by a wedge probe.

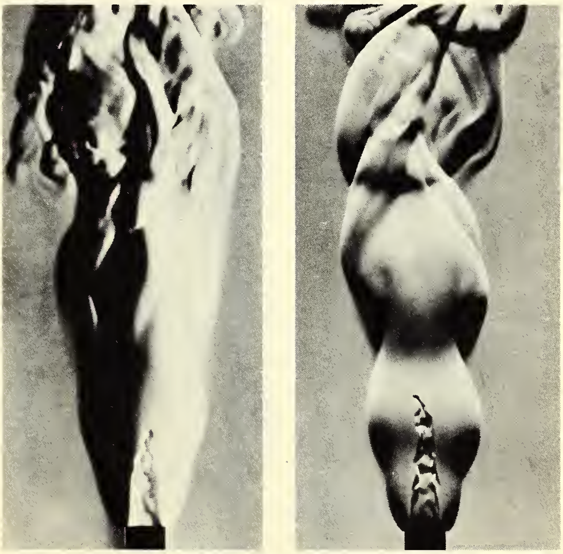

Plate J,4. Schlieren photographs of Bunsen flame, showing effect of position of knife edge. Left, knife edge vertical; right, knife edge horizontal.

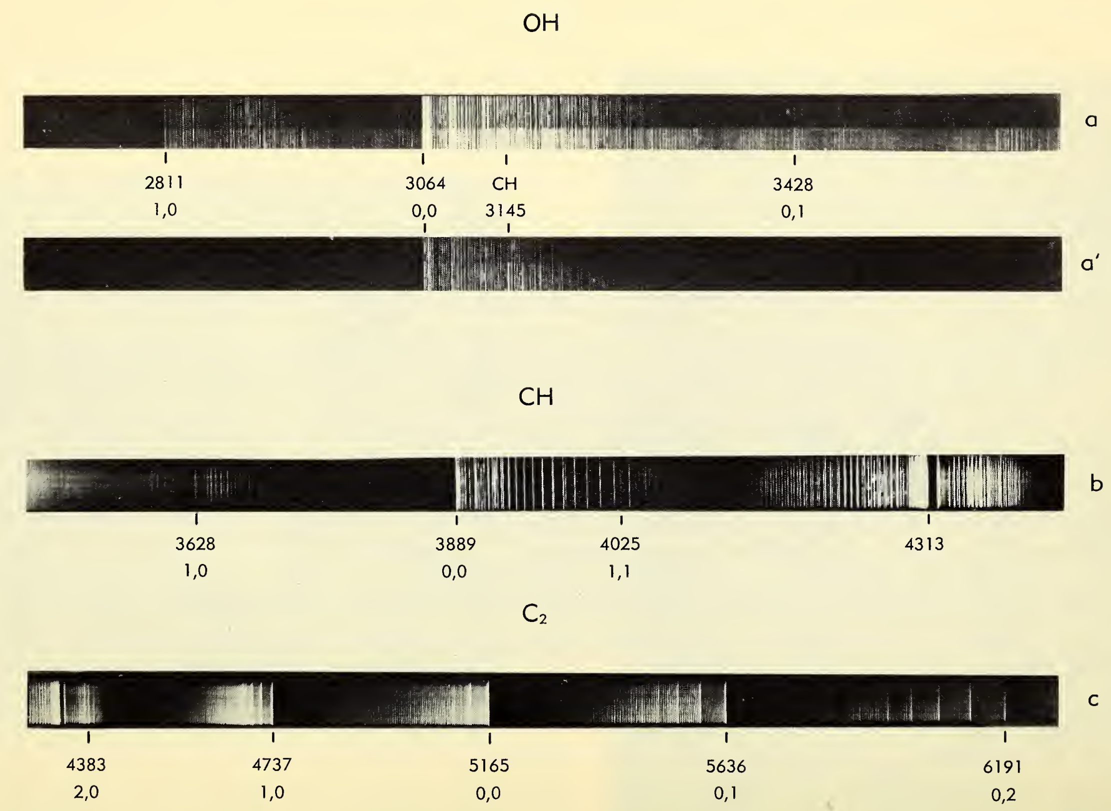

Plate M,3. The spectrum of a hydrocarbon flame from 2800A to 6200A. In Plate 3a the upper half is from the outer cone, the lower half from the inner cone. Plates 3b and c are from the inner cone.

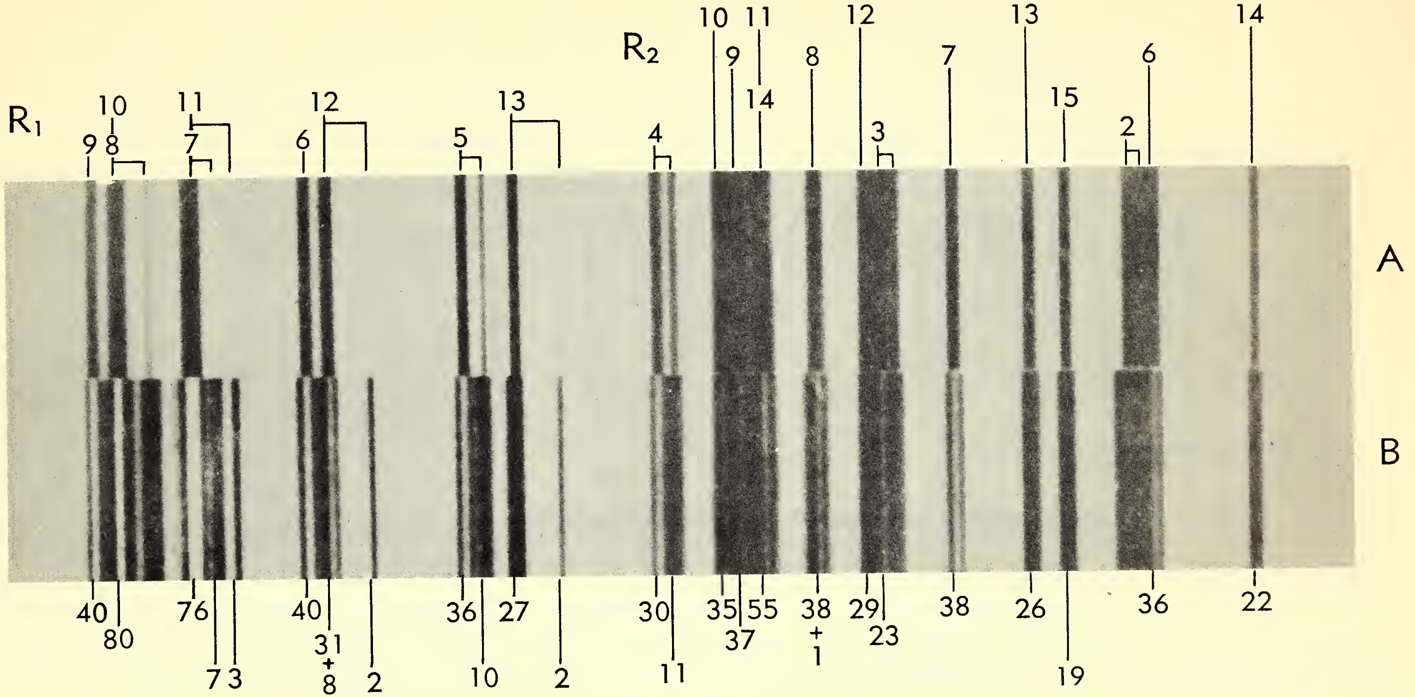

Plate M,4. Self-reversal in the 3064 OH band. (A) Spectrum from a small oxyacetylene flame. (B) Spectrum from a large flame seen along the axis. Below are given the relative intensities of the unreversed lines. It is seen that all lines with $I_0 > 20$ are self-reversed. Note particularly R_1 4–8, also R_2 7. The latter is a single line not confused with any other line.

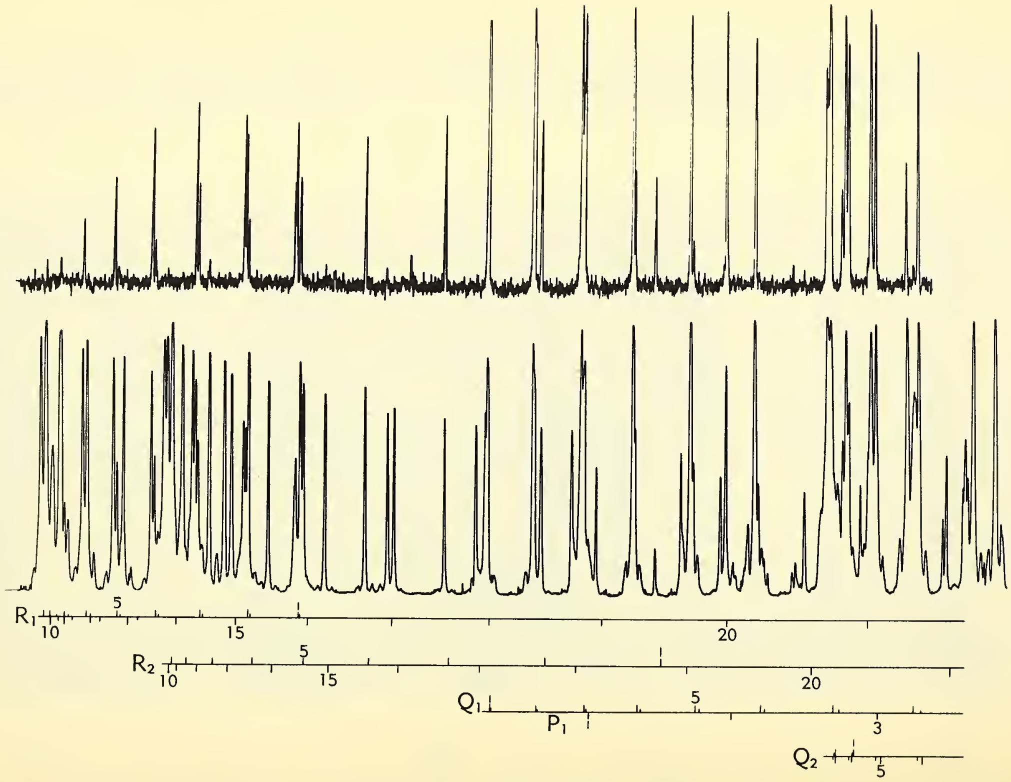

Plate M,5a. The short wavelength part of the 3064 OH band. Upper half, discharge in helium with H_2O impurity; lower half, oxyacetylene flame ($T \cong 3{,}000°K$).

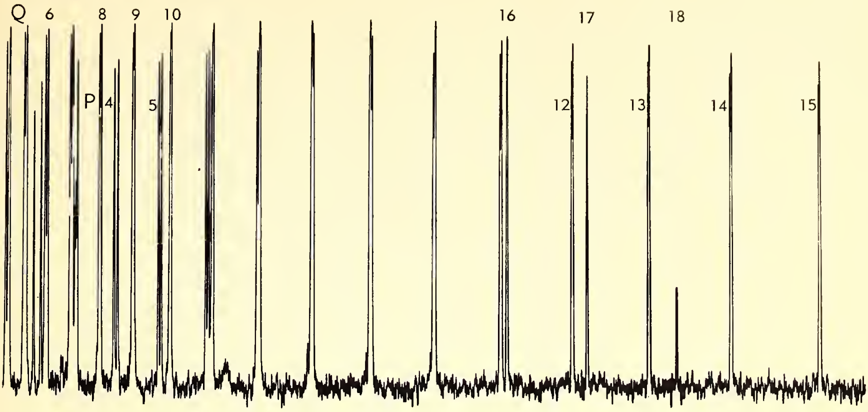

Plate M,5b. The 3871A band of CH. Confused region near the head omitted. The numbered lines are those best suited for temperature measurements.

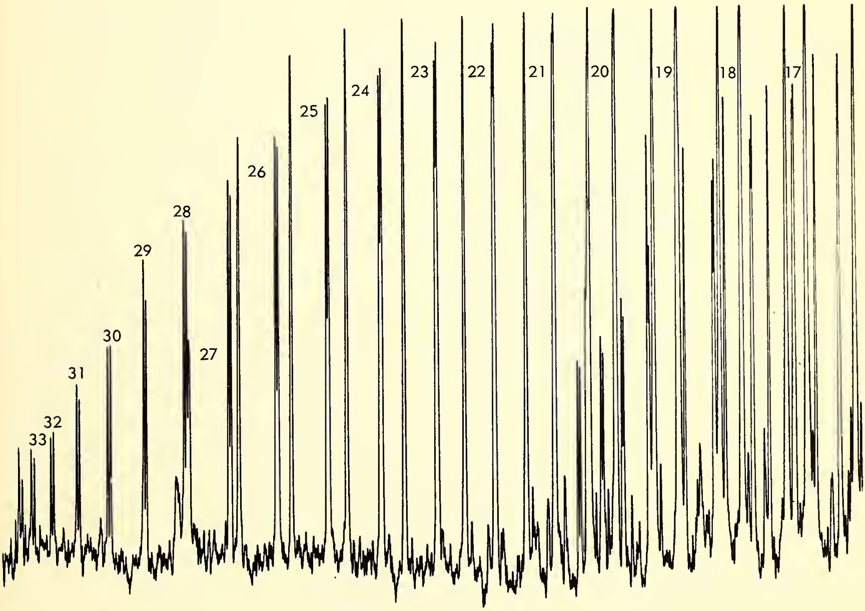

Plate M,5c. Short wavelength end of the 4300A CH band. This is relatively free from overlapping even with moderate dispersion. The long wavelength components (appearing double for $K > 20$) are not predissociated.

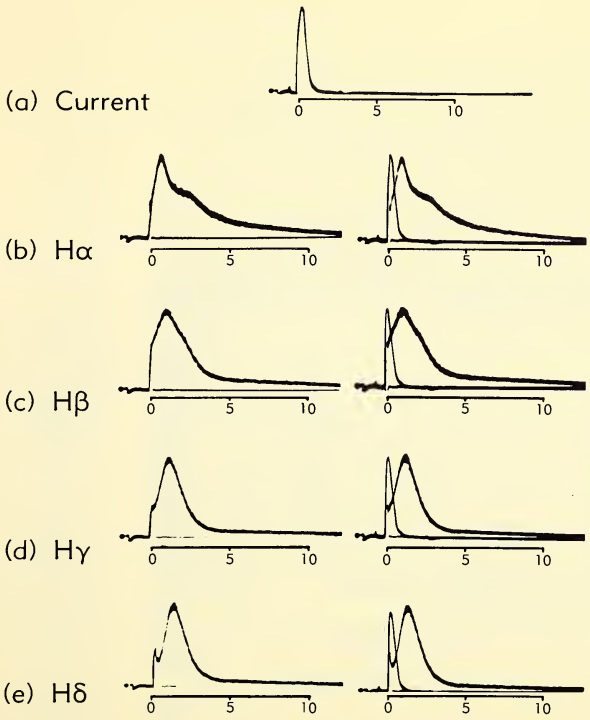

Plate M,6a. Pulse discharge through hydrogen. *(a)* Shape of current pulse; *(b)*–*(e)* atomic lines of hydrogen. The traces on the right have the current pulse superimposed. Time scale in microseconds.

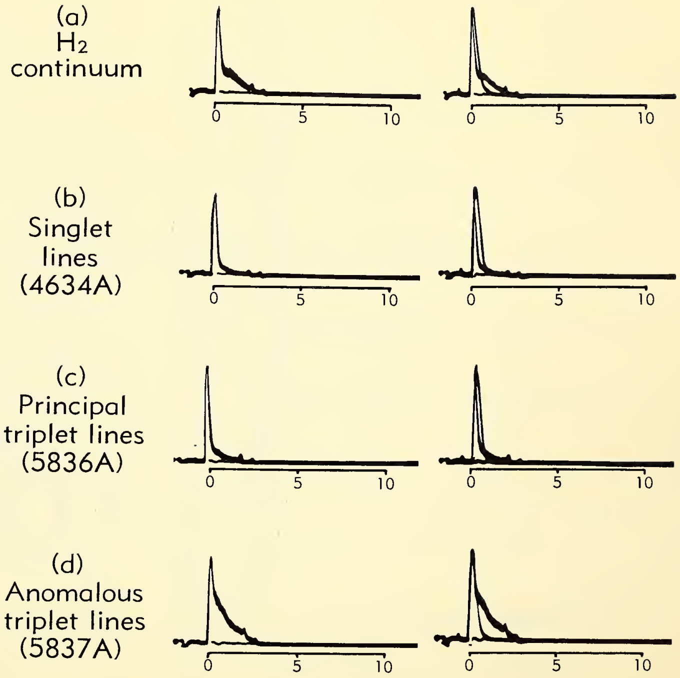

Plate M,6b. Pulse discharge through hydrogen, same conditions as for Plate 6a. Molecular lines of hydrogen.

and recorded along with the current required to maintain that temperature. After a range of such readings are recorded, the wire is placed in the flame where all burning reactions have been completed and the process of recording wire temperatures for different currents through the wire is repeated. It will be found that at wire temperatures below flame temperature, less current is required to maintain a given T than in a vacuum. At wire temperatures above flame temperature, more current is required to maintain a given temperature than in a vacuum because the flame gases then have a strong cooling effect on the wire. The two experiments give a pair of curves which must cross as illustrated in Fig. I,5f. The place where the curves cross marks the flame temperature, because at this point the flame conducts no heat from or to the wire and the radiation and conduction loss is the same as it is in a vacuum.

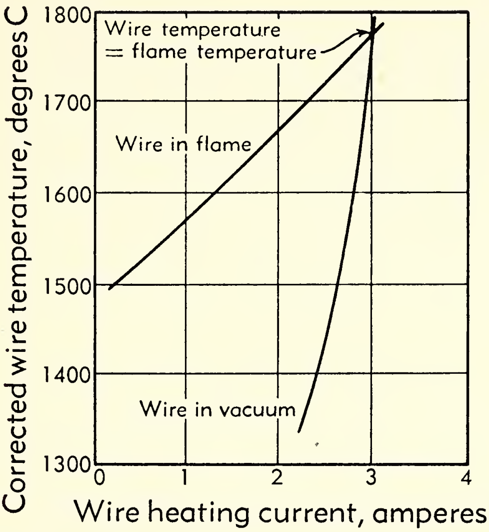

Fig. I,5f. Typical curves, flame temperature measurement by hot wire method (from Griffiths and Awbery).

This method is useful for calibrating other temperature-measuring methods. It has been used by Schmidt [*26*], Kohn [*27*], and Griffiths and Awbery [*28*] for this purpose.

I,6. Gas Temperature from Pneumatic Apparatus. The volume flow rate of a gas through a nozzle increases with the applied pressure until the flow velocity at the throat of the nozzle reaches the local velocity of sound, at which point the ratio of the entrance pressure to the throat pressure reaches a critical value which cannot be exceeded regardless of the inlet pressure. After the critical pressure ratio has been reached the volume flow rate measured at the inlet pressure and temperature also remain constant. This constant critical volume flow rate for a given gas and nozzle depends only on the entrance temperature and is given by the expression

$$\begin{aligned} w_e &= CA\left(\frac{2\gamma}{\gamma+1}\right) r^{1/\gamma}\left(\frac{p_e}{\rho_e}\right)^{\frac{1}{2}} = \kappa A T_e^{\frac{1}{2}} \\ r &= \left(\frac{2}{\gamma+1}\right)^{\frac{\gamma}{\gamma-1}} \end{aligned} \tag{6-1}$$

where C is the discharge coefficient (0.95 to 1.00), A is the throat area, r is the critical pressure ratio, and p_e and ρ_e, are the pressure and density, respectively, at the entrance. The critical mass flow rate is, then,

$$m_N = \rho_e w_e = \kappa_N p_e T_e^{-\frac{1}{2}} \tag{6-2}$$

where κ_N is characteristic of the gas and the throat area and T_e is the temperature at the entrance.

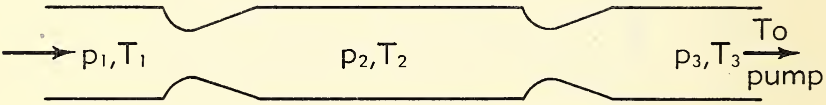

Fig. I,6. Two critical-flow nozzles in series.

As early as 1893 [*29*] an apparatus based on this relationship in critical flow nozzles was used to determine gas temperature. Recently, Moore [*30*] and Wildhack [*31*] have given the method more attention in applying it to the measurement of flame temperatures. In these methods the mass flow rate is effectively determined by use of a second critical flow nozzle in series with the first, as shown in Fig. I,6, so that the mass flow is necessarily the same in both. Equating the mass flow rates in the two nozzles, a relationship between the respective temperatures, pressures, and nozzle coefficients is obtained:

$$\frac{T_2}{T_1} = \left(\frac{\kappa_{N_2} p_2}{\kappa_{N_1} p_1}\right)^2 \tag{6-3}$$

Thus, if the nozzle coefficients and p_1, p_2, and T_2 are known, the temperature T_1 may be calculated.

The pressures may be readily measured with conventional pressure gauges of sufficient accuracy. The temperature T_2 may be established by surrounding the volume between the two nozzles with a jacket having thermostatically controlled temperature and adequate heat exchange surface to insure that the gas acquires the jacket temperature. If the gases contain condensable components, such as water vapor, it is necessary either to maintain T_2 high enough to prevent condensation and make the vapor act as an approximately perfect gas, or to hold T_2 low enough for practically all of the vapor to be condensed out so that it may be measured and allowed for in the corrected mass flow rate through the second nozzle. The difficulties arising from condensable vapors may also be avoided by using some dry gas, such as nitrogen, for the working gas in the pneumatic apparatus and bringing this gas through a suitable heat exchanger in good thermal contact with the flame gases before introducing it into the first nozzle. This method, however, introduces a different set of obvious difficulties, such as thermal lag, radiation from the heat exchanger and first nozzle, impedance to flow of flame gases, etc.

The upper limit to the temperature T_1 that can be measured by this method is set by the melting point or other critical temperature characteristics of the material of which the first nozzle is made. This nozzle should also be resistant to corrosion or fouling from the action of flame gases because its flow coefficient depends critically upon its exact dimensions and somewhat upon its surface condition if it has a small aperture.

The response time of the instrument is of interest in those applications in which changing temperatures T_1 are encountered. The pneumatic time response to changes of T_1 depends upon the volume of the internozzle space compared to the flow rate of the system. Wildhack [*31*] has shown that the pneumatic "time constant" is given by the expression

$$\tau = \frac{\rho_0 V T_0}{\kappa_{N_2} p_0 \sqrt{T_2}} \tag{6-4}$$

where ρ_0, T_0, and p_0 are the initial density, temperature, and pressure, respectively, in the internozzle space, and V is the volume of that space. In addition to this pneumatic time delay there is also a thermal lag of the entrance portion of the first nozzle. This effect becomes less pronounced as the size of the aperture of the first nozzle is increased because the heat transfer from the gas to the nozzle is decreased.

Orifices may be used in place of nozzles, but in this case a constant critical flow condition is never reached and a more complicated law of mass flow applies. In such a case the pressure drops across both orifices must be measured. In one of the recent adaptations of this method [*30*] the area of the second orifice is controlled by the temperature T_2, and the pressure drop across this orifice is held constant by a suitable regulator, so that the temperature T_1 is indicated by the pressures p_1 and p_2.

The pneumatic type of instrument requires a vacuum pump to maintain the necessary pressure differentials across the nozzles or orifices unless the initial gas pressure is large enough in comparison with ambient atmospheric pressure. The required volume displacement rate of such a pump may be decreased by use of properly designed exit cones on the nozzles, as these exit cones can give considerable pressure and density recovery. The minimum flow rate required to make this type of instrument give accurate results is set by that size of the nozzle aperture at which the effect of viscosity on the flow rate becomes negligibly small.

I,7. Temperature from Velocity of Sound. As early as 1873 it was suggested by Mayer [*32*] that the dependence of the velocity of sound on the temperature of the gaseous medium through which it propagates might be employed as the principle of a pyrometer. Anderson and Smith [*33*] explored the special advantages of this method for high temperature gases in their study of the temperature of the metal vapor formed during the explosive vaporization of wires by strong surges of electric current. They reflected the sound wave generated by the explosion back into the discharge region of hot vaporized metal and observed its rate of propagation there. Later, the method was developed further and used by Suits [*34;35;21*, p. 720] to measure the temperature of the gases in the flames of various kinds of electric arcs. Recently, ultrasonic techniques have been applied to the measurement of the velocity of sound in gas streams from which the temperature can be deduced.

In any of the methods which determine temperature from the velocity of sound it is essential first to know how the velocity of sound varies with the temperature in the particular gas, or gas mixture, being studied. In general, the velocity of propagation a of a small amplitude pressure wave through an elastic medium is given by $(K/\rho)^{\frac{1}{2}}$, where K is the volume modulus of elasticity and ρ is the density. For adiabatic pressure changes in gases

$$K = \rho \frac{dp}{d\rho} = \gamma p \tag{7-1}$$

Whence

$$a^2 = \frac{\gamma p}{\rho} \tag{7-2}$$

For perfect gases p/ρ is independent of the pressure and both p/ρ and γ are characteristic of the gas. Since ρ varies inversely as the absolute temperature T of the perfect gas, a varies as $T^{\frac{1}{2}}$.

In the cases of very hot flames in which dissociation and ionization are appreciable, account must be taken of the change of density due to dissociation as well as the temperature dependence of γ. These effects have been considered in detail by Poritsky and Suits [*35*] and the result of their analysis for air is given in Fig. I,7a. Similar analyses can be made for flame gases of different compositions from available thermodynamic data [*36,37*]. Once the variation of the velocity of sound with temperature at a given pressure for the flame gases has been determined, flame temperature can be deduced from the observed velocity of sound in the flame.

There are various ways of measuring the velocity of sound in flames. For electric arc flames, Suits [*34*] used an arrangement illustrated schematically in Fig. I,7b. The sound was produced in the discharge by a condensed spark discharge between the tungsten probe C and the arc cathode. The breakdown voltage at which the spark occurred was determined by the external gap *H*. A sound wave of sufficient intensity and sharpness was initiated by a discharge of 150 coulombs at 14 kilovolts. The "receiver" consisted of another spark gap *G*, placed just outside the flame, which was provided with enough external ballast resistance to make it nonoscillatory. The passage of the sound wave through this gap during its discharge period caused sudden changes in the voltage drop across it as illustrated in Fig. I,7c at t_1. The time of origination of the sound pulse is indicated by the beginning of the damped oscillation at t_0 produced by electromagnetic disturbances associated with the source spark. The end effects associated with abnormal sound propagation at and near the source spark and at the boundary between the flame and

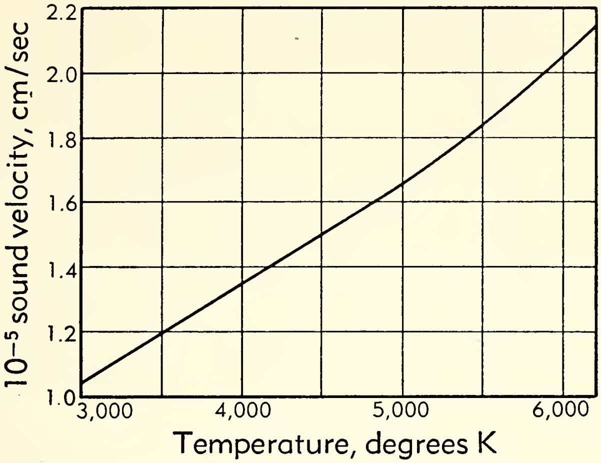

Fig. I,7a. Velocity of sound in air as a function of the temperature (Poritsky and Suits).

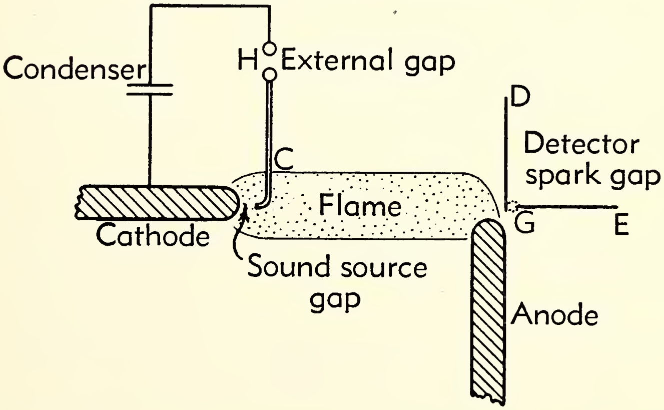

Fig. I,7b. Schematic arrangement of apparatus for measurement of velocity of sound in an electric arc flame (Suits).

the receiving gap were eliminated by taking observations over different path lengths in the arc flame, keeping other parts of the sound path constant and plotting the time of travel against the distance between the sound source and the anode. An example of this is shown in Fig. I,7d, which gives some of Suits' data for a copper arc in air.

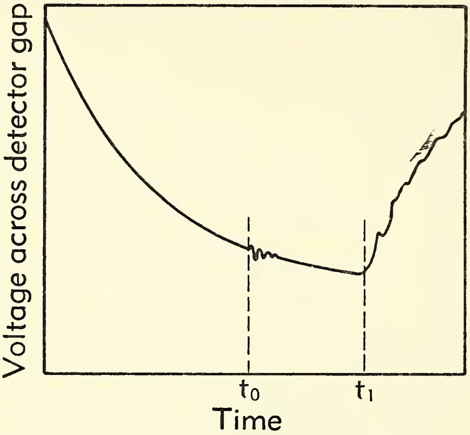

Fig. I,7c. General shape of the discharge curve for the receiver arc when disturbed by the passage of a sound pulse (Suits).

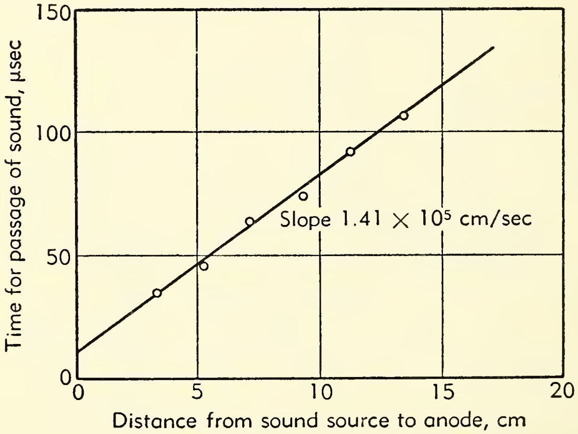

Fig. I,7d. Typical data for a 6-amp copper arc in air, showing end effects (Suits).

An optical method, also used by Suits [*38*], is illustrated in Fig. I,7e. The lens L_1 formed an image of the arc on the narrow horizontal slit S and the second lens L_2 formed an image, via the rotating mirror, on the photographic film in the cylindrical holder. The sound pulse was generated by a condensed spark discharge so placed that the sound wave traveled across the arc flame in a direction perpendicular to the axis of the optical system and parallel to the slit. A shutter located in front of the slit was opened immediately before the initiation of the sound spark and closed after a half revolution of the rotating mirror. A typical record is illustrated in Fig. I,7f. The shutter opened at 1, the condensed spark fired at 2, the sound wave front entered the arc flame at 3 and left it at 4. The compression part of the sound wave front manifested itself by increased brightness of the flame due to adiabatic compression. The slope of the wave front line on the film, together with the known rate of scan of the slit image along the film, gave the velocity of sound propagation in the flame. The largest source of error in this method was in determining the slope of the sound front line on the film. However, when the rate of discharge of the source spark was very high the wave front was very sharp and this source of error, together with errors in calibration of mirror rotation speed and the like, gave a total error of only about

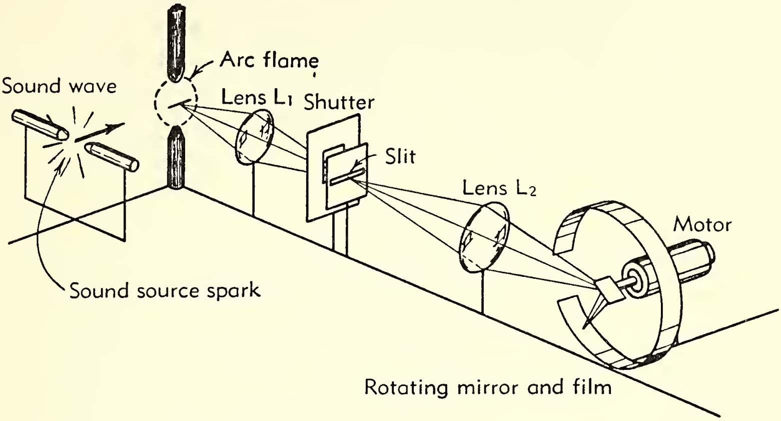

Fig. I,7e. Schematic layout of Suits' optical method of measuring the velocity of sound in electric arc flames.

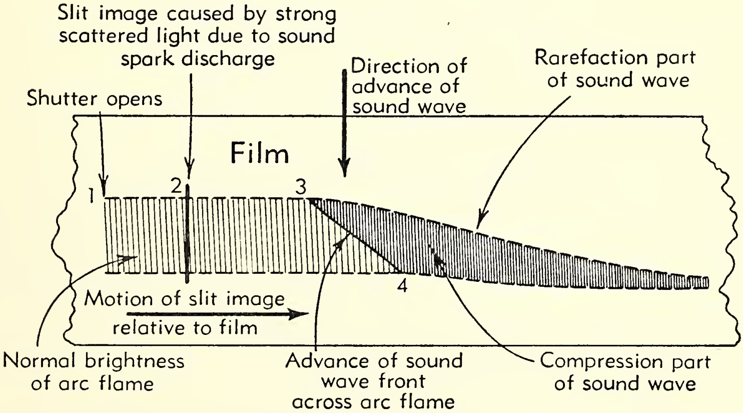
Slit image caused by strong scattered light due to sound spark discharge
Shutter opens
Direction of advance of sound wave
Rarefaction part of sound wave
Film
1
2
3
4
Motion of slit image relative to film
Normal brightness of arc flame
Advance of sound wave front across arc flame
Compression part of sound wave

Fig. I,7f. Typical record obtained from the apparatus shown in Fig. I,7e (Suits).

±100°C at 5500°K. This method can be applied to stationary chemical flames as readily as to electric arc flames. In all high temperature applications the chief difficulty is in getting a reliable relationship between temperature and the velocity of sound.

In the ultrasonic methods [*39,40*], the sound source is a high frequency piezoelectric crystal which radiates a narrow beam of ultrasonic radiation into the gas under observation as illustrated in Fig. I,7g. The sound waves advancing in the gas are observed by spark photography using schlieren or shadow techniques. From the photographs the wavelength of the sound in the gas is determined, and as the frequency is known with great accuracy, the velocity of sound may be determined with considerable exactness; from the velocity the temperature may be determined.

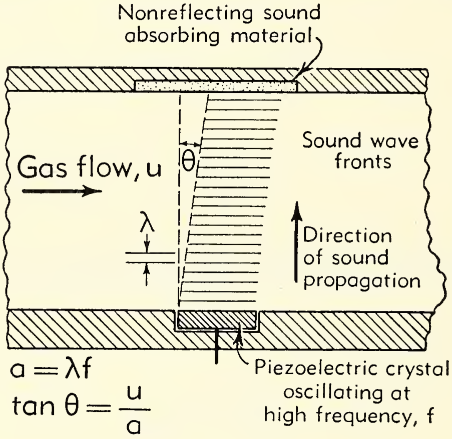
Nonreflecting sound absorbing material
Sound wave fronts
Gas flow, u
θ
λ
Direction of sound propagation
$a = \lambda f$
$\tan\theta = \frac{u}{a}$
Piezoelectric crystal oscillating at high frequency, f

Fig. I,7g. General arrangement of apparatus for projecting a beam of ultrasonic radiation into a gas duct (Marlow, et al.).

This method can be applied to advantage in those cases where the temperatures are low enough to permit the piezoelectric crystal to work, and where the general turbulence and self-noise due to gas flow do not obscure the sound wave pattern set up by the ultrasonic source.

I,8. Gas Velocity in Supersonic Flames.

General considerations. The measurement of gas velocities in hot supersonic flames is much more difficult than it is in cool subsonic gas streams because probes of any kind inserted in the flame set up strong shock waves which modify the very flow that is being measured, and the probes themselves are subjected to extremely high temperatures and mechanical forces by the blast of hot gas which often quickly destroys them. Some of the methods which may be resorted to are the measurement of the thrust force and mass flow rate of the apparatus which produces the flame, the determination of the Doppler shift of wavelength of a characteristic spectral radiation from the flame, and finding the shock angle produced by a thin wedge-shaped probe held in the flame.

Specific impulse method. Consider a simple example of a rocket motor utilizing liquid fuel and liquid oxidizer which are forced into the head end of the motor with a velocity u_1 parallel to the axis of the motor and its flame. Let the combined mass flow rate be $\dot{m}$. The release of chemical energy by reaction in the combustion chamber expands the reactants to hot gases at constant pressure and these are accelerated to a supersonic velocity u_2 as they expand through the nozzle to outside ambient pressure. The thrust force arising from the acceleration of the liquids is $F_{\text{liq}} = \dot{m}u_1$ and that arising from the acceleration of the gases is $F_{\text{gas}} = \dot{m}(u_2 - u_1)$. The total thrust force is then $F = F_{\text{liq}} + F_{\text{gas}}$. Thus by measurement of the total thrust force on the captive rocket motor, and the mass flow rate through it, the gas velocity is easily calculated as the ratio $F/\dot{m}$. This is the method most commonly used on test stands.

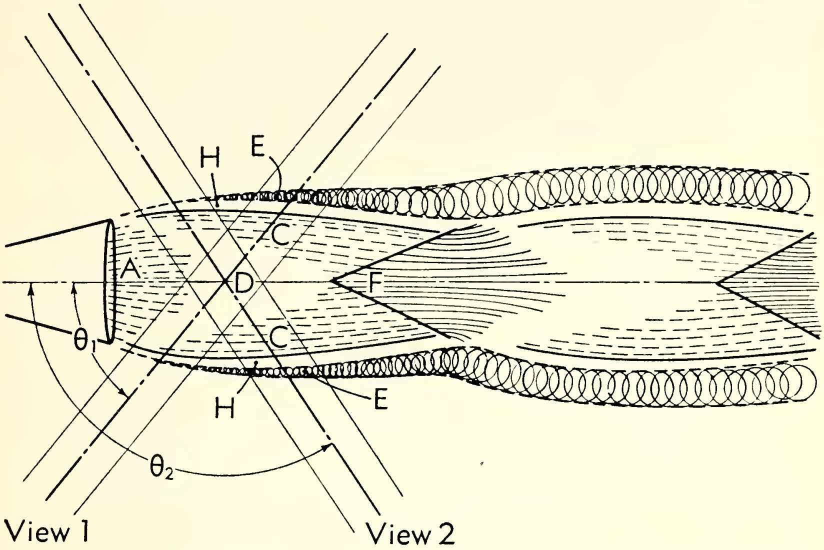

Fig. I,8a. Lines of sight in rocket flame for Doppler velocity measurement.

Spectral Doppler shift method [*41*]. If the flame gases contain a trace of the vapor of some alkali metal, such as sodium or lithium, which is thermally excited by the flame gases to radiate its resonance spectral lines, the small difference in wavelength of the light emitted in the upstream and downstream directions caused by the Doppler shift can be used to determine the average gas velocity. Consider the two angles of view of a rocket flame illustrated in Fig. I,8a. The fractional wavelength difference between these two angles of view is

$$\frac{\delta\lambda}{\lambda} = \frac{u}{c}(\cos\theta_1 - \cos\theta_2) \tag{8-1}$$

where λ is the normal wavelength of the radiation, $\delta\lambda$ the change in wavelength, u the gas velocity parallel to the flame axis, c the velocity of light, and the θ's are as shown in the drawing. The rocket gas velocity is known to be of the order of 2×10^5 cm/sec and thus the ratio u/c is about 0.7×10^{-5}. The flame geometry is such that $(\cos\theta_1 - \cos\theta_2)$ cannot be made much greater than unity. Consequently, the ratio $\delta\lambda/\lambda$ is about 10^{-5}, which for sodium yellow radiation (λ = 5390 and 5396A) gives a $\delta\lambda$ of less than 0.1A. As this shift is less than the width of the spectral lines themselves any method used to measure the shift requires the formation and comparison of two separate spectra, one for each angle of view of the flame. The accuracy of measurement of the shift is greatest when the width of the spectral lines is as small as possible. For resonance-type spectral lines the minimum width is set by the temperature and pressure of the gas, and the actual width becomes greater than this as the number of radiating atoms in the line of sight increases [*5*]. It has been found by experiment that the line width is satisfactorily small if the number of optically active sodium atoms per cm^2 in the line of sight is less than 4×10^{12}.

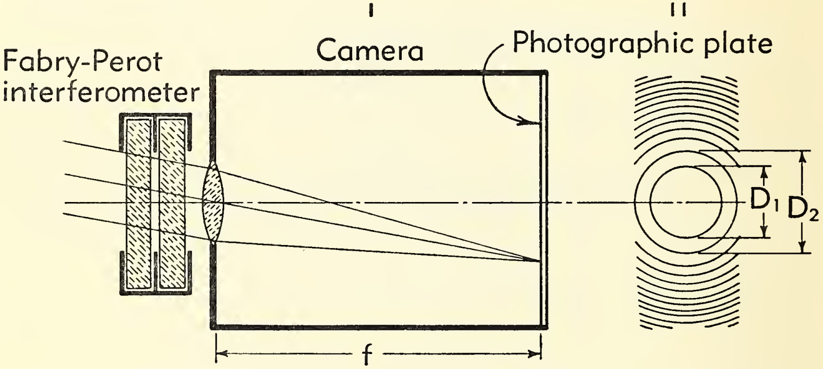

Fig. I,8b. Interferometer-camera assembly and a Fabry-Perot interference pattern.

The instrumentation selected for the measurement of these small changes of wavelength under the rigorous physical conditions which exist around a rocket test stand was a combination of a Fabry-Perot interferometer and a camera illustrated in Fig. I,8b(i). The interference pattern formed on the camera plate consists of concentric circular fringes as shown in Fig. I,8b(ii). For constant spacing of the interferometer plates the diameters of the fringe circles change with a change in wavelength, $\delta\lambda$, in such a way that the product of the diameter D and the change in diameter δD is the same for all fringes in the pattern. It can be shown that

$$\delta\lambda = -\frac{\lambda}{4f^2} D\delta D \tag{8-2}$$

where f is the focal length of the camera lens. As several fringes appear in each pattern, several values of $D\delta D$ may be obtained from each pair of Doppler shift patterns and these values may be averaged to give a more accurate result.

The intensity contour of each fringe is essentially that of the spectral line which produces it, and each fringe repeats this intensity contour. Thus sharp spectral lines produce sharp, easily measured fringes in the interference pattern. If the spectrum of the flame has two lines which are so close together that one cannot be eliminated by optical filters, as is the case for the sodium D line doublet, the spacing of the interferometer plates may be adjusted to make the two sets of fringes corresponding to the two wavelengths coincide in the interference pattern. For the sodium D lines this is accomplished by making the plate spacing an integral multiple of 0.02906 cm. The seventh multiple of this, 0.2034 cm, has been found satisfactory.

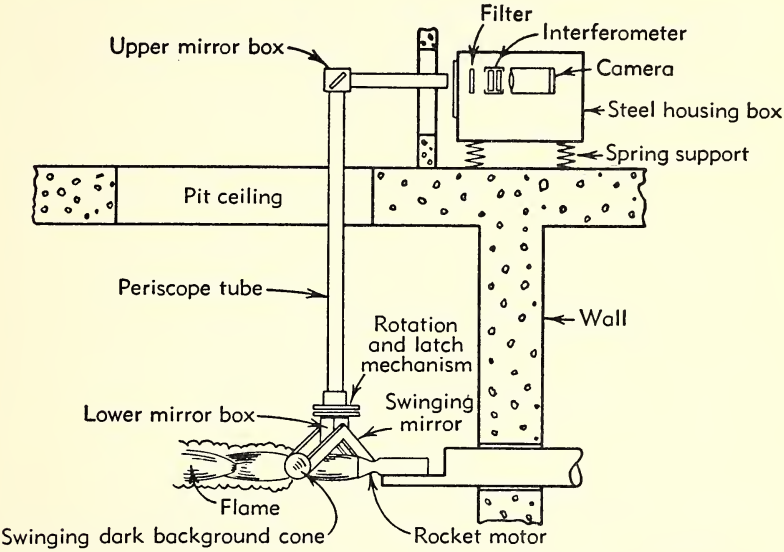

Fig. I,8c. Arrangement of the optical equipment at a rocket test stand.

As the vibration conditions near a rocket flame are quite severe, it is important that the sensitive optical equipment be placed at a safe distance from the flame and be well isolated from any mechanical disturbances. The arrangement used by the authors is illustrated in Fig. I,8c. The light from the flame was reflected into the periscope tube by a swinging mirror system which could be quickly swung from an upstream to a downstream view during the rocket test. The periscope tube was fitted with a "2f" lens system [*42*] which formed a real image of the flame on the window of the housing box where a mask could be placed to exclude all light except that coming from the region of interest in the flame. The interferometer-camera assembly was protected from air-borne and ground-borne vibrations by an airtight, spring-mounted, heavy steel box. An optical filter was placed in front of the interferometer to exclude as much as possible any radiation except the spectral line being used in the interference patterns. The camera was equipped with remote control devices for operating the shutter and quickly shifting the photographic plate from one frame to the next at the same time the swinging mirror was changed from one view to the other. Thus it was possible to photograph during a rocket test run the two interference patterns required for the Doppler velocity measurement. A typical Doppler pair of interference patterns is shown in Plate I,8a.

Table I,8. Gas velocities in rocket exhaust flames.

Nominal run no.	Spectral lines used	10^{-5} Velocity, cm/sec		Per cent difference
		Doppler	Impulse	
1	Sodium 5890, 5896A	1.96	2.07	−5.3
2		2.26	2.20	+2.7
3		2.17	2.17	0.0
4		2.14	2.16	−0.9
5		2.34	2.18	+7.3
6		2.28	2.16	5.5
7	Lithium 6707A	2.26	2.11	7.1
8		2.31	2.10	10.0
9	Sodium 5890, 5896A	2.30	2.29	0.4
10		2.35	2.19	7.3
11		2.51	2.19	14.6
12		2.39	2.12	12.7

The two lines of view shown in Fig. I,8a were selected on the basis of being freest of pressure zones which would give spurious wavelength shifts due to the pressure shift effect, as well as for containing the minimum of zones of widely differing temperatures which would cause confusing distortions of the fringe contours [*5*]. However, even in these two lines of sight the net luminosity favors the zones of higher velocity and thus does not represent accurately the average mass flow. For this particular pair of lines of sight it has been estimated from the zone temperatures and depths that a velocity 2 to 6 per cent higher than the average for the total mass flow should be indicated.

Some results of the Doppler method are listed in Table I,8 and compared with those of the specific impulse method made on the same rocket test runs. These velocities given by the Doppler method average about 6 per cent higher than those from the impulse method. The variation of the differences shown in Table I,8 is irregular and indicates that the accuracy of any one measurement by the Doppler method is probably not better than ±8 per cent, or $\pm 1.5 \times 10^4$ cm/sec. With this degree of accuracy it would be practical to use the method only on flames with gas velocities in excess of 10^5 cm/sec.

Shock angle method. The Mach number in a flame can be determined by inserting a thin wedge-shaped probe such as illustrated in Fig. I,8d. In order to make such a probe survive in a rocket flame it must be made of a material having very high thermal conductivity, such as copper; it must be strongly cooled from within by flow of a coolant; and it must be very firmly mounted on a strong supporting structure because of the great force and high temperature of the flame. The presence of the probe causes strong shock waves to be formed in which the rise of temperature and luminosity are so great that they can be photographed readily without any special equipment. Such a photograph is shown in Plate I,8b.

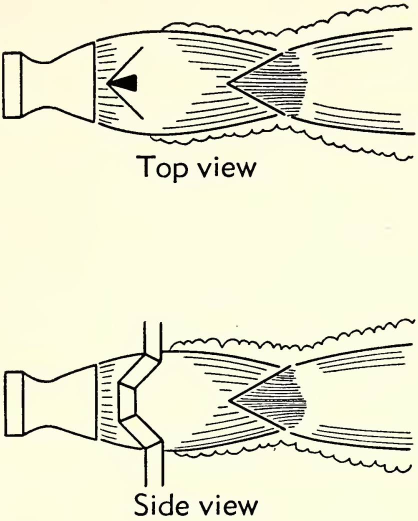

Fig. I,8d. Sharp wedge-shaped probe in rocket flame for Mach number measurement.

The geometry of the flow is shown in Fig. I,8e. The gas approaches with Mach number M_1 along streamlines parallel to the flame axis, then at the shock front suddenly changes to Mach number M_2 in a direction parallel to the wedge face. On the basis of one-dimensional flow, the relationship among the variables is given by the equation

$$\frac{\tan(\theta - \alpha)}{\tan\theta} = \left(\frac{\gamma - 1}{\gamma + 1}\right)\frac{(M_1 \sin\theta)^2 + 2}{(M_1 \sin\theta)^2} \tag{8-3}$$

where γ is the ratio of specific heats. The value of γ is known with fair accuracy from the flame-gas composition, and since θ and α can be measured from the photograph, M_1 can be calculated. By definition the Mach number is

$$M \equiv \frac{u}{\sqrt{\dfrac{\gamma R T}{\mathfrak{M}}}} \tag{8-4}$$

where R is the molar gas constant and $\mathfrak{M}$ the mean molecular weight of the flame gases (which is also known quite accurately from the flame-gas composition). Thus if the gas temperature is known the gas velocity can be calculated. The absolute accuracy of this method depends strongly upon the accuracy of the temperature measurement. Usually it leaves the experimenter with a feeling of uncertainty because there is always uncertainty as to the values of γ, $\mathfrak{M}$, and especially T.

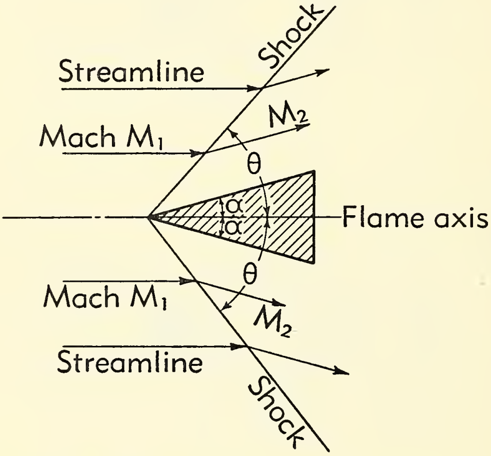

Fig. I,8e. Supersonic flow past a symmetrical wedge.

I,9. Gas Pressure in Supersonic Flames.

General considerations. In a supersonic flame the stream velocity is greater than the velocity of sound in the gases. Under these circumstances it is possible for regions to exist within the flame boundary in which the static pressure is higher or lower than that in the atmosphere surrounding the flame. In all cases the pressure gradients must be maintained by acceleration of the gases. The compressions often occur suddenly in the form of shock fronts. In general a supersonic stream will always contain shock fronts of various kinds unless the nozzle releases the gases at exactly atmospheric pressure and with the flow lines all parallel to the stream axis.

The drawing in Fig. I,8a shows the system of shocks which develop from a nozzle with a 15-degree exit angle and 4:1 ratio of mouth area to throat area when the combustion chamber pressure is about 25 times the ambient atmospheric pressure. It is found that this nozzle does not provide for full expansion of the gas to atmospheric pressure by the time it reaches the mouth so the gas expands around the edge of the nozzle at an angle greater than the 15-degree exit angle. As a result of the divergence of the flow the gas overexpands; then the flow is overcorrected toward the axis and this results in a strong compression shock from which the gas expands again. Thus in Fig. I,8a the region at *A* is above atmospheric pressure, at *D* is below atmospheric pressure, at *C* is equal to atmospheric pressure, at *F* is considerably above atmospheric pressure, etc. A simple photograph of the flame shows these zones to have different luminosities and hence different temperatures.

Spectroscopic pressure shift method. After the interferometer-camera apparatus described in Art. 8 was developed it became apparent that this apparatus was capable of measuring the small shifts of wavelength of resonance spectral lines associated with changes in pressure of the flame gases, and consequently it was adapted to the measurement of the gas pressures in the regions *A*, *D*, and *F* of Fig. I,8a. This was done by setting the swinging mirror of Fig. I,8c to view the flame perpendicularly (to eliminate Doppler shift) so that the line of sight passed through the region of interest. In addition, a mask was placed on the window of the interferometer-camera housing box in such a manner that only light from the section of interest in the flame was transmitted to the interferometer-camera assembly. After the rocket test run was completed a standard sodium vapor lamp was placed in the same position originally occupied by the flame and a second interference pattern was taken. By comparing the flame light pattern with the sodium vapor lamp pattern the wavelength shift was determined by use of Eq. 8-2. Then from a laboratory calibration of the pressure shift of wavelength for sodium in the presence of flame gases the pressure in the flame could be determined.

The pressure shift of wavelength of resonance-type spectral lines is known to be proportional to the absolute pressure, inversely proportional to the square root of the absolute temperature, and also to depend on the kind of foreign gas in which the emitting atoms are placed. The only data that could be found in the literature were for sodium vapor in such nonoxidizing gases as hydrogen, nitrogen, and argon [*43*]. It was necessary therefore to make measurements in the laboratory of the shift of the sodium D lines from sodium vapor in the presence of flame gases at known pressures. This was done by burning a mixture of oxygen and propane gases in a special blast lamp in a flame chamber which was capable of operating up to pressures of 5 atmospheres or more. The flame was located in the line of sight of two windows, one in each end of the chamber, so that the flame temperature could be measured by the sodium line reversal method. The pressure shift of wavelength was measured with the same interferometer-camera apparatus which was used at the rocket test station.

The temperatures obtained for the oxygen-propane flame at different pressures are shown in Fig. I,9a. The rise in flame temperature with pressure is to be expected because there is less dissociation of the products of combustion at higher pressures. However, this increase in flame temperature has little effect on the pressure shift because the increase in $T^{\frac{1}{2}}$ was only about 2.5 per cent while the pressure increased fivefold.

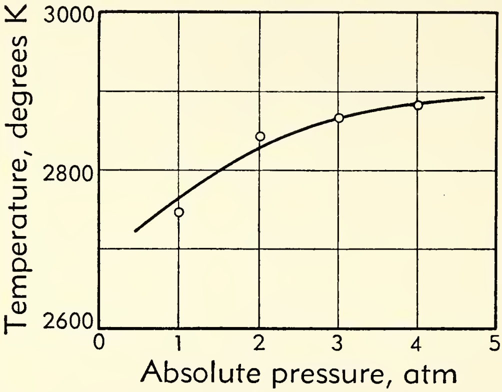

Fig. I,9a. Variation of temperature of oxygen-propane blast lamp flame with combustion chamber pressure.

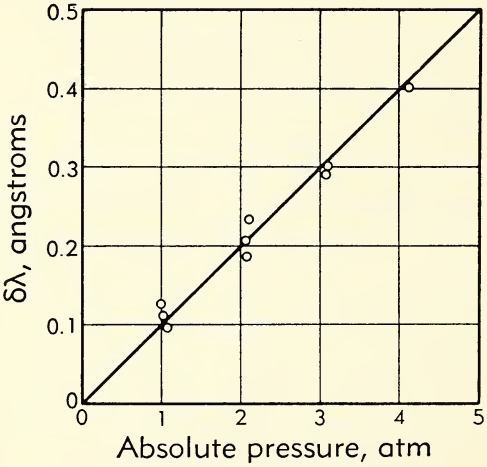

Fig. I,9b. Pressure shift of wavelength of sodium D line radiation from sodium atoms in an atmosphere of flame gases.

Fig. I,9b shows the results of the pressure shift calibration measurements corrected to a temperature of 2600°K. The shift is proportional to the pressure, as it should be according to theory, and has a magnitude of 0.010A per atmosphere at 2600°K.

Comparison of the pressure shift of wavelengths observed in the rocket flame with those given in the above calibration indicated that the gas pressure on the flame axis at A (Fig. I,8a) at the mouth of the nozzle was 2.5 atmospheres (absolute), at D in the region of overexpansion was 0.5 to 0.8 atmosphere, and at F in the front half of the shock cone about 2.5 to 2.8 atmospheres. Taking into account the uniform rise in temperature of the gases with time in this region of the flame due to continued chemical activity, the pressures observed are consistent with the temperatures obtained for the same regions [*8*].

The accuracy of this method of gas pressure measurement is limited by the smallness of the shift, the natural width of the spectral lines, and the distortion of the intensity contour of the spectral lines by the presence of several zones of different pressures and temperatures in the line of sight. It is estimated that the absolute accuracy of any one measurement of this kind is ±0.3 atmosphere, and hence the method is applicable only in those cases in which there are rather large and distinct changes of pressure in different zones of the flame.

I,10. Cited References and Bibliography.

Cited References

1. Gaydon, A. G., and Wolfhard, H. G. *Proc. Roy. Soc. London A199,* 89 (1949).
2. Féry, Ch. *Compt. rend. 137,* 909 (1903).
3. Kohn, H. *Ann. Physik 44,* 749 (1914).
4. Frieser, H., and Reuther, R. *German Arch. 38/1 G.K.* English translation by H. Liebhafsky, *Hermes Library GE DF 8514.* Gen. Elec. Co., 1947.
5. Bundy, F. P., and Strong, H. M. *Project Hermes Rept. 55275.* Gen. Elec. Co., Sept. 1948.
6. *Third Symposium on Combustion.* Williams and Wilkins, 1949.
7. Strong, H. M., Bundy, F. P., and Larson, D. A. *Project Hermes Rept. 49A0517.* Gen. Elec. Co., 1949.
8. Bundy, F. P., Johnson, R. H., and Strong, H. M. *Project Hermes Rept. R50A0506.* Gen. Elec. Co., 1950.
9. Tolansky, S. *High Resolution Spectroscopy.* Methuen, 1947.
10. Hett, J. H., and Gilstein, J. B. *J. Opt. Soc. Amer. 39,* 909 (1949).
11. Sanderson, J. A., Curcio, J. A., and Estes, D. V. *New York Univ. Project Squid Tech. Mem. NYU-2,* 1948.
12. Hottel, H. C., and Broughton, F. B. *Ind. Eng. Chem. 4,* 166 (1932).
13. Bundy, F. P., and Strong, H. M. *Phys. Rev. 76,* 457 (1949).
14. Mie, G. *Ann. Physik 60,* 297 (1908).
15. Becker, R. *Ann. Physik 28,* 1017 (1909).
16. Wolfhard, H. G., and Parker, W. G. *Nature 162,* 259 (1948).
17. Wolfhard, H. G., and Parker, W. G. *Proc. Roy. Soc. London B62,* 523 (1949).
18. Rössler, F., and Behrens, H. *Optik 6,* 145 (1950).
19. Rössler, F. *Z. angew. Phys. 2,* 161 (1950).
20. Uyehara, O. A., Myers, P. S., Watson, K. M., and Wilson, L. A. *Trans. Am. Soc. Mech. Engrs. 68,* 17 (1946).
21. Mullikin, H. F. *Temperature, Its Measurement and Control in Industry.* Reinhold, 1941.
22. Dahl, A. I., and Fiock, E. F. *Trans. Am. Soc. Mech. Engrs. 71,* 153 (1949).
23. Zhukovskiĭ, V. S. *J. Tech. Phys. U.S.S.R. 5,* 968 (1939).
24. Hottel, H. C., and Kalitinsky, A. *J. Appl. Mech. 67,* A-25 (1945).
25. Olsen, L. O., Dahl, A. I., and Freeze, P. D. Performance of butt-welded thermocouples in high-velocity air streams. *Natl. Bur. Standards Rept.,* Oct. 1948.
26. Schmidt, H. *Verhandl. deut. physik. Ges. 11,* 87 (1909); *Ann. Physik 29,* 971 (1909).

27. Kohn, H. *Ann. Physik 44*, 749 (1914).
28. Griffiths, E., and Awbery, J. H. *Proc. Roy. Soc. London 123*, 401 (1929).
29. Ühling, E. A., and Steinbart, A. *German Patent 7701*, 1893.
30. Moore, D. W. Jr., *Aeronaut. Eng. Rev. 7*, 30 (1948).
31. Wildhack, W. A. *Rev. Sci. Instr. 21*, 25 (1950).
32. Mayer, A. M. *Phil. Mag. 45*, 18 (1873).
33. Anderson, J. A., and Smith, S. *Astrophys. J. 64*, 359 (1926).
34. Suits, C. G. *J. Appl. Phys. 6*, 190 (1935).
35. Poritsky, H., and Suits, C. G. *J. Appl. Phys. 6*, 196 (1935).
36. Hirschfelder, J. O., et al. Thermodynamic properties of propellant gases. *Office Sci. Research Develop. Rept. 1087, Natl. Defense Research Comm. Rept. A-116*, 1942.
37. Geyer, E. W., and Bruges, E. A. *Tables of Properties of Gases.* Longmans, Green, & Co., London, 1948.
38. Suits, C. G. *J. Appl. Phys. 6*, 315 (1935).
39. Hubbard, J. C., Zartman, I. F., and Larkin, C. R. *J. Opt. Soc. Amer. 37*, 832 (1947).
40. Marlow, D. G., Nisewanger, C. R., and Cady, W. M. *J. Appl. Phys. 20*, 771 (1949).
41. Bundy, F. P., and Strong, H. M. *Gen. Elec. Tech. Rept. 55269*, June, 1948.
42. Bundy, F. P., and Strong, H. M. *J. Opt. Soc. Amer. 39*, 393 (1949).
43. Margenau, H., and Watson, W. W. *Revs. Mod. Phys. 8*, 22 (1936); *Phys. Rev. 44*, 92 (1933).

Bibliography

Andersen, J. W., and Fein, R. S. *J. Chem. Phys. 17*, 1268 (1949).

Barret, P. *Compt. rend. 226*, 396 (1948).

Bredt, I. *Compt. rend. 228*, 1927 (1949).

Cowan, R. D., and Dieke, G. H. *Revs. Mod. Phys. 20*, 418 (1948).

Ferri, A. *Elements of Aerodynamics of Supersonic Flows.* Macmillan, 1949.

Gaydon, A. G. *Spectroscopy and Combustion Theory*, 2nd ed. Chapman and Hall, London, 1948.

Gaydon, A. G., and Wolfhard, H. G. *Proc. Roy. Soc. London A194*, 169 (1948); *A199*, 89 (1949); *A201*, 561, 570 (1950).

Hyde, E. P., Cady, F. E., and Forsythe, W. E. *Phys. Rev. 10*, 395 (1917).

Jacobs, D. H., and Scholnick, S. *North Amer. Aviation, Inc. Rept. 86*, 1947.

Kandyba, V. V. *Izvest. Akad. Nauk S.S.S.R. 12*, 387 (1948).

Liepmann, H. W., and Puckett, A. E. *Introduction to Aerodynamics of a Compressible Fluid.* Wiley, 1947.

Malpica, J. T. *Gen. Elec. Rev. 44*, 439 (1941).

Mitchell, A. C. G., and Zemansky, M. W. *Resonance Radiation and Excited Atoms.* Macmillan, 1934.

Penner, S. S. *Am. J. Phys. 17*, 422, 491 (1949).

Richtmyer, F. K. *Introduction to Modern Physics.* McGraw-Hill, 1947.

Russell, H. W., Lucks, C. F., and Turnbull, L. G. See [*21*], p. 1159.

Silverman, S. *J. Opt. Soc. Amer. 39*, 275 (1949).

Sobolev, N. N. *J. Exptl. Theoret. Phys. U.S.S.R. 19*, 25 (1949).

Sobolev, N. N., and Shchetinin, T. I. *J. Exptl. Theoret. Phys. U.S.S.R. 20*, 356 (1950).

White, H. L. *Introduction to Atomic Spectra*, Chap. 21. McGraw-Hill, 1934.

Wolfe, C. M. *Aerojet Eng. Co. Rept. 327*, 1948.

Wolfe, C. M. See [*11*], p. 27.

SECTION J

FLAME PHOTOGRAPHY

WILLIAM T. REID

SECTION J

FLAME PHOTOGRAPHY

WILLIAM T. REID

J,1. Introduction. Photography as a research tool for studying flames is becoming more important as techniques are improved and better photographic materials are available. More and more investigators, needing to provide permanent, objective records of the appearance of flames or of the action of flames under different imposed conditions, use a camera. Others, wishing to observe phenomena occurring too rapidly to be visible to the unaided eye, turn to a special photographic technique such as spark photography or as provided by high speed cameras. Still others, to visualize phenomena not otherwise perceivable, use the interferometer, the schlieren system, or shadow photography.

Unfortunately, many workers are not aware of the many ways in which photography can be useful to them in their study of flames. The purpose of this section is to point out the photographic techniques proven most useful in flame studies, in order that the advantages of photography as a research tool may be utilized still further.

J,2. Direct Photography. The direct photography of flames appeals to those studying combustion processes because of its simplicity and availability. Generally, only a simple camera is required, together, possibly, with a few optical filters. Despite these advantages, however, the method has not enjoyed the greatest popularity, mainly because the visible image has only a limited usefulness. In a few cases, however, direct photography can be very helpful in studying combustion.

PHOTOGRAPHY THROUGH OPTICAL FILTERS. A typical method of investigating combustion by direct photography has been described by Bonhoeffer and Eggert [*1*]. They photographed the flame of a Teclu burner and that of a slot burner, using Agfa optical filters to isolate spectral regions of particular interest. To assure the utmost photographic sensitivity, Agfa photographic plates with spectral characteristics suited to the filters were used.

Bonhoeffer and Eggert explained by their photographs a three-step mechanism for combustion in a Bunsen flame. First, the inner cone radiated in the blue-green and ultraviolet regions because of the presence of OH, CH, and C_2 free radicals. Second, the intermediate zone radiated in the red and infrared regions because both CO_2 and H_2O exist in this zone in relatively high concentrations. Third, the outer mantle again radiated in the blue end of the spectrum because CO and H_2, in equilibrium with the CO_2 and H_2O in the intermediate zone, were burned in the outer mantle with oxygen available there, again providing free radicals. Their photographs confirm this mechanism, pictures with a blue-sensitive plate taken through a blue filter showing the inner zone and the outer mantle, and pictures made simultaneously through a red

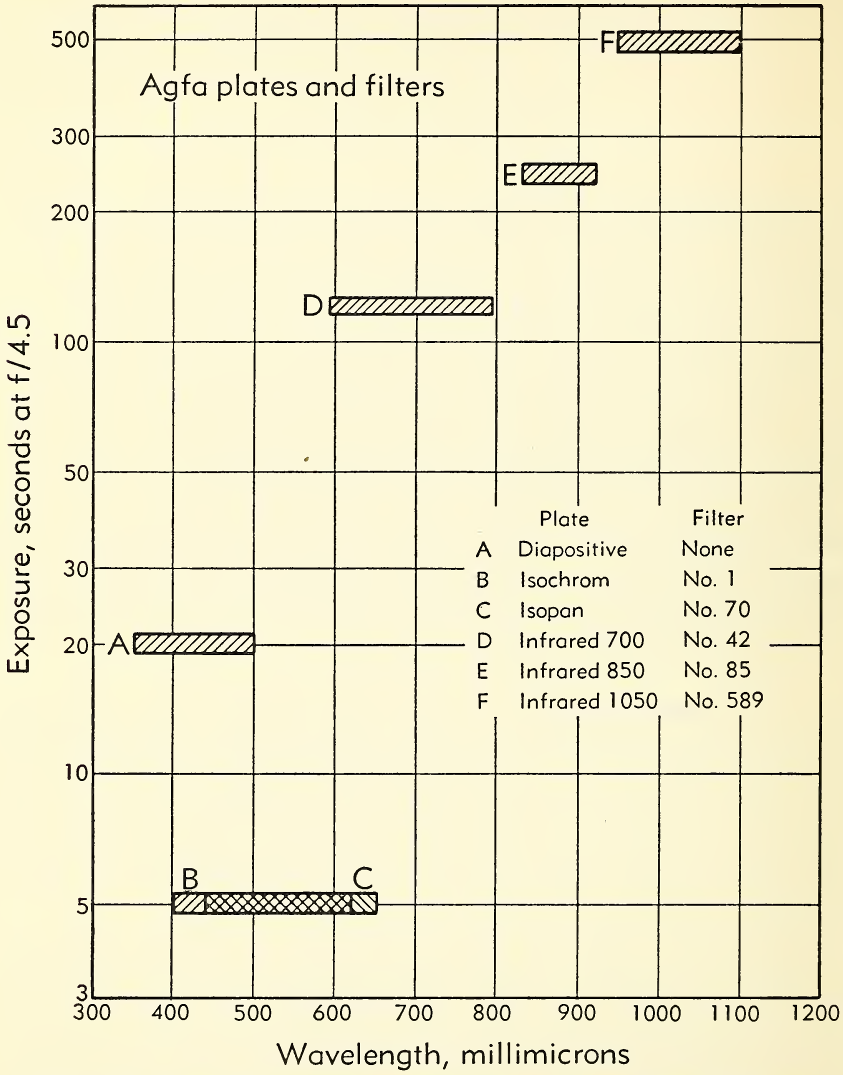

Fig. J,2. Exposure required when photographing flame of Teclu burner in various spectral regions (data of Bonhoeffer and Eggert).

filter on an infrared plate showing the intermediate zone. They also indicate that some thermal radiation occurred in the chemiluminescent zones, and that the chemiluminescent outer mantle is surrounded by a thermal-radiating zone.

By this method, sections of flames radiating predominantly in the ultraviolet and the visible spectrum can be identified as compared with those radiating in the infrared region. Thus, areas in which free radicals exist can be located with respect to those zones where carbon dioxide and water vapor predominate. The technique can be applied only very broadly, but it can serve as a useful qualitative tool.

Fig. J,2 summarizes the combinations of filters and photographic emulsions used by Bonhoeffer and Eggert, and the duration of the exposures required to obtain a satisfactory image of the flame of a Teclu burner. The long exposures in the infrared region result both from the small amount of radiation and from the relative insensitivity of the infrared plates in moderately narrow spectral zones. Photographs of the flame of a slot burner by these same investigators required even longer exposures, amounting to as much as 30 minutes at *f*/4.5 in the infrared region.

The plates used by Bonhoeffer and Eggert are not available at present in this country, but special emulsions supplied by the Eastman Kodak Company may be used for the same purpose.

Table J,2. Eastman photographic plates specially suited for flame photography.

General region	*Over-all spectral sensitivity of plate, millimicrons*	*Best spectral range for plate, millimicrons*	*Eastman designation of plate*	*Wratten filter to isolate best spectral range*
Ultraviolet	200– 500	200– 240	103-O, UV Sensitive	None
Blue	240– 500	240– 500	103-O	None
Green	240– 640	460– 620	103-D	57A
Yellow[1]	240– 630	550– 610	103-T	21
Red	240– 720	570– 670	103-E	23A
Extreme Red	660– 760[2]	680– 740	103-U	29
Infrared	240– 890	770– 840	I-N	88
Far Infrared[3]	720–1220	1010–1160	I-Z	88

[1] Maximum peak at 580 mμ; most suitable for D lines of sodium.
[2] Responds also in blue-violet region.
[3] Requires hypersensitizing.

Table J,2 lists special Eastman plates [*2*] selected for the photography of flames in relatively narrow spectral regions, as well as the Wratten filter best suited to isolating the region [*3*]. The plates are furnished in ten types of emulsions, most of which can be sensitized in any of sixteen spectral regions. Wherever possible, the Type 103 emulsion has been specified because it provides high speed, medium contrast, and low granularity. If greater contrast is required with some sacrifice in graininess, Type I emulsions can be specified, rather than Type 103. For greater resolution, but with loss of sensitivity, most of these plates are available as Type V. Maximum resolving power of 1,000 lines per millimeter can be obtained in the Class GH sensitizing of the Type 649 emulsion, peaking at 546 mμ.

These plates are supplied only on special order through Kodak dealers. Film also can be furnished.

Photography of Colored Flames. Nonluminous Bunsen flames are commonly used in studying the rate of flame propagation in gaseous mixtures because they permit ready observation of the inner cone. For other purposes, however, the nonluminosity of the flame is undesirable. Typical exposure to delineate the cone in a Bunsen flame may be $\frac{1}{5}$ second at *f*/11 with film having a speed of ASA 100. In such cases, materials are sometimes added to the air or to the fuel to make the flames more photogenic.

Although sodium ion is generally added, because of the brilliance obtained at the D line doublet (589 and 590 millimicrons), other materials may be used to take advantage of other spectral regions. Chief among these are cesium (456 mμ), boron (548 mμ), barium (554 mμ), strontium (606 mμ), and lithium (671 mμ). The method of addition varies, but schemes involving a spark discharge to promote the formation of a large number of small particles are widely used. The additive may enter the flame region with either the fuel gas or the combustion air, but usually the latter because of its greater volume.

Barret [4] used a 15-mm spark discharge at 20,000 volts from a platinum wire cathode in the bottom of a shallow tray inside a horizontal glass cylinder through which passed either the fuel gas or the combustion air. The anode was an annular ring of platinum supported above the surface of the solution in the tray. A somewhat simpler scheme is to support an electrically heated platinum helix just above the surface of a solid salt, such as sodium chloride. When the helix is heated to 2000–2200°F, and the combustion air is passed over it, enough salt is decrepitated to color the flame intensely. It is generally agreed that compounds normally considered volatile are not essential to produce good coloring, but that colloidal droplets or submicron solid particles are suitable. These particles are then volatilized by the high temperature of the flame. The chlorides are generally used.

Diborane, B_2H_6, is an intense coloring agent for flames. When present in hydrocarbon-air mixtures, such as propane-air, it provides a brilliant blue-green flame that is easy to photograph. Definite coloration occurs when the fuel-air mixture contains as little as 0.03 volume per cent of B_2H_6; at 0.25 volume per cent B_2H_6, the photographic exposure can be one-tenth that when no diborane is present. At this concentration, the additive has only an insignificant effect on flame speed.

Colored flames also can be produced by burning solids such as ethyl carbamate or ethyl oxamate if they contain small amounts of a coloring additive, for instance, strontium chloride, and an equal amount of a color-intensifying material such as ammonium chloride [*5*].

Color film, such as Kodachrome, Ektachrome, and Ansco Color, has not been used widely in photographing flames because of its low emulsion speed, ASA 8. For intense flames, as in rocket exhausts, it offers great possibilities. Spectral study of such color photographs, rather than of the original flame, is not satisfactory because the color of the image varies both with exposure and with processing conditions.

Photography of Fuel Beds. Many of the photographic methods developed in the study of fuel beds can be helpful in flame photography. An excellent review of the more important papers on the subject has been provided recently by Beral and Cooper [*6*]. Probably of greatest interest is the relationship shown between the required exposure time of photographs and the temperature of fuel beds. Based on original data taken from test exposures correlated with temperature indicated by a total-radiation pyrometer, it is possible to show that

$$\log \text{exposure} = -0.00277T + 1.106$$

where the exposure is in seconds, T is the temperature in degrees centigrade, the lens aperture is $f/6.3$, and the film speed is ASA 50. Although only an approximation, this relation may prove useful in estimating exposures in other cases where the radiation is essentially from a black body.

High Speed Photography. The study of rapid events, such as the motion of a flame front, can be done by making a single photograph with a very short duration and examining it in great detail, or by making a rapid series of such short-duration photographs and then viewing them as a motion picture. Both methods have been widely used, generally with the aid of the schlieren technique because the luminosity of flames is usually too low for direct photography with very short time intervals. Streak photography, where the image is deliberately made to move with respect to the film, offers still another method of investigation. Good reviews of the subject of high speed photography have been written recently [*7,34*].

Single exposure. Exposure times ranging from 1 to 500 microseconds can be achieved by an electric spark discharging a high-voltage capacitor through a gas-filled tube, or still shorter exposures by pulsing a continuous source of light by passing it through a Kerr cell.

Commercially available gas-filled tubes may dissipate as much as 600 watt-seconds in a single flash, with a total useful light output of about 24,000 lumen-seconds and a peak brilliance of 72×10^6 lumens. The largest commercial photoflash bulb has a useful light output of

95,000 lumen-seconds but a peak brilliance of only 5.2×10^6 lumens. In this example, the gas-filled tube produces useful light for about 300 microseconds and the photoflash bulb for 17,000 microseconds.

Special techniques have been developed for short exposures. These usually involve changes in the structure of the flash tube itself, and the use of small capacitors charged to a higher voltage. For example, the high pressure mercury-vapor capillary-type B-H6 lamp, made by General Electric, when discharged across a 3-microfarad capacitor charged to 1350 volts produces a 13-microsecond flash. Decreasing the size of the capacitor will shorten the flash duration still further, but at the expense of lumen output.

The Kerr cell, described recently by Zarem and Marshall [*8*], is an electro-optical type of shutter utilizing rotation of the plane of polarized light passing through a glass cell filled with nitrobenzene or phenyl cyanide, and containing two parallel flat electrodes. By newly developed electronic techniques of producing sharp pulses, these authors have been able to achieve exposures as short as 0.04 microsecond. The Kerr cell, however, is an inefficient light transmitter at best, half of the randomly polarized light entering the system being absorbed by the first polarizer. Thus, in no case can it have a transmission greater than 50 per cent. It has been used only in special applications.

Motion pictures. Repetitive flashing of gas-filled tubes synchronized with the motion of a strip of film can produce high speed motion pictures of nonluminous phenomena. This technique has been credited largely to Edgerton [*9*]. Picture-taking rates of 7,000 frames per second can be achieved by this method.

Most high speed motion pictures of flames have been taken with optical-compensating mechanically driven cameras. Two cameras of this type commercially available are the Eastman Type III, using 16-mm film and operating at speeds up to 3,000 frames per second, and the Wollensak Fastax, of which the 8-mm version with auxiliary voltage booster can achieve speeds as high as 14,000 frames per second. Both of these cameras have been very popular for research studies because of their ready availability, moderate price, and ability to use conventional film spooled on special reels.

Much has been learned about the mechanism of detonation in piston engines by means of high speed motion pictures, beginning largely with the work of Withrow and Rassweiler [*10*]. Later, Rothrock and Spencer [*11*] also used the high speed camera in similar studies. More recently, Miller [*12*] has studied detonation intensively with this same technique. Two different cameras were used [*13*] in Miller's early work, one operating at 40,000 frames per second and the other at 200,000 frames per second. When projected at the normal rate of 16 frames per second, the time scales were thus magnified by factors of 2,500 and 12,500 respectively.

Utilizing the schlieren principle, they showed conclusively the steady advance of the flame front across the cylinder with normal combustion, and the explosive knock reaction completed within 50 microseconds when a detonation wave followed autoignition of the end gas. Still more recently, photographs have been made with the second camera at 500,000 frames per second. Because these methods permit visualization of progress in even the fastest combustion reactions, they provide a powerful tool for combustion research.

Image dissection cameras capable of operating at speeds of up to 10^8 frames per second have been devised recently [*34*]. In general, these split the field of view into parallel narrow images by photographing through a moving grid which is also used later to view the developed image, or by placing the narrow dissected images end to end and reassembling them later for viewing. Image converter tubes capable of repetition rates as high as 10^7 frames per second also have been constructed, but the electronic equipment needed is complex. These highly specialized techniques are useful mainly for transient phenomena of exceedingly short duration. The resolution obtainable is not comparable with slower cameras, although it is usually adequate for ultrarapid events.

STREAK PHOTOGRAPHS. If a photographic film be moved normal to the motion of the image of a moving flame, with a slit to control the width of the image, a "streak" photograph is obtained. This provides a direct plot, in Cartesian coordinates, of the displacement of different points in the flame as a function of time. Knowing the speed of the moving film, the velocity of the flame image can be calculated, and, thus, the rate of flame propagation. Easily adapted to the schlieren principle by interposing a diaphragm in the light path, streak photographs also are useful in measuring the speed of detonation waves. Shepherd [*14*, pp. 301–316] shows excellent examples of how the principle is used for following ignition in various mixtures of gases where shock waves are present.

HYPERSENSITIZATION AND LATENSIFICATION. Usually, direct photography of flames is hindered because so little visible energy is radiated from the flame. As a consequence, exposures may be longer than the photographer wishes, particularly if optical filters are used to limit the spectral region. Many methods exist to increase the speed of emulsions, such as (1) hypersensitizing, as by treating the film before exposure; (2) latensification, by promoting growth of the latent image between exposure and development; (3) treating the film during exposure, as by heating it; (4) using specially formulated developers; and (5) intensification of the developed image. Miller and his coworkers [*15*] presented a good review of these methods in 1946. By their use, it is possible to increase emulsion speeds by a factor as great as three. A doubling of speed can be achieved most simply by using special developers, such as Eastman's SD-19a, containing hydrazine dihydrochloride.

J,3. Interferometry. Interference techniques for examining flames have never been so popular as the schlieren or the shadow methods. Two shortcomings of interferometry are responsible, the relatively high cost and complexity of the apparatus required, and the difficulty in the interpretation of the results. Nevertheless, the interferometer may be a valuable tool in studies of combustion.

PRINCIPLES OF INTERFEROMETRY. Basically, all interferometers operate on the same principle, the alternate reinforcement and cancellation occurring when two beams of light are superimposed with a difference in phase. Thus, if a monochromatic beam of light from a single source is split into two separate beams, one of which traverses a medium of different refractive index than the other, the velocity of light in one beam will be greater than in the other. Then, when the beams are recombined, they will be out of phase by an amount depending upon the difference in indexes of refraction of the media and upon the length of the path. Since this phase difference varies from point to point in the recombined beam, the image consists of alternate light and dark bands, the spacing of which is a measure of the difference in refractive indexes.

Application of this principle is very old. Mach [*16*], who describes the theory of interferometry in great detail, refers to many experiments prior to 1850.

TYPES OF INTERFEROMETERS. Although many interferometric systems have been devised, the Fabry-Perot and the Mach-Zehnder types have been used most in studying flames. The latter is the more important.

Fabry-Perot interferometer. Even with monochromatic light, the interference fringes produced by a simple interferometer are broad, and not sharply defined. If the interference does not occur between two separate beams, but by multiple reflection between two half-silvered surfaces, the fringes are narrow and bright against a black background. This principle of multiple internal reflectance is used in the Fabry-Perot interferometer. A detailed treatment of this subject is included in A,3.

Basically, the Fabry-Perot interferometer consists of two plane, parallel, half-silvered films mounted at a slight angle to the plane wave front of incoming light [*17*]. Being at a slight angle, some of the light is reflected from the second surface to the first, and thence again to the second, back to the first, and so on. Because each reflection is accompanied by the transmission of a part of the light, a collecting lens beyond the second surface forms a real image displaying interference effects.

Bundy and Strong [*18*, pp. 647–654] used the Fabry-Perot principle to good advantage in measuring the Doppler shift of the sodium D line in the exhaust flames of rockets. Here, the instrument was used to detect slight changes in wavelength, from which they deduced the velocity of the supersonic stream.

Mach-Zehnder interferometer. This type of interferometer has been used largely for studying flow in supersonic gas streams, and to a lesser extent in studies of heat transfer. Recently, it has been applied to the study of flames. An extension in principle of the Michelson interferometer, it utilizes the separation of light from a single source into two separate beams, one of which passes through the phenomena being observed. A great many variations have been proposed in the general style of the instrument, but generally it consists of a half-silvered mirror to split the beam, and two plane mirrors to reflect the resultant beams to a second half-silvered mirror which reassembles the beams for viewing.

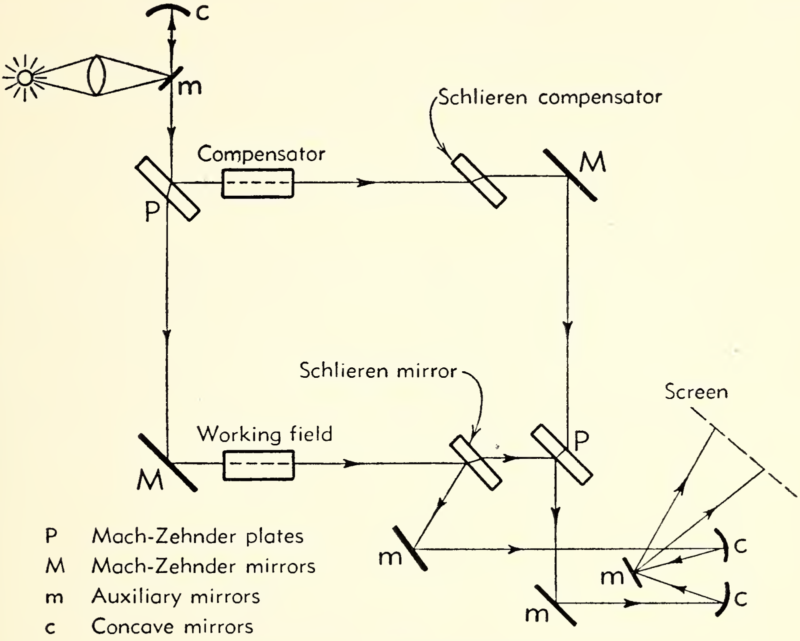

Fig. J,3. Arrangement of Mach-Zehnder interferometer with combined schlieren system.

Fig. J,3 shows the arrangement used in a Mach-Zehnder interferometer built at Wright Field in 1948 for the study of flames, as well as of problems in the fields of aerodynamics and thermodynamics [*19*]. It is unique in that since a schlieren system is built as part of the interferometer, simultaneous schlieren and interference records of the same phenomena can be obtained. Combining a schlieren system with an interferometer simplifies interpretation of the interferometric image. Where many complex fringes are present in the interferometer, the schlieren image serves to provide a first qualitative evaluation to assist in obtaining quantitative data from the interferometer photograph.

The Mach-Zehnder interferometer is difficult to adjust, usually requiring many hours to produce parallel image planes and fringes with white light. Price [*20*] has recently suggested a simple auxiliary light source and plane mirror to simplify this tedious job.

APPLICATIONS OF INTERFEROMETRY. The ability of interferometry to determine directly the index of refraction of transparent media fits it uniquely to quantitative measurements. Once the interferometer is properly adjusted, photographs made without particular care insofar as image density and contrast are concerned furnish all the data required to determine the index of refraction for a gas interposed for a known distance in the light path. Because the index of refraction is a linear function of the density of the gas, the method thus provides quantitative data on composition of a two-component gas mixture in a constant temperature field. Where both temperature and composition vary, no unique solution is possible, but variations in density at varying positions in the field can still be determined.

Excellent examples of the use of the Mach-Zehnder interferometer in examining flames have been given by Eckert, Drake, and Soehngen [*19*]. Because of the complex nature of the interferometer fringes in the steep temperature gradients present in flames, they used the schlieren system simultaneously as a qualitative guide to the interpretation of the interferometer image. The sensitivity of their system was sufficient to have the temperature difference between two successive lines only 4°F, making visible the boundary layer surrounding a horizontal, heated plate. Although candle flames also were photographed with the double system, only the most elementary observations were made and no data were reported. Olsen [*21*, pp. 663–667] used such an interferometer for examining the mixing of a jet of heated oxygen with surrounding air. His experiments included the use of various filters with white light, as well as sodium D line illumination. Although the accuracy obtained was not satisfactory, refinements in the technique are possible. With better control of test conditions, and with monochromatic illumination, Olsen expects to be able to make precision measurements.

J,4. Schlieren Photography. Probably the most widely used of all photographic techniques for studying flames is the schlieren method. Based on a principle due originally to Foucault and developed by Toepler [*22*], who originated the name meaning "striations," it has been described most completely by Schardin [*23*]. Liepmann and Puckett [*33*, pp. 89–101] give an excellent description of the schlieren method, as well as of shadow photography and interferometry. Reference is also made to A,2 for further details. Essentially, the schlieren method consists of focusing the image of a bright source limited by one sharp edge onto a knife edge parallel with the first one, so that most of the light passing the first edge is intercepted by the second. If the light beam is deflected between the two edges by other than the fixed optical system, as by some gradient in the index of refraction in the space through which the beam passes, the corresponding rays will be deflected past the second knife edge or be intercepted more completely by it to vary the illumination falling on a screen.

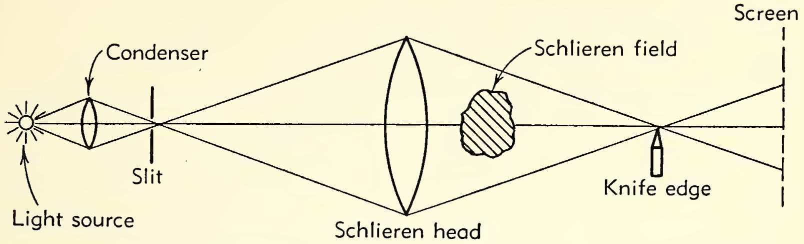

Fig. J,4a. Basic schlieren system.

Fig. J,4a illustrates the basic schlieren principle. Many variations of this simple arrangement have been devised; for example, the two-mirror system described by Barnes and Bellinger has been widely used [*24*]. It consists of two similar paraboloidal mirrors with the light source displaced to one side of the beam between the two mirrors, and with the camera on the opposite side. This symmetrical arrangement tends to cancel coma and there is a long path of parallel light in which to place the schlieren field.

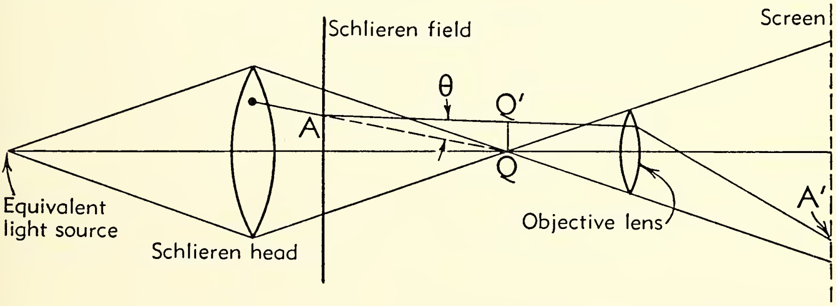

Fig. J,4b. Optical principle of schlieren system.

Optical principle. Fig. J,4b illustrates the optical principle of the schlieren method, as described in a recent Rand report [*25*]. Light from the source is focused by the schlieren head at *Q*, from whence it passes through an objective lens to form an image on the screen. The schlieren field and the screen are conjugate about the objective lens, and the light source and the point *Q* are conjugate about the schlieren head. Thus, an object in the schlieren field will produce a real image on the screen, and the light source will be imaged at *Q*.

If the light rays at A are refracted upward at some angle θ, called the angular deviation, the image they form will be at Q'. But all the rays leaving A will arrive at the same point A' on the screen, regardless of the angle at which they deviate from the normal path at A. Thus, two effects exist: (1) the image of the source is displaced depending upon the angular deviation in the schlieren field, and (2) all rays passing through a given point in the schlieren field will gather at a corresponding point on the screen. In the first case, the displacement of the image of the light source is independent of the position of the point in the schlieren field, and, in the second, the location of the point on the screen is independent of the angular deviation. Therefore, if a sharp edge is interposed in the bundle of rays at Q so that it will intercept a part of the rays having no angular deviation, the over-all illumination of the screen will be reduced. But those rays shifted to Q' because of the angular deviation will pass to the screen without interruption, producing additional illumination. The intensity of light on the screen, therefore, will depend upon the angular deviation.

A lens may be used as the schlieren head, but it must be of excellent quality and free from spherical or chromatic aberrations. Also, because the size of the field is fixed by the schlieren head, large lenses are usually required. For these reasons, first-surface paraboloidal mirrors are usually used.

In addition, straight knife edges are not required. Circular light sources, rather than ribbon sources, may be used, in which case the second knife edge may be replaced with a simple round hole. In some schlieren systems, no deliberate schlieren diaphragm is provided, the small diameter of the objective lens serving as the second knife edge to discard all rays deflected from the main bundle of rays entering the lens.

Plate J,4 illustrates the effect of changing the orientation of the knife edge.

Location of schlieren image. For the case of the schlieren system where a parallel light beam traverses the schlieren field, as when a two-mirror system is used, the location of the schlieren image can be calculated from basic optical principles.

It has been shown [*25*], for instance, that

$$-t = \frac{-f_n(x_1 + d)}{x_1 + d + f_n} + d$$

where $-t$ is the distance from the second schlieren mirror to the final image. In this analysis,

$$x_1 = \frac{f_m S}{f_m + S}$$

and S is the distance from the schlieren field to the second mirror; d is the distance from the second schlieren mirror to the camera objective; f_m is the focal length of the schlieren mirror, a negative dimension; and f_n is the focal length of the objective lens, also negative.

Size of schlieren image. It is also desirable to know the size of the image to be obtained with a given schlieren system. If r/R is the ratio of the radius of the field size to the radius of the beam entering the second mirror, then

$$\frac{r}{R} = \frac{1}{f_m f_n} [t(d + f_m + f_n) + d(d + f_m)] - 1$$

where the other dimensions are the same as given above.

With the aid of these two relationships, it is possible to design a schlieren system to fit the requirements of a given set of experimental conditions.

Quantitative application of the schlieren method. Although the schlieren method is used mainly as a qualitative indication of a gradient in the refractive index, it can also be applied quantitatively to such problems as the mixing of gases. Keagy, Ellis, and Reid [*25*] investigated three possible methods: (1) the use of a Ronchi grating in place of the conventional schlieren knife edge; (2) comparison of photographs made at different settings of the regular knife edge, and consequently at different sensitivities of the system; and (3) calibrating the photographic densities in the schlieren picture by including a gas-filled bubble in the schlieren field. The last of these, the "reference-schlieren" method, was most useful. By it, they were able to determine the refractive index of the mixture, and consequently the axial time-mean concentration of helium in a freely expanding jet at distances as great as 100 orifice diameters downstream. The method can be applied only to rotationally symmetric fields. Other quantitative procedures are possible with two-dimensional fields.

Quantitative application of the schlieren method to the study of flames will be difficult. Because the index of refraction of gases is related to density, and since density, in turn, is a function of temperature, pressure, and composition, all three of which vary simultaneously in flames, the measurement of the refractive index as a measure of flame properties would not be very helpful. This same basic shortcoming has limited the usefulness of interferometry in flame studies.

J,5. Shadow Photography. If a flame having steep temperature gradients is interposed between a bright point source of light and a screen, a shadow image of the flame will be obtained. This shadow, which can be photographed most simply by mounting a piece of film on the screen and using an intense spark as the light source, is a different representation of the gradients in the refractive index than is given by the schlieren method.

As pointed out by Lewis and von Elbe [*26*, p. 218], an optical gradient parallel to the light rays causes no visible change in illumination, whereas a gradient normal to the rays causes refraction and the appearance of an image on the screen. Density gradients in gases, and therefore gradients in the index of refraction, must be changing to produce good shadowgraphs; a constant gradient causes little change in illumination on the screen, and, thus, no useful image.

This property of the shadow method of producing an image proportional in density to the derivative of the gradient in the refractive index can be particularly useful. It permits recording photographically areas in flames where rapid changes in the gradients in the index of refraction are more important than the gradients themselves. Thus, in combination with the schlieren method, more information can be obtained on the change in the refractive index than is possible with either method alone. By removing the knife edge and slightly defocusing the camera, a schlieren system can be used to obtain shadowgraphs.

Shock waves are defined well by the shadow technique. In a shock wave, the density rises abruptly at the front of the wave, causing a rapid variation in the rate of change of density and producing a dark line in the shadow photograph. At the rear of the wave, there is a correspondingly rapid decrease in density, producing a lighter line in the photograph. This combination of a closely spaced dark line and a light line produces a good presentation of the shock wave.

Despite the advantage of an apparently simple relation between the blackening of a photographic emulsion and the derivative of the gradient in the refractive index, no quantitative application of the shadow method has been found in the literature. Rather, it has been used mainly for visualizing flow patterns in flame studies, and for determining the position of the flame front in the study of Bunsen flames.

J,6. Solids in Flames.

Small particles. By adding finely divided particles of noncombustible material to a gas mixture entering a burner, and then illuminating these particles stroboscopically and photographing them as they move through the flame, much information can be obtained about flame structure. The technique, used by Lewis and von Elbe [*27*] and reported in 1943, consists of adding microscopic MgO dust to the inlet of a burner, while illuminating the flame by the light from a photoflash bulb interrupted with a sector disk providing about seven pulses of light each millisecond. The light is limited by slits to a beam 2 millimeters wide parallel to the burner flame; the camera views this beam at right angles. Reflectors are provided, so that the particles are illuminated from both sides. Andersen and Fein [*28*] used a similar method with particles ranging from 20 microns to 40 microns in diameter. Stroboscopic pictures were taken to measure the emergent velocities, and streak photographs to determine the emergent angle. Their best measurements were made with the smallest particles.

Success for the method is based on the particles following the motion of the gases in the flame. Although small particles are used, their inertia keeps them from following exactly changes in direction of gas flow. The basic premises of Stokes' law may be applied generally, although the gravitational field is relatively unimportant here. It states

$$V = \frac{2ga^2(d_1 - d_2)}{9\mu}$$

where V is the terminal velocity, g the gravitational constant, a the radius of the particle (assuming it to be a sphere), d_1 and d_2 the densities of the particle and the medium, respectively, and μ the coefficient of viscosity of the medium. To attain maximum compliance between the particle and the gas, the terminal velocity should be as low as possible. Therefore, the particle should be small, its density should be low, and the viscosity of the gas should be high.

Smoke. Smoke also may be added to a flame to show the direction of flow lines. Lewis and von Elbe [*27*] used stannic chloride hydrate, which decomposes on heating and reappears after passage through the reacting zone. Thus, they were able to demonstrate the extent of the flow of heat from the combustion zone into the unburned gas by observing the zones in which the smoke was visible.

Ammonium chloride, zinc oxide, and ferric oxide also have been used as smokes to trace the thickness of the reaction zone. In the experiments of Broeze [*29*, pp. 146–155], the smokes had a terminal velocity of less than 1 millimeter per second, for which it should be possible to detect reaction zones as thin as 0.15 millimeter. He also showed that if there is a discontinuous surface in which the flow velocity increases abruptly, smokes acquire 90 per cent of the velocity increase within a distance d of the surface of discontinuity, where this distance is given as

$$d = \frac{U_0}{g}(2.3U_1 + 1.4U_2)$$

and where U_0 is the mean rate of free fall of the smoke, U_1 is the flow velocity before the discontinuity, U_2 is the added flow velocity due to the discontinuity, and g is the acceleration due to gravity.

Thus, temperature-sensitive solids in flames offer a good tracer method, not only for discontinuities in temperature, but for velocity as well.

In adding solids to flames, great care must be taken not to affect the combustion process. Because the thermal capacity of such solids is usually high, compared with that of the gas stream, the minimum quantity necessary to visualize the flow patterns should be added. Even then, a check should be made to see that the length of the flame does not increase when the solids are added. Andersen and Fein [*30*] showed that the addition of solid particles to mixtures of propane and air leaner than 3.8 per cent propane caused a significant decrease in combustion velocity.

It should be noted that the residence time of particles in flames increases with lean mixtures, because the burning velocity is lower and the flame zones are thicker. The thermal capacity of the added material then becomes even more important, for more time is available for the particles to absorb thermal energy from the flame.

J,7. Comparison of Photographic Methods of Locating Flame Front. As has already been shown, the interferometer method permits direct measurement of the index of refraction of gases, the schlieren technique discloses the gradient in the index of refraction, and the shadow method produces an image proportional in density to the derivative of the gradient in the refractive index. Direct photography, on the other hand, by selecting the spectral region, can be used to observe specific zones in the luminosity pattern of flames. Combinations of these methods can be used to provide more information than any one method alone. For instance, combinations of direct photography, schlieren photographs, and shadowgraphs have been extremely useful in locating the flame front in experimental flames.

Broeze [*29*, pp. 146–155] has compared direct flame photographs with schlieren pictures. In his illustrations, the schlieren cone lies well inside the cone shown by the direct photograph. By consideration also of photographs of smoke-laden flames, he was able to confirm earlier suggestions [*31*] that the schlieren image indicates the true location of the reaction zone. According to Broeze, the schlieren image should be used in all considerations of energy release and combustion velocity, the larger visible image being unsuitable for such measurements.

Andersen and Fein [*30*], on the other hand, found that the schlieren method was too sensitive to give a well-defined flame cone. When using the Gouy method for determining the burning velocity, where the area of the flame surface must be known, they preferred to use shadow photographs. By varying the distance between the flame and the film and by extrapolating to zero distance, their data agreed well with powder photographs of richer mixtures. Ashforth [*32*] and his coworkers preferred to take both direct photographs and shadowgraphs. By plotting the apparent burning velocities at different points in both the shadowgraphed cone and the luminous cone as a function of the radius of the flame cone at the point where the measurement is made, they arrived at two curves that intersected. This point they considered a true measure of the burning velocity.

J,8. Cited References.

1. Bonhoeffer, K. F., and Eggert, J. *Z. angew. Phot. Wiss. u. Tech. 1,* 43–47 (1939).
2. Anon. *Photographic Plates for Scientific and Technical Use,* 6th ed. Eastman Kodak Co., 1949.
3. Anon. *Wratten Light Filters,* 16th ed., revised Eastman Kodak Co., 1940.
4. Barret, P. *Compt. rend. 226,* 470–472 (1948).
5. Joyce, J. A. Colored-flame candle. *U.S. Pat. 2,481,019,* Sept. 6, 1949.
6. Beral, L., and Cooper, W. T. *Fuel 27,* 10–18 (1948).
7. Chesterman, W. D. *The Photographic Study of Rapid Events.* Clarendon Press, 1951.
8. Zarem, A. M., and Marshall, F. R. *Rev. Sci. Instr. 21,* 514–519 (1950).
9. Edgerton, H. E. *J. Appl. Phys. 8,* 2 (1937).
10. Withrow, L., and Rassweiler, G. M. *J. Soc. Automotive Engrs. 39,* 297–303 (1936).
11. Rothrock, A. M., and Spencer, R. C. Photographic study of combustion and knock in spark-ignition engine. *NACA Tech. Rept. 622,* 1938.
12. Miller, C. D. *S.A.E. Quart. Trans. 1,* 98–143 (1947).
13. Miller, C. D. High-speed camera. *U.S. Pat. 2,400,885,* May 28, 1946; High-speed motion picture camera. *U.S. Pat. 2,400,887,* May 28, 1946.
14. Shepherd, W. C. F. *Third Symposium on Combustion, Flame and Explosion Phenomena.* Williams & Wilkins, 1949.
15. Miller, H. A., Henn, R. W., and Crabtree, J. I. *J. Phot. Soc. Amer. 12,* 586–610 (1946).
16. Mach, E. *The Principles of Physical Optics.* Dutton, 1925.
17. Williams, E. W. *Applications of Interferometry.* Methuen, 1950.
18. Bundy, F. P., and Strong, H. M. *Third Symposium on Combustion, Flame and Explosion Phenomena.* Williams & Wilkins, 1949.
19. Eckert, E. R. G., Drake, R. M., Jr., and Soehngen, E. Manufacture of a Zehnder-Mach interferometer. *Air Materiel Command Tech. Rept. 5721,* 1948.
20. Price, E. W. *Rev. Sci. Instr. 23,* 162 (1952).
21. Olsen, H. L. *Third Symposium on Combustion, Flame and Explosion Phenomena.* Williams & Wilkins, 1949.
22. Toepler, A. *Ostwalds Klass. exact. Wissenschaften 157,* 1906.
23. Schardin, H. *Ver. deut. Ing. Forschungsheft,* 367 (1934).
24. Barnes, N. F., and Bellinger, S. L. *J. Opt. Soc. Amer. 35,* 497 (1945).
25. Keagy, W. R., Ellis, H. H., and Reid, W. T. Schlieren techniques for the quantitative study of gas mixing. *RAND Corp. Rept. R-164,* 1949.
26. Lewis, B., and von Elbe, G. *Combustion, Flames and Explosions of Gases.* Academic Press, 1951.
27. Lewis, B., and von Elbe, G. *J. Chem. Phys. 11,* 75–97 (1943).
28. Andersen, J. W., and Fein, R. S. *J. Chem. Phys. 17,* 1168–1273 (1949).
29. Broeze, J. J. *Third Symposium on Combustion, Flame and Explosion Phenomena.* Williams & Wilkins, 1949.
30. Andersen, J. W., and Fein, R. S. *J. Chem. Phys. 18,* 441–443 (1950).
31. van de Poll, A. N. J., and Westerdijk, T. *Z. tech. Phys. 22,* 29–32 (1941).
32. Ashforth, G. K., Long, R., and Garner, F. H. *J. Chem. Phys. 18,* 1112–1113 (1950).
33. Liepmann, H. W., and Puckett, A. E. *Introduction to Aerodynamics of a Compressible Fluid.* Wiley, 1947.
34. Miller, C. D., and Shaftan, K. *Product Eng. 23,* 168–182 (1952).

SECTION K

MEASUREMENT OF BURNING VELOCITY

ERNEST F. FIOCK

SECTION K

MEASUREMENT OF BURNING VELOCITY

ERNEST F. FIOCK

K,1. Introduction. The practical operation of many devices for producing heat and power depends upon the transformation, by the process of combustion, of the chemical energy latent in the fuel into more readily usable forms. An important factor in fixing over-all performance and space requirements is the rate at which this transformation can be accomplished, i.e. the rate of energy release as determined by the mass rate at which combustible mixture is converted into reaction products. Thus the rate of transformation of energy by combustion is of both practical and theoretical interest, since the process of combustion can be controlled and utilized most effectively only when its basic nature is understood thoroughly. One of the requisites to such an understanding is a knowledge of the rate at which flame advances into and transforms combustible mixture, and of effects thereon of all possible operating variables.

Much confusion exists in the literature on flame speeds from loosely used terms and from a lack of understanding of the conditions prevailing in the actual flames which have been studied. Obviously, flame speed is related to the rate of energy transformation by combustion, but several kinds of flame speed may be induced by changing the equipment in which a given mixture is burned. It is thus desirable to select and define a particular flame speed which is characteristic of the combustible mixture but independent of the surroundings. Such a flame speed may be designated as the burning velocity and defined as the normal component of the velocity of the reaction zone relative to nonturbulent unburned gas. Although various expressions have been used in this sense, the term burning velocity as used here is the "standard" burning velocity of Lewis and von Elbe [*6*, p. 240], so designated to indicate the absence of extraneous sources or sinks of heat and active particles. It is characteristic of the unburned mixture, and its numerical value depends only upon the composition, temperature, and pressure of this gas. Obviously these must be specified if the numerical value of burning velocity is to be significant. It is also obvious that, knowing the composition, temperature, and pressure, burning velocity may be expressed as either the mass rate or the volume rate at which unburned mixture is transformed per unit area of the flame.

No truly direct method has been developed for determining burning velocity, primarily because the burning process itself gives rise to complex physical manifestations which may impart motion to the unburned gas in the vicinity of the flame. Perhaps the most important of these is the drop in pressure which always occurs across the flame as a result of the acceleration of the products. Sharp curvature of the flame, as at the tip of a Bunsen inner cone, may also influence the state and the motion of the approaching unburned gas.

Because of the experimental difficulties inherent in establishing the velocity of the unburned gas relative to the flame, values recorded in the literature under a variety of names should be regarded as apparent flame speeds. These approximate the corresponding burning velocities to a greater or lesser extent, depending upon the experimental conditions and upon how the observed quantities are interpreted. The reviewer of existing methods of measurement and interpretation experiences considerable difficulty in attempting to determine how closely each set of reported flame speeds may actually approach the desired burning velocities. Thus it is important that the distinction between apparent flame speed and burning velocity be kept in mind by reviewer and reader alike in evaluating the various methods of measurement.

The scope of this section is limited to homogeneous mixtures of gases in the absence of mass transport due to turbulence or eddy diffusion. It is also limited as to range. The normal burning velocity is only one component of the turbulent burning velocity (II,H). The much higher velocities attained in detonations, wherein the waves are sustained solely by the liberation of energy within themselves, are treated in II,N.

Most sources of information summarized here are given in the Cited References (Art. 7). Additional details and source material will be found in the pertinent books and collections of papers listed in [*1* to *9*], as well as in the subsequent references.

K,2. Effects of the Structure of the Combustion Wave. The term combustion wave is used here in conformity with Lewis and von Elbe [*6*, Chap. VII], who have treated the case of interest in detail. (See also II,G.)

The structure of the wave would be immaterial to the determination of burning velocity if the ideal condition of the plane wave moving relative to gas in parallel flow could be attained in practice, because then only the relative velocity would have to be determined. However, most of the methods that have been devised for evaluating burning velocity involve deviations from these ideal conditions, principally curvature of the wave and changes in the direction of the unburned gas near and within the wave. Most experimental methods involve determinations of flame shape and position, and those utilizing moving flames usually require knowledge of their rates of displacement. Images of the same wave recorded by direct, shadow, and schlieren photography do not coincide [*10*;*11b,c*;*12e*;*13c*;*14*], and the true path of the unburned gas as it passes through the wave is difficult to establish. Thus the structure of the wave is of considerable importance in interpreting the observed quantities in terms of the burning velocity, since different flame shapes and areas will be obtained by the different methods of recording. Proper interpretation is further complicated by the fact that the thickness of the wave normally becomes relatively great [*8*, p. 405; *15*;*16*] at the lowest pressures at which stable combustion can be maintained.

The direct image is farthest from the unburned gas, the schlieren image is adjacent to it, and the shadow image is normally between the two but very much nearer the schlieren image. The methods of recording which use external illumination have the obvious advantages that the time of exposure is less, so that random fluctuations in the position of the flame are less troublesome, and that weakly luminous flames may be studied. The size of the shadow of a Bunsen inner cone depends somewhat upon the positions of the light source and the film relative to the flame. Correction for this effect can be made by taking pictures at various distances between flame and film and extrapolating to zero distance [*11b,c*;*12e*], a process which requires a completely steady flame and extra observations. Thus, from an experimental standpoint, the schlieren method seems best suited to the present purpose.

An indication of the direction of flow of the unburned gas may be had by introducing inert solid particles into the gas stream and photographing their movement by means of reflected light from an external source (Sec. J). How closely such particles follow the path lines, particularly right at the combustion wave, remains an open question. There is experimental evidence [*12c,e*] that, inside a Bunsen cone, they remain parallel to the burner axis until they reach that part of the combustion wave which is indicated by shadow and schlieren methods. Thereafter they begin to curve before the visible region is reached [*6*, p. 253; *12c,e*]. At the base and tip of the cone they curve even before the regions indicated by the shadow and schlieren methods are reached.

In addition to the more widely used methods of direct, shadow, and schlieren photography, the position of moving flames has been determined by the use of fusible wires [*17*], ionization gaps [*18*], and photoelectric cells [*19*,*20*]. Except for thin combustion waves, or unless two identical devices are used for measuring the time required for flame to travel the known distance between them, the use of such devices in the process of evolving burning velocities involves the question of what region in the wave actually triggers the sensing unit.

With this background, let us now proceed to a discussion of the methods which have been used in attempts to determine burning velocities. These may be treated in two major classes, according to whether the flames are stationary or moving.

Numerical values of experimentally determined flame speeds are summarized in Table K,6. In both the text and the table, compositions are always expressed in volume per cent.

K,3. Burning Velocities from Stationary Flames. Four more or less distinct methods involving stationary flames may be recognized. These utilize one type of Bunsen cone in which the velocity distribution in the unburned gas is parabolic, one in which the gas velocity is uniform, the tracing of path lines in the unburned gas by means of stroboscopically illuminated particles, and inverted and plane flames. In each method the gas must be nonturbulent, and appropriate accessory equipment must be provided for controlling, metering, and mixing the fuel and oxidant, and for measuring initial temperatures and pressures. Thus the composition and volume rate of flow of the homogeneous mixture issuing from the burner port are known.

For the sake of accuracy it is important that the flow from the burner port be extremely steady, because small pulsations, such as those introduced by periodic operation of pressure-regulating valves, may be amplified by resonance in the burner tube. It is important also that the flow pattern of the effluent mixture be steady and symmetrical, that there be no temperature gradients in the unburned gas, and that the velocity of the unburned gas does not suffer any unknown changes in either magnitude or direction between the burner port and the flame. Finally, the flow must be laminar, for otherwise the mixture will be consumed at the higher rate commensurate with turbulent flow (II,H).

The device which has been used more than any other in studying flame propagation is the Bunsen burner. If the inner cone of a Bunsen flame were a geometric cone whose base coincided with the burner port, the burning velocity S_u, as defined above, would be simply the volume of unburned gas entering unit area of the flame in unit time, or

$$S_u = \frac{\text{area of port} \times \text{average gas velocity through port } (U_u)}{\text{area of flame cone}}$$

Expressed in terms of the radius (R) of the port, the height (h) of the cone, and the angle (α) which one side of the cone makes with its axis, this becomes

$$S_u = \frac{RU_u}{\sqrt{R^2 + h^2}} = U_u \sin \alpha \tag{3-1}$$

In the above hypothetical case all of the unburned gas must have the same velocity, all of it must move parallel to the axis of the burner, there can be no heating of the unburned gas as it passes upward within the cone of flame, the reaction zone must be infinitely thin, and there can be no thermal or aerodynamic disturbances at the burner port, for only under these conditions can the flame be truly conical.

Actual burners and their flames differ so much from the above hypothetical requirements that many difficult problems arise in any attempt to calculate burning velocity from the observed shape of a Bunsen cone. Such calculations require knowledge not only of the shape of the flame, or at least some part of it, but also of the magnitude and direction in which stream tubes of unburned gas enter the diffusion zone of the flame in the region under consideration.

The quantities of primary importance in determining the shape of a flame on a given burner are the composition, temperature, velocity, and pressure of the unburned gas. In addition the following factors may influence the shape of the recorded image of a Bunsen flame: the method by which the image is produced (Art. 2); velocity and temperature gradients across the port; resonance effects in the burner tube; a change in velocity with height above the port; the radius of curvature of the flame; the pressure change due to burning; curvature of the path lines; and disturbances at the base and tip of the flame. Obviously many of these are interrelated.

Since so many factors combine to determine the shape of a Bunsen flame, it is not surprising that numerous methods have been proposed for interpreting the flame shape in terms of burning velocity, or perhaps that no completely satisfying method has yet been developed.

If the burner consists of a long tube of smooth, cylindrical bore, the flow therefrom is laminar at Reynolds numbers below about 2300, and the velocity distribution in the effluent gas is parabolic. The familiar laboratory Bunsen burner is of this type. Its possibilities for determining burning velocities will be presented first, because it was used in the earliest attempts to make such measurements, and because it has been used more widely for this purpose than any other device.

Bunsen flames above cylindrical tubes. As indicated previously, the burners under consideration are smooth-bore right cylinders, always with the length many times the diameter of the bore. The axis of the tube is vertical, the upper end or port is in a horizontal plane, and the unburned gas must not be caused to flow at Reynolds numbers above the critical value for the change from laminar to turbulent flow. This means that such a burner is useful only for mixtures that burn relatively slowly.

Interpretation of results obtained with this type of burner is complicated by the varying velocity in the unburned gas and by disturbances at the base and tip of the inner cone. However, the velocity distribution is amenable to reliable calculation from the Poiseuille equation. At the tip, diffusion toward the unburned gas in the axis changes both the composition and the state of the mixture. Thus the higher burning velocity at the tip is not characteristic of the mixture in its initial state. At the base of the flame the burner lip serves as a sink for heat and active particles and thus tends to quench the reaction. The excess pressure within the cone tends to impart lateral motion to the gas, and the difference in velocity between the gas and the surrounding atmosphere promotes mixing. These effects combine to produce a distortion of the flame at its base which depends upon several factors besides the burning velocity and the axial gas velocity. Thus flame speeds derived from the total area of the Bunsen cone cannot be characteristic of the unburned mixture in its initial state, although the errors caused by including both base and tip in the total tend to compensate each other.

Earlier measurements based on the total area of the visible cone have been reviewed by Smith [*5*, p. 389]. With the subsequent development of the shadow and schlieren methods, many other possible methods of interpretation based on both the angle of the cone and the areas of truncated cones away from the base and tip have been suggested [*7*, p. 85; *11*;*12*;*13*;*14*]. The writer agrees with Linnett [*12i*] and Wohl [*13c*] that flame speeds based on the area of the schlieren cone probably approximate the burning velocities more closely than those obtained by other interpretations of Bunsen flames. However, despite the evidence obtained from particle tracks, the writer is not wholly convinced that no small departures from axial flow in the unburned gas occur before it reaches the schlieren cone, since it would be difficult to follow deviations small enough to cause errors of only a few per cent in the derived flame speeds.

Space limitation precludes a complete review of all recent work on flame speeds. In many instances a particular research group has made repeated applications of one or more methods, developing and improving techniques in the process. Hence it is convenient to group the reports on this basis, both in the text and in the Cited References (Art. 7).

In 1943 Wolfhard [*21*] studied the combustion of stoichiometric mixtures of C_2H_2 and O_2 over the range of pressures from 3 to 760 mm Hg abs. The lower pressure limit was set by the capacity of his vacuum pump, rather than by inability to burn at still lower pressures. Cylindrical quartz burner tubes having diameters from 0.5 mm (at one atm) to 35 mm (at 3 mm Hg) were installed in a large glass pressure vessel having plane glass windows for observation. From direct photographs of the flames, the areas of the innermost surfaces of the visible cones were obtained with a planimeter. The apparent flame speed of a stoichiometric mixture of C_2H_2 and O_2 was found to be about 900 cm/sec, regardless of the pressure, exit gas velocity, or burner diameter.

Tube-type Bunsen burners have been used extensively at the University of Leeds in studies of flame speeds, flashback, blow-off, and of the dead space between the burner port and the flame. This work has been described in various reports by Townend and coworkers [*22*]. For the calculation of flame speed, an image of the visible cone is projected on a screen and traced. Areas are obtained on the assumption that each of a number of small horizontal slices is the frustum of a geometric cone. Apparent flame speeds are reported for CO-air, ethylene-air, and propane-air as functions of mixture ratio and pressure in the range 20 to 76 cm Hg. Those familiar with the equipment feel that the observed apparent flame speeds are in fact burning velocities when the experiments are made with large enough burners and when the gas flow rates are not too low. Under these conditions the observed values become independent of burner size and gas flow rate.

Equipment patterned after that developed at Leeds was used at Princeton [*23*] for measuring flame speeds of 1,3-butadiene with N_2-O_2 and He-O_2 mixtures at atmospheric pressure and below. Silica burner tubes were located within a larger glass tube for control of the pressure. The flame speed of the mixture containing He increased to a maximum as the pressure fell to 30 cm Hg, then decreased at still lower pressures. At atmospheric pressure it was increased 3.7-fold when He was substituted for N_2.

Sachsse and Bartholomé [*24*], using glass burner tubes and measuring the heights of visible cones, determined flame speeds for a wide variety of fuels mixed with air. Subsequent use of a nozzle-type burner [*25*] led them to suggest that the numerical values reported in [*24*] were low by about 25 per cent.

Linnett and coworkers at Oxford [*7*, p. 195; *12*] have measured flame speeds, using both tube-type burners and soap bubbles (Art. 4). Their burners are water-jacketed cylindrical tubes, and although they have used both shadow and schlieren methods, the latter is now favored. Results by the burner method are reported for ethylene-air, ethylene-O_2-N_2, and ethylene-air-CO_2 mixtures at room temperature and pressure. No specific mention is made of the concentration of water vapor.

Garner, Ashforth, and Long [*14*] at the University of Birmingham, using tube-type burners and both direct and shadow images, have studied the effects of pressure on flame speeds in mixtures with air of benzene, *n*-heptane, and 2,2,4-trimethyl-pentane at 50°C. Measurements of cone angle are made over the region in which the visible and shadow images are parallel.

At the University of Wisconsin, Andersen and Fein [*11*] measured flame speeds in mixtures of propane and air with a tube-type burner operated at room temperature and pressure. By extrapolation of the shadow cone areas to zero distance between flame and film, they found a maximum flame speed of 45.5 cm/sec. The moisture content of their unburned mixtures is not specified.

Several reports from the Bureau of Mines in Pittsburgh [*7*, p. 80; *8*, p. 374; *26*] contain experimental values of flame speed, together with data on flashback, blow-off, and quenching distances. All of these measurements were made with tube-type burners operated at atmospheric conditions. The visible images have been analyzed by both angle and area methods, and studies have been made by the use of stroboscopically illuminated particles (Sec. J).

Using a brass burner tube 0.071 cm in internal diameter, with a static pressure tap near the port, von Elbe and Mentser [*26d*] measured the cone height, the maximum diameter of the cone at its base, and the pressure difference due to accelerating the gases in flames of C_2H_2-O_2. Flame speeds were calculated from the areas of geometric cones having the measured bases and altitudes, and from the measured differences in pressure (Δp). The latter computations were made using the following equation for the pressure change across the flame due to the unavoidable change in momentum during burning:

$$p_u - p_b = \Delta p = \frac{\rho_u}{\rho_b}(\rho_u - \rho_b)S_u^2 \tag{3-2}$$

in which p is static pressure and ρ is density. Values of ρ_b were calculated from equilibrium data, and ρ_u and Δp were measured, so that S_u could be derived. The values obtained by the two methods agree remarkably well, but the flame speed amounts to only about 63 per cent of that reported by Wolfhard [*21*] and 50 per cent of that reported by Bartholomé [*25*].

Harris, Grumer, von Elbe, and Lewis [*7*, p. 80] used burner tubes of Pyrex, quartz, porcelain, and copper, with various diameters and each more than 40 diameters long, for measuring flame speeds, quenching distances, and the stability of flames of methane and propane with dry O_2 and N_2. Measurements of both area and angle were made on visible images, excluding portions of the inner cone near the base and tip. The two methods of computation gave values of flame speed which agreed within 10 per cent over the part of the image selected for measurement, with higher values by the angle method. The bending of path lines in the gas before it reaches the visible cone was recognized [*26c*], and the area method was considered to be more accurate because the errors from the bending tend to compensate over the measured surface. For dry propane-air, the maximum flame speed was found to be 37.6 cm/sec.

Dugger and his coworkers at NACA [*27a,b,d*] have used a heated burner tube operated at atmospheric pressure, shadow images, and the area method for determining the effect of varying mixture ratio and temperature on flame speeds for methane, ethylene, propane, and 2,2,4-trimethyl-pentane in air. For the latter fuel, the ratio of O_2 to N_2 in the mixtures was also varied. All mixtures contained 0.5 per cent of water vapor.

Also at NACA, and with similar equipment and technique, McDonald [*27e*] found that the flame speeds in a mixture containing 42 per cent CO and 58 per cent air, to which was added separately 1 per cent of ordinary H_2O and 1 per cent of D_2O, were 39.5 and 32.9 cm/sec, respectively.

At the University of Delaware, Wohl and coworkers have measured flame speeds and other burning characteristics of butane-air mixtures at atmospheric pressure [*13a*], and of methane-air and butane-air at various pressures [*13b*]. In [*13a*] visible images of butane-air flames were photographed through a green filter, which led to sharper definition of the innermost surface of the cone. Determinations were made with nearly dry mixtures (0.08 per cent H_2O), and with mixtures containing about 2.8 per cent of moisture. The maximum flame speeds were found to be 40.5 and 36.9 cm/sec, respectively. In [*13b*] flame speeds were determined from the areas of the visible images for methane-air mixtures at pressures between 0.25 and 6.3 atm, the values being 46 and 14 cm/sec, respectively. Pressure had the opposite effect on mixtures of butane-air, the flame speed being about 32 cm/sec at 0.25 atm and 41 cm/sec at one atm. Some of the flame images were analyzed by the angle method also, giving values which were nearly constant in the range from 0.3 to 0.7 of the radius of the port. As in [*7*, p. 80], flame speeds by the two methods agree to within 10 per cent, but here the values by the angle method are higher. Using butane-air flames, these observers present in [*13c*] a comparison of various methods of interpretation, leading to the conclusions that the most reliable method involves the area of the schlieren image, and that differences obtained when the visible image is used amount to only a few per cent.

In summary, the tube-type Bunsen burner has been used by many investigators in studying various phenomena of combustion, including the burning velocity. With its stationary flame, such a burner provides a convenient means for determining the over-all rate at which a combustible mixture is transformed. The many reasons why it is difficult to determine, from this over-all rate, the rate at which the transformation takes place per unit area of flame and in a direction normal to the flame have been discussed. Cylindrical curvature of the cone can be avoided by using slot-type burners, but flames of this type are difficult to treat on an area basis because of effects at either end of the slot.

A parabolic distribution of gas velocity across the port is characteristic of laminar flow in the tube-type burner. Even without any curvature of the path lines, such a velocity distribution causes some curvature in the trace of the central portion of the flame cone. An obvious method of straightening this element is to make the burner port the throat of a properly shaped nozzle. Such a nozzle discharging from an appropriate calming chamber gives a uniform velocity distribution, except in a thin boundary layer, and in addition gives laminar flow at higher Reynolds numbers than the critical value for tubes.

Except at their extremes, flames above nozzles should approach geometric cones more closely than do ordinary Bunsen flames. Thus their images should be less difficult to interpret in terms of burning velocity. However, since the method came into use rather recently, it is doubtful that its advantages and limitations have been fully explored. Attempts which have been made to use nozzle-type burners for determining burning velocities will be discussed next.

Bunsen flames above nozzles. In Johnston's apparatus [*28*] the nozzle serving as the burner port was located within a chamber whose pressure could be controlled. The large tube terminating in the nozzle could be heated for control of the temperature of the effluent mixture. A schlieren method was used to produce images which were projected on a screen where the angle between the traces was measured with a protractor. At the end of the tube opposite the nozzle, a vaporizer was provided so that fuels which are liquid at ordinary temperatures could also be studied.

Johnston reported distortion of his flames under extreme conditions of low pressure and low flow. Recognizing that values calculated as the product of the mixture velocity and the sine of the angle between the axis and the side of the schlieren image were probably dependent in some unknown degree upon the characteristics of the apparatus, he was careful to call such values flame velocities, as distinguished from burning velocities.

Bartholomé [*25*] studied flames at atmospheric conditions on nozzles of from 1 to 8 mm in diameter, so shaped that if d was the port diameter, the approach section had a diameter of at least $3d$, the converging portion had a length of $2d$, and the tip was a cylindrical section of length d. Flame speeds in the approximate range from 30 to 1200 cm/sec were derived from photographs of the visible cones by the angle method. For the fast-burning mixtures, Bartholomé considers these to be within 3 per cent of the burning velocity; for the slow-burning mixtures the error is thought to be about twice this figure. The results are stated to be independent of the gas velocity.

Some of the same mixtures with air had been run previously using a cylindrical burner tube, and Bartholomé points out that when the latter are multiplied by 1.25, moderate agreement is obtained with the values obtained above nozzles. He suggests that most of the values of flame speed derived from measurements on conventional Bunsen flames should have this correction applied to convert them to true burning velocities. It seems doubtful that such a generalization can be justified, except for his own results, which were obtained from cone heights and without considering the dead space or overhang.

At NACA, Dugger and Heimel [*27c*] used a burner having a ceramic nozzle in determining flame speeds of methane, ethylene, and propane in air at very low temperatures.

Equipment patterned after that of Johnston [*28*] is in use at the

National Bureau of Standards [*9*, p. 2731]. Values of flame speeds for methane-air at atmospheric pressure and over a wide range of fuel-air ratios, for stoichiometric mixtures of CH_4-O_2, C_2H_2-O_2, C_3H_8-O_2, H_2-O_2, and for these mixtures containing varying amounts of the diluents N_2, A, and He are available but not yet published. Water vapor was removed in traps cooled by dry ice. Experience with this equipment has shown the importance of keeping the burner nozzle at the same temperature as the effluent gas, and of controlling the moisture content even with hydrocarbon fuels. No method has been found for deriving flame speeds that are completely independent of gas velocity, although the spread in present results from this cause is only about twice the accidental error of observation.

Illuminated particle tracks. As described in Sec. J, the paths of flow of gas into and through a flame may be followed with a fair degree of approximation by introducing a few small particles of inert solid (for example MgO) into the stream of unburned gas and illuminating them externally. Photographed at right angles to the light, the traces of individual particles show the direction of flow in the plane of the light. If the particles are illuminated stroboscopically at a known frequency, their speed as well as their direction can be determined.

If such a method is to be exact, the particles must follow the path lines in the gas. Since the particles are heavier than the gas, their ability to follow the path lines will increase as their size is reduced. On the other hand they must not be too small to photograph, and if they are to be useful in measuring burning velocities they must have no sensible effect upon the rate of burning.

Smith [*5*, p. 389] used the stroboscopically illuminated particle method to study the velocity distribution above the port of a cylindrical burner tube in the absence of flame. Subsequently Lewis and von Elbe [*26c*] employed the method in a study of the variation in apparent flame speed over both normal and inverted flame cones. They point out that the burning velocity is affected by the solid particles, and therefore do not recommend the method for the actual determination of such velocities. Nevertheless these studies were useful in showing that the path lines in the unburned gas do curve before the gas reaches the visible Bunsen flame cone. From the registered path lines they were able to calculate flame speeds at various limited areas of the cone. These were found to increase gradually with distance from the burner wall, then to become essentially constant over the straightest part of the trace, and finally to increase sharply in the vicinity of the axis.

With the stoichiometric mixture of air and natural gas at atmospheric pressure, the flame speed determined over the central portion of the trace from particle tracks was about 22 cm/sec. The flame speed of the same mixture without added solids, as determined from the area of the visible cone over a cylindrical tube, was 23.4 cm/sec. These values indicate that the particles reduced the flame speed somewhat, and that, since the observed values differ so little, the effects of the high flame speed at the tip and the low value at the base approximately cancel when the area method is used.

Andersen and Fein [*11a*] used the same method as Lewis and von Elbe [*26c*], except that their burner terminated in a nozzle with a half-inch throat. Using MgO particles less than 20 microns in maximum dimension, they found that the speed of these particles in a given stream, with and without flame, was the same to within 1 per cent. They determined the variation of flame speed with mixture ratio, and concluded later [*11c*] that the illuminated particle method was of limited application in the measurement of burning velocity, primarily because of the high heat capacity of the solid particles. They felt, however, that this effect is negligibly small for stoichiometric mixtures, and that their maximum value of 45.0 cm/sec for propane-air is a good approximation of the burning velocity. However, their values for mixtures which differ considerably from stoichiometric, particularly on the lean side, depart markedly from the values observed by other methods.

On this point, a progress report from the University of Delaware [*13d*] suggests that submicroscopic particles, rather than those which are large enough to form tracks, may be responsible for reducing the rate of burning. At any rate, no change in the meniscus-shaped flames of very lean butane-air flames could be detected when powder free of dust was introduced.

In the course of their investigations of various methods of measuring flame speed, Linnett and his coworkers [*12*] used particle tracks to check the paths of flow, and found that these remain parallel to the axis until the shadow and schlieren cones are reached.

Inverted and plane flames. A solid obstruction placed in a stream of combustible gas flowing at a velocity greater than the burning velocity can be made to serve as an anchor for flame. Such a flame holder in the stream of gas from either a cylindrical tube or a nozzle gives a flame in which the inner cone is inverted and contains burned instead of unburned gas. Therefore, in flames of this type, the expansion due to burning has considerable effect upon the shape of the cone of primary combustion.

Exactly as with normal Bunsen flames, inverted flames can be used for determining burning velocity, provided the normal component of unburned gas velocity can be evaluated. Apparent flame speeds may, of course, be derived from measurements on inverted flames. However, unless the deviation of the flow lines from the axis is taken into account, these differ more from the burning velocity than do the corresponding values derived from normal flames. This is illustrated by the results of Wohl and Kapp [*13b*], which apply to inverted flames of butane-air stabilized over a nozzle by a 0.4-mm heated Pt wire stretched across a diameter at a distance of 0.2 mm above the nozzle. Apparent local burning velocities, calculated by the angle method without correcting for the direction of gas flow, were from three to four times the burning velocity, and varied greatly with the average velocity of the gas as it left the nozzle. Using an area method, but still neglecting the direction of flow, an average apparent flame speed was also calculated. This average value was likewise greater than the burning velocity (by about 25 per cent), and varied with the mixture velocity.

Lewis and von Elbe [*26c*] showed that the method of stroboscopically illuminated particles can also be applied to inverted flames, but did not attempt to measure burning velocities thereby. Because of the greater deflection of the particles away from the axis of the burner and because of the reverse slope of the flame trace, the particles approach the flame nearly tangentially. This tends to increase the difficulty of estimating the exact angle at which they enter the reaction zone.

It does not seem that the possible application of inverted flames in the study of burning velocities has been fully exploited. For example, an inverted flame can be stabilized above a nozzle by a small wire located above and in the axis of the nozzle. If the gas velocity is decreased slowly, such a flame becomes essentially flat, except around its periphery, where the interaction between the jet and the surrounding atmosphere is effective. Preliminary studies of this method, now in progress at the National Bureau of Standards, show that the flames may be stabilized some distance below the flame holder, but still above the nozzle. Such a flame will often remain in its stable position after the wire is removed. In the latter case the reaction of the flame itself causes enough divergence in flow to permit continued stability. These observations are additional evidence of the importance of extremely small forces, which may be thought of in terms of pressure, thrust, or change in momentum, in fixing the position of a flame.

The method just described for producing relatively flat flames which are isolated from any solid parts of the burner is closely akin to that used by Powling [*29*]. His burner was designed to stabilize slow-burning flames above a 6-cm tube filled almost to the port with straightening means whereby the effluent gas has a uniform velocity in laminar flow. The boundary layer is accelerated by means of a surrounding stream of inert gas. It was found necessary to place a 30-mesh screen above the flames in order to make them completely stable. This serves to reduce infiltration, and may also have some stabilizing action such as that ascribed above to the axial wire. Powling reports that this burner is satisfactory only for mixtures having burning velocities below about 15 cm/sec, and that the back pressure of the flame itself causes some divergence of the effluent jet, so that leeway is automatically provided as to the gas velocity required for stabilization. Burning velocity is calculated as the volume rate of flow divided by the area of the flat flame. Since the jet diverges, the latter is somewhat greater than the area of the burner port.

Beside its usefulness in determining burning velocities, Powling's burner has the advantage that it affords a clear view of the preflame zone for spectroscopic studies, and that, from curves of burning velocity and volume per cent of fuel near the lean limit, it provides an independent method for determining the lower limit of flammability. The latter is true because the burning velocity decreases very sharply with fuel concentration near the lean limit, and extrapolation to the zero of burning velocity is nearly linear. The cool and the blue flames of rich mixtures of ether-air and acetaldehyde-air have been stabilized simultaneously, and the two then made to coalesce by changing the mixture ratio.

K,4. Burning Velocities from Moving Flames.

Open-tube method. If a plane flame could be made to propagate from the open end toward the closed end of a tube filled with quiescent explosive mixture, the directly measurable speed in space would be identical with the burning velocity. This possibility has attracted many investigators seeking a simple and practicable method. However it must be concluded from the results which have been obtained with open tubes that no really satisfactory interpretation of these in terms of burning velocity has yet appeared.

The required interpretation is difficult since any actual flame, even though initiated as a plane combustion wave, soon bulges toward the unburned gas because of wall friction, quenching, and convection; since acoustic effects are frequently initiated by the flame, which then assumes a vibratory motion; and since the unburned gas about to be overtaken by the flame can scarcely be expected to remain at rest, in view of the disturbing factors just mentioned.

Until these disturbances were recognized, it was logical to assume that the major one might be the effect of the wall, and to experiment with larger and larger tubes. However the speed of uniform movement continued to increase as the diameter of the tube went up to nearly 1 meter. For the larger tubes this increase was due, at least in part, to the presence of folds which increased the area of the flame. It was found also that the speed of uniform movement depended somewhat upon the orientation of the axis of the tube, which is evidence of the importance of convection.

Coward and Hartwell [*30*] showed that some of the effects of the tube itself upon the movement of flame could be taken into account by considering the areas of the flames for which the speed of uniform movement was known. From successive photographs of the flame during the period of uniform velocity, taken at known time intervals, they calculated the average volume of unburned gas entering unit area of the flame per unit time. This treatment largely eliminated the variations due to tube diameter, except for the large sizes in which the flame was folded so that its area could not be estimated. However, insofar as the derivation of accurate burning velocities is concerned, this method is approximate at best, because of the uncertainty in determining the area of a three-dimensional surface from a photograph, and because it assumes that the flame touches the walls, that the burning velocity is uniform over the entire flame surface, and that the average gas velocity along the axis of the tube is negligible.

Wheatley [*12d*], in an attempt to extend the method of Coward and Hartwell to faster-burning mixtures of ethylene and air, found abrupt changes in both the speed of uniform motion and the flame shape. He was not able to correlate the observed flame areas with areas calculated from flame speed determined by another method, and concluded that the tube method involves so many uncertainties that it was unsuitable for determining the burning velocities of his mixtures.

On the other hand, Friedman and Burke [*9*, p. 2772] found no abrupt changes in speed or shape in their application of the method to mixtures of air with ordinary acetylene and with di-*deut*-acetylene.

Gerstein and coworkers at NACA [*20*] were able to establish uniform motion in a 2.8-cm tube much shorter than those used by Coward and Hartwell, by constricting the firing end to 0.8 cm and introducing a bleed, 0.17 cm in diameter, at the opposite end. They measured the speed of uniform motion with photocells and an appropriate timer, the flame area from photographs, and attempted to evaluate the velocity of the unburned gas at the flame by determining the volume of this gas which escaped through the 0.17-cm bleed into a soap bubble while the flame traveled between the two photocells. Flame speeds for a wide variety of pure hydrocarbons mixed with dry air at essentially atmospheric pressure have been determined using this equipment.

It seems to the author that the greatest value of the open-tube method is in yielding comparative values of flame speed, in order to show the effects of fuel structure [*20*; *9*, p. 2770].

Soap bubble method. Stevens [*31*] developed a method of measuring flame speeds which involved blowing an aqueous soap bubble with explosive mixture, firing it by a spark at its center, and photographing the resulting explosion. In applying this technique, it has been found expedient to suspend the bubble from a support which offers a minimum of resistance to the subsequent movement of the gases, and to introduce the firing electrodes either from above, through the support, or from below. In this way, complete freedom is provided for expansion in the horizontal direction. It is convenient to record the motion of the combustion wave on a film moving at a known constant speed, through a slit which leaves only the horizontal midsection, including the spark, visible.

The horizontal distance (r_1) between the firing spark and at least one wall of the bubble must be known. However, it is not necessary that the bubble be spherical, or even symmetrical, about the spark gap in the horizontal plane. Obviously the soap solution must form films which last long enough to permit the blowing, measurement, and firing of bubbles several centimeters in diameter, and it can contain no volatile, combustible solvent. It is also obvious that the explosive mixture can contain no constituent which dissolves in or permeates the film.

If the speed with which flame moves away from the spark is small compared with the velocity of sound in the surrounding atmosphere, the pressure ahead of the combustion wave does not increase significantly. The pressure required to distend the soap film is also negligible. Thus the explosion of a mixture within a soap film takes place at the constant pressure of the surroundings, the unburned gas suffers no sensible change in temperature before it is overtaken by the reaction zone, and flame speed remains constant throughout. The advancing flame remains spherical in form, and can impart only radial motion to the unburned gas, i.e. the direction of gas motion is everywhere normal to the combustion wave. Finally, if the mechanism for blowing and holding the bubble, and the igniter, are kept small, and if these elements are mounted vertically, burning along the horizontal diameter takes place without any restraint, and its rate is completely independent of the apparatus. Thus, except for the limitations imposed by the soap film, the method would be ideal for the determination of burning velocities.

In case the composition of the mixture within the bubble can be controlled, the image left by the advancing flame upon a film moving at constant velocity is a straight line originating at the spark, terminating when all of the gas along a horizontal radius has been consumed, and making an angle α with the image of the spark gap. If the magnification factor (m) and the linear film velocity (S_f) are known, the final radius (r_2) of the flame and the angle α can be read from the photograph. The speed of the flame in space (S_s) is given by

$$S_s = mS_f \tan \alpha \tag{4-1}$$

and the expansion ratio (E) at constant pressure is

$$E = \left(\frac{r_2}{r_1}\right)^3 = \frac{\rho_u}{\rho_b} \tag{4-2}$$

The mass of gas entering and leaving a given area of the combustion wave per unit time is

$$S_u\rho_u = S_s\rho_b$$

or

$$S_u = \frac{S_s\rho_b}{\rho_u} = \frac{S_s}{E} \tag{4-3}$$

Thus the burning velocity may be calculated directly from the results of a bubble experiment.

Fiock and Roeder [*32a*], in a detailed investigation of the method proposed by Stevens [*31*], used films containing glycerine, water, and soap. They found that the partial pressure of H_2O within such a film rapidly becomes equal to that of the surrounding atmosphere. Their films were considered unsatisfactory for use with hydrocarbon fuels, because these passed rapidly into and probably through the bubbles. Using CO as the fuel and controlling the water vapor in the mixtures by blowing the bubbles in an enclosure of regulated temperature (25°C) and humidity (2.69 volume per cent of H_2O), flame speeds of CO-O_2 and of the corresponding mixtures diluted with A or He [*20b*] were measured at atmospheric pressure. Effects of pressure could not be studied because the concentration of water vapor within the bubbles varied with pressure at constant temperature.

For this reason the results of Stevens [*33*] and of Kolodstew and Khitrin [*34*] on the effects of pressure on explosions of CO mixtures are open to serious question.

Recently, Linnett and coworkers [*12g*], using an unspecified solution of the soap Aphrosol, freed from alcohol but containing a little water, reported that observed burning velocities for 10 per cent C_2H_2 in air were sensibly constant if the bubbles were fired within 7 to 15 seconds after the blowing was started. Since firing within 15 seconds was normally feasible, they were not concerned that the flame speed decreased when the bubbles were allowed to stand longer. They modified the method to include schlieren photography [*12i*] and applied it to ethylene-O_2-N_2 mixtures and to C_2H_2-O_2-inert gas mixtures [*12j*] over the pressure range 20 to 76 cm Hg abs. The observed flame speeds were found to be independent of pressure, within the limits of experimental error. Since water vapor concentration is not specified, its possible effects on these results cannot be estimated.

Although combustion results are not yet available, promising attempts are being made to use materials other than aqueous soap solutions for retaining explosive mixtures, yet permitting them to burn at sensibly constant pressure. Kaufman and Cook [*35*] report that satisfactory bubbles can be blown from solutions of certain detergents in glycerol, and that such films appear satisfactory for use with hydrocarbon fuels and with oxidants other than NO and NO_2. Price and Potter [*36*] used transparent rubber balloons for studying the effect of adding H_2O and H_2 to mixtures of CO and O_2, the total fuel being always present in stoichiometric proportion. Their results are not yet available for review.

The writer feels that properly conducted experiments in films which permit the burning of a sphere of gas at constant pressure yield flame speeds which are in fact burning velocities. The principal limitation of this method lies in the difficulty of knowing the exact composition of the mixture at the time of firing.

Spherical bomb with central ignition. It is well known that the initial phases of explosions in closed containers are identical with those of the same mixtures at constant pressure, the flame spreading for a time as an expanding sphere in both cases. However the constant-volume bomb has the great advantage that the composition of the mixture can be varied at will, so long as all constituents remain gaseous.

For the determination of the volume of unburned gas transformed in unit time per unit area of the flame, i.e. the burning velocity, it is obvious that the flame in a closed container must remain spherical, that the velocity imparted to the unburned gas by the expansion of the flame must remain radial, and that these ends can be achieved only in a spherical bomb with central ignition. In such explosion vessels these conditions of symmetry are maintained during the entire burning period, although at least two exceptions have been noted in certain mixtures.

Schlieren pictures taken by Manton [*6*, p. 309] of the Bureau of Mines show that local irregularities sometimes appear in the flame surfaces as a result of the changes in composition of the gas immediately ahead of the flame by selective forward diffusion of constituents which are light as compared with the other gases in the mixture. In some mixtures both the flame front and the pressure become vibratory in character as the walls of the bomb are approached. It has been suggested that such vibrations may be due to delays in the establishment of equipartition, or perhaps in the transfer of energy to the low lying electronic level of O_2 [*8*, p. 529].

These irregularities are comparatively uncommon, and do not seriously limit the usefulness of the method. For the determination of burning velocities it is necessary that reliable time-pressure records of the explosion be obtained, and this requires special instrumentation.

It has been shown [*32d*] that the pressure-sensitive element of an indicator suitable for this purpose must be exposed directly to the gas, and not separated from it by any kind of passages. Diaphragm type indicators which respond with sufficient rapidity to follow the rapid changes of pressure, yet which are sufficiently flexible to give the necessary sensitivity, have been developed and applied successfully for this purpose.

The indicator developed by Lewis and von Elbe [*26a*] consists essentially of an integral body and diaphragm machined from one piece of nickel steel. The diaphragm is mounted flush with the wall of the bomb, and its deflections are used to tilt a mirror through a lag-free mechanical linkage. The position of the mirror as a function of the pressure was determined by a dynamic calibration. This instrument gives a continuous time-pressure record for each explosion in the bomb.

Indicators developed by Fiock, Marvin, Caldwell, and Roeder [*32c*] are of the balanced diaphragm type, and utilize stretched diaphragms of clock-spring steel mounted flush with the walls of the bomb. The space behind the diaphragm is sealed, and an adjustable insulated electrode is provided to indicate when the diaphragm is in its neutral position as well as to support the latter after contact is made. This instrument records a single point of the time-pressure curve, namely the time at which the explosion pressure becomes equal to the known backing pressure applied before the charge was fired.

The indicators described above are mentioned only because they have been applied successfully in the study of gaseous explosions in spherical bombs. It is probable that more recent developments in the measurement of rapidly changing pressures could now be applied to good advantage in the development of improved indicators.

In the following discussion of the measurement of burning velocity by means of spherical bombs with central ignition, the reasonable assumptions are made that the pressure at any stage of the reaction can be measured with the necessary accuracy; that the rate of heat loss from the burned gas to the unburned gas and to the walls is negligible; that the pressure at any instant is sensibly uniform throughout the bomb; that the flame front remains smooth and spherical; that the convective rise of the sphere of burned gas is negligible; that the gases are perfect; and that no reactions occur ahead of the flame. Under these conditions, burning velocities determined at constant volume apply to mixtures at temperatures and pressures which increase simultaneously as the burning progresses. Isolation of the individual effects of these two factors is difficult, but can be accomplished [*5*, p. 367] by varying the initial conditions over moderate ranges.

Using the relation suggested by Flamm and Mache [*37*] between the fraction of the gas inflamed at any instant and the corresponding pressure, Lewis and von Elbe [*26b*] developed a method for calculating burning velocities from the time-pressure record alone. This method, which makes use of certain thermodynamic data, simplifying assumptions, and graphical correlations, was applied in studies of explosions of gaseous ozone, and has been discussed by Gaudry [*8*, p. 521]. It is suggested that the sources mentioned be consulted for further details.

Suppose that a flame initiated at the center of a spherical bomb of radius R has a radius r at time t after ignition. In the next increment of time, dt, a shell of unburned gas of thickness $S_u dt$ is transformed. The total expansion occurring in time dt within the sphere of radius $r + S_u dt$ increases the pressure from p to $p + dp$ and compresses the remaining unburned gas so that its inner surface changes in radius from $r + S_u dt$ to $r + dr$. Since the flame front advances a total distance dr in time dt, its instantaneous velocity in space is $S_s = dr/dt$.

In this formulation of the problem it is to be noted that dp is the rise in pressure due to all possible processes taking place within the sphere of radius $r + S_u dt$, including shifts of chemical equilibrium and transfers of energy incident to the establishment of equipartition. Thus no knowledge is required of the thickness of the combustion wave or of the temperature state of the burned gas.

The subscript u is here used to indicate the unburned gas at pressure p, so that quantities with this subscript vary as the flame progresses. For example, γ_u is the ratio of the heat capacities of the unburned gas at temperature T_u, corresponding to the prevailing pressure p.

The unburned gas outside the shell of radius $r + S_u dt$ is compressed in the amount $-dV_u = 4\pi r^2(dr - S_u dt)$ from an initial volume of $4\pi(R^3 - r^3)/3$. Applying the adiabatic law in differential form to this compression,

$$\frac{dp}{p} = \frac{3\gamma_u r^2(dr - S_u dt)}{R^3 - r^3}$$

which reduces to

$$S_u = S_s - \frac{R^3 - r^3}{3\gamma_u p r^2}\frac{dp}{dt} = S_s\left(1 - \frac{R^3 - r^3}{3\gamma_u p r^2}\frac{dp}{dr}\right) \tag{4-4}$$

From experimental time-displacement records of the flame, values of r and $S_s = dr/dt$ can be obtained; corresponding time-pressure records yield values of p and of dp/dt; or values of dp/dr may be had from curves of p as a function of r. For any observed value of p, the adiabatic temperature T_u can be calculated, and the corresponding value of γ_u can be found in existing tables. Since all quantities in the right-hand members of Eq. 4-4 can be thus evaluated, instantaneous burning velocities may be derived from the experimental data.

This method was applied [*32c*] to stoichiometric mixtures of CO and O_2, and of the fuels *n*-heptane, iso-octane, and benzene with 36.7 per cent O_2 plus 63.3 per cent N_2.

K,5. Effects of Operating Parameters on Burning Velocity. The effects of various operating parameters upon the burning velocity are of great practical importance in the conversion of the chemical energy latent in a fuel into usable heat and power. Unfortunately only broad generalizations can be made from available data, and most of these must be based upon relative apparent flame speeds rather than upon actual burning velocities.

Fuel composition. Mixtures of H_2 and C_2H_2 with O_2 have the highest burning velocities that have been published. According to Bartholomé [*24,25*], H_2-O_2 burns slightly faster than C_2H_2-O_2. Using a nozzle-type burner, he found that H_2 flames could be made luminous by addition of up to 3 per cent of C_2H_2 without altering the burning velocity appreciably. On the other hand, Bone, Fraser, and Lake [*38*] report that the speed of uniform movement in H_2-O_2 in an open tube was approximately halved by adding 1 per cent of C_2H_2. Reported maximum flame speeds in C_2H_2-O_2 range from 570 to 1130 cm/sec, and it is believed that the higher values are closer to the true burning velocity. The fuels H_2 and C_2H_2 are believed to burn so rapidly because of the high concentration of hydrogen atoms formed in the flame, and because these are so small and light that they diffuse rapidly into the unburned gas ahead of the flame.

Carbon monoxide is particularly sensitive to the concentration of H_2O vapor. Because the C is already partially oxidized, the burning velocity in CO-O_2 is low compared with the mixtures of other fuels with O_2.

Maximum flame speeds in air mixtures of all hydrocarbons other than C_2H_2, under atmospheric conditions, lie in the approximate range 25 to 100 cm/sec. For pure and mixed hydrocarbons that warrant consideration as motor fuels from the standpoint of availability, this range is more nearly 30 to 40 cm/sec.

Among the straight chain paraffin hydrocarbons, the burning velocity of methane appears to be lowest, ethane highest, and others exhibit no significant differences. Branching of the carbon chain seems to reduce the burning velocity slightly.

The most comprehensive results for other types of hydrocarbons are those of Gerstein, et al. [*20*], who found that the maximum flame speeds in air mixtures of hydrocarbons increase in the order alkanes, alkenes, alkadienes, and alkynes.

Maximum flame speeds in mixtures of motor fuels and air do not differ by more than 20 per cent, there being no relation between these speeds and octane number. Of the antiknock and proknock derivatives which have been tried, none has a significant effect on the speed of flame in normal combustion.

Fuel-oxygen ratio. Almost without exception, recorded values of maximum flame speed occur in mixtures which contain slightly more fuel than the stoichiometric proportion. Curves of burning velocity as a function of fuel-O_2 ratio have relatively flat maxima, so that less precise knowledge of mixture composition is required here than in regions farther toward the rich or lean side. The method suggested by Powling [*29*] for determining flame speeds near the lean limit furnishes a means whereby this limit can be established without including effects of the measuring equipment.

Mixture temperature. Without exception, recorded values of flame speed increase with the initial temperature of the mixture. The rate of increase is moderate, and certainly much lower than the well-known exponential increase in chemical reaction rate with temperature. Thus, while the chemical reaction rate may make some contribution in establishing the burning velocity, it does not seem to be a controlling factor. Rather, the effect of initial temperature in producing a moderate increase in S_u indicates the importance of the transfer of matter and energy from the flame to the adjacent unburned gas by virtue of molecular motion (II,G).

Mixture pressure. Experimental evidence of the effect of pressure on the burning velocity is more confusing than that of the effect of temperature. Recorded maximum flame speeds for various mixtures of benzene [*14a*], methane [*13b*], and 1,3-butadiene [*23a*], for example, increase consistently as the pressure is reduced from atmospheric to about 30 cm Hg. On the other hand, maximum flame speeds in *n*-butane-air mixtures [*13b*] decrease with initial pressure. Those in ethylene-air and C_2H_2-air [*7*, p. 208; *12i,j*] change but little with pressure. Wolfhard [*21*] reports no appreciable change in flame speed with pressure for C_2H_2-O_2. Thus it seems that the effect of pressure must depend in some way upon the mechanism by which each specific fuel is transformed into products of combustion (II,G).

In examining the recorded data on the effects of pressure it is well to recall that the difference between observed, apparent flame speed and the corresponding burning velocity becomes more uncertain as the reaction zone thickens with decreasing pressure. Thus some of the confusion may be due to experimental error in burning velocities at reduced pressure.

Additive and inert gases. As already stated in this article, proknock and antiknock additives are without substantial effects on the burning velocities of mixtures of motor fuels with air.

In the recorded studies of burning velocity, too little attention appears to have been paid to the effects of H_2O vapor, except in the case of CO, where the extreme importance of moisture concentration is recognized. As may be seen in Table K,6, many observers have not troubled to record the moisture content of the mixtures studied. In some cases it may have been of little importance. That it can have an appreciable effect on flame speed in mixtures of fuels containing hydrogen is shown by the data of Kapp, Snow, and Wohl [*13a*], who found that adding 2.8 per cent of H_2O to nearly dry mixtures of butane-air decreased the maximum flame speed by about 10 per cent. Similar results were obtained at the National Bureau of Standards [*9*, p. 2731] with mixtures of CH_4-air. A possible explanation, advanced by Wohl and von Elbe [*39*], is that part of the energy of newly formed OH radicals and H_2O molecules may be dissipated upon collision with normal H_2O molecules.

Scattered studies have been made of the effects of inert diluents, particularly N_2, A, and He, on burning velocities. It seems probable that failure to find a plausible theory for the observed results may be due to the use of inexact values of thermal conductivity, as computed by the law of mixing, when one constituent is small and light [*25*].

K,6. Summary of Recent Determinations. Recent determinations of flame speeds approximating burning velocities are summarized in Table K,6, which provides a source list of information on individual fuels

Table K,6. Summary of recent determinations of flame speeds approximating burning velocities.

Additional values for the fuels listed are given in references [*1* to *9*]. For fuels not listed: see [*24*] for ethers, alcohols, and nitroparaffins; [*20a*] for alkenes, alkynes, and cyclohexane; [*20b*] and [*9*, p. 2771] for alkadienes, alkynes, and cyclic compounds.

Mixed fuels such as gasoline and city gas are not included.

Method[1] & reference	Mixture composition				Initial temp. T_u, °C	Initial press. p_u, atm	For maximum speed, mixture at T_u	
	Fuel	Oxidant	H_2O, volume %	Other			S_u (max) cm/sec	Fuel, volume %
Dvd[*31*]	CO	O_2	– – –[2]		room	1	104	69
Dvd[*32a*]	CO	O_2	3.31		30	1	109	69
Dvd[*32b*]	CO	O_2	2.69		25	1	101	69
Dvd[*32b*]	CO	O_2	2.69	A, He	25	1		
Avb[*40*]	CO	air	4.19		30	1	43	47
Dvd[*34*]	CO	air	2.31		room	1	47	49
Asa[*27e*]	CO	air	1.0		room	1	39.5[3]	41.6[3]
Asa[*27e*]	CO	air	0.0	1% D_2O	room	1	32.9[3]	41.6[3]
Jva[*41*]	N_2H_4	O_2	– – –		150	1	570[4]	
Bvb[*25*]	H_2	O_2	– – –		room	1	1175	74
Ata[5]	H_2	O_2	0.0		room	1	1067[4]	66.7[4]
Avb[*40*]	H_2	air	4.19		30	1	252	42
Bvb[*25*]	H_2	air	– – –		room	1	320	42
Bta[5]	H_2	air	0.0		room	1	224[4]	29.6[4]
Bvb[*25*]	H_2	Cl_2	– – –		room	1	410	63
Ava[*21*]	C_2H_2	O_2	– – –		room	0.1–1.0	900[6]	29
Ivc[*26d*]	C_2H_2	O_2	dry		room	1	570	30
Bvb[*25*]	C_2H_2	O_2	– – –		room	1	1140	36
Ava[*16*]	C_2H_2	O_2	– – –		room	1	800[4]	28.6[4]

[1] Key to experimental methods:

First letter is type of apparatus	Second letter is flame image used	Third letter is measurement on image
A. cylindrical burner tube	s. shadow	a. area
B. burner with nozzle	t. schlieren	b. angle
C. open tube	v. visible	c. height
D. soap bubble		d. volume
E. spherical bomb		
F. flat flame		
G. modified open tube		
H. particle track		
I. pressure drop across flame		
J. orifice serves as burner port		

[2] Dashes – – – indicate concentration of water vapor not specified in the original article.

[3] Not for maximum speed mixture.

[4] For stoichiometric mixture.

[5] Unpublished National Bureau of Standards results.

[6] Essentially independent of pressure.

Table K,6 (continued)

Method & reference	Mixture composition				Initial temp. T_u, °C	Initial press. p_u, atm	For maximum speed, mixture at T_u	
	Fuel	Oxidant	H_2O, volume %	Other			S_u (max) cm/sec	Fuel, volume %
Ata^5	C_2H_2	O_2	0.0		room	1	892^4	28.6^4
Ava[*16*]	C_2H_2	O_2	– – –	73% A	room	1	240^4	7.7^4
Dtd[*12j*]	C_2H_2	O_2	– – –	70% A	room	1	228	11
Dtd[*12j*]	C_2H_2	O_2	– – –	70% He	room	1	336	11
Dtd[*12j*]	C_2H_2	O_2	– – –	70% CO_2	room	1	41	11
Dtd[*12j*]	C_2H_2	O_2	– – –	70% O_2	room	1	416	11
Dtd[*12j*]	C_2H_2	O_2	– – –	71% A	room	0.26–1.0	215^{3,6}	10^3
Avb[*40*]	C_2H_2	air	4.19		30	1	145	10
Btb[*28*]	C_2H_2	air	– – –		318	0.13	591	10.9
Btb[*28*]	C_2H_2	air	– – –		318	0.30	514	11.7
Btb[*28*]	C_2H_2	air	– – –		318	0.46	502	11.5
Bvb[*25*]	C_2H_2	air	– – –		room	1	173	9
Ava[*16*]	C_2H_2	air	– – –		room	1	150^4	7.7^4
Cva[*9*, p. 2772]	C_2H_2	air	dry		25	1	154	9.8
Cva[*9*, p. 2772]	C_2D_2	air	dry		25	1	129	9.5
Bta^5	C_2H_2	air	0.0		room	1	156^4	7.7^4
– – –^{7}	C_2H_2	air	– – –		room	1	157	
Gva[*20c*]	C_2H_2	air	dry		room	1	141	10.3
Dtd[*12j*]	C_2H_2	air	– – –		room	1	156	11
Dtd[*12j*]	C_2H_2	air	– – –		room	0.26–1.0	146^{3,6}	10^3
Bvb[*25*]	C_2H_4	O_2	– – –		room	1	550	7.2
Dtd[*12i*]	C_2H_4	O_2	– – –		room	1	183.3^3	9^3
Asb[*12f*]	C_2H_4	O_2	– – –	N_2	15	1		
Asb[*12f*]	C_2H_4	O_2	– – –	CO_2	15	1		
Dtd[*12i*]	C_2H_4	O_2	– – –	72% N_2	room	1	55.1^3	9^3
Dtd[*12i*]	C_2H_4	O_2	– – –	70% N_2	room	1	83.7^3	9^3
Dtd[*12i*]	C_2H_4	O_2	– – –	66% N_2	room	1	98.5^3	9^3
Dtd[*12i*]	C_2H_4	O_2	– – –	56% N_2	room	1	132.2^3	9^3
Dtd[*12i*]	C_2H_4	O_2	– – –	32% N_2	room	1	172.5^3	9^3
Ava[*22a*]	C_2H_4	air	– – –		20	1	60	6.9
Bvb[*25*]	C_2H_4	air	– – –		room	1	80	7.5
Asb[*12f*]	C_2H_4	air	– – –		15	1	68.8	7.5
Atb[*12h*]	C_2H_4	air	– – –		room	1	68.2	7.8
Dtd[*12i*]	C_2H_4	air	– – –		room	0.26–1.0	66^{3,6}	7.0^3
Dtd[*12i*]	C_2H_4	air	– – –		room	1	67^{3,6}	8.0^3
Gva[*20d*]	C_2H_4	air	dry		room	1	67.8^8	7.6

---

[3] Not for maximum speed mixture.

[4] For stoichiometric mixture.

[5] Unpublished National Bureau of Standards results.

[6] Essentially independent of pressure.

[7] Values of Experiment Inc., quoted in [*9*, p. 2719]; method not specified.

[8] Adjusted by reference to values for ethylene-air obtained by Linnett and Hoare [*12f*].

Table K,6 (continued)

Method & reference	Mixture composition				Initial temp. T_u, °C	Initial press. p_u, atm	For maximum speed, mixture at T_u	
	Fuel	Oxidant	H_2O, volume %	Other			S_u (max) cm/sec	Fuel, volume %
Bsa[*27c*]	C_2H_4	air	0.0		−73	1	36	6.9
Asa[*27b*]	C_2H_4	air	0.5		34	1	78	7.3
Asa[*27b*]	C_2H_4	air	0.5		94	1	102	7.3
Asa[*27b*]	C_2H_4	air	0.5		150	1	125	7.3
Asa[*27b*]	C_2H_4	air	0.5		206	1	150	7.5
Asa[*27b*]	C_2H_4	air	0.5		261	1	179	7.5
Asa[*27b*]	C_2H_4	air	0.5		344	1	233	7.3
Ata[5]	CH_4	O_2	0.0		room	1	393[4]	25[4]
Cva[*30*]	CH_4	air	dry		room	1	27.5	9.8
Avb[*40*]	CH_4	air	4.19		30	1	38	10
A–c[*42*]	CH_4	air	– – –		room	1	36.4	9.7
Ava[*13b*]	CH_4	air	0.2		21	6.3	14.3	9.7
Ava[*13b*]	CH_4	air	0.2		21	1.0	33.4	10.3
Ava[*13b*]	CH_4	air	0.2		21	0.5	38.5	10.4
Ava[*13b*]	CH_4	air	0.2		21	0.25	46.0	10.0
Gva[*20a*]	CH_4	air	dry		room	1	33.8	10
Bsa[*27c*]	CH_4	air	0.0		−132	1	13	10.4
Bsa[*27c*]	CH_4	air	0.0		−73	1	20	10.4
Asa[*27b*]	CH_4	air	0.5		34	1	39	10.6
Asa[*27b*]	CH_4	air	0.5		96	1	53	10.6
Asa[*27b*]	CH_4	air	0.5		149	1	69	10.7
Asa[*27b*]	CH_4	air	0.5		207	1	89	10.8
Asa[*27b*]	CH_4	air	0.5		260	1	107	10.7
Asa[*27b*]	CH_4	air	0.5		342	1	148	10.4
Bta[5]	CH_4	air	0.03		28	1	38.1	10.1
Bta[5]	CH_4	air	0.0		room	1	37.5[4]	6.5[4]
– – –[9]	CH_4	air	– – –		25	1	43.6	
Avb[*40*]	C_2H_6	air	4.19		30	1	60	8
Gva[*20a*]	C_2H_6	air	dry		room	1	40.1	6.3
Bvb[*25*]	C_3H_8	O_2	– – –		room	1	390	17
Ata[5]	C_3H_8	O_2	0.0		room	1	357[4]	16.7[4]
Avb[*40*]	C_3H_8	air	4.19		30	1	45	6
Bvb[*25*]	C_3H_8	air	– – –		room	1	45	4
H-b[*11a*]	C_3H_8	air	– – –		room	1	45.0	4.1
Fva[*29*]	C_3H_8	air	– – –		room	1	Lean mixture only	
Asa[*11c*]	C_3H_8	air	– – –		room	1	45.5	4.1
Gva[*20a*]	C_3H_8	air	dry		room	1	39.0	4.5
– – –[7]	C_3H_8	air	– – –		room	1	45.6	
Asa and Ava[*14c*]	C_3H_8	air	– – –		room	1	48	4.5

---

[4] For stoichiometric mixture.

[5] Unpublished National Bureau of Standards results.

[7] Values of Experiment Inc., quoted in [*9*, p. 2719]; method not specified.

[9] Method not described.

Table K,6 (continued)

Method & reference	Mixture composition				Initial temp. T_u, °C	Initial press. p_u, atm	For maximum speed, mixture at T_u	
	Fuel	Oxidant	H_2O, volume %	Other			S_u (max) cm/sec	Fuel, volume %
Bta[5]	C_3H_8	air	0.0		room	1	45.7[4]	4.0[4]
Ava[*13e*]	C_3H_8	air	– – –		room	1.0	40.6	4.3
Ava[*13e*]	C_3H_8	air	– – –		room	1.5	38.0	4.3
Ava[*13e*]	C_3H_8	air	– – –		room	1.8	35.8	4.3
Ava[*13e*]	C_3H_8	air	– – –		room	2.7	32.3	4.4
Asa[*27c*]	C_3H_8	air	0.0		−73	1	23	4.4
Asa[*27c*]	C_3H_8	air	0.5		29	1	47	4.5
Asa[*27c*]	C_3H_8	air	0.5		93	1	62	4.5
Asa[*27c*]	C_3H_8	air	0.5		149	1	78	4.4
Asa[*27c*]	C_3H_8	air	0.5		204	1	98	4.4
Asa[*27c*]	C_3H_8	air	0.5		260	1	119	4.3
Asa[*27c*]	C_3H_8	air	0.5		343	1	160	4.2
Ava[*13a*]	n-C_4H_{10}	air	0.08		room	1	40.5	3.3
Ava[*13a*]	n-C_4H_{10}	air	2.8		room	1	36.9	3.3
Fva[*29*]	n-C_4H_{10}	air	– – –		room	1	Lean mixture only	
Ava[*13b*]	n-C_4H_{10}	air	0.2		21	0.25	32.5	3.6
Ava[*13b*]	n-C_4H_{10}	air	0.2		21	0.5	37.1	3.3
Ava[*13b*]	n-C_4H_{10}	air	0.2		21	1	40.7	3.2
Gva[*20a*]	n-C_4H_{10}	air	dry		room	1	37.9	3.5
Ava[*16*]	n-C_4H_{10}	air	– – –		room	1	40[4]	3.1[4]
– – –[7]	n-C_4H_{10}	air	– – –		room	1	45.9	
Fva[*29*]	n-C_5H_{12}	air	– – –		room	1	Lean mixture only	
Gva[*20a*]	n-C_5H_{12}	air	dry		room	1	38.5	2.9
– – –[7]	n-C_5H_{12}	air	– – –		room	1	44.4	
Gva[*20d*]	n-C_5H_{12}	air	dry		room	1	37.1[8]	2.8
Gva[*20a*]	n-C_6H_{14}	air	dry		room	1	38.5	2.5
Avc[*24*]	n-C_7H_{16}	air	– – –		16	1	46[10]	1.9
Avc[*24*]	n-C_7H_{16}	air	– – –		100	1	60[10]	1.9
Gva[*20a*]	n-C_7H_{16}	air	dry		room	1	38.6	2.3
– – –[7]	n-C_7H_{16}	air	– – –		room	1	42.4	
Ava[*14b*]	n-C_7H_{16}	air	– – –		50	0.53	63	1.9
Ava[*14b*]	n-C_7H_{16}	air	– – –		50	0.66	58	1.9
Ava[*14b*]	n-C_7H_{16}	air	– – –		50	0.79	54	2.0
Ava[*14b*]	n-C_7H_{16}	air	– – –		50	0.92	51	2.0
Ava[*14b*]	n-C_7H_{16}	air	– – –		50	0.99	50	2.0
Avc[*24*]	C_8H_{18}[11]	air	– – –		18	1	42[10]	1.7
Avc[*24*]	C_8H_{18}	air	– – –		100	1	55[10]	1.7

[4] For stoichiometric mixture.

[5] Unpublished National Bureau of Standards results.

[7] Values of Experiment Inc., quoted in [*9*, p. 2719]; method not specified.

[8] Adjusted by reference to values for ethylene-air obtained by Linnett and Hoare [*12f*].

[10] Corrected as suggested by the investigator.

[11] All tabulated results are for 2,2,4-trimethyl-pentane.

Table K,6 (continued)

Method & reference	Mixture composition				Initial temp. T_u, °C	Initial press. p_u, atm	For maximum speed, mixture at T_u	
	Fuel	Oxidant	H_2O, volume %	Other			S_u (max) cm/sec	Fuel, volume %
Asa and Ava[*14b*]	C_8H_{18}	air	---		50	0.53	57	1.7
Asa and Ava[*14b*]	C_8H_{18}	air	---		50	0.66	52	1.8
Asa and Ava[*14b*]	C_8H_{18}	air	---		50	0.79	49	1.7
Asa and Ava[*14b*]	C_8H_{18}	air	---		50	0.92	45	1.7
Asa and Ava[*14b*]	C_8H_{18}	air	---		50	0.97	43	1.7
Ata[*27d*]	C_8H_{18}	air	0.4		38	1	34.6	1.7
Ata[*27d*]	C_8H_{18}	air	0.4		94	1	44.8	1.7
Ata[*27d*]	C_8H_{18}	air	0.4		149	1	57.5	1.7
Ata[*27d*]	C_8H_{18}	O_2	dry	73.5% N_2	38	1	52.1	2.1
Ata[*27d*]	C_8H_{18}	O_2	dry	73.5% N_2	149	1	83.1	2.1
Ata[*27d*]	C_8H_{18}	O_2	dry	68.9% N_2	38	1	69.7	2.4
Ata[*27d*]	C_8H_{18}	O_2	dry	68.9% N_2	149	1	108.0	2.4
Ata[*27d*]	C_8H_{18}	O_2	dry	63.5% N_2	38	1	89.1	2.8
Ata[*27d*]	C_8H_{18}	O_2	dry	63.5% N_2	149	1	138.0	2.8
Ata[*27d*]	C_8H_{18}	O_2	dry	48.4% N_2	38	1	152.2	4.0
Ata[*27d*]	C_8H_{18}	O_2	dry	48.4% N_2	149	1	229.9	4.0
Avc[*24*]	C_6H_6[12]	air	---		20	1	54[10]	2.8
Avc[*24*]	C_6H_6	air	---		100	1	69[10]	2.8
Gva[*20a*]	C_6H_6	air	dry		room	1	40.7	3.3
Asa and Ava[*14b*]	C_6H_6	air	---		50	0.39	77	3.1
Asa and Ava[*14b*]	C_6H_6	air	---		50	0.53	65	3.0
Asa and Ava[*14b*]	C_6H_6	air	---		50	0.66	63	3.1
Asa and Ava[*14b*]	C_6H_6	air	---		50	0.79	61	3.1
Asa and Ava[*14b*]	C_6H_6	air	---		50	0.92	57	3.2
---[7]	C_6H_6	air	---		room	1	47.8	

---

[7] Values of Experiment Inc., quoted in [*9*, p. 2719]; method not specified.

[10] Corrected as suggested by the investigator.

[12] All tabulated results are for benzene.

and on the methods that have been used with each. Insofar as is possible, the following are also specified: mixture composition, initial temperature and pressure, the maximum observed flame speed, and the volume per cent of fuel in the maximum speed mixture. In most instances the latter two quantities were read from smooth curves of flame speed as a function of mixture ratio, so that they involve graphical smoothing of experimental results. Neither mixed fuels, such as gasoline and city gas, nor values quoted in previous reference works [*1* to *9*] are included in the table.

Although recognizing the desirability of suggesting which of the various values quoted for each fuel may approximate the burning velocity most closely, the reviewer feels that such selection involves more personal opinion than actual fact, and that it would therefore be of doubtful value. One of the major difficulties is the lack of information on moisture content, and on its possible contributions to the measured values.

K,7. Cited References.

1. Mache, H. *Die Physik der Verbrennungserscheinung.* Veit, Leipzig, 1918.
2. Bone, W. A., and Townend, D. T. A. *Flame and Combustion in Gases.* Longmans, Green & Co., London, 1927.
3. Jost, W. *Explosion and Combustion Processes in Gases.* Transl. by H. O. Croft. McGraw-Hill, 1946. Originally published by Springer, Berlin, 1932.
4. Jahn, H. *Der Zündvorgang in Gasgemischen.* Oldenbourg, Berlin, 1934.
5. A symposium on gaseous combustion. *Chem. Revs. 21,* 1937.
6. Lewis, B., and von Elbe, G. *Combustion, Flames and Explosions of Gases.* Academic Press, 1951.
7. *Third Symposium on Combustion, Flame, and Explosion Phenomena.* Williams and Wilkins, 1949.
8. International symposium on the kinetics and mechanism of ignition and combustion in gases. *Rev. Inst. franç. pétrole et Ann. combustibles liquides 4,* 1949.
9. Symposium on combustion chemistry. *Ind. Eng. Chem. 43,* 2717–2870 (1951).
10. van de Poll, A. N. J., and Westerdijk, T. *Z. tech. Phys. 22,* 29 (1941).
11. Andersen, J. W., and Fein, R. S. Univ. of Wisconsin.
    a. *J. Chem. Phys. 17,* 1268 (1949).
    b. *Univ. of Wisconsin CM-552,* July, 1949.
    c. *J. Chem. Phys. 18,* 441 (1950).
12. Linnett, J. W., and coworkers at Oxford Univ.:
    a. and Sherratt, S. *Trans. Faraday Soc. 44,* 596 (1948).
    b. and Wheatley, P. J. *Nature 164,* 403 (1949).
    c. *Fuel 29,* 13 (1950).
    d. and Wheatley, P. J. *Fuel 29,* 80 (1950).
    e. Grove, J. R., and Hoare, M. F. *Trans. Faraday Soc. 46,* 745 (1950).
    f. and Hoare, M. F. *Trans. Faraday Soc. 47,* 179 (1951).
    g. Pickering, H. S., and Wheatley, P. J. *Trans. Faraday Soc. 47,* 974 (1951).
    h. and Conan, H. R. *Trans. Faraday Soc. 47,* 981 (1951).
    i. and Pickering, H. S. *Trans. Faraday Soc. 47,* 989, 1101 (1951).
    j. and Wheatley, P. J. *Trans. Faraday Soc. 48,* 338 (1952).
13. Wohl, K., and coworkers at Univ. of Del.:
    a. and Kapp, N. M., and Snow, B. The effect of water vapor on the normal burning velocity and on the stability of butane-air flames burning above tubes in free air. *Project Meteor Rept. UAC-30,* Nov. 1948.
    b. and Kapp, N. M. Flame stability at variable pressures. *Project Meteor Rept. UAC-42,* Oct. 1949.
    c. and Kapp, N. M., Coon, D. C., Jr., and Fulmer, R. F. Methods of deter-

mining burning velocities and stability measurements of tube and nozzle flames. *Project Meteor Rept. UAC-49,* Dec. 1950.
  d. *Project Squid Semiannual Progr. Rept.,* p. 107, Apr. 1951.
  e. *Project Squid Semiannual Progr. Rept.,* p. 87, Oct. 1951.
14. Garner, F. H., Ashforth, G. K., and Long, R. at the Univ. of Birmingham:
  a. *Fuel 28,* 272 (1949).
  b. *Fuel 30,* 17 1951.
  c. *Fuel 30,* 63 (1951).
15. Gilbert, M. The investigation of low-pressure flames. *Calif. Inst. Tech. Jet Propul. Lab. Rept. 4-54,* Aug. 1949.
16. Gaydon, A. C., and Wolfhard, H. G. *Proc. Roy. Soc. London A196,* 105 (1949); *Fuel 29,* 15 (1950).
17. Wheeler, R. V. *Trans. Chem. Soc. 105,* 2606 (1914).
  Mason, W., and Wheeler, R. V. *J. Chem. Soc. 111,* 1044 (1947).
  Coward, H. F., and Greenwald, H. P. *U.S. Bur. Mines Tech. Paper 427,* 1928.
18. Schnauffer, K. *S.A.E. Journal 34,* 17, (1934).
  Rabezzana, H., and Kalmar, S. *Automotive Inds. 72,* 324, 354, 394 (1935).
  Mason, W. A., and Brown, K. M. *Automotive Inds. 72,* 582 (1935).
19. Vichnievsky, R., and Monnot, G. See [*8*], p. 130.
20. Gerstein, M. and coworkers at NACA.
  a. Levine, O., and Wong, E. L. Fundamental flame velocities of pure hydrocarbons, Part I. *NACA Research Mem. E50G24,* Sept. 1950.
  b. Levine, O., and Wong, E. L. Fundamental flame velocities of pure hydrocarbons, Part II. *NACA Research Mem. E50H25,* Nov. 1950.
  c. and Levine, O. Fundamental flame velocities of pure hydrocarbons, Part III. *NACA Research Mem. E51J05,* Dec. 1951.
  d. Simon, D. L., and Wong, E. L. Flame velocities over a wide concentration range for pentane-air, ethylene-air, and propyne-air flames. *NACA Research Mem. E51H09,* Oct. 1951.
21. Wolfhard, H. G. *Z. tech. Phys. 24,* 206 (1943).
22. Townend, D. T. A. and coworkers at Leeds.
  a. *Inst. Gas Engrs. Communs. 220,* 1939; *244,* 1941; *255,* 1943; *J. Inst. Fuel 18,* 175 (1945); *Fuel 29,* 64 (1950).
  b. Culshaw, G. W., and Garside, J. E. *Inst. Gas Engrs. Communs. 306,* 1946; *See* [*7*], p. 204.
23. Pease, R. N. and coworkers at Princeton.
  a. Badin, E. J., and Stuart, J. G. *J. Chem. Phys. 17,* 314 (1949).
  b. *Project Squid Semiannual Progr. Rept.,* p. 114, Apr. 1951.
24. Sachsse, H., and Bartholomé, E. *Z. Elektrochem. 53,* 183 (1949).
25. Bartholomé, E. *Z. Elektrochem. 53,* 191 (1949); *Naturwissenschaften 36,* 171 (1949).
26. Lewis, B., and von Elbe, G. at the Bureau of Mines in Pittsburgh. (See also [*6*])
  a. *J. Am. Chem. Soc. 55,* 504 (1933).
  b. *J. Chem. Phys. 2,* 283 (1934).
  c. *J. Chem. Phys. 11,* 75 (1943).
  d. and Mentser, M. *J. Chem. Phys. 13,* 89 (1945).
27. Dugger, G. L., and coworkers at NACA.
  a. *NACA Tech. Note 2170,* Aug. 1950; *J. Am. Chem. Soc. 72,* 5271 (1950).
  b. *NACA Tech. Note 2374,* May 1951.
  c. and Heimel, S. *NACA Tech. Note 2624,* Feb. 1952.
  d. and Graab, D. D. *NACA Tech. Note 2680,* Apr. 1952.
  e. and McDonald, G. E. *NACA Research Mem. E50C10,* July 1950.
28. Johnston, W. C. *S.A.E. Journal 55,* 62, 1947.
29. Powling, J. *Fuel 28,* 25 (1949).
30. Coward, H. F., and Hartwell, F. J. *J. Chem. Soc. 1932,* 2676.
31. Stevens, F. W. *NACA Rept. 176,* 1923.
32. Fiock, E. F., and coworkers at the Natl. Bur. Standards.
  a. and Roeder, C. H. *NACA Rept. 532,* 1935.

b. and Roeder, C. H. *NACA Rept. 553*, 1936.
c. Marvin, C. F., Caldwell, F. R., and Roeder, C. H. *NACA Rept. 682*, 1940.
d. and Caldwell, F. R. *J. Research Natl. Bur. Standards 26*, 175 (1941).

33. Stevens, F. W. *NACA Rept. 372*, 1930.
34. Kolodstew, Kh., and Khitrin, L. *J. Tech. Phys. U.S.S.R. 3*, 1034 (1936).
35. Kaufman, F., and Cook, H. J. Non-aqueous soap bubbles for flame studies. *Ballist. Research Lab. Tech. Note 575*, Jan. 1952.
36. Price, T. W., and Potter, J. H. Unpublished papers prepared for Am. Soc. Mech. Engrs. in June 1952 and for fourth symposium on combustion in Sept. 1952.
37. Flamm, L., and Mache, H. *Wien. Ber. 126*, 9 (1917).
38. Bone, W. A., Fraser, R. P., and Lake, F. *Proc. Roy. Soc. London A131*, 1 (1931).
39. Whol, K., and von Elbe, G. *Z. physik. Chem. 5*, 241 (1929).
40. Smith, F. A., and Pickering, S. F. *J. Research Natl. Bur. Standards 17*, 7 (1936).
41. Murray, R. C., and Hall, A. R. *Trans. Faraday Soc. 47*, 743 (1951).
42. Denues, A. R. T., and Huff, W. J. *J. Am. Chem. Soc. 62*, 3045 (1940).

SECTION L

MASS SPECTROSCOPY

JOHN A. HIPPLE

SECTION L

MASS SPECTROSCOPY

JOHN A. HIPPLE

CHAPTER 1. METHODS OF MASS ANALYSIS

L,1. Introduction. The development of mass spectroscopy has paralleled the growth of atomic physics from the early days of discovery in this field. J. J. Thomson with his parabola method of sorting out the components in an ion beam clearly illustrated the nature of "canal rays" and provided evidence for the isotopic nature of some of the stable elements. His published work shows admirably his prophetic vision of the future importance of this new tool to chemistry. This importance was recognized by others who followed soon in active participation in the growth of mass spectroscopy and who made contributions which shaped the course of early growth. Aston and Dempster were particularly active in these early developments. Down through the years to the beginning of World War II activities centered in a surprisingly few "schools" where the emphasis was dominated by the interests of a few key figures. This history has been told in the literature [*1*; *2*; *3*, p. 167; *4*]. Until 1940 only research of interest in basic chemistry gave fulfillment to Thomson's prophecies. These concerned on the one hand the elucidation of the isotopic nature of the elements with detailed information on their relative abundances and accurate masses, and on the other hand the study of the ionization and dissociation of molecules by electron impact. During this period, isolated instances occurred in which an available mass spectrometer was applied to a problem of chemical analysis; these instances were rare and only incidental to the justification of the existence of the mass spectrometer. No attempt was made to develop the mass spectrometer for precise routine analyses until about 1940. The time was then ripe for this development in many ways: sufficient information on ionization and dissociation processes had been accumulated to indicate clearly the soundness of the general principles; in designing instruments for the study of ionization processes, scientists had concomitantly devised the key principles that are requisite for an instrument for analytic work; and finally, the technological advances in electronics and vacuum techniques made possible the effective use of the knowledge that had been acquired from many years of basic research. The wartime need for this analytic tool provided the urgency for the promotion of the rapid development and acceptance of the mass spectrometric method for analytic work in laboratory and industry. Mass spectroscopy is now so widely used by chemists in research and analysis that there are at present many more instruments being used by chemists than by physicists and it is recognized as a most powerful and effective method of attacking many chemical problems. In combustion research the mass spectrometer plays an important role both as an analytic tool for gas and hydrocarbon analysis, and as a means of directly probing the intricacies of combustion processes by the study of combustion products and of reaction intermediates.

L,2. Types of Analyzers of Current Interest to Chemists.

Following Thomson's pioneering work, Aston and Dempster devised instruments that have served as models of the two types used for almost all of the work in mass spectroscopy to the present time. The Dempster type instrument will be described in some detail because most of the research and analytic work in mass spectroscopy of interest in combustion studies has been performed with instruments of this general class. Reference should be made to the description by Bleakney [*5*] of the combinations of electric and magnetic fields that will permit a mass analysis.

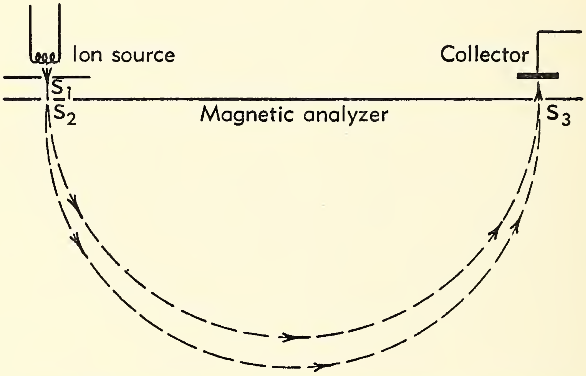

Fig. L,2a. Mass spectrometer of the Dempster type.

In Fig. L,2a the ion source is shown as a filament, but any source may be used which will create ions having a narrow range of kinetic energy. Most commonly, a gas or vapor is admitted to the source and is ionized by an electron beam. The ions are accelerated by a potential difference between s_1 and s_2 passing through s_2 into the magnetic field perpendicular to the plane of the figure. The radius of curvature r (in centimeters) of a singly charged ion of mass M (in atomic mass units) in the magnetic analyzer is given by the relation

$$r = \frac{144\sqrt{Mv}}{B}$$

where B is the strength of the magnetic field in gausses and v is the voltage difference through which these ions have been accelerated before entering the analyzer. For a selected value of the magnetic field, ions of a particular value of mass-to-charge ratio will have the proper radius of curvature to pass through the exit slit s_3 to the detector after a deflection angle of 180°; other ions will have a different radius of curvature in the magnetic field and cannot reach the collector without a suitable adjustment of either the accelerating voltage between s_1 and s_2 or the magnetic field. The ions passing through s_2 will have an appreciable angle of divergence and the deflection angle of 180° is chosen because these divergent ions will be approximately refocused after traversing a semicircle. The focusing is not perfect and the image at s_3 is broadened by the amount $\alpha^2 r$ (neglecting terms of higher order) where α is the half angle of divergence of the ion beam as it enters the magnetic analyzer at s_2.

The ion source in Fig. L,2a is shown as a filament for simplicity. Sources of this type have an essential role in mass spectroscopy, but the gaseous source is the type that has the greatest importance in combustion studies. The gas or vapor passes through the ion source at a low pressure and some of the molecules are ionized by electrons emitted from a hot filament. A complete mass spectrometer suitable for research and analysis involves a rather complex system of electronic circuits and controls; the vacuum and gas handling systems must be excellent, the electrode voltages and the magnetic field must be very carefully regulated by electronic circuits, the ion beam leaving the source must be unvarying, and the current of less than 10^{-10} amperes which reaches the ion collector must be linearly amplified and accurately recorded.

Nier [*6*] first introduced into analytic mass spectroscopy the magnetic deflection of less than 180°. Barber [*7*] and Stephens [*8*] had discovered this generalization of the 180° focusing condition and demonstrated that the image width was the same as for 180°. The method of focusing with the sector-shaped magnetic field was used first in precision mass spectroscopy with direct photographic detection by Bainbridge and Jordan [*9*] before Nier adapted it to the mass spectrometer employing electrical detection of the ions. On past performance there appears to be no particular advantage between the sectored field instrument and the original Dempster mass spectrometer. Both types are widely used for analytic work and detailed descriptions are available in the literature. (See, for example, Nier [*10*] and Washburn and coworkers [*11*].)

Aston first used the term mass spectroscopy and for many years—until Bainbridge entered this field—was the only person applying the technique to the accurate measurement of isotopic masses. He employed a two-stage combination of an electrostatic deflecting field followed by a magnetic field in order to obtain high resolution with an ion source emitting ions having a heterogeneous distribution in energy. Major improvements in Aston's original idea did not appear until the 1930's; since then, many papers have described systems involving improvements in the ion optics of mass spectrographs permitting the construction of instruments which produce a sharper and more intense image of the source slit. The large amount of work that appeared in the years following World War II shows that this continued to be a fertile field. These investigations have aimed to increase the intensity and resolving power by attaining two-directional focusing and by eliminating second order aberrations, i.e. the defects in focusing due to terms proportional to α^2 previously mentioned.

Until very recently the resolution required for analytic mass spectroscopy could be attained with a magnetic analyzer only if the ion source was carefully designed to inject into the analyzer a narrow energy band. The resolution had only to be sufficient to measure the ion current corresponding to types of ions differing in mass by only one part in several hundred. However, the ion optical principles developed primarily for the sequential arrangement of electric and magnetic fields are now taking on importance for mass spectrometry because of the trend toward very high resolution in the analyses of gases and vapors. One reason for the great interest in this can be ascribed to the success in handling very heavy hydrocarbons in the mass spectrometer. A second reason is that of extending the range of usefulness of the mass spectrometer by taking advantage of the "fine structure" at each nominal mass number. A notorious example of the difficulties encountered when two substances have their dominant peaks at the same mass number is that of CO and N_2. This overlap is a serious difficulty in the analysis of gas mixtures as well as in isotopic analysis. The $N^{14}N^{15}/N_2^{14}$ ratio is affected by the presence of CO, which is difficult to eliminate entirely from the background in the usual mass spectrometer tube. However, the mass of CO in atomic mass units is 28.004 and that of N_2 is 28.015; a mass spectrometer having a resolving power of one part in 2600 would completely separate the CO and N_2 ions. Overlapping spectra frequently mean that a suitable analysis can be made only by using other methods, usually chemistry, to assist the mass spectrometer. The recent researches aimed at the improvement of the resolving power and sensitivity of the mass spectrometer and the availability of more sensitive detectors will surely result in instruments that can exploit the small differences in masses of compounds having the same mass number. Nier and associates [*12*] have recently made an important step in this direction in their instrument designed for precision mass measurement using electric recording of the ion current. Fig. L,2b shows the multiplet at mass 28 obtained on this instrument. The ethylene, nitrogen, and carbon monoxide peaks which are not separated on the usual analytic instrument are here seen as three distinct peaks. For the task of analysis, there remains the challenging problem of extending the range of intensity of ion current that can be handled successfully at this high resolution and, if possible, simplifying the equipment required.

The latest theoretical and experimental developments in ion optics of interest to mass spectroscopists were described at a symposium at the National Bureau of Standards. For information on this and on results of other recent research by physicists in the field of mass spectroscopy, reference should be made to the published proceedings of this conference [*13*].

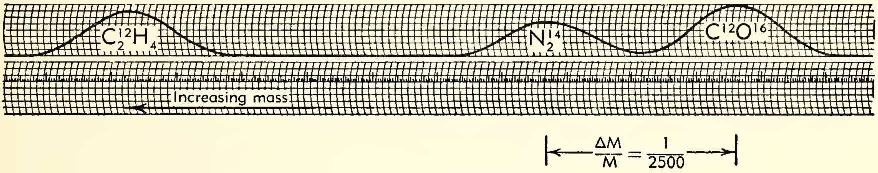

Fig. L,2b. Multiplet at mass 28 obtained by Nier and coworkers.

Even a brief survey of the present status of mass analyzers must take cognizance of the recent work on time-of-flight instruments. These fall naturally into two classes: those without a magnetic field (the "nonmagnetic" mass spectrometer) and those which are based on the cyclotron resonance of ions in a uniform magnetic field. The nonmagnetic instrument of Bennett [*14*] and his associates has attained a resolution of about 1 to 20 and has been applied to problems requiring only low resolution. More recently Glenn [*15*] has reported outstanding performance with his nonmagnetic instrument. This device can separate ions differing by one mass unit even for the heaviest elements and an unusually large portion of the ions created in the ion source reach the final collector. Glenn has applied his apparatus to the separation of isotopes for research studies, but other applications will doubtless be made of this important development.

The time-of-flight devices utilizing cyclotron resonance have already attained high resolution and will certainly make important contributions in the accurate measurements of the masses of the isotopes. Cyclotron resonance may be most promising for chemical analysis in the high resolution range. The general principle of the schemes utilizing the theory of cyclotron resonance is illustrated in Fig. L,2c. This particular method was introduced by Goudsmit [*16*]. A pulse of ions is injected into a uniform magnetic field and allowed to "coast" in a helical path, as shown. The time to travel one complete turn of 360° depends only on the mass-to-charge ratio of the ion and the magnitude of the uniform magnetic field. The initial velocity and direction of the ions do not affect this time. For a given pulse length Δt, the resolution is increased by increasing the flight time of the ions from source to receiver and this is most effectively done by allowing the ions to take a large number of complete cycles between source and receiver. From the cyclotron condition the time-of-flight for singly charged ions of mass M_0 (in atomic mass units) to travel N complete cycles in a magnetic field B is given by

$$t = 651 \frac{NM_0}{B} \text{ microseconds}$$

Other methods, utilizing the cyclotron condition, time the flight with a continuous sine wave rather than by pulsing techniques. The extremely high resolution potentially possible has thus far been limited to approximately 1 in 10,000 and the limitation has generally been attributed to the presence in the analyzer of unwanted weak electric fields. Varying degrees of success have been achieved in several laboratories with the inverted cyclotron [*17*], the mass synchrometer [*18*], the omegatron, and by timing in crossed fields [*19*].

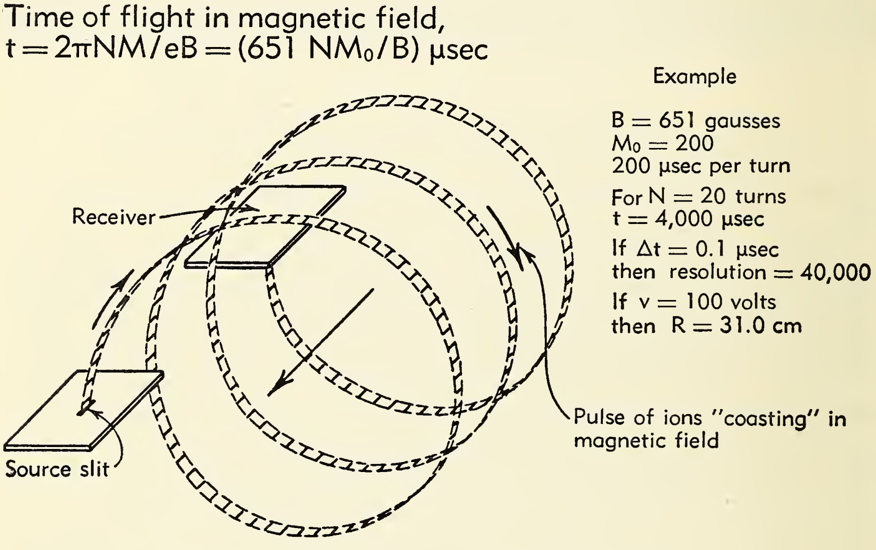

Fig. L,2c. Method of timing the flight of the ions using the cyclotron frequency condition.

L,3. The Production and Detection of Ions. In the sources used for the early work on electron impact, the electron beam was poorly controlled and the ions entered the analyzer with a rather wide distribution of energy. The resulting mass spectra were not very reproducible and the resolution was limited severely by the spread of energy. An important refinement was the introduction by Bleakney [*20*] of the source in which the electron beam is confined to a narrow region by a uniform magnetic field and the ions are drawn out of the ionization region by a weak electric field transverse to the electron beam. Greatly improved data on the primary processes of ion formation by electron impact in gases and vapors could now be obtained. Other sources have been developed for special purposes, but they will not be mentioned because they were not used for any of the work to be described here.

The expanding application of mass spectroscopy has promoted the development of amplifying and recording systems that have increased the speed and accuracy with which very weak ion currents can be measured. These and other advances in electronics cannot even be summarized at this point, and must be left to the references [*21*]. Beryllium-copper and silver-magnesium multipliers have been used thus far in only a few mass spectroscopy laboratories; in these, many experiments have been possible only because of the ability to measure much weaker ion currents than heretofore possible.

CHAPTER 2. APPLICATION TO CHEMICAL ANALYSIS

L,4. Ionization and Dissociation Processes. The application of the mass spectrometric method to chemical analysis is founded on the studies of ionization and dissociation by electron impact that were started about the time of World War I. For the next twenty years these studies were usually concerned with measurement of the minimum energy of the colliding electrons at which the various ions would first appear (appearance potentials) and an interpretation of the measured results in relation to known thermochemical and spectroscopic data. The relative intensities of the ions formed by primary electron impact in the pure substances were of secondary interest. This emphasis is evident in Smyth's review [*2*] of 1931. The interest in the mass spectra of pure compounds, now sometimes called cracking patterns, began to be stressed only after 1940 when the power of the mass spectrometer as an analytic tool had been demonstrated.

The mass spectrometer had its first major success in analytic chemistry when applied to hydrocarbon mixtures. The rapid advances in technique are indicated by the history of the study of methane. In 1928, Hogness and Kvalnes [*22*] were able to find only two primary products of ionization in methane, namely CH_4^+ and CH_3^+. With the improved instruments available eight years later [*23*] the cracking pattern of methane was identified as we now know it (CH_4^+, CH_3^+, CH_2^+, CH^+, C^+, H^+ and some less abundant ions). In a few more years it was demonstrated that instruments could be built that produced mass spectra of sufficient stability and reproducibility that complex mixtures of hydrocarbons could be analyzed.

The mass spectrometer has shown itself to be a powerful method for studying the energetics of various dissociative processes [*24*]. For the simpler molecules the self-consistent interpretation of the appearance potentials corroborates other work and in many instances provides new data on ionization potentials of molecules and free radicals, electron affinities, dissociation energies, and other thermochemical data. In this brief survey this subject cannot be treated adequately. Fortunately, two papers, one by Hagstrum [*25*] and the other by Stevenson [*26*], have recently appeared which provide critical discussions of the current status and can serve as a reference point.

Hagstrum presents a detailed account of the work on CO, N_2, NO, and O_2 and includes much new data that he has obtained. His new data generally confirm earlier mass spectrometric measurements and include a direct measurement of the kinetic energy of the ionic fragment. This eliminates one of the points that has been questioned regarding the interpretation of appearance potentials. The method of electron impact gives no information on the excitation or kinetic energy of the neutral fragment (or fragments in the case of multiple dissociation of polyatomic molecules) and usually this information is not known for an ionic fragment. The internal consistency of the interpreted data has shown that generally for the simpler molecules the ion will first appear at the minimum value of the electron energy corresponding to a negligible amount of excitational or kinetic energy. An example of the way the mass spectroscopic results can provide some illumination for controversial points in thermochemistry is illustrated by the dissociation energy of carbon monoxide $D(\mathrm{CO})$ and the heat of sublimation of carbon. Hagstrum finds that one cannot consider any value but $D(\mathrm{CO}) = 9.6$ ev "without doing considerable violence to a set of data for the molecules CO, N_2, NO, O_2, and H_2 which is not only internally consistent but agrees within limit of experimental error with spectroscopic values wherever they are available." A consistent interpretation of electron impact data is possible only with a value $L(\mathrm{C}) = 136$ kilocalories per mole for the heat of sublimation of carbon. Based on spectroscopic measurements of CO, the heat of sublimation of carbon must have one of the values 125, 136, or 170 kilocalories per mole [*27*]. Vapor pressure measurements [*28,29*] have supported the high value except for one very recent experiment [*30*] in which a preliminary result of 141 kilocalories is reported. At the present time universal agreement on the value of this important constant has not been reached.

The information on the dissociation energy of methane $D(\mathrm{CH_3{-}H})$ obtained by electron impact will serve to illustrate the study of polyatomic molecules. Table L,4 is a summary by Stevenson and shows the

Table L,4. Various determinations of $D(CH_3—H)$.

Method	*Process*	$D(CH_3—H)$, *ev*
Direct electron impact	(a) $CH_3 \rightarrow CH_3^+ + \overline{E}$ with	
	(b) $CH_4 \rightarrow CH_3^+ + H + \overline{E}$	$4.4_4 \pm 0.2$
	(c) $CH_3OH \rightarrow CH_3^+ + OH + \overline{E}$	$4.4_8 \pm 0.4$
Indirect electron impact	(d) $C_2H_6 \rightarrow C_2H_5^+ + H + \overline{E}$ with $C_3H_8 \rightarrow C_2H_5^+ + CH_3 + \overline{E}$	$4.3_8 \pm 0.2$
	(e) $C_3H_8 \rightarrow C_3H_7^+ + H + \overline{E}$ with iso $C_4H_{10} \rightarrow C_3H_7^+ + CH_3 + \overline{E}$	$4.3_4 \pm 0.2$
	(f) $C_3H_6 \rightarrow C_3H_5^+ + H + \overline{E}$ with iso $C_4H_8 \rightarrow C_3H_5^+ + CH_3 + \overline{E}$	$4.4_8 \pm 0.2$
	(g) n-$C_3H_7Cl \rightarrow C_3H_7^+ + Cl + \overline{E}$ with n-$C_4H_{10} \rightarrow C_3H_7^+ + CH_3 + \overline{E}$	$4.4_2 \pm 0.2$
	(h) $CH_3OH \rightarrow CH_2OH^+ + H + \overline{E}$ with $C_2H_5OH \rightarrow CH_2OH^+ + CH_3 + \overline{E}$	$4.4_2 \pm 0.2$
Electron impact average		4.42 ± 0.04
Photochemical	(i) $CH_4 + Br \rightarrow CH_3 + HBr$ $HBr \rightarrow H + Br$	4.43 ± 0.05
Pyrolysis	(j) $CH_3I \rightarrow CH_3 + I$ $HI \rightarrow H + I$	4.45 ± ?

(a) Hipple, J. A., and Stevenson, D. P. *Phys. Rev. 63,* 121 (1943).

(b) Smith, L. G. *Phys. Rev. 51,* 263 (1937).

(c) Cummings, C. S., and Bleakney, W. J. *Phys. Rev. 58,* 787 (1940).

(d) Stevenson, D. P. *J. Chem. Phys.* 10, 291 (1942).

(g) Stevenson, D. P., and Hipple, J. A. *J. Amer. Chem. Soc. 64,* 2766 (1942).

(h) See (c).

(i) Kistiakowsky, G. B., et al. *J. Chem. Phys. 10,* 305 and 653 (1942); *J. Chem. Phys. 11,* 6 (1943).

(j) Polanyi, M., et al. *Nature 146,* 129 and 685 (1940); *147,* 542 (1941); also *Trans. Faraday Soc. 37,* 377 and 648 (1941); *39,* 19 (1943).

internal consistency that establishes confidence in the interpretation. In this table the direct electron impact method for the determination of $D(CH_3—H)$ involves measurements on the CH_3 ion directly. Thus $D(CH_3—H)$ can be calculated as the difference between the ionization potential of the CH_3 ion formed directly from the free methyl radical and the appearance potential of this ion when formed from methane. The latter measurement involves a rupture of the C—H bond in methane plus possible additional factors such as excitational and kinetic energies of the products and an activation energy for the process $H + CH_3^+ \rightarrow CH_4^+$. The experimental observation that these factors are small is illustrated for the various direct and indirect determinations of $D(CH_3—H)$ listed in the table. The indirect electron impact determinations require the use of thermochemical data to supplement the electron impact measurements. For example, referring to method (d), $D(CH_3—H)$ is calculated from the appearance potentials of the ethyl ion in the mass spectra of ethane and propane, together with the heats of formation of methane, ethane, and propane and $D(H—H)$, the dissociation energy of hydrogen into hydrogen atoms. The accuracy of the value thus calculated is conditioned by the same factors enumerated during the discussion of the direct method and again are believed to be small on the basis of the consistency of Table L,4. The seven electron impact values for $D(CH_3—H)$ are mutually consistent within experimental error. The table also gives for comparison the values $D(CH_3—H)$ as determined from photochemical reactions and pyrolyses; good agreement with the electron impact results is apparent.

A particularly favorable example has been chosen in the case of the determination of $D(CH_3—H)$. In general, caution must be exercised in inferring information of interest to thermochemistry from measurements of appearance potentials. Confidence in the correctness of these inferences may be established in many cases, but there are clear limitations to the method. Stevenson and Hagstrum discuss these limitations.

In addition to the limitation imposed by the indeterminacy of the "excess" energy, the accuracy of the measurements of ionization and appearance potentials has been restricted to about 0.1 volt by the spread in energy of the electrons emitted from the hot filament. Two recent approaches to this problem give promise of relieving this limitation. They will be described briefly.

Foner, Kossiakoff, and McClure [*31*] have shown that a numerical treatment of the data permits, in their words, the "deboltzmannizing" of the experimental curve, i.e. the effect of the Boltzmann spread in energy of the electrons may be removed and the curve for probability of ionization may be drawn as it would be obtained with a monoenergetic electron beam. The data must be taken with great care because the method requires values of the first and second derivatives of the original curve. Fig. L,4a illustrates the method with a synthetic curve. The method has been shown in practice to improve the accuracy by a factor of approximately 10. Unfortunately it is tedious and rather difficult to use because of the necessity of obtaining the first and second derivatives with good accuracy.

Fox, Hickam, Kjeldaas, and Grove [*32*] use an experimental method for obtaining the true probability curve $P(E)$, which can be understood by reference to Fig. L,4b. In this schematic diagram of a simplified ion source, the electrons leave the filament with the distribution in energy indicated by the dotted curve between the filament and electrode 4. If a retarding voltage of the proper magnitude is applied to electrode 4, only those electrons having velocities greater than a certain minimum value will be able to pass beyond 4 and reach the ionization region 5. The resulting distribution is indicated by the dotted curve inside electrode 5 in the figure. Of course, the electrons may be accelerated to a higher velocity between 4 and 5 after the slower ones have been removed from

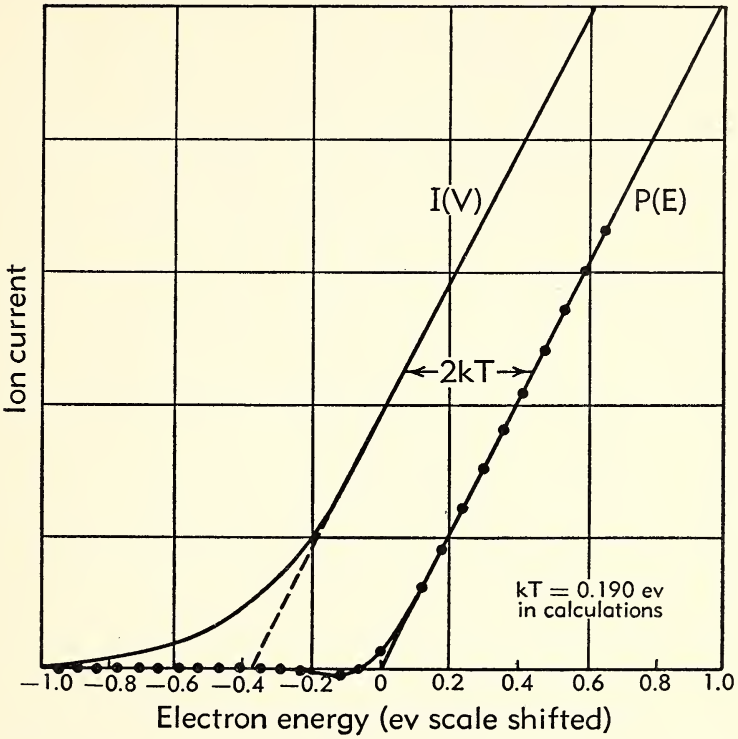

Fig. L,4a. The straight line on the right is an assumed curve for probability of ionization $P(E)$. The spread in velocities of the electrons from a hot filament shifts this curve to the left and produces the long tailing as illustrated by the solid curve $I(V)$. Starting from $I(V)$, the numerical method of Foner, Kossiakoff, and McClure produces the circled points which coincide with $P(E)$ except for slight deviations near vanishing ion current. For this example $kT = 0.190$ ev.

the beam by the retarding voltage between 4 and the filament. The ion current received at the ion collector of the mass spectrometer is measured for one value of V_R and then again after V_R is changed by ΔV_R. The difference between these two measured values of the ion current is the ion current contributed by the electrons in the narrow energy band ΔV_R, indicated by the lower curve in Fig. L,4b. This method has also increased the accuracy of the measurement of appearance potentials by a factor of about 10. One objection to this procedure is that it can correct for only one component of the velocity distribution. The electron gun has an electrode arrangement much more complicated than that shown in the simplified drawing and the authors claim that the combination of their electrode arrangement with the action of the axial magnetic field holding the electrons on their path from the filament to the collector makes ineffective the components of velocity perpendicular to the magnetic field. A difficulty is that the ion current used is rather weak in intensity because it is produced only by electrons in the range ΔV_R. Both this technique and the numerical one described previously are interesting innovations and will produce some improved data on appearance potentials.

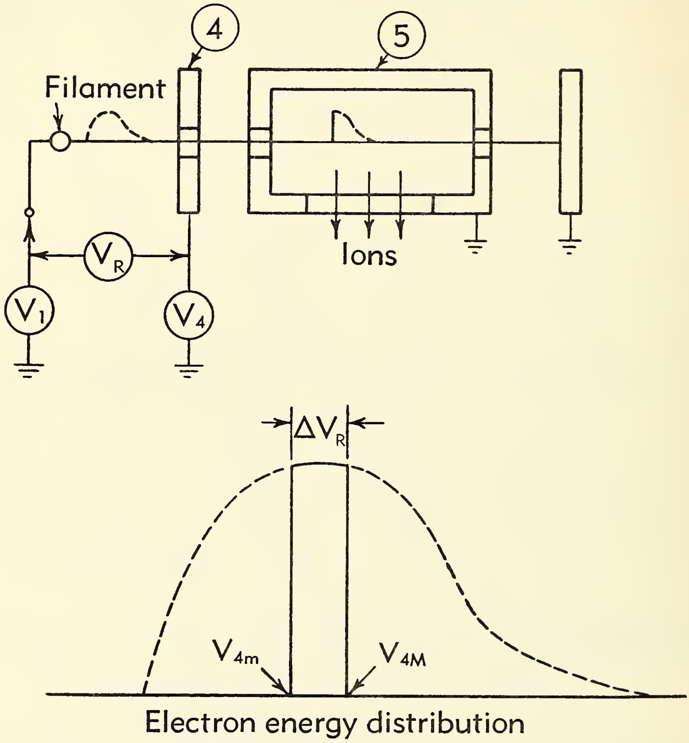

Fig. L,4b. Method of improving measurements of ionization potentials by reducing the effect of the thermal spread of electrons from the hot filament.

L,5. Special Requirements for Analysis. The instruments that were developed purely for research provided a necessary basis for the application to quantitative analysis of gas mixtures. However, some rather stringent additional requirements now appear. In the first place, the ion current corresponding to a particular component of a mixture of gases in a sample must be a linear function of the partial pressure of that component independent of the other components, i.e. the instrument must provide output data that is a linear superposition of the mass spectra of the separate components. The previously mentioned ion source of the Bleakney type provides the best control of the electron beam and is the one that has been used exclusively for the most accurate analytic work. The effects on the electrons and ion beams of surface charging are minimized, although surfaces facing the region in which the ions are formed may still produce discriminating effects unless properly designed and sufficiently clean.

The mass spectra of pure compounds obtained with different instruments can be matched only approximately. Tables of mass spectra [*33*] serve as a valuable qualitative guide, but cannot be used directly for accurate analyses; each instrument must be calibrated with pure substances and periodically recalibrated. Several factors produce this discrimination [*34,35*]. All the ions produced by the electron beam in the ion source do not reach the final detector in any instruments currently available: the relative proportions that are detected depend on the mass and the initial kinetic energy. This discrimination occurs in the ion source and analyzer and some discrimination will probably be present as long as the ions pass through slits of finite width and length. The temperature [*36,37*] can also affect the mass spectrum, although this variable can be brought under control by regulation of the temperature of the ion source. The necessity for individual calibration of each instrument is not too troublesome for a large organization; on the other hand, the acquisition and stocking of a large number of pure calibrating standards for many smaller groups becomes a considerable undertaking and the development of an instrument free of discrimination would be a rewarding achievement. The mass spectra may also be affected by the action of the hot filament on the sample or by the degree of adsorption and elution from the walls of the mass spectrometer tube and gas handling system.

Selective and nonlinear effects may also occur in a poorly designed gas flow system. Satisfactory methods of insuring that the concentration of the components in the ionization region of the mass spectrometer is representative of that in the original sample have been reviewed [*38,39*].

L,6. Recent Developments. The intensive application of the mass spectrometer to chemical analysis in the decade 1942–1952 has brought forth many articles describing technical details of the analytic method and the extension to an ever-widening number of compounds [40]. Only a few developments illustrative of the trend at the end of this decade can be mentioned here.

The early analyses were limited to gases and those substances which had sufficient vapor pressure for the calibration to be made in the same manner as for gases. Even so, some compounds could not be analyzed quantitatively because of adsorption. In recent years these difficulties have been largely surmounted by heating the sample system and mass spectrometer tube, relocating the leak which throttles the gas into the tube and following certain empirically determined procedures in operation [41]. These improvements coupled with the introduction of the micropipet and mercury-covered sintered disk for introducing a known amount of liquid [42] extended the mass spectroscopic method to a wide range of liquids having a very low vapor pressure at room temperature. With the use of molten gallium in place of mercury with the sintered disk, very heavy hydrocarbons such as petroleum waxes have been handled successfully [43]. A portion of the mass spectrum of a petroleum wax in the range of 42 to 45 carbon atoms obtained on the mass spectrometer at Shell Oil Company is illustrated in Fig. L,6a. The success in this higher range of molecular weights has been of practical importance to the petroleum industry and the extension to still higher molecular weights will undoubtedly be pushed forward through the interest of petroleum chemists and those in many other fields.

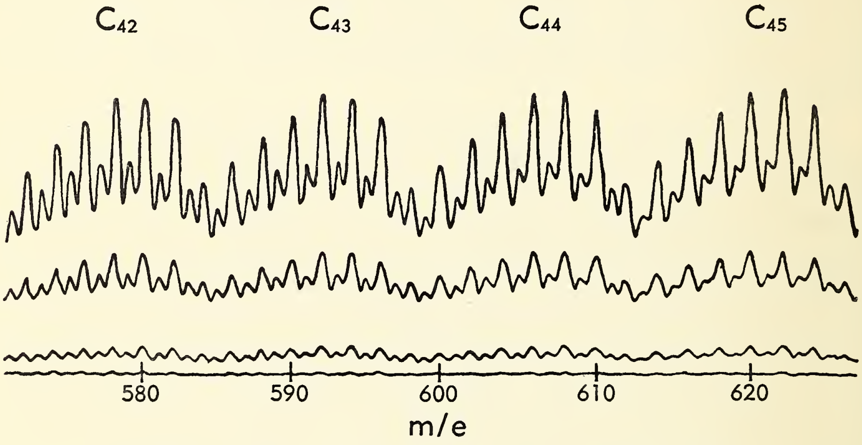

Fig. L,6a. Mass spectrum of a petroleum product of high molecular weight obtained by O'Neal and Wier.

Because the mass spectrum quickly reflects the change in composition of the sample, the mass spectrometer has been recognized as a promising method for monitoring processes in which the composition is continually changing, such as plant streams in a refinery or the exhaust from combustion processes. The equipment and the problem of operating under adverse conditions have been too complex for wide application of the method thus far. In several cases an elaborate installation has justified itself, and the success in these recent cases coupled with simplifications permitted by future technological advances will make this type of monitor more commonplace in the future. Continuous process analysis played an important role during World War II in the separation of U^{235} in the gaseous diffusion plant at Oak Ridge [*44*]. The change in composition of the sample stream was automatically printed on the chart within a minute after it occurred. A more recent application has been to the analysis of respiratory gases. Fig. L,6b shows a schematic diagram of a system of process monitoring in an ethylene recovery plant [*45*]. The essential components of any process monitor are illustrated here. The control valve permits the periodic switching from the stream to a standard used for

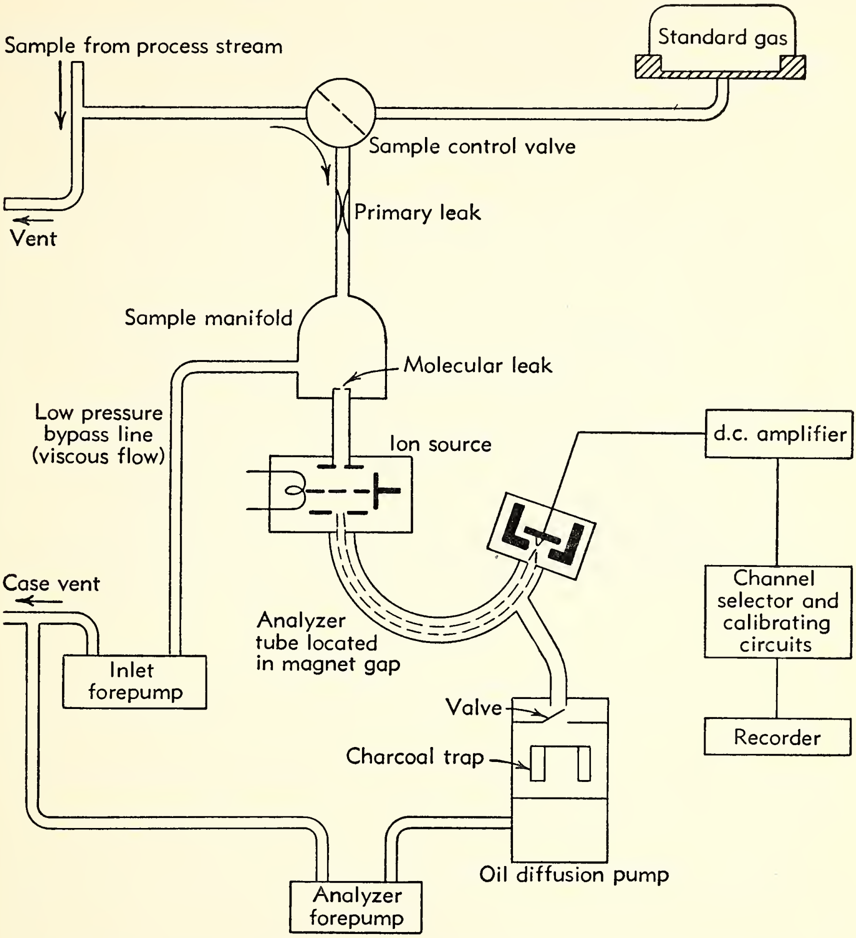

Fig. L,6b. General arrangement of mass spectrometer and sampling lines for process monitoring at Esso Standard Oil Company.

reference. The changing proportions of CH_4, C_2H_4, and C_2H_6 indicated by this monitoring system are shown in Fig. L,6c. The two figures are from the Baton Rouge plant of Esso Standard Oil Company and these workers conclude that "the increased efficiency of plant operation . . . clearly demonstrates the great value of the monitor type mass spectrometer in plant control."

Appreciable progress has been made in the analysis of solids with the mass spectrometer. The isotope dilution method [*46*] has been applied recently [*47*] to the measurement of extremely small amounts of uranium in minerals—as little as one part in 10^{12}. It involves no major change in the ordinary instrument for analyzing gases. The procedure is complicated and requires expert personnel, but it is the only method that can handle such low concentrations.

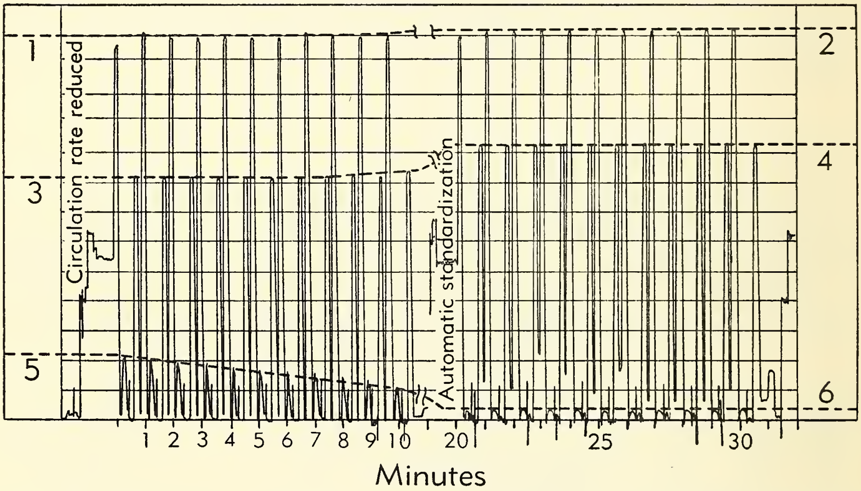

Fig. L,6c. Changing proportions of CH_4 (1–2), C_2H_4 (3–4), and C_2H_6 (5–6) obtained by the system of process monitoring shown in Fig. L,6b.

Dempster [*48*] introduced the high frequency vacuum spark into mass spectroscopy and did some exploratory work which showed it had great promise for the analysis of solid samples. He pointed out its big advantage for analytic work of no blind spots—ions will be produced from any element present in the sample. The method has been adapted to electric recording [*49*] and quantitative analyses of stainless steel samples have been made with good accuracy.

CHAPTER 3. APPLICATIONS TO FLAMES

L,7. Early Studies of Chemical Reactions. The mass spectrometer has had much appeal to chemists for the study of reaction kinetics because of its ability to make continuous measurements of the changing concentration in a reaction chamber. Physicists started work along these lines, as illustrated by the investigations of Hagstrum and Tate [*50*] who studied the thermal activation of the oxygen molecule on a hot platinum filament, investigating with the mass spectrometer the compounds formed by the scavenging effect of the excited oxygen molecule on the walls of the glass vessel. In another experiment they studied the formation of atomic hydrogen on a hot tungsten filament.

Leifer and Urey [*51*] studied the kinetics of the thermal decomposition of dimethyl ether and acetaldehyde. A leak was inserted into the hot reaction chamber and the concentration of the stable intermediates could be measured continuously.

One result of the studies of ionization and dissociation of hydrocarbons was the realization that the mass spectrometer might be used to study unstable reaction intermediates. The first work in this field was that of Fraser and Jewitt [*52*]. Although no mass spectrometer was used in their work and consequently they could make no mass analyses of the ions, the method was the same as that later used to study free radicals in the mass spectrometer. Tetramethyl lead was passed through a hot quartz tube and the dissociation products emerged as a molecular beam. This molecular beam was then subjected to the ionizing influence of a controlled electron beam. From the ions thus created they hoped to detect free methyl radicals emerging from the quartz tube and to determine the ionization potential. The ionization potential of the free methyl radical is lower than that of the appearance potential of the CH_3^+ ion formed directly from the tetramethyl lead without the agency of the hot quartz furnace; if the electron energy is adjusted to a value higher than the ionization potential of the radical but lower than the appearance potential of the radical ion formed from a parent molecule, the presence of the free radical may be uniquely confirmed.

In the same period, Eltenton [*53*] studied the possibility of the application of the mass spectrometer to the detection of short-lived reaction intermediates occurring during low pressure combustion and to the thermal decomposition of hydrocarbons. Eltenton's work was the primary effort in this field, and clearly indicated the feasibility of the method while demonstrating that the technique was a difficult and elaborate one. Eltenton describes three different reaction chambers which he used. One of these is illustrated in Fig. L,7. The reactor was placed closely adjacent to the ionization chamber of a Dempster type mass spectrometer (180° type) having a radius of 3.5 cm. A difficulty with an experiment of this type is that of insuring that the radicals produced by the chemical reaction at the relatively high pressure in the reactor have a practically collision-free path to the ionization chamber. The reactor was separated from the ionization chamber by a thin diaphragm containing a small hole, and by a collimating chamber. Oil diffusion pumps evacuated the ionization and collimating chambers and permitted the pressure in the ionization chamber to be kept at approximately 10^{-3} mm for a pressure of 100 mm in the reactor. In addition to the quartz reactor shown, Eltenton used one with carbon filaments and another with stainless steel lined with gold.

With the electron-accelerating voltage set at 14 volts, Eltenton did detect CH_3^+ ions formed directly from the free radicals and not dissociated by the electron beam from the tetramethyl lead. He showed, for instance, that CH_3 radicals were definitely present in a helium stream containing 0.6 per cent tetramethyl lead at a reaction pressure of 0.4 mm.

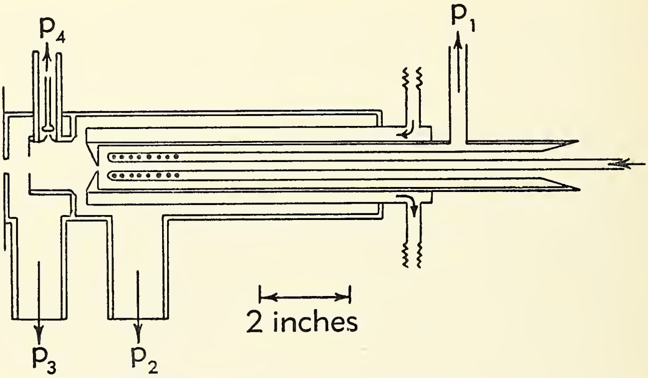

Fig. L,7. Reaction chamber used by Eltenton to study flames.

Eltenton, having demonstrated the workability of the method, subsequently applied it to a survey of the intermediates occurring in the thermal decomposition of various molecules, studying the effect of the pressure and temperature and then making a preliminary survey of the intermediates formed during the combustion of methane, propane, and carbon monoxide at pressures ranging from 30 to 140 mm. The gases were introduced separately and he made tentative identification of CH_3O, CH_2O, CHO, C_2H_2, and CH_3.

L,8. Flame Studies with the Mass Spectrometer at Johns Hopkins Applied Physics Laboratory. At the meeting of the Division of Chemical Physics of the American Physical Society in May, 1952, Foner and Hudson [*54*] of the Johns Hopkins Applied Physics Laboratory described an extension of the Eltenton method for the study of flames with a mass spectrometer. They applied more recently developed electronic techniques, faster pumps, a mass analyzer of the sector field type which allowed greater flexibility in positioning the burner and its associated gadgetry in the vicinity of the ion source, and introduced a method of modulating the beam of the neutral reaction products, discriminating strongly thereby in favor of these rather than the gas in the ion source. The burner which they used is illustrated in Fig. L,8a. The orifice through

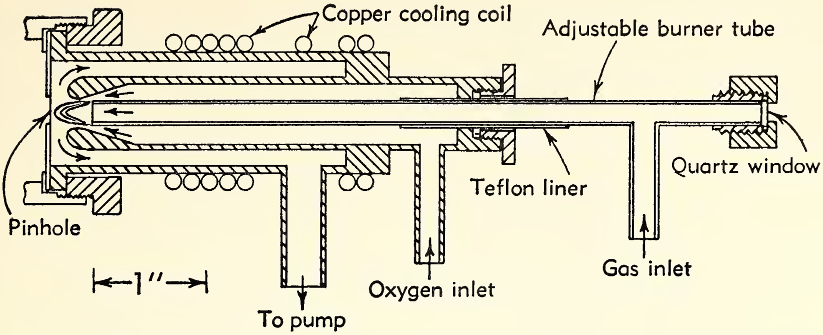

Fig. L,8a. Burner system used with mass spectrometer at Johns Hopkins Applied Physics Laboratory.

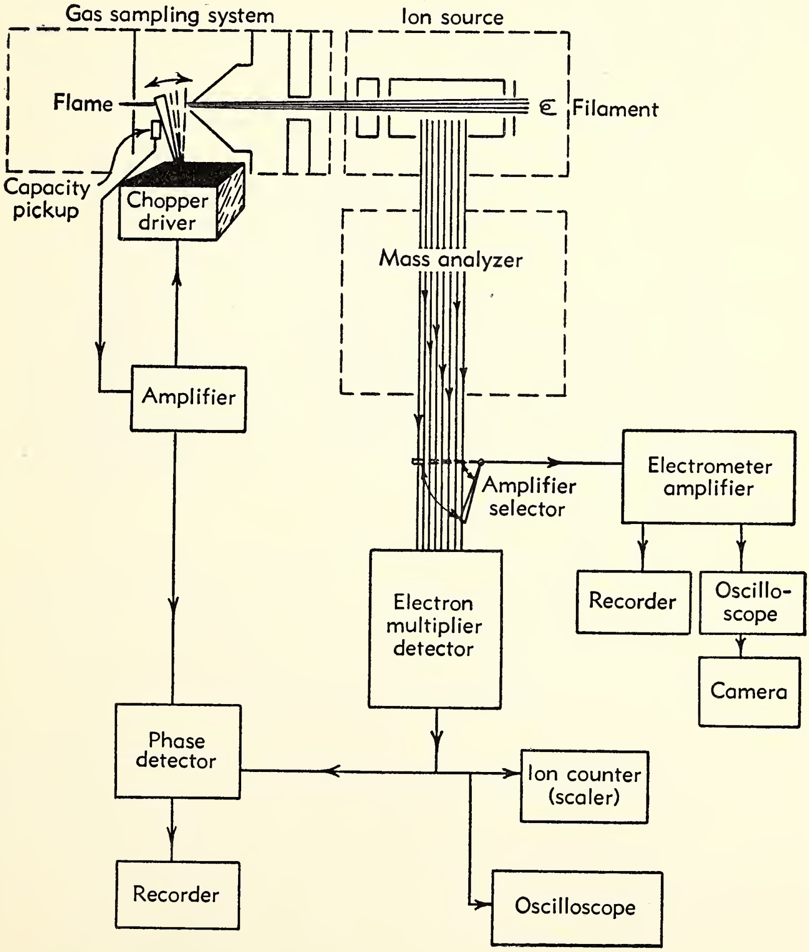

Fig. L,8b. System for analyzing flame products with the mass spectrometer (Johns Hopkins Applied Physics Laboratory).

which the reaction products pass was a pinhole of diameter 0.001 to 0.004 in. in 1-mil thick gold foil. The burner tube was adjustable and could be brought to within 0.050 in. of the gold diaphragm. Fig. L,8b is a block diagram of the main components in this experimental setup. The products emerging from the pinhole pass into a region evacuated by a 50-liter-per-second pump to a hole in an adjustable snout whose distance from the pinhole can be varied. The beam passes next through a chamber evacuated with a 10-liter-per-second pump and onward through a channel to the ion source connected to a pump having a speed of 250 liters per second. Because the molecular beam travels countercurrently to the electron beam, an estimated factor of 10 in intensity is gained. An enormous increase in sensitivity in favor of the molecular beam from the flame over the gas existing in the ion chamber was gained by mechanically

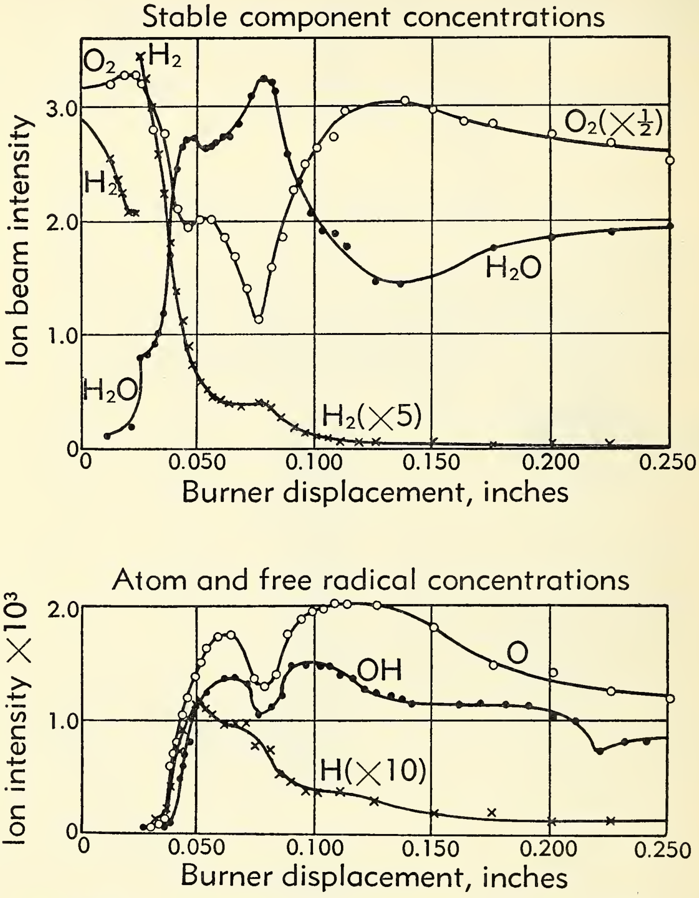

Fig. L,8c. Combustion products from the hydrogen-oxygen flame detected by the mass spectrometer.

interrupting the beam emerging from the pinhole in front of the flame at a frequency of 200 cycles per second and synchronously detecting the ion current measured by the multiplier after passing through the magnetic analyzer. This method of "tagging" the neutral beam from the flame gives an estimated factor of 10,000 favoring the detection of these components rather than gas admitted directly to the ion source of the mass spectrometer. Coupled with the factor of 10 mentioned earlier, the resultant gain is estimated to be of the order of 10^5. Thus it can be seen that this beautiful method practically assures that the analyzed ion current originates from the ionization of the flame products.

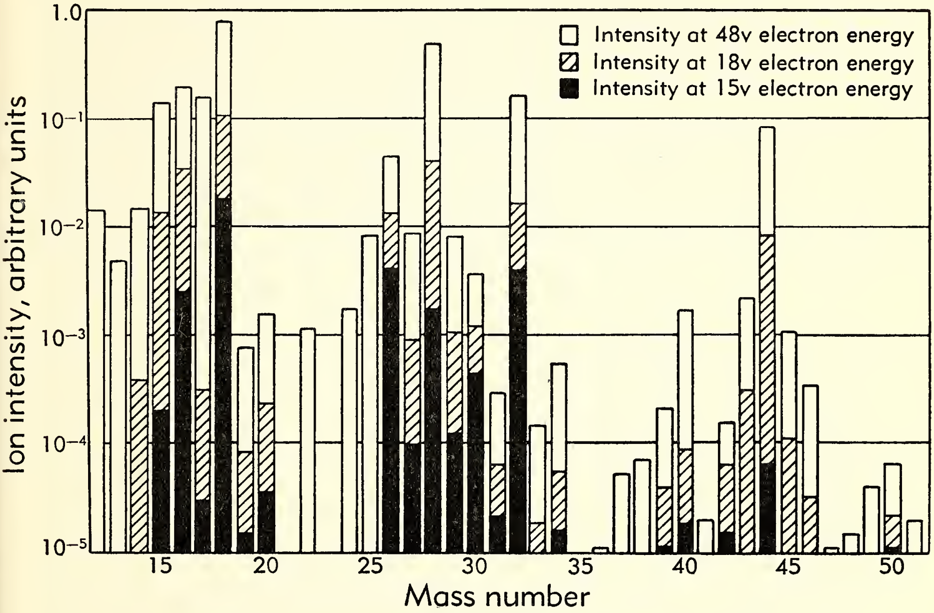

Fig. L,8d. Mass spectrum of the methane-oxygen flame.

Some typical results for the hydrogen-oxygen flame are shown in Fig. L,8c. The operating pressure was 6 cm and the orifice had a diameter of 0.004 in. The upper curve shows the ion beam intensity of the stable components for various burner positions, i.e. the ion current detected at relatively high values of the electron energy. The zero position of the abscissa corresponds to a burner distance of 0.050 in. from the gold diaphragm. One sees here the gradual decrease of the fuel gas and the increase of the water vapor as the burner displacement starts to increase. The lower curve taken at an electron energy of 18 electron volts shows the variation in the concentration of the oxygen and hydrogen atoms and the OH free radicals. The experiments have thus far been confined largely to the hydrogen-oxygen flame because it offered the best hope for possible interpretations. The complexities encountered with other fuels are illustrated in Fig. L,8d which shows the spectrum obtained from the combustion products of the methane-oxygen flame. The free radicals would appear more markedly in the solid lines corresponding to ion current detected at an electron energy of 15 electron volts. Thus the solid portion of mass 15 would be attributed to the CH_3 radical. The solid portion of mass 26 is clear proof of the formation of acetylene in the methane-oxygen flame. Prominent peaks can be clearly attributed to CH_4, H_2O, O_2, CO_2, and C_2H_6. A more detailed study will reveal the presence of other components. The $O^{16}O^{18}$ molecule accounts for the current at mass 34. Under these conditions of burner operation no trace of HO_2 or H_2O_2 was detected.

After the completion of this manuscript an interesting report by Lossing and Tickner [*55*] appeared which describes the measurement of the methyl radical concentration in the stream of a carrier gas by means of a suitably modified mass spectrometer. Rate constants of the decomposition of di-*tert*-butyl peroxide have been measured. For mercury dimethyl the decomposition rate was dependent on the pressure of the carrier gas in the working range of pressure of 5 to 20 mm. In this case an estimate could be made of the collision frequency for recombination of methyl radicals.

L,9. Cited References.

1. Aston, F. W. *Mass Spectra and Isotopes.* Longmans, Green & Co., London, 1942.
2. Smyth, H. D. *Revs. Mod. Phys. 3*, 347 (1931).
3. Inghram, M. G. *Advances in Electronics*, Vol. 1. Academic Press, 1948.
4. Bruche, E. *Electronengerate.* Springer, Berlin, 1941.
5. Bleakney, W. *Am. Phys. Teacher 4*, 12 (1936).
6. Nier, A. O. *Rev. Sci. Instr. 11*, 212 (1940).
7. Barber, M. F. *Proc. Leeds Phil. Lit. Soc. Sci. Sect. 2*, 427 (1933).
8. Stephens, W. E., and Hughes, A. L. *Phys. Rev. 45*, 123, 513 (1934).
9. Bainbridge, K. T., and Jordan, E. B. *Phys. Rev. 50*, 282 (1936).
10. Nier, A. O. *Rev. Sci. Instr. 18*, 398 (1947).
11. Washburn, H. W., Wiley, H. F., and Rock, S. M. *Ind. Eng. Chem. Anal. Ed. 15*, 541 (1943).
12. Nier, A. O., and Roberts, T. R. *Phys. Rev. 81*, 507 (1951).
13. Mass spectroscopy in physics research. *Proceedings of conference held at the Natl. Bur. Standards in Sept. 1951. Natl. Bur. of Standards Circ. 522*, Jan. 23, 1953.
14. Bennett, W. *J. Appl. Phys. 21*, 143 (1950).
15. Glenn, W. E. *Univ. of Calif. Radiation Lab. Rept. 1628*, Jan. 1952.
16. Hays, E. E., Richards, P. I., and Goudsmit, S. A. *Phys. Rev. 82*, 345 (1951).
17. Bloch, F., and Jeffries, C. D. *Phys. Rev. 80*, 305 (1950); Jeffries, C. D. *Phys. Rev. 81*, 1040 (1951).
18. Smith, L. G. *Rev. Sci. Instr. 22*, 115 (1951); *Phys. Rev. 85*, 767 (1952).
19. Sommer, H., Thomas, H. A., and Hipple, J. A. *Phys. Rev. 82*, 697 (1951); Sommer, H., and Hipple, J. A. *Phys. Rev. 83*, 229 (1951).
20. Bleakney, W. *Phys. Rev. 34*, 157 (1929).
21. Hipple, J. A., and Shepherd, M. *Anal. Chem. 21*, 32 (1949).
    Shepherd, M., and Hipple, J. A. *Anal. Chem. 22*, 23 (1950).
    Dibeler, V. H., and Hipple, J. A. *Anal. Chem. 24*, 27 (1952).
22. Hogness, T. R., and Kvalnes, H. M. *Phys. Rev. 32*, 942 (1928).

23. Hipple, J. A., and Bleakney, W. *Phys. Rev. 47*, 802 (1935).
Smith, L. G. *Phys. Rev. 51*, 263 (1937).
24. Wallenstein, M. B., Wahrhaftig, A. L., and Eyring, H. *Atomic Energy Commission unclassified document 1484*, June 15, 1951.
25. Hagstrum, H. D. *Revs. Mod. Phys. 23*, 185 (1951).
26. Stevenson, D. P. *Discussions Faraday Soc. 10*, 35 (1951).
27. Herzberg, G. *Molecular Spectra and Molecular Structure*, Vol. I: *Spectra of Diatomic Molecules*, 2nd ed. Van Nostrand, 1950.
28. Brewer, L., Gilles, P. W., and Jenkins, F. A. *J. Chem. Phys. 16*, 797 (1948).
29. Simpson, O. C., Thorn, R. J., and Winslow, G. H. *Argonne Natl. Lab. Rept. ANL-4264*, 1949.
30. Doehaerd, T., Goldfinger, P., and Waelbroeck, F. *J. Chem. Phys. 20*, 757 (1952).
31. Foner, S. N., Kossiakoff, A., and McClure, F. T. *Phys. Rev. 74*, 1222 (1948).
32. Fox, R. E., Hickam, W. M., Kjeldaas, T., Jr., and Grove, D. J. *Phys. Rev. 84*, 859 (1951). Also [*13*].
33. Tables of mass spectral data. *Am. Petroleum Inst. Project 44*. Carnegie Inst. of Technol. See also many publications of Mohler, F. L., Dibeler, V. H., et al. in [*21*].
34. Coggeshall, N. D. *J. Chem. Phys. 12*, 19 (1944).
35. Berry, C. E. *Phys. Rev. 78*, 597 (1950).
Washburn, H. W., and Berry, C. E. *Phys. Rev. 70*, 559 (1946).
36. Fox, R. E., and Hipple, J. A. *J. Chem. Phys. 15*, 208 (1947).
37. Stevenson, D. P. *J. Chem. Phys. 17*, 101 (1949).
38. Honig, R. E. *J. Appl. Phys. 16*, 646 (1945).
39. Halsted, R. E., and Nier, A. O. *Rev. Sci. Instr. 21*, 1019 (1950).
40. Gifford, A. P., Rock, S. M., and Comaford, D. J. *Anal. Chem. 21*, 1026 (1949).
Langer, A., and Fox, R. E. *Anal. Chem. 21*, 1302 (1949).
Thomas, B. W., and Seyfried, W. D. *Anal. Chem. 21*, 1022 (1949). Also [*21*].
41. Washburn, H. W., Berry, C. E., and Hall, L. G. See [*13*].
42. Taylor, R. C., and Young, W. S. *Ind. Eng. Chem. Anal. Ed. 17*, 811 (1945).
43. O'Neal, M. J., Jr., and Wier, R. P., Jr. *Anal. Chem. 23*, 830 (1951).
44. Nier, A. O., Abbott, T. A., Pickard, J. K., Leland, W. T., Taylor, T. I., Stevens, C. M., Dukey, D. L., and Goertzel, G. *Anal. Chem. 20*, 188 (1948).
45. Starr, C. E., Jr., Johnson, F. B., Purdy, K. M., Charlet, E. M., and Lanneau, K. P. Presented at Twelfth International Congress of Pure and Applied Chemistry, 1951. See also, Robinson, C. F. *Chem. Eng. 58*, No. 12, 136 (1951).
46. Rittenberg, D. *J. Appl. Phys. 13*, 561 (1942).
Nier, A. O. *Preparation and Measurement of Isotopic Tracers*. J. W. Edwards, 1946.
47. Hess, D. C., Brown, H., Inghram, M. G., Patterson, C., and Tilton, G. See [*13*].
48. Dempster, A. J. *Rev. Sci. Instr. 7*, 46 (1936).
49. Gorman, J. G., Jones, E. J., and Hipple, J. A. *Anal. Chem. 23*, 438 (1951).
50. Hagstrum, H. D., and Tate, J. T. *Phys. Rev. 59*, 509 (1941).
51. Leifer, E., and Urey, H. C. *J. Am. Chem. Soc. 64*, 994 (1942).
52. Fraser, R. G. J., and Jewitt, T. N. *Phys. Rev. 50*, 1091 (1936); *Proc. Roy. Soc. London A160*, 563 (1937).
53. Eltenton, G. C. *J. Chem. Phys. 15*, 455 (1947).
54. Foner, S. N., and Hudson, R. L. *J. Chem. Phys. 21*, 1374 (1953).
55. Lossing, F. P., and Tickner, A. W. *J. Chem. Phys. 20*, 907 (1952).

SECTION M

SPECTROSCOPY OF COMBUSTION

G. H. DIEKE

SECTION M

SPECTROSCOPY OF COMBUSTION

G. H. DIEKE

M,1. Introduction. The present section deals with the spectroscopic techniques that are of use in the study of combustion processes. Emphasis is placed throughout more on the methods than on the results. Specific results are given to illustrate the methods but completeness is not claimed. When spectroscopic methods can be applied to the study of reaction kinetics, they are liable to furnish data that cannot be obtained in any other way. The interpretation of these data, however, may be quite difficult and the numerical data themselves subject to corrections that are not always easy to evaluate. Very careful scrutiny of the experimental technique and of the fundamental assumptions is always indicated.

An illustrative example for this is furnished by the spectroscopic methods of temperature determination in flames. This is treated in some detail in Art. 5. If the intensities of a number of lines are measured and the relative transition probabilities are known, the temperature of the flame can be determined by standard methods. A routine application of these methods may, however, give quite wrong results. The mistakes may be due to the neglect of experimental errors. The influence of the continuous background on photographic intensity measurements may have been overlooked. The lines may show strong self-absorption which can falsify the results very markedly. If the resolution of the spectrograph is not sufficient systematic errors can be made, etc. In addition there may be difficulties of another kind if there is no general thermodynamic equilibrium. In such cases it is pointless to attempt to determine the temperature, as one can speak about a temperature only if there is statistical equilibrium for all degrees of freedom. The spectroscopic technique of temperature measurement usually involves only one degree of freedom—for instance, rotation. The intensity distribution may indicate an equilibrium distribution over the rotational degrees of freedom and, therefore, a rotational temperature can be determined. However, this rotational temperature may be quite different from the temperature determined in some other way. Such considerations are particularly important for reaction zones. They show that routine methods which are quite safe in the majority of cases must be examined very carefully before they can be used in the reaction zone. On the other hand the fact that equilibrium does not exist should not discourage any one from spectroscopic studies. On the contrary, the nonequilibrium conditions are the most interesting ones as the particular reaction mechanism is then reflected in the intensity distribution, whereas at equilibrium all traces of it have disappeared.

Quantitative spectroscopic data are obtained either by wavelength or by intensity measurement. The former would be of importance only when hitherto unknown spectrum lines were discovered. This, on the whole, will occur only rarely. Therefore, the bulk of the data useful for reaction studies must be obtained from intensity measurements. For this reason particular attention is given in this section to the modern methods of intensity measurement. The general spectroscopic techniques may be found in textbooks on this subject [*1*,*2*,*3*].

M,2. Instrumentation. A device, usually called a spectrograph,[1] which produces the spectrum and means by which the spectrum can be recorded and measured, is needed for any kind of spectroscopic work. For this purpose the photographic plate (or film), photoelectric devices, thermocouples, bolometers, and similar devices are available. In this article some of the most important features of instrumentation are discussed, with particular emphasis on their usefulness for spectroscopic flame studies.

The dispersive element in most spectrographs is either a prism or a grating. For some special purposes interferometers may be useful. For instance, when the line shape is to be studied or temperatures determined from self-reversal of lines, the high resolving power of an interferometer may be needed. This may also be required for very narrow absorption lines (see Art. 4). The interferometer is an instrument that is very wasteful of light and requires considerably higher experimental skill in its use than an ordinary prism or grating spectrograph. Therefore, it is of relatively little importance for flame spectroscopy except in such special problems as those just mentioned.

FILTER SPECTROSCOPY. On the other extreme is the possibility of flame spectroscopy without a spectrograph through isolating by filters the part of interest in the spectrum. This requires a preliminary study of the spectrum with a spectrograph to make sure of the structure of the spectrum and the particular line or band that is to be isolated. The presence of the line and its intensity, as functions of flame conditions, may then be studied quantitatively. The filter isolation method has the advantage of being cheap and simple, but is limited by the fact that it can be used only when the problem has been reduced to the study of a well-defined line or band. The presence of metallic impurities can be measured quantitatively with a filter. The yellow sodium lines, for instance, can be isolated with relative ease. Temperature measurements based on the intensity distribution in the continuous spectrum may be made by isolating a small interval in the short and long wavelength part of the spectrum and by measuring the relative intensity of the two sections. This is analogous to the method, long used in astronomy, of determining the color index of stars. This color index method is even more primitive than isolation by filters, and is now largely obsolete.

---

[1] Often a distinction is made between *spectroscope*, an instrument for observing the spectrum visually; *spectrograph*, an instrument for photographing the spectrum; and *spectrometer*, an instrument for making measurements on the spectrum. No such distinction is made here.

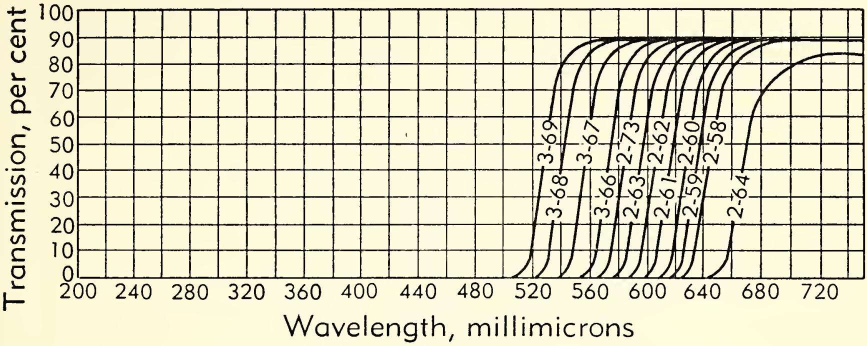

Fig. M,2a. Violet cutoff filters (Corning).

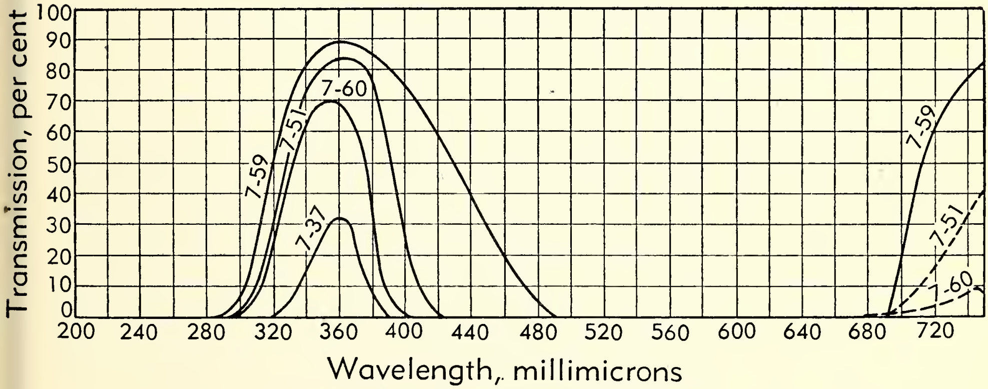

Fig. M,2b. Filter with cutoff on both sides of transmission band (Corning).

The possibilities of filter spectroscopy have increased considerably in recent years because of the availability of filters with very narrow band pass. The useful filters may be grouped into two classes:

Absorption filters. These usually are made of glass or gelatine with coloring matter added. Filters that have a cutoff at a certain wavelength so that everything below this wavelength is absorbed and everything above it is transmitted are very common. The cutoff region can be placed practically anywhere in the spectrum (see Fig. M,2a). Another type of absorption filter,[2] generally more useful for our purpose, has a broad transmission band (see Fig. M,2b).

Interference filters. Narrower bands can be obtained with interference filters, of which a great variety of different types have been developed in recent years. The simplest of these is the Fabry-Perot type of transmission filter [*4*,*5*], which consists of two metal layers separated by a thin dielectric layer—all mounted on a glass plate. Fig. M,2c shows the transmission of such filters as a function of wavelength. There is a transmission band at a frequency ν_0 and all its multiples. By selecting the proper material and thickness of the layers, ν_0 can be chosen to have any desired value in the visible and the near infrared and ultraviolet. The transmission at the maximum is of the order of magnitude of 40 per cent, and the half width, that is the width of the transmission curve at half the maximum transmission, is about 100A. These filters are available commercially and are relatively inexpensive. Fig. M,2d shows the empirical transmission curve of such a commercial filter. The transmission at the multiples of ν_0 can easily be cut out by an absorption filter of the first type. Filters with a smaller band width (about 60A) can be obtained by increasing the number of layers.

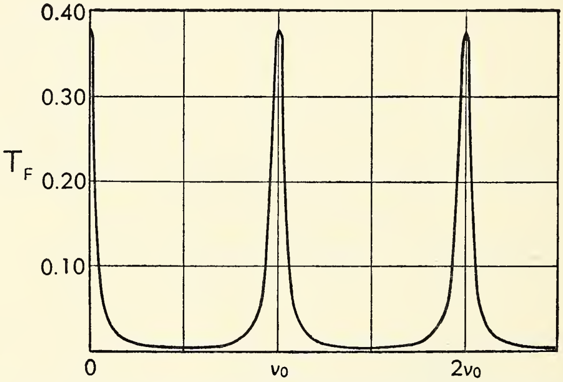

Fig. M,2c. Transmission curve of an interference filter (after Hadley and Dennison).

Much narrower band widths can be obtained with polarization interference filters [*6*]. The so-called Turner frustrated total reflection filter [*7*,*8*,*9*] (a diagram of which is given in Fig. M,2e) when combined with birefringent materials [*10*] is said to be capable of having a band width of 10A and a maximum transmission of perhaps 70 to 80 per cent.

A further development of these filters [*6*,*10*] makes it possible to obtain a band width of only 1A. Moreover, the center of transmission can be shifted over a range of about 3A by combining it with a device of variable and controllable birefringence such as the Kerr cell. Filters of the last-mentioned type can very well replace a spectrograph of moderately high resolving power for the isolation of individual spectrum lines. The complexity and price of such filters are quite high so that in general they would have hardly any advantages over a conventional spectrograph-type monochromator.

---

[2] Details on available absorption filters are contained in:
Glass Color Filters. Corning Glass Works, Optical Sales Dept., Corning, N.Y.
Wratten Light Filters. Eastman Kodak Co., Rochester, N.Y.

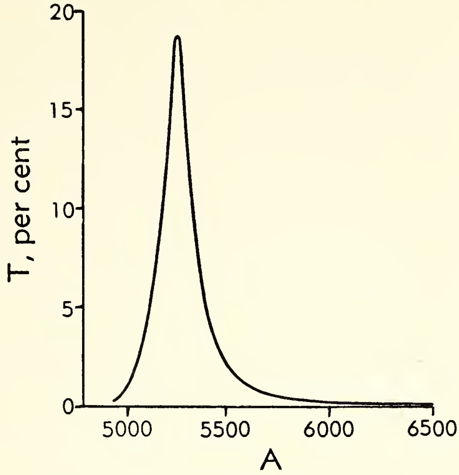

Fig. M,2d. Empirical transmission curve of an interference filter with center at 5275A. Maximum transmission 18.8 per cent, half width 82A.

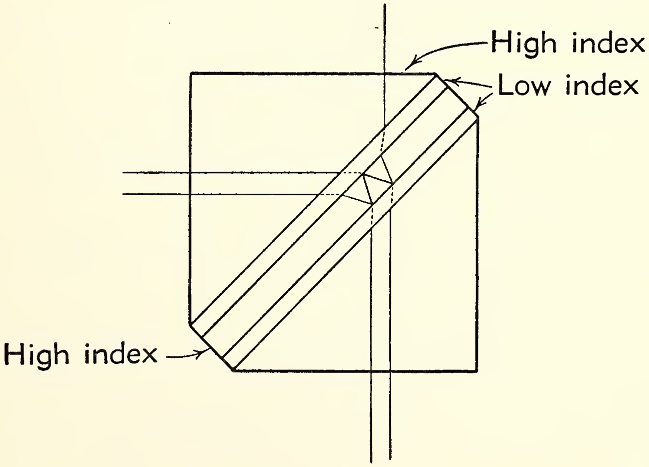

Fig. M,2e. Arrangements of the elements and path of the rays in the Turner frustrated total reflection filter (Billings).

When such high resolution is not required the simpler types of interference filters may be used; they should be given serious consideration for the isolation of narrow spectrum regions. The techniques of making interference filters are still relatively new, and new developments may be expected in the coming years.

Spectrographs. For any fundamental research in flame spectroscopy and for most applications, a grating or prism spectrograph will be needed. There are now available a great variety of good commercial spectrographs, so that only in very rare cases will anyone find it necessary to design and build his own instrument. On the other hand, the proper choice of a spectrograph is very important for success in any particular task. Unfortunately there is no one instrument which can be considered best for every purpose. This is not due to any shortcoming in design but to the fundamental limitations in any spectrograph or, for that matter, any optical instrument. The principles of design and performance of spectrographs will be found in any book on spectroscopy or physical optics [*1*,*2*,*3*]. For our purpose it will be useful to look at the extreme cases.

If high resolution is required, such as is necessary for the resolution of the rotational structure of the more complicated molecular bands, a large grating spectrograph with a focal length of 21 feet or more and a 6- or 8-inch grating, preferably with 30,000 lines per inch, may be required. Such instruments have a reciprocal dispersion[3] of about 1.2A/mm or better in the first order. Because of their bulk, they cannot be easily moved and must be specially designed and built.

While a large spectrograph will be able to resolve all the details, it is necessarily very wasteful of light and requires very bright flames if the exposure times are not to become excessive. Moreover, the spectrum is very much spread out and many plates are required to cover it completely, which may be a big handicap if a general survey of the spectrum is required. Furthermore, diffuse bands have the tendency to disappear under high dispersion.

On the other hand, high dispersion is absolutely essential when the lines are close together, particularly when weak lines are to be found among groups of much stronger lines. It should be stated that with the large spectrographs, for instance, a 21-foot, 30,000-line-per-inch grating in the second order which has a dispersion of about 0.6A/mm, the actual resolution with ordinary flames (where the gases are near atmospheric pressure at fairly high temperatures), is limited by the actual width of the lines and not the performance of the spectrograph. Therefore, a spectrograph of even higher resolution would offer no advantages.

---

[3] Strictly speaking, the dispersion of a spectrograph has, of course, nothing to do with its resolving power. Most spectrographs are designed, however, so that the resolving power is limited by the resolution of the photographic emulsion rather than the resolving power of the prism or grating. This means that the dispersion actually determines the resolution of the instrument. For this reason we may take the dispersion of an instrument as an indication of its actual resolving power. However, it must be understood that this may not be true for some instruments. For the spectrographs usually encountered no large deviations from this rule occur.

At the other extreme is a prism spectrograph of short focal length and very high relative opening (e.g. $f/2$ or better). Here the length of the whole visible and near ultraviolet may be only a few centimeters or less; resolution is sacrificed for speed. For weak flames this is essential, as it may be better to get only a rough idea of the spectrum than nothing at all.

A large grating spectrograph will have a relative speed of about $f/40$. A small $f/2$ spectrograph is, therefore, 400 times faster for sharp lines. For diffuse bands (and the continuous spectrum) there is another factor in favor of the smaller instrument equal to the ratio of the linear dispersions, so that the latter will be many thousand times faster than the large one. In judging the relative exposure times the failure of the photographic reciprocity law must also be taken into account, which fact works against the larger instruments. A spectrum that could be photographed satisfactorily in 10 seconds with the smaller instrument would not register on the larger instrument with exposures of 24 hours or more. This shows that the larger instruments would be completely useless for such weak flames.

The average worker in flame spectroscopy will choose an instrument between the two extremes. If he is more interested in detail of structure and works with strong flames, one of the larger commercial grating instruments (dispersion about 5A/mm in the first order) will be found most useful. If his interest is chiefly the exploration of weak flames or if he is not interested in detail, a short focus instrument will be more suitable.

The question of whether the spectrograph should be a prism or a grating instrument is of very little consequence as long as it is understood that instruments with similar performance (resolving power, dispersion, and speed) are compared. On the whole, experience has shown that if high dispersion is required a grating spectrograph will be found more suitable, but that for small spectrographs a prism instrument is generally more practical.

For the intermediate size the choice may depend on the particular purpose. On the whole, grating instruments probably will be found more convenient because of the more constant linear dispersion and the greater flexibility as various orders are available. When great freedom from scattered light is required, particularly in the ultraviolet, a prism instrument, but not one of the Littrow type, may have advantages. In a grating instrument the amount of scattered light depends very much on the individual grating. Naturally a nearly perfect grating will be better for almost any purpose than one with many faults. Rowland ghosts, which are the most common grating fault, are not very important for flame spectroscopy unless they are very strong (say, stronger than 0.25 per cent of the main line).

Photography of the Spectrum. For most purposes photography is perhaps still the commonest method of recording the spectrum. This can be accomplished without great difficulties from the short wavelength limit near 2,000A—which is due to the beginning of O_2 absorption—to about 12,000A. Properly sensitized emulsions[4] must be used outside the interval 2300A to 5000A. Beyond about 8600A the sensitivity of the available emulsions falls off rapidly so that much longer exposures must be counted on. Hypersensitization with ammonia is essential beyond 8600A and may be useful throughout the whole red and near infrared.

The photographic method is most useful for survey purposes and when identification and wavelength measurements are the chief purpose. Ordinarily, quantitative intensity measurements are better done by a photoelectric method. Photographic intensity measurements are quite feasible if the emulsion is properly calibrated, and may actually be more advantageous than photoelectric ones if many lines are involved or when the intensity is very weak. For details of technique see, for instance, Harrison, Lord, and Loofbourow [*2*] and the literature cited therein.

Photoelectric Methods of Recording. When intensity measurements are the chief consideration, photoelectric methods of recording the spectrum are more advantageous than photography. This is particularly true when changes in the spectrum are to be measured as functions of flame conditions. Naturally, in the infrared beyond 1.2μ nonphotographic methods must be used.

For the ultraviolet and visible, experience of recent years has shown that the use of multiplier phototubes is so much more convenient and accurate for spectroscopic intensity measurements than any other method that this method has hardly any rival in the wavelength region for which it is suited.

The following types of tubes are most commonly used for spectroscopic purposes [*11*] (all manufactured by RCA):

931-A: All-purpose tube. May be used from about 3100A to 6500A. There is considerable individual variation from tube to tube. In particular, the sensitivity near the long wavelength limit may be very much different for different tubes.

1P21: Identical to 931-A but more carefully selected for maximum sensitivity and stability.

1P22: Goes slightly farther to longer wavelengths. Is of advantage in the red but often the same results may be achieved there with a specially selected 931-A tube, as the 1P22 tube has more dark current and less amplification.

1P28: In general identical with 931-A but with an ultraviolet transparent envelope. It must be used in the ultraviolet below 3100A. Above

---

[4] Detailed data on photographic emulsions will be found in *Photographic Plates for Scientific and Technical Use.* Eastman Kodak Co., Rochester, N.Y.

3100A it is somewhat inferior to 931-A or 1P21 because the higher temperature necessary for dealing with the harder glass has an unfavorable effect on the photosurfaces. The latest tubes seem to be much improved in this respect.

There are sometimes special experimental tubes available which may be useful for certain purposes. The cost of such special tubes is considerably higher than that of regular tubes.

One such special tube—now discontinued, unfortunately—had a cesium oxide photocathode which rendered it sensitive to about 10,000A (1μ). Although inferior in the visible range to the regular 931-A, it made it very easy to penetrate the near infrared without making a change in technique except interchanging tubes.

Another experimental tube has a quartz envelope which is attached to the glass base through graded seals. Quartz has a higher ultraviolet transparency in the ultraviolet than the hard glass used for 1P28. Apparently, the use of the graded seals obviates the necessity for high temperatures during manufacture so that the sensitive surfaces are not impaired. This tube cannot be used interchangeably with the regular ones as it is considerably longer.

There are some British tubes which have the photocathode on the glass. Their performance for spectroscopic purposes seems to be as good as that of the RCA tubes but not superior.

A number of special tubes were developed for nuclear crystal scintillation measurements. They appear not to have any advantages for spectroscopic measurements.

The multiplier phototubes are distinguished from ordinary photodiodes in that through secondary emission on nine successive dynodes the original photocurrent is amplified inside the tube up to a million times. This amplification is nearly noise-free. The output of a photomultiplier can, therefore, be measured with a reasonably sensitive instrument without further amplification. While this is possible except for very weak intensities it will be found advantageous to use an amplifier with a current amplification of a few hundred times between photomultiplier output and recording instrument. The advantage of this is that it will be possible to work at a lower intensity level, with the avoidance of fatigue phenomena, and to use at the same time rather rugged measuring instruments. The output current of a photomultiplier can then be kept below one microampere, which also enables one to avoid the difficulties due to fatigue [*12*]. The lower limit is determined by statistical current fluctuations.

When the light source is weak, the intensity fluctuations which are due to the atomic nature of electricity and the quantum nature of light may become excessive. If, on the average, n_0 photoelectrons per second are emitted, due to statistical fluctuations, the exact number in a given time interval Δt is not $n_0\Delta t$, but differs from this by a certain amount d. Probability theory shows that the average square of this deviation is

$$\overline{d^2} = n_0\Delta t$$

From this it follows that the average relative root-mean-square deviation is

$$R_t = \frac{\sqrt{\overline{d^2}}}{n_0\Delta t} = \frac{1}{\sqrt{n_0\Delta t}} = \frac{4 \times 10^{-10}}{\sqrt{i_0\Delta t}}$$

where i_0 is the average photocurrent expressed in amperes. R_t gives the relative accuracy with which a given photocurrent can be measured under the most ideal conditions. The subsequent amplification in the photomultiplier tube will add additional fluctuations, but these will not change the order of magnitude of R_t.

With the proper technique (i.e. using noise-free circuits and, if necessary, having the phototube cooled) these statistical fluctuations are actually limiting the accuracy, when we go to low enough intensities and short times of observation.[5]

With a time constant of one second the fluctuations are about 1 per cent at an output current of about 1.5×10^{-9}A with a multiplication factor of 10^6. Considerably smaller currents than this can be observed, but with decreased accuracy.

If the signal fluctuations limit the accuracy, the only remedy is either to increase the signal strength or, if this is not possible, to increase the time of observation. This usually can be done by increasing the time constant of the electric circuit through the introduction of large capacitances. As the speed of recording must be reduced if this is done, there is a practical limit beyond which it is not ordinarily advisable to go. The technique of using the photomultiplier tubes is quite simple if some elementary precautions are observed, but this is not the place for detailed instructions [*12*].

As there is practically no inertia in the electrons, the photomultiplier tubes can be used to follow rapidly varying intensities. Intensity measurements within one-millionth of a second are not particularly difficult, if the intensity is adequate and the measuring circuit properly designed. Such short-interval measurements are most easily displayed on the screen of a cathode ray oscillograph, although there are other methods which give more accuracy.

As a measuring instrument, any reasonably sensitive galvanometer may be used without an amplifier. There are now dial microammeters, which, though not quite as accurate as a good galvanometer, are easier to use. For many purposes recording microammeters are advisable. These are extremely rugged instruments and can be obtained with a current sensitivity of 10^{-8} amperes per scale division or better. They contain a built-in amplifier but can be used with an additional amplifier between phototube and recorder. The recorders most commonly used are made by Leeds and Northrup or the Brown Instrument Company.

---

[5] For higher currents the imperfections in the meter or recorder may set a limit to the accuracy. If there is a considerable amount of dark current, its fluctuations determine the accuracy rather than the fluctuation in the signal current. Naturally, if there are other sources of noise in the amplifier or other parts of the circuit, they may cover up the statistical signal fluctuations. With some care it is usually possible to suppress all extraneous sources of fluctuations to below 1 per cent so that when R_t exceeds 0.01 the statistical signal fluctuations will be the dominant factor.

Even when a phototube is kept in complete darkness an output current will flow which is called the dark current. It is due partly to thermal emission from the photocathode, and partly to internal leakage.[6] The magnitude of the dark current depends very much on the individual tube. Under normal operating conditions it is of the order of magnitude of 10^{-8} amperes. This dark current sets a lower limit to the signal that can be measured.

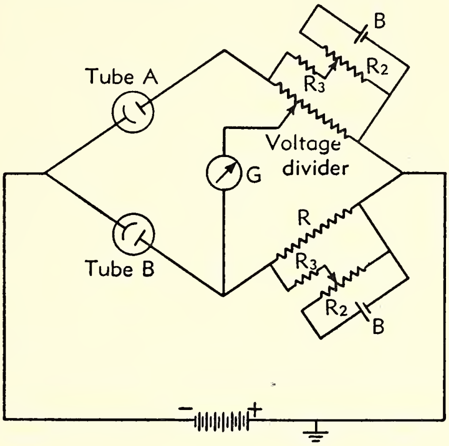

Fig. M,2f. Fundamental circuit for direct measurement of intensity ratios. Note the two bucking circuits for eliminating the dark currents.

The dark current can be eliminated in various ways. In the first place a bucking potential can be applied which compensates the dark current (cf. Fig. M,2f). In this way the dark current could be eliminated completely if it would remain constant. However, there are short and long period fluctuations. The long period fluctuations can be eliminated by adjusting the bucking potential manually from time to time. This, however, is not satisfactory unless the variations are slight and very gradual.

[6] When the external circuit is not properly designed or inferior insulation materials are used, particularly when one works in a very moist atmosphere, there is an external leakage dark current. It can be recognized by the fact that it persists when the tube is removed from the socket unless it is in the tube base itself. It should be eliminated by proper design. Air conditioning the laboratory room will help considerably.

A better way to eliminate the dark current is to modulate the light by a rotating sector in front of the slit. The photocurrent consists then of pulses which can be amplified by a tuned a.c. amplifier. This eliminates the dark current and also any pickup which does not have the same frequency as the light pulses. This also makes it possible to use an a.c. amplifier, which is usually more stable than a d.c. amplifier.

While the steady and slowly varying components of the dark current are eliminated in this way, the components of the dark current fluctuations with the same frequency as the light pulses are amplified; these set a measurable lower limit to the signal.

In order to eliminate the dark current completely, the tube must be cooled. Cooling to the temperature of dry ice is quite sufficient and is achieved easily by surrounding the tube with the cooling mixture. Under these conditions the limitations in sensitivity and accuracy are entirely those determined by the fluctuations in the signal itself. It is not so easy to avoid condensation of moisture after a prolonged period of operation. Insulation breakdown will then produce considerable noise. However, when one deals with very faint light sources (output currents considerably below 10^{-8} amperes), cooling of the tubes is the only practical way to obtain enough sensitivity.

When actual intensity measurements are needed over a considerable wavelength interval, the sensitivity of the combination phototube, spectrograph, and optical system must be calibrated as a function of the wavelength. In the visible and near ultraviolet and infrared, this is most conveniently done with a tungsten ribbon lamp. The temperature of the ribbon must be known as a function of the current. Then the intensity distribution as a function of the wavelength can be calculated with the help of the known emissivity of tungsten.

Often, the chief interest is in the relative intensity of two spectrum lines. The intensity ratio can, of course, be obtained by measuring both lines separately, but there are often great advantages in measuring the ratio directly. Fig. M,2f shows the fundamental circuit with which this can be achieved. The output current of one tube (the reference tube B) goes through a fixed resistance R, that of the second tube (A) through a slidewire resistance (voltage divider) with the resistance R_X on the ground side of the contact. When the galvanometer in the bridge shows no current, the ratio of the photocurrents is $i_A/i_B = R/R_X$. It is very important that the balance not be upset by quick fluctuations in the intensities. Therefore, the circuits must be dynamically balanced, which means not only that the resistances must have the proper values, but also that the time constants of the two circuits must be adjusted. This requires very careful design of the circuits.

A ratio recorder has been constructed by Leeds and Northrup which records automatically the ratios of two lines. For ratio measurements it is important that the dark currents be completely eliminated. In Fig. M,2f the necessary bucking circuits are indicated. A better way to do this is by modulating the light with a rotating sector and using a.c. amplification, as explained earlier.

Use of Phototubes with the Spectrograph. Almost any spectrograph can be adapted for photoelectric intensity measurements, although some are more suitable for this purpose than others. When a series of lines is to be measured, there are two ways of doing this.

Fixed tubes. A separate exit slit and phototube may be placed at each line and the output of all tubes measured simultaneously. This requires as many measuring devices as there are lines and, therefore, is practical only if the number of lines is moderate. The width of each phototube is 25 mm. When two lines are closer than this, the phototubes cannot be placed side by side. By a suitable arrangement of slits and mirrors (for instance, as illustrated in Fig. M,2g), lines fairly close together can be dealt with. In a spectrum fairly rich in lines when narrow exit slits must be used, a fixed-slit system is very sensitive to changes in temperature and to any other disturbance that would displace the slits even slightly. On the other hand, the fact that all lines are measured simultaneously guarantees freedom from difficulties due to fluctuating light sources.

When a number of lines are to be measured simultaneously it is probably not very practicable to use elaborate devices such as automatic recorders or even galvanometers. Fairly simple devices have been designed for this purpose. The current from each phototube charges a condenser. This may be a small condenser which is charged to a fixed voltage many times during one exposure. The number of times the condenser is charged is automatically recorded and is proportional to the photocurrent [*13*]. Another way of measuring the photocurrent is to charge a larger condenser for a fixed time and to measure the voltage on the condenser [*14*].

Scanning. The simultaneous measurement of several lines with fixed slits obviously is only practical when the number of lines to be measured is relatively small. In all other cases the spectrum is scanned by the phototube. In the author's experience scanning is the best way to use the phototubes for practically any purpose provided a few precautions are observed.

The scanning can be done either by moving the slit with the phototube along the focal curve of the spectrograph or by keeping the tube fixed and rotating the grating or prism in order to change the wavelength. With the first method any spectrograph can be used that is suitable for photographic recording, while the second method is best suited for use with a monochromator.

There are many ways in which the motion of the tube along the

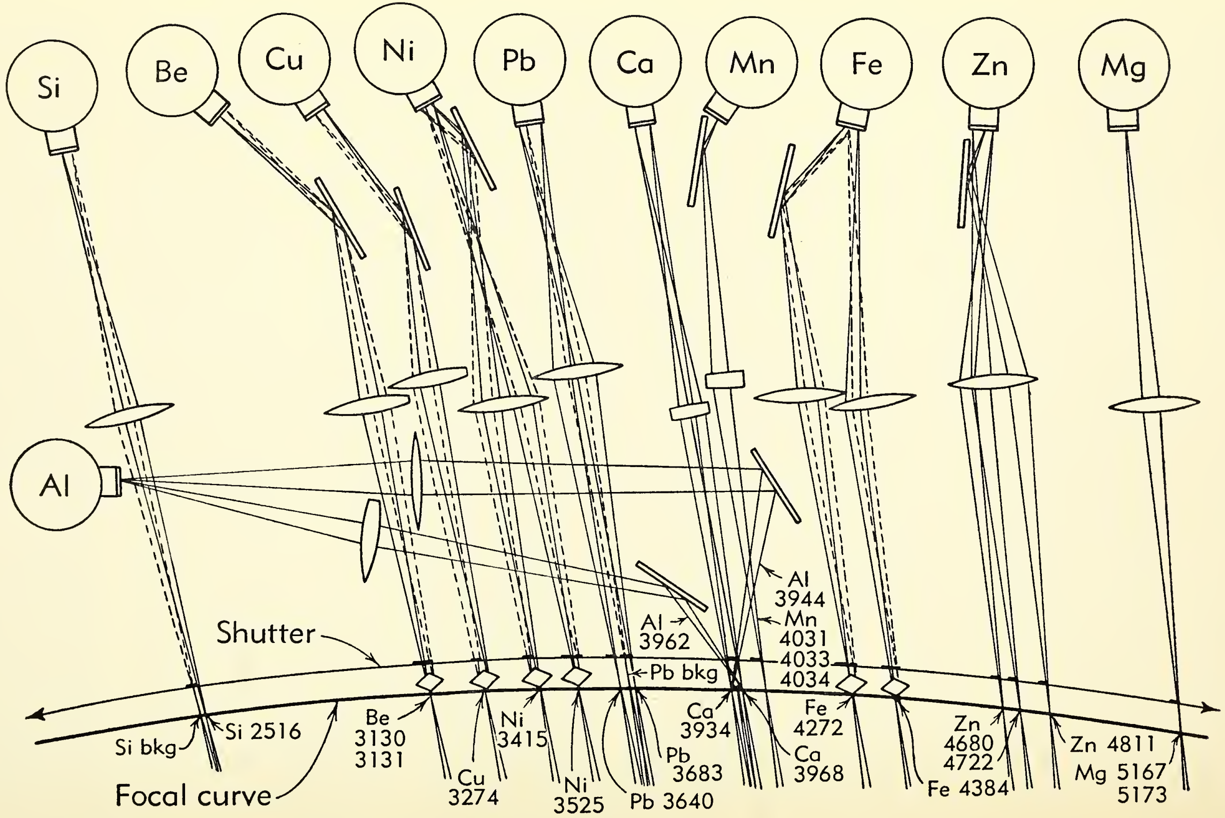

Fig. M,2g. Optical details in the arrangement of phototubes, exit slits, prisms, mirrors, and lenses when a number of lines lying fairly close together are to be observed with fixed phototubes. (After Saunderson, Caldecourt, and Peterson [*14*].)

focal curve can be realized, and the choice of the best way depends on the construction of the particular spectrograph. When the required wavelength interval is small, the motion may be along a straight line and can be carried out with a screw. When considerable distances have to be covered the tube must be made to travel along the focal curve and, moreover, its axis must always point in the direction of the grating or prism. However, considerable deviation from this last condition can be tolerated.

On the whole, scanning with a properly constructed monochromator and a fixed tube is considerably less cumbersome than using a movable phototube in a conventional spectrograph. The latter has decided advantages when more than one line is to be recorded at the same time and makes ratio recording more straightforward. Commercial plane-grating monochromators for photoelectric scanning are to be available in the near future.

With the scanning method, different lines are recorded successively. The results will be meaningful only if the light source is constant or if steps are taken to render harmless the effects of light source fluctuations. For this reason it is always advisable and often necessary to resort to direct ratio measurements, unless, of course, the changes in the light intensity themselves are to be studied.

For ratio measurements one tube scans the spectrum while a second one is fixed on a reference line or a group of lines. There is no difficulty in arranging this when the scanning tube moves. It is more difficult when scanning is done in a monochromator by moving the spectrum. In this case it is often advisable to use as a reference some of the beam before it strikes the grating or prism. A thin quartz plate between slit and grating will reflect part of the light onto the reference tube. Better results can be obtained when a second monochromator is available for the reference tube.

In the infrared, photographic methods cannot be used and multiplier phototubes or ordinary photodiodes do not reach beyond the photographic limit.

For wavelengths between 1μ and 3μ, lead sulphide photoconductive cells have proved by far the most convenient and sensitive receiver. Beyond this range to about 6μ, lead selenide and lead telluride cells may be used, although they have not yet been perfected to such an extent as the lead sulphide cells. Beyond 6μ, thermocouples or bolometers must be used; these are considerably less sensitive than the photoconductive cells.

The spectroscopic technique in the near infrared, where photoconductive cells can be used, does not differ much from that in the visible. Glass prisms are not feasible beyond about 2μ; beyond that, rock salt, potassium bromide, and other materials must be used. For high resolution, gratings are recommended. Infrared spectroscopy is hampered by water vapor absorption. This can be overcome by having the light path in a dry atmosphere or, better, in a vacuum. However, this will not entirely remove the difficulties for flame spectroscopy because of the water vapor in the flame itself.

M,3. Identification of Flame Constituents. In any combustion process the initial substances—fuel and oxygen supply—as well as the final products (e.g. water and carbon dioxide) are usually well known. In addition, short-lived intermediate compounds are often formed in the flame. Their recognition is of prime importance for an understanding of the combustion mechanism. Because of their short life these compounds usually cannot be dealt with by the ordinary methods of chemical analysis. In many cases spectroscopic methods are ideal for the study of these intermediate compounds.

Besides the substances formed in the flame as essential links in the combustion mechanism, other substances appear which may be mere impurities or which play a secondary role in the combustion mechanism. Until this mechanism is completely clarified, however, one will do well not to overlook any compound found in the flame.

One task of the spectroscopic flame study is, then, the identification of the various compounds found in the flame. The first aim is usually a qualitative study. This may be quite easy for some molecules, more difficult for others, and next to impossible for a few. Quantitative studies may then follow, and these will try to connect the behavior of the various substances in the flame with the reaction mechanism.

Such substances that emit light in the flame—whether in the visible, infrared, or ultraviolet is immaterial—and, therefore, produce an emission spectrum are most easily accessible for spectroscopic study. On the other hand, the experimental technique of studying the absorption spectrum is usually much more difficult, but may yield results that cannot be obtained in any other way (see Art. 4).

We may take as an example a typical hydrocarbon flame such as that produced with a Bunsen burner. The different coloration of the inner and outer cones indicates that the spectra of the two zones are different.

The initial ingredients of the flame are hydrocarbons (for example, acetylene and oxygen), and the final products are H_2O and CO_2. In the emission spectrum of the flame when observed under ordinary conditions, none of these substances show up except in the infrared. The reason is that none of them have emission spectra that can be excited in a flame in the visible or near ultraviolet. This shows that one must be very careful in drawing conclusions from spectroscopic observations as to the presence of certain molecules, as some of the most prevalent ones may be spectroscopically inert.

The prominent structures in the spectrum of a hydrocarbon flame are bands originating from the radicals OH, CH, and C_2. The former occurs throughout the flame, the latter two only in the inner cone. Plate M,3 shows the principal bands of these molecules under moderate dispersion. The rotational structure can be resolved at least partly with medium dispersion, say, about 5A/mm. For complete resolution a large grating spectrograph with a dispersion of 1A/mm, or better, is necessary and even then the vicinity of the heads of the C_2 bands will remain unresolved.

Because of the general prevalence of these bands in most flame spectra and their importance when quantitative studies are attempted, a description of the principal features of these bands will be given.

The OH Bands. They form an extensive band system in the ultraviolet that has been the subject of many investigations. The 0,0 band with its head at 3064A is the most prominent band. All the bands are shaded toward the red. The whole system is given in Table M,3a. The wavelengths of the principal heads are indicated, as well as the relative intensities. The bands in italics in Table M,3a are treated in detail in a recent review of the system by Dieke and Crosswhite [*15*]. The numbers in parentheses are the intensities in an acetylene flame. The data for the other bands which are of minor importance for flame studies are taken from older papers listed in that review.

Table M,3a. The ultraviolet OH bands.

$V'\backslash V''$	0	1	2	3	4
0	*3064* (1000)	*3428* (4)			
1	*2811* (86)	*3122* (156)	*3485* (2)		
2	2609	*2875* (55)	*3185* (23)		
3	2444	2677	*2945* (8)	*3254* (5)	
4		2517	2753	3022	3331

In a flame the 3064 and 2811 bands can be obtained relatively free from superposition of other bands. As 3064 is by far the strongest band, it is most useful for detailed studies. In the inner cone the CH band 3134 interferes from about 3100 to longer wavelengths. The rotational structure is seen in Plate M,4 and Plate M,5a.

The OH bands may also be obtained in absorption (see Art. 4).

The CH Bands. These bands occur with appreciable strength only in the inner cone. There are three band systems, as follows:

$^2\Sigma \rightarrow {}^2\Pi$ bands near 3900A. They have, in principle, the same structure as the OH bands, but appear simpler because the coupling is closer to type *b* coupling. They can be resolved fairly well (except for the R branches) with moderate dispersion. The vibrational scheme is given in Table M,3b.

Table M,3b. The $^2\Sigma \rightarrow {}^2\Pi$ system of CH.

	R_2 heads	
$V'\backslash V''$	0	1
0	3871.4	
1	3627.2	4026.3

The 0,0 band at 3871A is by far the strongest and is the only one that ordinarily can be used for detailed studies. It is reasonably free from interference by other systems (see Plate M,3b).

$^2\Sigma \rightarrow {}^2\Pi$ band at 3134A. This band has the lines very closely spaced so that reasonable resolution can only be achieved with the largest spectrographs. Moreover, it lies in the 3064 OH band, and is confused with it. For this reason it ordinarily is not suitable for detailed study in flames.

$^2\Delta \rightarrow {}^2\Pi$ bands near 4300A. The system consists of the very strong 0,0 band, the weaker 1,1 band, and the even weaker 2,2 band. The three bands overlap. Moreover, each individual band has a very complicated structure. Near the center the very close jumble of lines, as it appears in a flame, cannot be resolved, even in the largest spectrographs.[7] The R branches extending toward the shorter wavelengths, however, are reasonably well resolved and may be quite useful for detailed studies, as the 4300 band is the most intensive structure in the CH spectrum (see Plate M,5c).

THE C_2 BANDS. A number of band systems appear in the flame spectrum of which the so-called Swan bands are the most prominent. These form $^3\Pi \rightarrow {}^3\Pi$ transitions and lie in the visible range with the strongest bands in the green. They give to the inner cone its characteristic green color.

The vibrational scheme of the Swan bands is given in Table M,3c (see also Plate M,3a).

Table M,3c. The Swan bands ($^3\Pi \rightarrow {}^3\Pi$) of C_2.

$V'\backslash V''$	0	1	2	3	4	5
0	5165.2 (10)	5635.5 (8)	6191.2 (3)			
1	4737.1 (9)	5129.3 (6)	5585.5 (8)	6122.1 (4)		
2	4382.5 (2)	4715.2 (8)	5097.7 (1)	5540.7 (6)	6059.7 (3)	6677.3 (1)
3		4371.4 (4)	4697.6 (7)		5501.9 (4)	6004.9 (3)
4			4365.2 (5)	4684.8 (4)		5470.3 (2)
5					4678.6 (2)	4668.7 (1)

The bands are shaded toward the violet. They have sharp edges and consist of triple P and R branches. (Short Q branches near the origin are lost in the crowded section.) The bands can be only partly resolved.

Table M,3d. The $^1\Pi \rightarrow {}^1\Pi$ system of C_2.

$V'\backslash V''$	0	1	2	3	4
0	3852.2 (10)	4102.3 (9)			
1	3607.3 (8)	3825.6 (5)	4068.1 (6)		
2	3399.7 (5)	3592.9 (7)		4041.8 (3)	
3		3398.1 (5)	3587.6 (7)		4026.9 (1)

---

[7] In an electric discharge at low pressure these bands are simplified, and, moreover, the lines are sharper than in a flame and the central parts can be resolved.

The so-called Deslandres-d'Azambuja bands (Table M,3d) form a $^1\Pi \rightarrow {}^1\Pi$ transition. Their structure is similar to that of the Swan bands, but simpler, as all the lines are single. They are, moreover, much weaker, but they appear quite frequently and usually are clearly seen at high resolution when the heads stand out and the individual lines are part of the general background. Other C_2 band systems that occur in flames but that were recognized only recently are given in Tables M,3e and M,3f.

Table M,3e. Fox-Herzberg system of C_2.

$V'\backslash V''$	0	1	2	3	4	5	6
0			2732	2855	2987	3129	3283
1			2656	2772	2996		
2	2486		2589	2699			
3	2430		2528				
4	2378						
5							

Table M,3f. $^1\Sigma \rightarrow {}^1\Pi$ system of C_2 (Philips' infrared bands).

$V'\backslash V''$	0	1	2
0	--		
1	10,133.8[1]		
2	8750.8		
3	7714.6	8980.5	
4		7907.7	9131.
5			8108.2

[1] The 1,0 band has not been reported previously in the literature. It, as well as the other bands, is observed with great strength in an acetylene-oxygen flame.

The OH, CH, and C_2 Swan bands are the most conspicuous feature in the spectrum of any hydrocarbon flame. They appear prominently in the spectrum at any dispersion.

OTHER BANDS IN HYDROCARBON FLAMES. When the spectrum is examined carefully at high dispersion or when the flame burns under special conditions, a number of other bands appear.

In the first place, there are the various weaker C_2 systems mentioned above. Herman and Hornbeck [*16*] found that the Schumann-Runge bands of O_2 appear in hydrocarbon flames, particularly when there is an excess of oxygen. The chief bands[8] noticed by them are:

0,12 (3104A); 0,13 (3333A); 2,15 (3356); 0,14 (3370); 2,16 (3500); 0,15 (3516); 1,16 (3583); 0,16 (3673); 1,17 (3742); 0,17 (3841); 1,18 (3913); 2,19 (3987); 0,18 (4021); 1,19 (4096); 2,20 (4173); 1,20 (4292); 2,21 (4373).

Also found is the $^1\Sigma \rightarrow {}^3\Sigma$ system of O_2 in the near infrared usually called the atmospheric absorption bands. The origin of the principal heads is given in Table M,3g.

---

[8] These are the results from the CO-O_2 explosion spectrum. Hornbeck and Hopfield [*17*] state that these bands are similar in the CO flame and also in hydrocarbon flames, though less conspicuous in the latter.

In the spectrum of the inner cone of an ethylene flame (and also present in most other hydrocarbon flames) is a set of diffuse bands degraded toward the red. They lie between 2700 and 4100A, and are most strongly developed near 3300 to 3400A. The origin of these bands is still in doubt. W. M. Vaidya [*18*], who was the first to observe them, attributed them to HCO. Herman and Hornbeck [*16*] suggested that they might actually be due to O_2, CH, and/or other bands unresolved at low dispersion. Close inspection, however, seems to indicate that the bands are real. Attempts to determine the molecule responsible for them by substituting deuterium for hydrogen in the fuel have given no clear-cut results. That they are due to HCO, is still a strong possibility, but has not been proved. Some of the evidence is given by Gaydon [*19*]. A clear-cut identification of the molecule responsible for the hydrocarbon bands would be of great value to flame reaction kinetics. The matter is complicated by the fact that so far these bands have not been obtained with sufficient dispersion to unravel the rotational structure.

Table M,3g. Heads of principal bands of the atmospheric absorption bands of O_2.

$V'\backslash V''$	0	1	2	3
0	7594	8598		
1	6867	7685	8698	
2	6277		7779	8803
3	5788			7879
4	5380			

Details about the spectra of other types of flames will be found in Gaydon [*19*].

M,4. Absorption. The identification of constituent compounds in flames by their absorption spectrum presents experimental problems which often differ very substantially from those encountered when studying the emission spectra. Two reasons are chiefly responsible for this.

When a luminous gas emits certain spectrum lines, these same lines appear in absorption if light from a source with a continuous spectral distribution traverses the gas. Light of the wavelength of a spectrum line is weakened by the absorption but strengthened by the emission in the gas. It has been shown in Sec. I that when the temperature of the continuous source is higher than that of the flame, the lines appear as absorption lines, and otherwise, as emission lines. The method of line reversal for temperature measurements depends on this fact.

In a gas in equilibrium at high temperature, there would be no particular advantage in using absorption lines, as every line observable in absorption should also show in emission. This is not true when there is no equilibrium, or when the gas temperature is low and the continuous background comes from a substance at a temperature much higher than that of the gas. In that case we may easily detect a compound by its absorption spectrum when its emission spectrum cannot be found.

We have to recognize one essential difference between an emission and an absorption line. In any spectrograph the actual width of an emission line depends chiefly on three things, namely, the width of the slit, the resolving power of the spectrograph, and the true width of the line. The finite resolving power of the instrument with an infinitely narrow slit and a line of negligible true width produces a line of half width ϵ, the instrument half width. On the other hand, we would obtain a line with the true half width δ in an instrument with infinite resolving power and negligible slit width.

The actual width of a line is due to all three causes, but may be controlled, in a given instance, by only one of the three causes, with the other two being negligible.

If, now, we have an isolated emission line, we see immediately that the total amount of energy contained in it is independent of the instrument and is proportional to the slit width. With a weak line we can increase its chance of being observable by using a high speed spectrograph of low resolution and, therefore, large instrument width. Also, we may open the slit wide. This will increase the signal in photoelectric observations. It will increase the blackening of the photographic image as long as the effective slit width (the width of the geometrical image of the slit on the focal plane) is not large compared with the instrument width.

The situation is quite different with an absorption line. Suppose we have a spectrograph of unlimited resolution and an infinitely narrow slit. The intensity distribution in an absorption line is then like the narrowest curve (with $\epsilon/\delta = 0.1$) of Fig. M,4a, and this represents nearly the true shape of the line, independent of instrumental restrictions. This figure will not change appreciably as long as slit width and instrument width are small compared to the true width δ of the line. Suppose we now employ a spectrograph of which the instrument width ϵ is not small compared to δ. Then each monochromatic component in the continuous spectrum spreads laterally, and the dark parts on the photographic plate encroach on the light parts. The result is that the same absorption line now looks like the other curves of Fig. M,4a. The minimum is much shallower and consequently the line is less easily detected. Fig. M,4b shows the intensity of the minimum below the continuous background as a function of the ratio of instrument width to true line width. The effect of finite slit widths is similar to the effect of the instrument width.

With an instrument of small dispersion or with wide slits, the conditions for discovering sharp absorption lines are extremely unfavorable. True line widths of 0.01A are not infrequent. Such lines can be detected efficiently only with a spectrograph having an instrument width of

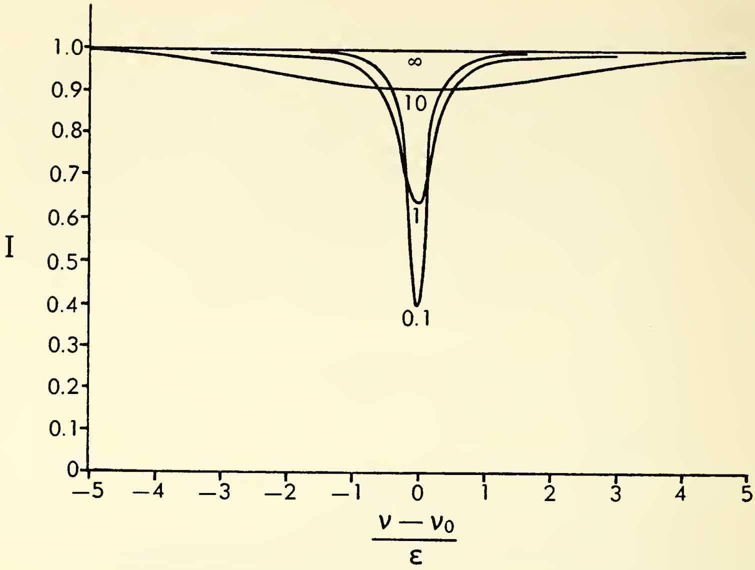

Fig. M,4a. Intensity in an absorption line with varying ratio ϵ/δ of instrument width to true width of the line. The numbers near the minima are the values of ϵ/δ.

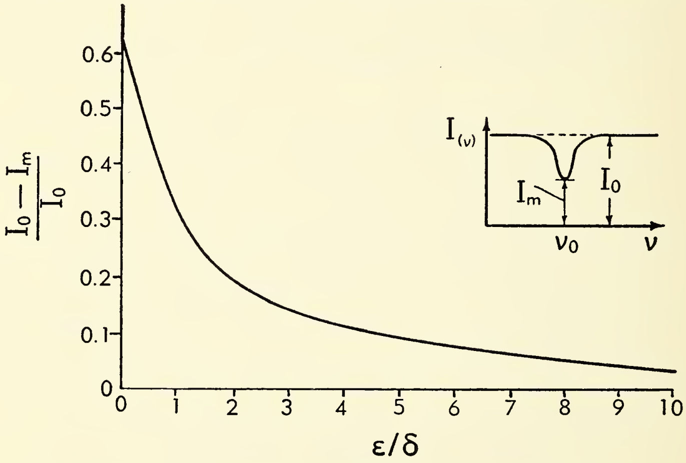

Fig. M,4b. Visibility of an absorption line as a function of the ratio ϵ/δ of instrument width to true width.

the same order of magnitude as the true width or even smaller, which means a resolving power of several hundred thousand. For the detection of weak absorption lines, therefore, spectrographs of the highest resolving power are needed. This means large gratings, or interferometers (which, however, present other difficulties). This condition must be even more rigorously fulfilled for quantitative intensity measurements on absorption lines, if complicated and uncertain corrections are to be avoided.

The attempt to make such measurements with inadequate resolution has in the past often led to difficulties.

Of the molecular bands occurring in flames, only the OH bands in absorption have been studied to any extent. In numerous papers Oldenberg and his coworkers have solved the problem of observing the OH absorption spectrum and have obtained some very interesting results regarding the reaction kinetics of OH. Most of this work was done with electric discharges through water vapor and hydrogen peroxide. In order to avoid the trouble of having emission and absorption at the same time, an intermittent discharge was used together with a synchronized shutter on the spectrograph. The spectroscopic observations were made only when the discharge was off and the gas nonluminous. In the second order of a large, 21-foot spectrograph there was enough resolving power (220,000) to observe the absorption spectrum even though the true width was only about one-third of the instrument width. In this way Oldenberg [*20*] found that under favorable conditions the lifetime of the OH radicals in their normal state is about $\frac{1}{8}$ second. At the same time, it was possible to investigate the reaction mechanisms by which OH radicals disappear and actually to measure the rate constants [*21*].

In order to do this it is necessary to find the actual concentration of OH. This can be done through the intensities of the absorption lines if the absolute transition probabilities are known. Oldenberg and Rieke [*22*] determined these probabilities by measuring the absorption coefficient of OH lines in water vapor[9] at fairly high temperatures (1200°C), where a small but sufficient fraction of the molecules is dissociated and where the concentration of OH radicals can be calculated from the thermal equilibrium. They found f values[10] of the order of magnitude of 10^{-4} to 10^{-3} and lifetimes of a typical excited level of 2.5×10^{-6} sec.

The resolving power of a large grating spectrograph is not sufficient to obtain good quantitative results with sharp absorption lines such as those of OH. For this reason Oldenberg and Rieke [*21,23*] availed themselves of the considerably higher resolution of a Fabry-Perot interferometer. Because of its small, free spectral range,[11] a continuous background could not be used. For this reason, they used another discharge tube for the emission background, and endeavored to broaden the lines of this source in order to see the absorption as narrow dark lines on the background of broad emission lines. However, they were only partly successful with this procedure.

We have discussed the state of affairs when there are individual, sharp absorption lines. When such lines are crowded very closely together, as they are near the head of a band, absorption can be observed even with moderate dispersion. One should make sure, however, that the actual lines, i.e. when observed under very high resolution, are crowded together, and that this is not caused by the insufficient resolution of the spectrograph. Even then one must be very careful in drawing quantitative conclusions from absorption under such conditions.

---

[9] Actually a mixture $\frac{2}{3}H_2O + \frac{1}{3}O_2$.

[10] The f values give the ratio of the energy emitted by the actual molecule to that of a classical elastically bound electron of the same frequency.

[11] The free spectral range of a grating, interferometer, or similar device is the wavelength interval between successive orders.

The situation can be made much more favorable when the lines can be broadened by high pressure. Explosions in a closed vessel are, therefore, much more favorable for absorption experiments [*24*].

When there is actually continuous absorption, there will be no difficulty in observing this quantitatively, even with small spectrographs. Such continuous absorption is observed with a number of molecules—for instance, H_2O_2 and O_3, both in the ultraviolet. Unfortunately, a continuous spectrum is not a very characteristic thing by which the presence of a substance can be easily recognized. It may be used for quantitative measurements only after it has been demonstrated to which molecule it belongs. Also, one must be sure that continuous absorption of different origin does not interfere.

If there is sharp line absorption one can avoid the difficulties inherent in the limited resolving power of a spectrograph by using as emission background not a continuous spectrum, but a sharp line emission spectrum as nearly as possible identical with the absorption spectrum which is being investigated.

For instance, if the presence of normal OH is to be investigated, the emission spectrum of OH is used from a flame or an electric discharge. By traversing the absorbing gas, the emission lines are weakened; this can be observed with a spectrograph of moderate resolution or, in favorable cases, even with filters without a spectrograph. The problem of the quantitative evaluation of such results is exactly the same as that of the weakening of spectrum lines by self-absorption, which has been treated by Cowan and Dieke [*25*]. If the line widths of emission and absorption lines are identical, there are no particular difficulties, although the results are different depending on whether the line shape is controlled by the Doppler effect or by so-called collison broadening.[12] When the line widths of emission and absorption lines are different, complications arise. One way of dealing with this is to use extremely high resolution, as was done by Oldenberg and Rieke [*21*] when they employed the Fabry-Perot interferometer. If the line widths of both emission and absorption lines can be determined empirically, the total weakening of the line obtained with moderate resolution can be used to determine the concentration (see Cowan and Dieke [*25*]). Plate M,4 shows the absorption in the centers of the OH lines when the light has to pass from the center of the flame through a considerable layer of cooler gas containing OH [*15*].

[12] Theory and experience have shown that in most light sources, particularly if the pressure is not extremely low, the line shape is controlled by collision broadening.

If the absorbing gas is also luminous, as is the case with flames, the following procedure can be adopted. Call the emission source A, the luminous absorption flame B. Line up A and B on the optical axis of a spectrograph so that A is farther away from the slit. An image of A is formed on the slit so that the light from A has to pass through B. The intensities in the spectrum are now measured under the following three conditions:

1. Both A and B present: Intensity $I_1 = I_B + (1 - b)I_A$
2. Only A present: $I_2 = I_A$
3. Only B present: $I_3 = I_B$

where b is the fraction of I_A absorbed in B.

When there is no absorption ($b = 0$), we have

$$I_1 = I_2 + I_3$$

but if there is absorption present, we have

$$I_1 < I_2 + I_3$$

and we obtain b from

$$I_3 + I_2 - I_1 = bI_2$$

These experiments can be performed easily with two flames. If the measurements are made with the OH bands, considerable absorption is found, which indicates that there is a considerable concentration of normal OH radicals in the flame. This agrees with the observation of long life of OH in an electric discharge.

On the other hand, no appreciable absorption is found in the CH and C_2 bands [*26,27*]. This indicates a very small concentration of normal CH and C_2 radicals in the flame, which must be caused by a very short lifetime of these two radicals.

M,5. Data on Equilibrium Conditions.

Criteria for Equilibrium. Whenever there is thermodynamic equilibrium in a system, the distribution of the molecules over the various energy levels is entirely determined by the temperature, and a knowledge of the temperature is sufficient to characterize the equilibrium, given the number and kind of molecules present. Therefore, a knowledge of the temperature is important for almost any kind of equilibrium system. This article deals with spectroscopic criteria by which equilibrium can be recognized, if it exists. Spectroscopic methods for measuring the temperature are also treated. The next article deals with the more complicated and more interesting cases where no equilibrium exists.

When it is desirable to know the temperature at a particular spot in a flame, the methods of measurement suitable for liquids and solids or for nonburning gases are of little use. In the first place, there would be very few thermometer substances capable of withstanding the high temperatures. Furthermore, a thermometer of any bulk would interfere with the combustion mechanism. Also, it would not be at all certain that if a thermometer could be introduced into the flame and a temperature recorded with it, that this temperature would be that of the surrounding flame gases. The metal surface of a thermocouple, for instance, could act as a catalyzer, and the heat of reaction would then heat the junction to a temperature considerably above that of the surrounding. This actually does occur when, for instance, metal is introduced into a gas containing atomic hydrogen.

For all these reasons, optical methods of temperature measurement are preferable, for with them there is no necessity to interfere in any way with the flame itself. The so-called line-reversal method, which is treated in Sec. I, is in this category. In the present article, the spectroscopic methods for temperature determinations are treated. Before dealing with any experimental details, it is very important to have a clear concept of the fundamental principles involved.

One can define the temperature of a gas only if there is statistical equilibrium. In this case the distribution over the various energies is according to Boltzmann's law. This means that if the energy is quantized the number of molecules having a certain value E_n is

$$N_n = CG_n e^{-E_n/kT} \tag{5-1}$$

or, when there is a continuous range of energies,

$$n(E)dE = g(E)e^{-E/kT}dE \tag{5-2}$$

where G_n and $g(E)$ are the so-called a priori probabilities (G_n would be the degree of degeneracy of the state E_n).

Ordinarily, the energy of a molecule is distributed over a number of degrees of freedom. We have translational energy which is continuously variable, vibrational and rotational energies which have usually discrete values, and electronic energies which are also discrete unless there is an appreciable degree of ionization. Naturally, when there is equilibrium, there must not only be equilibrium over a particular degree of freedom, but also all degrees of freedom must be in equilibrium with one another.

If it is possible to determine empirically the distribution of molecules over the different energies—in other words, if we can determine $N(E)$ as a function of the energy E—the temperature can be found. For from (5-1) follows

$$\ln N_n = \ln C + \ln G_n - \frac{E_n}{kT} \tag{5-3}$$

If N_n is known for two values $E^{(1)}$ and $E^{(2)}$ of E_n, the unknown constant C can be eliminated.

$$\ln \frac{N_n^{(1)}G_n^{(2)}}{N_n^{(2)}G_n^{(1)}} = -\frac{E_n^{(1)} - E_n^{(2)}}{kT} \tag{5-4}$$

The knowledge of the particular states involved assures knowledge of G_n. With N_n empirically determined everything in Eq. 5-4 is known except the temperature, which thus can be calculated. An analogous expression holds when we have a continuous energy range and start with Eq. 5-2.

If the distribution of molecules over the different energy states can be determined empirically, the temperature can be found. Except under very special circumstances, the only way to determine this distribution is by spectroscopic intensity measurements.

The intensity of any particular atomic or molecular transition is given by

$$I_{n'n''} = A_{n'n''}h\nu_{n'n''}N_{n'} \tag{5-5}$$

where $\nu_{n'n''}$ is the frequency of the line, $A_{n'n''}$ the transition probability, and $N_{n'}$ the number of molecules in the initial state. When there is statistical equilibrium

$$N_{n'} = Ce^{-E_{n'}/kT} \tag{5-6}$$

with C a constant independent of $E_{n'}$. This is identical with Eq. 5-1 except that the a priori statistical weights $G_{n'}$ have been omitted, as the transition probabilities $A_{n'n''}$ may be defined so as to include them.

Suppose we can measure the intensities $I_{n'n''}$ for a number of lines. Of course, only relative values are of significance as we have usually no way of knowing the total number of molecules present and, therefore, do not know the constant C in Eq. 5-6. Also, the fraction of light originating in the light source and finally reaching the receiver (photographic emulsion or phototube) is usually unknown. Calling F the product of all the constants, we can write Eq. 5-5 as

$$I_{n'n''} = FA^*_{n'n''}e^{-E_{n'}/kT} \tag{5-7}$$

if $A^* = \nu A$, or as

$$Y = \log \frac{I_{n'n''}}{A^*_{n'n''}} = \log F - \frac{E_{n'}}{kT}\log e \tag{5-8}$$

if common logarithms are used.

When a spectrum is properly analyzed, the values of $E_{n'}$ are known. Only relative values are required. A shift in the energy scale will leave Eq. 5-7 or Eq. 5-8 unchanged except for a different value of the constant F. Suppose we also know the transition probabilities $A^*_{n'n''}$. Again, only relative values are required. If the intensities $I_{n'n''}$ are measured we can plot

$$Y = \log \frac{I_{n'n''}}{A^*_{n'n''}}$$

as a function of $E_{n'}$, and all points must lie on a straight line (see Fig. M,5a), the slope of which is $-\log e/kT = -0.62445/T$ if the energies are given in wave numbers and the temperatures in degrees Kelvin. Therefore, the slope of this experimentally determined line will give the temperature of the gas.

As a straight line is determined by two points, the temperature can be obtained from intensity measurements on two lines belonging to the same atom or molecule, having $Y^{(1)}$, $E^{(1)}$ and $Y^{(2)}$, $E^{(2)}$ respectively. Eq. 5-8 gives, then,

$$Y^{(1)} - Y^{(2)} = -(E^{(1)} - E^{(2)}) \frac{0.62445}{T} \tag{5-9}$$

It does not make any difference what lines are chosen, provided they come from different initial levels and provided the transition probabilities are known. For the actual applications, however, some particular line groups are more suitable than others. Those cases which have been found most useful are discussed in some detail below.

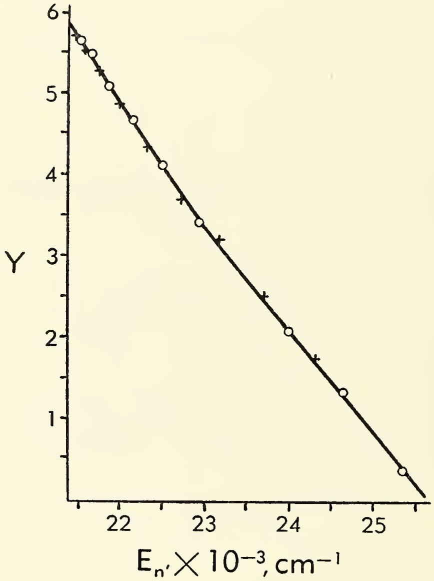

Fig. M,5a. Log I/A against energy plot for rotational levels in the He_2 molecule.

While two lines are, in principle, sufficient to determine the temperature, more lines will yield better accuracy as each line has a certain error of measurement which will result in a temperature error. If many lines are measured and plotted, this will not only result in increased accuracy but also give a check on the assumption that statistical equilibrium exists. For equilibrium it is necessary that all points lie on one straight line. If they do not, there are two possibilities. Either there is something wrong with the method of intensity measurements so that the values found do not represent the true intensities, or there is no equilibrium and, therefore, no temperature. Examples of the second alternative are given in Art. 6, while some of the possibilities for errors in intensity measurements are discussed below under *Sources of error*. It should be emphasized that even if a number of lines lie on a straight line, this is not necessarily a valid proof that equilibrium exists. It is conceivable that lines of different origin would not fall on the same line. In order to establish proof of equilibrium, the initial states should be distributed over all possible degrees of freedom. This, in general, is not possible, and it may be necessary for experimental reasons to confine the variations in the energy to variations in one particular degree of freedom. We have the following possibilities:

1. Translation
2. Rotation
3. Vibration
4. Electronic motion

If we vary the energies only over one of these degrees of freedom, we may speak, for instance, of a rotational temperature, or, in another case, of an electronic temperature. If there is real equilibrium all these temperatures are the same and are equal to the true temperature. A rotational temperature is, therefore, the true gas temperature if we can assure ourselves that there is not only equilibrium among the rotational states but *general* equilibrium. If there is a rotational temperature, the general nature of the gas may indicate that there is equilibrium and that the rotational temperature is the gas temperature. There are, however, cases where this is not true. Equilibrium is established by collisions. Departures from equilibrium may be brought about by chemical reactions or electrical discharges. The more collisions there are in the average before the light is emitted, the better are the chances for equilibrium. Therefore, high pressures favor equilibrium, whereas reactions and discharges in gases at low pressures may produce a spectrum that indicates a considerable departure from equilibrium.

TRANSITION PROBABILITIES. In order to convert spectroscopic intensity measurements into temperature measurements, a knowledge of the relative transition probabilities $A_{n'n''}$ is required. There are two ways of obtaining these quantities. It may be possible to calculate them theoretically. This is the most satisfactory way where it can be done reliably. Otherwise, the transition probabilities must be determined empirically. A reliable calculation of this kind is possible only in relatively simple cases. These quantities can be calculated with any desired accuracy for the atomic hydrogen spectrum, which, however, has little or no significance for the determination of flame temperatures. In most cases, rotational transition probabilities for diatomic molecules may be found theoretically, although there are some exceptions. This is discussed below under *Theoretical transition probabilities*. Vibrational transition probabilities have been calculated in a few cases, but they are in general less reliable than the rotational probabilities. All other values must be found empirically.

Most Favorable Lines. Suppose we want to determine the temperature from two lines. We want to know what accuracy we can expect and what lines are the most favorable for this purpose. From Eq. 5-9 we get

$$\frac{1}{T} = -\frac{Y^{(1)} - Y^{(2)}}{E^{(1)} - E^{(2)}} \cdot a = -a\frac{\log I_1/I_2}{E^{(1)} - E^{(2)}} + a\frac{\log A^{(1)}/A^{(2)}}{E^{(1)} - E^{(2)}} \qquad (5\text{-}10)$$

where $a = k/\log e$.

We may assume that for our purpose the energy levels are known with ideal accuracy, and we shall assume the same thing about the transition probabilities. Even if the latter assumption is not true, we may be sure that the ratio $A^{(1)}/A^{(2)}$ remains at least constant, which means that there may be errors in the absolute values of the temperature, but that the values will be reproducible to a much higher degree. We may then have a somewhat distorted temperature scale, but the accuracy of the temperatures on this scale will be determined by the separation of the energy levels and the accuracy with which the intensities can be measured. The farther apart the initial levels from which the two lines come, the higher the accuracy.

The accuracy with which an intensity ratio can be measured is highest when the two lines have nearly the same intensity and when they lie close together in the spectrum. That this is so is immediately obvious for photographic measurements, where uncertainties in the plate calibration make themselves felt more if the lines have greatly different intensities. However, the statement is true also for photoelectric measurements when self-absorption and continuous background affect the reliability of the intensities more if they have greatly different intensities. More about this is found on pp. 506–508.

It may be said, therefore, that the line pairs most suitable for temperature determination are those where the two lines come from widely separated energy levels and they have nearly the same intensity.

It is perhaps not superfluous to emphasize again that temperature determinations from just a single line pair should never be relied on until a survey has been made with a larger number of lines, because such a survey indicates that the two lines are suitable lines. This survey should establish, first, that equilibrium exists; second, that the lines in question are free from blends; and third, that self-absorption or continuous background cannot affect the results.

The accuracy that can be expected from spectroscopic intensity measurements may be derived from Eq. 5-9. Suppose $E^{(1)} - E^{(2)} = 1{,}000$ cm^{-1} and that the ratio I_1/I_2 can be determined to within 1 per cent. This will mean an accuracy of 0.5 per cent in $\log I_1/I_2$, and an accuracy of roughly 1 per cent of $1/T$ or the same relative accuracy in T. At 3,000°K this could mean an uncertainty of ±30°K. Intensity measurements accurate to 1 per cent can only be made under favorable circumstances by photoelectric measurements. Otherwise, the accuracy will be less than that indicated above. On the other hand, the accuracy can be increased by choosing energy levels farther separated. A separation of 10,000 cm^{-1}, which quite often can be obtained, would increase the accuracy by the factor 10, which at 3,000°K would reduce the uncertainty to ±3°K.

We shall now consider some particular cases and discuss more fully some of the experimental details where this seems appropriate.

Translational Temperatures. The only way translational motion enters into spectroscopic observations is by the Doppler effect. This effect applies equally well to both molecules and atoms. If a molecule has a component v_s in the line of sight, a spectrum line of frequency ν is shifted by an amount $\nu v_s/c$ to the violet when the molecule approaches, to the red when it recedes. The number of molecules with a given v_s is determined by Maxwell's distribution law. Instead of a single sharp line with a frequency ν_0 which would be emitted by a molecule at rest, we get now a broadened line where the distribution of intensity as a function of the frequency is given by

$$I(\nu) = I_0 e^{-\frac{\ln 2}{\delta^2}(\nu - \nu_0)^2} \tag{5-11}$$

where δ is the so-called Doppler half width, that is, the distance from the center to where the intensity has decreased to half the maximum value. We have

$$\delta^2 = \frac{2RT\nu_0^2 \ln 2}{\mathfrak{M}c^2}$$

or (5-12)

$$\delta = 0.71 \times 10^{-6}\sqrt{\frac{T}{\mathfrak{M}}}\,\nu_0 \text{ cm}^{-1}$$

where R is the gas constant, $\mathfrak{M}$ the molecular weight, and T the absolute temperature. If it is possible to determine the half width δ experimentally, the temperature can be found from Eq. 5-12.

Unfortunately, there are serious drawbacks to using the Doppler width for temperature measurements. In the first place, Eq. 5-11 holds only if the sole reason for broadening the line is the Doppler effect, or, in other words, if the width of the line due to other causes is negligible compared with the Doppler width. It is well known that a completely undisturbed molecule at rest emits a line of finite width. This natural width for normal lines is so small that it usually can be neglected. However, interactions between molecules broaden the lines due to shortening of the life of excited states because of collisions, the influence of electric fields, or similar reasons. This broadening will, of course, become stronger when higher pressure brings the molecules closer together and increases the number of collisions. Under conditions such as occur in a flame or an arc at atmospheric pressure, the width due to these causes is usually several times the Doppler width. Under these circumstances, Eq. 5-11 and 5-12 become completely invalid and cannot be used for any temperature determinations. Should the pressure width and the Doppler width be of the same order of magnitude, Eq. 5-11 can be modified, but its value for temperature measurement would be doubtful.

While there may be conditions where Eq. 5-11 and 5-12 do hold, such as low pressure, absence of fields, and very light molecules, they cannot ordinarily be used for temperature measurements. Accordingly, attempts to use the Doppler width for this purpose [*28*] have not been very successful.

As the Doppler width is small (about 0.01A for a CH line at 3,000°K), any line width determination must be made with a spectrograph of very high resolution. An interferometer is necessary for this. Such measurements have been made occasionally in the past to determine the molecular weight $\mathfrak{M}$, rather than the temperature T, in order to identify the emitter of unknown spectrum lines; even for this purpose the method has often proved unreliable. Recently, Gaydon and Wolfhard [*28*] tried to use it for temperature measurements and came to the conclusion that it was unreliable. In view of what was said before, this could hardly be expected to be otherwise.

ELECTRONIC TEMPERATURES. The distribution of atoms or molecules over the various electronic states, if there is equilibrium, determines an electronic temperature. We may use this fact most profitably when dealing with suitable atomic spectra where there are many different electronic states. It is to be expected that in an electric discharge the electronic temperature may be very considerably higher than the gas temperature, as the field may accelerate the electrons to energies considerably higher than the kinetic energy of the atoms.

When the excitation is purely thermal the electronic temperature must, of course, be equal to the gas temperature. In flames we may add metal atoms by adding a spray of a metal salt solution to the fuel. Only a very small amount need be added to produce the metal spectrum with good intensity. The metal atoms are completely inert as far as the combustion process is concerned, and can be assumed much more readily to have the actual gas temperature than radicals which participate in the combustion process.

Those metals seem to be more useful which have many electronic levels spread over a wide energy range. Iron is typical of these. Iron carbonyl, which is a liquid, can easily be added to the fuel of practically any flame. The iron spectrum which results shows immediately in most flames that it corresponds to a much lower electronic temperature than does the spectrum of the ordinary iron arc. In order to be able to use the iron intensities for temperature determinations, the transition probabilities must be known, and in this case they can be determined only empirically. The temperature of a given hydrocarbon flame can be determined with the help of the OH bands when conditions are right. Then the transition probabilities may be determined as indicated above. For a selection of the proper iron lines, the table given by Crosswhite [*29*] is very useful. Self-absorption must be particularly watched for. The effect of self-absorption can be obtained from a few index lines. Then the amount of self-absorption of all other lines can be predicted and, if necessary, corrected for. It is, however, best always to avoid lines with appreciable self-absorption.

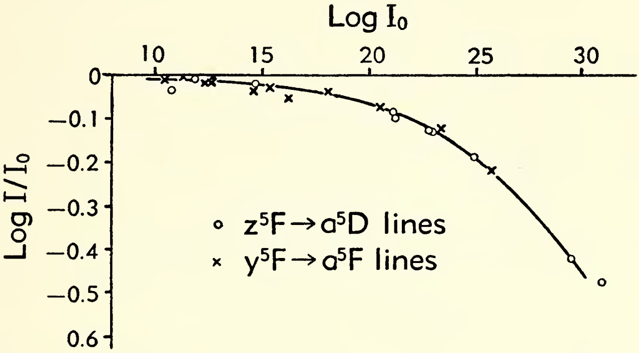

Fig. M,5b. Self-absorption of iron lines as a function of their intensity.

The factors that affect self-absorption [*25*] most are as follows: (1) Concentration of the metal vapor, the higher the concentration the stronger the self-absorption. (2) Intensity of the line; Fig. M,5b shows a typical example of how self-absorption, measured by log I/I_0 (when I_0 is the intensity the line would have without self-absorption), depends on the intensity of the line. (3) Height of the lower state. Lines ending on the ground state are more absorbed than those ending on higher states. This effect is often much smaller than generally assumed and is absent if there is uniform excitation. Fig. M,5b indicates that there is no appreciable difference in self-absorption between the lines ending on the ground level a^5D of iron, or on the a^5F level, which is about 7,000 cm^{-1} higher. This must be the case if there is thermal equilibrium and if all lines have approximately the same wavelength. Therefore, Fig. M,5b is proof that thermal equilibrium exists.

Crosswhite [*26*] has measured the relative transition probabilities of a number of lines in the near ultraviolet. He found that if he used these lines to obtain temperatures in other types of flames, there was very good agreement with the temperatures obtained in other ways.

The greatest drawback of this type of measurement is that self-absorption is not negligible unless the lines are so weak that their measurement presents difficulties. The amount of self-absorption can be determined experimentally with considerable accuracy and then corrected for. If there is general thermal equilibrium, these corrections are relatively simple, since in a given wavelength region they are only a function of the intensity, and not of the origin, of the lines. In that case, relatively strong lines may be used successfully.

If the effect of self-absorption is disregarded, the stronger lines, which are usually those coming from the lower levels, are weakened, so that those from the higher levels appear abnormally strengthened. This effect may suggest a much higher temperature than is actually present.

In most combustion processes, the atoms with relatively low ionization potentials are partly ionized. The degree of ionization increases with rising temperatures. Therefore, at first sight, it seems that measurement of the degree of ionization should be a way to determine the temperature. There are a number of elements of sufficiently low ionization potential, which can be added to the fuel. In order to determine the degree of ionization spectroscopically, it is necessary that the ion itself have also a relatively low excitation potential. The alkaline earths are particularly well suited since prominent lines of the ion as well as of the neutral atom fall in the visible or near ultraviolet, with the result that their relative intensities can easily be measured.

Unfortunately, the ionization equilibrium depends not only on the temperature but also on the concentration of the metal in the flame. This equilibrium is given by the Saha formula. Measurements made by Riesz [*26*] at the Johns Hopkins University with strontium in an acetylene flame confirmed the validity of the Saha formula under these conditions. This means that no reliable method for temperature determinations can be derived in this way.

Vibrational Temperatures. On the whole, there is no simple way to calculate reliable vibrational transition probabilities, so that such values as are needed must be determined empirically. In some cases, such as those of OH [*30*] and C_2 [*31,32,33*], theoretical values for the vibrational transition probabilities have been calculated, but it is not easy to say how accurate they are.

Vibrational temperatures may occasionally be useful when the dispersion is not high enough to resolve the rotational structure. In such cases intensities of band heads may be used, although great caution is required when quantitative conclusions are to be drawn from the intensities of partially resolved structures.

In the infrared, vibrational temperatures may be quite useful either in absorption or in emission.

Rotational Temperatures. Groups of lines from diatomic or polyatomic molecules—due to transitions in which the electronic and vibrational changes are the same while the rotational transitions vary—are commonly called bands. The structure of bands is simplest for diatomic molecules, and these alone are considered here. Molecular bands are perhaps better suited for spectroscopic temperature measurements than any other groups of lines and therefore deserve some detailed treatment.

One of the reasons is that usually a band is composed of a group of lines, all in the same wavelength region and of comparable intensity. Furthermore, in most cases the relative transition probabilities can be calculated with considerable accuracy, which simplifies matters greatly. For flames, the ultraviolet OH bands are probably of the greatest importance. Next in importance are the CH bands and to a lesser degree the C_2 bands [*27,34*]. Before going into these specific bands we shall discuss a few general features.

Theoretical transition probabilities. These are particularly simple for unperturbed singlet bands. The matrix components of the square of the dipole moment can be calculated fairly easily. Multiplied by ν^4, they are proportional to the transition probabilities $A^*_{n'n''}$ required in Eq. 5-7.

$$A^*_{nm} = d^2_{nm}\nu^4_{nm}$$

The values of d^2 for the most common types of bands are given in Table M,5a.

Table M,5a. Intensity factors d^2 for unperturbed singlet bands.

Type of band	$P(K)$	$R(K)$	$Q(K)$
$\Sigma \rightarrow \Sigma$	K	$K + 1$	0
$\Sigma \rightarrow \Pi$	$\frac{1}{2}(K + 1)$	$\frac{1}{2}K$	$\frac{1}{2}(2K + 1)$
$\Pi \rightarrow \Sigma$	$\frac{1}{2}(K - 1)$	$\frac{1}{2}(K + 2)$	$\frac{1}{2}(2K + 1)$
$\Pi \rightarrow \Pi$	$\frac{(K - 1)(K + 1)}{K}$	$\frac{K(K + 2)}{K + 1}$	$\frac{(2K + 1)}{K(K + 1)}$
$\Pi \rightarrow \Delta$	$\frac{(K + 1)(K + 2)}{2K}$	$\frac{(K - 1)K}{2(K + 1)}$	$\frac{(2K + 1)(K + 2)(K - 1)}{2K(K + 1)}$
$\Delta \rightarrow \Pi$	$\frac{(K - 1)(K - 2)}{2K}$	$\frac{(K + 2)(K + 3)}{2(K + 1)}$	$\frac{(2K + 1)(K + 2)(K - 1)}{2K(K + 1)}$
$\Delta \rightarrow \Delta$	$\frac{(K - 2)(K + 2)}{K}$	$\frac{(K - 1)(K + 3)}{K + 1}$	$\frac{4(2K + 1)}{K(K + 1)}$

These values should be correct when there is no resultant electronic spin—that is, if the bands are singlet bands—and if there are no strong interactions. One common type of interaction gives rise to the so-called Λ-doubling. For very large values of the Λ-doubling (the so-called L-decoupling) the values in Table M,5a are incorrect. Such strong interaction is to be expected only in very light molecules (e.g. H_2 and He_2) and particularly for high lying electronic levels. Other types of interactions which are not always easily recognized in a casual study of the bands also may affect the transition probabilities. Such interactions may sometimes be recognized by perturbations in the position of certain lines or by the presence of predissociation.

When there is a resultant electronic spin S we have doublet bands for

$S = \frac{1}{2}$ and triplet bands for $S = 1$. Higher multiplicities are only rarely encountered. The values of Table M,5a are still approximately correct if the doublet or triplet separation is small and if the total intensity of a doublet or triplet is taken. The lowest values of the rotational quantum number K may then have to be excluded.

Formulas for doublet $^2\Sigma \rightarrow {}^2\Pi$ bands have been given by Earls [*35*]. These are important since the 3064 OH and the 3900 CH bands which commonly occur in flames are of this type. All transition probabilities for the 3064 OH band have been tabulated by Dieke and Crosswhite [*15*].

When, for some reason, it is impossible to calculate the required transition probabilities, it is necessary to measure them. This can be done in emission and sometimes in absorption.

For this purpose it is necessary to have in thermal equilibrium a light source of which the temperature is known. This makes it possible to calculate the distribution over the various energy states, i.e. to obtain relative values of N_n. If the $I_{n'n''}$ are measured, then the transition probabilities may be obtained from

$$I_{n'n''} = A^*_{n'n''} N_{n'}$$

The temperature may be determined originally with line groups of known transition probabilities; for instance, if the OH bands can be observed in a flame and if one can be sure of equilibrium.

In a certain sense, absorption measurements are more reliable if we deal with stable gases. We can then work at lower temperatures which can be measured with ordinary thermometers. Unfortunately, there are very few stable gases which at moderate temperature have band absorption in the accessible regions. Besides, we have the optical difficulties of dealing with the narrow absorption lines discussed in Art. 4. For these reasons very few transition probabilities of interest to us have been determined from absorption measurements. It is likely that transition probabilities of infrared bands of such molecules as H_2O can now be obtained with sufficient accuracy from absorption measurements and that they would be quite useful for flame studies. An advantage of absorption transition probabilities is that absolute values can be determined which will be useful for quantitative determination of the amount of the substance present.

The empirical determination of transition probabilities through intensity measurements in emission or absorption is not restricted to the rotational lines of a band but can be used for any kind of transition. Often it is the only way to obtain vibrational or electronic transition probabilities (see below: *The CH Band*).

Application of method (*standard method*). A suitable band is first selected. It should be at least partly resolved, for only intensity measurements on free lines are reliable. The choice of the spectrograph will depend on the particular molecule. For hydrides good results can be obtained with medium dispersion. For most other molecules usually the highest possible resolution compatible with the intensity of the source should be used.

At the beginning of the investigation, as many as possible of the individual band lines should be measured and their log I/A values plotted against the initial energy $E_{n'}$. The resulting plot will show that there is statistical equilibrium if all the lines clearly fall on a straight line. If they do, with a few exceptions, it is safe to use the band for temperature measurements, unless when a new survey is made light source conditions are quite different. The points that fall consistently off the straight line are probably blends or otherwise unsuitable lines, and should be avoided in the future. An idea of the accuracy of the intensity measurements is obtained by observing the way in which the points fit the straight line.

Should the preliminary measurements indicate that the band is suitable, the technique may be simplified by using fewer lines, with two lines the minimum number. These two are best chosen as lines of moderate and nearly equal intensity, one near the beginning and one near the end of the band (see further under *Isointensity method*). If the temperature varies between wide limits, different pairs may have to be selected for different temperature ranges.

Sources of error. If the preliminary investigation reveals that the points on the log I/A versus energy plot do *not* lie on a straight line, this may be due to a number of reasons which should be investigated. The reason for the departure from a straight line may, of course, be due to a genuine departure from equilibrium. If this is so, no temperature measurements can be made, as no temperature is defined. More is said about such cases in Art. 6.

The decision that there is no equilibrium should not be made, however, without making sure that departures from a straight line are not due to other causes.

Widely scattered points are an indication that the measuring technique is unreliable and should be improved. If the resolution of the spectrograph is not adequate, it is possible that no satisfactory remedy can be found. If most points lie on a smooth curve which, however, is not a straight line, the indication is that the measurements are at least consistent. Faulty plate calibration may be a reason for the curvature. Perhaps the best way to be sure that plate calibration cannot be responsible is to avoid photography and to make the intensity measurements photoelectrically, in which case, with reasonable precautions, the intensity scale must be correct.

If there are no errors in the intensity measurements, there still may be deviations from linearity even if there is equilibrium. One source of error is due to the presence of a continuous background when the measurements are made by photographic methods. Suppose that there is a uniform continuous background on which the lines are superimposed. This adds a constant amount to the intensity of each line. The percentage error due to this is relatively large for a weak line but small for a strong line. On the log I/A diagram this will push up the points for the weaker lines relatively more than those for the stronger lines. This is shown in Fig. M,5c.

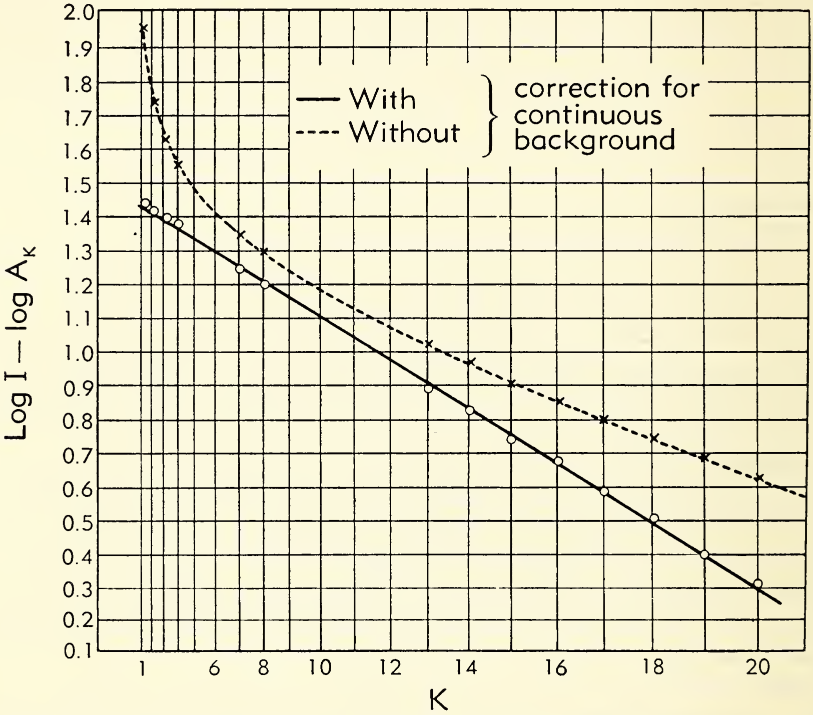

Fig. M,5c. Influence of a continuous background on apparent intensity distribution.

The crosses connected by the dotted line represent the original measurements, and the plot shows a decided curvature. The strength of the continuous background was then determined, and a constant amount was subtracted from the I values (*not* from log I). The dots in Fig. M,5c represent the so-corrected log I/A values, which now fall on a straight line.

There is a continuous background in almost every flame spectrum. On weak exposures it may easily be overlooked but nevertheless cause the trouble discussed here. The correction outlined may be made with photographic measurements. It is, however, often uncertain and always clumsy and inconvenient. The problem of a continuous background does not present itself with photoelectric measurements, for the intensity in this case is measured as the height of the peak above the continuous background. No corrections are required.

Self-absorption. The technique of determining temperatures from the intensities of individual spectrum lines is based on the assumption that the light of the various lines reaches the observer with the same relative intensity as when it was emitted by the molecules. This is true only when it does not undergo any appreciable absorption on its path through the flame from the point of emission. Strictly speaking, this would be true only for an infinitely thin luminous layer. For practical purposes we can be satisfied if the optical path length is thin, which would mean that the absorption would be small within the flame.

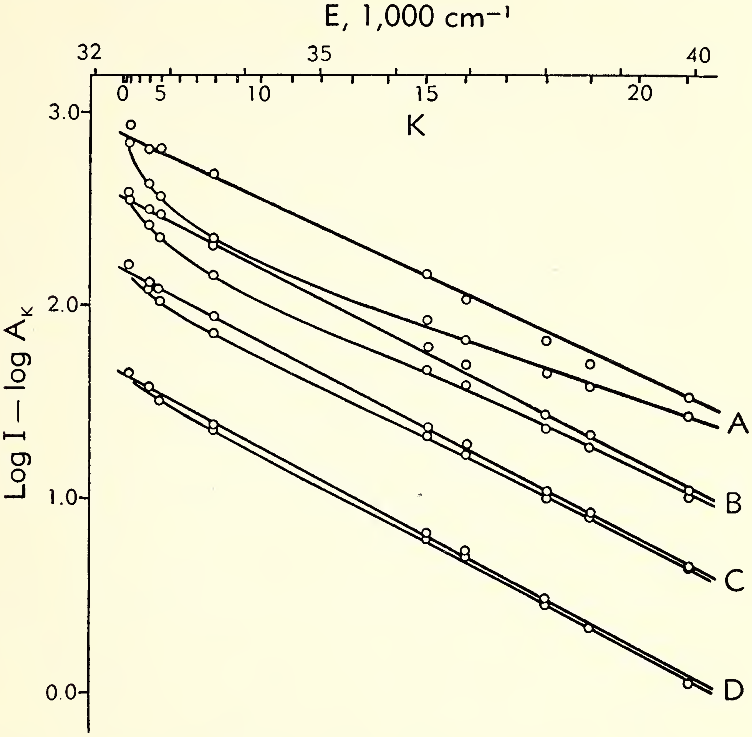

Fig. M,5d. Intensity plots for the OH band in acetylene flames of varying sizes. The lower curves give the data uncorrected, the upper curves after corrections for self-absorption are applied.

When temperature measurements are made from the intensity distribution in a continuous spectrum such as that of a black body or from line reversal measurements, just the opposite condition should be fulfilled, namely, the optical path should be long. Then equilibrium between radiation and the molecules, which is essential for those methods, can establish itself.

When there is appreciable absorption in the flame, when line intensities are used, errors are introduced which may be considerable (see also above under Electronic Temperatures). Fig. M,5d gives the effect of self-absorption for flames of varying size. The data [*26*] are as follows:

	A	*B*	*C*	*D*
Diameter of burner tip	0.093″	0.043″	0.027″	0.013″
C_2H_2 flow, cm^3/min	5,000	2,000	600	160
O_2 flow, cm^3/min	12,500	5,000	1,500	400

In each case, the lower curve represents the actually measured intensities, and the upper one represents the intensities after corrections for self-reversal have been made. It is seen that the departure from a straight line can here be quite satisfactorily explained by self-reversal and does not require the assumption of nonequilibrium.

It is clear that large errors would have been made in the temperature for the large flame *A* if the right part of the uncorrected curve had been used, whereas in the smallest flame (*D*) the corrections were negligible. A further example of strong self-absorption is shown in Fig. M,5f.

Light sources such as flames are never homogeneous. The temperature varies from the center toward the periphery. In spectroscopic temperature measurements an average is taken along the line of sight. The resultant intensity distribution is the superposition of the distributions occurring at various localities along the line of sight. In general, the log I/A plot that one gets this way will not be a straight line. It is readily seen that the places which are at low temperatures contribute relatively more for low energies than for high energies. If one drew tangents to the log I/A curves and extrapolated to high values of K, one would get the maximum temperature along the line of sight, provided that the state of affairs were not modified by self-absorption or other causes. For a discussion of these factors see Lochte-Holtgreven and Macker [*36*] and Huldt [*37*].

Isointensity method. We have now seen that a temperature determination can be made from the two suitably chosen spectral lines. It was also apparent that as the lines become more nearly equal in intensity, and as the initial levels of these lines become more separated, the better is the accuracy that can be achieved. While the procedure of plotting the whole log I/A versus E curve is always more reliable, in routine operations the use of a single line pair may save a great deal of time and be sufficiently accurate if the lines are properly chosen.

The so-called isointensity method comes close to using one line pair only and avoids some of the pitfalls that otherwise may affect the results adversely. Fig. M,5e illustrates the method which differs from the general method for rotational temperatures only in the way the measurements are carried out. Fig. M,5e shows the intensity distribution for two different temperatures.

If we take one particular line with a low K value (b), we find that there is another K value toward the tail of this branch which has the same intensity. This K value, K_b, is not necessarily an integer; that is, it does not necessarily correspond to an actual line, but it can be determined by interpolation if the intensity curve is known in the vicinity of K_b. This value $K_b = x$ for a fixed b is a function only of the temperature, and the form of this function can be determined with relative ease.

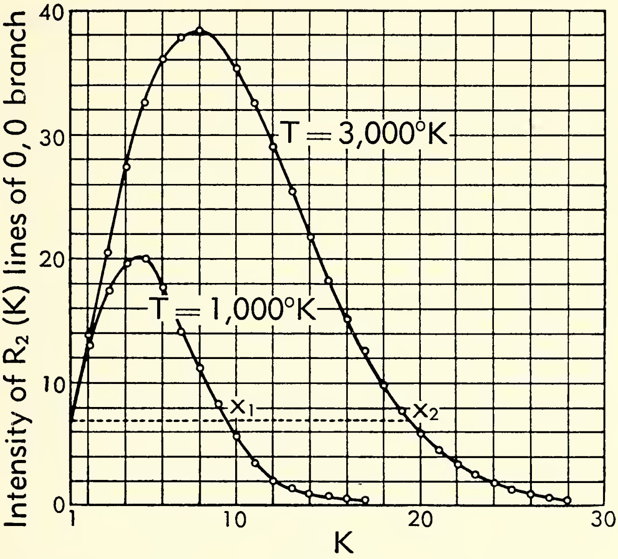

Fig. M,5e. Intensity distribution in the 3064 OH band at two different temperatures.

We have

$$A_b e^{-E_b/kT} = A_x e^{-E_x/kT}$$

or

$$\frac{E_x - E_b}{kT} \log e = \log A_x - \log A_b$$

$$\frac{(E_x - E_b) \log e}{k(\log A_x - \log A_b)} = T$$

Everything except T is known for integer values of x and, therefore, T can be calculated as a function of x for x, an integer. For noninteger values of x, T can be found by interpolation.

In Fig. M,5e, $b = 1$ is chosen as an example. For $T = 1{,}000°$ x is between 9 and 10 and for $T = 3{,}000°$ x is between 19 and 20.

For this method, the temperature determination depends only on the determination of equality of intensity and is completely independent of plate calibration. Also, the continuous background is immaterial, provided it is the same for both lines. Therefore, the advantages are greatest when the photographic method is used.

As far as the influence of self-absorption is concerned, it is also eliminated if there is uniform excitation. In this case, the self-reversal depends only on the intensity and, therefore, does not affect the equality of two lines. If, however, the absorption takes place chiefly in an outer layer of lower temperatures, the line with the lower K will be more strongly absorbed and the temperature determined will be too high. It has been shown [*26*] that this condition may be appreciable in some flames.

Tables and curves for applying this method with the 3064 OH band were given by Dieke and Crosswhite [*15*].

Special examples. The OH and CH bands are present in most flame spectra. They have a relatively wide structure so that the rotational lines are fairly well separated even for spectrographs with moderate dispersion. For this reason these bands are usually most useful and therefore will be treated here in some detail. Other bands can be treated in a similar manner.

The OH bands.[13] The 0,0 band with its principal head at 3064A is the band best suited to temperature measurements. It has the typical structure of a $^2\Sigma \rightarrow {}^2\Pi$ transition; that is, it consists of twelve different branches. There is a great deal of overlapping so that not all branches are very suitable. From 3122A on, the presence of the 1,1 band complicates matters still further. Plate M,4 is a photograph of the band in the vicinity of the head. Plate M,5a shows a microphotometer trace at fairly low temperatures and one at fairly high temperatures.

The lines of most of the stronger branches are accompanied by so-called satellite lines. These are lines less intense than the main lines and at varying distances from them (see Plates M,4 and M,5a). Whether the satellite is completely separated from the main line depends on the dispersion of the spectrograph and on the slit width. The lines with satellites are, therefore, not very safe for intensity measurements. The R_2 and P_1 branches are the only ones free of satellites. Of these, the R_2 branch is the better and is, therefore, usually used for temperature measurements. The lines have medium strength and all lie in a very small wavelength interval. They are listed in Table M,5b with the data necessary for their use. The lines marked C in the fifth column are useless under any circumstances; the ones marked B can be used only in large spectrographs with narrow slits; and those marked A can be used in medium spectrographs, particularly those marked A^*, which are more than 0.50A from the nearest interfering line.

There is every reason to believe that the transition probabilities given in Table M,5b are correct within the limits of experimental errors. The largest sources of error probably are self-absorption and continuous background. Both are present to an appreciable extent in all flames.

---

[13] See also Table M,3, Art. 4, and Plate M,4.

Fig. M,5c shows the effect of the continuous spectrum. The dotted curve is obtained from photographic measurement without correction for the continuous background. After the correction has been applied the solid line is obtained, which shows that there is rotational equilibrium. Without the correction, one might be inclined to believe that there are appreciable deviations from equilibrium. The uncorrected part beyond $K = 12$ approaches a straight line, and if this part were used for the temperature determination, the temperature would come out much too high.[14]

Table M,5b. Data on the R_2 branch of the 3064 OH band.

K	λ	A	$I_{3,000}$		E'	log A
1	3084.050	2.7	68	A^*	101.48	0.43
2	80.231	5.7	138	B	202.95	0.75
3	77.028	8.9	204	A^*	337.99	0.95
4	74.369	12.8	273	A^*	506.55	1.11
5	72.199	16.7	325	C	708.23	—
6	70.478	20.7	359	C	942.76	—
7	69.177	24.8	378	A	1209.88	1.39
8	67.929	28.8	383^{+}	C'	1509.17	—
9	67.775	32.9	373	C	1840.14	—
10	67.661	37.0	352	C	2202.42	—
11	67.929	41.0	323^{+}	C'	2595.36	—
12	68.608	45.1	290	C	3018.52	—
13	69.675	49.1	255	B	3471.09	1.69
14	71.145	53.2	218	A^*	3952.74	1.73
15	73.028	57.2	183	A	4462.40	1.76
16	75.334	61.3	151	B	4999.65	1.79
17	78.071	65.3	125	A	5563.43	1.82
18	81.255	69.3	98	A	6153.12	1.84
19	84.894	73.4	77	A	6768.49	1.87
20	89.008	77.4	59	A^*	7406.70	1.89
21	93.609	81.4	45	B	8068.73	1.91
22	98.715	85.4	34	C	8753.01	—
23	3104.348	89.5	25	A^*	9458.36	1.95
24	07.852	93.5	19	C		—
25	14.622	97.5	14	C		—

Results. Temperatures obtained from some characteristic hydrocarbon flames (small torch) are given in Table M,5c. The values in parentheses were obtained under unfavorable conditions and are not very accurate. In all cases, corrections were made for self-absorption. The temperatures given in Table M,5c are, of course, only representative values, as they do depend on the particular spot in the flame.

Measurements of OH temperatures have been made in the past by many observers [*27,38*]. Occasionally, very high values were obtained, particularly in the inner cone. We have seen that the presence of both self-absorption and a continuous background in photographic measurements without corrections yields apparent rotational temperatures which may be much too high. It is very difficult to judge from some of the data given in the literature how much these effects might have influenced the results. Unquestionably, in a reaction zone at low pressures where strong deviations from equilibrium may be expected, values as high as 9,000°K are not too surprising. On the other hand, at higher pressures the high values may very well be partly due to self-absorption. Also, the fact that Q lines (which have satellites and which show particularly strong self-absorption) were usually used may have influenced the results. In particular, we have never been able to find the high temperature of 5400°K, which Gaydon and Wolfhard [*38*,*39*] found for all hydrocarbon flames at atmospheric pressure.

---

[14] The deviations from a straight line for small values of K have been attributed to shortcomings in the transition probabilities. There are indications that a remnant of these deviations remains even with photoelectric measurements. However, these deviations, if present, are much smaller than those indicated in Fig. M,5c. The effects of self-reversal produce the same type of deviations as does the influence of the continuous spectrum.

Table M,5c. OH temperatures in some characteristic flames.

	Lean °K	*Stoichiometric* °K	*Rich* °K
Ethylene-C_2H_4			
inner cone	(4400°) ± 200°	(4400°) ± 200°	4000°
outer cone	2800°	2750°	2650°
Acetylene-C_2H_2			
inner cone	4020°	3570°	3550°
outer cone	2730°	2900°	2850°
Propane-C_3H_8			
inner cone	3050°	3050°	3000°
outer cone	2750°	2750°	2650°
Methane-CH_4			
inner cone	—	2800°	(2900°) ± 100°
outer cone	—	2650°	2650°

Very high apparent temperatures (4800°K) are obtained in an ethylene flame when CO_2 is mixed with the gas. Self-absorption is very strong under these conditions, but even after correction for self-reversal the temperature is high (3900° or 4800°, depending on how the self-absorption correction is determined). Fig. M,5f shows the effect of self-absorption. The corrections were here determined by actually measuring the absorption of light passing through the flame and by then assuming that the light of the flame itself would undergo, on the average, half the absorption. This gave a temperature of 3900°K. If uniform excitation was assumed and the amount of self-reversal determined experimentally from the lines with low rotation and extrapolated for high rotation, 4800°K was obtained. The discrepancy in the two values shows the uncertainty in the temperature if such high self-absorption is present.

The absorption measurements (Fig. M,5g) show a temperature of 2520°K for the unexcited OH radicals. The CH temperatures gave approximately 2700°K for the same flame. The discrepancy of the various values shows that there can be no general equilibrium here. Similar departures from equilibrium have been observed in reaction zones by several investigators.

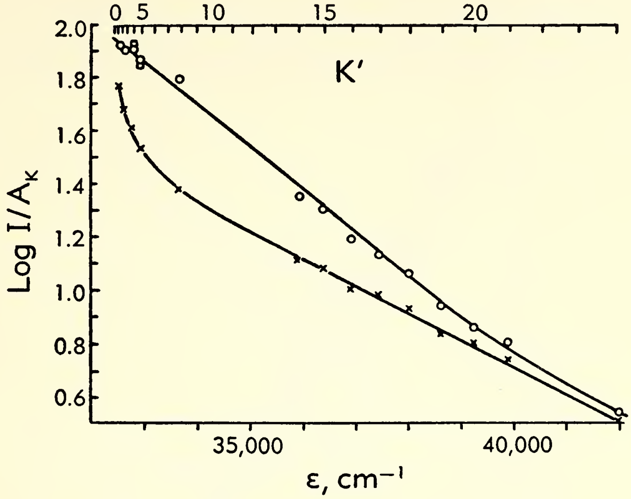

Fig. M,5f. OH intensity distribution in an ethylene flame.

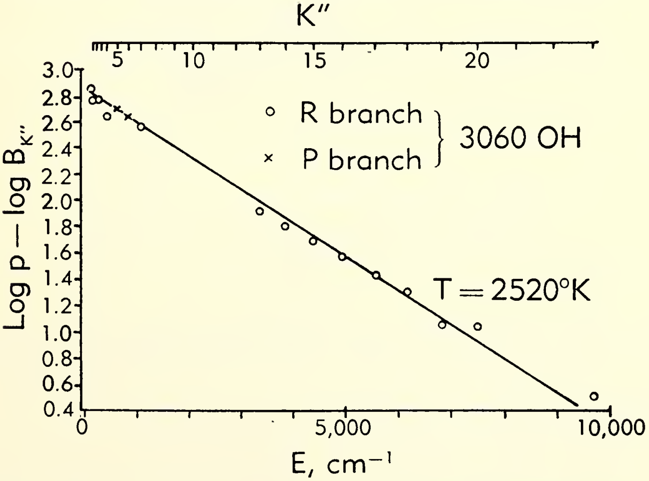

Fig. M,5g. OH absorption distribution in an ethylene flame.

The CH bands. The two bands at 3870A ($^2\Sigma \rightarrow {}^2\Pi$) and 4300A ($^2\Delta \rightarrow {}^2\Pi$) are very strong and lie in a very suitable region for temperature measurements. The 3870 band has a simpler structure but the 4300 band is stronger. Although its center is too crowded, the short wavelength end has a rather open structure and may be used even with instruments of moderate dispersion. Plates M,5b and M,5c give details of the two bands with those lines numbered which are most suitable for intensity measurements. While in the OH bands the calculated transition probabilities give satisfactory results, this is not true in general for the CH bands, so that the transition probabilities must be determined empirically.

The reason for the discrepancies is very probably interaction with an unstable state which removes a certain percentage of the molecules from the upper state before the molecule has had a chance to radiate. Therefore, the lines coming from such states are weakened.

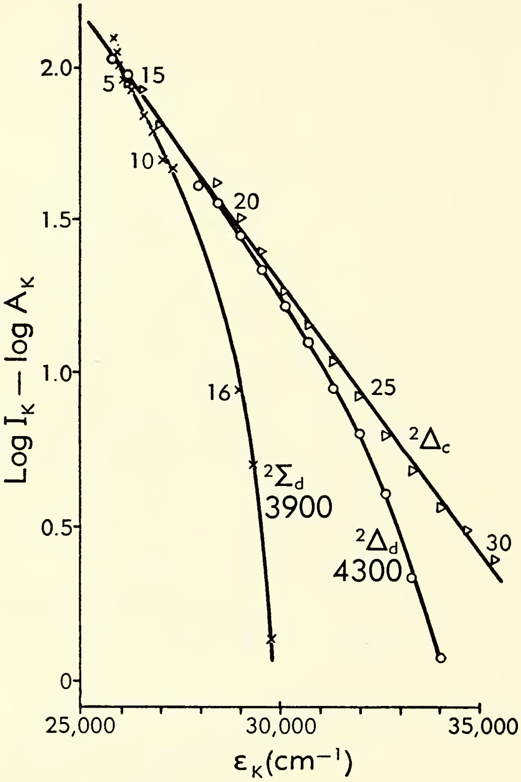

Fig. M,5h. Intensity distribution in CH bands showing effect of predissociation in the $^2\Delta_d(^2\Delta^-)$ and $^2\Sigma_d(^2\Sigma^-)$ levels. (From photographic measurements.)

In the 4300 band, half the upper states ($^2\Delta^-$) are so affected and the other half ($2\Delta^+$) are normal. The calculated values of the transition probabilities can, therefore, be used for lines coming from the $^2\Delta^+$ state, whereas this is not possible for lines from the $^2\Delta^-$ state (half the lines in the 4300 band) and the $^2\Sigma^-$ state (all the lines of the 3870A band).

This is illustrated in Fig. M,5h, which was drawn with the theoretical transition probabilities.[15] The triangles represent lines from the $^2\Delta^+$

---

[15] For all but the lowest K values of the $^2\Delta \rightarrow {}^2\Pi$ it is sufficient to use the values of Table M,5b for the corresponding singlet transition. The formulas for the exact

(= $^2\Delta_c$) levels. (The long wavelength component of the R branches, appearing double for $K > 20$, are shown in Plate M,5c.) They lie reasonably well on a straight line and define a definite rotational temperature. It is seen in Fig. M,5h that the lines coming from the $^2\Delta^-$ (Δ_d) and $^2\Sigma^-$ states do not fall on a straight line. This does not mean that there is departure from equilibrium but simply that the transition probabilities are smaller than their theoretical values because of an increasing loss of molecules in these states by predissociation. Fig. M,5i gives again the distribution in an acetylene flame with the $^2\Delta^-$ lines left out. The temperature obtained from the $^2\Delta^+$ lines is 3680°K, which compares with the value 3650°K obtained for the same flame with the OH bands.[16] This close agreement between the temperatures obtained from the two different molecules is good evidence for statistical equilibrium in the flame.

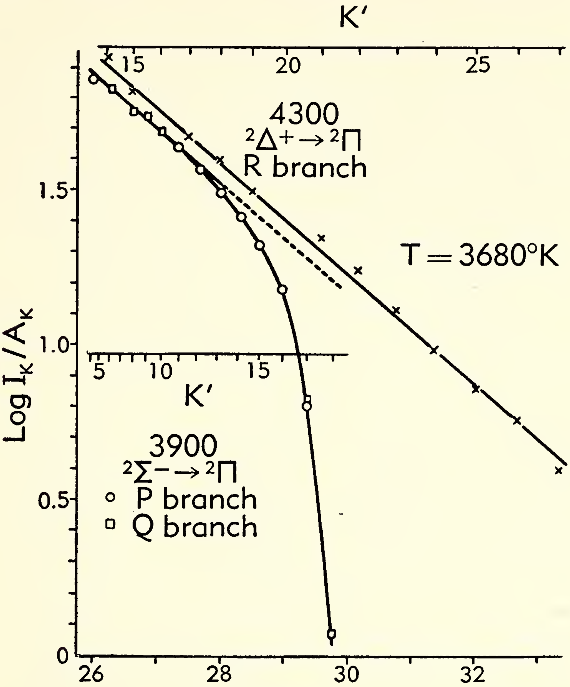

Fig. M,5i. CH intensity distribution (photoelectric measurements).

The 3870 band, because of the simplicity and openness of its structure, would be one of the simplest bands for temperature measurements were

---

values of the $^2\Delta \rightarrow {}^2\Pi$ transition are fairly complicated and have never been given explicitly.

[16] Determinations of CH temperatures by Gaydon and Wolfhard [*28*] neglected the corrections to the transition probabilities. Some of their discrepancies may be explained in this way.

it not for those abnormally low intensities of the higher lines. The situation can be saved by calculating the transition probabilities of the 3870 band empirically from such measurements as those given in Fig. M,5i. Table M,5d gives the necessary data for the use of the 3870A CH band for intensity measurements.

The lines that are listed can be obtained with a spectrograph of moderate dispersion. The slit should not be too narrow, so that the doublets of widths given in the third column are not resolved.

The CH molecule, in contrast to the OH molecule, is very short-lived in the flame. Attempts to obtain it in absorption have failed.[17] From this fact it may be concluded that the concentration of CH radicals in the ground state is always very small, so that self-absorption will be negligible. Accordingly, no evidence of self-absorption has been found. This makes CH temperatures particularly useful in cases where OH temperatures are unreliable because of too large self-absorption.

Table M,5d. Data for the 3900 CH band.

				log A	
K	λ	$\Delta\lambda$	E'	Theoretical	Experimental
			Q branch		
6	3998.23	0.31	527.11	1.021	1.021
8	4005.79	0.24	898.80	1.135	1.135
9	10.44	0.21	1120.04	1.181	1.181
10	15.70	0.18	1364.03	1.221	1.221
17	74.44	0.07	3655.62	1.417	0.940
18	87.03		4054.76	1.435	0.274
			P branch		
4	3908.02	0.50			
5	14.22	0.41	251.96	0.678	0.678
12	72.35	0.21	1630.46	0.988	0.988
13	83.10	0.19	1918.49	1.016	0.999
14	99.60	0.18	2227.54	1.040	1.003
15	4006.91	0.18	2556.72	1.063	1.007
16	20.11	0.17	2905.20	1.084	0.984
17	34.31	0.16	3271.85	1.102	0.920
18	49.64	0.16	3655.62	1.118	0.624

M,6. Departure from Equilibrium Conditions.

Long-Time Averages. In an equilibrium state, the distribution over the variation energy states and, therefore, the intensity of the spectral lines are determined by one parameter, the temperature T. If the temperature is given, everything is determined. Equilibrium may be the final stage in a number of reactions, but any particulars that characterize the reactions have disappeared from the equilibrium state. For this reason, no information on the nature of the reaction can be gained from observations on the equilibrium state.

---

[17] Recently (1952) CH absorption has been observed in the author's laboratory within 20 microseconds after the passage of a spark.

Therefore, a study of nonequilibrium distributions should be of considerably greater interest. When there is departure from equilibrium, the particular mechanism that has led to this distribution is revealed. So far, relatively little work has been done in this field. Some cases of reported departures from equilibrium may be due to such causes as self-absorption. The field, however, is very promising.

As equilibrium is established by collisions, the best chance to observe marked departures from equilibrium naturally is presented at very low pressures. The particular distribution produced by the reaction is then preserved in the intensity distribution. Higher pressures will tend to obliterate it and equilibrium is then approached. A few examples may illustrate this point.

If an electric discharge is passed through water vapor at pressures of a millimeter or less, the H_2O molecule is broken up into $OH + H$. The study of the ultraviolet OH bands reveals the rotational and vibrational energy distribution of the excited OH radicals so formed.

Fig. M,6a shows this distribution represented by the usual plot of $\log I/A$ against energy at a water vapor pressure of 0.05 mm. If there were equilibrium, all points should lie on one straight line. Here we see that subsequent rotational levels for $V = 0$ lie on one curve, those for $V = 1$ on another curve, etc. This shows that there is no equilibrium between rotation and vibration, and the departure from linearity shows that there is nothing like rotational equilibrium. It appears that the low K values lie approximately on a straight line which corresponds to a temperature of 600°K. A somewhat better idea of the significance of this distribution can be had if we turn to Fig. M,6b, where N_K is plotted instead of $\log N_K$. The solid curve for $V = 0$ that results has two maxima, one near $K = 4$ and the other, broader one near $K = 16$. The curve can be regarded as a superposition of two curves, one an equilibrium distribution for 600°K, the other a curve with a broad maximum at $K = 16$. The first curve corresponds to the actual temperature of the gas (the gas was at room temperature but was heated somewhat by the discharge). The second curve corresponds to the distribution created by the reaction. This means that the particular mechanism creates OH radicals preferentially with rotations around $K = 16$ which would be entirely absent from the equilibrium distribution at 600°K.

We expect that collisions will remove the excess rotational energy, transfer it to other degrees of freedom, and thus raise the temperature. Fig. M,6c shows that this is exactly what happens. It corresponds to Fig. M,6b, but the data were taken at a water vapor pressure of 10 mm. The temperature has risen to 1220°K. The maximum at $K = 16$ is very much reduced, showing that the number of molecules in thermal

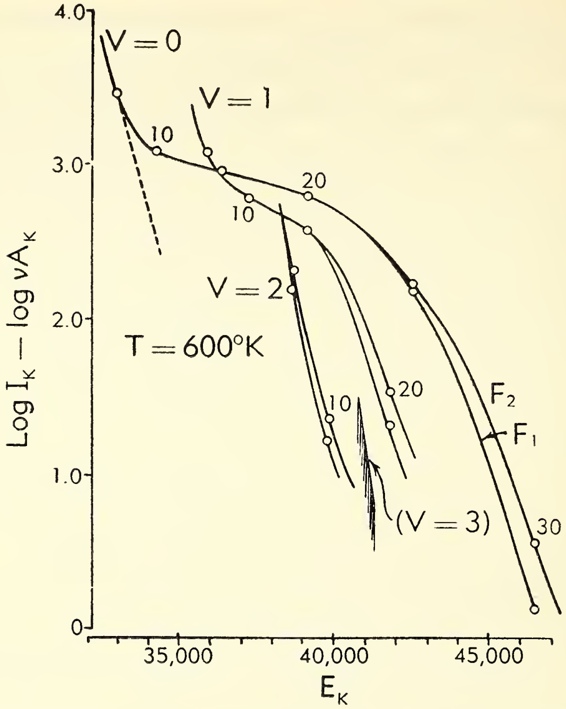

Fig. M,6a. OH distribution in low pressure (p = 0.05 mm) discharge through water vapor showing strong deviations from equilibrium. The values for V = 3 lie lower than those indicated.

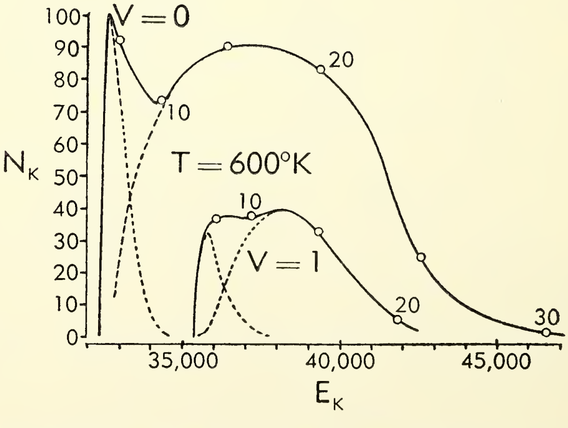

Fig. M,6b. Same as Fig. M,6a but nonlogarithmic plot.

equilibrium has increased at the expense of the molecules with the anomalous rotations.

Finally, Fig. M,6d shows analogous data for a discharge in 15-mm helium with traces of water vapor. Here, the excited molecules with the anomalous rotations will predominately collide with helium atoms and lose their excess energy to them. The second peak has, therefore, almost entirely disappeared, but there has been no strong rise in the rotational OH temperature, which is only 400°K.

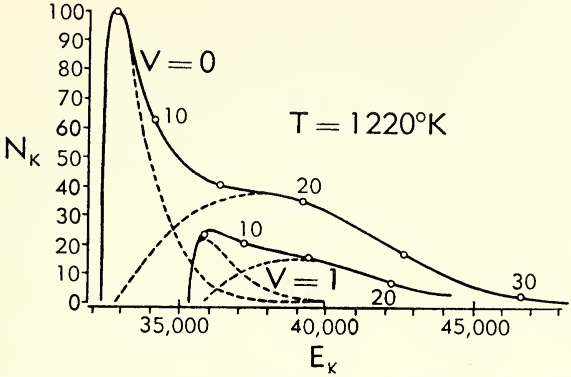

Fig. M,6c. Same as Fig. M,6b but pressure higher (p = 10 mm).

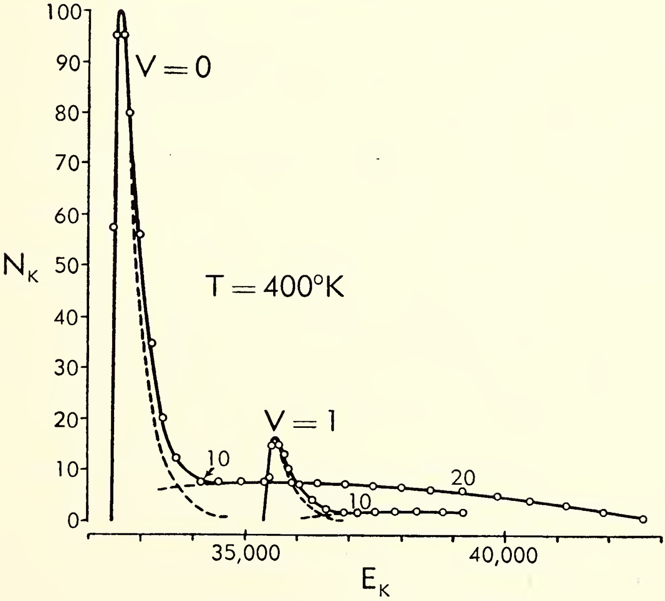

Fig. M,6d. Same as Fig. M,6b but discharge in 15 mm helium with 0.05 mm water vapor (see also Plate M,5a).

The exact mechanism which produces this anomalous distribution has not been entirely cleared up, but it is evident that the data of this and similar studies may be of great help in elucidating the mechanism of the reaction.

There have been numerous other cases of nonequilibrium distribution reported. Several observers have reported unreasonably high rotational temperatures. Usually, no detailed investigation was made to find out whether there was equilibrium distribution over the rotational states. In particular, when abnormally high rotational OH temperatures are found in flames at low pressure [*38*] there is no indication of the second maximum which is so characteristic for the excitation in a discharge tube. Gaydon and Wolfhard [*28,38,39,40,41*] have studied extensively the temperatures of low pressure flames and have found high rotational temperatures for OH and C_2, normal CH temperatures, and evidence for high excitation of iron that was introduced into the flame. While these results seem to indicate clearly that there can be no general thermal equilibrium in the reaction zone—a fact which cannot be too surprising—the details of the reaction mechanism that might account for these results are not clear.

It is more likely that more interpretable information can be obtained from reactions that are simpler than those which occur simultaneously in a flame. Such reactions are those in a gas at low pressure under the influence of an electric discharge.

Under favorable conditions it may, then, be possible to observe the gradual transition toward equilibrium. This can be done most easily by increasing the pressure and giving the molecules more opportunities for collision during the lifetime of the excited states. From such observations, relaxation times can be calculated. When the observations are made on emission spectra, these will be relaxation times of the excited states and quite possibly different from the relaxation times of the normal molecule. To obtain the latter it would be necessary to make absorption measurements with high time resolution, which is much more difficult to do.

The case of excited OH in an electric discharge showed an excess of high rotation. In the following example, an abnormally low rotational temperature is found combined with an excess of vibrational energy. This is a particularly simple case where the mechanism is quite clear and also where the transformation into an equilibrium distribution at higher pressures can be followed.

If the H_2 spectrum is observed in an electric discharge in hydrogen at low pressure and if the rotational temperature is determined, that temperature is found to be very low, actually below room temperature, and there is an excess of vibrational energy which suggests high vibrational temperatures. Because the transition probabilities are unknown, no vibrational temperatures can be determined, and it is questionable whether or not they exist. This state of affairs is due to the change in internuclear distance in the excitation process. Electrons which hit the unexcited H_2 molecule bring the molecule into an excited state, and in this transition the moment of inertia increases approximately by a factor 2 or the internuclear distance by about 40 per cent. This, according to the Franck-Condon principle, has as a consequence that, by preference, high vibrational states are excited. Also, for the same reason, the exciting electron cannot effect any substantial changes in the angular momentum of rotation. This means that the distribution over the rotational quantum numbers is approximately the same as for the unexcited atoms. This distribution, because of the Boltzmann factor $e^{-E_n/kT}$, is determined by the exponent

$$\frac{E_n}{kT} = \frac{\hbar^2 K(K+1)}{2kIT}$$

of which the significant part is the constant IT. As the rotational distribution is the same before and after excitation, the product IT is the same. As I has increased by a factor 2, the apparent temperature T must have decreased by a factor $\frac{1}{2}$. This explains the abnormally low rotational temperatures which are observed. Thus we have here excited molecules with too little rotational energy and too much vibrational energy for the temperature of the gas, which temperature might be erroneously identified with the translational temperature.

When the gas pressure is increased and the molecules have, therefore, more chance to collide before they emit the light, we expect that the rotational temperature will be increased and the vibrational temperature decreased. This is exactly what is observed, and this can be followed quantitatively by spectroscopic intensity measurements.

Rapid Changes. The methods described in the preceding paragraphs can be applied when the distribution is stationary or varies only slowly with time. The intensities that are obtained are averages over a considerable time. When photographic methods are used, the averaging time is equal to the exposure time. With photoelectric methods, the time constant of the electric measuring circuit or that of the recorder (or the meter), whichever is the larger, determines the averaging time. The circuit time constant can be given any value between wide limits. The recorder or galvanometer time constants are usually of the order of one to two seconds. Intensity variations with shorter periods than this cannot be observed with this method.

The cathode ray oscillograph in connection with the multiplier phototube is a device with very little inertia and can, therefore, follow very fast intensity variations, such as might be found in an explosion, a spark-initiated chemical reaction, or an a.c. gas discharge. The basic circuit is given in Fig. M,6e.

The question naturally arises as to how rapid variations can be recorded with this system and what the limiting factors are. It is desired to have on the screen of the oscillograph a faithful reproduction of the intensity changes in the light source. In order to obtain this, some precautions must be observed.

While the electron beam in the cathode ray tube can follow the voltage fluctuations on the deflection plates practically without inertia, there are other parts of the setup which impose limitations. The inability of the electric circuit to follow fast current fluctuations may set an upper limit to the frequency of intensity changes that can be recorded. In a simple circuit this is determined by the time constant CR where R is the resistance and C the capacitance of the circuit. When one tries to make this quantity as small as possible, C is the stray capacity in the circuit and cannot be reduced any further. This shows that the input resistance R should be made small in order to have a small time constant. This reduces the voltage across the resistor and requires higher amplification with higher inherent noise. In order to be able to obtain a satisfactory oscillograph trace, the signal should be as high as possible. This is required for another reason which comes from the statistical fluctuations discussed in Art. 2. The mean fluctuations are inversely proportional to $\sqrt{i_0 \Delta t}$ where i_0 is the average photocurrent and Δt the time interval during which the measurements are made. In our case, Δt is approximately equal to the controlling time constant of the whole combination. If this is kept small in order to achieve high time resolution, the fluctuations become necessarily large. This can be compensated for by a large signal current i_0 but only to a certain extent, because care must be taken that saturation is not reached anywhere in the system.

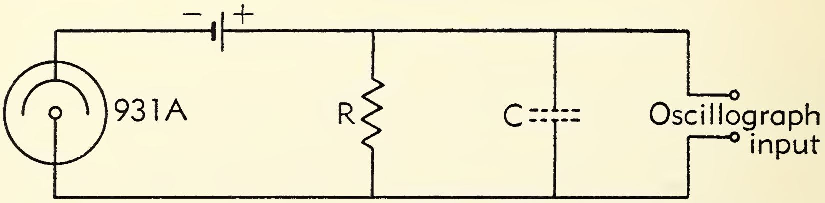

Fig. M,6e. Schematic circuit diagram for use of phototube with oscillograph.

From what has been said it is clear that in order to avoid excessive fluctuations, the time constant should not be made unnecessarily short. It should be of the order of magnitude of the time interval during which significant intensity changes can be expected.

Experience has shown that there is no particular difficulty in working with time intervals down to 10^{-6} seconds but that the difficulties rise quickly if one wants a time resolution considerably beyond this. Here is not the place to discuss in detail the numerous electronic problems that arise if the time resolution is to be pushed to the limit.

As an example of what results can be obtained see Plates M,6a and M,6b. These show the light emitted in a reaction initiated by the passage of a spark through hydrogen at one-millimeter pressure [*42*]. The current pulse (Plate M,6a) lasts about one microsecond. Plate M,6a shows the intensity traces of the atomic lines on the left-hand side. The right-hand pictures always give the same line with the current superimposed. If excitation and light emission were to occur without time delay, the current and intensity traces should coincide. Actually the light of the atomic lines lasts considerably longer, which shows that it must come at least partly from secondary reactions. This is confirmed by the fact that the shape of the intensity traces depends markedly on the pressure, that is, on the number of collisions. The light from the molecules represented in Plate M,6b, on the other hand, is generally due to primary electron excitation, as there is very little difference between the shape of the exciting current and the intensity of the molecular lines.

The intensity traces are highly reproducible, as can be judged from the similarity of the right and left traces, which represent different exposures. Also, each photograph usually represents the superposition of about ten successive sweeps. The sharpness of the traces shows that there was practically no variation during the ten successive flashes. This example shows that considerable information can be obtained from the spectrum even in very simple cases and that the method promises to be successful in many other cases, although so far it has not been consistently applied.

While the combination of phototube and cathode ray oscillograph presents the quickest and most direct means of measuring fast intensity fluctuations, there are other ways that may be applied advantageously under certain conditions, particularly when the times are not extremely short.

Display of the whole spectrum on the screen of an oscillograph. The method described above makes it possible to observe accurately the intensity of a single spectrum line as a function of time. Sometimes it is desirable to observe the relative changes in the spectrum as the reaction proceeds. If only a few wavelengths are involved this can be done by employing one phototube for each wavelength, each with an oscilloscope. There are now available oscilloscopes, with multiple electron beams, which are particularly well suited for this purpose. Each beam can be controlled independently of the other so that the effect is that of several oscillographs with a common screen. The sweeps of all the beams can be synchronized. These instruments make it possible to display the intensities of two or more lines as functions of the time, and to make an accurate study of the changes in relative intensities.[18]

---

[18] Another way of achieving the same result is by means of an electronic switch. This device makes it possible to switch rapidly from one circuit to another, and through the persistence of vision to give the effect of having both displayed simultaneously. The electronic switch is not designed for very fast events and cannot resolve times shorter than one millisecond.

Sometimes it is desirable to watch changes in the whole spectrum. Such observations will usually be of a qualitative nature. Often they are useful as preliminary studies from which the proper lines may be selected for a more detailed quantitative study.

Several persons have produced a spectrum on the screen of an oscillograph by sweeping through the spectrum and having the sweep synchronized with the horizontal sweep of the oscillograph. The repetition frequency of the sweep can be adjusted between wide limits. If it is faster than about 16 cycles per second the persistence of vision will create the impression of a steady curve representing the intensity distribution in the spectrum. Even with slower repetition frequencies this impression can be maintained by the use of a persistent screen. Relatively slow changes in the intensity distribution may be directly observed. Faster changes may be studied by photographing the screen with a movie camera. Obviously, the best time resolution is obtained if the camera is synchronized with the oscillograph so that one picture is taken for every sweep.

This method can be used with photomultiplier tubes in the visible or ultraviolet or with lead sulfide crystals in the near infrared. Bullock and Silverman [*43,44*] studied in this way the infrared spectrum of explosions. The sweep through the spectrum was achieved by a mirror which could be rocked with a frequency of up to 150 cycles per second. The time of an individual sweep was about 0.002 second.

Another way, long practiced, when time variations in a spectrum are to be observed photographically, is to have the plate move perpendicularly to the dispersion of the spectrum. The plate or film can move either continuously or in steps as in a motion picture camera. In well-designed instruments a time resolution of close to 10^{-3} seconds can be achieved, with moderate dispersion and light of high intrinsic brightness. With rotating mirrors higher resolution can be obtained.

M,7. Cited References and Bibliography.

Cited References

1. Brode, W. R. *Chemical Spectroscopy*, 2nd ed. Wiley, 1943.
2. Harrison, G. R., Lord, R. C., and Loofbourow, J. R. *Practical Spectroscopy*. Prentice-Hall, 1948.
3. Sawyer, R. A. *Experimental Spectroscopy*, 2nd ed. Prentice-Hall, 1951.
4. Hadley, J., and Dennison, D. M. *J. Opt. Soc. Amer. 37*, 451–465 (1947).
5. Hadley, J., and Dennison, D. M. *J. Opt. Soc. Amer. 38*, 483–496 (1948).
6. Billings, B. H. *J. Opt. Soc. Amer. 37*, 738–746 (1947).
7. Billings, B. H. *J. Opt. Soc. Amer. 40*, 471–476 (1950).
8. Billings, B. H., and Pittman, M. A. *J. Opt. Soc. Amer. 39*, 978–983 (1949).
9. Leurgans, P., and Turner, A. F. *J. Opt. Soc. Amer. 37*, 983–989 (1947).
10. Billings, B. H., Sage, S., and Draisin, W. *J. Opt. Soc. Amer. 40*, 262 (1950).
11. Engstrom, R. W. *J. Opt. Soc. Amer. 37*, 420–431 (1947).
12. Dieke, G. H. Photoelectric intensity measurements in spectra. *Trans. Instr. Measurements Conference Stockholm*, 1947.

13. Hasler, M. F., and Dietert, H. W. *J. Opt. Soc. Amer. 34,* 751 (1944).
14. Saunderson, J. L., Caldecourt, V. J., and Peterson, E. W. *J. Opt. Soc. Amer. 35,* 681–697 (1945).
15. Dieke, G. H., and Crosswhite, H. M. The ultra violet bands of OH. *Johns Hopkins Univ. Appl. Phys. Lab. Bumblebee Rept. 87,* 1948.
16. Herman, R. C., and Hornbeck, G. A. *J. Chem. Phys. 17,* 1344 (1949).
17. Hornbeck, G. A., and Hopfield, H. S. *J. Chem. Phys. 17,* 981–987 (1949).
18. Vaidya, W. M. *Proc. Roy. Soc. London A147,* 513–521 (1934).
19. Gaydon, A. G. *Spectroscopy and Combustion Theory,* 2nd ed. Chapman and Hall, London, 1948.
20. Oldenberg, O. *J. Chem. Phys. 3,* 266–275 (1935).
21. Oldenberg, O., and Rieke, F. F. *J. Chem. Phys. 7,* 485–492 (1939).
22. Oldenberg, O., and Rieke, F. F. *J. Chem. Phys. 6,* 439–447 (1938).
23. Oldenberg, O., and Rieke, F. F. *J. Chem. Phys. 6,* 779–782 (1938).
24. Hornbeck, G. A. *J. Chem. Phys. 16,* 845–1005 (1948).
25. Cowan, R. D., and Dieke, G. H. *Revs. Mod. Phys. 20,* 418–455 (1948).
26. Dieke, G. H., and Crosswhite, H. M. *Periodic Repts. Contract Nav. Ord. 8036 JHB-3a, Johns Hopkins Univ.,* (1947–1951).
27. Wolfhard, H. G. *Z. Physik 112,* 107–128 (1939).
28. Gaydon, A. G., and Wolfhard, H. G. *Proc. Roy. Soc. London A199,* 89–104 (1949).
29. Crosswhite, H. M. *Spectrochim. Acta 4,* 122–151 (1951).
30. Shuler, K. E. *J. Chem. Phys. 18,* 1221–1226 (1950).
31. McKellar, A., and Buscombe, W. *Pubs. Dominion Astrophys. Observatory, Victoria B. C., 7,* 361–381 (1948).
32. McKellar, A., and Tawde, N. R. *Astrophys. J. 113,* 440 (1951).
33. Tawde, N. R., and Patel, J. M. *Astrophys. J. 112,* 210–212 (1951).
34. Lochte-Holtgreven, W. *Z. Physik 64,* 443–451 (1930).
35. Earls, L. T. *Phys. Rev. 48,* 423–424 (1935).
36. Lochte-Holtgreven, W., and Macker, H. *Z. Physik 105,* 1–15 (1937).
37. Huldt, L. *Eine Spektroskopisch Untersuchung des elektrischen Lichbogens und der Azetylen Luftflamme.* Uppsala, 1948.
38. Gaydon, A. G., and Wolfhard, H. G. *Proc. Roy. Soc. London A194,* 169–184 (1948).
39. Gaydon, A. G., and Wolfhard, H. G. *Proc. Roy. Soc. London A201,* 561–569 (1950).
40. Gaydon, A. G., and Wolfhard, H. G. *Proc. Roy. Soc. London A201,* 570–586 (1950).
41. Gaydon, A. G., and Wolfhard, H. G. *Proc. Roy. Soc. London A205,* 118–134 (1951).
42. Hirshfeld, M., and Dieke, G. H. *Johns Hopkins Univ. Appl. Phys. Lab. Bumblebee Rept. 129,* 1950.
43. Bullock, B. W., and Silverman, S. *J. Opt. Soc. Amer. 39,* 200–201 (1949).
44. Bullock, B. W., and Silverman, S. *J. Opt. Soc. Amer. 40,* 608–615 (1950).

Bibliography

Banning, M. *J. Opt. Soc. Amer. 37,* 792–797 (1947).

Behrens, V. H., and Rössler, F. *Z. Naturforsch. 5a,* 311–317 (1950).

Buc, G. L., and Stearns, E. I. *J. Opt. Soc. Amer. 40,* 336 (1950).

Bullock, B. W., Hornbeck, G. A., and Silverman, S. *J. Chem. Phys. 18,* 1114 (1950).

Daly, E. F., and Sutherland, G. B. M. *Proc. Phys. Soc. London 59,* 77–87 (1947).

Deal, W. E., Bradshaw, W., and Matsen, E. A. *J. Chem. Phys. 16,* 638 (1948).

Dieke, G. H., Crosswhite, H. M., and Loh, H. Y. *J. Opt. Soc. Amer. 36,* 185–191 (1946).

Durie, R. A. *Proc. Phys. Soc. London A63,* 1292–1294 (1950).

Frost, A. A., and Oldenberg, O. *J. Chem. Phys. 4,* 642–648 (1936).

Frost, A. A., and Oldenberg, O. *J. Chem. Phys. 4,* 781–784 (1936).

Gaydon, A. G., and Wolfhard, H. G. *Proc. Phys. Soc. London A63,* 778 (1950).

Ginsburg, N., and Dieke, G. H. *Phys. Rev. 59*, 632–644 (1941).
Herman, R. C., Hopfield, H. S., Hornbeck, G. A., and Silverman, S. *J. Chem. Phys. 17*, 220–221 (1949).
Herman, R. C., Hornbeck, G. A., and Laidler, K. J. *Science 112*, 497–498 (1950).
Herzberg, G. *Spectra of Diatomic Molecules*, 2nd. ed. Van Nostrand, 1950.
Holt, R. B., McLane, C. K., and Oldenberg, O. *J. Chem. Phys. 16*, 225–229 (1948).
Hornbeck, G. A., and Herman, R. C. *J. Chem. Phys. 17*, 842 (1949).
Hornbeck, G. A., and Herman, R. C. *J. Chem. Phys. 18*, 763 (1950).
King, J., Temple, R. B., and Thompson, H. W. *Nature 158*, 196–197 (1946).
Laidler, K. J. *J. Chem. Phys. 17*, 221 (1949).
Laidler, K. J., and Shuler, K. E. Symposium on combustion chemistry. *Meeting Am. Chem. Soc. Cleveland*, April, 1951.
Lochte-Holtgreven, W. *Z. Physik 67*, 590–600 (1931).
Oldenberg, O. *Phys. Rev. 46*, 210–215 (1934).
Oldenberg, O. *J. Chem. Phys. 2*, 713–714 (1934).
Oldenberg, O., and Sommers, H. S., Jr. *J. Chem. Phys. 9*, 573–578 (1941).
Pearse, R. W. B., and Gaydon, A. G. *The Identification of Molecular Spectra*, 2nd. ed. Wiley, 1950.
Plyler, E. K. *J. Research Natl. Bur. Standards 40*, 113–120 (1950).
Plyler, E. K., and Humphreys, C. J. *J. Research Natl. Bur. Standards 41*, 449–456 (1950).
Plyler, E. K., and Humphreys, C. J. *J. Research Natl. Bur. Standards 42*, 567–578 (1950).
Quinn, H. F. *Can. J. Research A28*, 411–432 (1950).
Shuler, K. E. *J. Chem. Phys. 18*, 1466–1470 (1950).
Shuler, K. E. Total transition probabilities and the energetic distribution of OH ($^2\Pi^+$) and O_2 ($^3\Sigma^-$) in the oxy-hydrogen flame. *Johns Hopkins Univ. Appl. Phys. Lab.*, 1951.
Shull, H. *Astrophys. J. 112*, 352–360 (1950).
Silverman, S. *J. Opt. Soc. Amer. 39*, 275–277 (1949).
Silverman, S., and Herman, R. C. *J. Opt. Soc. Amer. 39*, 216–218, (1949).
Silverman, S., Hornbeck, G. A., and Herman, R. C. *J. Chem. Phys. 16*, 155–156 (1948).
Smith, F. D., and Turner, A. F. *J. Opt. Soc. Amer. 40*, 261 (1950).
Sulzer, P. *Helv. Phys. Acta 23*, 531–535 (1950).

SECTION N

ANALYSIS OF THE COMBUSTION WAVE BY PRESSURE EFFECTS AND SPECTROSCOPY

N. THOMAS

SECTION N

ANALYSIS OF THE COMBUSTION WAVE BY PRESSURE EFFECTS AND SPECTROSCOPY

N. THOMAS

N,1. Introduction. Some studies of the effect of pressure variation on flame properties were made prior to 1940, e.g. the work of Ubbelohde [*1*] and of Khitrin [*2*], but it is only since that date that results of real significance have been obtained. This is due partly to improved experimental equipment, and also to the application of spectroscopy to flame studies and the development of rational theories of flame propagation which can be correlated with the experimental data.

The major advance in this field was made by Wolfhard [*3*]. Working in Germany during 1942, he developed the current type of low pressure burner and initiated the program of experimental observations on it. In this fundamental paper Wolfhard determined the stability properties of the low pressure burner over a wide operating range, and indicated the possibilities of further experimental work.

In 1939 Wolfhard [*4*] had published some observations on the apparent rotational temperature of OH radicals in Bunsen-type flames. He noted that it was abnormally high, relative to the equilibrium temperature of the flame, but owing to the shape of the flame and the thinness of the reaction zone it was not possible to locate, spatially, the source of the abnormal radiation. It seemed possible, however, that as pressure was reduced, and the mean free path of the reacting molecules lengthened, the reaction zone, in which processes involving a definite number of molecular collisions were presumed to occur, should broaden. This expectation was fulfilled and, owing to the rapid decrease of viscosity effect with decreased pressure leading to disappearance of wall drag, an almost flat velocity profile was obtained across the burner tube for sufficiently low pressures. The thickened reaction zone resembled a flat disk, sitting above the burner port. Its thickness and symmetry made it a far easier object of detailed study than the reaction zone of a conventional flame.

Since that time a long series of observations have been made, mainly by Gaydon and Wolfhard, upon thick reaction zones of this type, and the methods developed have found other uses. At first, the more obvious physical properties, reaction zone thickness and temperature, were measured. More recently, the free radical concentrations and their influence upon flame properties have been studied and discussed. This aspect of the work is still largely open.

In 1947, Tanford and Pease [*5*] remarked that their free radical theory of flame propagation predicted an increase in burning velocity with reduced pressure, and cited the early observations of Khitrin in support of this thesis. Subsequent investigators have tried to check this point, and to use the effect of pressure on flame velocity as a means of differentiating between thermal and free radical theories of flame propagation.

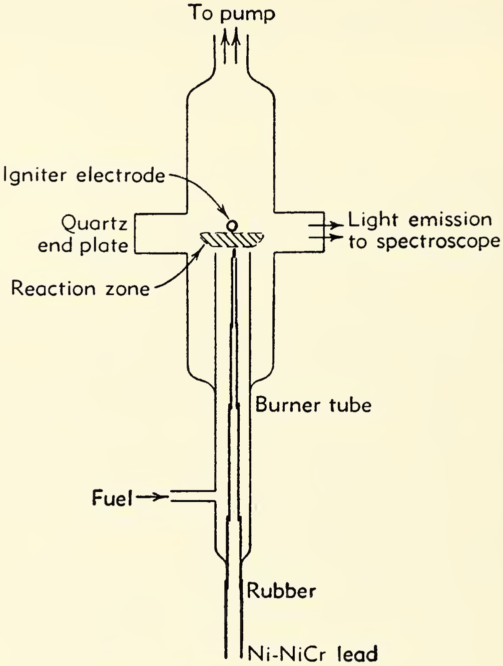

Fig. N,2a. Cross section of burner.

Pressure effects in flames provide an invaluable tool which, if suitably used, can supply much information, not otherwise obtainable, about what might be called the fine structure of flames, and about the details of the propagation mechanism. The development is still incomplete, but the material obtained to date is set out in what is hoped to be a fairly coherent form in this section.

N,2. Burner Design and Characteristics. The low pressure burner designed by Wolfhard [*3*] is illustrated in Fig. N,2a. As can be seen, it consists of a burner of large diameter enclosed in a cylindrical Pyrex vessel, with short side arms ending in flat quartz plates to make spectroscopic observation possible. Ignition is effected by making a discharge between two flat metal electrodes, as shown. A large capacity pump is required and arrangements are made to insert a pressure buffer in the form of a large metal tank in the exit line.

A typical stability chart obtained by Wolfhard is shown in Fig. N,2b. Here, the ordinate is the linear velocity of the gas mixture in the burner pipe, and the abscissa is the pressure in mm of Hg. Each plot is made for a specific diameter of the burner pipe, as indicated. The need for wide tubes at the lower pressures is apparent.

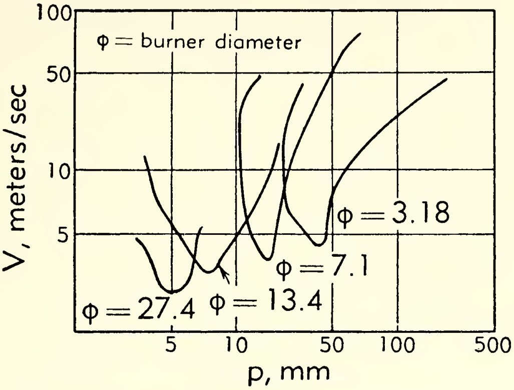

Fig. N,2b. Burner stability regions.

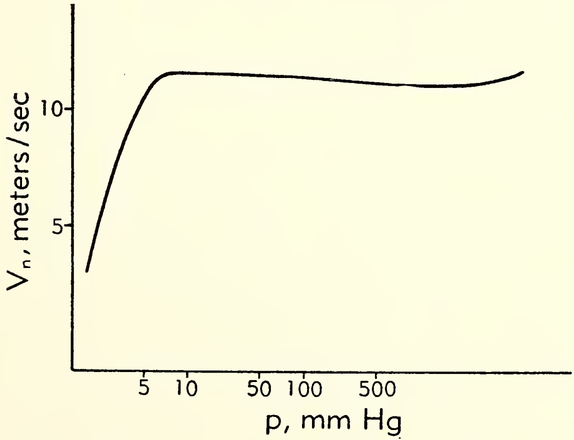

Fig. N,2c. Effect of pressure on burning velocity.

Wolfhard and Hubner (unpublished) have endeavored to explain this effect on the assumption that the decrease in surface area to volume ratio of the flame, obtained with a wide burner tube, is needed to offset the loss of heat from the flame caused by the reduction in pressure, with accompanying increase in surface area. This tacitly assumes that the flame is a system in thermal equilibrium.

Near the tips of the stability regions it was found that the reaction zone of the flame degenerated into a flat disk, while the outer cone gases became completely separated. This, of course, is due to the flattening of the velocity profile in the burner tube at low pressures. By giving the reaction zone cylindrical symmetry, this effect greatly facilitates systematic observations of the zone structure.

In his 1943 paper Wolfhard also plotted the apparent burning velocity V_n, against pressure. This is illustrated in Fig. N,2c. It can be seen that above the very low pressure range V_n remains almost constant with pressure. This observation, it should be noted, applies only to the C_2H_2-O_2 flame studied. The values of V_n were determined by the Gouy method.

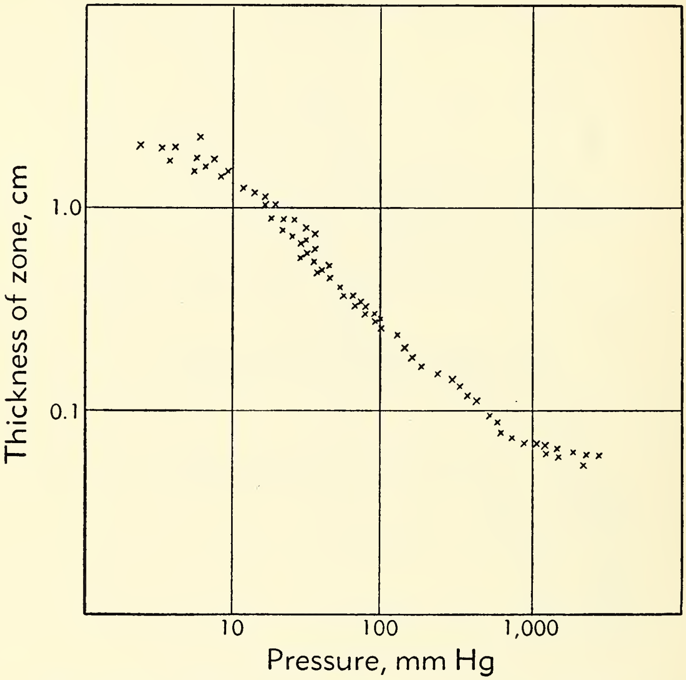

Fig. N,2d. Effect of pressure on reaction zone thickness.

It was also possible to measure the thickness and volume of the luminous reaction zone at various pressures. Graphs showing these quantities are given in Fig. N,2d and N,2e. The approximate linearity of the graph of thickness versus pressure, over a considerable range, is of interest.

More recently Gilbert [*6*], at the California Institute of Technology, has constructed a larger and more elaborate low pressure burner than the original Wolfhard design. Modifications included the use of a rectangular burner pipe and ignition by an oxygen-propane pilot flame rather than by an electric discharge. A very detailed account of this equipment is given in [*6*].

In the next article some of the photographic and thermocouple measurements made on the flame are described in more detail.

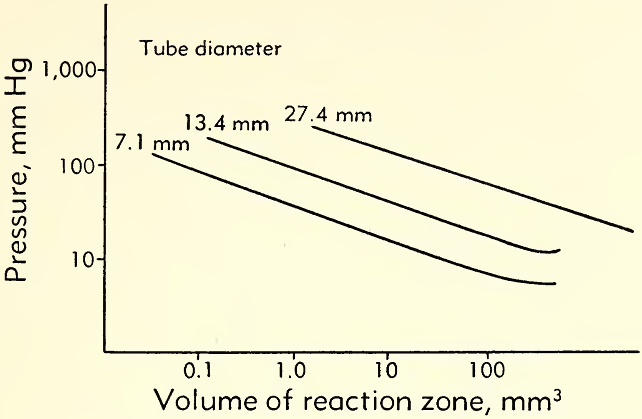

Fig. N,2e. Effect of pressure on reaction zone volume.

N,3. Reaction Zone Structure. Klaukens and Wolfhard [*7*] reported schlieren-photographic and direct temperature measurements on their low pressure flames. The schlieren results verified the observation, made previously by van de Poll and Westerdijk [*7a*], of the separation of schlieren and emission images of the reaction zone, the schlieren image lying ahead of the emission image on the cold side. This property was common to all hydrocarbon flames studied.

The shape of the reaction zone at a few mm Hg, and its thickness, made possible direct temperature measurements by a thermocouple across the reaction zone. Also, insertion of a thermocouple from below into the flame front causes the whole front to rise a little when it is introduced, rather than a marked distortion as is the case at normal pressures.

The thermocouple, then, was inserted through a rubber joint at the base of the burner pipe. It was enclosed in a telescopic ceramic tube. Chromel-alumel couples of 0.3 mm or 0.1 mm Ni-NiCr were used, and the difference between measurements was negligible, so it was assumed that the 0.1-mm wire gave a fairly accurate reading. Results are shown in Fig. N,3a. The extension of the flame is plotted as seen through a telescope.

Radiation losses were corrected by attaching a small fused bead to the end of the thermocouple. The heat loss from this sphere could be calculated by the T^4 law, while the heat transfer (q) to the wire was estimated by a Nusselt-type relation.

$$q = hF(T_2 - T_1)$$

where T_2 = gas temperature, T_1 = thermocouple temperature, F = area of bead, and h = heat transfer coefficient, which is related to the Nusselt number Nu by the equation

$$Nu = \frac{hd}{\lambda}$$

where d = diameter of bead (assumed spherical) and λ = heat conductivity coefficient. Nu is obtained from the Reynolds number of the sphere, which can be calculated. The relation $Nu = f(Re)$ is known only empirically and for long cylinders. Gilbert [*6*] has noted this point and has endeavored to correct it by using an analogy between fluid friction and heat transfer, writing

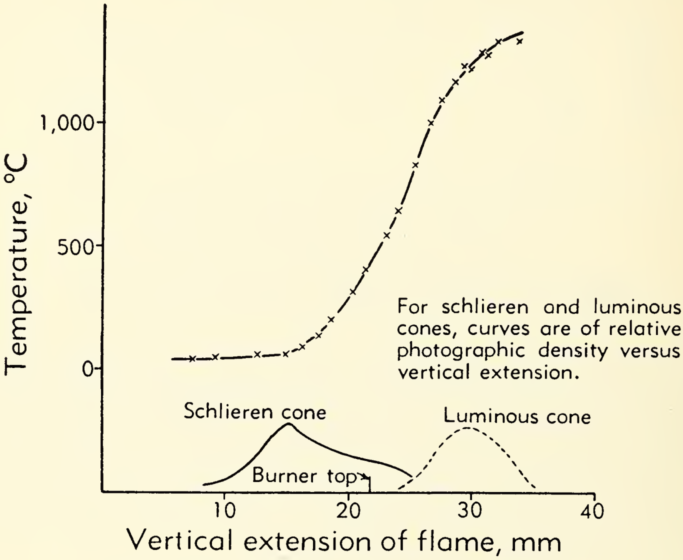

Fig. N,3a. Structure of reaction zone (1).

$$\frac{Nu\text{ (sphere)}}{Nu\text{ (cylinder)}} \sim \frac{C_D\text{ (sphere)}}{C_D\text{ (cylinder)}}, \quad C_D = \text{drag coefficient}$$

This ratio was found by Gilbert to vary from 2 to 10 in the range of Reynolds numbers encountered. Thus the use of Nu (cylinder) would appear to give too high a value for T_2. Rough comparisons with the data of Klaukens and Wolfhard suggest that this is indeed the case.

Catalytic effects were apt to cause irregular thermocouple readings, particularly in the low temperature regions of the flame. Gilbert [*6*] discusses these effects in some detail.

For the C_2H_2-O_2 flame, Klaukens and Wolfhard obtained a temperature distribution curve across the reaction zone, which they considered accurate enough for a detailed study. They made piecewise calculations of the heat flow in the direction of the cold mixture, using the conductivity expression $\lambda A(dT/dx)$ over each section. They found that up to about 800°C the heat flow by conduction accounted satisfactorily for the observed temperature of the zone, but that above this point an additional source of heat, clearly the exothermic reaction, was needed to account for the observations. This is shown in Fig. N,3b. Also, the cold boundary of the schlieren image was found to occur at about 200°C.

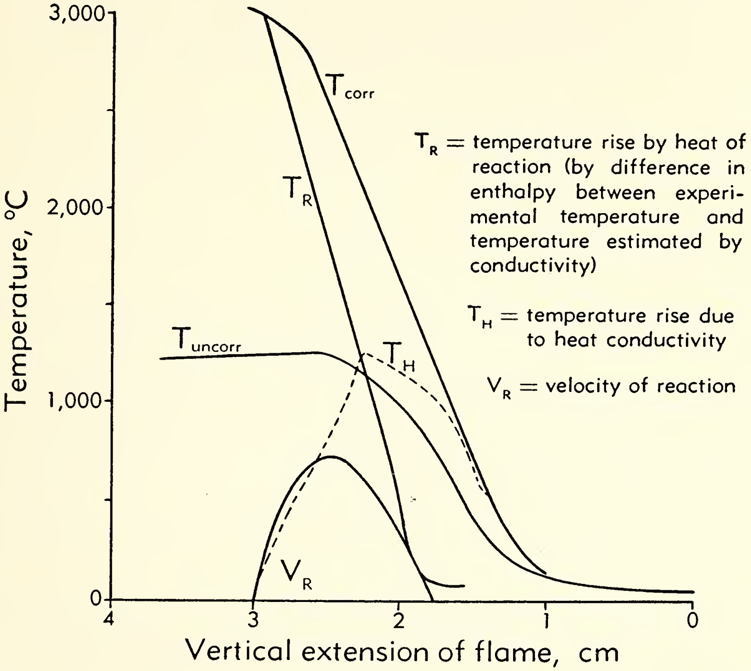

Fig. N,3b. Structure of reaction zone (2).

The validity of this result is affected to some extent by Gilbert's remarks, mentioned above. It does, however, suggest that the true ignition temperature in these flames is remarkably low, which rather contradicts some work done on thermal theories of flame propagation. However, discussion of this point is given in Art. 7.

Gilbert has made measurements similar to those of Klaukens and Wolfhard and, like them, has noted the existence of an extensive preheating zone in the flames. However, the measurements described above are probably not sufficiently accurate to serve as a check on any model of the reaction zone structure. Aside from experimental error, certain physical constants (e.g. λ) entering into the interpretation are not known with tolerable accuracy.

N,4. Spectroscopic Temperature Measurements. The thermocouple measurements described in the previous article were obviously limited in accuracy, especially as far as high temperature readings were concerned, because of the use of the rather dubious heat transfer approximation. It was clearly necessary to make spectroscopic estimates of flame temperature.

In 1939, Wolfhard [*4*] had measured the apparent rotational temperature of OH radicals in a Bunsen-type flame at atmospheric pressure and had noted some abnormally high rotational temperatures. With the low pressure flame available it was possible to follow up this work in much more detail.

The method of measuring the rotational temperature of OH is described at some length in Sec. M by Dieke, and consequently need not be dealt with in detail here. It is assumed that the reader is familiar with the theory of the method.

A full account of the work on OH is given in a paper by Gaydon and Wolfhard [*8*].

The temperature was measured by the usual method of plotting the rotational energy (in wave numbers) against ln $(I - P\nu^4)$, where I is intensity, ν frequency of the line, and P the transition probability. The temperature is given by the slope of the plot. A method of calculating P for simple diatomic emitters was given by Earls [*12*] using a procedure due to Van Vleck. This was used in the low pressure flame work on OH, CH, and C_2. However, the recent tabulation by Dieke and Crosswhite [*13*] has relieved the worker in this field of the trouble of making the numerical computations in the case of OH.

The first measurements were carried out on the OH system, since work previously carried out by Wolfhard could be utilized. Observations were made on the C_2H_2-O_2 flame at various pressures and with a vertical traverse through the reaction zone to estimate any variation in temperature across the zone.

The results showed that the apparent rotational temperature of OH was indeed abnormally high. Temperatures as high as 8700°K were recorded. In addition, there was surprisingly little variation across the reaction zone, though a certain decrease was noted in the bluish corona at the top of the zone.

On the other hand, the rotational temperature was altered significantly by changes in pressure, as is shown by the following table:

Gas pressure, mm Hg	*Rotational temperature, °K*
13	5700
5.5	6200
2.5	7000
1.5	8750

At a pressure of 6 mm the temperature distribution across the flame was thus

Flame base	6200°K
Flame center	6000°K
Flame top (corona)	5300°K

Relative total strengths of the OH band in these three regions were about as 5:2:1. Observed temperatures were highest in mixtures containing excess C_2H_2, as can be seen from these figures:

Pressure, mm Hg	*Temperature, °K*	*Gas mixture*
5.5	6200	Stoichiometric
3	6800	$C_2H_2 + 2.5\ O_2$
6	6800	Rich
3	8600	$1.5\ C_2H_2 + 2.5\ O_2$
7	5850	Lean
3.3	6200	$C_2H_2 + 3.75\ O_2$

In the acetylene-oxygen flames, good straight-line plots were obtained, indicating that a Maxwell-Boltzmann distribution of rotational energy holds for the molecules. With the oxyhydrogen flame, a rotational temperature for the 0,0 band of OH of about the theoretical value for the low pressure flame (2300°K) was obtained, but the introduction of a trace of acetylene had a remarkable effect. The intensity of OH emission was greatly increased and the rotational temperature plot became "two-sloped," the part at low rotational levels remaining at a slope corresponding to 2300°K, while at the higher levels the slope corresponded to a temperature of 8,000 to 9,000°K (Fig. N,4a).

The same type of plot was also noted for flames of acetylene-air and acetylene-N_2O mixtures. Here, the upper portion of the plot gave a low apparent rotational temperature ($\cong$ 3,000°K), while the rest of the slope, covering the region of higher rotational energy states, gave a high apparent temperature corresponding to those indicated above. No clear interpretation of this has been given. The specificity of this abnormal temperature effect should be noted. It was not observed with H_2 or CO flames, nor with flames of certain organic compounds, such as methyl alcohol and formaldehyde. Also, the abnormal temperatures were never detected in the burnt gases immediately above the reaction zone.

The 2811A band (1,0) and the 2,1 band were examined, and it was found that there was an abrupt decrease in intensity of the higher rotational levels in the 1,0 band and that the 2,1 band was abnormally weak in low pressure flames. The type of plot obtained is shown in Fig. N,4b. It was found that the change in slope of the plot did not set in with the same absolute rotational energy in all the vibrational states. For the 1,0 band the effect set in at $E = 40{,}712\ \text{cm}^{-1}$, as indicated, while in the 2,1 band it seemed to set in at 38,221 cm^{-1}. In the 0,0 band it was not clearly observed, but there was some indication that it might set in at about 42,600 cm^{-1}. If the effect were due to chemical causes it would seem likely that the limit would occur at the same energy in all cases. However, it is normal for predissociation of the molecule to occur in the higher vibrational state at lower energy, and predissociation also shows up more strongly at low pressure. Furthermore, the abnormal portion of the temperature plot splits into two, one for each component of the spin

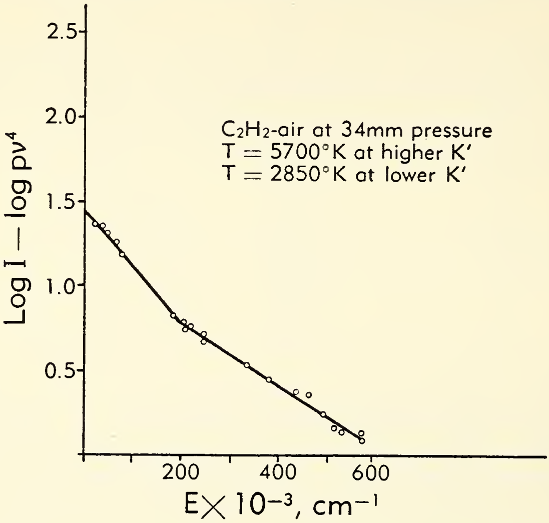

Fig. N,4a. Rotational temperature plot.

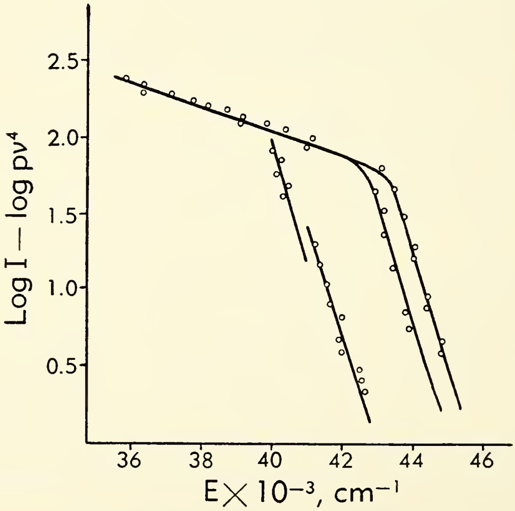

Fig. N,4b. Predissociation effects in OH.

splitting. This unequal effect on the spin component also is not explicable on chemical grounds.

This reasoning was checked by an examination of OH bands emitted by a discharge tube containing water vapor, and the same effect was observed here. This seemed to eliminate the possibility of a chemical cause. The nature of the predissociation involved is discussed in detail by Gaydon and Wolfhard [*10*]. Their analysis is of considerable spectroscopic interest, for the predissociation is of a most unusual type, but it will not be reproduced here.

The rotational temperature measurements were subsequently extended to other diatomic emitters. The technique was essentially the same, however. With CH, the 3900A and 4315A bands were measured.

A straight-line temperature plot was obtained in all cases. For the 3900A band, rotational temperatures corresponding to the equilibrium flame temperature were obtained. For the 4315A band, they were about 10 per cent above theoretical. Finally, measurements were carried out on C_2 to obtain the rotational temperature.

Over a considerable range of values of rotational energy a straight-line temperature plot was obtained, indicating a Maxwell-Boltzmann distribution of the usual type. Some typical results are set out below.

	Gas mixture	*Pressure*	*Temperature, °K*
C_2H_2-O_2:	stoichiometric	1 atm	4950 ± 200
	stoichiometric	8.5 mm	3800 ± 400
	rich	8 mm	4200 ± 300
	stoichiometric	2.1 mm	3800 ± 500
	rich	2.0 mm	4020 ± 400
C_2H_2-air:	stoichiometric	1 atm	3400 ± 300
	rich	62 mm	3240 ± 300
$1.33\ H_2 + 0.133\ C_2H_2 + 1.0\ O_2$	(stoichiometric)	9 mm	3000 ± 500
CH_4-O_2:	rich	1 atm	3900 ± 800
	rich	40 mm	3250 ± 400
C_2H_6-O_2:	almost stoichiometric	25 mm	4100 ± 400
	stoichiometric	1 atm	4100 ± 400

All of these data show that the C_2 rotational temperature is well above equilibrium except in the H_2-C_2H_2-O_2 mixture. It falls with pressure (compare OH) and is apparently reduced by diluents, at least in the two examples of acetylene-oxygen and acetylene-air flames. Details of the work are given in the paper by Gaydon and Wolfhard [*11*]. The results on OH at atmospheric pressure given by Dieke are not in complete agreement with those of Gaydon and Wolfhard. However, abnormally high rotational temperatures on the low pressure flame have recently been reported by Penner and coworkers [*29*]. They obtained temperatures up to 8,000°K, and to this extent have confirmed the previous results.

Temperature measurements on the rotational energy levels of molecules have been handled most extensively, since the transition probabilities are calculable and the technique of measurement is fairly well known to spectroscopists. However, temperature measurements using the translational and vibrational modes of motion of the molecules have been made and are described below.

The term "temperature" as generally used is directly related to the translational motion of molecules, and it would be of interest to determine this for an emitting radical. Gaydon and Wolfhard [*9*] were able to do this for the CH radical, using the Doppler broadening effect. As the method used is not adequately described elsewhere in this series, it is outlined below.

The width of a spectrum line depends on the following factors: the natural width, collision broadening due to interference by surrounding inert molecules, resonance broadening due to interference with similar molecules, and Doppler broadening due to random thermal motions of emitting molecules. The natural breadth of a line is negligible above room temperature, and while resonance broadening is very serious in the case of atomic spectra, it can be neglected for molecular spectra. Collision broadening is, of course, present, but in the low pressure flame we assume that it is negligible, though some microwave data suggest that the assumption is not completely justifiable.[1]

The spectrum line half-breadth b due to Doppler broadening is given by $b = 2\sqrt{\ln 2}\,\sqrt{(2RT/\mathfrak{M}c^2)}\,\nu$ cm^{-1} [cf. *9*], where $\mathfrak{M}$ is the molecular weight, R the gas constant, c the velocity of light, T the absolute temperature, and ν the wave number of the line. Since $b \sim \sqrt{T}$, a method depending on direct measurement of b will not be particularly sensitive for temperature measurement, but it should serve to determine any marked departure from equilibrium temperature.

To obtain a value for T from the above formula it is sufficient to measure b, but to find whether there is any departure from a Maxwell-Boltzmann translational energy distribution, the intensity contour, or cross section, of a spectral line must be compared with that expected theoretically for pure Doppler broadening. Hence, the line must be examined with very large dispersion and its intensity accurately measured.

It is possible for the line contour to be altered by self-absorption, but in the case of CH, at low pressures, such an effect is very small.

Now, the intensity contour of the spectral line results from a combination of the true contour of the line and the instrumental contour given by the interferometer fringe system. The instrumental contour breadth was obtained from mercury lines, since the Doppler broadening of the mercury lines is small compared with that of CH, owing to water cooling of the arc and the high atomic weight of mercury. Pressure broadening also appeared small. Typical intensity contours for a CH line and for a nearby Hg line are shown in Fig. N,4c. The mercury arc spectrum was, in practice, superposed on that of the flame to avoid errors due to differing conditions of exposure.

---

[1] For a discussion of the theoretical background of line broadening, on which the present analysis is based, see [*41*].

The mean half-breadth, b, of the spectral line was derived from the measured half-breadth m and the instrumental fringe breadth, i, by a rather tedious procedure, as follows: For collision broadening only can we use the simple $m = b + i$ relation. For Doppler broadening we have to use a relation of type $m^2 = b^2 + i^2$. But for the combined Doppler and instrumental broadening there does not seem to be any such simple relation, the resultant being, apparently, intermediate between the linear and quadratic summations. So, an ideal Doppler contour for an assumed temperature was plotted using the expression

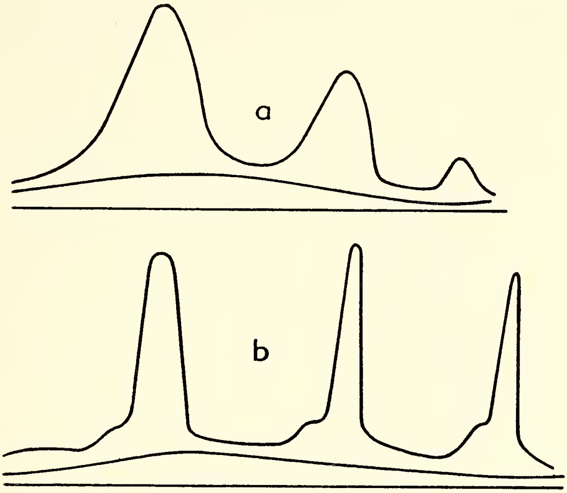

(a) Intensity contour of three CH fringes
(b) Intensity contour of Hg line at 4077.8A
Lower curve is background from flame

Fig. N,4c. CH line contours.

$$I = e^{-2\,[\sqrt{\ln 2}(x/b)]^2}$$

where x is the distance, in wave numbers, from the center of the line. The observed instrumental contour was also plotted, and the resultant curve obtained by a piecewise graphical summation. This is shown in Fig. N,4d. The resultant curve was compared with the observed intensity contour, and the guessed temperature adjusted till a fit was obtained. With practice only two trials were required.

The CH band at 3900A was used; but the lines are double, due to spin splitting, and only one could be adequately resolved with the wide slit used for photometering the spectral lines. Long exposures, ranging up to two hours, were required.

The results obtained are summarized below:

Flame	*Pressure*	*Temperature*
C_2H_2-O_2 stoichiometric	1 atm	2600°K
	14 mm	4000°K
	5 mm	4000°K
	2 mm	4250°K

The first of these results is rather lower than the equilibrium flame temperature, but not by more than the possible experimental error, estimated at ±600°K. This result indicated that pressure broadening, even at atmospheric pressure, was negligible. The low pressure measurements show a marked departure from equilibrium, but little variation with pressure. However, some variation was noted across the reaction zone. (The above values are for the center of the zone.) This is shown in the following table:

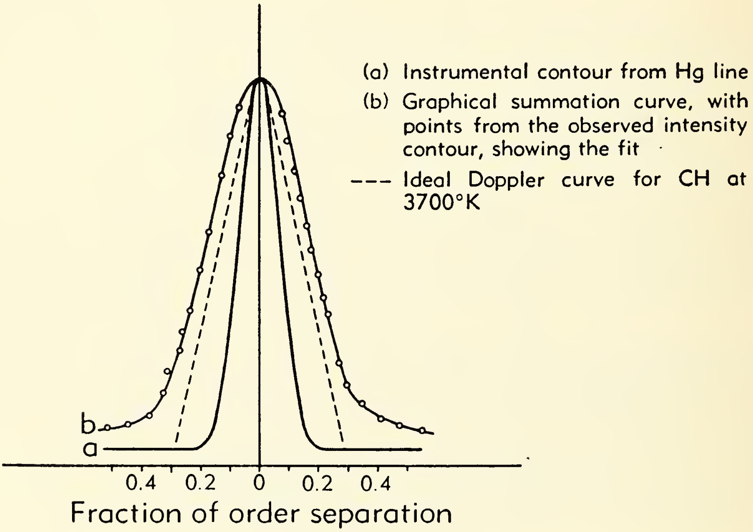

Fig. N,4d. CH line contour analysis.

Region	*Temperature*
Top	4475°K
Center	4000°K
Base	3125°K

It should be added in conclusion that the margin of error with this method is very appreciably greater than that involved in rotational temperature measurement. The experimental procedure is also much more laborious.

Measurements of the vibrational temperatures of molecules can be carried out, by a procedure strictly analogous to the rotational temperature measurements described in the article on spectroscopy. Measurements of this type have been carried out on CN by Thomas, Gaydon, and Brewer [*14*], and by Shuler [*15*] on OH. Their work dealt with flames at normal pressure, but is of some interest to the main theme of this article and will be described briefly.

In carrying out vibrational temperature measurements, the intensities of the band heads are photometered, and a graph of the type $\ln\,(I - P\nu^4)$ against the vibrational energy state is plotted. This should give a straight line, from the slope of which the temperature is derived. However, the number of points available for plotting is much less than with rotational line systems, which increases the possibility of error. More serious is the fact that the transition probability, P, cannot be calculated readily from the theory. In a few cases, however, transition probabilities have been obtained empirically by comparison with other methods of temperature measurement.

This is the case for the CN radical, where Ornstein and Brinkman [*16*] in 1932 carried out a direct comparison of vibrational and rotational temperatures for a carbon arc burning in nitrogen. Their values of the transition probabilities for the CN bands were utilized to measure apparent vibrational temperatures from the intensities of CN band heads in the outer cone of a cyanogen-oxygen flame. A temperature of 4800°K was recorded for a stoichiometric mixture, which is in agreement with the equilibrium temperature calculated assuming $D(N_2)$ to be 9.76 ev. It was significant, too, that immediately above the reaction zone the apparent vibrational temperature dropped to little over 3000°K, as can be seen from these figures.

Height above reaction zone	*Temperature*	*Remarks*
10 mm	4800°K	C_2N_2-O_2 stoichiometric
5 mm	3800°K	Margin of error = ±400°K
2 mm	3200°K	

Measurements of the rotational temperature of CN, carried out in the reaction zone of these flames, yielded a mean value of 2600°K. By contrast, the rotational temperature of C_2 was about 4700°K, and showed surprisingly little variation with mixture strength. This agreed with the results of Gaydon and Wolfhard on the rotational temperature of C_2 in hydrocarbon flames.

Shuler [*15*] obtained vibrational transition probabilities for the OH molecule by a graphical integration of assumed wave functions, a procedure which had been previously employed in work on hydride molecules. For a detailed account the reader is referred to the original paper. Shuler made measurements on OH emission from the outer cone of the CH_4-O_2 flame at atmospheric pressure, obtaining both vibrational and rotational temperatures. The latter was derived by using the isointensity method described by Dieke. Good agreement was obtained between the values and also with the equilibrium temperature of the flame, which was 2600°K. Vibrational temperatures for the outer cone of the C_2H_2-O_2 flame yielded the abnormally high value of 3750°K.

We have not given any account of the well-known sodium-line reversal method. This is because a very full account of recent work on this method is given in Sec. I by Bundy and Strong, and because the method breaks down in the reaction zones of flames, as will be seen below.

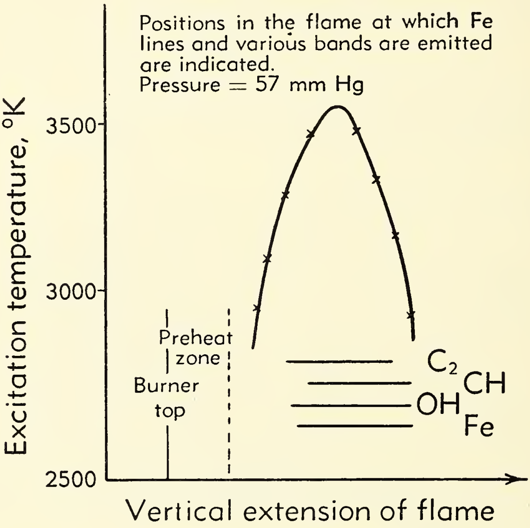

Fig. N,4e. Abnormal line reversal temperatures.

Early in their work on temperature measurement, Gaydon and Wolfhard introduced iron carbonyl into low pressure C_2H_2-O_2 flames and measured the reversal temperature of the Fe resonance lines. The results, shown in Fig. N,4e, show that the apparent reversal temperature varies across the reaction zone and greatly exceeds the theoretical flame temperature.

Gaydon and Wolfhard [*17*] followed up this line of work in a more detailed investigation of the excitation of metal atoms in reaction zones of flames. They used a double burner with two concentric tubes. The gas stream passing through the inner tube only was contaminated with a metallic compound, e.g. $Fe(CO)_5$, and a region in the center of the low pressure flame was so obtained, which emitted metallic lines. This was done to obtain a region of uniform temperature emitting metallic lines.

Results for the resonance lines of Fe involving the ground state are summarized thus

Wavelength of line, angstroms	*Reversal temperature, °K*
3859–9	2565
3440–6	2880
3020–6	3058
2936–9	3100
2522–8	3465
2483–3	3450

These temperatures all exceed the equilibrium value for the mixture used (≅ 2350°K) and increase as we go to lines of shorter wavelength. Each line represents an electronic transition between different levels in the electron shells of metal atoms. These transitions, and the energy changes they represent, have been tabulated by the atomic spectroscopists and are available in such compilations as Bacher and Goudsmit's *Atomic Energy States.*

Accordingly, it was possible to obtain values of E, the energy of the transition for each line. A graph of E versus E/KT was plotted. Results are shown in Fig. N,4f, for lines of several metals. It is clear that such a plot should be linear and that the slope should give a value of T. Also, the line should pass through the origin. The apparent temperature obtained from the plot for Fe was ≅ 8,000°K. Similar abnormalities seemed to occur for Pb lines. This result certainly made it clear why some lines would not reverse against any background source available.

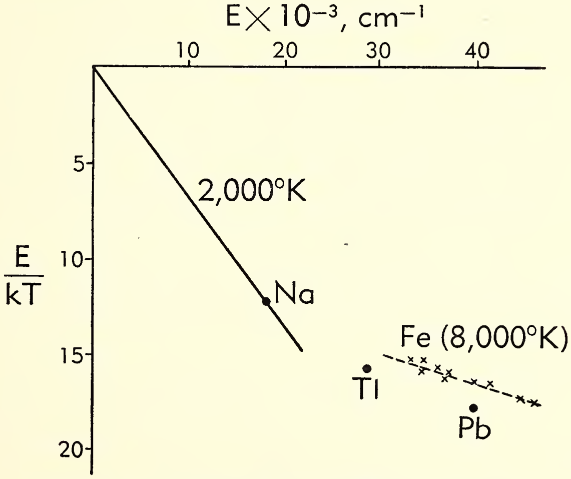

Fig. N,4f. Abnormal line reversal temperatures.

Little variation in excitation temperature with pressure was noted, and the temperature was also rather insensitive to variations in mixture strength. Some comparisons of the intensity of the 4050A Fe group for different fuels were made; they showed an 8:1 ratio of C_2H_2 to CH_4 and 35:1 of C_2H_2 to CH_3OH. In H_2-O_2 and CO-O_2 flames, excitation effects completely disappeared.

Burgoyne and Thomas [*18*] noted that Fe lines excited in the reaction zone of a hydrocarbon flame did not extend into the interconal gas region. In the work on low pressure flames, a spectrum of Fe lines extending down to 2300A was found; also in ammonia-oxygen and cyanogen-oxygen flames (cf. [*14*]). It was not found in H_2-O_2 or CO-O_2 flames. The maximum energy transition associated with any of the observed lines was 7.53 ev = 173 kcal.

The above results suggest that line reversal methods can give highly anomalous results in the reaction zone. However, it should be noted that the NaD line gave reasonably satisfactory results, though the data suggest that a line of longer wavelength, such as the Li red line, would be more reliable. Nonresonance lines are certainly unreliable.

Apart from abnormal excitation effects, it is possible that the line reversal method may fail if the flame is not in radiative equilibrium. In a closed system, depopulation of excited states by radiation will be balanced by absorption of radiation. In small open flames, this is not so. Only when the collision processes responsible for exciting or deactivating atoms are far more important than radiation effects will the reversal temperature approach the true temperature. In low pressure flames, where radiative life and time between collisions become comparable, the errors may be serious. Thus, reversal temperatures for interconal gases, using Na, were obtained several hundred degrees below equilibrium. While this may be due partly to heat losses, radiative equilibrium effects probably contributed.

A discussion of the bearing of these nonequilibrium effects on the mechanism of flame propagation is postponed to the concluding article.

N,5. Free Radical Concentration Measurements. Some work has been carried out on spectroscopic determination of the free radical concentration in flames. This work is still in an early stage of development, but has already yielded some interesting results.

Gaydon and Wolfhard [*19*] have carried through the outstanding piece of work in this field to date, on the C_2 emission from low pressure flames. The low pressure flame was peculiarly suitable for this work as it was free of carbon emission, which might have interfered with intensity measurements. It was decided to measure the absolute intensity of C_2 emission from the flame. This involved direct comparison with the light emitted by a known area of a tungsten strip lamp. The energy radiated by the lamp, J_λ, in watts per steradian, is given by

$$J_\lambda = \frac{Ac_1\lambda^{-5}}{e^{c_2/\lambda T} - 1} \cdot E_\lambda d\lambda$$

Here λ is wavelength in cm, A is area in cm^2, and T is absolute temperature. E_λ is the emissivity of tungsten, and c_1 and c_2 are radiation constants. Since the lamp radiates over a sphere, its total emission is $4\pi J_\lambda$.

As the brightness measurement was over the whole reaction zone and was not expressed in terms of brightness/unit area, it was necessary to use a spectrograph alone, without a condensing lens, placed at such a distance, and with a sufficiently wide slit to collect light from the whole of the reaction zone. A small quartz instrument with wide aperture ($f/4.5$) and a wide slit ($\cong 0.1$ mm) was accordingly used. The lamp was set at a measured distance between flame and slit and a length of the center of the filament selected by an aperture stop. From a knowledge of the width and distance of the stop and the width of the strip filament, the effective area of filament exposed was determined. A rotating sector was used to vary intensities of the flame and lamp, for comparison purposes. It was necessary to use an inverse square law correction to allow for different distances of flame and lamp from the slit. But with this correction, spectrograms of the flame and lamp, taken on the same plate, could be directly compared.

Measurements of the plate density of the flame spectrum were made at 25A intervals for the 1,0; 0,0; and 0,1 bands of C_2. Using the lamp continuum, curves of optical density against log intensity were plotted at 100A intervals over a region from 4500 to 5800A. From the formula given above, the intensity could be derived in terms of energy units (watts). From the curves for the lamp continua and the measurements of plate density of the flame spectrum, a curve of intensity versus wavelength could be constructed for the flame, and the area beneath it gave the actual energy emitted in the C_2 sequence. The value for a stoichiometric oxyacetylene flame was 21×10^{-3} w. This was raised by a factor of 10 per cent, to allow for reflection at the quartz window of the burner.

This result was converted to photons/molecule by using the Planck relation $E = h\nu$ to get the number of photons, and dividing by the number of molecules entering the flame per second, as obtained from the gas flow and Avogadro's number. The final result was 11.3×10^{-5} quanta/O_2 molecule.

This absolute calculation was very laborious, and other measurements were made in a relative way by photometering the 0,0 band of C_2. The above value for C_2H_2-O_2 was taken as standard. The main results are summarized below.

There was a marked variation in C_2 light yield with pressure. It was not possible to follow the C_2H_2-O_2 flame up to atmospheric pressure, but a comparison was made with a propane-oxygen flame. This showed that the light yield at atmospheric pressure was $\frac{1}{20}$ that at 12 mm. The effects of mixture strength for various fuels were noted, and are summarized in the following table.

			$\lambda = O_2/(O_2$ at stoichiometric)		
Fuel	Light yield ($\times 10^{-5}$) (stoichiometric)	Pressure, mm	Light yield (maximum)	λ (maximum)	Pressure, mm (maximum)
CH_4	0.049	13	1.05	0.59	30
C_2H_2	11.3	5.5	112	0.42	16
C_3H_8	0.78	12	6.1	0.55	24
C_6H_6	16.3	7.6	33.5	0.66	16

The general trend of the results is clear from the table. It is notable that the maximum always occurs in a rich mixture. Measurements on the C_2H_2-O_2 flame indicated an extremely sharp maximum, as can be seen (Fig. N,5a).

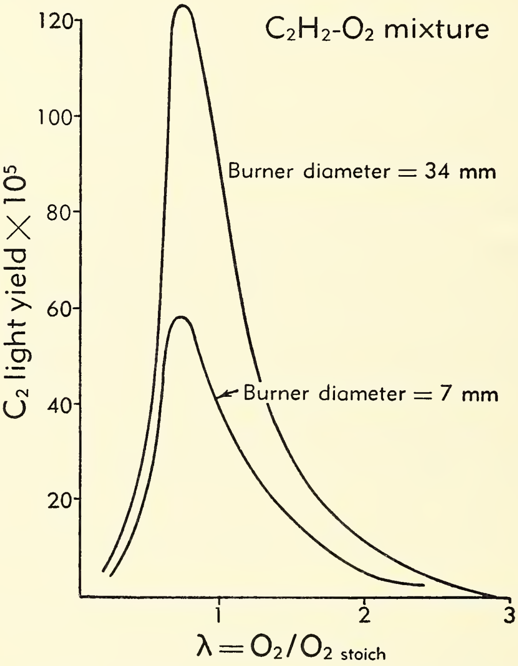

Fig. N,5a. Variation of C_2 emission with mixture ratio.

The effect of diluents on the light yield provides some very interesting data. Dilution of a stoichiometric C_2H_2-O_2 mixture with nitrogen led to a moderate decrease in light yield, probably attributable to the rise in pressure on adding the diluent. On the other hand, dilution with oxygen caused a very rapid fall in light yield. Increases in light yield obtained on adding hydrogen and (to a slight extent) on adding CO are probably due to the effect of these gases on the oxygen equilibrium. In some cases, the light yield from stoichiometric mixtures was measured while the hydrocarbon was gradually replaced by H_2 or CO in amounts sufficient to keep the mixture stoichiometric. The results for ethane are shown in Fig. N,5b. It is apparent that the light yield does not fall off linearly with hydrocarbon concentration. The curve for CO is perhaps not too accurate, because of interference by the continuous and slightly banded emission of burning CO.

It was found, in general, that the light yield fell off roughly as a power of the hydrocarbon concentration, though the relation is not exact. For various hydrocarbons, "power laws" were obtained as follows:

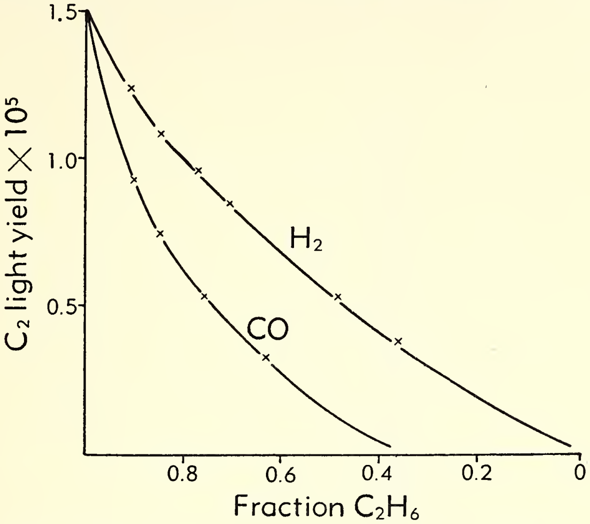

Fig. N,5b. Replacement of C_2H_6 with CO and H_2.

a. H_2 replacement

Light yield L $\sim (CH_4)^2$
$\sim (C_2H_2)^2$
$\sim (C_2H_6)^2$ (rather more than 2)
$\sim (C_6H_6)$ (rather more than linearly)

b. CO replacement

L $\sim (CH_4)^6$
$\sim (C_2H_2)^3$
$\sim (C_2H_6)^6$
$\sim (C_6H_6)^3$

The above data are on stoichiometric flames, but some rough observations on rich C_2H_2-O_2 flames indicate similar effects.

The concentration of C_2 in the flame could be found readily as follows: The number of light quanta emitted per second by the stoichiometric C_2H_2-O_2 flame is known; it is 6×10^{16} quanta/second. The radiative life of C_2 has been obtained by Brewer, Gilles, and Jenkins [*20*] and is approximately 8×10^{-9} sec. Combining these two factors, we see that the flame contains at any instant 5×10^8 excited molecules. Since the reaction zone in a low pressure flame is a regular cylinder, its volume can be estimated, and the concentration of excited C_2 was found to be 10^8 molecules/cm^3.

Now Brewer, Gilles, and Jenkins have determined the partial pressure of C_2 molecules in equilibrium with hot, solid carbon. At 2700°K, corresponding to our equilibrium flame temperature, they get a partial pressure of 9×10^{-10} atm for unexcited C_2. Multiplying this by the Boltzmann factor, $e^{-E/kT}$, one gets 3×10^{-16} atm for excited C_2. From the value of 10^8 molecules/cm^3 we get a partial pressure (in the flame at 1/100 atm) of 6×10^{-11} atm. This is 10^3 times as great as the value from the data of Brewer, et al. and suggests that C_2 is not produced by thermal evaporation from solid carbon.

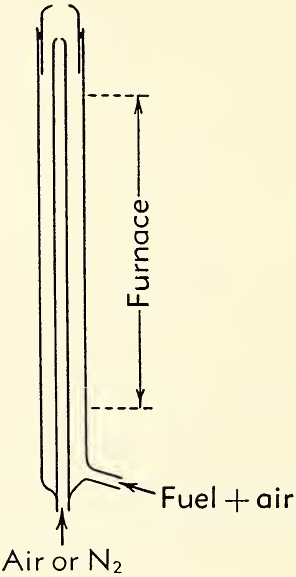

Fig. N,5c. Preheat burner design.

This work of Gaydon and Wolfhard is the only absolute measurement on a free radical yet carried out in flames. Some work on relative intensities, carried out, however, at atmospheric pressure, has been reported by the author [*21*]. This will be described rather shortly, although the results have some bearing on the low pressure flame work.

The author measured the effect of preheating on the C_2 and CH emission from hydrocarbon-air flames, using a special type of burner designed to give constant mass flow over a wide range of preheat, without encountering flashback troubles due to the increase in flame velocity on heating. In this burner, the flame was supported on a fine jet of nitrogen or air, directed up a central concentric tube. Preheating of the mixture was carried out using a small quartz spectrograph with wide slit, over a fairly wide temperature range. The burner is shown in Fig. N,5c.

The nature of this variation of intensity with temperature is shown in Fig. N,5d. It is seen that a peak is reached at about 450°C, followed by an abrupt drop at 620°C, when the whole character of the flame changes. Below this temperature, it was a normal Bunsen-type flame, but above it a fairly uniform cylinder of flame was formed. The intensity showed a slight rise with temperature from this point on.

The work of Wohl and his associates [*22*] was also carried out at atmospheric pressure. They used a special type of burner giving a uniform and flat reaction zone, a "two-dimensional flame," in their terminology. The reaction zone in this flame was very thin (about 0.4 mm), but by the use of a special burner mounting and of two successive slits placed between the spectroscope and the flame, it was possible to make traverses of the flame with some accuracy.

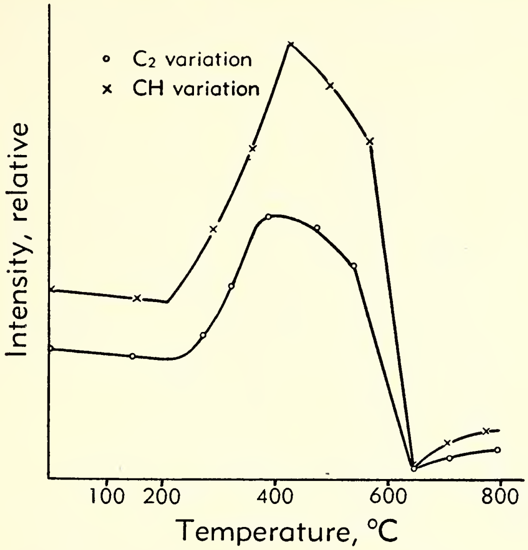

Fig. N,5d. Effect of ambient temperature on C_2 emission.

Using a Perkin-Elmer spectrograph fitted with a photomultiplier tube, Wohl determined the relative intensity of emission of various radicals across the reaction zone. Owing to his optical arrangements, only a small fraction of emitted light reached the spectrograph, after the two slits had been used to narrow the effective aperture. However, the sensitive photomultiplier overcame this disadvantage. The instrument used by Wohl could be adapted to measure infrared emission of H_2O vapor produced in the reaction, using a lead selenide detector in place of the photomultiplier. The results obtained by Wohl, using a butane-air flame, are indicated in Fig. N,5e. The rapid fall of radical emission intensity behind the reaction zone is noticeable, while the H_2O emission continues to rise in intensity. Wohl considers that the maximum of H_2O emission indicates completion of the reaction and attainment of chemical equilibrium, and notes that this is accompanied by a rapid fall in radical concentration.

In the course of their work on OH in low pressure flames, Gaydon and Wolfhard attempted to measure the OH concentration in the reaction zone of the flame by an absorption method. The difficulties encountered in absorption spectroscopy are described by G. H. Dieke (Sec. M) where it is explained that for the detection and measurement of OH in absorption, an instrument of very high resolution is required, i.e. of small instrument width, or the relatively weak OH lines will be swamped by the spread of the monochromatic radiation. The quartz Littrow spectrograph employed in the work was not fully adequate, but some approximate measurements were made in the following manner.

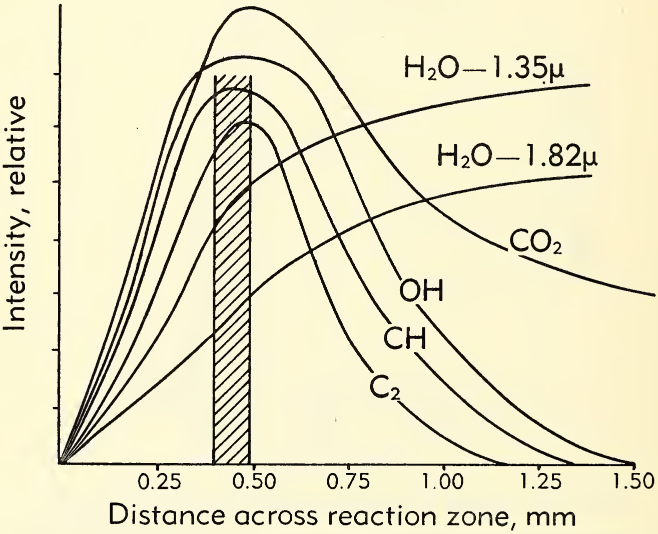

Fig. N,5e. Reaction zone structure; radical concentrations.

It was not possible to determine the OH concentration by measuring $\int \alpha l d\nu$, where α = absorption coefficient, l = length of absorbing layer, and ν = frequency. However, it was assumed that the loss of light due to absorption was proportional to αl for weak absorption. This value was obtained by photometering the lines directly with a photometer slit greater than the line width. Multiplication by the slit width (in cm^{-1}) gave a value for $\int \alpha l d\nu$. By comparing these values of $\int \alpha l d\nu$ with those of Oldenberg and Rieke, the concentration of OH could be directly determined (cf. Sec. M).

A carbon arc was used as a background source, and a weak oxyacetylene or C_2H_2-air flame was used. The result, shown in Fig. N,5f, is not too satisfactory, but it does indicate an unusually high concentration of OH in the preflame zone, a concentration which is certainly much higher than for thermal equilibrium.

These measurements complete the record of those made to date on reaction zones of premixed flames. Some work by Wolfhard and Parker [*23*] on the reaction zone of symmetrical diffusion flames is, however, worth discussing.

Wolfhard and Parker obtained their symmetrical diffusion flame by feeding fuel and air from two parallel and adjacent rectangular slots

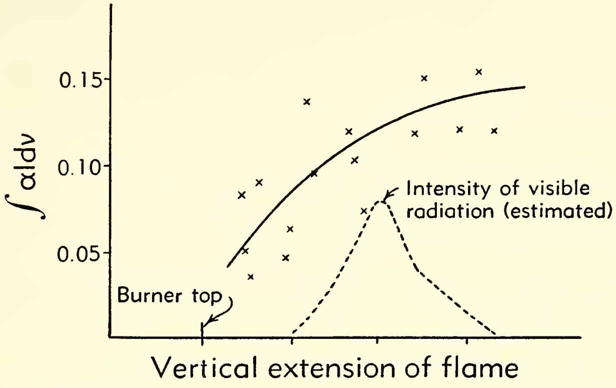

Fig. N,5f. Reaction zone structure; OH concentration (at low pressure).

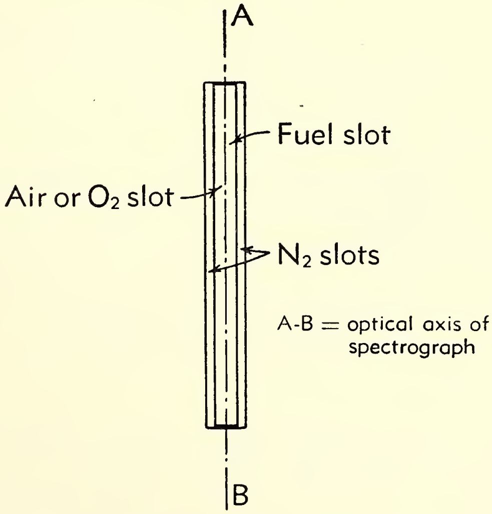

Fig. N,5g. Plan view of diffusion burner.

(Fig. N,5g). A nitrogen jacket for the flame was formed by the flow of N_2 from two outer enclosing slots. The reaction zone which formed about the mixing line of the fuel and oxygen jets was symmetrical and fairly thick, and could be studied in some detail spectroscopically. This flame has also been operated at varying pressures, and the results so obtained are extremely interesting.

Wolfhard and Parker worked on ammonia-oxygen, hydrogen-oxygen, hydrogen-NO, and hydrocarbon-oxygen flames. The flames used had an average optical depth of 5 cm. Emission spectra were obtained in a cross traverse of the reaction zone, which was about 5–10 mm thick. Later, by using a large Littrow-type spectrograph, they obtained absorption measurements of OH. The concentration of this radical was determined by comparison with absorption in a premixed flame of similar optical depth, burning over a narrow slot burner. The concentration of OH in the premixed flame was calculated assuming chemical equilibrium and was used as a datum point from which to estimate OH concentrations in various portions of the diffusion flame. Similar measurements were carried out on the oxygen absorption system in the 2200 to 2500A region, which was, rather surprisingly, found by Wolfhard and Parker in these flames.

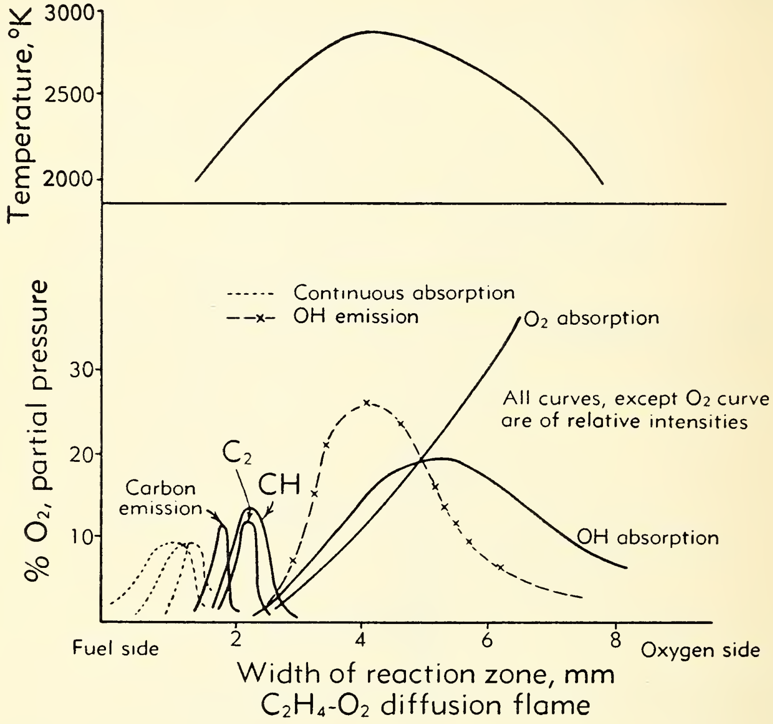

Fig. N,5h. Reaction zone structure—diffusion flame.

The results obtained by Wolfhard and Parker for the ethylene-oxygen flat diffusion flame are summarized graphically in Fig. N,5h. Results of the same general character were obtained for the ammonia-oxygen flame. The weakness and localization of C_2 and CH emission, as compared with a hydrocarbon-oxygen premixed flame, is particularly striking. The temperature plot in the upper part of the drawing was obtained both by the sodium line reversal method and an OH line reversal procedure, using a calibrated hydrogen discharge tube as background source. The results obtained by the two methods were practically identical.

Absorption spectra of acetylene and of benzene were noted on the fuel-rich side of the flame, the benzene spectrum disappearing before the region of continuous absorption (pyrolysis absorption) indicated in the figure.

In an examination of the H_2-O_2 diffusion flame the line reversal temperature of O_2 in the reaction zone of the flame was measured, and was found to be 3070°K ± 60°, which agrees well with the equilibrium temperature.

The C_2 and CH bands were emitted rather strongly in a small region immediately above the flame base. On reducing pressure, the intensity of the C_2 and CH emission over the whole flame greatly increased, while carbon formation gradually disappeared. The flame, in fact, assumed the characteristics of an ordinary premixed hydrocarbon flame at low pressures.

The abnormally excited spectrum of Fe, as produced in premixed flames, was not found in diffusion flames when $Fe(CO)_5$ was introduced into them. At low pressures, however, the nonthermal lines extending into the far ultraviolet showed up.

This work completes the summary of data on reaction zone structure. Its implications for the theory of flames are discussed in the concluding article.

N,6. Pressure Effects and Burning Velocity. As remarked in the introductory article, Tanford and Pease, in setting out a theory of flame propagation by free radical diffusion, tried to determine the effect of pressure on flame velocity. Their argument runs as follows:

By using a very simplified model of the reaction zone of a flame, an expression for the flame velocity can be derived. The derivation is given in the original papers and it is not necessary to reproduce it here. Tanford and Pease get

$$u = \left(\sum_i \frac{K_i C p_i D_i}{Q B_i}\right)^{\frac{1}{2}}$$

where K_i = rate constant of ith species of active radical, C = concentration of combustible, p_i = partial pressure of ith species of active radical, D_i = diffusion coefficient of ith species of radical, B_i = recombination coefficient of ith species of radical, and Q = mole fraction of *potential* combustion products in the fuel mixture. Of the terms occurring in this equation, only three, C, p_i, and D_i, depend on pressure. Now, for a mixture of given composition, the concentration, C, of combustion in molecules/cm^3, is directly proportional to the pressure, while the diffusion coefficients, D_i, are inversely proportional to the pressure. So these two effects cancel, and we are left with the pressure dependence of the radical partial pressures, p_i. It is assumed by Tanford and Pease that, since free radicals are products of dissociation, their partial pressures will decrease with increasing pressure, roughly as $1/p^{\frac{1}{2}}$. Thus, since $u \sim p_i^{\frac{1}{2}}$, it should vary as $p^{-\frac{1}{4}}$ where p is pressure.

The early observations of Ubbelohde and Khitrin, on both hydrocarbon and carbon monoxide flames, tend to confirm the ideas of Tanford and Pease. More recently, Wheatley and Linnett [*24*] made measurements on hydrocarbon-air flames at reduced pressure (down to the 25 to 30 cm range) with a view to checking the Tanford-Pease theory. They used a rather simple form of low pressure flame, burning an ordinary Bunsen-type laminar flame, and measured the burning velocity by projecting a shadow of the flame cone onto a photographic plate, the burning velocity being derived from the linear gas velocity (assumed known with a parabolic distribution across the burner tube) and the sine of the angle which the burner zone makes with the vertical (Gouy's formula). The calculation was carried out piecewise over the cone.

Wheatley and Linnett found that there was, indeed, an increase in burning velocity with reduced pressure. By plotting burning velocity against $p^{-\frac{1}{4}}$, they obtained a fairly linear plot. It was found that the burning velocity of 7 per cent ethylene-air mixtures increased from 70 cm/sec at 76 cm pressure to 97 cm/sec at 27 cm. In their discussion, they point out that the thermal theory of flame propagation put forward by Boys and Corner predicts a decrease of flame velocity with lowering of pressure. As this is not so, their results certainly provide evidence against purely thermal theories of flame propagation and in favor of Tanford's hypothesis.

Belles and Simon [*32*] have carried out measurements of inflammability limits in tubes and rectangular slots at low pressure, and have found, as did Wolfhard in his work on the burner, that a wider inflammability range exists at low pressures in large diameter tubes. They correlated the "critical" or limiting diameter with pressure and found an almost linear relation, thus $d_{\text{cr}} \sim p^{-0.97}$. It was also found that d_{cr} was related inversely to the flame speed and directly to the square root of the minimum ignition energy for the mixture. Plots of d_{cr} versus 1/flame speed and versus $\sqrt{\text{ignition energy}}$ were linear.

This work confirms and extends Wolfhard's results on burner stability. Simon and Belles have tried to combine the Tanford-Pease theory with Semenov's expression for free radical diffusion on the walls of a container of known shape and size, in order to get a relation between flame speed, tube diameter, and shape. By taking account of the variation of diffusion coefficient with pressure, they could account for the pressure effect on limits. In general, their results, like those of workers on low pressure burners, suggest that a radical-diffusion mechanism is the rate-determining step in flame propagation at reduced pressures.

Edse [*25*] has recently studied the burning velocities of H_2-O_2 flames at high pressures. As this work is the only example of its kind so far available, it merits some description, and this is given below.

The apparatus consisted essentially of a cylindrical steel combustion chamber, pressurized by inert gas fed up the sides, and maintained at constant pressure by a suitable back pressure regulator. The burner tube was inserted through a sealed opening in the bottom of this. Quartz windows were provided for observation. Flows of H_2 and O_2 under pressure were measured by noting the pressure drop experienced when they passed through a cotton plug in a copper tube. Ignition of the flames was effected by an electrically heated platinum wire, mounted on a retractable plunger.

In operating the apparatus, serious difficulties were experienced because of the frequency with which flames flashed back at high pressure. It was found that reproducible flashback conditions were only obtained when the burner tube was water-cooled; otherwise, heating of the burner rim greatly increased the possibility of flashback. The operating procedure adopted was to ignite a stream of H_2 from the burner tube in a concentric stream of pressurizing air, then gradually to add O_2 to the H_2 flame, and finally to replace the air with nitrogen. The nature of the pressurizing gas was found not to affect flashback conditions.

The flashback velocities for rich mixtures were obtained by increasing the O_2 flow rate, without changing that of H_2 up to the limit. For lean mixtures, the H_2 flow in a very lean mixture was gradually increased till the flashback occurred.

Edse found, as might be expected, that flow conditions were turbulent in burner tubes of the narrow diameter which he used (0.122 cm to 1.031 cm). He also studied flashback conditions in turbulent flames burning at atmospheric pressure, by means of a control experiment. Burning velocities were derived from photographs of the flames simply by measuring the angle of the inner flame cone as it appears at the rim of the burner tube and by using the Gouy formula. This method is obviously inaccurate for an absolute determination of burning velocity, but Edse considers it adequate for relative measurements carried out at varying pressures. It was found that the size of the inner cone recorded photographically depended on the sensitivity of the emulsion; thus different values of flame velocity were obtained on plates sensitive to infrared, red, and blue regions. This is probably similar to the effect first noted by van de Poll and Westerdijk [*7a*] when they found that schlieren and luminous cone images did not coincide. The stability limits of the turbulent flames could be accounted for by a critical velocity gradient model similar to that of Lewis and von Elbe for laminar flames. Edse uses an expression for the velocity gradient model similar to that of Lewis and von Elbe for laminar flames. He uses an expression for the velocity gradient at the tube boundary originally given by Prandtl and Tietjens, thus,

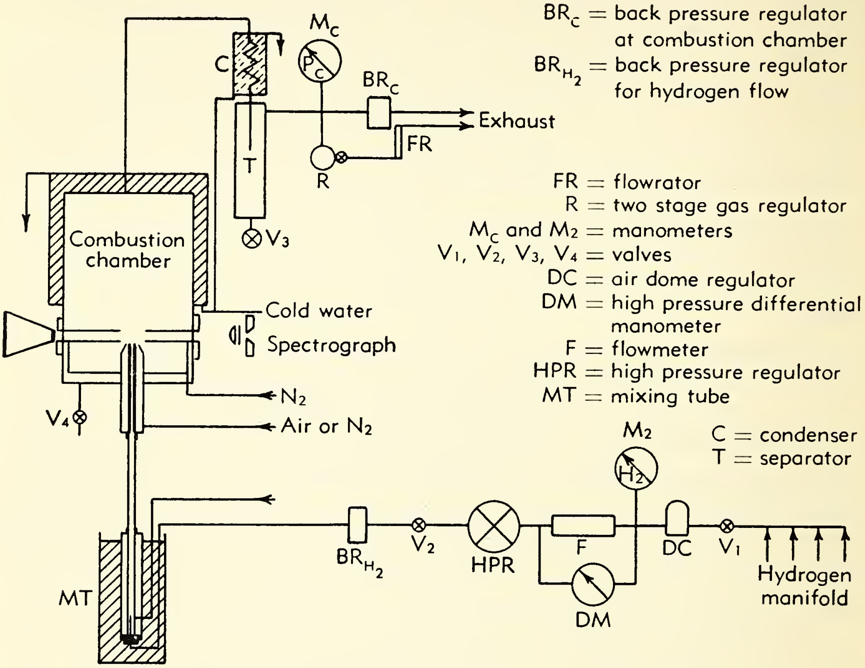
BR$_c$ = back pressure regulator at combustion chamber
BR$_{H_2}$ = back pressure regulator for hydrogen flow
FR = flowrator
R = two stage gas regulator
M$_c$ and M$_2$ = manometers
V$_1$, V$_2$, V$_3$, V$_4$ = valves
DC = air dome regulator
DM = high pressure differential manometer
F = flowmeter
HPR = high pressure regulator
MT = mixing tube
C = condenser
T = separator
M$_c$
P$_c$
C
T
BR$_c$
Exhaust
FR
R
V$_3$
Combustion chamber
Cold water
Spectrograph
N$_2$
Air or N$_2$
V$_4$
M$_2$
H$_2$
MT
BR$_{H_2}$
V$_2$
HPR
F
DM
DC
V$_1$
Hydrogen manifold

Fig. N,6a. Diagram of apparatus for study of high pressure Bunsen burner flames.

$$\frac{du}{dx} = \frac{0.0392}{Re^{\frac{1}{4}}} \cdot \frac{\bar{u}^2}{\nu}$$

where ν is the kinematic viscosity and the other symbols have the usual meaning. Edse writes

$$\nu = \nu_0 \frac{p}{p_0}$$

Using this equation, we can correlate the flashback limit with the critical velocity gradient, provided the temperature of the burner port was controlled by cooling.

An attempt was made by Edse to evaluate the effect of turbulence on the velocity of high pressure flames by burning turbulent flames at atmospheric pressure, and by obtaining their velocities by the "flame pressure" formula of Mache,

$$p_F = p_u \frac{\mathfrak{M}_u}{RT_u} u_F^2 \left(\frac{T_F n_F}{T_u n_u} - 1\right)$$

The subscripts F and u refer to flame and unburned gas, respectively, n is the number of moles present, and the other symbols have their usual meaning. T_F and n_F are given by calculation of equilibrium conditions in the flame. Comparing these values with the velocities of laminar flames burning under similar conditions, Edse found no difference. Thus he assumes the change in burning velocity caused by increased pressure is due only to pressure effects.

From the data on the equilibrium flame temperature and composition, Edse found that the flame velocities reached a maximum at about maximum flame temperature, and that they generally varied much in the temperature. No such correlation was noted between flame velocities and relative concentration of active radicals in the flame (Fig. N,6a to N,6d). (Edse divides the concentration of radicals by pressure to allow for the effect of pressure on the diffusion coefficient.) He concludes that flame propagation in his flames is controlled purely by thermal conduction.

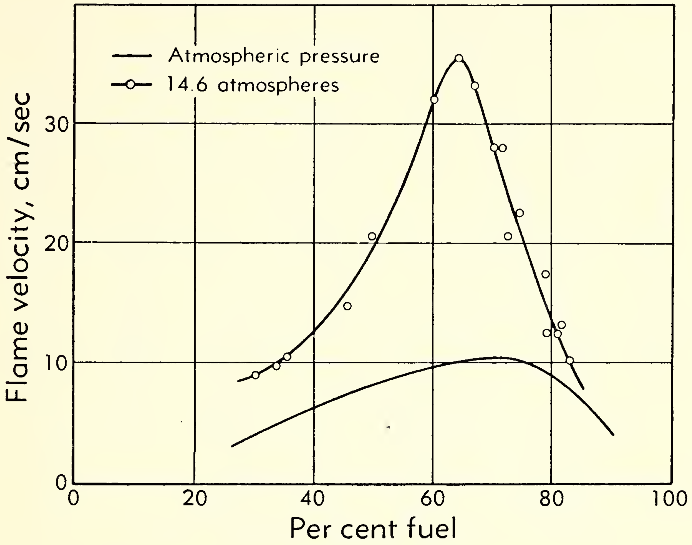

Fig. N,6b. Flame velocities of hydrogen-oxygen mixtures burning on cylindrical tubes.

The results which were obtained on turbulent flame velocity certainly seem questionable, for they contradict all previous work on this subject. Consequently, it is difficult to say how far Edse's results are valid.

Wolfhard [*3*], in his early work on low-pressure flames, observed that the burning velocity did not appear to vary with pressure in the case of acetylene-oxygen mixtures, as is shown in Art. 2 of this section. Subsequently Gaydon and Wolfhard [*26*] set out an approximate theory of free radical diffusion in an attempt to account for this result. From the results obtained by Klaukens and Wolfhard on reaction zone thickness and temperature distribution, they estimate the time of passage of an element of gas through the zone, taking into account the change in gas velocity with temperature. (Reaction zone thickness at atmospheric pressure was estimated by extrapolation of Wolfhard's results on flame thickness at low pressures.) This "time of passage" was substituted in the expression $x = \sqrt{2Dt}$ for diffusion of particles. Here, D is the diffusion coefficient for H atoms, assumed to vary as $T^{\frac{3}{2}}$ over the temperature range involved, and x then will be the average distance traveled by a hydrogen atom during the "time of residence" of the gas in the luminous zone.

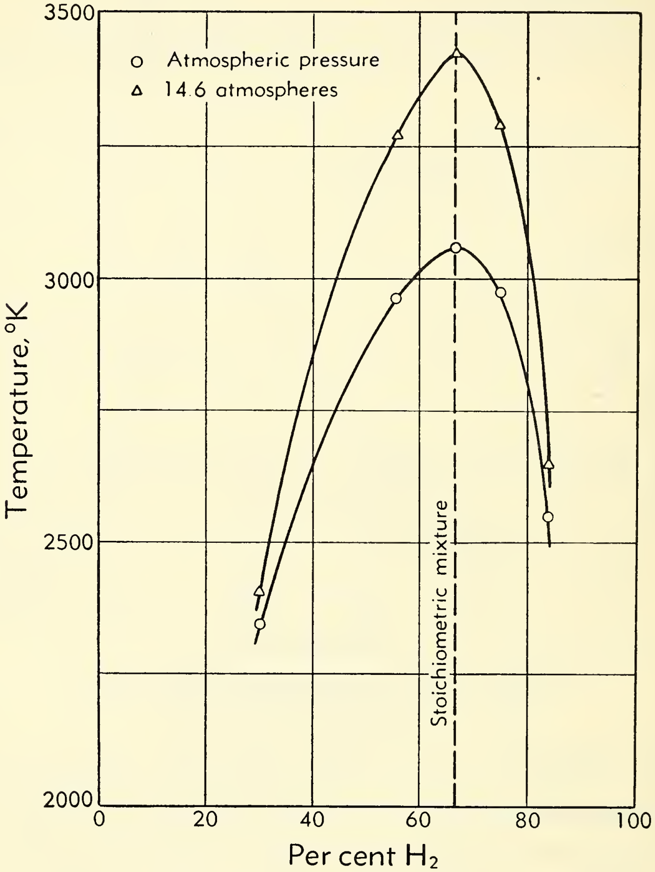

Fig. N,6c. Theoretical temperature of H_2-O_2 flames.

It was found that a linear relation existed between x and the experimentally derived thickness of the luminous reaction zone, δ_l. Roughly, $x = 3\delta_l$. Now, if the expression $x = \sqrt{2Dt}$ is differentiated with respect to t and equated to a gas velocity v at the ignition point, a value of $x = 2\delta_r$ is obtained, where δ_r is the reaction zone thickness, assumed constant.

Gaydon and Wolfhard proceed by taking v_r, the gas velocity in the reaction zone, as δ_r/t_r, and get t_r from the $x^2 = 2Dt$ relation, using a value of x in terms of δ_r. They thus get $v = D/2\delta_r \times$ (temperature factor), or, setting $\bar{u}\delta_r = vn_c$, where $\bar{u}$ is reaction velocity, v gas velocity, and n_c number of combustible molecules present initially, $v^2 = D\bar{u}/2n_c \times$ (temperature factor).[2]

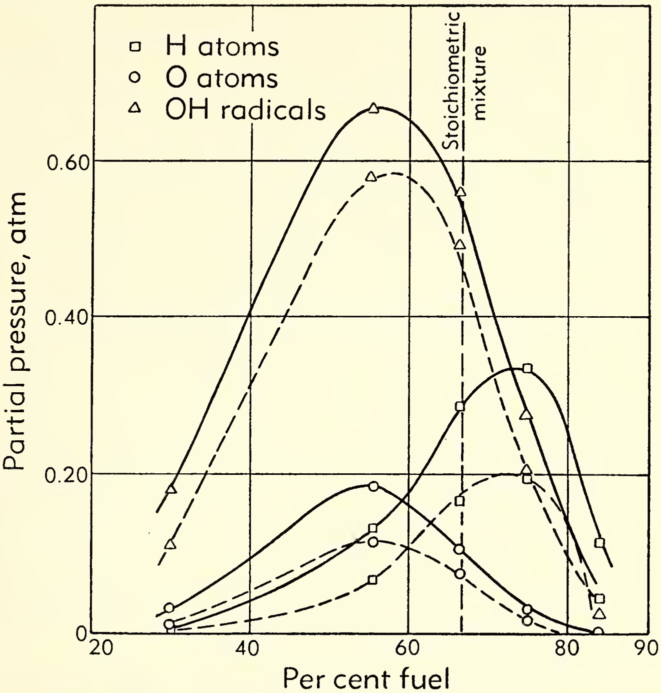

Fig. N,6d. Concentrations of H, OH, and O in H_2-O_2 flame gases.

Gaydon and Wolfhard argue that this relation implies that v should be independent of pressure, since $D \sim 1/p$, $n_c \sim p$, and $\bar{u} \sim p^2$ if it depends on two-body collisions. These contradictory data have not been clearly resolved.

The theories so far put forward are very approximate. The Tanford-Pease theory assumes the combustion process to occur as a single-stage reaction, and, rather arbitrarily, divides the reaction zone into a hot zone producing hydrogen atoms, and a cooler "diffusion zone" in which none are produced. The Gaydon-Wolfhard theory makes drastic approximations about the diffusion mechanism, and equates the linear rates of flow of free radicals and gas, rather than using a conservation-of-mass equation for the whole combustion process, such as Tanford and Pease used. Essentially, both theories postulate a linear relation between the rate of diffusion of free radicals and the over-all rate of combustion, an assumption which is probably incorrect.

---

[2] Manson [*40*] has put forward a theory of flame propagation, treating the flame as a flow discontinuity the pressure difference across which is said to be due to the "projection" of free radicals into the unburned gas. This pressure difference is taken as the excess pressure of H atoms at equilibrium flame temperature over that at room temperature. Substituting this in the normal shock equation, values of flame velocity can be calculated. The physical basis of the "projection" mechanism is unclear, and, although some agreement with experiment has been obtained, it is less consistent than with more conventional diffusion or thermal conduction theories.

It should be remarked, however, that the combustion processes in acetylene may differ appreciably from those in other hydrocarbons. Thus, Bartholomé [*35*] in plotting flame velocities against free radical or hydrocarbon-oxygen mixtures, obtained a smooth curve for a large number of hydrocarbons, with the sole exception of acetylene. Since acetylene is the only triple-bonded hydrocarbon fuel to have been studied much to date, it is not altogether surprising that some of its properties should seem anomalous. Recently, Wheatley and Linnett [*24*] have studied the flame velocity of acetylene-air and acetylene-oxygen mixtures at various pressures by the soap bubble method, and have substantially confirmed Wolfhard's result that burning velocity is independent of pressure. On the other hand, work on other hydrocarbons by the burner method (Badin, Stuart, and Pease [*33*] and Garner, Long, and Ashforth [*34*]) shows that burning velocity is increased by a decrease in pressure. Some of the discrepancies are explicable by the fact that the equilibrium temperature of the C_2H_2-O_2 flame is pressure sensitive, as compared to that of air flames of lower temperature. Thus, in such a flame, the equilibrium concentration of free radicals will fall off at reduced pressure and will partly offset the effect of the inverse fourth root law mentioned above. This, however, is a very incomplete explanation.

The diffusion theories of flame propagation, outlined above, suggest that the flame velocity should vary with $\sqrt{D}$, where D is the diffusion coefficient of the radical, or radicals, which is responsible for the propagation process. However, thermal theories of flame propagation, such as those put forward by Zeldovich [*38*] and by Boys and Corner [*37*], predict a dependence of flame velocity on the square root of the thermal conductivity. The analysis in both cases follows rather similar lines, but with different assumptions. Now, the thermal conductivities and diffusion coefficients of gases are closely related transport properties, and it is difficult to distinguish between variations of the two factors without rather precise measurements. The data for these do not exist, particularly in the case of thermal conductivities. Some progress has been made in calculating exact values of D for gas mixtures at high temperatures from the kinetic theory, but similar calculations for thermal conductivity involve assumptions about the manner in which energy is transferred during molecular collisions and have not been particularly successful. Presumably, both heat and free radicals are capable of initiating reactions in a flame front, but the faster-diffusing free radicals, such as H atoms, play the main part in the low temperature zone of the flame front. Tanford showed by a rough calculation that the hydrogen atom concentration in a flame front fell off much more slowly than the temperature, and there is not much doubt of the qualitative correctness of this result. This effect would be increased at low pressures, with the spreading out of the reaction zone, the increase in diffusion coefficients of the free radicals, and the reduction in thermal conductivity of the gases. At sufficiently low pressures free radicals may play a predominant part, but at high pressures the tendency will clearly be in the reverse direction, and the result obtained by Edse, that flame velocity is only dependent on temperature, would not be surprising.

Since flames of technical interest operate at atmospheric or above atmospheric pressures, it is possible that thermal effects together with changes in flow conditions (absent at low pressures) are the main factors in propagating them. The difficulties experienced by Edse illustrate this point. This conclusion, however, is rather tentative, and as can be seen from the work cited above, no final definitive result has been obtained to date.

Added note. Since this section was written, some new results have become available from the United States Bureau of Mines on burning velocities of hydrocarbon-air flames over a pressure range of $\frac{1}{20}$ to 2 atmospheres. Measurements were carried out on a slot burner, which gave a wedge-shaped reaction zone, eliminating errors due to cone curvature on the Bunsen-type burner. They were checked against values obtained in bomb experiments (cf. [*36*]) on similar mixtures and were found to agree within very close limits. Essentially, the results show a constant burning velocity over the above range of pressures. This directly contradicts the Tanford-Pease theory, and casts doubt on the validity of earlier burning velocity measurements in Bunsen-type flames, although no adequate explanation is yet available for the experimental discrepancies. On the Gaydon-Wolfhard assumption that total reaction rate varies as p^2 it is possible, as shown above, to develop a pressure-independent expression for burning velocity. However, this theory only assumes diffusion of radicals to occur well *within* the boundary of the thermal conduction wave to the point of apparent ignition temperature, and its direct application is as yet restricted to low pressure flames.

It would seem that these new data tend to support the conclusion reached above, that thermal conduction, not radical diffusion, is the determining factor in flame propagation, except perhaps at low pressures.

N,7. Discussion. In this article the validity of some results cited previously is discussed, and their bearing on the mechanism of flame propagation is indicated.

Penner [27] has lately criticized the rotational temperature measurements made on OH by Gaydon and Wolfhard, and others, on the ground that self-absorption effects may falsify the interpretation of the data. A summary of Penner's arguments is given below.

Penner has constructed plots of ln $(I - p\nu^3)$ against E_u, corresponding to the experimental plots for rotational temperature, by the following procedure: A value for the coefficient of self-absorption is assumed and is multiplied by the intensity ratio for two levels of a transition (obtained from Dieke and Crosswhite's tabulation and the ratio of the frequencies for the levels), giving the upper value of the coefficient. From this the corresponding intensity is readily deduced, and finally the term ln $(I - p\nu^3)$ is obtained and plotted against values of the rotational energy levels, E_u. The slope of the plot gives T_u, the apparent temperature of the isothermal region over which the calculation is performed.

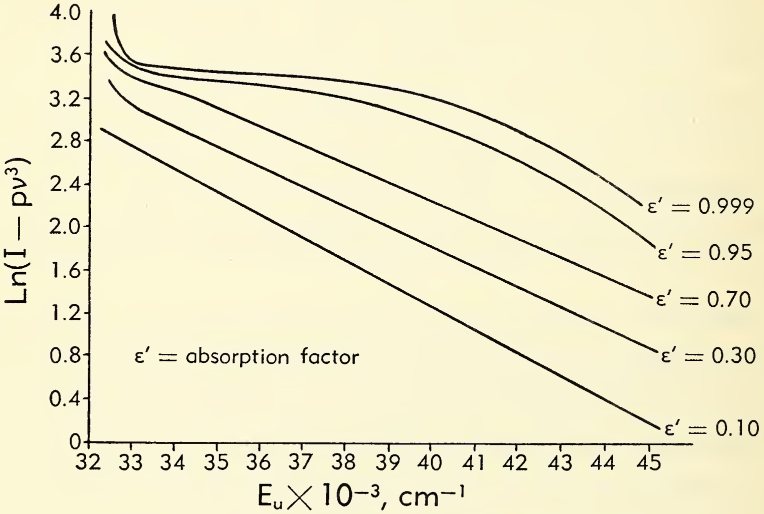

Fig. N,7. Computed rotational temperature plots.

Penner has carried through these computations for certain OH transitions. He finds that with increasing self-absorption the plots show increasing curvatures until they simulate very high apparent temperatures (Fig. N,7). He suggests that a limited number of experimental points at lower values of E_u could be correlated as two intersecting straight lines, and this certainly applies to the results of Gaydon and Wolfhard on acetylene-air and acetylene-nitrous oxide flames. Penner also found that for sufficiently large values of E_u, all curves become parallel independently of the assumed self-absorption. Hence, in this region, at the right of the figure, the experimental data should yield apparent temperatures in agreement with the true temperature. It was originally suggested that the change in slope which Gaydon and Wolfhard explained by a predissociation mechanism was due to this effect, but an experimental check showed that this was not so, as the apparent temperature given by the slope at high E_u is much lower than the true flame temperature. Physically, Penner's computations are based on the assumption that there is a good deal of self-absorption in the low pressure flame. Some numerical estimates by him, based on Oldenburg's absolute intensity measurements for OH, suggest that this factor is large enough to cause temperature abnormalities in low pressure flames.

As against Penner's criticism, it should be remembered that the occurrence of abnormal rotational temperatures is highly specific, as was mentioned earlier. It is localized in the reaction zone only and is not found in certain fuels. Also, the majority of temperature plots obtained were single, straight lines without any indication of the "two-slope" effect characteristic of Penner's abnormal plots.

In addition, Penner's calculations were carried out on the assumption that only Doppler broadening was occurring. Some recent calculations by him [*42*], covering the case of combined Doppler and collision broadening, show that the plots remain straight and give true values of temperature, even when self-absorption is present. Of course, as pointed out by Penner himself, calculations carried out for a simple isothermal model cannot be directly applied to a complex system such as a flame, except with very great caution.

It is unlikely that self-absorption affected the measurements on C_2 or CH, and a direct experimental check on C_2, noting whether the intensity changed when the flame was backed by a mirror, gave a negative result. Gilbert (unpublished work) has carried out a similar experiment on his low pressure flame, but has only obtained evidence for a small amount of OH self-absorption.

It may be noted that Broida has lately obtained abnormally high rotational temperatures for OH in hydrocarbon flames (considerably diluted with inert gases) at atmospheric pressure. This effect does not appear explicable by self-absorption [*43*]. In general, the results published by Broida [*30,31*] on oxyhydrogen and methane flames at atmospheric pressure confirm the results of Gaydon and Wolfhard on OH rotational temperatures, except that in the CH_4-O_2 flame no abnormal effects were noted.

Broida has also worked on vibrational temperature measurements, using the methods developed by Shuler, and has obtained some curved plots in the inner cones of oxyhydrogen flames. These plots indicate non-equilibrium vibrational distributions of energy. It will be remembered that Thomas, Gaydon, and Brewer obtained abnormally low vibrational temperatures for CN in the region immediately adjacent to the reaction zone in C_2N_2-O_2 flames. Low rotational temperatures were also obtained. However, for the outer cone, the same method gave a temperature of

4800°K, corresponding to equilibrium calculated assuming $D(N_2) = 9.76$ ev. This later result was confirmed by Kistiakowsky and coworkers [*39*] who determined $D(N_2)$ from detonation speeds in cyanogen-oxygen mixtures.

This summary suggests that the temperature measurements so far made by various workers have a certain self-consistency, and that no direct contradictions have so far appeared. The relation of these results to current theories of flame propagation is by no means clear at present. Some of the data on diffusion flames, abnormal excitation, and C_2 formation have been used by the author [*28*] to develop a tentative theory of the processes which may occur in the reaction zone of the hydrocarbon flame.

The author's theory starts from the result of Gaydon and Wolfhard on C_2 concentration in flames. It has been described above how they found, comparing their results with the data of Brewer and coworkers on the evaporation of C_2 from solid carbon, that the C_2 concentration was too high to be accounted for by evaporation from carbon particles. On the other hand, they were able to eliminate the suggestion, previously made by Smith, that carbon formation was due to polymerization of C_2 radicals in flames, since the concentration of C_2 is much too small to provide an adequate supply of C_2 radicals which can polymerize by direct collision during their "residence time" in a reaction zone. As a possible alternative they suggested that C_2 might be formed by the breakdown of a polymer, since C_2 formation seemed associated with carbon formation, and since the latter process had previously been thought to occur because of some form of polymerization.

The mechanism suggested by the author involves two alternative paths of polymerization, one occurring in the presence of oxygen, the other in its absence. In the first case, the polymerization is accompanied by dehydrogenation to give a highly unsaturated product; in the second case a relatively saturated polymer is formed, which goes eventually to form graphite rings. In the first case, however, a vibrational breakdown of the unsaturated polymer is postulated to occur at sufficiently high temperatures, and C_2 and CH radicals are formed simply by the breakdown of the polymer skeleton.

The direct reaction of C_2 with oxygen would supply enough energy to account for the observed abnormal excitation effects, and such a mechanism would not contradict the observations of the dependence of C_2 intensity on hydrocarbon and oxygen concentration. It also accounts for the "power law" effect noted by Gaydon and Wolfhard, in which the C_2 emission was shown to be roughly dependent on a power of the fuel concentration. This would follow if C_2 were assumed to be the end product of a polymerization of the nonbranching-chain type.

The vibrational breakdown of a highly unsaturated polymer is discussed in the original paper, and an analysis of the possible mode of breakdown is given. This leads to the conclusion that the highly unsaturated polymers will be more stable at high temperatures than saturated ones, but that the breakdown, when it does occur, will do so with greater speed than is the case with saturated chains. Such thermodynamic data as are available confirm the above conclusions on stability of the polymer.

The results of Wolfhard and Parker on hydrocarbon diffusion flames can be qualitatively explained by this theory, since, in the absence of oxygen, hydrocarbon polymerization will proceed by way of saturated polymers to carbon. As unsaturated polymers are not formed, no C and CH is found, and no abnormal excitation effects are noted. Reduction of pressure, by increasing the diffusion coefficients, leads to rapid mixing and contact of the fuel with oxygen before any large amount of thermal polymerization occurs. It has not been possible to give any reasonable theory of the way in which the energy released by the vibrational breakdown of the chain is partitioned between the rotational and translational energies of the fragments. So the abnormal temperature values for C_2 and CH cannot be interpreted with any certainty.

The explicit mode of formation of OH in the reaction zone is not known, but Gaydon and Wolfhard [*8*] have discussed their observations and have concluded that the rotational energy of OH is mostly removed by collision with CO and CO_2, while electronically excited OH radicals are removed by collision with O_2. Their removal will give a higher rotational temperature. This explanation has been extended by Broida to cover his work on diluted flames, but its tentative nature should be emphasized.

The work outlined in this article casts some doubt on one of the assumptions used in current theories of flame propagation, namely, the use of a uniform reaction rate mechanism through the combustion wave. The existence of regions of nonthermal equilibrium suggests gross differences between the reaction rate mechanism in different portions of the flame. It may be that the combustion wave model postulated by Lewis and von Elbe [*36*] in which the flame front is somewhat arbitrarily divided into separate zones, is a nearer approach to the true state of things than might have been expected. In any event, it is likely that future work on flame propagation will have to take account of the existence of nonthermal equilibrium in the flame, and, by so doing, may find it possible to treat the unsteady regions of flame propagation, such as the predetonation region, which have hitherto defied even a qualitative explanation.

N,8. Cited References.

1. Ubbelohde, L. *J. Gasbeleucht. 59*, 49 (1916); *60*, 225 (1917).
2. Khitrin, L. *J. Tech. Phys. U.S.S.R. 3*, 926 (1936).

3. Wolfhard, H. G. *Z. tech. Phys. 24,* 206 (1943).
4. Wolfhard, H. G. *Z. Physik 112,* 107 (1939).
5. Tanford, C., and Pease, R. N. *J. Chem. Phys. 15,* 862 (1947).
6. Gilbert, M. *Jet Propul. Lab. Rept. 4-54,* Aug. 1949.
7. Klaukens, H., and Wolfhard, H. G. *Proc. Roy. Soc. London A193,* 512 (1948).

7a. van de Poll, A. N. J., and Westerdijk, T. *Z. tech. Phys. 22,* 29 (1941).

8. Gaydon, A. G., and Wolfhard, H. G. *Proc. Roy. Soc. London A194,* 169 (1948).
9. Gaydon, A. G., and Wolfhard, H. G. *Proc. Roy. Soc. London A199,* 89 (1949).
10. Gaydon, A. G., and Wolfhard, H. G. *Proc. Roy. Soc. London A208,* 63 (1951).
11. Gaydon, A. G., and Wolfhard, H. G. *Proc. Roy. Soc. London A201,* 561 (1950).
12. Earls, L. T. *Phys. Rev. 48,* 423 (1935).
13. Dieke, G. H., and Crosswhite, H. M. *Johns Hopkins Univ. Appl. Phys. Lab. Bumblebee Rept. 87,* 1948.
14. Thomas, N., Gaydon, A. G., and Brewer, L. *J. Chem. Phys. 20,* 369 (1952).
15. Shuler, K. E. *J. Chem. Phys. 18,* 1221, 1466 (1950).
16. Ornstein, L. S., and Brinkman, H. *Proc. Acad. Sci. Amsterdam 34,* 33 (1932).
17. Gaydon, A. G., and Wolfhard, H. G. *Proc. Roy. Soc. London A205,* 119 (1951).
18. Burgoyne, J. H., and Thomas, N. *Nature 163,* 765 (1949).
19. Gaydon, A. G., and Wolfhard, H. G. *Proc. Roy. Soc. London A201,* 570 (1950).
20. Brewer, L., Gilles, P. W., and Jenkins, F. A. *J. Chem. Phys. 16,* 797 (1948).
21. Thomas, N. *Trans. Faraday Soc. 47,* 958 (1951).
22. Wohl, K., Welty, F., Bernath, L., et al. *Inst. Mech. Engrs. London J. & Proc.,* Sept. 1951.
23. Wolfhard, H. G., and Parker, W. G. *Proc. Phys. Soc. London A, 65,* 2 (1952).
24. Wheatley, P. J., and Linnett, J. W. *Trans. Faraday Soc. 48,* 338 (1952).
25. Edse, R. Paper presented at ASME Symposium at Columbus, Ohio, June 1952.
26. Gaydon, A. G., and Wolfhard, H. G. *Proc. Roy. Soc. London A196,* 105 (1949).
27. Penner, S. S. *J. Chem. Phys. 20,* 507 (1952).
28. Thomas, N. *J. Chem. Phys. 20,* 899 (1952).
29. Penner, S. S., Gilbert, M., and Weber, D. *J. Chem. Phys. 20,* 522 (1952).
30. Broida, H. P. *J. Chem. Phys. 19,* 1383 (1951).
31. Broida, H. P., and Shuler, K. E. *J. Chem. Phys. 20,* 168 (1952).
32. Belles, F. E., and Simon, D. *NACA Repts. Mem. E51J09, E51 L18,* 1951.
33. Badin, E., Stuart, L., and Pease, R. N. *J. Chem. Phys. 17,* 314 (1949).
34. Garner, F. H., Long, R., and Ashforth, G. K. *Fuel 30,* 17 (1951).
35. Bartholomé, E. *Naturwissenschaften 36,* 171, 206 (1949).
36. Lewis, B., and von Elbe, G. *Combustion, Flames and Explosions in Gases,* Chap. VII. Academic Press, 1951.
37. Boys, S. F., and Corner, J. *Proc. Roy. Soc. London A197,* 90 (1949).
38. Zeldovich, J. Theory of combustion and detonation of gases. *Air Materiel Command Transl. F-TS-1226-LA,* 1949.
39. Kistiakowsky, G. B., Knight, H. T., and Malin, M. E. *J. Chem. Phys. 20,* 876 (1952).
40. Manson, N. *Rev. Inst. franç. pétrole et Ann. combustibles liquides 4,* 338 (1948).
41. Born, M. *Optik.* Springer, Berlin, 1933.
42. Penner, S. S. *J. Chem. Phys. 21,* 686 (1953).
43. Broida, H. P. *J. Chem. Phys. 21,* 1165 (1953).

INDEX

Abel's integral equation, 12, 18
absolute radiation methods, 359–365
absorption,
  broadening, 348, 349
  measurements of radical concentration, 544–553
  of electrons, 106
  of spectra (see spectral absorption)
  of X rays, 97
  selective, 362
absorptivity, 344
acoustic anemometry, 152ff.
  in shock tube, 153
acoustic Mach meter, 152
  quartz crystal type, 153, 154
active nitrogen, 79, 80
  energy of, 84
additive and inert gases, effect on burning velocity of, 430
afterglow, 79ff.
  effect of impurities on appearance of, 81
  flow studies by, 85
  intensity of, 81
  Lewis-Rayleigh, 79
  pressure effect in nitrogen, 81
  pressure range in air, 82
  production of, 83
  shock wave studies using, 85
  spectrum in air, 82
  temperature effects in nitrogen, 81, 84
  theoretical models in nitrogen, 80
  volume effects in nitrogen, 81, 84
afterglow technique,
  application of, 85
  flow photography with, 85
  shock wave studies with, 85
air, afterglow in, 82
air, glow discharge in, 86
alignment of impact tubes, 119
α particle absorption, 104
  density measurements by, 104
  probe for, 104
aluminum flakes as luminous tracers, 142ff.
amplifier, hot wire, 253ff. (see circuitry, hot wire)
analogy, electric (see electric analogy)
analogy, hydraulic (see hydraulic analogue)
anemometry (see hot wire probe; turbulent flow; velocity measurement)
angle method for measurements of burning velocity, 412
angle of attack at hot wire probes, 240, 249
angle of incidence for Mach-Zehnder, 54
angular deviation of light due to gradients, 29, 36
aperture of light source, 52
  limitations on, 53
apparatus (see instrumentation)
appearance potentials, 447, 452
area method for measurements of burning velocity, 414
averaging of hot wire signals, 263, 264, 272
axially symmetric flow,
  in electric analogy, 330
  interferometric evaluation of, 12, 13, 63

beam splitter, 47ff.
  dispersion by, 57
  effect on allowable aperture of the Mach-Zehnder interferometer, 53
Bendix pressure gauge, 129
black body, 344, 359
  temperature of, 344
Boltzmann equation applied to theory of shock front thickness, 207
boundary conditions in electric analogy, 330, 331
boundary layers,
  density in, 73
  on impact tube, 114
  recovery temperatures in, 177ff.
  temperature measurements in, 195
  transition of, 215, 217
Bourdon tube pressure gauge, 129
box turbulence, 220
brightness,
  flame, 347, 350ff., 361
  grading, 356
  mirrored, 359
  spectral background, 348
  unmirrored, 359
Buck and Barkas pressure gauge, 128ff.
Bunsen burner,
  method for studying flame propagation by, 412
  nozzle-type, 418
  tubular, 413
Bunsen flames,
  curvature at base and tip of, 411

  cylindrical tubes above, 413
  nozzles above, 418
burner,
  high pressure, 555–557
  laminar diffusion, 551
  low pressure, 527–531
  two-dimensional, 551
burning velocity,
  apparent flame speed and, 410
  definition of, 409
  effect,
    of additive and inert gases on, 430
    of flame shape on, 410
    of flow irregularities on, 410
    of flow pattern on, 410
    of fuel composition on, 428, 429
    of fuel-oxygen ratio on, 429
    of inert gases on, 430
    of initial state on, 428
    of mixture ratio on, 429
    of pressure on, 430
    of structure of combustion wave on, 410, 411
    of temperature on, 429
  influence,
    of hydrogen atoms on, 553, 554, 558
    of radicals on, 528, 560
  laminar, 409
  measurement of,
    by angle method, 412
    by area method, 414
    by bubble method, 423–426
    by Bunsen burner method, 413–420
    from inverted flames, 420
    from moving flames, 422–428
    from plane flames, 420
  normal, 409
  numerical values of, 414–421, 428–435
  open-tube method for determination of, 422, 423
  pressure variation on, 529, 553–561
  recent values of, 431–435
  significance of, 409
  spherical bomb method for determination of, 426–429
  stationary flames from, 412–422

C_2 bands, 484, 485, 518
  concentration in flame, 545
  rotational temperature of, 537
cameras, commercial, for high speed motion pictures, 394
carbon dioxide, 482
carbon formation in flame, 564
cascade flow in electric analogy, 329, 334
cathode ray oscillograph, 519
ceiling-to-floor ratio, 254
central ray, 49
CH bands, 483, 484, 518
  Plate M,3
  rotational temperature of, 537, 565
  vibrational temperature of, 538
chemiluminescence, 363
"China clay" method, 217
chronograph,
  for traveling waves, 162
circuitry,
  amplifier design, 258, 262
  bandwidth, 270
  compensation units, 253
  hot wire, 253
  noise factor, 260
circulation in electric analogy, 327ff. 334–335
CN,
  rotational temperature of, 541
  vibrational temperature of, 541
coefficient,
  of entrainment of luminous particles, 142
  of heat transfer, 182
  of spectral absorption, 89, 92, 94
  of X-ray absorption, 97, 98
collision broadening, 490
collisions, 515
combustion, fluctuating, 360, 361
combustion wave,
  methods of recording, 411
  structure of, 410, 411
commercial cameras for high speed motion pictures, 394
compensating chamber, interferometric, 10, 54
compensation for hot wire thermal lag, 250
  at high frequency, 251
  calibration of, by square wave signals, 251
  circuits for, 253–256
  constant temperature negative feedback, 256
  effect on noise level of, 258
  in shock tube, 252
  "poor man's," 259ff.
  relation of, to ceiling-to-floor ratio of amplifier, 254
compressible flow in electric analogy, 333–335
computation of density, 63, 64 (see also evaluations, interferometric)
computing machines, use of, in conjunction with optical analysis, 17, 24
condensation, optical study of, 289ff.
condensation particle, measurement of size of, 298, 301
conical flow,
  studied by electric analogy, 337, 338
  test for, 63, 64

constant temperature hot wire system, 256
continuous background, 496, 504, 507
continuous spectra, 490
cooling of phototubes, 476, 478
corona discharge, 147, 148
correlation,
  between mass flow and stagnation temperature, 248
  between two signals, 264, 265
  from shadowgraphs of turbulent flow, 280–282
  shear, 265
  time, 266, 268
  triple, circuit for, 267
  velocity temperature, 266
critical,
  flow nozzle, 369–371
  pressure ratio, 369
  volume flow rate, 370
current fluctuations of hot wire, 244ff.
current function in electric analogy, 322, 323
curvature at base and tip of Bunsen flames, 411
cyanogen flame, temperature of, 541, 563
cyclotron resonance mass spectrometer, 445, 446

dark current of phototubes, 477, 478
densitometer recordings, 356, 358
density,
  errors in (see errors in density determination)
  gradient, effect on evaluation, 67
  in boundary layer, 73
  measured by,
    α particle absorption, 104
    electron absorption, 105, 106
    interferometry, 62–69 (see also evaluations, interferometric)
    spectral absorption, 91–93
    X-ray absorption, 100–103
  registration by interferometry, 6
  registration by schlieren photography, 7
  registration by shadowgraph, 20
density change,
  across shock, 204
  modified by relaxation, 209
density fluctuations,
  correlation in isotropic turbulence, 281, 282
  hot wire response to, 248
  measured by shadow methods, 279, 280
  microscale of, 282
deshocking,
  of interferograms, 19
  of schlieren records, 20
Deslandres-d'Azambuja bands, 485
detonation in piston engines, photography of, 394, 395
deuterium, effect on flame speed, 417, 431
diborane, effect on photography of flames, 392
diesel engine, combustion chamber gas temperatures of, 362ff.
diffraction rings of condensation particles, 298
diffuser, supersonic, hydraulic analogue of, 319
diffusion flame, laminar, 551–553
direct image of combustion wave, 411
discharge in OH, 515–518
discrimination in mass spectrometers, 453
dissociation energy, CH_3—H, 449–450
Doppler broadening, 490, 497, 498
  measurement of CH temperature by, 538–540
Doppler width of spectral lines, 345
double traverse coincident schlieren system, 32

effects of,
  deuterium on flame speed, 417, 431
  fuel composition on burning velocity, 428, 429
  mixture ratio on burning velocity, 429
  moisture content on flame speed, 415–417, 431–435
  pressure on burning velocity, 430
  temperature on burning velocity, 429
electric analogy,
  boundary conditions in, 330ff.
  Dirichlet problem in, 331
  for axially symmetric flows, 329ff.
  for cascade flow, 328ff., 334
  for circulation, 327ff., 334ff.
  for compressible flows, 333–335
  for conical flows, 337ff.
  for lifting surface problems, 332, 333
  for velocity potential, 322ff.
  instrumentation for, 325ff.
  scale constants in, 323
  thickness parameter in, 323
electrical discharge, 146ff., 515–518
  effect of pressure on, 147
  types of, 146
electrodynamometer used for two signal correlation, 265
electron absorption, 106
Electronic Transit-Time Anemometer (ETTA), 145
electrophoresis, schlieren system for, 33
emissivity, 344, 359
energy spectrum of turbulence, 268ff.
  measurement of, 269, 279ff.

  - relation between one-dimensional and three-dimensional, 279
- entrainment of luminous particles, 142
  - coefficient of, 142
- equilibrium, thermal, 491ff.
- errors in density determination, 17ff., 64ff.
  - at shock wave, 19, 65, 68
  - by X-ray absorption, 89
  - in boundary layer, 67, 68
  - refraction (density gradient) type, 67
- ethylene flame, 510, 511
- evaluations across shock wave, 19, 62, 65, 68
  - basic equations for, 9
  - errors in (see errors in density determination)
  - in axially symmetric flow, 12, 63
  - in isentropic flow, 63, 64
  - interferometric, 61ff.
- excitation of line spectra in flames, 542–544
- explosion waves, shadowgraph analysis of, 21ff.
- extinction coefficient, 296ff.
  - dependence on particle size, 296
  - dependence on wavelength, 297

- Fabry-Perot interferometer, 355, 378
- fatigue of photocathodes, 475, 477
- feedback, negative, (see negative feedback)
- "figure of merit," 224
- filter spectroscopy, 468–471
- filters,
  - absorption, 469
  - interference, 361, 470
  - photography through, 389–392
- flame constituents, 482
- flame photography,
  - additives to increase luminosity, 392–393
  - exposures for, 393, 394
  - recommended plates and filters for, 391
  - use of color film in, 393
- flame position,
  - direct method of recording, 410
  - methods of recording, 411
  - schlieren method of recording, 411
  - shadow method of recording, 411
- flame speed, 409ff.
  - apparent, 409, 410
  - effect of deuterium on, 417, 431
  - effect of flame shape on, 411
  - effect of flow pattern on, 413
  - effect of moisture on, 415–417, 431–435
- flame structure, small particles, defining, 402, 403
- flame studies by mass spectrometry, 458–462
- flame temperature by compensated hot wire method, 368, 369
- flame velocity, measurement of, 403
- flames,
  - coloring for photography, 392, 393
  - complex, 352, 354, 358
  - direct photography of, 389
  - electric arc, 372–376
- fluctuations of physical variables, 243ff., 248
  - large, 248, 249
- focusing effects in shadowgraphs, 21
- Franck-Condon principle, 519
- free flight interferometry, 73ff. (see also interferometry, applications of)
- free molecule flow, use of impact tube in, 120ff.
- free radicals,
  - concentrations by mass analysis, 460ff.
  - detection by photography, 389, 391
- fringe, interference, 378
- fringe shift, 7ff., 10ff.
  - measurement of, 61ff.
    - across shocks, 62
    - superposition method of, 62, 73
- fringes,
  - available number of, 52
  - contour (isopycnal), 62
  - formation of, 49ff.
  - "islands" of, 51, 61
  - location of, 55
  - orientation (direction) of, 50ff., 54ff.
  - "wash-out" of, 51
  - white light, 57, 62
- Froude number,
  - in free surface flow, 310
  - measurement of, 313
- fuel beds, photography of, 393
- fuel composition, effect of, on burning velocity, 428, 429
- fuel-oxygen ratio, effect of, on burning velocity, 429

- gas pressure, in supersonic flames, 382
  - measurement by spectroscopic pressure shift, 383
- gas temperature, determination of,
  - pneumatic method for, 369–371
  - ultrasonic methods for, 376
  - velocity of sound method for, 372ff.
- gas velocity,
  - in rocket exhaust, 380
  - measurement by Doppler shift, 396
  - measurement of, in supersonic flames, 376
  - specific impulse method for determination of, 377

  spectral Doppler shift method for determination of, 377ff.
gauges, pressure (see pressure gauges)
Geiger counter, for X-ray measurements, 102
General Motors pressure gauge, 129
geometric optics, use of, in flow analysis, 4
Gladstone-Dale formula, 48, 63
glow discharge, 86
  alternating current, 151
  application to flow studies, 86
  in air, 86
  in nitrogen, 86
  in supersonic flow, 150
  study of turbulence with, 150
  velocity sensitivity in, 148, 150
gradient, density (see also density gradient), 21, 23
gradients, impact tube measurements in, 119
gravity waves, used in hydraulic analogy, 310ff., 317ff.

half width, spectral lines, 348
heat loss of hot wire, 228ff.
  effect of finite wire length on, 239
  equations for, 238, 243ff., 247
  graphic representation of, 42
  in steady incompressible flow, 230ff.
  in steady, supersonic flow, 233ff., 236
  in unsteady flow, 241ff.
  pertinent parameters affecting, 229
  variation in, with Reynolds number, 232, 233
heat transfer, 181ff.
  coefficient of, 182
  design of models for, 183
  in presence of internal temperature gradients, 183
  response time, 184
heating, aerodynamic, 176ff.
high resolution apparatus, 358
high speed motion pictures,
  commercial cameras for, 394
  Edgerton technique, 394
  image dissection type, 395
  optical compensating, 394
  repetitive light source, 394
high speed photography, 393ff.
  Kerr cell, 394
  single exposure, light sources for, 393ff.
H_2O, 482, 502
  infrared emission in flames, 549
H_2O_2, 490
hodograph tank, 335ff.
hot wire method for flame temperature measurements, 368, 369
hot wire probe, 223ff.
  advantage of, 221
  analysis of signals from, 263ff.
  at angle of attack, 240
  calibration, 250ff.
  equilibrium temperature of, 234ff.
  equivalent circuits for lag, 253
  "figure of merit" of, 224
  length correction of, 239
  length-diameter ratio of, 224, 229, 233
  materials for, 223ff.
  mechanical loading of, 223
  multiple wire types of, 227
  operation of, 221
  parameters of, 220, 221
  principle of, 219
  resolution length of, 222
  response of, in two- or three-dimensional flow, 248, 249
  response of, to large fluctuations, 249
  response of, to shock wave, 252
  sensitivity of, 244, 247ff.
  technique for making, 223ff., 225ff.
  temperature loading of, 234ff., 237
  thermal wave propagation along, 252
  time constant of, 243, 245
  transresistance of, 246
  using constant temperature negative feedback operation, 256
  wire length corrections for, 274ff.
  with "poor man's" compensation, 259ff. (see also compensation, correlation, heat loss, and information analysis)
hot wire temperature (see hot wire probe)
hydraulic analogue, 309ff.
  applied to supersonic diffuser, 319
  appraisal of, 320
  choice of water height, 313
  for shocks, 316, 319ff.
  of viscosity and heat conduction, 315
  ratio of specific heats in, 314ff.
  role of surface tension in, 317
  techniques for, 311ff.
  validity of, 314ff.
  wave propagation in, 317ff.
hydrocarbon bands, 486
hydrocarbon flame, 485
hydrogen, discharge in, 518, 519
hydrogen atoms, influence of, on burning velocity, 553ff., 558

illuminated particle track method, 411
impact pressure, 111
impact tube, 111
  alignment tolerances in transverse velocity gradients of, 119
  effect of turbulence on, 120
  relaxation effects with, 118
  response time of, 122
  shock wave formation at, 116

- stagnation point of, 111ff.
- theory of use of, in free molecule flow, 120ff.
- viscous corrections for use of, in compressible flow, 116, 117
- viscous corrections for use of, in incompressible flow, 113ff.
- viscous corrections for use of, in slip flow, 116–118

impurities, effect on appearance of afterglow, 81 (see also afterglow)
incoherent scattering, 294
index of refraction,
  - change in, across shock, 204
  - determination of, 10ff., 20, 21

indicators of explosion pressure, 426ff.
inert gases, effect of, on burning velocity, 430
information analysis,
  - for energy spectrum, 268
  - for shear correlation, 265ff.
  - for time correlation, 266, 268
  - for triple correlation, 266ff.
  - for velocity temperature correlation, 266
  - of hot wire signals, 263ff.
  - of two signals, 264ff.

infrared,
  - lead sulfide receptors for, 170, 171
  - pyrometer, 171
  - technique, 481
  - temperature measurement by, 170ff.

instrumentation,
  - electrolytic plotting tank, 325, 326
  - for acoustic anemometry, 152ff.
  - for condensation studies, 303, 304
  - for glow discharge measurements, 149
  - for heat transfer studies, 183
  - for infrared pyrometry, 171ff.
  - for light screen measurements, 162
  - for projection thermography, 176
  - for shock thickness measurements, 205
  - for tracer measurements, 140–145
  - for X-ray absorption measurements, 100ff.
  - free surface water table, 311ff.
  - hot wire, 223ff., 250, 253, 257–262, 270
  - shielded thermocouple, 190ff.
  - spectral absorption, 91ff.

intensity distribution, 346
intensity measurements,
  - accuracy of, 478
  - photoelectric, 478

interference,
  - light, 47
  - use in pressure gauge, 128

interference pattern, optical, 378, 380, 383
interferograms,
  - of axially symmetric flows, 12
  - of two-dimensional flows, 10
  - reduction of, 8ff.

interferometer, 468, 488, 489
  - Erdmann (phase contrast), 60
  - Fabry-Perot, 355, 378, 396
  - Jamin, 48
  - Kraushaar (diffraction grating), 60
  - Mach-Zehnder, 6, 48ff., 397, 398 (see also Mach-Zehnder interferometer)
  - Michelson, 48

interferometry,
  - applications of,
    - to channel flow, 61, 72
    - to free flight studies, 61, 73ff.
    - to jets, 69
    - to shock tube, 61, 75
    - to wind tunnels, 61, 73
  - density determination by, 61ff.
  - errors in (see errors in density determination)
  - examination of flames by, 398
  - for turbulence measurements, 282
  - observation of gas mixing by, 398
  - precision or sensitivity of, 64ff.
  - principles of, 396
  - results of, compared with manometric readings, 73
  - schlieren combined with, 398

inverted flames, burning velocities from, 420ff.
ion detection in mass spectrometry, 447ff.
ion production for mass spectrometry, 447ff.
ion tracers, 139ff.
  - methods of production, 140
  - temperature measurements by, 199
  - velocity measurements by, 139ff.

ionization, 500
  - potentials, 452
  - probability, 451
  - processes in mass spectrometers, 447–449

ionization chamber for X-ray measurements, 102
iron lines, 498, 499, 518
isentropic flow, interferometric evaluations of, 63, 64
isointensity methods, 506ff.
isopycnal, 62
isotope dilution method in mass spectrometry, 456

jets,
  - freely expanding analysis of, by schlieren photography, 401

  studied by interferometry, 69ff. (see also interferometry, applications of)
  studied with hodograph tank, 336

Kármán vortex street, 241
Kerr cell as light shutter, 42
King's law, theory of, 230ff.
Kirchhoff's radiation law, 344, 346
kurtosis of probability density, 273
Kutta-Joukowski rule, in electric analogy, 327ff., 335

laminar burning velocity, 409ff.
lamp, tungsten ribbon, 346ff., 359ff.
lead sulfide cells, 170ff., 481
  response time of, 171
  spectral sensitivity of, 171
  temperature range of, 172, 173
lift problems in electric analogy, 332, 333
light path (see optical path)
light reflection from a shock front, 204ff.
light scattering (see scattered light)
light screen technique, 159ff.
  accuracy of, 163
  instrumentation for, 162
  reflection type, 161
  schlieren type, 159, 160
light source,
  for Mach-Zehnder interferometer (see Mach-Zehnder interferometer)
  for vacuum ultraviolet, 91, 92
  short duration, 41
light yield of C_2 spectrum, 544–548
line reversal temperature measurement, anomalies in, 542–544
line width, 487–490
luminous tracer particles, 142ff.
  injection of, 143
  observation of, 143
  rotating mirror technique for measurement of, 144, 145

Mach angle measurements, 37, 40
Mach meter, acoustic, 152ff.
Mach number, 365–368
  as parameter in hot wire theory, 229, 234ff.
  measured by spectral absorption, 94
Mach-Zehnder interferometer, 6, 48, 397
  adjustment of, 58ff., 397, 398
  angle of incidence of light of, 54
  basic principle of operation of, 6ff.
  dimensions of, 56
  fringes, location of, 55
  geometry of, 49, 54ff.
  mechanical features of, 58
  modifications of, 60
  optical arrangement of, 54
  properties of optical elements of, 56ff.
  required properties of the light source of, 51ff.
  theory of ideal, 49ff.
  with single plate control, 56
manometers, 125ff. (see also pressure gauges)
mass analyzers, time-of-flight, 445, 446
mass spectrometer,
  cyclotron resonance, 445
  Dempster, 442, 443
  for analysis, 442–446
  for monitoring, 454, 455
  Nier, 443ff.
  nonmagnetic, 445
  180° deflection, 443
mass spectrometer analysis,
  discrimination in, 453
  ionization processes in, 447–449
  special requirements for, 453
mass spectrometry,
  cracking patterns in, 447
  detection of short-lived intermediates by, 457
  flame studies in, 458–462
  for ion production, 447
  in ion detection, 447
  ion sources in, 442, 443
  isotope dilution method in, 456
  monitoring by, 454, 455
  precision of, 444
mass spectroscopy,
  history of, 441
  reaction kinetics by, 456–458
mass spectrum,
  of methane-oxygen flame, 461
  of petroleum product, 454
measurement of burning velocity, 409–438
mercury vapor, spectral absorption by, 93ff.
methane, ions from, 447ff.
methane-oxygen flame, mass spectrum, 461
microscale,
  of turbulence, 220, 270, 271, 282
  relation to spectrum, 270
MIT temperature probe, 191
mixture ratio, effect on burning velocity, 429
moisture, effects on flame speed, 415–417, 423, 431, 433ff.
molecular collisions, in shock front, 210
momentum loss in flame, 416
monitoring by mass spectrometry, 454, 455
monochromators, 479, 481
moving flames,
  burning velocities from, 422–428
  location of,
    by fusible wires, 411

        by ionization gaps, 411
        by photocells, 411, 423
    position of, 410, 411
moving plate, 522

negative feedback, hot wire circuit, 246, 247
nitrogen,
    afterglow spectrum, 80
    glow discharge in, 86
    heat of dissociation in, 80
nitrogen-carbon monoxide mass ratio, 444
noise level in hot wire amplifiers, 258ff.
nonequilibrium conditions, 514–522
nonlinearity in hot wire response, 248ff.
normal burning velocity, 409
nozzle,
    coefficient of, 370
    design, test of, 23
    sluice, 311
nozzle-type Bunsen burners, 418, 419
Nusselt number, for hot wire probe, 229ff.

O_2, bands, 485, 486
OH, 483ff., 489ff., 499–502, 508–511, 516–518
    concentration in low-pressure and diffusion flames, 550–552
    rotational temperature of, 534–537, 563
    vibrational temperature of, 541
optical density wedge, rotating spiral disk, 355, 356
optical depth, flames, 348
optical methods,
    comparison of, 23, 24
    error sources in, 11, 17ff.
    for study of turbulence, 277ff.
    of flow analysis, 3ff.
optical path
    first order equations of, 9
    in homogeneous medium, 8ff.
    in interferometric systems, 10ff.
    in schlieren systems, 10ff.
    in shadow systems, 20ff.
optical system for shock reflectivity measurements, 205
oscilloscope, 360, 361, 363
oxygen, spectral absorption by, 90ff.
ozone, 490
    spectral absorption by, 92, 93

particle track method, 411
path difference, 49, 50
    compensation for, 10, 54
periscope for rocket exhaust observation, 379, 380
phosphorescence,
    efficiency of, 175
    materials exhibiting, 175
    response time of, 175
    sensitivity of, 174
    temperature-sensitive, 173
photoconductive cells, 474, 475, 481
photoelectric,
    intensity measurements, 478
    pyrometer, 359ff.
photographic emulsions, 474
    hypersensitization of, 395
    latensification with, 395
photographic methods,
    comparison of, 404
    used with water table, 313
photography,
    detection of free radicals by, 389, 391
    of detonation in piston engines, 394, 395
    of flames, coloring for, 392, 393
    of fuel beds, 393
    spark, 374–376
    through filters, 389–392
photomultiplier tubes, 474ff.
phototubes,
    cooling of, 476, 478
    dark current of, 476ff.
piezoelectric crystal, 376
piezoelectric pressure gauge, 130
    frequency response of, 132
    materials for, 132, 133
    pyroelectric effect in, 131
    sensitivity of, 131
Pitot tube formula, 111, 112
plane flames, burning velocities from, 420ff.
plane of centers, 49
"poor man's" compensation, 259ff.
Prandtl number, as parameter in hot wire theory, 229, 231, 234
Pratt and Whitney temperature probe, 192
precision of the interferometric method, 64ff.
predissociation, 512
    of OH in flame, 536, 537
pressure,
    change across a flame, 413
    effect on burning velocity, 430
    indicators, 426, 427
    shift of wavelength of spectral lines, 383ff.
    spectroscopy, 527–566
pressure gauges, 124ff.
    Bendix, 129
    Bourdon tube, 129
    Buck and Barkas, 128
    crusher, 133, 134
    elastic diaphragm type, 127, 128
    frequency response of, 124ff.
    General Motors, 129

  indentor, 133, 134
  mechanical, 133, 134
  pertinent characteristics of, 124ff.
  piezoelectric (quartz crystal) type, 130ff.
  use of optical interference in, 128, 129
  use of pyroelectric effect in, 131, 132
  Wiancko, 129
probability functions, 271ff.
  joint probability density, 274
  kurtosis, 273
  skewness, 273
probe,
  hot wire (see hot wire probe)
  temperature (see temperature probe)
  used in electrolytic plotting tank, 325
profile, temperature, of flame, 532, 533
pyrometer,
  infrared, 171
  photoelectric, 359ff.
pyrometry, two-color, 361ff.

radiation losses, thermocouple, 365
radicals,
  concentration in flames, 544–553
  formation in flames, 564, 565
  influence on burning velocity, 528, 560
  temperatures of, 534–542
ratio recording, 478
Rayleigh formula for light scattering, 292
ray tracing, use in optical analysis, 22
reaction kinetics by mass spectroscopy, 456–458
reaction zones in flames,
  detection by smoke, 403
  pressure-thickness relation of, 530
  structure of, 532, 533
recovery factor, 177ff., 187, 367 (see also recovery temperature)
recovery temperature, 177ff.
  dependence on surface roughness, 180
  dependence on turbulence, 181
  factor, 177, 187
  factors influencing, 177, 178, 180, 181
  for laminar boundary layer, 177, 178
  for turbulent boundary layer, 177, 178
  measurement of, 177–179
"reds," 301
reflectivity of shock front, 203ff.
  limitations on measurement of, 206
  measuring technique for, 205ff.
  scaling law of, 206
  theory of, 204
refraction,
  error, 67, 68
  error due to neglect of, 6
  hypothesis of infinitesimal, 5
  index of, 47
relaxation,
  effect on shock front thickness, 209
  effects in impact tube measurements, 118
reservoir pressure, 111, 112
residual colors, relation to condensation particle size, 298
resistance fluctuations,
  of hot wire, 244ff.
  thermometer for determination of, 196
resolving power, spectroscopic, 348, 355
response time, 519
  of pneumatic thermometer, 371
Reynolds number of hot wire probes, 232, 233
rocket exhaust velocity, shock angle measurement of, 381, 382
rotating mirror,
  optical studies with, 42
  use in interferometry (see interferometry, application of)
rotating sector, 478
rotational relaxation in nitrogen, 208ff.
rotational temperature,
  influence of, on self-absorption, 563
  of C_2, 537
  of CH, 537ff., 565
  of CN, 541
  of OH, 534–537, 563

scaling in electric analogy, 323
scanning of spectrum, 479ff.
scattered light, 290ff.
  dissymmetry of, 299
  incoherent, 294
  intensity of, 290, 299
  measurements in hypersonic flow, 303
  modes of, 292, 293
  polar diagrams for, 292
  polarization of, 300
  Rayleigh's formula for, 292
scattering coefficient, X ray, 98
schlieren light screen, 159ff.
schlieren records,
  analysis of, 10
  in axially symmetric flows, 17
  in two-dimensional flows, 10, 11
  of shock waves, 18
  reduction of, 17
  relative brightness of, 7, 10
schlieren system,
  compared with shadow, 43
  diffraction effects in, 35
  edge, 7
  effect of orientation of knife edge in, 400
  examples of, 27, 29, 32
  flame position by, 411
  inclined slit type, 33

  light path representation in, 10
  location of image plane by, 400
  principle of, 7, 28, 399, 400
  quality of components of, 30
  quantitative techniques by, 376, 401
  Ronchi, 35
  sensitivity of, 28, 32, 35, 36
  sharp focusing, 34
  size of image, 401
  stop, 8
  typical arrangements for, 399
Schumann-Runge bands, 485
scintillation counter for X-ray measurements, 103
self-absorption, 490, 491, 499, 500, 505, 506, 508
  influence of, on rotational temperature, 563
sensitivity,
  of hot wire method, 244, 247ff.
  of interferometric method, 64ff.
sensitivity calibration in spectra, 478
shadow systems, 4ff., 38ff., 401, 402
  analysis of, 20ff.
  applications of, 40
  capabilities of, 40
  compared with schlieren, 43
  description of, 38ff.
  detection of shock waves by, 402
  for transient phenomena, 41
  for turbulence measurements, 217, 218, 277ff.
  schlieren combined with, 102
shape factor in spectral lines, 348
shear correlation, 265, 266
shear spectrum, 271
shields, thermocouple with, 365
shock angle, 381, 382
shock front, 203ff.
  density change across, 204
  in supersonic flames, 382
  light reflection from, 204
  molecular collisions in, 210
  production of, 205, 206
  refractive index change across, 204
  rotational relaxation at, 209
  shape of, 204
  thickness in argon, 207
  thickness in nitrogen, 207
shock tube,
  acoustic anemometry with, 153
  interferometry with, 75 (see also interferometry, applications of)
  light screen technique for, 159ff.
  used for hot wire transient response, 252
shock waves,
  density evaluation errors, 19, 65, 68
  detection by shadow photography, 402
  hydraulic analogue for, 316, 319
  interferograms of, 19
  measurement of velocity of, 160
  on impact tube, 116
  photography of, by afterglow, 85
  schlieren records of, 11
  shadowgraphs of, 21
  speed measurements of, 159
short-lived intermediates, detection of, by mass spectrometry, 457
skewness of probability density, 273
slope-o-meter, 298
soap bubble method, 423–426
sodium,
  method of adding to flames, 392
  optically active, 378
sodium D lines, 346, 347
sodium line reversal, 346
  high resolutions method for determination of, 354ff.
sodium vapor, 349
  lamp, 355, 358
solids in flames, effect on combustion process of, 403, 404
Sonic True Air Speed and Mach Number Indicator (STAMNI), 155ff.
  transit time, 155, 157
  two receiver type, 156
spark photography, 374–376
spectral absorption, 89ff.
  coefficient of, 89, 90, 92, 94
  dependence of, on pressure, 94
  dependence of, on temperature, 94, 95
  determination of density by, 89, 91, 93
  determination of Mach number by, 94
  instrumentation for, 91, 92, 95
  of air, 89
  of mercury vapor, 93ff.
  of oxygen, 90, 91
  of ozone, 92, 93
spectral line,
  half width, 348, 349
  resonance, 377
  reversal, 345
spectral line contour, 349, 361, 379
spectrographs, 468, 472ff.
  dispersion of, 472
  speed of, 473
spectroscopy,
  filter, 468ff.
  pressure effects and, 527–566
spectrum, continuous, 362
  light yield of C_2, 544–548
  of interferometer light source (see Mach-Zehnder interferometer)
  scanning of, 479, 481
spherical bomb with central ignition, 426–428

stability limits, low pressure burner, 529, 530
stagnation temperature, 187
STAMNI (see Sonic True Air Speed and Mach Number Indicator)
static pressure, 111
static temperature, 186
stationary flames, burning velocities from, 412–422
statistical fluctuations in spectra, 475, 476
Stieltjes integrator, use of, in evaluation of interferograms, 13
streak photography, 395
stream function, electric analogy for, 324
stroboscopically-illuminated particles, 419
Strouhal number, 241
structure of combustion wave, 410, 411
supersonic diffuser, hydraulic analogue data for, 319
surface temperature measurement, 167ff.
  by infrared, 170, 171
  by phosphorescence, 173ff. (see also temperature measurement)
  by thermocouples, 169, 170
  of fast-moving objects, 171–173
  principles of, 167, 168
Swan bands, 484, 485

tank,
  electrolytic plotting, 324–326
  hodograph, 335, 336
temperature, 491ff.
  accuracy of spectroscopic measurement of, 494, 496, 497, 510
  apparent black body, 362
  effect on burning velocity, 429
  effective, flames of complex structure, 352
  electronic, 498–500
  flame, 345
  inner zone, 352
  monochromatic color, 362
  rotational, 500–514, 534–538, 562, 563
  static, 365
  translational, 497, 498, 538
  vibrational, 500, 541, 542, 563
temperature fluctuations, 244ff.
temperature loading of hot wire, 237, 243
temperature measurement,
  by ions, 199, 200
  by STAMNI, 198, 200 (see also surface temperature measurement)
  by ultrasonic waves, 199
  in moving fluid, 186, 187
  thermocouple probes for, 186ff.
  with resistance thermometer, 196
  with vortex thermometer, 196
temperature probe, 187
  conduction error of, 188, 189
  design of, 188ff.
  diffuser type, 191
  for boundary studies, 195
  for engine superchargers, 190
  for gas turbines, 190
  for high temperature range, 193
  general requirements, 187, 188
  high velocity type, 190, 191, 194, 195
  MIT type, 191
  of small dimensions, 195
  Pratt and Whitney type, 192
  radiation error of, 189
  sensitivity of, 192, 193
  short lag type, 195
temperature-velocity correlation, 266
thermal lag of hot wire, 245
thermocouple measurements on flames, 531–533
thermocouples,
  for flame temperature measurements, 364
  for mean square fluctuations, 262
  in high velocity gas streams, 366
  probe type (see temperature probe)
  radiation losses, 365
  surface type, 169
thermography,
  contact, 175
  projection, 176
thermometry (see surface temperature measurement, temperature measurement, temperature probe)
thickness of shock front, 204, 207
time constant, 519
  calibration of, 250ff. (see also hot wire probes)
  hot wire, 242ff.
time correlation, 266
time-of-flight mass analyzers, 445, 446
total temperature, 186
Townsend discharge, 147
tracers, 139ff.
  ion, 139, 140
  luminous, 142ff.
  thermal, 145
transconductance of hot wire amplifier, 246
transformer compensation of hot wire, 253, 259
transition,
  detection of, 214–217
  in boundary layer, 215–217
transition probabilities, 495
  rotational lines, 538, 541, 562
  vibrational lines, 541
transmission factor, 348ff.

transmitted light,
  diffraction ring formation by, 298
  for study of small particles, 295
transverse contamination, 214, 217
triple correlation, 266
  circuit for, 267
tubular Bunsen burners, 413ff.
turbidity of a scattering medium, 296
turbulence measurements, classification of, 214
turbulent flow,
  averaging processes for, 220, 272
  box type, 220
  correlations, 264, 265, 280, 281 (see also correlation)
  energy spectrum, 268, 269, 279
  measurement of, by glow discharge, 150
  measurement of, by shadow methods, 278ff.
  microscale, 220, 270, 282
  shear spectrum, 271 (see also heat loss, hot wire probes, information analysis)
"2f" lens system, 379
Tyndall spectra of higher order, 301

ultraviolet absorption (see spectral absorption)
unburned gas,
  direction of flow, 411
  velocity pattern in, 411

velocity, burning, 409ff.
  distribution above nozzles, 419
  distribution above tubes, 417
velocity fluctuations, 243
  in supersonic flow, 247
  large, 248, 249
velocity gradient parameter, 114
velocity measurement, 139ff.
  by acoustic anemometry, 152ff.
  by corona discharge, 147, 148
  by glow discharge, 148ff.
  by ionization, 139ff.
  by light screen technique, 159ff.
  by luminous particles, 142ff.
  by Townsend discharge, 147, 148
  with rotating mirror, 144, 145
velocity potential, analogy for, 322, 323
velocity profile, turbulent, 215, 216
vibrational temperature
  of CH, 538
  of CN, 541
V meter, 227
voltage fluctuations of hot wire, 244ff.
vortex thermometer, 196
vorticity meter, 227
  response of, 228

wall temperature (see surface temperature)
water surface, analogue flow equations using, 310
waves,
  hydraulic analogue of propagation of, 317, 318
  on free water surface, 312
  shock (see shock waves)
Wiancko pressure gauge, 129
Wien's radiation law, 344, 345, 359, 361, 362
wind tunnel, use of interferometer with, 73 (see also interferometry, applications of)

X meter, 227
X-ray absorption, 97
  apparatus for, 100ff.
  coefficient of, 97, 98
  measurement time of, 100
  measurements of boundary layers with, 103
  receiving instruments for, 102
  relative error in density measurements of, 98, 99
  tubes for intensity measurements of, 102, 103
  wavelength range of, for air density measurements, 100

zones, flame, 347ff.

3-5-55

CENTRAL SCIENCE LIBRARY

3 1262 04012 6871

629.1323
H629
v. 9

ENGINEERING
SCIENCES
LIBRARY